

JAERI - M
85-213

DEPARTMENT OF CHEMISTRY

PROGRESS REPORT

(January 1984 - December 1985)

February 1986

Department of Chemistry

日 本 原 子 力 研 究 所
Japan Atomic Energy Research Institute

JAERI-Mレポートは、日本原子力研究所が不定期に公刊している研究報告書です。
入手の問い合わせは、日本原子力研究所技術情報部情報資料課（〒319-11茨城県那珂郡東海村）あて、お申しこしください。なお、このほかに財団法人原子力弘済会資料センター（〒319-11茨城県那珂郡東海村日本原子力研究所内）で複写による実費頒布をおこなっております。

JAERI-M reports are issued irregularly.

Inquiries about availability of the reports should be addressed to Information Division
Department of Technical Information, Japan Atomic Energy Research Institute, Tokai-mura, Naka-gun, Ibaraki-ken 319-11, Japan.

©Japan Atomic Energy Research Institute, 1986

編集兼発行 日本原子力研究所
印刷 いばらき印刷(株)

Department of Chemistry
Progress Report
(January 1984 - December 1985)

Department of Chemistry
Tokai Research Establishment, JAERI

(Received December 12, 1985)

Described are the research activities in the Department of Chemistry during the last 2 years and publications from 1981 to 1985. The activity was mainly focused on the basic researches for further development of the nuclear fuels and materials, for establishing the nuclear fuel cycles, and for obtaining basic data for the environmental safety. Intensive effort was also paid to service analysis of various fuels and materials.

Keywords: Progress Report, Fuels, Nuclear Materials, Environmental Safety, Basic Research, Radionuclides

Board of Editor for Progress Report
E. Tachikawa (Chief Editor), T.A. Sasaki (Associate Chief Editor),
S. Ohno, K. Ohwada, M. Saeki, N. Shinohara, A. Nakamura, K. Watanabe

化学部プログレスレポート
(1984年1月-1985年12月)

日本原子力研究所東海研究所
化 学 部

(1985年12月12日受理)

化学部における最近2年間の研究活動に重点をおいてまとめた。研究内容は主として核燃料・材料の開発、核燃料サイクルの確立、環境安全に資するための基礎研究である。他に所内外からの、種々材料および燃料についての依頼測定にもこたえている。

化学部プログレスレポート編集委員会

立川圓造(委員長), 佐々木貞吉(副委員長), 大野新一, 大和田謙, 佐伯正克, 篠原伸夫, 中村彰夫,
渡部和男

CONTENTS

FOREWORD	1
1. ANALYTICAL CHEMICAL STUDIES ON NUCLEAR FUELS AND REACTOR MATERIALS	3
1.1 Studies on Ion-exchange Separation Using HF-H ₃ BO ₃ Media	3
1.2 Studies on the Determination of Hydrogen and Sulfur by Isotope Dilution Mass Spectrometry ...	12
1.3 Determination of Gaseous Elements in Reactor Materials	22
1.4 Analytical Chemical Studies of Plutonium and Uranium	27
1.5 Studies on Atomic Spectroscopy	37
1.6 Studies on Faradaic Ion Transfer across the Interface of Two Immiscible Electrolyte Solutions and Potential-generating Process at an Ion-selective Electrode	48
1.7 Determination of Boron in Boronated Graphite Pellets by Mass-spectrometric Isotope Dilution and Acid-base Titrimetry	55
1.8 Mass-spectrometric Isotope Dilution Analysis of Boron in Highly-irradiated U-Al-B Alloy Fuel Elements	56
1.9 Other Activities	58

2. PREPARATION, ANALYSIS AND CERTIFICATION OF	
REFERENCE MATERIALS	61
2.1 Reference Materials of Zirconium and Its	
Alloys, JAERI-Z11 to -Z16	61
2.2 Certification of JAERI-Z17 and -Z18 for Carbon ..	79
2.3 Preparation, Analysis and Certification of	
a Uranium Isotope Certified Reference Material	
JAERI-U5	80
2.4 Evaluation and Perspective of Measurement	
Techniques for Uranium Isotopic Assay in	
Nuclear Fuel Cycle	82
3. ANALYTICAL CHEMICAL SERVICE AND SCIENTIFIC	
GLASSBLOWING UTILIZATION	83
3.1 Service Analysis	83
3.2 Glassblowing	86
4. RADIOCHEMICAL STUDIES OF NUCLEAR FUELS	89
4.1 Separation and Determination of Neptunium,	
Plutonium and Americium of Tracer Levels	89
4.2 Acid Digestion of Combustible Wastes	
Containing Plutonium	95
5. RADIOCHEMICAL STUDIES OF TRITIUM	103
5.1 Chemical Interaction of Tritium with Materials ..	103
5.2 Sorption and Desorption Behavior of Tritium	
on Material Surfaces	114
5.3 Removal of Tritium by Various Solid Adsorbents ..	123

6. CRUD BEHAVIOR AND CHEMICAL DECONTAMINATION FOR NUCLEAR REACTOR	132
6.1 Corrosion Behavior of SUS-304 in High Temperature Water	132
6.2 Measurement of Specific Activities of ^{55}Fe and ^{63}Ni in CRUD	140
6.3 Development of Chemical Decontamination Process with Sulfuric Acid-cerium(IV) for Decommissioning	149
7. SOLID-STATE CHEMISTRY OF RADIATION DAMAGE	158
7.1 Chemical Reactions Induced by Low-energy Ions ..	158
7.2 Surface Chemical Changes of Refractory Materials by Hydrogen Bombardments	168
7.3 Lattice Defects and Structural Changes in Ion-irradiated Metals and Ceramics	178
8. SERVICE WITH Co-60 IRRADIATION FACILITY AND ANALYTICAL EQUIPMENTS	187
8.1 Irradiation Service	187
8.2 Analytical Service	188
9. THERMODYNAMIC STUDY OF NUCLEAR FUEL	195
9.1 The Nature of Small Polarons and the Oxygen Potential in Nonstoichiometric Uranium Oxides ..	195
9.2 On the Nonstoichiometry, Point Defects and Fe^{2+} - Mg^{2+} Interdiffusion in Olivine	203

9.3	Phase Relations and Thermodynamics of Ternary Uranium Oxides	215
9.4	Magnetic Susceptibilities of UO_2 - ThO_2 Solid Solutions	232
10.	SOLIDIFICATION OF HIGH-LEVEL RADIOACTIVE WASTE INTO SYNTHETIC MINERAL-LIKE COMPOUNDS	245
10.1	Phase Study	245
11.	NUCLEAR CHEMISTRY RESEARCH	256
11.1	Measurements on Burnup Characteristics of the Japan Power Demonstration Reactor-I Full-core Fuel Assemblies	256
11.2	Experiments of Nuclides far from β -stability by JAERI ISOL	265
11.3	Actinides Synthesized by Heavy-ion Nuclear Reaction	271
11.4	Isotope Correlation Techniques for Verifying Input Accountability Measurements at a Reprocessing Plant	276
11.5	Measurements and Evaluation of Gamma-ray Intensities of ^{239}Pu	282
12.	DEVELOPMENT OF RADIOCHEMICAL ANALYSIS METHODS	288
12.1	Rapid Ion Exchange Separation of Transplutonium Elements	288
12.2	Electrodeposition of Actinides	293

12.3	Analysis of Biological Shielding Concrete of JPDR	296
13.	SOLUTION CHEMISTRY OF RADIOACTIVE ELEMENTS	301
13.1	On the Particle Size Distribution of Hydrolyzed Plutonium(IV) Polymer	301
13.2	Solution Chemistry of Ruthenium	308
14.	ANALYTICAL SERVICES FOR IRRADIATED FUELS	311
14.1	Burnup Measurements of Spent Fuel from Power Reactors	311
14.2	Measurements of Absolute Fission Number of NSRR Test Fuels	315
15.	STUDIES ON FIXATION OF VOLATILE RADIONUCLIDES	319
15.1	Application of Silver-free Zeolites to Remove Iodine from the Dissolver Off-gas	319
15.2	Interaction of RuO_4 with Metal Surfaces	329
16.	STUDIES OF TRITIUM SEPARATION BY ISOTOPICALLY SELECTIVE LASER EXCITATION OF MOLECULES	340
16.1	Development of Laser for Isotope Separation	340
16.2	Hydrogen Isotope (tritium) Separation Using Selective IR Multiple-photon Dissociation	349
17.	STUDIES OF FLUORINE COMPOUNDS	357
17.1	UV Effect on Etching of Fission Tracks in Polyvinylidene Fluoride Film	357

17.2	Study on Direct Fluorination of Polymers	366
17.3	The Application of an Effective Nuclear Charge Model to the Prediction of Valence Force Constants in Uranyl Tetrachloride and Pentafluoride Complexes	370

目 次

序 論	1
1. 核燃料・炉材料等の分析化学的研究	3
1.1 フッ化水素酸－ホウ酸系イオン交換分離法の研究	3
1.2 同位体希釈質量分析法による水素及びイオウの定量に関する研究	12
1.3 炉材料中のガス成分の定量	22
1.4 プルトニウム，ウランの分析化学的研究	27
1.5 原子スペクトル分析法の研究	37
1.6 異種溶液界面におけるイオン移動反応及びイオン選択性電極での電位発生機構 の研究	48
1.7 ホウ素添加黒鉛ペレット中ホウ素の定量	55
1.8 同位体希釈質量分析法による高燃焼ウラン－アルミニウム－ホウ素合金燃料要 素中ホウ素の定量	56
1.9 その他の研究活動	58
2. 標準試料の製作，分析及び表示値決定	61
2.1 ジルコニウム，ジルコニウム合金標準試料 JAERI-Z 11 ～ Z 16	61
2.2 JAERI-Z 17 及び Z 18 の炭素の表示値決定	79
2.3 濃縮度測定用ウラン同位体標準試料 JAERI-U5 の製作，分析及び表示値決定	80
2.4 ウラン濃縮度測定技術の現状－核燃料サイクルにおける対象と課題	82
3. 分析サービスとガラス工作	83
3.1 依頼分析	83
3.2 ガラス工作	86
4. 核燃料の放射化学的研究	89
4.1 微量の Np, Pu, Am の相互分離と定量	89
4.2 プルトニウムを含む可燃性廃棄物の湿式処理	95
5. トリチウムの放射化学的研究	103
5.1 材料中でのトリチウムの化学的挙動	103
5.2 材料表面におけるトリチウムの収着と脱離	114
5.3 固体吸着剤によるトリチウムの捕集	123
6. クラッド及び原子炉除染の化学	132

6.1	SUS-304の腐食と水中クラッドの挙動	132
6.2	クラッド中の ^{55}Fe と ^{63}Ni の比放射能測定	140
6.3	硫酸セリウム(V)系化学除染法の開発	149
7.	放射線損傷の固体化学的研究	158
7.1	低エネルギーイオン衝撃による化学反応	158
7.2	水素イオン衝撃による耐熱性材料の表面化学変化	168
7.3	金属及びセラミックスにおけるイオン照射欠陥	178
8.	Co-60照射室の運営並びに電顕等分析業務	187
8.1	Co-60照射室の運営	187
8.2	電顕等分析業務	188
9.	燃料の熱力学的研究	195
9.1	非化学量論性ウラン酸化物の酸素ポテンシャルとスモールポーラロンの性質	195
9.2	オリビンのノンストイキオメトリ、点欠陥及び Fe^{2+} - Mg^{2+} 相互拡散	203
9.3	三元系ウラン酸化物の熱力学	215
9.4	UO_2 - ThO_2 固溶体の磁気的性質	232
10.	高レベル廃棄物の合成鉱物化	245
10.1	相平衡状態の検討	245
11.	燃焼率測定に関連する核化学的研究	256
11.1	JPDR使用済燃料の全炉心測定	256
11.2	ISOLによる β 安定領域から離れた核種の測定	265
11.3	重イオン核反応により生成するアクチノイド	271
11.4	再処理インプット溶液測定データ検証のための同位体相関技術	276
11.5	プルトニウム-239の γ 線放出率測定	282
12.	放射化学分析法の研究	288
12.1	超プルトニウム元素の迅速イオン交換分離	288
12.2	アクチノイドの電着	293
12.3	JPDR生体遮蔽(コンクリート)の分析	296
13.	放射性物質の溶液化学的研究	301
13.1	プルトニウム加水分解重合体の粒度分布	301
13.2	ルテニウムの溶液化学	308

14. 使用済燃料の依頼分析	311
14.1 動力炉使用済燃料の燃焼率測定	311
14.2 NSRR 試験照射燃料の絶対核分裂数測定	315
15. 揮発性放射性核種の固定化の研究	319
15.1 銀を含まないゼオライトによる溶解工程オフガス中のヨウ素の除去	319
15.2 四酸化ルテニウムと金属表面の相互作用	329
16. 励起法によるトリチウム分離の化学的研究	340
16.1 同位体分離用レーザーの開発	340
16.2 赤外多光子解離を用いた水素同位体（トリチウム）分離	349
17. フッ素化合物の物理化学的研究	357
17.1 FF 照射ポリフッ化ビニリデン膜の化学エッチング時の UV 照射効果	357
17.2 ポリマーの直接フッ素化に関する研究	366
17.3 有効核電荷モデルの応用——四塩化ウラニル及び五フッ化ウラニル錯塩の力の定数の推定	370

FOREWORD

The Department of Chemistry consists of six laboratories which are listed in the following; their research subjects and total number of researchers and technicians engaged in (at the time of April, 1985) are also listed.

- Analytical Chemistry Laboratory : Analytical chemistry of nuclear fuels and reactor materials. (11 and 13).
- Radiochemistry Laboratory : Reactor chemistry of radioactive nuclides. (10 and 3).
- Solid State Chemistry Laboratory : Solid state chemistry of radiation damage. (5 and 5).
- Nuclear Fuel Chemistry Laboratory : High temperature chemistry of nuclear fuels. (6 and 1).
- Nuclear Chemistry Laboratory : Development of burn-up measurement. (6 and 7).
- Physical Chemistry Laboratory : Physical chemistry of volatile radioactive nuclides. (6 and 3).

Regarding nuclear fuels and materials, progresses are being made steadily in the field of thermodynamics of uranium oxides in binary and in ternary phases, and in mutual separation of Np, Pu, and Am. Advanced are the technologies of the nuclear safeguard and on-line analytical measurements of nuclear fuel materials. Various techniques are developed for quantitative measurements of trace amounts of elements in reactor materials such as zircalloys, hastelloy-X, and other heat-resisting alloys. Intensive efforts have also been paid to the studies of the radiation damage of various materials.

Within the framework of the studies on the environmental safety, extensive experiments have been done on the following subjects: i) release behaviors of volatile radioactive nuclides such as iodine and tritium from nuclear fuels, ii) laser isotope separation of tritium from waste solutions, iii) physical and chemical interactions of tritium with materials. Tritium decontamination of stainless steel is one of the concerns.

Service work in the Department included chemical analyses and electron microscopic measurements of nuclear fuels and reactor materials, burn-up measurements, ^{60}Co gamma-ray irradiation, and glassblowing. The work sometimes needed not only the special techniques but also design

and construction of special equipments and/or apparatus.

The Department is contributing to the JPDR Decommissioning Project, since 1981, particularly in the development of decontamination technology.

Kaoru UENO
Director,
Department of Chemistry

1. ANALYTICAL CHEMICAL STUDIES ON NUCLEAR FUELS AND REACTOR MATERIALS

T.Adachi, H.Aoyagi, Y.Baba, H.Fukushima, K.Gunji,
H.Hashitani*, A.Hoshino, S.Iso, M.Ito, K.Izawa*,
K.Kato, S.Kihara*, T.Komori, H.Muto, T.Nakajima*,
M.Ouchi, K.Takashima, H.Takeishi, K.Tamura,
S.Tamura, Y.Toida, K.Watanabe, C.Yonezawa* and
Z.Yoshida

1.1 Studies on Ion-exchange Separation Using HF-H₃BO₃ Media

The anion-exchange in HF-HCl or HF-HNO₃ solutions has been widely used for the separation of metals. In the absence of hydrochloric or nitric acid, separation can be done to only two groups, i.e., metals which form stable fluoride complexes and others. The presence of Cl⁻ or NO₃⁻ is believed to be effective in differentiating the adsorbabilities of metal fluoride complexes to the anion exchange resin. In more than 0.1M of HF, metals which form stable fluoride complexes form highly fluorinated complexes such as ZrF₆²⁻, TiF₆²⁻, and AlF₆³⁻, and hence the difference in the adsorbabilities of these complexes either on cation or anion exchange resin is not large enough to separate them from one another.

If the concentration of HF can be controlled to a certain value far less than 0.1M, at which such lower fluorinated complexes as ZrF₅⁻, TiF₃⁺, and AlF²⁺ are formed, the mutual separation of metals based on the difference in the charges of the fluoride complexes may be expected. However, it is not easy to control

HF concentration to a constant value far less than 0.1M in practical operations including the dissolution of the sample in hydrofluoric acid.

By adding boric acid, which is used as a masking agent for fluoride ions, the fluoride ion concentration is reduced to about one hundredth without reducing the total HF concentration, C_{HF} , as shown in Fig. 1. This reduction of the free fluoride ion concentration makes it easy to produce the metal fluoride complexes suitable for their separation.

1.1.1 Cation-exchange Separation [1]

The distribution coefficients, K_d , of 18 elements for cation-exchange resin (Diaion SK #1) in HF and HF- H_3BO_3 media are shown in Tables 1 and 2. Elution behavior of Zr(IV), Ti(IV), Al(III), U(VI), and Fe(III) was investigated in HF and HF- H_3BO_3 using a column filled with 4g of dry resin (10mm ϕ x 120mm). On the basis of the results shown in Fig. 2, a separation scheme for Zr(IV), Ti(IV), Al(III), U(VI), and Fe(III) was designed. These metals were eluted successively by the following solutions: Zr(IV) by 0.2M HF-0.65M H_3BO_3 , Ti(IV) by 0.5M HF-0.65M H_3BO_3 , Al(III) by 2.0M HF-0.65M H_3BO_3 , U(VI) by 0.1M HF, and Fe(III) by 0.5M HF. As the fluoroboric acid has a buffer action relating to the fluoride ion concentration, the distribution coefficients of metal ions are not affected by the increase in the concentrations of metal ions, even at a low concentration of fluoride ions in the solution.

1.1.2 Anion-exchange Separation [2,3]

The BF_4^- and BF_3OH^- produced in HF- H_3BO_3 media are adsorbed

strongly to the anion-exchange resin and the relative adsorbabilities of metal fluoride complexes are remarkably reduced. Using these properties of $\text{HF-H}_3\text{BO}_3$ and the adsorbabilities of other anions such as Cl^- or NO_3^- , a new anion-exchange method for the separation of such hard acid-metals as Ti(IV) , Zr(IV) , Nb(V) , and Ta(V) has been proposed.

The K_d of metals in $\text{HF-H}_3\text{BO}_3$ media containing HNO_3 are presented in Table 3. Elution behavior was investigated after adsorption of metals in a column (4g of Diaion SA #100 in dry form, 8mm ϕ x 180mm) in 0.2M HF. The elution curves are shown in Fig. 3. As expected from the K_d values obtained by the batch method, the mutual separation of metals is possible by the column.

The influence of anions on the K_d of hard acid-metals for a strongly basic anion-exchange resin was further investigated. The K_d of 18 hard acid-metal ions were determined in $\text{HF-H}_3\text{BO}_3$ media in the presence of Cl^- , NO_3^- , SO_4^{2-} , or ClO_4^- . The relation between the adsorbabilities of the coexisting anions and the K_d values of the metal ions was discussed. The fluoride ion concentration is quite low in $\text{HF-H}_3\text{BO}_3$ media because of the complex formation of the fluoride ion with boric acid, and most of the hard acid-metal ions have lower K_d values in $\text{HF-H}_3\text{BO}_3$ media than those in HF solution. By selecting the kinds of coexisting anions and varying their concentrations in $\text{HF-H}_3\text{BO}_3$ media containing less than 0.02M of fluoroborate ions, the K_d values of metal ions can be controlled to allow the anion-exchange separations such as Ti-Zr , Ti-U , Sn-Nb , and Mo-W .

1.1.3 Application to the Determination of Trace Elements in Zirconium Alloys

Determination of Uranium using Cation-exchange Separation[4]

In 0.1 to 1M HF - 0.4 to 0.65M H_3BO_3 media, U(VI) forms a cationic fluoride complex, whereas Zr(IV) exists as an anionic complex. Even if a considerable amount of the free fluoride ion is consumed by the complex formation with zirconium, the free fluoride ion concentration is kept constant because the fluoride ion is supplied by the dissociation of the fluoroborate ions in the media. By these characteristics of this media, a cation-exchange separation method was developed for the determination of traces of uranium in zirconium and its alloys.

Analytical result for NBS 360 reference materials was 0.73 ± 0.10 ppm ($n=3$) and agreed well with the certified value (0.7 ppm). In Table 4, analytical results for uranium in several zircaloy samples are shown. By the proposed method, 0.5 ppm to 10 ppm of uranium was determined with the relative standard deviation of 10% to 5%. Iron, tin, chromium, nickel, and metal elements usually included in zirconium alloys as the impurities did not interfere with the determination of uranium.

Successive Determination of Titanium and Aluminum using Cation-exchange Separation [5]

With the addition of H_3BO_3 to a dilute HF solution, Ti(IV) and Al(III) form cationic fluoride complexes due to the reduction of the free fluoride ion concentration, whereas Zr(IV) exists as an anionic fluoride complex. Further, fluoride ion concentration in HF- H_3BO_3 media is kept constant by the buffer action of this media. On the basis of these findings, a cation-exchange separation method was developed for the successive determination of micro quantities of Ti(IV)

and Al(III) in zirconium and its alloys.

Analytical results are shown in Table 5. By the method shown, more than 3 ppm of Ti(IV) and 2 ppm of Al(III) can be determined.

(T. Adachi)

Publication List

- [1] Adachi, T.: "Cation exchange separation of metal ions using HF-H₃BO₃ media", Bull. Chem. Soc. Jpn., 55, 802(1982).
- [2] Adachi, T.: "Anion exchange separation of hard acid-metals using HF-H₃BO₃ media", Bull. Chem. Soc. Jpn., 55, 1824(1982).
- [3] Adachi, T., Yoshida, H., Izawa, K., Kihara, S.: "The influence of anions on the distribution coefficients of hard acid-metals for anion-exchange resin in HF-H₃BO₃ media", Bull. Chem. Soc. Jpn., 57, 1487(1984).
- [4] Adachi, T., Yoshida, H., Izawa, K., Kihara, S., Hashitani, H.: "Determination of trace of uranium in zirconium and its alloys using cation exchange separation followed by Arsenazo III spectrophotometry", (in Japanese), Bunseki Kagaku, 33, 11(1984).
- [5] Adachi, T., Yoshida, H., Izawa, K., Hashitani, H.: "Successive determination of micro quantities of titanium and aluminum in zirconium by cation exchange separation in hydrofluoric acid-boric acid media", (in Japanese), Bunseki Kagaku, 33, 455(1984).

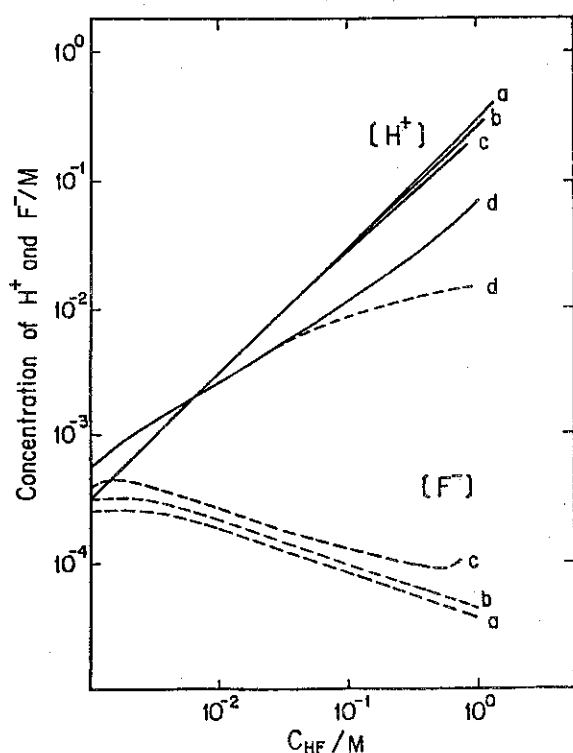


Fig. 1 Calculated concentration of H^+ and F^- in $HF-H_3BO_3$ media.

$[H_3BO_3]$; a:0.65M, b:0.4M, c:0.2M, d:0M

Table 1. Cation-exchange distribution coefficients of metal ions in $HF-0.65M H_3BO_3$ media

Metal ion	HF (M)				
	0.1	0.2	0.5	1.0	2.0
Fe(III)	$>5 \times 10^3$	$>5 \times 10^3$	4.5×10^2	800	177
Cd(II)	$>5 \times 10^3$	$>5 \times 10^3$	2.8×10^3	730	185
Mn(II)	$>5 \times 10^3$	$>5 \times 10^3$	2.5×10^3	581	164
Co(II)	$>5 \times 10^3$	$>5 \times 10^3$	2.4×10^3	562	154
Ni(II)	$>5 \times 10^3$	$>5 \times 10^3$	2.6×10^3	657	118
Cu(II)	$>5 \times 10^3$	$>5 \times 10^3$	1.9×10^3	427	97
Cr(III)	$>5 \times 10^3$	$>5 \times 10^3$	1.8×10^3	284	145
U(VI)	4.3×10^3	2.1×10^3	580	180	63
V(IV)	2.0×10^3	1.3×10^3	480	190	66
Al(III)	1.6×10^3	580	180	63	20
Ti(IV)	181	77	21	11	7
V(V)	125	90	68	60	58
Mo(VI)	16	10	7	5	3
Sn(IV)	15	7	6	5	3
Zr(IV)	13	10	8	4	<3
Hf(IV)	11	8	6	4	<3
W(VI)	10	6	5	3	<3
Nb(V)	10	8	6	5	<3
Ta(V)	10	6	5	<3	<3

Table 2. Cation-exchange distribution coefficients of metal ions in HF

Metal ion	HF (M)				
	0.1	0.2	0.5	1.0	2.0
Cd(II)	$>5 \times 10^3$	$>5 \times 10^3$	$>5 \times 10^3$	$>5 \times 10^3$	2.5×10^3
Co(II)	$>5 \times 10^3$	$>5 \times 10^3$	$>5 \times 10^3$	$>5 \times 10^3$	2.0×10^3
Mn(II)	$>5 \times 10^3$	$>5 \times 10^3$	$>5 \times 10^3$	$>5 \times 10^3$	1.9×10^3
Ni(II)	$>5 \times 10^3$	$>5 \times 10^3$	$>5 \times 10^3$	$>5 \times 10^3$	1.6×10^3
Cu(II)	$>5 \times 10^3$	$>5 \times 10^3$	$>5 \times 10^3$	$>5 \times 10^3$	1.5×10^3
V(IV)	420	180	80	31	13
Fe(III)	192	50	10	5	3
Cr(III)	45	32	25	11	10
V(V)	30	16	10	3	3
U(VI)	20	12	10	8	5
Al(III)	9	8	7	6	5
Ti(IV)	3	3	3	3	<3
Zr(IV)	3	3	3	3	<3
Hf(IV)	3	3	3	3	<3
W(VI)	<3	<3	<3	<3	<3
Mo(VI)	<3	<3	<3	<3	<3
Sn(IV)	<3	<3	<3	<3	<3
Nb(V)	<3	<3	<3	<3	<3
Ta(V)	<3	<3	<3	<3	<3

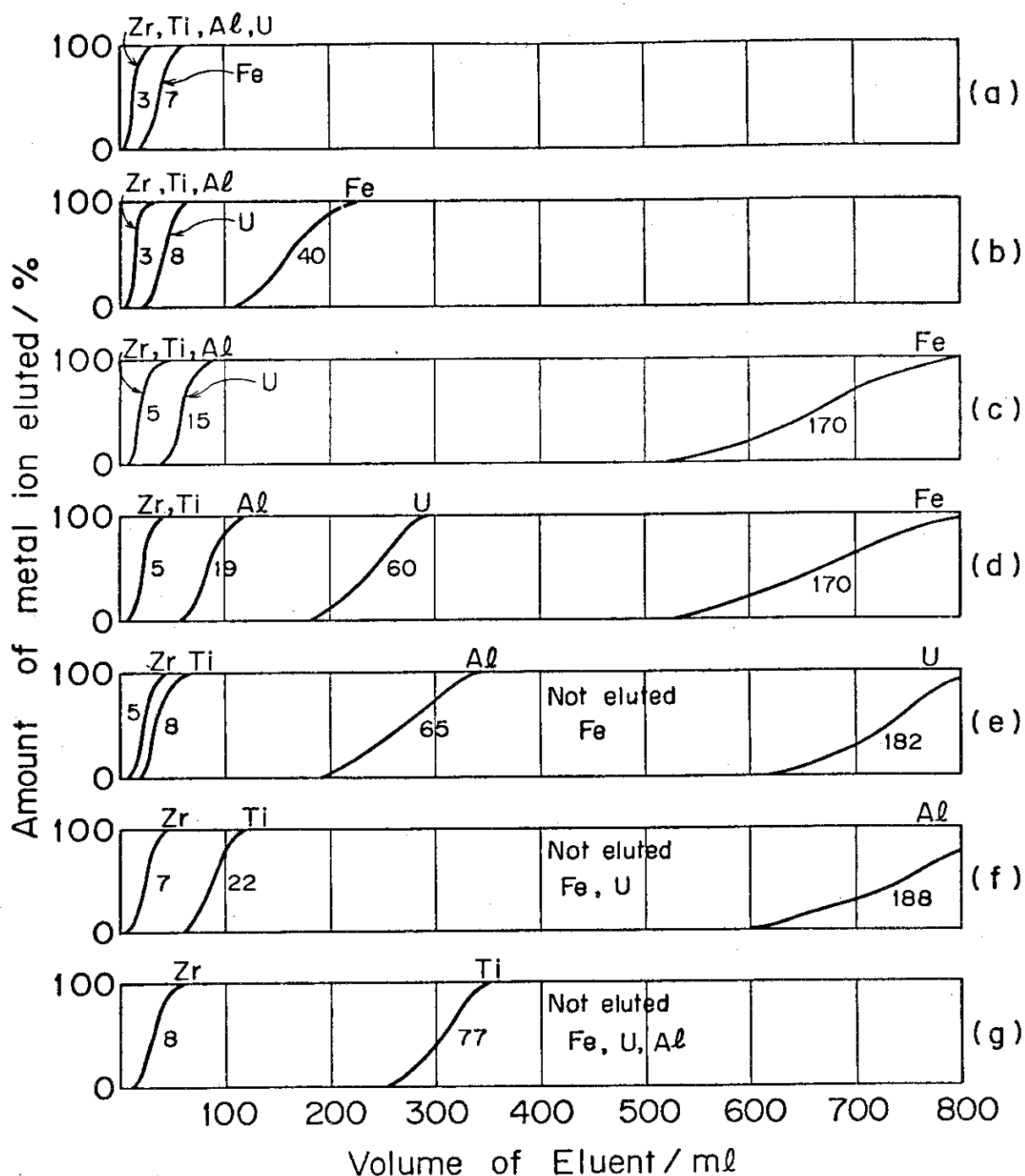


Fig. 2 Column elution behavior of metal ions in HF and HF-H₃BO₃ media onto cation exchange resin
Flow rate: 1.2 ml/min. Figures in each column are K_d values obtained. (a): 0.5M HF, (b): 0.2M HF, (c): 0.1M HF, (d): 2M HF-0.65M H₃BO₃, (e): 1M HF-0.65M H₃BO₃, (f): 0.5M HF-0.65M H₃BO₃, (g): 0.2M HF-0.65M H₃BO₃.

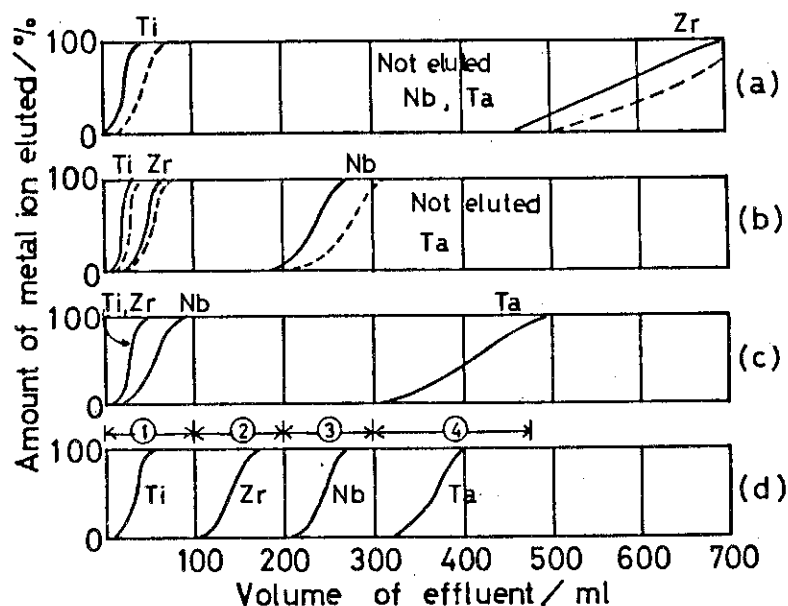


Fig. 3 Column elution behavior of Ti(IV), Zr(IV), Nb(V), and Ta(V) in HF-H₃BO₃ media containing HNO₃ onto anion resin. Flow rate: 1.0 ml/min. Concentration of HF-H₃BO₃-HNO₃ (M); (a) 0.1-0.5-0.01 (—), 0.01-0.5-0.03 (---), (b) 0.1-0.5-0.1 (—), 0.01-0.5-0.1 (---), (c) 0.5-0.5-0.1, (d) 1:0.1-0.5-0.01, 2:0.1-0.5-0.1, 3:0.5-0.5-0.1, 4:1-0.5-5.

Table 3 Anion exchange distribution coefficients of metal ions in HF-H₃BO₃ media containing HNO₃

Ion	HNO ₃ /M	0.1M HF-H ₃ BO ₃					HF-0.5M H ₃ BO ₃			
		H ₃ BO ₃ /M					HF/M			
		0	10 ⁻³	10 ⁻²	0.1	0.5	10 ⁻³	10 ⁻²	0.1	0.5
Ta(V)	10 ⁻²	> 5x10 ³	> 5x10 ³	4.1x10 ³	2.4x10 ³	2.3x10 ³	3.3x10 ³	5x10 ³	2.3x10 ³	606
	10 ⁻¹	4.0x10 ³	1.5x10 ³	1.2x10 ³	1.0x10 ³	790	102	955	790	315
W(VI)	10 ⁻²	> 5x10 ³	5x10 ³	765	97	232	4.3x10 ³	2.4x10 ³	232	13
	10 ⁻¹	115	110	28	14	56	182	112	56	5
Nb(V)	10 ⁻²	> 5x10 ³	5.0x10 ³	531	90	95	321	383	95	6
	10 ⁻¹	102	91	68	18	58	79	71	58	3
Hf(IV)	10 ⁻²	4.2x10 ³	2.2x10 ³	1.4x10 ³	181	152	1.0x10 ³	1.6x10 ³	152	19
	10 ⁻¹	360	320	245	7	< 3	< 3	10	< 3	< 3
Zr(IV)	10 ⁻²	> 5x10 ³	> 5x10 ³	5.0x10 ³	162	140	306	1.3x10 ³	140	4
	10 ⁻¹	375	346	282	6	< 3	< 3	8	< 3	< 3
Mo(VI)	10 ⁻²	1.2x10 ³	906	209	33	44	995	613	44	11
	10 ⁻¹	75	56	25	4	15	48	33	15	6
Ti(IV)	10 ⁻²	> 5x10 ³	> 5x10 ³	3.8x10 ³	70	15	18	150	15	3
	10 ⁻¹	405	355	302	18	< 3	< 3	< 3	< 3	< 3
Sn(IV)	10 ⁻²	> 5x10 ³	> 5x10 ³	5.0x10 ³	57	15	39	141	15	14
	10 ⁻¹	420	390	322	15	< 3	< 3	< 3	< 3	< 3
V(V)	10 ⁻²	92	76	15	11	< 3	4	3	< 3	< 3
	10 ⁻¹	4	< 3	< 3	< 3	< 3	< 3	< 3	< 3	< 3
U(VI)	10 ⁻²	72	49	5	< 3	< 3	20	15	< 3	< 3
	10 ⁻¹	< 3	< 3	< 3	< 3	< 3	< 3	< 3	< 3	< 3
Al(III)	10 ⁻²	30	20	12	10	7	8	5	7	3
	10 ⁻¹	< 3	< 3	< 3	< 3	< 3	< 3	< 3	< 3	< 3
Cr(III)	10 ⁻²	31	28	14	3	5	3	14	5	< 3
	10 ⁻¹	< 3	< 3	< 3	< 3	< 3	< 3	< 3	< 3	< 3
Fe(III), Cu(II), Cd(II),		< 3					< 3			
Ni(II), Mn(II), Co(II)		< 3					< 3			

Table 4 Analytical results for uranium in zircaloy samples⁺

Sample	Found (ppm U)	Av.	Cooperative results		
			$\bar{x} \pm \sigma$ (ppm U)	N	n
CRMs					
JAERI-Z11	0.8, 0.7	0.8	0.8±0.08	10	20
JAERI-Z12	0.9, 1.0	1.0	1.1±0.12	10	20
JAERI-Z13	(0.27, 0.27)	<0.5	<0.5 (0.34±0.07)	10	20
JAERI-Z14	(<0.3, <0.3)	<0.5	<0.5 (0.24±0.04)	10	20
Others					
A	(<0.3, <0.3)	<0.5	(<0.3)	3	7
B	(<0.3, <0.3)	<0.5	(<0.3)	3	6
C	3.7, 3.9, 3.9	3.8	3.9±0.22	7	20
D	6.6, 7.1, 6.9	6.9	7.1±0.20	7	21
E	1.3, 1.3, 1.3, 1.2, 1.1	1.3	1.3±0.07	9	29
F	1.0, 1.0, 1.0	1.0	1.0±0.05	7	19

+ A series of zircaloy CRMs, JAERI-Z11 to -Z14(disc) issued by Japan Atomic Energy Research Institute. Uranium was certified by collaborative analysis using the proposed method, after exercising with other zircaloy samples, A to F. Samples A and B are commercial grade zircaloy-2(1.5%Sn, 0.1%Fe, 0.1%Cr, 0.05%Ni), and E and F are zircaloy-4(1.5%Sn, 0.2%Fe, 0.1%Cr). N: Number of laboratories; n: Number of determinations.

Table 5 Analytical results for titanium and aluminum in zirconium and zircaloy samples

Sample	Found, ppm	Average	Certified value, ppm
(a) Titanium			
JAERI-Z11	23.3, 24.0, 23.7	23.7	28
JAERI-Z12	89.4, 93.3, 92.0	91.6	93
JAERI-Z13	3.5, 2.9, 2.5	3.0	4
JAERI-Z14	<3, <3, <3	<3	3
NBS 1234	14.6, 14.3	14.4	(20)
NBS 1235	84.2, 84.7	84.4	(90)
NBS 1236	167, 160	164	(185)
NBS 1237	15.3, 15.0	15.2	(30)
NBS 1238	98.0, 98.3	98.2	(100)
NBS 1239	50.7, 50.2	50.4	(40)
(b) Aluminum			
JAERI-Z11	16.9, 16.4, 16.1	16.5	15
JAERI-Z12	96.7, 97.5, 95.6	96.6	86
JAERI-Z13	57.2, 55.6, 55.1	56.0	53
JAERI-Z14	139, 136, 137	137	130
NBS 1234	33.1, 34.7	33.9	(25)
NBS 1235	129, 126	128	(105)
NBS 1236	320, 324	322	(350)
NBS 1237	19.8, 20.1	20.0	(15)
NBS 1238	134, 129	132	(105)
NBS 1239	70.6, 70.4	70.5	(50)

The certified values of Ti and Al in zircaloy CRM's JAERI-Z11 to Z14(disc), were determined by collaborative analysis(11 Labs. for Ti and 8 Labs. for Al), in which most of Labs. used the proposed cation exchange separation method. The values for NBS 1234 to 1236(zirconium metal) and 1237 to 1239(zircaloy-4) are not certified but are given as additional information.

1.2 Studies on the Determination of Hydrogen and Sulfur by Isotope Dilution Mass Spectrometry

1.2.1 Equilibrium Pressures of Hydrogen and Deuterium

Dissolved in Group IVa Metals at Low Concentration[5]

In the determination of hydrogen in titanium, zirconium and its alloys by isotope dilution mass spectrometry (IDMS), a significant difference in solubility between hydrogen and deuterium has been observed: hydrogen is more soluble than deuterium: hence the concentration ratios of hydrogen/deuterium in the metals are significantly larger than those in the surrounding gas phase under isotopic equilibrium.

The present study was undertaken to know the exact difference in the solubilities between hydrogen and deuterium in the group IVa metals. Equilibrium pressures of hydrogen and deuterium over titanium (420 - 970 °C), zirconium (480 - 940 °C) and hafnium (445 - 635 °C) were measured in the pressure range from 0.013 to 133 Pa using a modified Sieverts' apparatus.

The pressure-composition relationship obeyed Sieverts' law: the solubility of hydrogen and deuterium in the metals at low concentration is proportional to the square root of the pressure. The values of the Sieverts' constant at various temperatures were determined from the reciprocals of the slopes of the linear plots: the square root of pressure against the atom ratio. The logarithms of the Sieverts' constants obtained are plotted against the reciprocals of temperatures in Fig. 1. Arrhenius equations for the Sieverts' constants were determined from the linear portion of the plots in Fig. 1 by

the least squares method and are presented in Table 1. The slope denoted by b in the Arrhenius equations gives the enthalpy of solution in KJ/g-atom. There is a definite difference in the values of Sieverts' constants between hydrogen and deuterium. The values of the Sieverts' constants for hydrogen are larger than those for deuterium. At constant atomic fraction the equilibrium pressures of deuterium were found to be 1.1 to 1.4 times as high as those of hydrogen for all three metals over the temperature range examined.

1.2.2 Determination of Hydrogen in Titanium, Zirconium and its Alloys[6,7]

Hydrogen which is present in such metals as titanium, zirconium and its alloys in excess of the terminal solid solubility forms metal hydrides and causes serious embrittlement of the metals and alloys. The maximum permissible value for hydrogen in zirconium and its alloys for nuclear application is 0.0025 % by weight. Therefore, an accurate determination of hydrogen is of considerable industrial importance. Hot extraction methods are commonly used for the purpose. However the results obtained are highly dependent upon the extraction conditions. In order to test the accuracy of the hot extraction results, independent analysis techniques are required.

IDMS has been investigated for the absolute determination of hydrogen in metals using deuterium as spike. The results were found to be dependent upon the recovery of the isotopically equilibrated hydrogen because of the isotope effect on the solubilities between hydrogen and deuterium in the metals.

As hydrogen is more soluble than deuterium, the isotope composition of hydrogen in the gas phase differs significantly from that in the solid sample in the isotopic equilibrium. When the values of recovery are less than 10 % of total amount of the equilibrated hydrogen, analytical values become about 14 % lower than the true value. The recovery over 70 % of the total amount assures accurate result.

On the basis of above findings, a simple vacuum apparatus has been developed for the isotope equilibration between deuterium and hydrogen in metals. The apparatus is shown in Fig. 2. The sample was equilibrated with a known quantity of deuterium at 850 °C for 20 min. More than 90 % of the resulting equilibrated hydrogen gas was recovered using the mercury transfer diffusion pump in order to eliminate systematic errors caused by the isotope effect. Application of this technique to NBS and JAERI standard samples yielded results that were in good agreement with the certified values. The results are shown in Table 2.

1.2.3 Verification of Certified Sulfur Values in Steel

Reference Materials

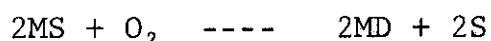
Sulfur present in metals and alloys even at trace levels often changes their properties significantly, so that a rapid and accurate determination of sulfur is indispensable for production control. Combustion methods are most commonly used for such analyses, but their accuracy depends greatly on the reference materials used for calibration. The gravimetric method employing barium sulfate has been used for certification despite its lack of sensitivity and accuracy. Samples

containing less than 0.005 % sulfur can not be analyzed by this method.

A procedure has been developed at this laboratory utilizing IDMS for the accurate and precise determination of sulfur in steels and heat-resisting alloys. And IDMS has been already applied to the various materials including zirconium and its alloys [1,2,3]. In 1979, the National Bureau of Standards (NBS) asked JAERI to perform IDMS analyses on five of their steel Standard Reference Materials (SRMs) for the certification of sulfur values.

Through correspondence, a significant discrepancy between the sulfur results obtained in the two laboratories (JAERI and NBS) was observed. The results are given in Table 3. The cause of the large discrepancy between the two sets of IDMS results for SRM 362 and 364 has been traced to the difference in the dissolution techniques adopted by the two laboratories: the open beaker dissolution (JAERI) and the sealed tube dissolution (NBS) [4]. It was found that part of the sulfur present in these samples was lost as sulfur dioxide during the open-beaker dissolution, and was suggested that when the sealed-tube dissolution technique was used, any sulfur dioxide evolved in the closed vessel was absorbed and oxidized to sulfate by the acid mixture ($\text{HNO}_3\text{-HCl}$) at high temperature and pressure. Despite the use of the sealed tube dissolution technique, the small discrepancy continued to exist. Prerinsing of the samples with water, ethanol and acetone prior to analyses was found to be contributed to this discrepancy. A significant amount of elemental sulfur which was easily removed by the rinsing was found to be present on the surface

of most sample chips. Depth distribution of sulfur in some of the standard chip samples was examined. And the sulfur concentration in the vicinity of the surface was found to be extremely high. Most of the sulfur in steels is known to be present in the form of iron sulfide and manganese sulfide. It was therefore assumed that the metal sulfides migrated to the surface and were gradually oxidized by atmospheric oxygen to elemental sulfur:



The free energy changes of this reaction are $\Delta G = -36.9$ kcal/mol for manganese sulfide and $\Delta G = -35.4$ cal/mol for iron sulfide, so it can take place spontaneously.

Sulfur in 26 steel reference materials from BCS, JSS and NBS was determined by IDMS applying both the sealed-tube and open-beaker dissolution techniques. All the results obtained by the use of both dissolution techniques agree with each other except for NBS SRMs 362 and 364. The results are shown in Table 4, the open beaker results are included in calculation of averages except for NBS SRMs 362 and 364. It seems that the sulfur present in most samples can be completely converted into sulfate by the conventional open-beaker dissolution technique. The results are in good agreement with the certified values for BCS samples and the recent or revised certified values for JSS and NBS samples. The ratios of the results to the certified values are 1.00 ± 0.04 for BCS samples, 0.97 ± 0.04 for JSS samples and 0.97 ± 0.03 for NBS samples.

(K. Watanabe)

Publication List

- [1] Watanabe, K.: "Determination of sulfur in steels by isotope dilution mass spectrometry after dissolution with sealed tube", (in Japanese), Bunseki Kagaku, 30, T103 (1981).
- [2] Watanabe, K.: "Determination of total- and sulfide-sulfur in geological materials by isotope dilution mass spectrometry", informal communication, (1983).
- [3] Watanabe, K.: "Accurate determination of sulfur at trace levels by isotope dilution mass spectrometry", Anal. Chim. Acta, 147, 417 (1983).
- [4] Watanabe, K.: "Verification of certified sulfur values in steel reference materials by isotope dilution mass spectrometry, and characterization of sulfur present on the solid samples", Talanta, 31, 311 (1984).
- [5] Watanabe, K.: "Equilibrium pressures of hydrogen and deuterium dissolved in titanium, zirconium and hafnium at low concentrations", J. Nucl. Mater., in press.
- [6] Watanabe, K., Ouchi, M.: "Isotope dilution technique applied to the determination of hydrogen in titanium, zirconium and zirconium alloy", (in Japanese), Bunseki Kagaku, 34, 677 (1985).
- [7] Watanabe, K., Ouchi, M., Gunji, K.: "Determination of hydrogen in titanium, zirconium and its alloys by isotope-equilibration mass spectrometry - Verification of certified values", Fresenius Z. Anal. Chem., in press.

Table 1 Summary of Sieverts' constants in the solubility equations for the group IVa metals:

$$\ln k = a + b(10^3/RT) \quad (k = \text{atomic ratio} \times \text{Pa}^{-1/2}; \\ R = 8.314 \text{ JK}^{-1} \text{ mol}^{-1})$$

System	temp. range (°C)	a	b
α -Ti-H	426 - 838	$-11.568 \pm 0.060^*$	$44.51 \pm 0.42^*$
α -Ti-D	420 - 846	-11.625 ± 0.049	43.82 ± 0.35
β -Ti-H	897 - 971	-11.283 ± 0.480	46.59 ± 4.80
β -Ti-D	897 - 973	-12.095 ± 0.434	53.99 ± 4.36
α -Zr-H	483 - 752	-12.069 ± 0.188	54.59 ± 1.32
α -Zr-D	499 - 749	-12.149 ± 0.148	54.38 ± 1.07
β -Zr-H	871 - 938	-12.564 ± 0.906	67.05 ± 8.85
β -Zr-D	869 - 940	-12.500 ± 0.599	65.59 ± 5.86
α -Hf-H	450 - 635	-10.897 ± 0.199	34.78 ± 1.33
α -Hf-D	446 - 634	-11.237 ± 0.094	36.35 ± 0.62

* Values are simply the statistical error (2 σ).

Table 2 Determination of hydrogen in titanium, zirconium and its alloy standard samples

Sample ^a	Hydrogen ($\mu\text{g/g}$)		
	Certified value	present study,	n
NBS SRM			
357, zirconium	19 ± 3	19.7 ± 0.4^b	4
358, zirconium	107 ± 3	107.2 ± 0.6	4
1086, titanium	116 ± 3	113.8 ± 1.1	4
1087, titanium	57.5 ± 2.5	56.1 ± 0.4	5
JAERI			
Z-8, zircaloy-2	-	7.5 ± 0.7	6
Z-10, zircaloy-2	$(8.2 \pm 1.1)^c$	9.3 ± 0.4	5
Z-17, zircaloy-2	-	15.8 ± 0.5	4
Z-18, zircaloy-4	-	13.4 ± 0.6	4

a. Sample sizes were 0.3 - 1.0 g.

b. Value is standard deviation.

c. Mean value obtained at the Sub-Committee on Reactor Materials, JAERI. Nine laboratories participated in the determination; all used vacuum hot extraction method.

Table 3 Results obtained by IDMS and ID-SSMS^a for sulfur in NBS steel SRMs

Sample NBS SRM	Sulfur found, $\mu\text{g/g}$			
	IDMS (JAERI)		ID-SSMS (NBS)	
	Open beaker (rinsed)	Sealed tube (rinsed)	Sealed tube (as received)	Open beaker (as received)
361	131 ± 0.6	132 ± 0.6	$144 \pm (0)^b$	-
362	301 ± 2.1	358 ± 1.1	$359 \pm (0.9)$	322
363	63 ± 0.2	64 ± 0.4	$67 \pm (0)$	-
364	213 ± 1.6	246 ± 1.0	$251 \pm (2.8)$	226
365	55 ± 0.2	$56 \pm (0.3)$	-	-
32e	181 ± 1.0	180 ± 0.7	$204 \pm (0.8)$	205
33d	$89 \pm (0.2)$	90 ± 0.6	$94 \pm (0.5)$	-
72f	$204 \pm (0.5)$	206 ± 0.8	$219 \pm (1.0)$	-

^a Isotope dilution spark source mass spectrometry.

^b Values in parentheses are range of two determinations.

Table 4 Determination of sulfur in steel reference materials
and elemental sulfur on the samples

Sample	Certified values		Average IDMS values, $\mu\text{g/g}^\dagger$		Elemental sulphur, $\mu\text{g/g}$	Mn content, (certified value, %)
	Year	%	(as received)	(rinsed)		
NBS						
32e, Ni-Cr steel	1957	0.021	204	180	18	0.798
33d, Ni-Mo steel	1955	0.010	94.2	90.0	3	0.537
72f, Cr-Mo steel	1957	0.024	219	206	17	0.545
133a, Cr-Mo steel	1956	0.329	3300	2720	594	1.03
361, low-alloy steel	1970	0.017*	144	132	14	0.66
362, low-alloy steel	1970	0.038	359	358§	0	1.04
363, low-alloy steel	1970	0.009*	67.5	64.4	2	1.50
364, low-alloy steel	1971	0.029*	251	246§	3	0.25
365, electrolytic iron	1970	0.006*	n.d.	56.1	0	0.0056
BCS						
211/1, 13% Cr rustless steel	1958	0.032	316	310	0	0.32
219/4, Ni-Cr-Mo steel	1977	0.027	267	257	5	0.81
232/2, carbon steel	1970	0.126	1250	1200	57	1.18
241/2, 9.9% W high-speed steel	1968	0.025	234	216	11	0.27
402, low-alloy steel	1971	0.023	245	236	8	0.19
403, low-alloy steel	1971	0.036	363	350	6	1.69
455, mild steel	1974	0.061	620	618	0	0.09
495, 13% Mn steel	1972	0.014	138	125	6	13.6
JSS						
152-4, alloy steel	1971	0.022	195	189	7	0.42
242-5, carbon steel	1973	0.031	303	281	4	0.72
508-2, Ni-Cr steel	1968	0.017	157	151	4	0.49
150-7, low-alloy steel	1979	0.034	328	n.d.	3	0.11
151-7, low-alloy steel	1979	0.017	164	n.d.	13	1.48
152-7, low-alloy steel	1979	0.043	425	n.d.	30	0.42
150-6, low-alloy steel¶	1979	0.035	348	—	—	0.11
151-6, low-alloy steel¶	1979	0.017	166	—	—	1.48
152-6, low-alloy steel¶	1979	0.043	440	—	—	0.42

n.d. = not determined.

*Most recent certified values are 0.015% for SRM 361, 0.0068% for SRM 363, 0.025% for SRM 364 and 0.0056% for SRM 365.

†Average for two or more determinations; relative standard deviation better than 1%.

§The results obtained by the open-beaker dissolution are 301 $\mu\text{g/g}$ for SRM 362 and 213 $\mu\text{g/g}$ for SRM 364.

¶Disk samples for spectroscopic analysis.

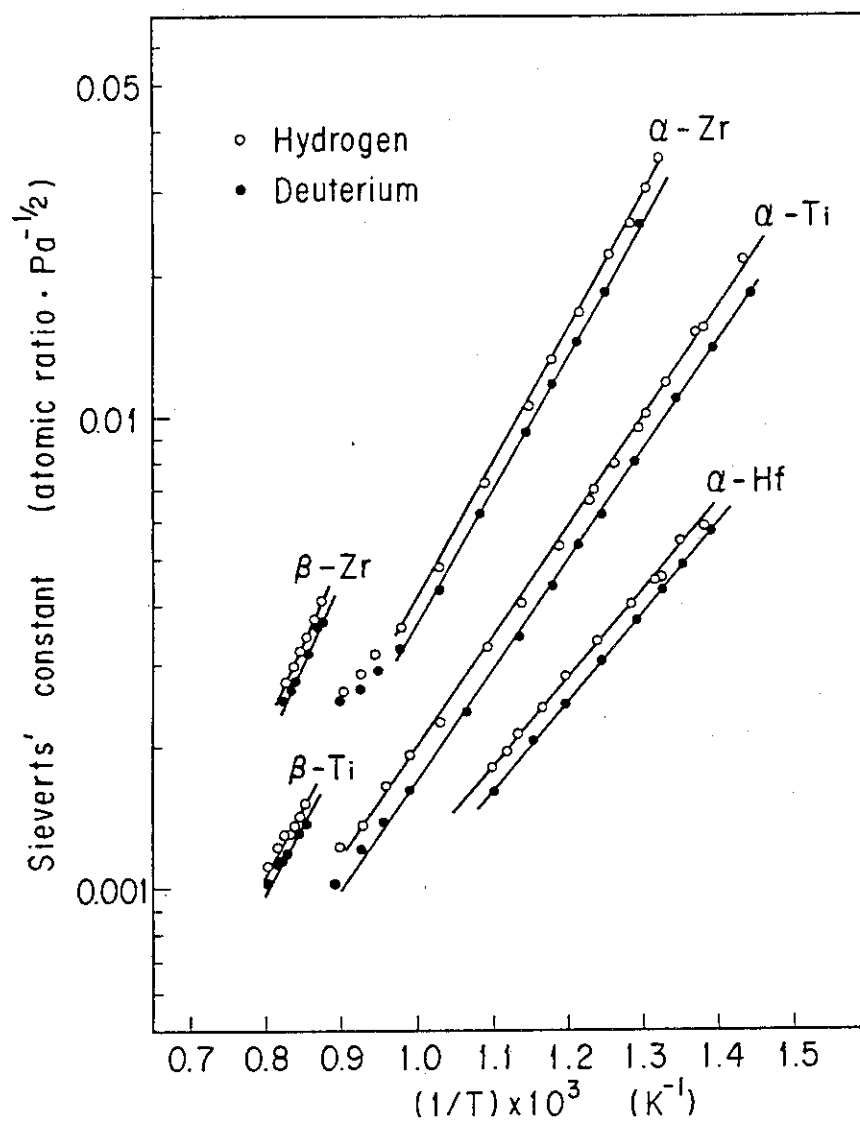


Fig. 1 Arrhenius plots of Sieverts' constants

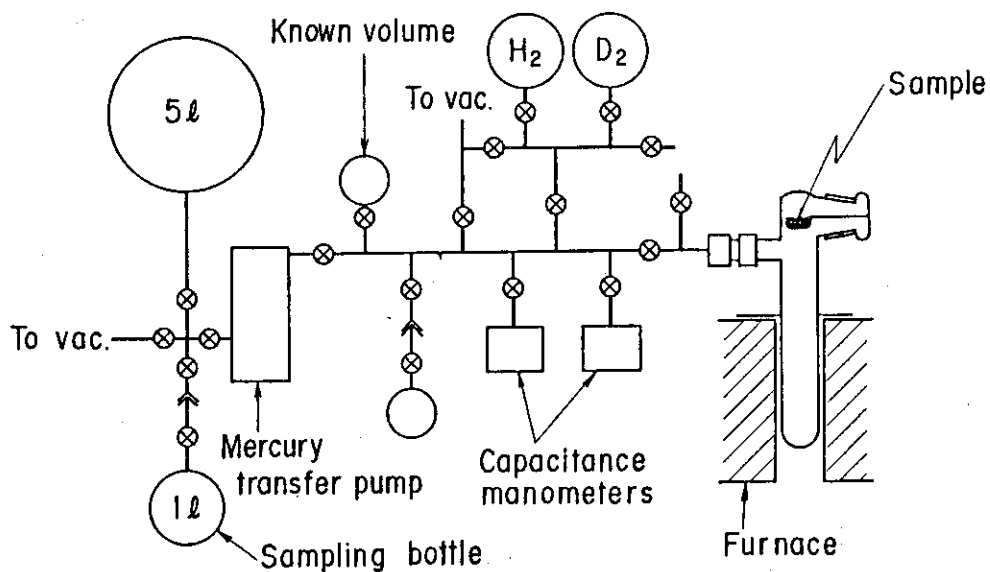
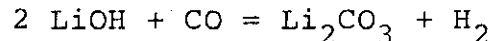


Fig. 2 Vacuum apparatus for hydrogen isotope equilibration

1.3 Determination of Gaseous Elements in Reactor Materials

1.3.1 Determination of Hydrogen in Lithium Oxide by Hot Extraction with Carbon Monoxide[1]

Lithium oxide is one of the candidate materials as a blanket in nuclear fusion reactor. Physical and chemical properties of lithium oxide are affected by the presence of impurity hydrogen and in most cases hydrogen are not favourable. A new method for the determination of hydrogen in lithium oxide has been established. Hydrogen in lithium oxide exists mainly in the form of hydroxide, which is formed from lithium oxide and atmospheric moisture during storage. The lithium hydroxide liberates hydrogen gas when it is heated in carbon monoxide and changes into lithium carbonate ;



Hydrogen evolved can be determined by means of gas chromatography. In the method developed, carbon monoxide is used not only as chemical reactant but also as carrier gas.

Schematic illustration of the apparatus used is shown in Fig. 1. One hundred to five hundreds mg of sample is placed in a reaction tube (15 mm in diameter, 200 mm long). Stream of carbon monoxide is passed through the tube at the flow rate of 80 ml/min, and then the tube is heated at 390 °C for 15 min. The hydrogen evolved from the sample is determined by using a thermal conductivity detector.

Evolution behaviour of hydrogen was found to be influenced by physical properties of lithium oxide, e.g., density, specific surface area and degree of sintering. Lithium carbonate did not interfere with the determination of hydrogen.

The lower limit of determination was 0.002 wt % for 500 mg of sample. Although the time required for the analysis depended on the amounts of sample used, in general, it took about 20 min after weighing the sample under a dried atmosphere in gloved box. Hydrogen contents in actual lithium oxide samples were 0.028 to 0.7 wt % as indicated in Table 1. The proposed method may also be applicable to the determination of hydrogen in sodium and potassium oxides.

1.3.2 Determination of Carbon in Zircaloy 2 and Zircaloy 4[2]

In the course of certification of carbon values for Zircaloy 2 and Zircaloy 4 reference materials, it was found that analytical results obtained by the conventional combustion methods were affected significantly with many factors such as fluxes, size of sample chips, and washing and drying of sample as treatments of sample prior to analysis.

In order to check the accuracy of the combustion methods, an acid decomposition method using HF-HNO_3 was also studied. Analytical results obtained by the acid decomposition method were in a good agreement with those by the combustion methods. This agreement may show that all the carbon in zircaloys exists in the form of combined carbon, because only combined carbon can be determined by the acid decomposition method. The preparation and certification of zircaloy reference materials for carbon are described in 2.2.

1.3.3 Thermogravimetric Analysis of Titanium- and Scandium-Deuterium Targets[3]

Titanium-deuterium (Ti-D) and scandium-deuterium (Sc-D)

targets which were used as a source of 14 MeV neutron in a performance test of Fusion Neutronics Source (FNS) were prepared by heating at 400 °C and 600 °C, respectively, in a deuterium atmosphere of about 70 kPa for two hours. The amounts of deuterium absorbed in the targets were determined by an impulse heating-argon carrier gas extraction-gas chromatographic method. The atom ratios of deuterium to titanium and scandium of the targets were 1.24 and 1.29, respectively.

Thermal behavior of the Ti-D and Sc-D targets was examined by thermogravimetric analysis (TGA). TGA curve of the two targets are shown in Fig. 2. Weight loss due to deuterium release for the Ti-D target is observed at 400 - 570 and 570 - 720 °C, and that of the Sc-D target is observed at 630 - 765 °C.

On the other hand, FNS group reported that the release of deuterium from the Ti-D target occurred at 120 °C and that from Sc-D target was negligible at 380 °C in their experiments. when the target was bombarded with proton beam. The discrepancy in the temperature of deuterium release for the Ti-D target at the two laboratories is assumed to be caused by the different experimental conditions adopted, i.e., with and without proton beam.

(A.Hoshino)

Publication List

- [1] Hoshino, A., Iso, S., Ito, M.: "Rapid determination of hydrogen in lithium oxide by carbon monoxide carrier gas method", (in Japanese), Bunseki Kagaku, 33, 226 (1984).
- [2] The Comm. on Anal. Chem. of Nucl. Fuels and Reactor Mat., JAERI : "Determination of carbon in Zircalloys", (in Japa-

nese), JAERI-M 83-035 (1984).

- [3] Hoshino, A., Iso, S., Ito, M.: "Preparation of deuterium target and determination of deuterium in the targets", (in Japanese), JAERI-M 83-110 (1983).

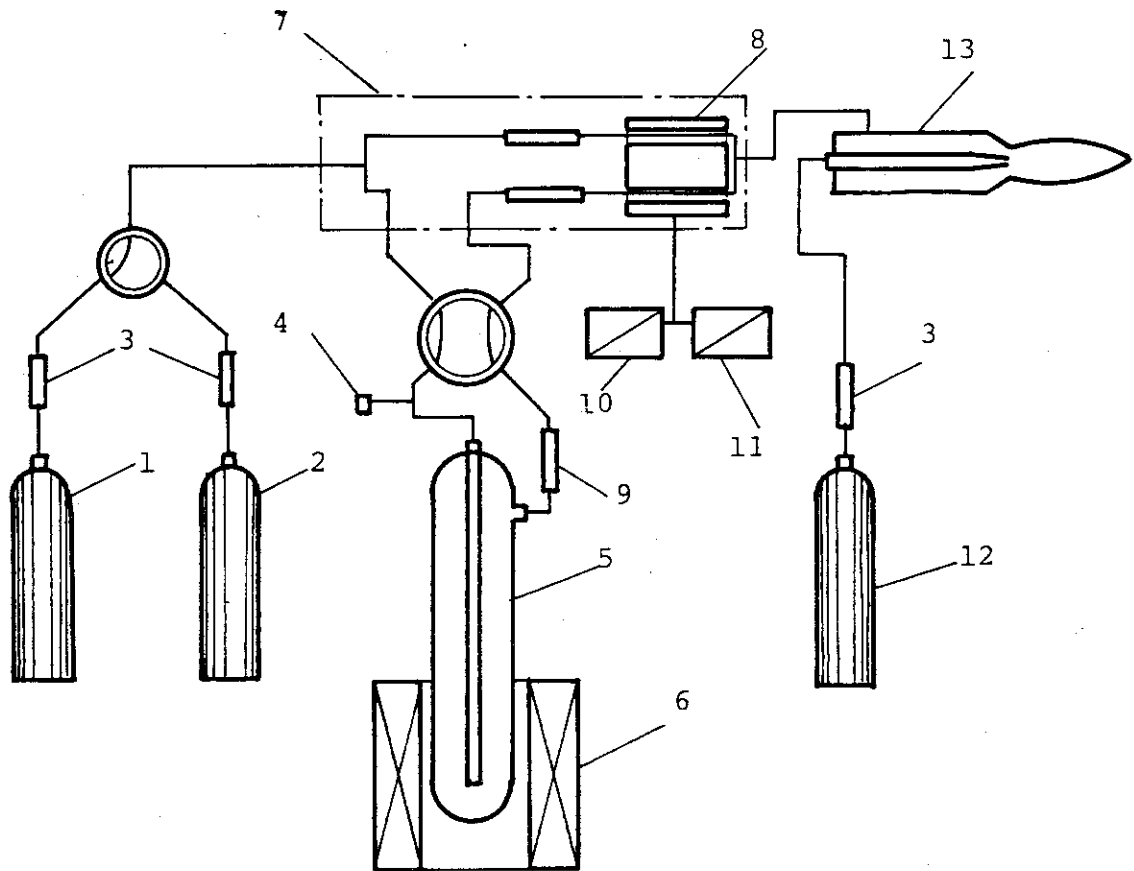


Fig. 1 Schematic illustration of the apparatus for the determination of hydrogen in lithium oxide

1:Carbon monoxide vessel, 2:Argon vessel, 3:Flow meter, 4:Hydrogen injection point for calibration, 5:Reaction tube, 6:Furnace, 7:Gas chromatograph, 8:Thermal conductivity cell, 9:Silica gel tube, 10:Recorder, 11:Integrator, 12:Oxygen vessel, 13:Burner for carbon monoxide

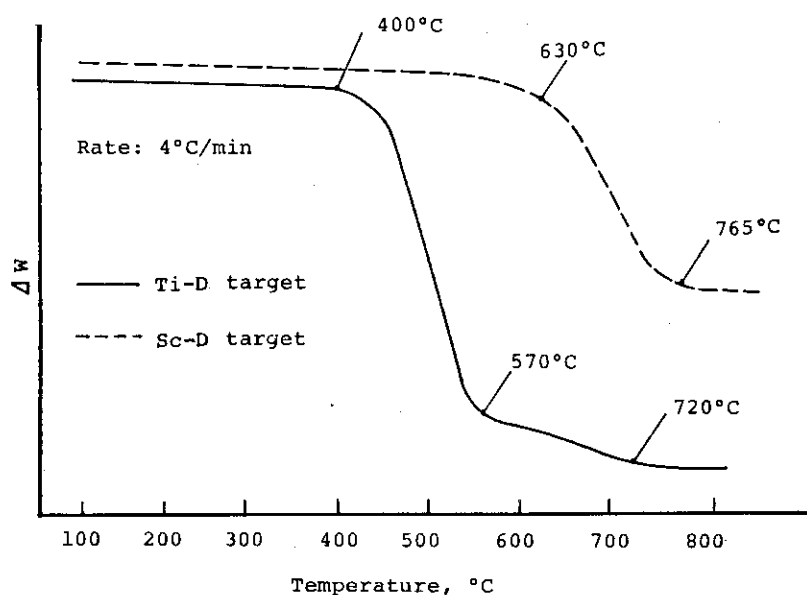


Fig. 2 TGA curves of Ti-D and Sc-D targets

Table 1 Analytical results of hydrogen in lithium oxide samples

Sample	Sample taken,mg	Hydrogen,%
A	110.3	0.75
	116.3	0.63
	144.9	0.74
	96.1	0.70
		$0.71 \pm 0.05\%$ *
B	452.1	0.029
	398.3	0.034
	460.5	0.025
	401.3	0.025
		$0.028 \pm 0.004\%$ *
C	199.3	0.18
	137.7	0.20
	293.0	0.17
		$0.18 \pm 0.01\%$ *

A,C: Chemical reagent, B: Sintered powder

* Standard deviation

1.4 Analytical Chemical Studies of Plutonium and Uranium

1.4.1 Study on Hydrolysis of Plutonium(III), (IV), and (VI) [1]

Plutonium ion which exists at such high oxidation states as Pu(III), (IV), and (VI) in the aqueous solution readily hydrolyzes and forms hydroxide-polymer and -precipitate. The formation of plutonium hydroxide frequently causes unexpected error in the analytical operations such as the chemical separation and the detection. Hydrolysis also influences the diffusion behavior of plutonium in the environment and in the human body. Many studies on hydrolysis of plutonium, therefore, have been done in the field of solution chemistry, analytical chemistry, and nuclear technology. Despite these great efforts there remains much uncertainty in the details of the hydrolysis or polymerization of plutonium.

In this work, the hydrolysis behavior of Pu(III), (IV), and (VI) in nitrate or chloride solution was studied by alkalimetry. The size of the plutonium hydroxide precipitate formed in the solution was investigated by the filtration of the precipitate. The chemical form of the hydroxide was estimated by consulting with the reported values of hydrolysis constants and oxidation-reduction potentials of plutonium ions.

Figure 1 contains the relations between pH of the solution and the volume of the titrant, when 0.5 M nitric acid or hydrochloric acid solution with about 10^{-2} M Pu(III), (IV), or (VI) was titrated by 0.1 M sodium hydroxide solution.

The recoveries of plutonium(III)- or (IV)- hydroxide precipitate (Fig. 2) were investigated by filtrating precipitate formed at various pH by using filters of different pore

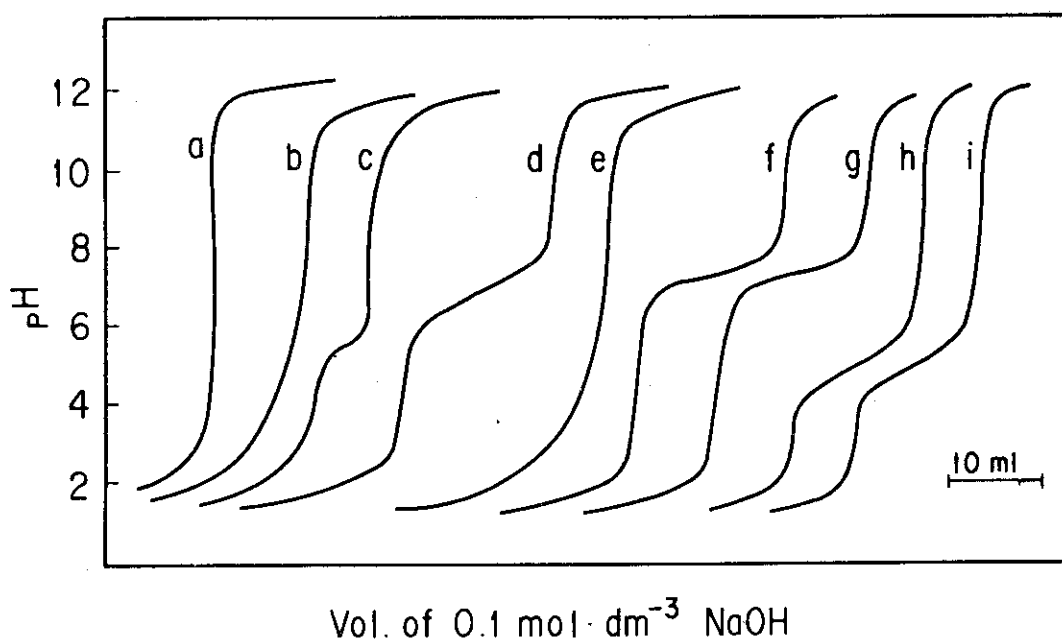


Fig. 1 Titration of plutonium with sodium hydroxide.

Solutions to be titrated: 50 ml of 1.29×10^{-2} M
 Pu(IV) (b,c), Pu(III) (d-g), and Pu(VI) (h,i),
 in 0.5 M HNO_3 (b,d,e,h) or 0.5 M HCl (c,f,g,i),
 with (d,f) or without (b,c,e,g-i) deaeration
 a: blank (0.5 M HNO_3 or HCl)

sizes.

In the deaerated nitrate or chloride solution of $\sim 10^{-2}$ M Pu(III), polymeric precipitate of $[\text{Pu}(\text{OH})_2]^+$ was formed at pH higher than 6 or 7, which corresponds to the pH-plateau in the titration curves d and f in Fig. 1. When the concentration of Pu(III) was $\sim 10^{-4}$ M, the polymeric hydroxide was precipitated in nitrate solution of pH higher than 3 and in chloride solution of pH higher than 3, and when the concentration of Pu(III) was $\sim 10^{-6}$ M, the hydroxide was precipitated in both nitrate and chloride solutions of pH higher than 2. Since Pu(III) of such a low concentration as less than $\sim 10^{-4}$ M was readily oxidized to Pu(IV) by oxygen dissolved in the solution, the precipitate

formed was identical to that of Pu(IV). Plutonium(III) in the nitrate solution was oxidized more rapidly than that in the chloride solution. The size of the precipitate was 10-40 μm in diameter.

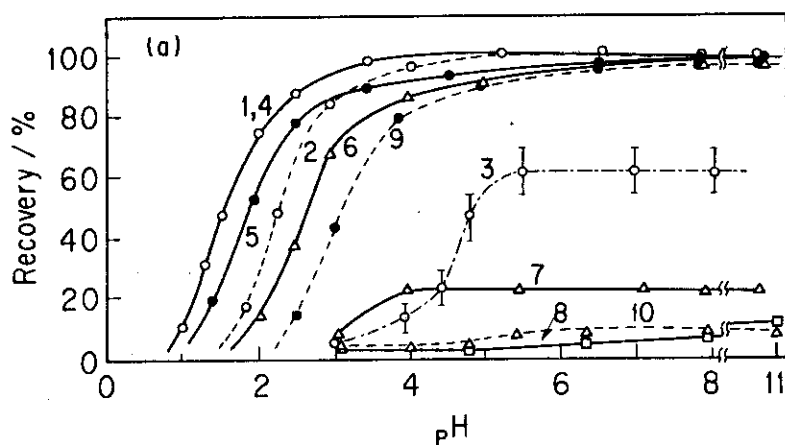


Fig. 2 Recovery of Pu(IV)- and Pu(III)-hydroxide precipitate

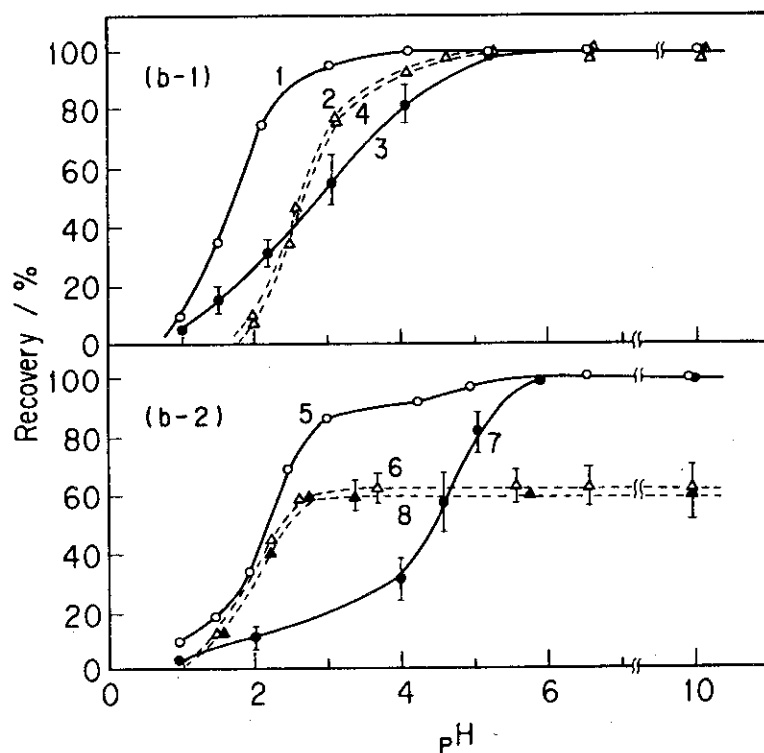
(a) Pu(IV)

Concentration of Pu in 0.5 M HNO_3 :

1,4-8; 2.58×10^{-4} M,
2,9,10; 1.29×10^{-6} M,
3, 1.29×10^{-9} M

Pore size of filters:

1-3; 0.45 μm ,
4; 3 μm ,
5,9; 5-10 μm ,
6,7,10; 20-30 μm ,
8; 40-50 μm



(b) Pu(III)

Medium: (b-1); 0.5 M HNO_3 ,

(b-2); 0.5 M HCl

Concentration of Pu:

1,3,5,7; 2.58×10^{-4} M,
2,4,6,8; 1.29×10^{-6} M,
3,4,7,8: with deaeration,

1,2,5,6,: without deaeration,

Pore size of filter:
0.45 μm

In nitrate or chloride solution containing 10^{-6} - 10^{-2} M Pu(IV), polymeric precipitate of $[\text{Pu}(\text{OH})_2]^{2+}$ was formed at pH higher than about 2. The precipitate, $[\text{Pu}(\text{OH})_2]^{2+}$ formed in the chloride solution changed to $[\text{Pu}(\text{OH})_3]^+$ by consuming one mole of hydroxide ion in the solution at pH 4-6 (see titration curve c in Fig. 1). The size of the precipitate formed in the nitrate solution, pH 10, of $\sim 10^{-6}$ M and $\sim 10^{-4}$ M Pu(IV) were 5-20 and 10-40 μm in diameter, respectively, whereas that of the precipitate formed at pH 4 was slightly smaller than those.

In nitrate and chloride solutions of Pu(VI), $\text{PuO}_2(\text{OH})_2$ was formed at pH higher than 5. Although hydrolytic Pu(VI) was not precipitated even when the concentration of Pu(VI) was 10^{-2} M, $\text{PuO}_2(\text{OH})_2$ was quantitatively coprecipitated with hydrolytic precipitate of Pu(IV) when Pu(VI)/Pu(IV) ratio in the solution was less than 0.2.

1.4.2 Determination of Uranium-oxygen Ratio in Non-stoichiometric Uranium Dioxide Based on Dissolution with Strong Phosphoric Acid

The uranium-oxygen ratio, O/U ratio, in UO_{2+x} is one of the most important factors which influence the compatibility between the cladding and the fuel, the fuel safety, and the fuel economy. Physical techniques for the analysis of the oxidation state such as X-ray diffraction analysis, X-ray photoemission spectrometry, and the measurement of electromotive force have some limitations, one of which is that these methods substantially need reference material having identical composition with that of the sample in order to calibrate the methods.

The chemical methods for oxidation-state analysis of

UO_{2+x} , on the other hand, seem to be promising because these are quantitative in their principles and they don't require the reference material, and therefore, they will be an independent and referee method to the physical methods as above.

The chemical method developed in this work is grounded on the fact that UO_{2+x} is dissolved with strong phosphoric acid (SPA) producing uranium ions whose oxidation states are the same as those in the solid UO_{2+x} . The O/U ratio can be calculated from the amounts, A, of U(VI), $A_{\text{U(VI)}}$, and of U(IV), $A_{\text{U(IV)}}$, in the SPA solution with the aid of the following equation,

$$\text{O/U} = 2 + [A_{\text{U(VI)}} / \{ A_{\text{U(VI)}} + A_{\text{U(IV)}} \}]$$

on the assumption that UO_{2+x} is the mixture of UO_2 and UO_3 . The amounts of U(VI) and U(IV) were determined by spectrophotometry and/or electrochemical method.

The spectrophotometry of U(VI) and U(IV) in the SPA solution was improved[2]. For the determination of U(VI), the large absorption in the wavelength region between 280 and 330 nm was measured where U(IV) has no absorption at all. In order to avoid any unexpected interference by impurities and/or colloidal polymers of U(IV)-phosphoric acid, the absorbances both at 290 and 310 nm were employed to determine U(VI). The proposed procedure can be applied to samples of O/U ratios 2.001-2.67. The reproducibility, related to the ratio, is ± 0.0002 .

The distribution of the oxidation states of uranium in the UO_{2+x} pellet was evaluated by dissolving the pellet with a continuous flow of SPA from surface to bulk and by determining the dissolved U(VI) and U(IV) consecutively by two-step flow-coulometry[3]. A schematic diagram of the apparatus used is

shown in Fig. 3. After setting the pellet in the sample room (a), it is rotated at a rate about 100 rpm. The SPA deaerated is allowed to flow using a micro pump (f) as indicated by broad arrows. Upon heating of the sample room at 180-200 °C, dissolution of the pellet begins with yielding U(VI) and U(IV). After the resulting solution is diluted to 3-6 times in a mixing room (h) with diluted SPA, the solution is introduced into the two-step flow-coulometric column electrode (j). Uranium(VI) in the solution is reduced quantitatively to U(IV) at the first-step column electrode, E-I, of -0.6 V vs Ag-AgCl reference electrode (SSE). Then at the second column electrode, E-II, of +0.85 V vs SSE, U(IV) which is both the reduction product at the E-I and the dissolution product of UO_2 , is oxidized to U(VI). The ratio of the current at the E-I to that at the E-II at a given time is calculated to the O/U ratio at the dissolving surface at the time.

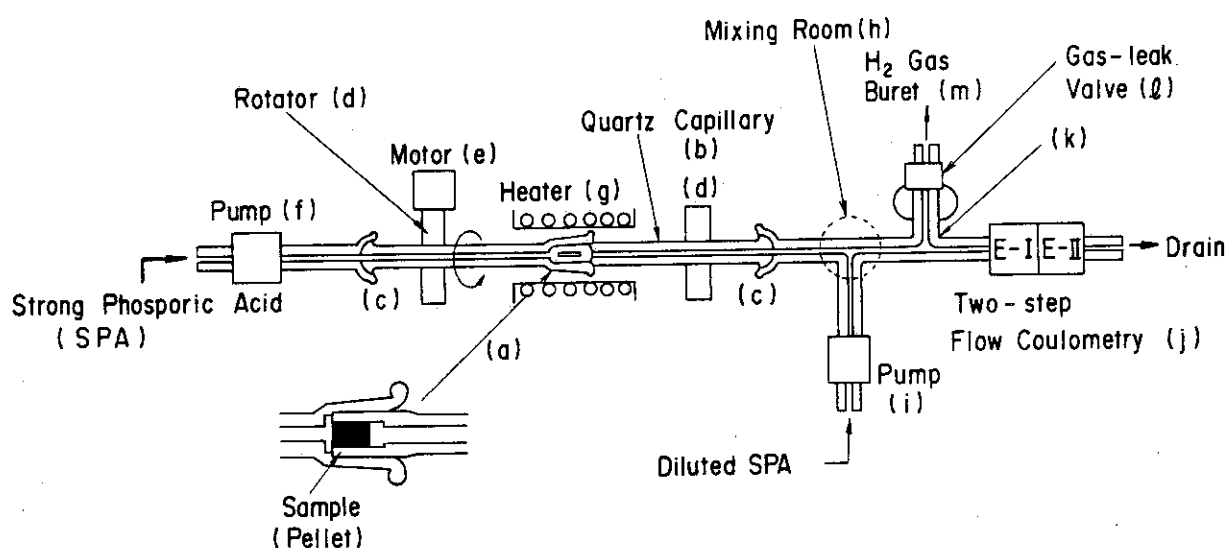


Fig. 3 Schematic diagram of apparatus

The proposed method was applied to the analysis of radial distribution of the O/U ratio in the UO_{2+x} pellet. The oxidized surface of about 20 Å of UO_{2+x} pellet which had been stood for about 10 years at room temperature in air was estimated to be $\text{UO}_{2.05}$, and the O/U ratio decreased toward the bulk until 0.1 μm. After the pellet was heated for 10 h at 300 or 430 °C in air, the oxidized surface layer increased to about 8 μm or about 820 μm, respectively.

The O/U ratio and also its distribution in the pellet may change by the neutron irradiation, and therefore, it is desired to determine the O/U ratio in the UO_{2+x} not only before but also after the irradiation. The applicability of the chemical method based on dissolution with SPA to the determination of the O/U ratio in the irradiated UO_{2+x} was investigated[4]. To know the distribution of the O/U ratio in the sample pellet, a piece of UO_{2+x} was taken out from a given part of the irradiated UO_{2+x} , and the sample piece was dissolved with SPA. It was confirmed that the oxidation states of uranium did not change through the sampling and the dissolution procedures, even in the presence of fission product elements and the radioactivity. The stability of U(VI) and U(IV) in SPA solution in the presence of radioactivity were investigated. For the determination of U(VI) and U(IV) in the solution, two methods based on different principles, i.e., spectrophotometry and flow-coulometry were employed to avoid unexpected error. The interference from plutonium and fission product elements in the determination was reduced by the pre-electrolysis of the diluted SPA solution. The proposed methods accompanied with spectrophotometry and flow-coulometry were feasible for the O/U ratios of more than

2.01 in UO_{2+x} with less than 5×10^3 MWd/t burnup and more than 2.001 in UO_{2+x} with less than 1×10^4 MWd/t, respectively.

1.4.3 Determination of Plutonium by Solvent Extraction-Liquid Scintillation Method[5]

A combined solvent extraction-liquid scintillation method was developed for the determination of plutonium. The quenching effects by eleven phosphorous compounds, eight amine compounds, and five beta-diketone compounds were examined with respect to the relation between the degree of the quenching and their molecular structures. Among compounds investigated the organo phosphorous compounds such as tributylphosphate (TBP), bis-(2-ethylhexyl) phosphoric acid (HDEHP), and tri-n-octylphosphine-oxide (TOPO) were shown to be least quenching. Choosing TOPO as an extractant, the recommended procedure for the determination of plutonium was established as follows; To 7 M nitric acid solution (10-50 ml) containing 0.1 ng-2 μg plutonium 5 ml of 0.1 M TOPO-xylene is added and plutonium is extracted into the organic phase. This procedure is repeated twice. Organic phase is transferred into 20 ml of glass vial and 5 ml of xylene containing 60 mg of 2,5-diphenyloxazole (PPO) is added and counted on a liquid scintillation counter. The count rates of alpha-ray were proportional to the amounts of plutonium from 0.1 ng to 2 μg , and the standard deviation was 5 % from 1 ng to 2 μg , and 10 % from 0.1 ng to 1 ng. The quenching by diverse inorganic ions and the effects of the radioactive elements were also investigated.

1.4.4 Determination of Uranium and Plutonium in Solution by Energy-dispersive X-ray Fluorescence Analysis[6]

An analytical system of energy-dispersive X-ray fluorescence spectrometer and glove box was constructed. The beryllium window of 4 μm thickness was mounted in the optical pass between sample solution and X-ray detector. Uranium from 100 $\mu\text{g/ml}$ to 5 mg/ml was determined with 1 % of relative standard deviation by using the $L\alpha_{1,2}$ lines, and plutonium from 500 $\mu\text{g/ml}$ to 5 mg/ml was determined with 2 %. The self absorption by uranium or plutonium of more than 5 mg/ml were corrected by using $\text{Pb}(\text{NO}_3)_2$ as the internal standard. Measuring the intensity ratio of $UL\alpha_{1,2}$ or $PuL\alpha_{1,2}$ to $PbL\alpha_{1,2}$, up to 200 mg/ml of uranium and up to 20 mg/ml of plutonium were determined with the relative standard deviations of 1 % and 2 %, respectively.

(Z. Yoshida and Y. Baba)

Publication List

- [1] Aoyagi, H., Yoshida, Z., Adachi, T., Kihara, S.: "Hydroxides of Pu(III), (IV), and (VI)", (in Japanese), Nippon Kagaku-kaishi, 1984, 1249 (1984).
- [2] Kihara, S., Adachi, T., Hashitani, H.: "Spectrophotometric determination of the O/U-ratio of non-stoichiometric uranium dioxide", Fresenius Z. Anal. Chem., 303, 28(1980).
- [3] Kihara, S., Yoshida, Z., Muto, H., Aoyagi, H., Baba, Y., Hashitani, H.: "Determination of oxidation states of uranium in uranium dioxide pellets by two-step flow-coulometry", Anal. Chem., 52, 1601(1980).
- [4] Takeishi, H., Muto, H., Aoyagi, H., Adachi, T., Izawa, K., Yoshida, Z., Kawamura, H., Kihara, S.: "Determination of

oxygen-uranium ratio in irradiated uranium dioxide based on dissolution with strong phosphoric acid", Anal. Chem., in press.

- [5] Baba, Y.: "Determination of plutonium by solvent extraction-liquid scintillation method", J. Radioanal. Chem., 79, 83(1983).
- [6] Baba, Y., Muto, H.: "Determination of uranium and plutonium in solution by energy-dispersive X-ray fluorescence analysis", (in Japanese), Bunseki Kagaku, 32, T99(1983).

1.5 Studies on Atomic Spectroscopy

1.5.1 Wavelength Shift Phenomena in an ICP

Atomic emission spectroscopy using an inductively coupled plasma (ICP) as light source, ICP-AES, is widely and acceleratively spreading to many different fields because of its excellent analytical characteristics such as high sensitivity and precision, wide analytical dynamic range, less chemical and ionization interferences, and sequential or simultaneous multi-element determination. In order to know the physical (spectroscopic) characteristics — temperature and electron number density — of the ICP which produces the above-mentioned excellent analytical characteristics, we have investigated on the observation of spectral line profiles emitted by an ICP[1].

Profiles of 16 spectral lines stemming from 8 elements (Ar, Na, Cu, Sr, Cd, Ba, Mg and Li) emitted by an ICP have been observed and measured with a pressure-scanning Fabry-Perot interferometer. In the process of profile observations, we have found wavelength shifts of spectral lines in an ICP and for the first time studied this phenomenon quantitatively and systematically in a spectrochemical source. The profiles of spectral lines emitted by the ICP have been compared with those emitted by hollow cathode lamps (HCLs). The magnitude of the wavelength shift to the red or the blue varied more or less with the plasma conditions, observation position and the concentration of a concomitant, cesium. In the present work the observed line profiles were not deconvoluted for the apparatus profiles. Typically the order of magnitude of the wavelength shift measured for spectral lines that show large shifts at an observation

height of ca. 4 mm in an "analytical" ICP is $n \times 10^{-3}$ nm, where n is ca. 4 for Ar I 427.2 nm and ca. 1 for Cu I 521.8 nm and Sr II 430.5 nm. With regard to the wavelength shift, several trends and/or regularities were found. The Stark effect is considered as the main cause of the phenomena.

The profile observation results obtained for each spectral line are summarized in Fig. 1 and Table 1 for the Ar I 427.2 nm line and in Fig. 2 and Table 2 for the spectral lines of metal species introduced with carrier gas, respectively. Table 3 shows the effect of concomitant Cs concentration on the Ba I 553.5 nm and Ba II 455.4 nm line profiles. The three different ICP conditions examined in the observation of Ar I 427.2 nm line profiles

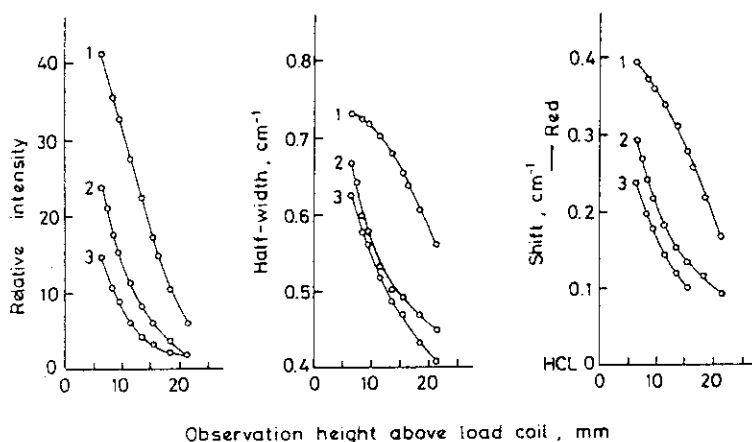


Fig. 1. Emission intensity, halfwidth and wavelength shift of the Ar I 427.2 nm line vs observation height above the load coil (curve 1—ICP (1), curve 2—ICP(2), curve 3—ICP(3)). The magnitude of wavelength shift is derived from the central wavelength of the Ar I 427.2 nm line emitted by an Ar-filled Ca-Mg HCL (HCL 0).

Table 1 Effect of observation position on the wavelength shift of Ar I 427.2 nm line emitted by ICP(2)

O.P.*	O.H.† (mm)	Shift (cm ⁻¹)	Illustration of each O.P.*
1	14.0	0	
2	14.0	0.015	
3	14.0	0.020	
4	8.0	0.127	
5	8.0	0.139	
6	8.0	0.169	

*Observation position.

† Observation height above load coil.

were the following:

- ICP(1): without carrier gas (without axial channel).
- ICP(2): water was nebulized and introduced with carrier gas (routine ICP, incident rf power of 1.6 kW, argon gas flows of 10.5, 1.5 and 1.0 l min⁻¹ for the outer, intermediate and carrier gas, respectively).
- ICP(3): no water was nebulized but carrier gas was introduced (the aspiration tube was plugged).

The conclusions of the trends and/or regularities of the wavelength shift phenomena found can be summarized as follows:

(1) In general, the central wavelengths of spectral lines emitted by the ICP tend to shift to the red in comparison with those emitted by HCLs.

(2) Depending on the observation height, however, central wavelength shifts to the blue have also been found, again in comparison with HCL lines.

(3) The magnitude of the wavelength shift of spectral lines increases with decreasing observation height. This suggests that the strength of the electric field increases with decreasing observation height and as a result the terms involved in the spectral transitions suffer more severely the perturbation effect of the electric field at lower positions in the ICP.

(4) The Ar I 427.2 nm line profiles show that the wavelength shift to the red increases not only lower in the ICP but also towards the periphery of the ICP. These enhancements may be related to the strength of the electric field.

(5) The magnitude of wavelength shift for spectral transitions to an intermediate level tends to be larger than that for transitions to the ground state.

Table 2 Observed spectral lines, their transition characteristics and results

Spectral line (nm)	Transition	Energy levels (cm ⁻¹)	Fine structure	Observation			Maximum shift from central wavelength of HCL [†]		
				Shift in ICP* (10 ⁻⁴ nm)	height interval (mm)	Observation height (mm)	(cm ⁻¹)	(10 ⁻⁴ nm)	(mm)
Na I 588.9 (D ₂)	3s ² S _{1/2} -3p ² P _{3/2}	0-16973		0.007	2.4	2.5-6.5	0.030	10.4	2.5
I 589.5 (D ₁)	3s ² S _{1/2} -3p ² P _{1/2}	0-16956		0.008	2.8	2.5-6.5	0.032	11.1	2.5
Cu I 510.5	4s ² D _{5/2} -4p ² P _{3/2}	11 203-30 784	o	0.011	2.9	4.2-13.5	—	—	—
I 521.8	4p ² P _{3/2} -4d ² D _{5/2}	30 784-49 942		0.042	11.4	4.2-13.5	0.036	9.8	4.2
I 578.2	4s ² D _{3/2} -4p ² P _{1/2}	13 245-30 535	o	—	—	—	—	—	—
Sr I 460.7	5s ² S ₀ -5p ¹ P ₁	0-21 698		0.003	0.6	2.5-16.5	0.024	5.1	2.5
II 421.5	5s ² S _{1/2} -5p ² P _{1/2}	0-23 715		0.012	2.1	6.5-19.5	0.020	3.6	6.5
II 430.5	5p ² P _{3/2} -6s ² S _{1/2}	24 517-47 737		-0.046	-8.5	4.2-19.5	-0.033	-6.1	4.2
Cd I 479.9	5p ³ P ₁ -6s ³ S ₁	30 656-51 484	o	-0.011	-2.5	6.5-14.5	~0.057	~13.1	14.5
I 508.5	5p ³ P ₂ -6s ³ S ₁	31 827-51 484	o	-0.012	-3.1	6.5-16.5	~0.050	~12.9	16.5
Ba I 553.5	6s ¹ S ₀ -6p ¹ P ₁	0-18 060		0.003	0.9	2.5-6.5	0.026	8.0	2.5
II 455.4	6s ² S _{1/2} -6p ² P _{3/2}	0-21 952		0.007	1.5	4.2-16.5	0.019	3.9	4.2
II 493.4	6s ² S _{1/2} -6p ² P _{1/2}	0-20 262		0.005	1.2	4.2-16.5	0.024	5.8	4.2
Mg I 518.3	3p ³ P ₂ -4s ³ S ₁	21 911-41 197		-0.010	-2.7	4.2-13.5	0.026	7.0	13.5
Li I 610.3	2p ² P _{3/2} -3d ² D _{3/2}	14 904.00-31 283.12	o	0.074	27.6	6.5-15.5	—	—	—
	2p ² P _{3/2} -3d ² D _{5/2}	14 904.00-31 283.08							
	2p ² P _{1/2} -3d ² D _{3/2}	14 903.66-31 283.08							

*Symbol "—" indicates that the central wavelengths shift to the blue with decreasing observation height.

†Symbol "o" indicates that the central wavelength shifts to the blue in comparison with that of the HCL.

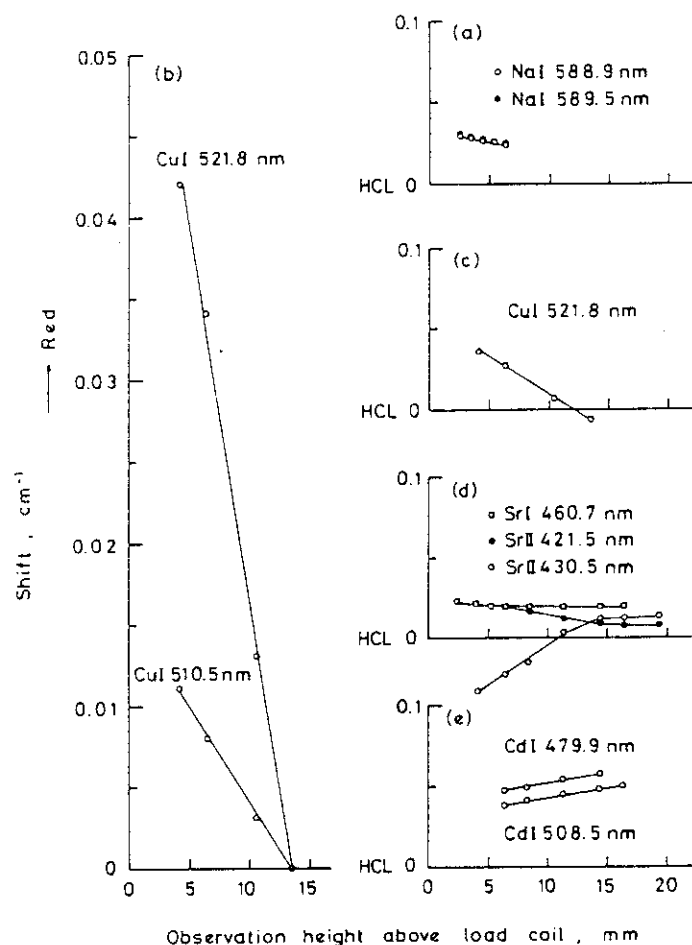


Fig. 2 Wavelength shift vs observation height above the load coil for the Na, Cu, Sr and Cd spectral lines emitted by the routine ICP. (a), (c), (d) and (e): the magnitude of wavelength shift is derived from the central wavelength of each spectral line emitted by HCLs (HCL 0), (b): the magnitude of the wavelength shift is derived from each central wavelength obtained at 13.5 mm of observation height above the load coil.

Table 3 Effect of concomitant Cs concentration on the Ba I 553.5 nm and Ba II 455.4 nm line profiles

Solution conc. ($\mu\text{g ml}^{-1}$)			Relative int.		Halfwidth (cm^{-1})		Shift (cm^{-1})	
			*	†	*	†	*	†
1	Ba 10 + Cs 0	0	9.15	13.7	0.122	0.173	0	0
2	Ba 10 + Cs 1000	14.7	13.1	14.7	0.126	0.176	0.003	0.002
3	Ba 10 + Cs 2000	16.5	12.9	16.5	0.126	0.176	0.006	0.004
4	Ba 10 + Cs 5000	18.5	12.1	18.5	0.126	0.179	0.008	0.006

* Ba I 553.5 nm, observation height above load coil: 3.5 mm.

† Ba II 455.4 nm, observation height above load coil: 7.5 mm.

(6) The wavelength shifts to the red for the Ba I 553.5 nm and Ba II 455.4 nm lines, produced by large amounts of a concomitant, Cs, may be attributed to the interactions of the emitting species, Ba, with other charged or uncharged particles produced in proportion to the amount of the concomitant.

(K.Kato)

1.5.2 Isotopic Analysis by Optical Spectral Methods

Isotope shifts in atomic spectra have been used for the isotopic analysis of several of the very light and very heavy elements in the periodic system. Since the isotopic shifts in the atomic spectra are very small, it is necessary to employ high-resolution spectroscopic techniques such as large grating spectrographs, prism-echell spectrographs, or Fabry-Perot interferometers.

In our laboratory, methods of isotopic analysis for lithium and uranium were developed. A pressure-scanned plane Fabry-Perot interferometer mounted internally within a 0.5 m focal length modified Czerny-Turner monochromator was used. A water-cooled hollow cathode discharge tube was specially designed as the excitation source.

A Procedure for Lithium Isotopic Analysis [2]

The isotope shift in the 670.7 nm resonance line of lithium is used. The line is a doublet with a small fine structure splitting (0.016 nm). The ^6Li - ^7Li isotope shift is nearly identical with the fine structure splitting, so that one observes three lines for mixtures in orders of increase in wave-length: the strong component of ^7Li , the weak component of

^7Li superimposed on the strong component of ^6Li , and finally the weak component of ^6Li .

The resonance line has a marked tendency to self-absorption and the presence of self-absorption makes precise intensity measurements difficult. Besides, the spectral line width of lithium is strongly affected by the mass dependent Doppler broadening, because lithium is a light element. Therefore, excitation of lithium atoms necessitates a low temperature source to minimize Doppler broadening and a low density of atoms to minimize self-absorption. In this report, the hollow cathode source loaded with 0.1 mg lithium is excited at currents as small as 0.8 mA.

A lithium acetate solution containing 0.1 mg of lithium is evaporated to dryness under an infra-red lamp in a graphite electrode, which is then loaded in the cathode cavity of the hollow cathode discharge tube. The discharge tube is operated in a continuously flowing atmosphere of pure argon at 1.05 Torr. A 75 Hz half-wave rectified power supply for operating the discharge tube is derived through a transformer from the power amplifier connected with the sine-wave generator. The emitted radiation is detected by a Hamamatsu R-928 photomultiplier, whose signals are amplified by a preamplifier and a lock-in amplifier.

When a cold trap was connected to the vacuum system for continuous purification of argon gas, there was a considerable increase in the intensity of the lithium resonance line. No variation in the $^6\text{Li}/^7\text{Li}$ intensity ratio was detected in a continuous source operation up to 2 hours, during which time a gradual increase in the intensities of both the lines was

observed.

Table 4 shows the reproducibilities of the ${}^6\text{Li}/{}^7\text{Li}$ intensity ratios.

Figure 3 shows the working curve obtained by plotting the intensity ratios versus the isotopic ratios obtained by mass spectrometry.

According to the sum rule for intensities,

the theoretical intensity ratio of

the fine structure

doublet is 2:1, and

the weak line of ${}^6\text{Li}$ and the strong line of ${}^7\text{Li}$ are used for the measurement. The intensity ratio R is calculated from the following equation,

$$R = 2 I_{{}^6\text{Li}} / I_{{}^7\text{Li}}.$$

Since the resulting working curve is found to be linear with unit slope in the concentration range investigated as shown

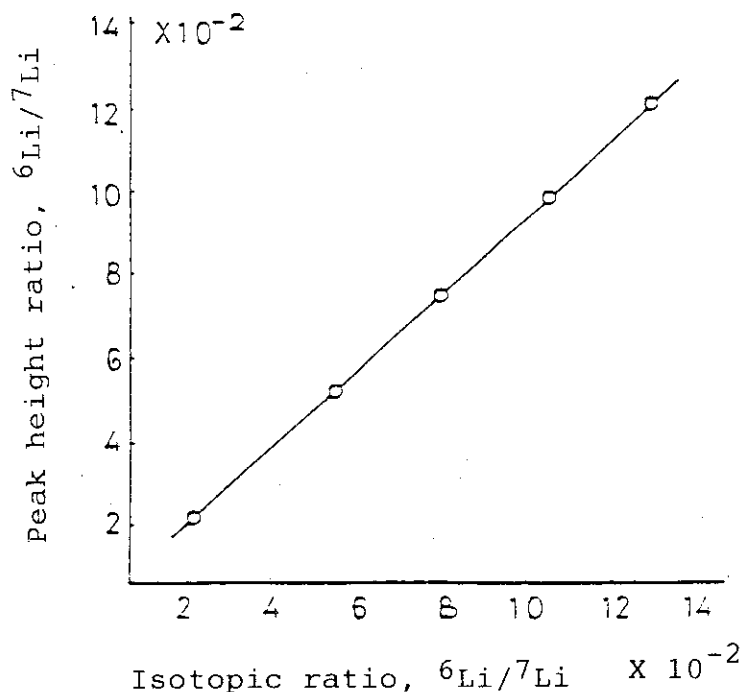


Fig. 3 Plot of peak height ratio found vs. isotopic ratio obtained by mass spectrometry.

Table 4 Reproducibility of the method.

Sample	Peak height ratio ${}^6\text{Li}/{}^7\text{Li}$	n	σ	Coefficient of variation %
A	0.06953	6	0.00018	0.26
B	0.06954	6	0.00018	0.26

Here, n is the number of determinations.

in Fig. 3, the emitted radiation appears to be practically free from self-absorption. The analysis time required per sample is less than 40 minutes.

A Procedure for the Determination of $^{235}\text{U}/^{238}\text{U}$ Ratios[3]

We chose the 502.7 nm line which contains unresolved hyperfine structure and is highly sensitive. Isotope shift of this line for $^{235}\text{U} - ^{238}\text{U}$ is 0.01 nm.

Our previous report showed that the ^{235}U line was nearly superimposed on a weak line arising from the excitation of a support gas in the hollow cathode discharge tube. The precision of the $^{235}\text{U}/^{238}\text{U}$ ratios was limited at low ^{235}U concentrations by this interfering line.

In this work, in order to eliminate both this interference and the background, which is also due to the emission of the support gas, we employed a technique using a lock-in amplifier (phase sensitive detector) with alternating current operation of the hollow cathode discharge tube. When the discharge tube works in an alternating current mode, the negative glow occurs at both electrodes of it alternately. During the half-cycle that the counter electrode is cathodic, only the support gas is excited in the region of the negative glow. As illustrated in Fig. 4, the reference signal is applied to the phase sensitive detector so as to be in phase with the composite signal of the uranium line and excited support gas, and to be 180 degrees out-of-phase with the signal of the excited support gas only, which is inverted by the phase detector and its integrated value is effectively subtracted from that of the composite signal at the hold circuit in the amplifier.

The discharge tube originally designed for use in alternating current is illustrated in Fig. 5. The discharge tube is operated with a 50 Hz alternating current at 40 mA.

A uranyl nitrate solution containing 2 mg of uranium is transferred to a graphite electrode, evaporated to dryness, and ignited to convert the uranyl nitrate to an adhering deposit of

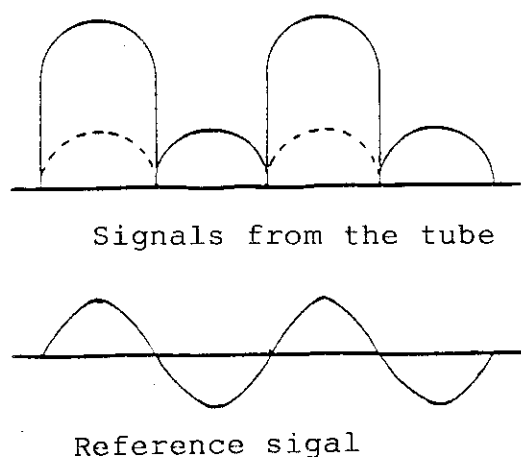


Fig. 4 Phase setting between the signals from the hollow cathode tube and the reference signal.

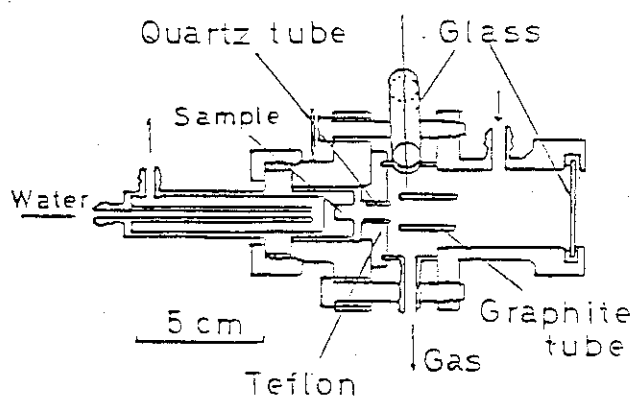


Fig. 5 Hollow cathode tube.

Table 5 Comparison of optical and mass spectrometric results.

Sample	Optical spectrometric			Mass spectrometric	
	Peak height ratio $^{235}\text{U}/^{238}\text{U}$	n	Coefficient of variation %	$^{235}\text{U}/^{238}\text{U}$ atomic ratio	$^{235}\text{U}/^{238}\text{U}$ atomic ratio
A	0.02251	10	0.38	0.02072	0.02065
B	0.02912	9	0.30	0.02787	0.02784
C	0.03619	10	0.20	0.03552	0.03548
D	0.02832	11	0.34	0.02701	0.02700
E	0.03484	10	0.31	0.03406	0.03423

n is the number of determinations.

uranium oxide. This electrode is loaded in the cathode cavity.

It was found that an addition of nitrogen to argon support gas was very effective to increase and maintain the uranium line intensities for a long period of time. The maximum intensity was obtained with a 7:1 (in mole) mixture of argon to nitrogen at 2.5 Torr.

The isotopic concentrations of 0.684 to 20.0 at% ^{235}U can be determined with a relative standard deviation ranging from 0.4 to 0.2 %. Table 5 shows the experimental results compared with mass spectrometric results on slightly enriched samples. The reproducibility of the $^{235}\text{U}/^{238}\text{U}$ intensity ratios obtained by this procedure was nearly comparable to that obtained by mass spectrometry.

(H. Fukushima)

Publication List

- [1] Kato, K., Fukushima, H., Nakajima, T.: "Observation of spectral line profiles emitted by an inductively coupled plasma - I. On the wavelength shift of spectral lines", Spectrochim. Acta, 39B, 979(1984).
- [2] Fukushima, H., Nakajima, T.: "Spectro-isotopic analysis using the hollow cathode discharge technique", Forty-first Conference on Analytical Chemistry held in Kohchi (1980).
- [3] The Comm. on Anal. Chem. of Nucl. Fuels and Reactor Mats., JAERI: "A committee report on the state-of-art of uranium isotope enrichment measurement techniques", (in Japanese), JAERI-M 82-051 (1982).

1.6 Studies on Faradaic Ion Transfer across the Interface of Two Immiscible Electrolyte Solutions and Potential-generating Process at an Ion-selective Electrode

1.6.1 Current-scan polarography at the aqueous/organic solutions interface

Recently the voltammetry at the aqueous/organic solutions (w/o) interface has been recognized as the powerful tool for the investigation of the ion transfer across the interface. The measurement of the voltammogram feasible for the quantitative analysis, however, is fairly difficult, mainly due to the distortion of the polarograms by considerable ohmic potential drop (IR drop) involved in the electrolytic cell. The current-scan polarography with the aqueous electrolyte dropping electrode (EDE) developed in this work[1] was found to be the most promising to obtain the satisfactory voltammogram at the w/o interface.

The electrolytic cell for the EDE is illustrated schematically in Fig. 1. The aqueous electrolyte solution was dropping upward into the organic solution such as nitrobenzene from a Teflon capillary (1.4 mm ϕ x 3 mm) with the mean flow rate $m=0.018 \text{ cm}^3 \text{ s}^{-1}$ and the drop time t about 2.2 s. To get the polarogram, the current, I , between CE1 and CE2 was scanned at a rate $v=0.5 \text{ } \mu\text{A s}^{-1}$ and the potential difference, ΔV , between RE1 and RE2 was detected. To compensate the IR drop between RE1 and RE2, a resistance, R_c , which is equivalent to a resistance, R , between RE1 and RE2 is put into the current supplying circuit in series and the voltage, IR_c , generated by R_c is subtracted from the potential difference measured between

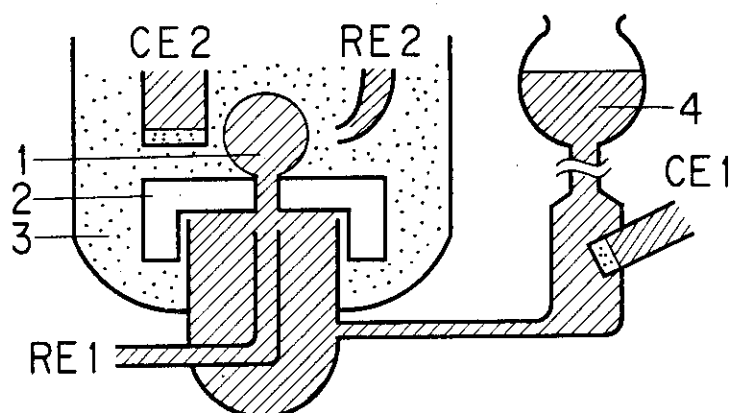
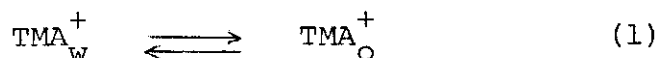


Fig. 1 Electrolytic cell

- 1, aqueous electrolyte dropping electrode;
 2, Teflon cylinder with small hole (1.4 mm ϕ x 3 mm)
 3, nitrobenzene phase; 4, reservoir for
 aqueous solution;
 RE1, RE2, Ag-AgCl electrode for potential
 measurement;
 CE1, CE2, electrode for scanning current

RE1 and RE2.

Current-scan polarograms obtained are shown in Fig. 2. Curve 1 is the polarogram when the EDE contains 0.05 M LiCl and 1 M MgSO_4 as supporting electrolytes and drops into the nitrobenzene solution containing 0.05 M tetrabutylammonium tetrphenylborate (TBA^+TPB^-). Since LiCl and/or MgSO_4 are hardly soluble in nitrobenzene and TBA^+TPB^- is hardly soluble in water, the w/o interface is polarized at the potential region where the current is negligible. Curve 2 was obtained with the same solution couple as that for curve 1 but in the presence of both 5×10^{-4} M tetramethylammonium bromide, TMA^+Br^- , in w and 5×10^{-4} M TMA^+TPB^- in o. This polarogram shows the composite wave due to the following ion-transfer reaction;



The polarogram sharply intersects the potential axis suggesting that the w/o interface is depolarized at the potential of zero-current, since TMA^+ is easily transferred from one phase to the other across the interface. Curve 3 in Fig. 2 illustrates the polarogram obtained in the same condition as that of curve 2 but without TMA^+ in o. The anodic wave in the polarogram is attributed to the ion-transfer reaction;

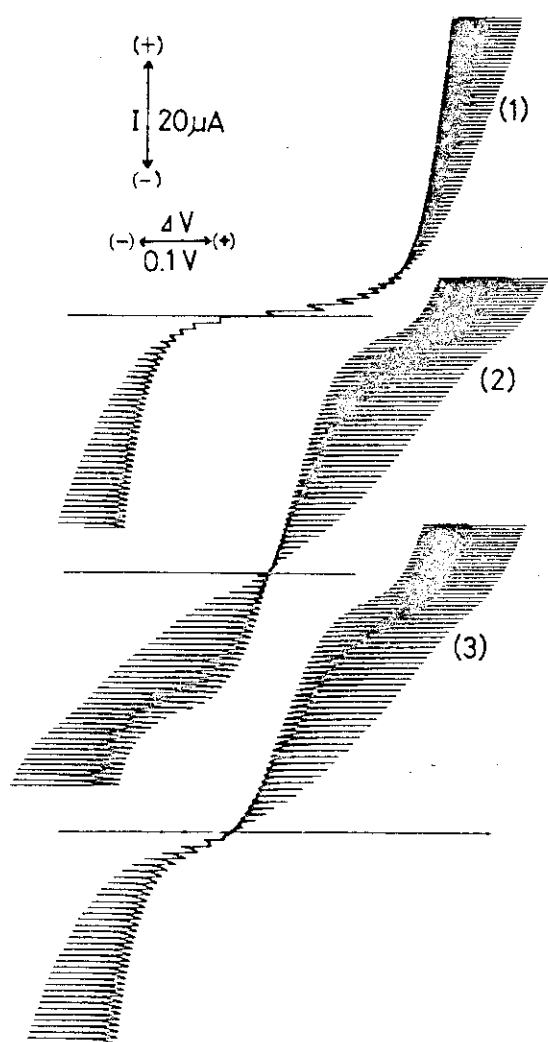
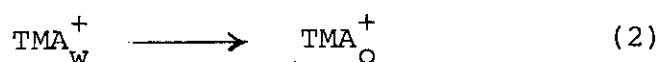


Fig. 2 Current-scan polarograms of TMA^+ at the aqueous electrolyte dropping electrode

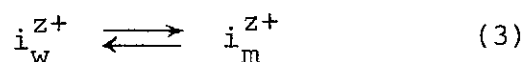
Supporting electrolyte; 0.05M LiCl+ 1M MgSO_4 in aqueous dropping electrode and 0.05M TBA^+TPB^- in organic phase

- (1) without TMA^+ in both w and o
- (2) with 5×10^{-4} M TMA^+ both in w and o
- (3) with 5×10^{-4} M TMA^+ in w and without TMA^+ in o

The current-scan polarography was satisfactorily applied to fundamental studies of the ion transfer involved in the solvent extraction systems[2,3] in order to know the extraction mechanism, and studies of the carrier-mediated ion transfer at the w/o interface[4].

1.6.2 Voltammetric interpretation of the potential at ion-selective electrode, based on current-scan polarograms observed at the w/o interface[5,6]

The equilibrium potential in potentiometry is attained when the rate of the anodic reaction is equivalent to that of the cathodic reaction. The potential at an ion-selective electrode (ISE) should also be interpreted in terms of the above mentioned concept, i.e., the ISE potential should correspond to the potential at the solution/ISE-membrane interface (w/m interface) where the rate of the anodic reaction is equivalent to that of the cathodic reaction of the ion transfer;



where i^{z+} is an objective cation with charge $z+$ in each phase.

The zero-current potential in the composite polarogram of i^{z+} , e.g., the composite polarogram of TMA^+ as shown in curve 2 in Fig. 2 corresponds to the potential generated at the ISE of i^{z+} such as TMA^+ . It is obvious from results in Fig. 2 that, only when the membrane (organic) phase contains an appropriate concentration of such objective ion as TMA^+ , the w/m or w/o interface is completely depolarized by the transfer of the ion and the composite polarogram sharply intersects the potential axis giving a stable zero-current potential.

The zero-current potential of the composite polarogram of TMA^+ shifts about 60 mV more negative when the concentration of TMA^+ in w is increased one order and the concentration of TMA^+ in o is constant (see curves 3 to 7 in Fig. 3). The shift of the zero-current potential in polarograms corresponds to the Nernstian response observed at the ISE.

The composite polarogram and the zero-current potential are affected by the anodic final rise or cathodic final descent of the residual current (curve 11 in Fig. 3), when the concentration of TMA^+ in w is sufficiently high or low. Consequently, the shift of the zero-current potential with the concentration of TMA^+ is small in these concentration ranges. The dynamic concentration range detectable at the ISE is

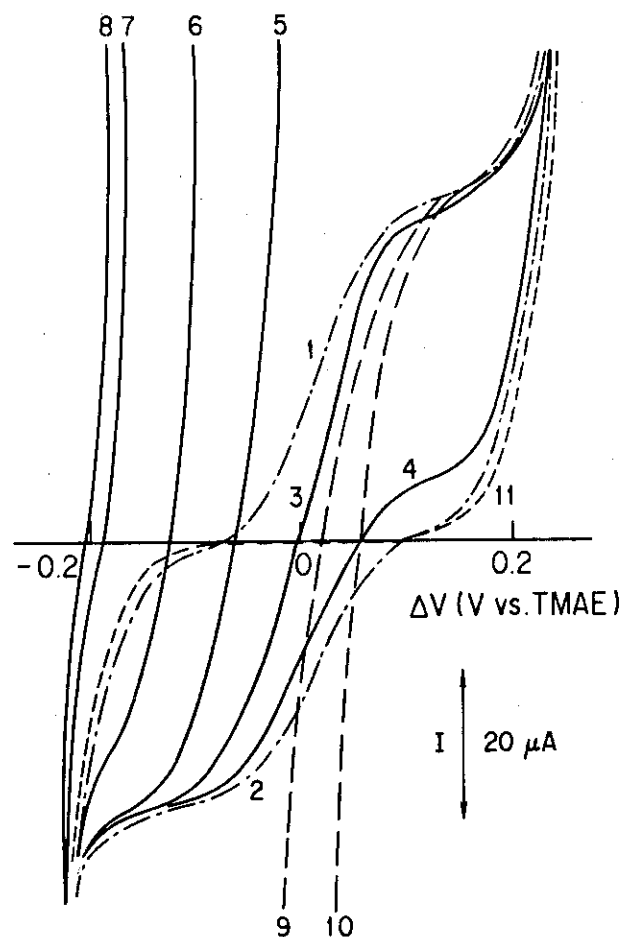


Fig. 3 Polarograms for the transfer of TMA^+ at the w/o interface

Concentration of TMA^+Br^- in w (M);
 (1,3,9,10) 5×10^{-4} , (4) 5×10^{-5} , (5) 5×10^{-3}
 (6) 5×10^{-2} , (7) 5×10^{-1} , (8) 5,
 (2,11) 0

Concentration of TMA^+TPB^- in o (M);
 (2-8) 5×10^{-4} , (9) 1×10^{-3} , (10) 5×10^{-3} ,
 (1,11) 0

Supporting electrolyte in w; 1 M MgSO_4 ,
 in o; 0.05 M TBA^+TPB^-

restricted by the same process as that which controls the shift of the zero-current potential as mentioned above. The interference from a second ion j^{z+} in the ISE measurement of i^{z+} can be explained by considering the effect of j^{z+} in w on the zero-current potential in the composite polarogram for i^{z+} .

The role of an ionophore in the membrane of the ISE can also be interpreted by considering the shift of the zero-current potential in the presence of ionophore in o .

Equations which express such characteristics of ISE as the generating potential, the interference, and the effect of an ionophore were derived using the polarographic equations for ion-transfer at the w/o interface.

(Z. Yoshida)

Publication List

- [1] Kihara, S., Yoshida, Z., Fujinaga, T.: "Current-scan polarography at the aqueous/organic solutions interface", *Bunseki Kagaku*, 31, E297(1982).
- [2] Yoshida, Z., Freiser, H.: "Ascending water electrode studies of metal extractants. Faradaic ion transfer of protonated 1,10-phenanthroline and its derivatives across an aqueous 1,2-dichloroethane interface", *J. Electroanal. Chem.*, 162, 307(1984).
- [3] Yoshida, Z., Freiser, H.: "Ascending water electrode studies of metal extractants. Role of kinetic factors in the faradaic ion transfer of metal-phenanthroline complex ions across an aqueous-organic solvent interface", *Inorg. Chem.*, 23, 3931(1984).
- [4] Yoshida, Z., Freiser, H.: "Mechanism of the carrier-mediated transport of potassium ion across water-nitrobenzene

interface by valinomycin", J. Electroanal. Chem., 179, 31(1984).

- [5] Fujinaga, T., Kihara, S., Yoshida, Z.: "Voltammetric interpretation of potential at ion-selective electrode using current-scan polarography at aqueous/organic solutions interface", Bunseki Kagaku, 31, E301(1982).
- [6] Kihara, S., Yoshida, Z.: "Voltammetric interpretation of the potential at an ion-selective electrode, based on current-scan polarograms observed at the aqueous/organic solution interface", Talanta, 31, 789(1984).

1.7 Determination of Boron in Boronated Graphite Pellets by Mass-spectrometric Isotope Dilution and Acid-base Titrimetry[1]

It is well known that boron contents in so-called boron carbides are largely dependent on the synthesis conditions.¹⁾ However, boron in homogeneous powder of a boron carbide can be determined by, e.g., acid-base titrimetry after sodium carbonate fusion with a precision of better than 1 % (relative standard deviation ; RSD). Isotope dilution combined with surface ionization mass spectrometry has given a better precision when analyzing B_4C particles (40 to 60, and 1000 mesh samples).

An acid-base titrimetric method was re-examined here in detail. Five to 10 mg of boron (boric acid solution) was added to nil to 0.5 g of purified graphite powder containing less than 0.1 ppm B, 2 to 8 ml of 5.6 w/v % calcium hydroxide suspension was added and ignited at 900 °C in a fused-silica dish for 3 to 4 h. The residue was dissolved in 5 ml of 3 M formic acid, diluted with water to 100 ml, and boiled to expel carbon dioxide for 3 min. The solution was allowed to cool to about 50 °C and 0.05 M NaOH was added to adjust the acidity at pH 6.4 to 7.0. Then, the titrimetric procedure using 0.05 M NaOH followed similarly to that described by Blumenthal.²⁾ Repeatability-precisions of 0.1 to 0.4 % (RSD) were obtained in the analysis of synthetic mixtures.

The relative standard deviations (five separate pellets) obtained in the titrimetric results for nine boronated graphite samples containing 1.75 to 8.2 wt % B (particle diameter of B_4C ; 3 to 810 μm) ranged from 1.5 % (8.13 wt % B, 270 μm) to

13 % (1.75 wt % B, 3 μ m).

It was suggested that these large scatters might be caused by an inhomogeneous boron distribution in a size (0.1 to 0.5 g) of samples taken.

(S.Tamura)

References

- 1) Beauvy, M.: J. Less-Common Metals, 90, 169 (1983).
- 2) Blumenthal, H.: Anal. Chem., 23, 992 (1951).

Publication List

- [1] VHTR Progress Report No.21, (in Japanese), informal communication, (1984).

1.8 Mass-spectrometric Isotope Dilution Analysis of Boron in Highly-irradiated U-Al-B Alloy Fuel Elements[1]

Analytical chemical procedures for determining boron contents and changes in boron isotopic compositions in highly-irradiated U20-Al80-B0.05 alloy nuclear fuel element specimens were investigated relating with an improvement program study aimed to gain high burnups of 90 % enriched ^{235}U fuel loaded in a research reactor (JRR-2).

Sample specimens (0.3 g, about 4×10^9 Bq) were decomposed with 10 ml of 1.8 M sulfuric acid. Separate aliquots weighed from the solution were utilized to determine boron contents using the isotope dilution analysis followed by Ta single filament ion source mass spectrometry, to evaluate the burnups by the ^{137}Cs method and $^{235}\text{U}/^{238}\text{U}$ ratio method. Chemical procedures involved the precipitation of Al and U by

aqueous ammonia, batch-wise anion exchange of boron using a boron-specific resin (IRA-943, 30 mesh) and methyl borate distillation. Recoveries of boron from each separation step were studied. Decontamination factors for ^{137}Cs , ^{106}Ru (^{106}Rh), ^{125}Sb ($^{125\text{m}}\text{Te}$), and whole gamma-rays radioactivities were traced in detail. Relative decontamination factors obtained were more than 5 to 40×10^3 in the above chemical procedure. The alpha- and gamma-rays activities of separated samples employed in mass spectrometry were observed as low as natural background levels. Boron contents in six specimens taken from different positions of an unirradiated fuel element plate were determined either by isotope dilution mass spectrometry or curcumin spectrophotometry. And a significant variation in the boron contents (518 to 640 ppm B) was found.

After accomplishing a study on unirradiated samples, hot-analyses were started. The amounts of boron in aliquots of irradiated sample solutions were 30 to 40 μg B. Boron blanks throughout the whole separation scheme were observed as less than 0.1 μg B.

Analytical results showed that depleted boron isotopic data could be plotted in several groups related to different burnups in the sample positions, but a detailed discussion on this matter was postponed for lack of a number of data concerned.

(S.Tamura)

Publication List

- [1] Tamura, S., Toida, Y., Yonezawa, C., Tamura, K.: "Isotope-dilution mass-spectrometric analysis of boron in highly-

irradiated U-Al-B alloy fuel-element specimens", (in Japanese), JAERI-M 82-070 (1982).

1.9 Other Activities

(1) The structure of mercury electrodeposited on platinum[1], and other metals[2] such as gold, copper, nickel, molybdenum, stainless steel, lead or zinc was investigated by the thermal evaporation technique combined with atomic absorption spectrophotometry of mercury. The structure of mercury layer was correlated with the electrolytic hydrogen evolution reaction at the mercury-film surface, which closely reflects the electronic property of the surface. Based on the results obtained, it was concluded that a nickel-based thin mercury film electrode, Ni-TMFE, was the most promising for such electrochemical uses as anodic stripping voltammetry. The electrochemical properties of the Ni-TMFE were investigated in detail[3]. This new electrode was applied to the anodic stripping voltammetry of 10^{-10} - 10^{-7} M of lead(II) and cadmium(II) in solution.

(Z.Yoshida)

(2) Titrimetric determination of uranium by Davies-Grays method combined with the gamma-ray spectrometric determination of the ^{137}Cs and ^{134}Cs was performed on the UO_2 pellet pieces taken out from the fuel rods which had been irradiated in JMTR [4]. It was confirmed that $^{134}\text{Cs}/^{137}\text{Cs}$ ratio showed linear relation with the burnup of the pellet with the relative standard deviation of less than $\pm 7\%$.

(Z.Yoshida)

(3) Application of X-ray emission induced by radioisotopic alpha-ray to trace analysis was investigated for $11 \leq Z \leq 23$ by KX-rays, and $30 \leq Z \leq 42$ by LX-rays, respectively. The lowest detection limit obtained for 40 ksec counting was 10^{-6} g for phosphorus, which is difficult to be analyzed by the X-ray fluorescence analysis using X-ray tube[5].

(Y.Baba)

Studies on surface analysis of the high temperature materials relating to thermonuclear fusion are described in Part 7.2.

Publication List

- [1] Yoshida, Z.: "Structure of mercury layer deposited on platinum and hydrogen-evolution reaction at the mercury-coated platinum electrode", Bull. Chem. Soc. Jpn., 54, 556 (1981).
- [2] Yoshida, Z.: "Preparation of an ideal mercury film electrode and its electrochemical property", Bull. Chem. Soc. Jpn., 54, 562 (1981).
- [3] Yoshida, Z., Kihara, S.: "Anodic stripping voltammetry at a nickel-based mercury film electrode", Anal. Chim. Acta, 172, 39 (1985).
- [4] Kawamura, H.^{*}, Komukai, B.^{*}, Sasaki, H.^{*}, Kawamata, K.^{*}, Izawa, K., Takeishi, H., Ito, T.^{*}, Sakurai, F.^{*}, Oyamada, R.^{*}: "Burnup evaluation of the fuel rods used as the fuel centerline temperature measuring experiment", (in Japanese), JAERI M-84-228 (1984).
- [5] Baba, Y.: "Application of X-ray emission by radioisotopic alpha-ray excitation to trace element analysis", Radio-

- chem. Radioanal. Lett., 56, 175 (1982).
- [6] Takashima, K., Nakajima, T., Okashita, H*, Shimizu, R*:
"Construction and performance of a newly developed X-ray
excited optical luminescence spectrometer", Spectrochim.
Acta, 36B, 687 (1981).
 - [7] Yahata, T*, Abe, J*, Hoshino, A.: "The effect of the con-
trolled oxygen on the incineration of radio contaminated
organic compounds", (in Japanese), JAERI-M 9974 (1982).
 - [8] Baba, S*, Ichikawa, S*, Gunji, K., Sekine, T*, Baba, H*,
Komori, T.: "The half-life of ^{152}Eu ", Int. J. Appl. Radiat.
Isot., 34, 891 (1983).
 - [9] Toida, Y.: "Spectrophotometric determination of traces of
boron in graphite", (in Japanese), informal communication,
(1984).
 - [10] Hoshino, A., Tamura, S., Fukushima, H., Watanabe, K.:
"Analysis of nuclear fuels and reactor materials ; A re-
view", (in Japanese), Bunseki, 1984, 834 (1984).
 - [11] Komori, T.: "Mass spectrometry in nuclear science and
technology ; A review", (in Japanese), Mass spectroscopy
(Japan), 33, 105 (1985).
 - [12] Kato, K.: "Deployment of inductively coupled plasma atomic
emission spectroscopy for analysis of radioactive samples
and for determination of radioactive elements ; A litera-
ture review", informal communication, (1985).
 - [13] The Comm. on Anal. Chem. of Nucl. Fuels and Reactor Mats.,
JAERI : "Cooperative analysis on hafnium in zirconium
and zirconium alloys using inductively coupled plasma
atomic emission spectrometry", (in Japanese), JAERI-M
85-028 (1985).

2. PREPARATION, ANALYSIS AND CERTIFICATION OF REFERENCE MATERIALS

T.Adachi, H.Fukushima, K.Gunji, H.Hashitani^{*},
A.Hoshino, S.Iso, M.Ito, K.Izawa^{*}, K.Kato,
T.Komori, T.Nakajima^{*}, K.Takashima, H.Takeishi,
K.Tamura, S.Tamura, Y.Toida and C.Yonezawa^{*}

2.1 Reference Materials of Zirconium and its Alloys, JAERI-Z11 to -Z16

2.1.1 Introduction

Several kinds of reference materials have been provided since 1968, under the cooperation of the Committee on Analytical Chemistry of Nuclear Fuels and Reactor Materials, JAERI, essentially for national needs in the field of nuclear science and technology.

Among these standards, zircaloy reference materials, JAERI-Z1 to -Z3 were widely used by many analysts working at nuclear energy facilities for calibration in X-ray fluorescence spectrometric (XRF) and in optical emission spectrometric methods, and for validation of the methods newly developed. Because of a small number of stock and the high demand for these standards, the inventories were rapidly depleted and the supply was exhausted within several years after their issue. In the trade of zircaloy material for cladding tube, however, some inconsistencies in the analytical values for hafnium happened to occur. After that, the reason was turned out to be due to the discrepancy in the standards used for calibration.

These situations stressed the importance and need for an accurate standard material. Therefore, we decided the renewal and started the production of raw materials in March 1974. One or two years later, National Bureau of Standards, U.S.A., planned to prepare new zirconium and zircaloy standard reference materials, and issued them in 1980 with certificates for hafnium, based on the results of isotope dilution spark source mass spectrometry (IDSSMS) and neutron activation analysis (NAA).

In June 1979, JAERI-Z11 to -Z14 were issued with provisional certificates for alloying elements (Sn, Fe, Cr and Ni), based on the results obtained by collaborative analyses using XRF, and for hafnium, based on the result obtained by NAA carried out at JAERI. In this case, the values of JAERI-Z1 to -Z3 were used as calibration standards.

In June 1983, JAERI-Z11 to -Z18 were issued after the certification through the collaborative analyses of alloying and impurity elements except hafnium. The certificates for hafnium were obtained by accurate isotope dilution surface ionization mass spectrometry (IDMS). The certificate for JAERI-Z11 to -Z16 is shown in Fig. 1.

(T.Komori)

2.1.2 Preparation and Homogeneity Test of JAERI-Z11 to -Z16

(i) Preparation of JAERI-Z11 to -Z16 [1]

JAERI-Z11 to -Z14 are intended for use in the calibration of apparatus and method used in the analysis of zircaloy for alloying elements (Sn, Fe, Ni and Cr) and impurity elements (Hf, B, Cd, U, Cu, Mn, Pb, Al, Si, Ti, Mo and W), and available

in disk form (32 mm in diameter, 20 mm thick and 110 g in wt.). The raw materials of the standard were obtained from Central Research Laboratories, Sumitomo Metal Industries Ltd., in March 1978. The material for each standard (Z11 to Z13) was doubly melted with a consumable electrode arc furnace in an argon atmosphere and in a vacuum. The material for Z14 was melted four times in order to obtain the intended concentration for each of added elements and achieve a uniform distribution throughout the material. Each ingot obtained by melting was forged, formed, lathe cut, numbered, and finally processed to each standard.

The preparation process for each standard is shown in Figs. 2 and 3.

JAERI-Z15 and -Z16, zirconium metals, are intended essentially for use in the analyses of low concentrations of hafnium and are available in plate form (30 mm square, 2 mm thick and 12 g weight). The raw materials of the standards were obtained from Technical Research Center, Nippon Mining Co., Ltd., in September 1976. The zirconium sponge used for Z15 and Z16 was obtained by purifying zirconium oxychloride (reactor grade) using thiocyanate-MIBK solvent extraction method. The zirconium sponge purified thus (hafnium contents ; 2 and 37 ppm) was melted with an electron beam skull furnace. Each ingot obtained by melting was forged, formed, rolled, washed with an acid, numbered, and finally processed to each standard.

The preparation process for each standard is shown in Fig. 4.

(ii) Homogeneity test

The homogeneity test was done on the alloying elements by XRF, and on hafnium by NAA, respectively, at JAERI. The criteria for homogeneity were as follows ; (1) the target precision was set at 1 % or better for the alloying elements by the above method, (2) that for more than 50 ppm on hafnium at 2 % or better, and (3) that for less than 50 ppm of hafnium at 5 % or better. The homogeneity test was done on the samples taken, in a ratio of one to nine , based on the table of random numbers. Based on the results of homogeneity test, the range for distribution was decided.

The specimens in the form of turnings, which were obtained from the ranges of the materials satisfying the criteria for homogeneity test, were used for the collaborative analyses for certification.

(K.Takashima)

JAPAN ATOMIC ENERGY RESEARCH INSTITUTE

Certificate of Analysis

Certified Reference Materials
 JAERI-Z11, Z12, Z13, Z14, Z15, Z16
 Zirconium and Zircaloy

Certified Value

	Z11	Z12	Z13	Z14	Z15	Z16
	%					
Sn	1.83	0.92	1.48	0.47		
Fe	0.209	0.129	0.136	0.093		
Cr	0.041	0.013	0.098	0.150		
Ni	0.021	0.094	0.058	<0.001		
	ppm					
Hf	71	128	72	220	2	37
B	1.1	3.7	<0.2	<0.2		
Cd	<0.1	<0.1	<0.1	<0.1		
U	0.8	1.1	<0.5	<0.5		
Cu	40	98	8	11		
Co	6	20	<3	49		
Mn	5	28	4	7		
Pb	12	11	5	3		
Al	15	86	53	130		
Si	57	95	21	124		
Ti	28	93	4	3		
Mo	10	46	<2	<2		
W	13	32	7	43		

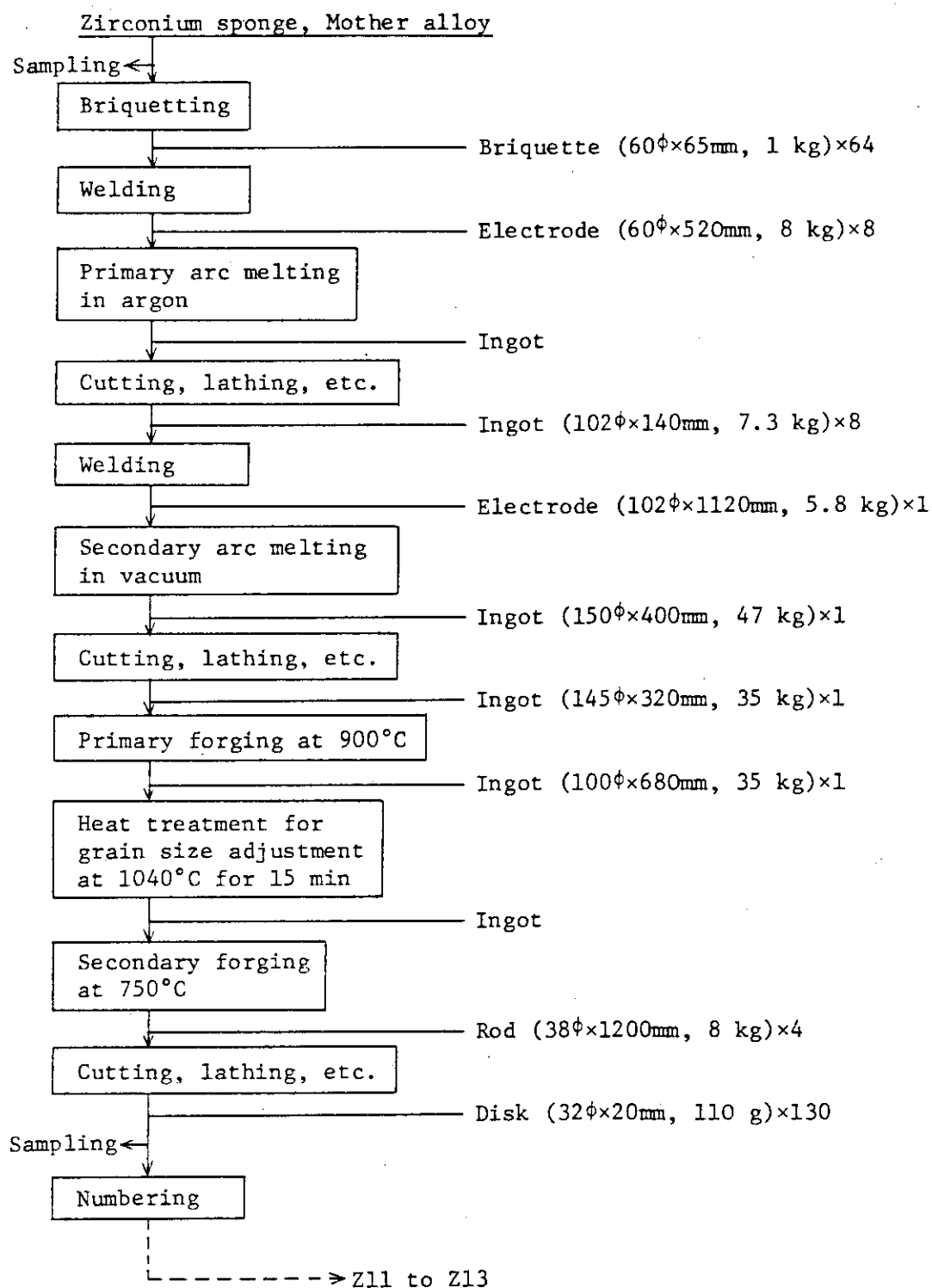
Additional information.

1. Analytical values for Hf(Average $\pm 3\sigma$) were : Z11 = 71.1 ± 0.5 (n=5), Z12 = 128.4 ± 0.8 (n=5), Z13 = 72.2 ± 0.8 (n=4), Z14 = 220.3 ± 1.5 (n=4), Z15 = 2.0 ± 0.2 (n=3), Z16 = 37.0 ± 0.5 (n=5).
2. Analytical values for B by ID-MS were : Z13 = 0.04, Z14 = 0.17.
3. Analytical values for U(Average) were : Z13 = 0.34, Z14 = 0.24.

July 1983

Analytical Chemistry Laboratory,
 Japan Atomic Energy Research Institute
 Tokai-mura, Ibaraki-ken, Japan

Fig. 1 Certificate of JAERI-Z11 to Z16



φ mark shows diameter in mm.

Fig. 2 Preparation process of JAERI-Z11 to Z13

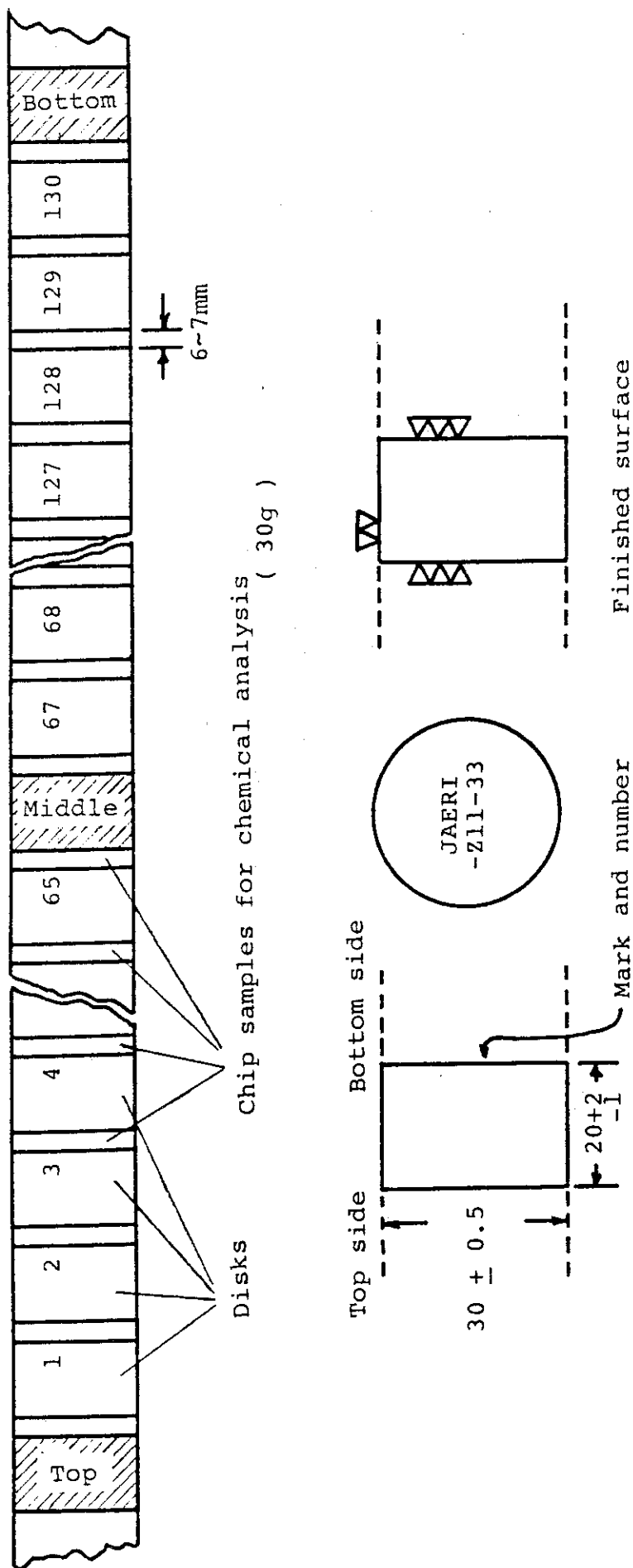


Fig. 3 Preparation and surface finish of the disk sample

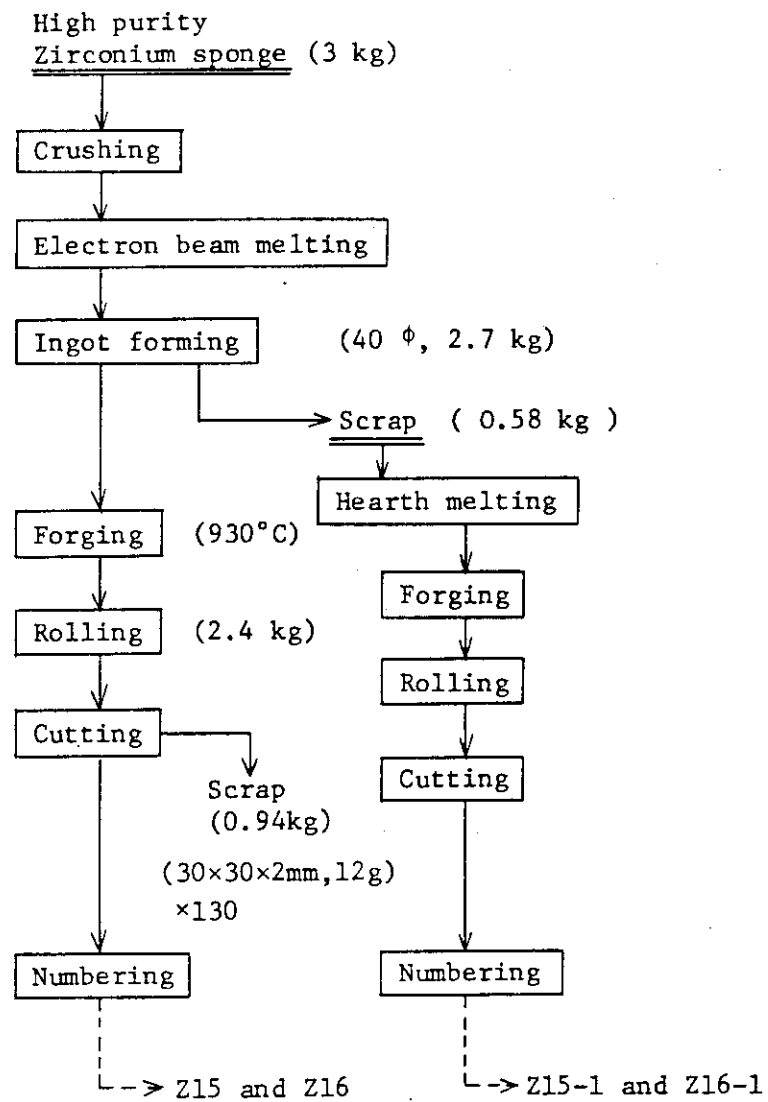


Fig. 4 Preparation process of JAERI-Z15 and Z16

2.1.3 Collaborative Analysis

Collaborative analysis for certification has been carried out according to the former mode ; (1) Proposal of the method of determination, (2) Development, verification and training of the method, (3) Performance of collaborative analysis. The principle to search for the true value became deeper by adopting the latest international concepts such as accuracy base chemical measurements and the hierarchy for methods of determination. In Table 1, the methods are summarized. The methods and modifications proposed for respective elements are as follows (for Hf, see 2.1.4).

Tin : The precise coulometry was developed as a definitive method. Iodate titrimetry as a reference method was modified.

Iron : The modified method for determining iron, nickel and chromium at the same time was proposed.

Chromium : High purity reagent has been used. Sensitivity gained about 20 % higher but iron interference was same as that using former reagent.

Boron : Various methods using curcumin were used for the analysis of the common samples. Curcumin photometry after distillation was finally adopted. The analytical results by isotope dilution mass spectrometry (IDMS) showed at first some 10 % higher values than those obtained by the above mentioned method. It was proved that small amount of spiked boron was co-distilled with water during dissolution. Only sulfuric acid was used to dissolve the sample in the IDMS method, to avoid co-distillation of spiked boron.

Cadmium, Copper, Cobalt, Manganese and Lead : Atomic absorption spectrophotometry after extraction or ion-exchange separation

was applied for these five elements using the same solution.

Uranium, Aluminum and Titanium : The new cation-exchange separation method using $\text{HF-H}_3\text{BO}_3$ media was developed (see 1.1).

Silicon : Effect of co-existing zirconium was investigated.

And it was modified so that the calibration curve was made in the presence of small amount of zirconium.

Molybdenum : The photometric methods were used without modification.

Tungsten : The modified thiocyanate-photometric method was proposed.

(T.Adachi)

Table 1 Methods used for collaborative analysis

Elements	Methods used
Sn :	①Coulometric titration (controlled current), ②Iodate titration after reduction with Al, ③8-Quinolinol extraction-photometry.
Fe :	①1,10-Phenanthroline photometry, ②Thiocyanate photometry.
Ni :	①Dimethylglyoxime extraction-photometry, ②Dimethylglyoxime bromine photometry.
Cr :	①Diphenylcarbazide photometry, ②Diphenylcarbazide photometry after separation of iron by ion exchange.
Hf :	Isotope dilution mass spectrometry, supported by isotope dilution spark source mass spectrometry (NBS) and isotope dilution neutron activation analysis.
B :	①Curcumine photometry, ②Isotope dilution mass spectrometry.
Cd, Co, Cu, Mr., Pb :	①Atomic absorption spectrophotometry after separation by ion exchange, ②Atomic absorption spectrophotometry after separation by DDTC extraction.
U :	Arsenazo III photometry after separation by ion exchange.
Al :	After ion exchange separation ; ①8-Quinolinol extraction-photometry, ②ICP emission spectroscopy, ③Atomic absorption spectrophotometry.
Si :	Photometry as molybdenum blue.
Ti :	①Diantipirylmethane photometry, ②Sulfosalicylic acid photometry, ③Thiocyanate photometry, ④ICP emission spectroscopy.
Mo :	①Thiocyanate extraction-photometry, ②8-Quinolinol extraction-photometry, ③Dithiol extraction-photometry, ④ICP emission spectroscopy.
W :	①Thiocyanate extraction-photometry, ②Dithiol extraction-photometry.

2.1.4 Determination of Hafnium in Certified Reference

Materials JAERI-Z11 to -Z16 and NBS SRM 1234 to 1239 by Isotope Dilution Surface Ionization Mass Spectrometry [2]

The contents of hafnium ranging 2 to 440 ppm Hf in seventeen certified reference materials prepared, in a separate manner, at Japan Atomic Energy Research Institute (JAERI) and National Bureau of Standards (NBS, USA) were accurately determined by isotope dilution surface ionization mass spectrometry (IDMS).

Approximately 1 to 1.2 g of the chipped sample was accurately weighed and decomposed in 20 ml sulfuric acid by heating with addition of some tens to hundreds micrograms of a spike isotope (89 atomic % ^{177}Hf). A weighed aliquot of the solution amounting to about 0.2 g of sample was taken into a 100 ml fused-silica dish and heated to dryness. The residue was dissolved in 10 ml of 0.63 M sulfuric acid and loaded on the top of a strongly-basic anion exchange resin column (Dowex 1X-8, 200 to 400 mesh, 20 dia. x 200 length, mm) to elute hafnium with 0.63 M sulfuric acid. Eluted fractions of hafnium (150 to 200 ml) were collected in a 300 ml fused-silica beaker and evaporated to dryness. Several elution curves were traced by means of inductively coupled plasma atomic emission spectroscopy (ICP-AES). The recovery of hafnium from the ion exchange was greater than 96 %.

The mass-spectrometric sample was prepared by dissolving the above residue in sub-ml of 0.63 M sulfuric acid after decomposing tiny resin particles by gently heating with a small portion of hydrogen peroxide water.

Isotope ratios of hafnium and zirconium were observed by

a carbonization technique.¹⁾ This involved coating several μl of sulfuric acid solution of the element (15 to 30 μg Hf or Zr) on a rhenium-ribbon filament with addition of deionized dilute glycerol solution (150 to 300 μg glycerol) and heating them in an ion source of a mass spectrometer to form intermediate carbon-containing compound states before high-temperature thermal ionization of the element. Stable ion currents of 0.3 to 1×10^{-11} A (total Hf^+ ion signals) could be detected using a Faraday cup collector and maintained for a few to several hours. Repeatability-precisions of 0.1 to 0.3 %, and 0.1 to 0.5 % (relative standard deviation ;RSD) on natural major isotope ratios for a short period of time (1 to 3 h), and for a long period of time (beyond several h), respectively, were observed. Ratio-taking was usually carried out on 8 to 10 ratios of each isotope pair. To confirm the accuracy of isotopic compositions calculated from the raw isotope ratios thus observed, a comparison was made with some of the worldwide reported values. Agreements between the observed values and reported ones converted to atomic weight were better than 0.002 %.

A strictly regulated analytical pattern was taken to obtain precisely repeatable isotope ratios in dilution works of the element. Besides, a rather slow heating-rate of the filament, one sample per day, enabled us to measure the isotope ratios of such a high ionization potential element with reasonable precisions.

The elemental concentrations of ^{177}Hf and ^{91}Zr spike solutions were calibrated by isotope dilution utilizing a variety of analyzed pure-metal reagents of which major impurity was due to zirconium or hafnium, vice versa. These were again deter-

mined by isotope dilution with a typical precision of 0.3 % (RSD). The estimated uncertainty in a sum of other impurities, except for Zr or Hf, seemed much less than 50 to 500 ppm, i.e., 0.00005 to 0.0005 in purity factors as unity.

In order to minimize the degree of the effect of so-called isotopic mass discrimination, inevitable in any mass spectrometry, the isotope dilution calculation was performed on multiple major isotope ratios, e.g., $^{178}\text{Hf}/^{177}\text{Hf}$, $^{179}\text{Hf}/^{177}\text{Hf}$, and $^{180}\text{Hf}/^{177}\text{Hf}$ in the hafnium determination, and its averaged value were taken to obtain the result in a separate analysis run. Anomalous isotope ratio values could thus be sensitively detectable by plotting multiple isotope ratios, e.g., $^{180}\text{Hf}/^{177}\text{Hf}$ ratio as abscissa, $^{178}\text{Hf}/^{177}\text{Hf}$ and $^{179}\text{Hf}/^{177}\text{Hf}$ ratios as ordinate.

Then, hafnium contents in zirconium (JAERI-Z15 and -Z16 and NBS SRM 1234 to 1236), Zircaloy 2 (JAERI-Z11 to -Z14) and Zircaloy 4 (NBS SRM 1238 and 1239) were confirmed with precisions nearest to 0.25 % (RSD) including sample inhomogeneity, if any. Two outliers were NBS SRM 1237 (32.7 ppm Hf, 1.3 C.V.%) and JAERI-Z15 (1.96 ppm Hf, 3.2 C.V.%).

A harmony test was performed between the intensity signals observed by other instrumental methods such as XRF and ICP (DCP)-AES and the results by isotope dilution analysis here reported. The test has covered a wide range of 2 ppm Hf (JAERI-Z15) to 440 ppm Hf (NBS SRM 1215) and revealed that the mass-spectrometric results were very excellent.

(S.Tamura)

2.1.5 Certification and Evaluation of Analytical Results[3]

In June 1979, JAERI-Z11 to -Z14 were issued with provisional certificate for Sn, Fe, Cr and Ni based on the result of collaborative analysis by XRF using the reference materials, JAERI-Z1 to -Z3. The certified values for these elements were decided in June 1980, based on the result of the collaborative analysis using absolute chemical methods.

The certified value for Hf was decided by IDMS at JAERI doing also NBS SRM 1234 to 1239. The results of this method agreed well with those of isotope dilution spark source mass spectrometry done at NBS and isotope dilution neutron activation analysis done at JAERI, and was found to be best estimate for Hf.

The certified values for other impurity elements were decided in July 1983, based on the result of collaborative analysis using absolute chemical methods.

Tin : Certified value was decided based on the collaborative result (titrimetry and photometry) and the result obtained by the definitive method (precise coulometry). Compatibility of certified value with those of JAERI-Z1 to -Z3 and NBS SRM was also checked by the collaborative analysis using XRF.

Iron : The analytical method was same as that used at the former time. The collaborative analysis showed a little higher result compared with the provisional certificate obtained by XRF. But the difference was less than 1 %.

Nickel : Nickel was determined at the same period with the determination of tin and iron, and any problem was not found.

Chromium : Collaborative analysis was delayed to obtain high purity reagent. The protocol was precisely prepared for the me-

thods (Table 1). The result showed no difference between the two methods. The mean values for Z11 to Z14 were a little smaller than provisional certificates. The effect of iron on photometric determination on chromium was not clear.

Hafnium : In June 1979, provisional values represented as Hf to Zr ratio were decided by NAA using values obtained by emission spectrography for JAERI-Z1 to -Z3. Certification was done using IDMS as a definitive method and isotope dilution neutron activation analysis (IDNAA) as a supporting method[4]. Analysis by IDMS took three years including the investigation on isotopic ratio measurements of hafnium. Calibrated spike values, obtained by several hafnium metals of different chemical purities, agreed well in less than 0.1 %. This showed that accuracy of the analytical results obtained was within 0.2 % at the 95 % confidence level. Compared with the results obtained at the former time by IDMS, excellent results having higher accuracy and precision were acquired.

The NBS SRM 1234 to 1239 were also analyzed at the same time in JAERI. In NBS, on the other hand, they didn't decide the certified value at that time, because there existed appreciable amount of discrepancy between the results obtained by isotope dilution spark source mass spectrometry (IDSSMS) and those by NAA. So they asked JAERI to analyze hafnium value using IDMS as an accurate method.

The result obtained by IDNAA as a supporting method carried out by JAERI agreed well with those by IDMS for JAERI CRM and NBS SRM.

Boron : Distillation curcumin spectrophotometry as a reference method was finally adopted for the collaborative analysis by

seven skilled laboratories. The most important thing in the determination of boron was to minimize the contamination. So collaborative analysis was done after practicing well with several kinds of common samples. Certified value was determined by this method considering IDMS result. It was informative that systematic error was found even in the precise IDMS method.

Cadmium : The results obtained by atomic absorption spectrophotometry (AAS) were less than 0.1 ppm for all CRM and common samples. By flameless AAS, some signals corresponding to 11 - 15 ng were found, but these were proved to be originated from reagents and water used.

Uranium : Collaborative analysis was carried out by ten laboratories using ion-exchange separation followed by Arsenazo III photometry after protocol was well examined using common samples. The results agreed well except one extraordinary result (See 1.1.3).

Copper : Analytical results were in good accordance except one laboratory for Z14. The reason was not known, but repeated analysis was done.

Cobalt : Analytical results varied widely for Z14. Some factors such as the bias between methods of analysis or inhomogeneity of samples were inquired. But the reason for such large scatters was not clear. Repeated analysis was done by two laboratories.

Manganese : Only in Z12 appreciable amount of manganese was found, and its analytical results were in good agreement.

Lead : Existence of lead in zirconium and zircaloy was neither considered at all in the beginning, nor was its certification

planned. In the course of practicing cadmium determination in common samples, it was recognized that lead was actually incorporated. No problem was found in the determination of lead. Analytical results for Z13 and Z14 were decided as certified values based on judgement.

Aluminium : Collaborative analysis was done without complete practice of the analytical method using common samples. So results for Z11 to Z14 varied somewhat large. The most important thing in the determination of aluminium is to prevent contamination from reagents and atmosphere. It was insufficient in the protocol of analysis to minimize such contamination. The certified values were considered to show a state of the art.

Titanium : In the four methods used, there were no discrepancy. Certified values for Z11 and Z12 were decided by the mean values and those for Z13 and Z14 by judgement.

Silicon : Except for the large scatters for lower content Z14, there was no problem in the collaborative analysis.

Molybdenum and Tungsten : Both elements do not exist actually in zircaloy. Mean analytical values were decided as certified values.

(T.Adachi)

Reference

- 1) Tamura, S.: Mass Spectroscopy (Japan), 23, 49 (1975).

Publication List

- [1] The Comm. on Anal. Chem. of Nucl. Fuels and Reactor Mats.,
JAERI : "Preparation of zirconium and zirconium-based alloy
certified reference materials JAERI-Z11 to -Z18", (in
Japanese), JAERI-M 83-241 (1983).
- [2] Tamura, S., Tamura, K., Kato, K.: "Determination of haf-
nium in zirconium and its alloy certified reference mate-
rials by isotope dilution surface ionization mass spectro-
metry", (in Japanese), 30th Annual Conf. Jpn. Soc. Anal.
Chem., Kyoto, Abstracts p.419 (1981).
- [3] The Comm. on Anal. Chem. of Nucl. Fuels and Reactor Mats.,
JAERI : "Collaborative analysis for certification of zir-
conium and zirconium base alloy reference materials JAERI-
Z11 to -Z16", (in Japanese), JAERI-M 85-038 (1985).
- [4] Yonezawa, C., Komori, T.: "Determination of hafnium in
zirconium and its alloys by stable isotope dilution-neu-
tron activation analysis", Anal. Chem., 55, 2059 (1983).

2.2 Certification of JAERI-Z17 and -Z18 for Carbon

JAERI-Z17 and -Z18 are intended for use in the determination of carbon, and are available in chip form, approximately 4 x 1 x 0.5 mm, in glass bottle, which contains nominal 25 g. The base materials for Z17 and Z18 were obtained from the commercially available Zircaloy 2 and Zircaloy 4 tube shells, respectively, which are used as cladding materials of fuel rods.

Collaborative analysis for certification were carried out with the participation of ten laboratories, using the methods of coulometry (5 labs.), infrared absorption (4 labs.) and thermal conductivity (1 lab.).

The averages of the total analytical values were 0.010 ± 0.001 % ($n = 30$) for Z17 samples, and 0.015 ± 0.001 % ($n = 30$) for Z18 samples, respectively, and the average of the values obtained for NBS SRM 360a at the same time was 136 ± 10 ppm, comparing with the certified value, 136 ppm.

In consideration of the chemical requirements (≤ 270 ppm) of zircaloy tube and the analytical precision, the certified values for carbon in Z17 and Z18 were decided as 0.010 % and 0.015 %, respectively[1].

(A.Hoshino)

Publication List

- [1] The Comm. on Anal. Chem. of Nucl. Fuels and Reactor Mats., JAERI : "Determination of carbon in Zircaloys", (in Japanese), JAERI-M 83-035 (1983).

2.3 Preparation, Analysis and Certification of a Uranium Isotope Certified Reference Material JAERI-U5

A series of uranium isotope certified reference material JAERI-U5, No.1 to No.6, the successive CRM to JAERI-U3, was prepared and certified under the recognition of the Committee on Analytical Chemistry of Nuclear Fuels and Reactor Materials, JAERI.

The reference material consists of six samples of a variety of uranium isotopic enrichment (0.2010, 0.7987, 1.500, 2.561, 3.601, 4.509 wt percent ^{235}U) and each sample contains 2.00 g of U_3O_8 powder. The materials are packed in bottles of low-potassium glass for a possible use in non-destructive gamma-rays spectrometric assay. The certified values of isotopic compositions were decided by evaluating a mass spectrometric collaborative analysis that was performed at two laboratories, i.e., Tokai Works, Power Reactor and Nuclear Fuel Development Corporation, and Analytical Chemistry Laboratory, JAERI.

Repeatability-precisions of certified isotopic compositions in JAERI-U5, No.1 to No.6, are several times better than those given on a predecessor JAERI-U3. Accuracy of certified values stands on NBS SRM U-005 to U-930 which are widely adopted in determining the instrumental and procedural bias.

Information on chemical impurity species and its amounts is also available.

The situation concerning necessity of these kinds of reference materials, preparation flowsheets, isotopic homogeneity test, evaluation of mass-spectrometric collaborative analysis, and measurement procedures were reported in details elsewhere[1].

(S.Tamura)

Publication List

- [1] Tamura, S., Hashitani, H.(eds.): "Preparation and certification of a uranium isotope certified reference material JAERI-U5", (in Japanese), JAERI-M 82-053 (1982).

2.4 Evaluation and Perspective of Measurement Techniques for Uranium Isotopic Assay in Nuclear Fuel Cycle

A sub-committee on uranium isotopic assay was temporarily organized during 1979 to 1982 under the auspices of the Committee on Analytical Chemistry of Nuclear Fuels and Reactor Materials, JAERI.

The sub-committee consociated fifteen specialists on the matter from eight independent organizations in this country. The following subjects were discussed ; (1) the perspective of facing importance of isotopic assay techniques in nuclear fuel cycle, (2) the reality of control analyses in fuel fabrication factories, (3) the technical pursuance in safeguard inspection analysis, (4) the evaluation of present-day state and its direction of near future development of techniques such as mass spectrometry, passive and active assay, optical spectral method, and (5) the necessity of analytical reference materials for destructive and non-destructive assay R/D.

A resulting activity report of the sub-committee was issued elsewhere[1] and this could be helpful to have a good grasp of the problems concerned.

(S.Tamura)

Publication List

- [1] The Comm. on Anal. Chem. of Nucl. Fuels and Reactor Mats., JAERI : "A committee report on the state-of-art of uranium enrichment measurement techniques", (in Japanese), JAERI-M 82-051 (1982).

3. ANALYTICAL CHEMICAL SERVICE AND SCIENTIFIC GLASSBLOWING UTILIZATION

3.1 Service Analysis

The laboratory performs a wide variety of analytical service work. Much of it is short-time in nature and comes from other laboratories and programs within JAERI. In order to carry out an elemental and isotopic analyses, the functions of service analysis cover the following items ; absorption spectrophotometry, electrochemical analysis (polarography, coulometry, flow-coulometry etc.), gas analysis (gas chromatography, inert gas fusion etc.), atomic absorption spectrophotometry, flame spectrophotometry, emission spectrometry, X-ray fluorescence spectrometry, X-ray optical luminescence technique, mass spectrometry, thermal analysis and so on. Sometimes, consultation, collaboration and quality assurance related to chemical measurements are also contained.

Some of the typical service analyses carried out for these several years are described in the followings.

For the chemical characterization of fuel compacts used in Very High Temperature Reactor Critical Assembly (VHTRC), analyses were performed on kernels, particles, compacts and graphite used as matrix of compacts. The analyses included uranium by gravimetry, isotopic composition of uranium by mass spectrometry, moisture by gravimetry and coulometry, hydrogen by impulse heating-inert gas extraction-gas chromatography, and metallic impurities (Al, Ag, B, Cd, Cr, Cu, Fe, Mg, Ni, Si, Sm, Eu, Gd and Dy) by emission spectrometry, X-ray excited optical luminescence and

spectrophotometry[1 - 4]. Boron in mixtures of boron carbide and graphite (burnable poison) was also determined. The heat resistant alloys, including improved ones, were analyzed for the impurities and/or components.

In relation to the nuclear fusion, the method developed (see 1.3.1) was applied to the determination of hydrogen in lithium oxides. The isotopic analyses of lithium in some lithium-containing compounds like Li_2O were carried out by mass spectrometry. In addition, an apparatus for isotopic analysis of lithium, based on the optical spectral method developed at the laboratory (see 1.5.2), was designed and installed at the Separation Engineering Laboratory for isotope separation work.

In the field of the nuclear safety, analyses of primary cooling water and some structural materials such as aluminum, zircaloy etc., were performed in relation to reactor operation. The gaseous components, generated from various kinds of solidified wastes and the low-level radwastes at the incineration, were identified and measured by mass spectrometry.

In relation to the basic research and developmental work, e.g., the irradiated UO_2 pellets were analyzed for the O/U ratios by flow-coulometry and spectrophotometry (see 1.4.2), uranium by titrimetry, and plutonium by isotope dilution mass spectrometry.

The latest states of service analysis will be published elsewhere in the near future.

(T.Komori)

Publication List

- [1] VHTR Progress Report No.19, (in Japanese), informal communication, (1982).
- [2] VHTR Progress Report No.21, (in Japanese), informal communication, (1984).
- [3] VHTR Progress Report No.22, (in Japanese), informal communication, (1985).
- [4] Oku, T., Eto, M., Imai, H., Hoshino, A.: "Physical, chemical and mechanical properties of ASR-0RB and ASR-1RB carbon", informal communication, (1985).

3.2 Glassblowing

K.Kimura, R.Sato, K.Obara
and T.Ideta

At Tokai Research Establishment, a glassblowing shop was established in 1958 to supply the specific needs for the chemists, physicists and associated technical people for research and development work in the nuclear-related fields. Owing to the unique properties of glass, such as transparency, strength, formability, cleanability, chemical inertness and electrical resistance, the scientific glassblowing services have been utilized for the large majority of broadly varied research and development programs throughout Tokai-site Laboratories (Tokai, Oarai and Naka Research Establishments).

The range of glassblowing shop services includes grinding, polishing, forming and molding, chemical silvering, annealing, encapsulation, fabrication of special glass equipment and bench systems, design and design coordination, preparation of models, and the development of new techniques concerned with glassblowing.

The glassworking equipments in the glassblowing shop are as follows ;

- (1) Lathe, glass
- (2) Drill
- (3) Lap
- (4) Cutting machine
- (5) Oven, annealing
- (6) Polishing machine
- (7) Vacuum system

The typical works made for these three years are written in the followings ;

- (1) An atomic hydrogen-generating apparatus : to support the development of stabilization of the vacuum in a thermonuclear fusion reactor by changing hydrogen atom into a getter.
- (2) A glass loop simulated with pressurized water reactor : to observe the behavior of the two phase flow at the loss of coolant accident[1].
- (3) An apparatus for incinerating the organic waste : to support the technical development for disposal of organic radioactive waste containing plutonium.
- (4) A thermosiphon apparatus : to contribute to the design and maintenance of a cold neutron source installed at JRR-3.

(K.Kimura)

Publication List

- [1] Kimura, K., Obara, K.: "Construction of a glass loop simulated pressurized water reactor", (in Japanese), JAERI-M 82-211 (1983).
- [2] Kimura, K., Obara, K.: "Vacuum sealing of platinum ampoule", (in Japanese), Honoho^{*}, No.21, 38 (1983).
- [3] Kimura, K., Obara, K., Sato, R.: "A flexible glass tube with O-rings", (in Japanese), informal communication, (1983).
- [4] Obara, K.: "A safety glassblowing apparatus for tritium-contaminated glass system", (in Japanese), J. At. Energy Soc. Jpn., 26, 134 (1983).
- [5] Kimura, K., Obara, K., Sato, R., Ideta, T.: "A device for connecting ball joints", (in Japanese), Honoho^{*}, No.26, 134 (1983).

* A bulletin of Japanese Society of Scientific Glassblowing.

A list of Patents and Utility Models

- [6] Kimura, K., Sato, R., Obara, K.: "A clamp for connecting joints", (a utility model), applied in 1982.
- [7] Sato, R., Obara, K., Ideta, T., Kimura, K.: "A jig of grooving a flange for O-ring", (a utility model), applied in 1983.
- [8] Sato, R., Obara, K., Ideta, T., Kimura, K.: "A simple glass lathe", (a utility model), applied in 1983.
- [9] Sato, R., Obara, K., Ideta, T., Kimura, K.: "An improved chuck device", (a Patent), applied in 1983.
- [10] Obara, K.: "An apparatus for glassblowing", (a patent), applied in 1983.
- [11] Kimura, K., Obara, K., Sato, R., Ideta, T.: "A shock-absorbent tube", (a patent), applied in 1985.

4. RADIOCHEMICAL STUDIES OF NUCLEAR FUELS

Y.Kobayashi, J.Akatsu and

T. Kimura

4. 核燃料の放射化学的研究

小林 義威・吾勝 常勲・木村 貴海

4.1 微量の Np, Pu, Am の相互分離と定量

4.1.1 緒言

環境放射能の測定や放射性廃棄物の処理処分に関連して、Pu などのように生体・環境におよぼす影響の大きい α 線放出核種の同定と定量を行うための簡便で信頼性の高い測定方法が必要である。これまで環境試料や放射性廃棄物中の α 放射能の測定は、主にイールドモニターを用いた水酸化物などへの共沈、イオン交換樹脂、溶媒抽出、電着などの方法で行われている。著者らは硫酸バリウムにトレーサー量の α 放射体が定量的に共沈するという Sill らの方法^{1)~3)}を応用し、より簡便で信頼性の高い測定法の開発を進めている。この方法は、簡便、迅速なこと、イールドモニターなしでも高い信頼性があること、さらに天然の α 放射体と超ウラン元素の同時定量が可能なことなどの利点がある。

α 放射体の硫酸バリウムへの共沈挙動は硫酸ナトリウム、硫酸カリウム、酸などの化学的要因により影響を受ける。しかし、これらの影響についてはあまり知られていない。これまでに、トレーサーレベルから数 mg までの範囲でウランとトリウムの硫酸バリウムへの共沈挙動〔1〕とその応用として可燃性固体廃棄物中の α 放射体の定量の研究〔2〕を行ってきた。ここでは、トレーサーレベルの Np, Pu, Am の硫酸バリウムの共沈挙動について、酸の種類と酸濃度、およびバリウム・硫酸ナトリウム・硫酸カリウム添加量の影響について検討を行った。その結果、これらの元素が少量のバリウム (0.25 mg) 添加により硫酸バリウムに定量的に共沈するだけでなく、同沈殿試料の α 線スペクトルの直接測定による核種の定量も可能であることがわかった。これらアクチノイドの 3・4 価が硫酸バリウムに共沈し、5・6 価が共沈しない性質を利用し、各元素 (U, Np, Pu, Am) の原子価を順次 3・4 価に調製することにより、連続的に各々硫酸バリウムへ共沈させ相互分離することが可能である。そこで Np, Pu, Am を連続的に相互分離するために使用する酸化剤・還元剤の選択およびその組合せを検討した。その結果、酸化剤に過マンガン酸を、還元剤に亜硝酸、ヒドロキシルアミンを順次使用することにより、簡単かつ定量的に Np, Pu, Am を相互分離できることがわかった。

4.1.2 実験

(a) 試料溶液

元素組成の異なる3種類の試料(① Np・Pu・Am, ② Pu・Am, ③ Am)をすべて1 M 硫酸に調製し使用した。試料を白金板上に乾燥焼付けし、全 α 線計数と α 線スペクトルを測定して決めた試料①のNp, Pu, Amの放射能比はそれぞれ全計数値の28.4%, 66.9%, 4.7%であった。試料②のPuとAmの放射能比は91.8%, 8.1%であった。試料溶液中の各元素の原子価は、酸化剤・還元剤を加えない場合の硫酸バリウムへの共沈挙動から、Npは4価が40%で5・6価が60%, AmとPuはそれぞれ3・4価であると考えられる。

(b) 沈殿試料の調製と α 放射能の測定

Figure 1に α 線計数、 α 線スペクトル測定のための硫酸バリウム沈殿試料調製の手順を示す。沈殿を0.45 μ mメンブランフィルター(47 mm ϕ)を用いて減圧ろ過した後、フィルターとともにステンレス試料皿にのせ赤外線ランプで乾燥した。沈殿試料の全 α 線計数は窓付き2 π ガスフローカウンタで測定し、 α 線スペクトルも同試料をSi表面障壁型検出器(450 mm²)で測定した。

4.1.3 結果および考察

(a) Np, Pu, Amの硫酸バリウムへの共沈挙動

Np, Pu, Amが定量的に硫酸バリウムに共沈し、かつ同沈殿試料の α 線スペクトル測定によりNp, Pu, Amをそれぞれ定量できる条件を検討した。共沈率は試料の全 α 線計数値から求めた。以下の実験で用いた試料は、 Fe^{2+} でNp(IV), Pu(IV), Am(III)に調製して使用した。

i) 酸と酸濃度の影響

0.35 M硫酸ナトリウム, 0.43 M硫酸カリウムが存在する場合は硫酸で2 N以下, 塩酸で1 N以下, 硝酸で0.5 N以下の酸濃度で, Np, Pu, Amは98%以上硫酸バリウムに共沈した。しかし, それぞれ酸濃度が上昇すると共沈率は急激に減少し, 硫酸10 Nでは5%, 塩酸, 硝酸3 N以上ではほとんど共沈しなかった。一方, 硫酸溶液でナトリウム, カリウムを加えない場合には0.1 Nで60%から10 Nで35%へと徐々に共沈率は減少した。この結果は酸の種類と酸濃度より, 硫酸ナトリウム・硫酸カリウムの存在がNp, Pu, Amの共沈に大きく影響することを示している。このことから以下の実験は0.5 N硫酸溶液中で行った。

ii) 硫酸ナトリウム, 硫酸カリウムの影響

0.43 M硫酸カリウムが存在し, 0.35 ~ 0.70 M硫酸ナトリウムが共存する条件で98%以上のNp, Pu, Amが共沈した。硫酸カリウムがない場合は同濃度の硫酸ナトリウムで約65%であった。硫酸ナトリウム濃度が増加すると共沈率は徐々に減少した。これから硫酸ナトリウムは適切な濃度では共沈を促進するが過剰になると抑制することがわかった。一方, 0.35 M硫酸ナトリウムが存在し, 0.29 ~ 0.72 M硫酸カリウムが共存する条件で98%以上が共沈した。硫酸ナトリウムがない硫酸カリウムだけの場合でも同濃度で約90%が共沈した。硫酸カリウムは, その溶解度により濃度範囲が制限されるため硫酸ナトリウムの場合のような共沈率の減少はみられなかった。以上の結果から硫酸ナトリウムに比べ硫酸カリウムは, Np, Pu, Am

の硫酸バリウムへの共沈に大きな影響をおよぼしていると考えられる。これはUの場合〔1〕と同様に、Np, Pu, Amがカリウムとの硫酸複塩をつくり硫酸バリウムへ共沈するためと考えられる。また硫酸ナトリウムの効果は、Npなどのカリウムとの複塩をつくる際の塩析剤として働いていると考えられる。

iii) バリウム添加量の影響

バリウムの添加量は共沈率と α 線スペクトルのエネルギー分解能の両方に影響するためそれらの相関々係を調べた。バリウムを0.25～1.25 mg 加えた場合は98%以上の共沈率を示すが、それより多い場合は実効的な共沈率はほとんど変わらないが沈殿試料の自己吸収による α 線計数の損失が多くなり、そのため見掛け上の共沈率は徐々に減少した。また0.25 mgより少ない場合は急激に共沈率は減少した。一方、エネルギー分解能（半値幅）はバリウム量0.25 mg以下では約110 KeV (5.16 MeV, $^{239}\text{Pu} + ^{240}\text{Pu}$) ではほぼ一定の値を示し、 α 線スペクトルから得たNp, Pu, Amの放射能比は誤差1%以内で焼付け試料から得られた値と一致した。この結果から以下の実験ではバリウムを0.25 mg 加えることにした。このときの沈殿試料の計算上の厚さは0.042 mg/cm²である。

(b) Np, Pu, Amの酸化剤・還元剤との反応

Np, Pu, Amを連続的に相互分離するために、各元素の原子価の調製に用いる酸化剤・還元剤の選択、組合せ、使用条件（添加量、温度、時間）について検討した。

i) Np, Pu, Amと酸化剤との反応

Fe^{2+} (6.5×10^{-4} M) を加えNp, Pu, Amを3・4価に調製した後、4種類の酸化剤を加え各元素の6価への酸化の割合を硫酸バリウムへの共沈率で調べた。 Fe^{2+} の添加量の約2倍のグラム当量の酸化剤を加えた結果、100℃（5分攪拌）において $\text{K}_2\text{S}_2\text{O}_8$ (Ag^+) と KMnO_4 はNp, Puを速やかに6価に酸化し、 $\text{K}_2\text{S}_2\text{O}_8$ (Ag^+)はAm(III)も約70% 6価に酸化した。 $\text{K}_2\text{Cr}_2\text{O}_7$ と KBrO_3 はそれぞれNpだけを速やかに6価に酸化した。一方室温（50分攪拌）において、 $\text{K}_2\text{S}_2\text{O}_8$ (Ag^+)によるNp, Pu, Amの酸化はいずれも不完全で、 KMnO_4 によるPu, KBrO_3 によるNpの酸化も不完全（50%）であった。以上から、Np・PuとAmの分離には KMnO_4 を、NpとPu・Amの分離には $\text{K}_2\text{Cr}_2\text{O}_7$ または KBrO_3 を100℃で用いるのが有効であることがわかった。ただし、 KMnO_4 を用いた場合は、Np, Puとの酸化還元反応と KMnO_4 自身の熱分解とにより MnO_2 が一部沈殿するため、沈殿試料の α 線スペクトルの分解能は悪くなった。

ii) 酸化剤と還元剤との反応

Np, Pu, Amを連続的に相互分離するためには、これらの元素と酸化剤・還元剤との反応だけでなく、酸化剤と還元剤との反応も考慮しなければならないため、前述の酸化剤に対応する最適な還元剤の選択を行った。酸化剤を加えた後、種々の還元剤を加え酸化剤の色の変化、 MnO_4^- (紫)・ MnO_2 (茶, 沈殿) $\rightarrow \text{Mn}^{2+}$ (淡紅), $\text{Cr}_2\text{O}_7^{2-}$ (橙) $\rightarrow \text{Cr}^{3+}$ (青緑), により酸化剤の還元反応の進行状況を定性的に評価した結果、 $\text{NH}_2\text{OH} \cdot \text{HCl}$, $\text{N}_2\text{H}_4 \cdot 2\text{HCl}$, Fe^{2+} , Ti^{3+} , H_2O_2 , NaHSO_3 は、100℃において速やかに上記の還元反応を進めることがわかった。ただし Ti^{3+} は4価に酸化された後、0.4 N以下の酸では TiO_2 (白) が沈殿した。また NaNO_2 によるCr(VI)の還元反応は上記の還元剤に比べ遅かった。

iii) Np, Pu と還元剤との反応

KMnO₄ (8.0×10^{-4} M) を加え, Np, Pu を 6 価に酸化した後, 前述の 7 種類の還元剤をそれぞれ加え, 4 価への還元を調べた。添加した KMnO₄ の約 2 倍のグラム当量の還元剤を加えた結果, H₂O₂, NaNO₂ を除きいずれの還元剤も 100 °C (5 分攪拌) において Np, Pu を速やかに 4 価に還元した。H₂O₂ の場合はさらに過剰に加える必要があった。NaNO₂ は 6 価の Np, Pu から Pu だけを選択的に還元するため, Np と Pu の分離に有効であることがわかった。このとき Np は 5 価であると考えられる⁴⁾。一方室温 (50 分攪拌) での Np, Pu の還元反応はいずれも不完全かまたは全く起きなかった。酸化剤・還元剤として加える金属イオンの共沈への影響を少なくするために, 還元剤は Np, Pu の還元には NH₂OH・HCl を, Pu の還元には NaNO₂ を用いた。

(c) Np, Pu, Am の連続相互分離

(a), (b) の結果をもとに Np, Pu, Am を連続的に相互分離する方法を検討した結果, 次の 3 通りの方法が考えられた。ここで沈殿生成はすべて Fig. 1 の条件で行い, 酸化剤・還元剤は初めに加える酸化剤・還元剤の約 2 倍当量ずつを順に加えて行った。

- ① 試料溶液に KMnO₄ を加え Np, Pu を 6 価に酸化し, まず 3 価の Am を硫酸バリウムへ共沈させ分離する。次に NH₂OH・HCl を加え Np, Pu を 4 価に還元し, 続いて K₂Cr₂O₇ を加え Np だけを再び 6 価に酸化し, 4 価の Pu を共沈分離する。最後に再び NH₂OH・HCl で Np を 4 価に還元し共沈分離する。
- ② ①の方法で K₂Cr₂O₇ のかわりに KBrO₃ を加え Np を 6 価に酸化する。
- ③ Np, Pu を KMnO₄ で酸化し, まず 3 価の Am を分離した後, NaNO₂ を加え Np を 5 価に, Pu を 4 価に還元し, Pu だけを共沈分離する。次に NH₂OH・HCl で Np を 4 価に還元し共沈分離する (Fig. 2)。

上記の①～③の方法に従って分離を行った結果, ②の方法ではほとんどの Pu が Np と共に最後の沈殿に共沈した。この原因を調べるために, まず KBrO₃ を加えるときに既に存在している Mn²⁺ と KBrO₃ との反応を検討したところ, KBrO₃ により Mn²⁺ が酸化されて MnO₂ が生成することがわかった。そこで Pu (IV) と KBrO₃, MnO₂ との反応を調べたところ, KBrO₃, MnO₂ それぞれ単独では Pu (IV) はほとんど酸化されないが, KBrO₃ と MnO₂ が共存すると速やかに Pu (IV) が 6 価に酸化されることがわかった。したがって, KMnO₄ と KBrO₃ を連続的に用いる②の方法では Np, Pu, Am の相互分離は不可能である理由が明らかとなった。一方, ①と③の方法では, ほぼ同様に良好な結果が得られた。③の方法で分離した結果を Table 1 に示す。各元素は硫酸バリウムの各フラクションへそれぞれ 97 % 以上が共沈し, 混入する他の元素はほぼ 1 % 以下であった。各フラクションの合計では Np が 97.2 % の他, Pu, Am は共に 99 % 以上が硫酸バリウムに共沈した。①, ③の方法は Sill が報告している方法³⁾ すなわち①の方法において還元剤として NH₂OH・HCl の代わりに酸化剤に対し過剰量の H₂O₂ を使用する方法に比べ, 簡便だけでなく分離の精度も高いことがわかった。さらに①と③の方法を比較すると, Np, Pu, Am の分離の結果はほぼ同様であるが, ③の方法が酸化剤として添加する金属イオンが少ないこと, アクチノイド元素の酸化還元の回数が少ないことなどから優れた方法である。またウランが含まれる場合は③の過程でウランは 6 価の

ままであると考えられるため、Np を分離後、 Ti^{3+} などの還元剤で4価に還元し硫酸バリウムに共沈分離できると予想される。

4.1.4 結 論

本実験において、トレーサーレベルで共存するNp, Pu, Amが硫酸バリウムに定量的に共沈するだけでなく、沈殿試料の α 線スペクトル測定により各元素を同時定量可能な条件 (Fig.1) を見出した。さらにこの条件のもとで得られたNp, Pu, Am の連続相互分離法 (Fig. 2), すなわち酸化剤に過マンガン酸を、還元剤に亜硝酸、ヒドロキシルアミンを用いる分離方法は、従来の方法に比べ酸化剤・還元剤として添加する金属イオンが少ない、アクチノイド元素の酸化還元回数が少ないなど、簡便だけでなく分離の精度も高い優れた方法であることがわかった。

(T. Kimura)

References

- 1) Sill, C.W., Puphal, K.W., Hindman, F.D.: Anal.Chem., **46**, 1725(1974).
- 2) Sill, C.W., Williams, R.L.: Anal.Chem., **41**, 1624(1969).
- 3) Sill, C.W.: Health Physics, **17**, 89(1969).
- 4) Lachapelle, T.C., Magnusson, L.B., Hindman, J.C.:
The chemistry of neptunium. The transuranium elements.
(Seaborg, G.T.) McGraw Hill. National Nuclear Energy Series,
Div.IV(14B) 1097, New York 1949.

Publication List

- [1] Kimura, T., Kobayashi, Y.: "Coprecipitation of uranium and thorium with barium sulfate", J.Radioanal.Nucl.Chem., Articles, **91(1)**, 59(1985).
- [2] Kimura, T., Kobayashi, Y.: "Determination of alpha emitters in combustible solid materials", J.Radioanal.Nucl.Chem., Letters, **94(6)**, 381(1985).

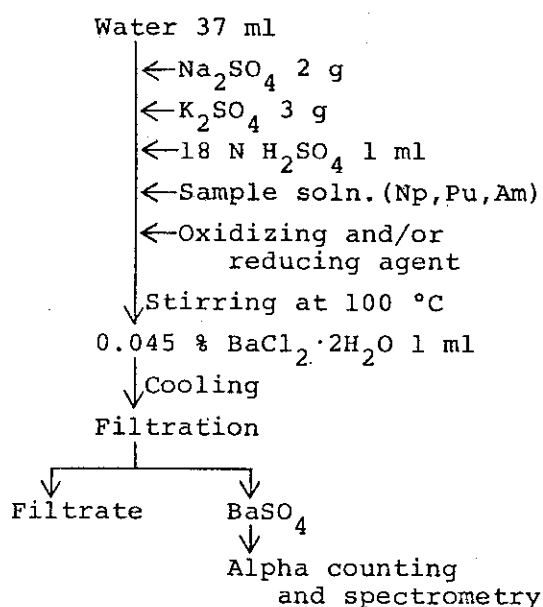


Fig.1 Coprecipitation procedure of Np, Pu, and Am with BaSO_4

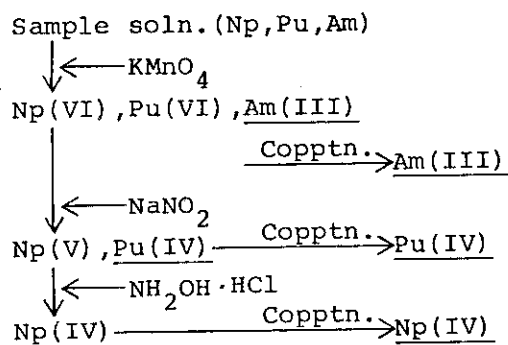


Fig.2 Sequential separation of Np, Pu, and Am from each other

Table 1 Distribution of Np, Pu, and Am during their sequential separation on BaSO_4

BaSO_4 pptn.	Np(%)	Pu(%)	Am(%)
Am fraction	—	—	99.1
Pu fraction	—	98.1	0.4
Np fraction	97.2	1.1	0.2
Total	97.2	99.2	99.7

4.2 プルトニウムを含む可燃性廃棄物の湿式処理

4.2.1 序 論

プルトニウム取扱い施設から発生する廃棄物はおもに、不燃性、可燃性廃棄物、および廃液に大別できる。こゝでは可燃性廃棄物に含有するプルトニウムの非破壊定量、ならびに同廃棄物の減容、無機化についてのべる。

固体廃棄物中のプルトニウムの定量方法として、中性子およびガンマ線を計測する非破壊分析法がある。中性子法は高エネルギーのガンマ線共存下でも測定可能であるが、自発核分裂中性子を測定するための同時計数技術が要求される。ガンマ線法は核種固有のエネルギーを測定するため高い識別能力をもつが、試料自身によるガンマ線減衰を補正する必要がある。プルトニウム取扱い施設では、一般に核分裂生成物から分離された後のプルトニウムを取扱う場合が多い。このことから、ガンマ線測定に限定して測定方法の確立をはかった。

他方、可燃性廃棄物は、かさ高、放射線分解によるガスの発生、可燃性などの理由から、長期保管に不適當であり、減容、無機化、プルトニウム回収などの処理が必要である。同廃棄物の大部分を炭酸ガスと水に分解して、気体状で廃棄し、溶液中に残るプルトニウムを回収することがのぞましい。処理方法として、乾式では空気調節燃焼、流動床焼却などがあり、湿式では酸分解がある。湿式法では、可燃性ガスや、粉塵の発生を制御できること、またプルトニウムは硫酸塩で得られることなどが期待できる。米国、ハンフォードでは濃硫酸に可燃性廃棄物を投入し、加熱しながら濃硝酸を添加して分解する硫酸-硝酸法を開発している。原研では、イオン交換樹脂やソルカブロックを対象に硫酸-過酸化水素(硝酸)での酸分解を開発している。本実験では、この方法を採用し、廃棄物を無機化すると共に、プルトニウムを回収して上記非破壊測定の定量値と比較した。

以下に、(I) ガンマ線測定による ^{239}Pu の定量、(II) 酸分解による廃棄物の湿式処理についてのべる。

4.2.2 ガンマ線測定による ^{239}Pu の定量

Fig. 1 に示すごとく、 ^{239}Pu は (320 - 470) keV 領域でガンマ線を放出する。本法では、検体外部からこのガンマ線を測定して、可燃性廃棄物中の ^{239}Pu を定量する。この際、プルトニウムの偏在、共存するアメリカシウムの影響およびまわりの廃棄物によるガンマ線減衰の補正を考慮して、定量方法の確立をはかった〔1〕〔2〕。

検 体 プルトニウム取扱いグローブボックス内では、一般に発生する可燃性廃棄物を、小型紙カートン (100 ϕ × 230 mm) に、またはラグビーフットボール大までポリエチレン袋に詰め、グローブボックスの廃棄ポートから、ビニールバッグにシールアウトし、これらの数個をさらに一般廃棄物用紙カートン (JIS-Z-4902, 280 ϕ × 350 mm, 実効容積, 17 ℓ) に梱包している。ガンマ線測定は、同カートンを検体の1単位として行い、プルトニウムを定量した。Fig. 2 に示すように、検体をスキャニング架台にのせ、 ^{239}Pu ガンマ線を 400 秒 (有効計数時間) 間測定した。架台は水平に毎分 1 回転、上下に 1 往復以上移動するように設定してある。NaI(Tl)

検出器 (76 ϕ × 76 mm) は検体の側面に設置してある。Fig. 3 はガンマ線測定値とプルトニウム重量に関する検量線を示している。

プルトニウム偏在の影響 既知量のプルトニウム線源を紙カートン内の任意の位置におき、スキヤニング測定し、線源の偏在の影響を調べた結果、定量値の変動は、+12%、-25%以内の誤差であることがわかった。

アメリシウムの影響 ^{241}Am はプルトニウム同位体 ^{241}Pu (半減期 14 年) の壊変生成物であり、常にプルトニウム中に存在する。 ^{241}Pu の存在比や、プルトニウム精製後の時間が異なるため、一義的に ^{241}Am 量を規定することができない。 ^{241}Am は 59 keV ガンマ線のほか、わずかではあるが 100 - 800 keV の範囲にわたりガンマ線を出す。そこで、Fig. 1 に示すように、プルトニウムのガンマ線測定領域 (A 領域) とそれ以外の領域 (B 領域) を設け、二領域を同時に測定する。B 領域の測定値を A 領域の ^{241}Am に帰因するバックグラウンド値に等しくなるようにエネルギー領域を決める。 ^{241}Am の線源を用いて二領域を同時に測定した。400 秒間の計数値をそれぞれ、 \underline{A}_0 , \underline{B}_0 とし、 ^{241}Am 量に殆んど関係なく $\underline{A}_0 = \underline{B}_0$ となるように、A 領域を (356 - 470) keV に設定した。この理由は 320 keV 近辺のアメリシウムのガンマ線をさけること、および装置校正用 ^{133}Ba 線源のガンマ線が 356 keV であり、このエネルギーピークが A 領域の低エネルギー端に選べることによる。設定した B 領域は (475 - 635) keV である。次に、 ^{239}Pu ガンマ線は、A, B 両領域で同時に測定する。400 秒間の A, B 領域の測定値を \underline{A} , \underline{B} とすると、 ^{239}Pu ガンマ線の計数値は ($\underline{A} - \underline{B}$) に相当する。なお、プルトニウムガンマ線は B 領域では殆んど検出されない。この方法で ^{241}Am の共存量にかかわらず、 ^{239}Pu ガンマ線を測定できることが明らかになった。Fig. 3 の検量線は空気中で ($\underline{A} - \underline{B}$) 値を測定して算出した重量換算グラフである。検体をスキヤニング架台に置いたときを想定して、その中心となるべき位置に、スパイラルワイヤーで線源を固定して測定した。

^{239}Pu ガンマ線減衰の補正 廃棄物中の ^{239}Pu ガンマ線は、まわりの廃棄物により吸収され減衰する。廃棄物のみかけの密度を因子として補正を行った。紙、布、ビニールシート、砂を詰めたカートンに既知量のプルトニウム線源を挿入して減衰度合を測定した。Fig. 4 は密度 0.05 - 1.5 g/cm³ の範囲で補正すべき係数 (f) に関するグラフを示した。検体の容積が一定であるから、重量を知れば見かけの密度がわかり、この密度から (f) 値が求まる。一方、検体のプルトニウムからのガンマ線測定で ($\underline{A} - \underline{B}$) 値を得れば、補正值は ($\underline{A} - \underline{B}$) × f となり、Fig. 3 の検量線からプルトニウム重量がわかる。本法では検体 1 個あたり、1 mg 以上のプルトニウムが存在すれば ± 25 % 以内の誤差で定量できることが明らかになった。

廃棄物の定量 Table 1 に示す 9 検体の見かけの密度は、0.1 - 0.2 g/cm³ であり、Fig. 4 から、それぞれ補正すべき (f) 値を求めると、約 20 % であった。一方、ガンマ線測定値に (f) を乗じ ($\underline{A} - \underline{B}$) × f を求め、この値から Fig. 3 の検量線を用いてプルトニウムの重量を求めた。その結果、9 検体中の全プルトニウムは 1117 ± 25 mg であった。

4.2.3 酸分解

この方法は可燃性廃棄物を炭酸ガスと水に分解して、その大部分を気体状で廃棄すること、ならびに、プルトニウムや他の金属イオンを分解槽にあつめ、必要に応じてプルトニウムを回収す

ることである。Fig. 5にそのフローシートを示す〔3〕。

組 成 本実験に使用した主な廃棄物の組成は、ゴム（20重量%）、紙（20%）、ビニール・ポリエチレン（50%）、その他、ウエス、イオン交換樹脂など（10%）であった。あらかじめ、廃棄物を選別することなく剪断した。

分解槽 Fig. 6にグローブボックス（巾、高、奥ゆき、各1m）内に設置した分解槽を示す。5ℓのガラス製分解槽に、2ℓの濃硫酸を入れ、攪拌しつつ側面から加熱して、約250℃に保つ。上部には廃棄物投入口、酸化剤注入口、温度計がある。また、分解ガスはラシヒリング管通過後水冷コンデンサー、フィルターを経て排気系に入る。冷却コンデンサー内での凝縮水は、コンデンサー底部から受けタンクに入る。

操 作 剪断した可燃性廃棄物を定期的に分解槽に投入する（～0.2 kg/回）。上部から酸化剤、すなわち、濃硝酸15 v/v %を含む30%過酸化水素水を徐々に（0.3 ℓ/h）注入する。分解槽の濃硫酸は徐々に減少するため、補充して常に2ℓに保つようにした〔4〕。

結 果 Table 2に示すように、約13 kgの可燃性廃棄物を処理した。ゴム、ビニールの分解を促進させるために、過酸化水素水単用のかわりに、濃硝酸－過酸化水素水の混合液を用いた。その全量は140 ℓであった。分解槽の濃硫酸を常に2ℓに保つために、時々濃硫酸を補充したが、その全使用量は8 ℓであった。排気ガスの冷却で約90 ℓの凝縮水が発生し、その酸濃度、およびアルファ放射能は、それぞれ、1.6 M（ $[H^+]$ ）、 1×10^{-2} mCi/ℓであった。分解槽に蓄積したプルトニウム（アメリシウム）は他の金属イオン、Fe（Ⅲ）、Ca（Ⅱ）などと共に沈殿となった。濃硫酸溶液中のアルファ放射能は約0.2 mCi/ℓであり、プルトニウム（アメリシウム）の大部分が沈殿となっていることがわかった。

プルトニウム、アメリシウムの回収 分解槽の溶液と沈殿を流し出し、両者をデカンテーションで分離した。沈殿を7 M硝酸水溶液で溶解した。一部に不溶性残渣が残る。溶液中のプルトニウムは陰イオン交換樹脂カラム（Dowex, 1×4 , 50～80 メッシュ）に通し、プルトニウムを吸着させ、分離回収した。回収量、および不溶性残渣中のプルトニウムは、それぞれ、1015, および175 mg であり、85%以上が可溶性プルトニウムである。他方、陰イオン交換カラムの流出液にはアメリシウムが含まれており、この流出液からアメリシウムを回収した。Fe（Ⅲ）イオンなどの沈殿が発生する寸前の酸濃度（～0.5 M）まで、溶液の硝酸を水酸化ナトリウムで中和する。次に、シュウ酸カリウムを加えて約0.1 M液をつくる。この溶液を攪拌しつつ、1 M硝酸カルシウム水溶液を滴下し、生成した少量のシュウ酸カルシウムの沈殿でアメリシウムを捕集する。上澄液のアルファ放射能は約0.2 mCi/ℓであった。沈殿からアメリシウムを回収した〔5〕。

4.2.4 結 論

含有プルトニウム可燃性廃棄物約13 kg を酸分解法で無機化し、また無機塩からプルトニウムを回収した。分解槽に蓄積した全プルトニウム量は、1190 mg であり、あらかじめガンマ線法で定量した値、1117 mg と誤差範囲内で一致した。

本ガンマ線測定法では、プルトニウムの偏在、 ^{241}Am ガンマ線の影響を考慮し、また、廃棄物によるガンマ線減衰に対する補正を行った。検体内に廃棄物を封入したビニールバッグや、小型紙カートンが数個入っており検体は決して均一体ではない。しかし測定時、検体を水平に回転し、

また上下にスキヤニングさせるため、見かけ上検体内の物性を均一とみなし得ると仮定している。廃棄物を分解して、全プルトニウムを定量した結果と、ガンマ線測定の結果がほぼ一致していることから、上記スキヤニング測定で検体を均一物体とみなしてよいことが明らかとなった。

酸分解では、可燃性ガスを発生しやすい紙類も、難燃性の塩化ビニール類も処理することができた。しかし、条件設定になお問題があった。廃棄物の均一な剪断、および濃硫酸の均一な攪拌が困難であった。硫酸の温度制御も重要であり、250℃以上となると硫酸の消費が著しくなる。また、200℃以下になると分解反応が緩慢となり、粘性が大きく発泡しやすくなる。そのほか、30%過酸化水素のみを酸化剤として使用すると、紙類は迅速に分解されるが、ゴム類の分解は緩慢である。このため、過酸化水素-硝酸の混合液を使用した。このことから、単位時間当りの処理量を明確に示すに至らなかった。プルトニウムの回収では、プルトニウムが可溶性の硫酸塩であるため、容易に回収できた。収率は85%以上となった。しかし、カルシウムなどの硫酸塩は7M硝酸溶液には難溶性であり、これら難溶性の溶解残査がある場合、それにプルトニウムが吸着、吸蔵されるためか、その回収率が低下する。本酸分解で可燃性廃棄物を無機化することができ、一応所期の目的を達成したが、上述の問題が今後留意すべき事項である。

(J. Akatsu)

Publication list

- [1] Akatsu, J.: "Determination of Pu amount in a waste carton by gamma-ray measurement", J. Nucl. Mater. Manag., X (4) 22 (1981).
- [2] Akatsu, J., Kobayashi, Y., Kimura, T.: "Non-destructive determination of ^{239}Pu in wastes by application of gamma-ray measurement", J. Radioanal. Nucl. Chem. Letters, 86 (3) 159 (1984).
- [3] Kobayashi, Y., Matsuzuru, H., Akatsu, J., Moriyama, N.: "Acid digestion of radioactive combustible wastes" J. Nucl. Sci. Technol., 17 (11) 865 (1980).
- [4] Matsuzuru, H., Kobayashi, Y., Dojiri, S., Akatsu, J., Moriyama, N.: "A comparison of the acid digestion of spent ion exchange resins using H_2SO_4 - H_2O_2 ", Nucl. Chem. Waste Manag., 4, 307 (1983).
- [5] Akatsu, J., Kobayashi, Y., Matsuzuru, H., Dojiri, S., Moriyama, N.: "Separation of Pu-Am from the leachant of a deposit in an acid digestion solution by calcium oxalate coprecipitation", Separation Science and Technology, 18 (2) 177 (1983).

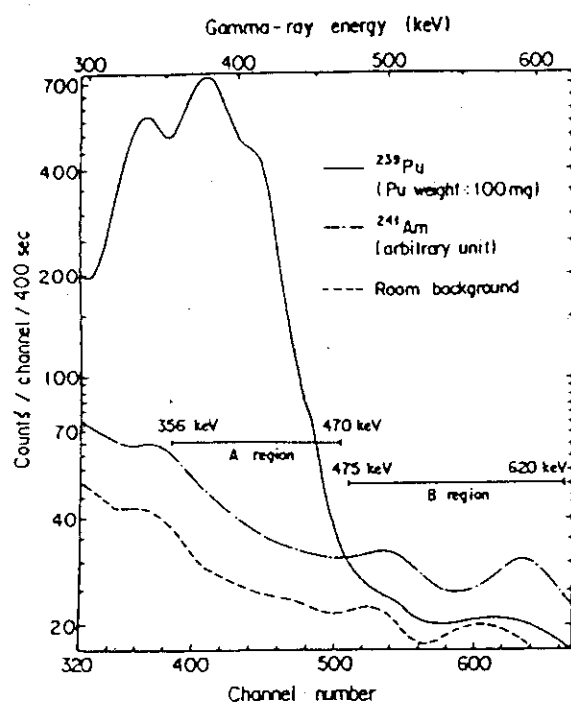


Fig. 1 Gamma-ray spectra of ^{239}Pu and ^{241}Am in 300-600 keV region

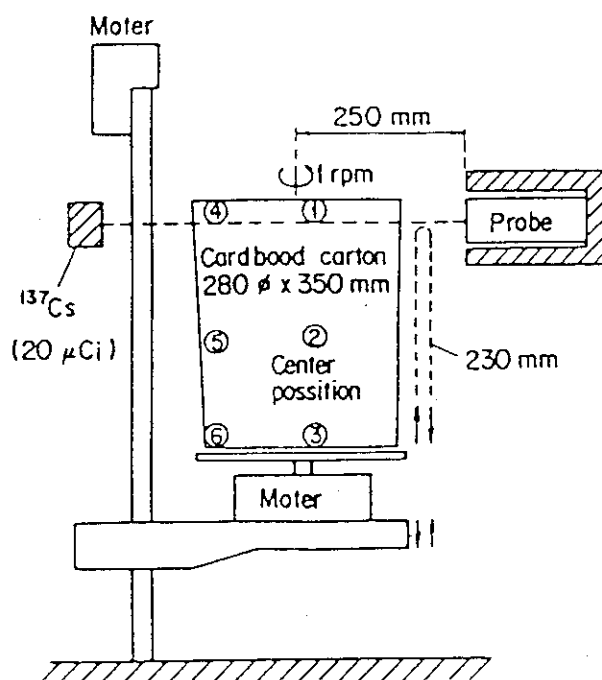


Fig. 2 Schematic view of Pu assay system

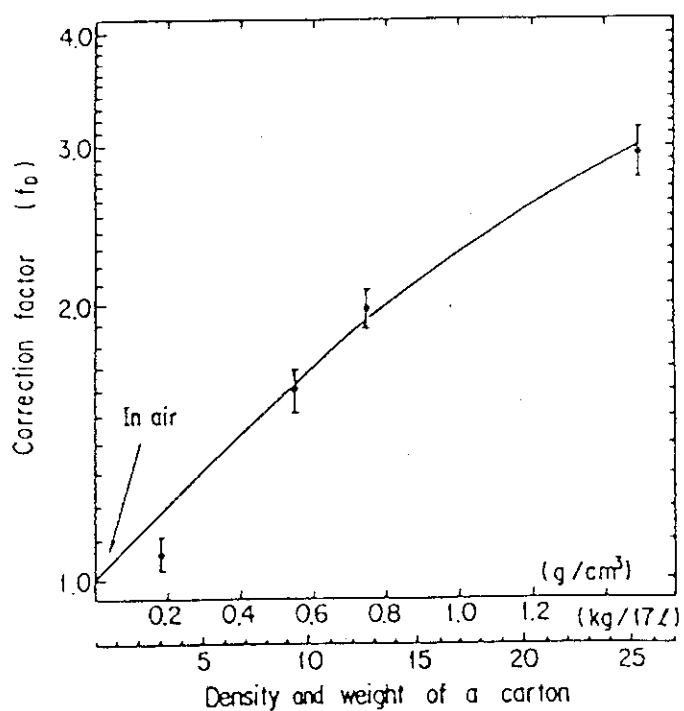
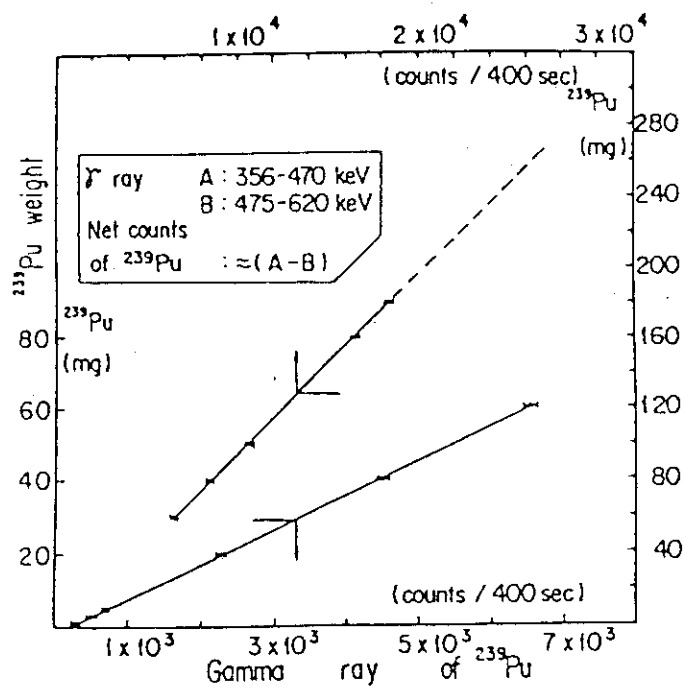


Table I Determination of Pu weight in waste carton by gamma-ray assay

No.	Density (g/cm ³)	(f)	(A - B) x f	Pu weight (mg)
1	0.123	1.12	(222 ±104) x 1.12	0.9 ± 0.9
2	0.168	1.17	(2503 ±114) x 1.17	26 ± 1
3	0.188	1.20	(873 ± 52) x 1.20	8 ± 1
4	0.153	1.16	(3378 ± 78) x 1.16	59 ± 1
5	0.180	1.18	(1075 ± 93) x 1.18	10 ± 1
6	0.123	1.12	(25276 ± 255) x 1.12	67 ± 1
7	0.165	1.17	(22253 ± 776) x 1.17	61 ± 2
8	0.105	1.10	(3497 ± 98) x 1.10	35 ± 1
9	0.162	1.17	(52110 ± 1614) x 1.17	850 ± 25
Total				1117 ± 25

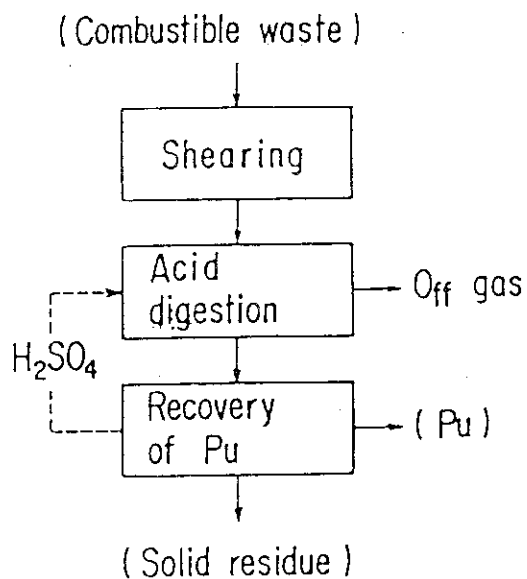


Fig.5 Flowsheet of acid digestion Process

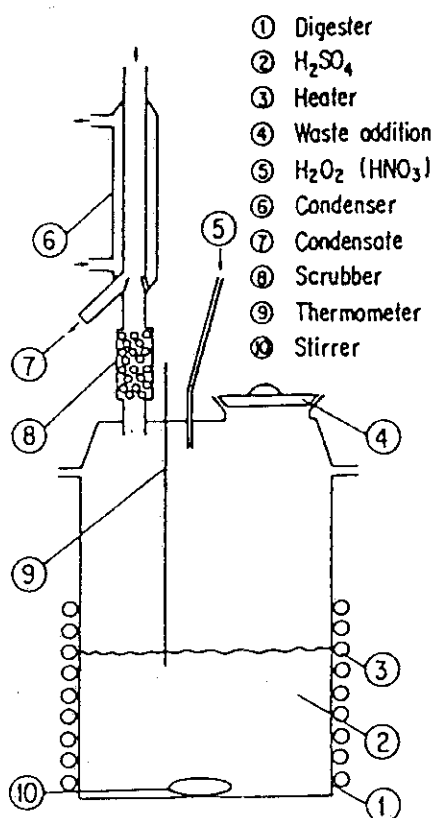


Fig.6 Schematic diagram of acid digestion apparatus

Table 2 Experimental results of acid digestion

Combustible waste (Kg)	13.5
rubber (weight %)	20
paper	20
vinyl sheet	50
others	10
Digestion solution (L)	13.8
30% H_2O_2 containing 15 v/v % of concentrated HNO_3	
Concentrated H_2SO_4 (L)	8
Pu recovery	
Pu weight (mg)	1015±15
efficiency (%)	85.3
Aqueous waste (L)	87
acidity, $[H^+]$ (M)	1.6
gross alpha-activity ($\mu Ci/L$)	11±9
Solid residue	
weight (dried) (g)	380
Pu weight (mg)	175±5

5. RADIOCHEMICAL STUDIES OF TRITIUM

M.Nakashima, T.Hirabayashi, Y.Aratono,
M.Saeki and E.Tachikawa

5. トリチウムの放射化学的研究

中島 幹雄・平林 孝圀・荒殿 保幸
佐伯 正克・立川 圓造

5.1 材料中でのトリチウムの化学的挙動

5.1.1 緒言

核反応で生成したり、プラズマから飛び出してくるトリチウムは高エネルギーを持っているため、熱平衡にあるトリチウムとは異った挙動をすることに注目し、研究を継続している。これまでに得た主な結果は以下の通りである。

5.1.2 高エネルギートリチウムの拡散挙動

黒鉛や熱分解炭素中に打込まれた高エネルギートリチウムは、炭素と化学結合を形成する。その結果非常に再放出されにくい。放出化学形は主に水素状トリチウム (HT) であり、水素同位体イオン (H^+ や D^+) ビーム実験時に見られる化学スパッタの主成分である CH_3 や CH_4 は非常に少ない〔2〕。

黒鉛の中性子照射に伴う損傷と黒鉛中のトリチウムの拡散係数の間には、Fig. 1 に示すような明らかな相関が認められ、損傷が進むとともにトリチウムは黒鉛中で拡散しにくくなることを見いだした〔11〕。これは炭素材料中での拡散が主に基底面間で起っていると仮定すると次のように説明できる。すなわち、黒鉛の中性子照射損傷は炭素原子の基底面間へのはじき出しが主であり、その結果照射量とともに、基底面の面間隔が大きくなって行く。トリチウムの拡散通路である面間へはじき出された炭素原子は、トリチウムの拡散を妨害するため、活性化エネルギーは大きくなり、拡散係数は小さくなる。

上記モデルを実験的に確かめるため、アルミナ核上にCVD (Chemical Vapor Deposition) 法により沈積した配向性 (異方性) の異なる熱分解炭素を用い、トリチウムの拡散係数を測定した〔24〕。熱分解炭素は基盤に対して平行に沈積して行く性質を持っているが、その度合は蒸着する条件により異なることが分っている。またその異方性は一般にBAF (Bacon Anisotropy Factor) により示される。得られた結果を Fig. 2 及び Table 1 に示す。異方性の大きな熱分解炭素中ではトリチウムが拡散しにくいことが明瞭であり、上記モデルの実証ということが出来る。

一方、高エネルギートリチウムのセラミックス (UO_2 , Si , Al_2O_3) 中での拡散は熱的に材料中へ導入したトリチウムに比べ、非常に遅いが、金属 (Al) 中ではこの現象は認められなかった〔1〕,〔9〕,〔13〕。(UO_2 中におけるトリチウムの拡散係数のアレニウスプロットを Fig. 3 に示す〔13〕。) 材料中にトリチウムと化学的親和性の高い元素が存在する場合、高エネルギートリチウムはこれらの元素と化学結合を形成するためであると予想した。そこで、低温固体キセノン中での高エネルギートリチウムの化学反応を利用して、この仮説の立証を試みた。その結果、高エネルギートリチウムが、材料中を通過する際、その飛跡に沿ってエネルギーを失い、そのため母材の格子が高度に乱れ、かつ高温となった領域、すなわちホットゾーンが形成され、最終的にトリチウムはその領域内で化学結合を形成することが明らかになった。実験結果と理論計算の比較から、ホットゾーンの大きさは半径 3~4 nm, その寿命は約 10^{-11} 秒程度であると結論した〔4〕。

しかし、アルミニウム中で差異が認められなかったのは、損傷の回復がセラミックスに比較し、より低温領域で起ってしまうためである可能性も考えられる。そこで、水素同位体に対する化学的親和性が大きい元素のみで構成され、かつ照射損傷についての研究例も多い、ケイ素単結晶を反応系に選り、トリチウムの拡散及び再放出挙動を調べた〔13〕。ケイ素結晶中でも高エネルギートリチウムによる拡散係数の方が非常に小さかった。詳細な実験の結果、トリチウムはケイ素結晶から 635 °C にピークを形成して放出されるが、この温度は Si-H 結合の切断温度及びケイ素結晶の荷電粒子による損傷の回復温度と、ほぼ完全に一致してしまうため、化学結合形成及び損傷による捕捉のいずれが優先しているのか特定するに至らなかった。

さらにこの点を明らかにするため、石英ガラス (SiO_2) に 80 keV の D^+ を打込み、その挙動を調べた〔23〕。導入した D^+ は母材中で OD 基を形成していることを FT-IR (フーリエ変換赤外分光) 測定により確認した。形成された OD 結合及び SiO_2 中に不純物として存在する OH 結合の低温における γ 線分解の割合を比較したところ、Fig. 4 に示すように、明らかに新しく生じた OD 結合の方が切断しにくいことが分った。これは D^+ 自身の作る損傷により、吸収された γ 線のエネルギー伝播が阻害されるためであろう。生成した H 及び D 原子の再結合速度を ESR (電子スピン共鳴) 測定により調べることににより、損傷は拡散の開始過程を主に抑制していることも明らかになった。

5.1.3 リチウム-アルミニウム合金中でのトリチウムの挙動〔10〕,〔15〕

リチウム-アルミニウム合金 (Li-Al 合金) は、トリチウムの大量製造用ターゲットとして使用される。しかし、一般に金属中のトリチウムの拡散速度は大きいため、ターゲットからの漏洩が懸念された。そこで、Li-Al 合金中でのトリチウムの拡散係数を測定した〔10〕。その結果、わずか 200 ppm のリチウムがトリチウムの拡散係数を、純アルミニウム中の値より 1 桁以上下げること、及び拡散係数はリチウム濃度とともにさらに小さくなって行き、逆に拡散の活性化エネルギーは大きくなって行くことを見いだした。その様子を Fig. 5 に示す。これは合金構成元素のトリチウムの拡散に及ぼす化学的親和力の効果をはじめて明らかにしたものである。さらに詳細に Li-Al 合金中のトリチウムの挙動を調べ、Li-Al 合金はリチウム濃度 1% 程度でも、室温付近では α 及び β 相に分相しており、水素同位体はリチウムとアルミニウムの金属間化合物

である β 相に集中し、その中でかなりの部分（トリチウム濃度約 5 ppm で約 16 %）が分子状（ T_2 及び HT）として存在していることを見いだした〔15〕。

5.1.4 材料中でのトリチウムの存在状態〔22〕,〔29〕

液体窒素温度で中性子照射したフッ化リチウム中におけるトリチウムの化学形と放出挙動の相関を、ESR 測定と重硝酸（ $DN O_3$ ）溶液への溶解時に放出されるトリチウムの化学形分析を組合せて調べた〔22〕。照射済試料中のトリチウムの化学形は、 $T^-(LiT)$ 、 $T^+(TF$ 又は $LiOT)$ 、 T^0 、HT 及び T_2 の 5 つであるが、相対量はアニーリング温度と共に変化する。350 °C では 95 % 以上が T^- として安定化する。しかし、この T^- は 350 °C 以上では再び分解をはじめ、分解後には溶解時に水（ $DT O$ ）となる化学種に変化する。これらの様子を Fig. 6 に模式的に示す。結晶からのトリチウムの放出は 350 °C 以上で T^- が完全に分解した後に開始されることも明らかになった。

一方、原子炉温度で照射したフッ化リチウムの重硝酸溶液への溶解時に放出されるガス状トリチウム成分は 36 % (4.8×10^{15} nvt)、61 % (4.8×10^{16} nvt) 及び 98 % (1.2×10^{18} nvt) と明らかな中性子照射量依存性を示した。試料中に不純物として含まれる OH 基は 4.8×10^{15} nvt の照射で完全に消滅してしまうが、650 °C でアニーリングすると完全に回復した。 1.2×10^{18} nvt まで照射したフッ化リチウム単結晶を 650 °C までアニーリングした後、赤外吸収スペクトル測定を行うと、 3578 cm^{-1} と 2225 cm^{-1} に鋭い吸収ピークが認められた。Fig. 7 にこれらのスペクトルを示す。それぞれのピークの ^{60}Co γ 線による放射線分解挙動及びアニーリングによる回復率が良く一致すること及び同位体シフト値が理論値と一致することから、 2225 cm^{-1} のピークは OT 基に帰属するものであると結論した〔29〕。さらに、実測波数から分光学的パラメータを計算し、OT 基の解離エネルギーは約 5 eV であることを明らかにした。

(Y. Aratono and M. Saeki)

Publication List

- [1] Nakashima, M., Aratono, Y., Tachikawa, E. : "Diffusivity of recoil-injected tritium in aluminium", J. Nucl. Mater., **98**, 27 (1981).
- [2] Saeki, M. : "Release behavior of tritium from graphite heavily irradiated by neutrons", J. Nucl. Mater., **99**, 100 (1981).
- [3] Nakashima, M., Tachikawa, E., Saeki, M., Aratono, Y. : "Removal mechanism of tritium by variously pretreated silica gel", J. Inorg. Nucl. Chem., **43**, 369 (1981).

- [4] Aratono, Y., Tachikawa, E., Miyazaki, T., Sakurai, M., Fueki, K. : "The characteristic behavior of recoil tritium atom in solid neopentane at 77K. The application of a hot zone model", Bull. Chem. Soc. Japan, 54, 1627 (1981).
- [5] Nakashima, M., Saeki, M., Aratono, Y., Tachikawa, E. : "Release of radioiodine from UO_2 during reactor operation", Inter. J. Appl. Radiat. Isotopes, 32, 397 (1981).
- [6] Aratono, Y., Tachikawa, E. : "Formation of tritiated compounds upon dissolution of lightly-irradiated $\text{UO}_2(\text{LiF})$ pellets in nitric acid", J. Inorg. Nucl. Chem., 43, 2191 (1981).
- [7] Aratono, Y., Tachikawa, E., Miyazaki, T., Kawai, Y., Fueki, K. : "Temperature effect on recoil tritium in solid alkanes at 20-300 K. Comparison of recoil T atoms with H(D) atoms in gamma radiolysis", J. Phys. Chem., 86, 248 (1982).
- [8] Aratono, Y., Tachikawa, E., Miyazaki, T., Fueki, K. : "Isotope effect on hydrogen atom abstraction reaction by recoil T atoms in solid $n\text{-C}_{10}\text{D}_{22}$ - $n\text{-C}_{10}\text{H}_{22}$ mixtures. Comparison of recoil T atoms with D atoms in gamma radiolysis. (Note)", Bull. Chem. Soc. Japan, 55 1957 (1982).
- [9] Aratono, Y., Nakashima, M., Saeki, M., Tachikawa, E. : "The diffusivities of fission-created or thermally-doped tritium in UO_2 ", J. Nucl. Mater., 110 201 (1982).
- [10] Nakashima, M., Saeki, M., Aratono, Y., Tachikawa, E. : "Diffusivity of tritium in Li-Al alloys", J. Nucl. Mater., 116, 141 (1983).
- [11] Saeki, M. : "Influence of radiation damage on diffusivity of tritium in graphite", Inter. J. Appl. Radiat. Isotopes, 34, 739 (1983).

- [12] Saeki, M., Hirabayashi, T., Aratono, Y., Hasegawa, T., Tachikawa, E. : "Preparation of gas chromatographic column for separation of hydrogen isotopes and its application to analysis of commercially available tritium gas", J. Nucl. Sci. Technol., 20, 762 (1983).
- [13] Saeki, M., Yokoyama, A., Aratono, Y., Tachikawa, E. : "Origins of diffusivity-retardation of tritium in bombarded silicon crystal", Radiochim. Acta, 33, 139 (1983).
- [14] Aratono, Y., Tachikawa, E., Miyazaki, T., Nagaya, S., Fujitani, Y., Fueki, K. : "Isotope effect on hydrogen atom abstraction reaction by recoil tritium atoms in Xe-C₂H₆-C₂D₆ mixtures at 77 K", J. Phys. Chem., 87, 1201 (1983).
- [15] Saeki, M., Nakashima, M., Aratono, Y., Tachikawa, E. : "Effects of lithium concentration on chemical behavior of tritium in Li-Al alloys", J. Nucl. Mater., 120, 267 (1983).
- [16] Aratono, Y., Nakashima, M., Saeki, M., Tachikawa, E. : "Release behavior of tritium from UO₂ during reactor operation", J. Nucl. Mater., 114, 234 (1983).
- [17] Hirabayashi, T., Saeki, M. : "Sorption of gaseous tritium on the surface of type 316 stainless steel", J. Nucl. Mater., 120, 309 (1984).
- [18] Saeki, M., Tachikawa, E., Miyazaki, T., Fujitani, Y., Fueki, K. : "Selective hydrogen atom abstraction by T and D atoms in radiolysis of tritiated decane at 77 K. Mass effect on solid state reaction", J. Phys. Chem., 88, 3108 (1984).
- [19] Saeki, M., Hirabayashi, T. : "Sorption mechanisms of tritium on the surface of borosilicate glass", Radiochim. Acta, 35, 233 (1984).
- [20] Saeki, M., Hirabayashi, T. : "Desorption behavior of carrier

- free tritium from the inner surface of glass ampoule", Radioisotopes, 33, 776 (1984), (in Japanese).
- [21] Hirabayashi, T., Saeki, M., Tachikawa, E. : "A thermal desorption study of the surface interaction between tritium and type 316 stainless steel", J. Nucl. Mater., 126, 38 (1984).
- [22] Aratono, Y., Nakashima, M., Saeki, M., Tachikawa, E. : "Tritium centers in neutron-irradiated LiF studied by ESR spectroscopy and dissolution in deuterated nitric acid", Radiochim. Acta, 37, 101 (1984).
- [23] Saeki, M., Ohno, S., Tachikawa, E., Azuma, N., Miyazaki, T., Fueki, K. : "Comparison of 80 keV D⁺ ion implantation with thermal D₂ doping in silica by FT-IR and ESR spectroscopy", J. Amer. Ceram. Soc., 68, 151 (1985).
- [24] Saeki, M. : "Effects of pyrolytic carbon structure on diffusivity of tritium", J. Nucl. Mater., 131, 32 (1985).
- [25] Aratono, Y., Nakashima, M., Saeki, M., Tachikawa, E. : "Design and installation of "In-Pilr Tritium-Release Experimental Apparatus" In-situ study of tritium release from uranium dioxides", J. At. Energy Soc. Japan, 27, 139 (1985), (in Japanese).
- [26] Hirabayashi, T., Saeki, M., Tachikawa, E. : "Effect of surface treatments on the sorption of tritium on type 316 stainless steel", J. Nucl. Mater., 127, 187 (1985).
- [27] Hirabayashi, T., Saeki, M., Tachikawa, E. : "Chemical decontamination of the tritium-sorbing surface of type 316 stainless steel", J. Nucl. Mater., 136, 179 (1985).
- [28] Saeki, M., Hirabayashi, T. : "Effects of ionizing radiation on the amount and the chemical forms of tritium sorbed on

the surface of borosilicate glass", Radiochim. Acta, 38, 37 (1985).

- [29] Aratono, Y., Nakashima, M., Saeki, M., Tachikawa, E. :
 "Infrared spectrum of tritiated hydroxyl ion (OT^-) in
 neutron-irradiated LiF crystal", J. Phys. Chem., in press.
- [30] Tachikawa, E., Kobayashi, Y., Muromura, T., Aratono, Y. :
 "Chemistry of radioactive waste treatment", J. At. Energy
 Soc. Japan, 23, 154 (1981), (in Japanese).

Table 1

Best fit values of frequency factor (D_0)
 and activation energy (Q)

Material	BAF	$\ln (D_0)$ (cm^2/s)	Q kJ/mol
H-1	>1.78	-(4.8 \pm 0.8)	261 \pm 8
H-2	1.78	-(6.0 \pm 1.8)	249 \pm 17
G-32	1.07	-(17.4 \pm 1.0)	105 \pm 9

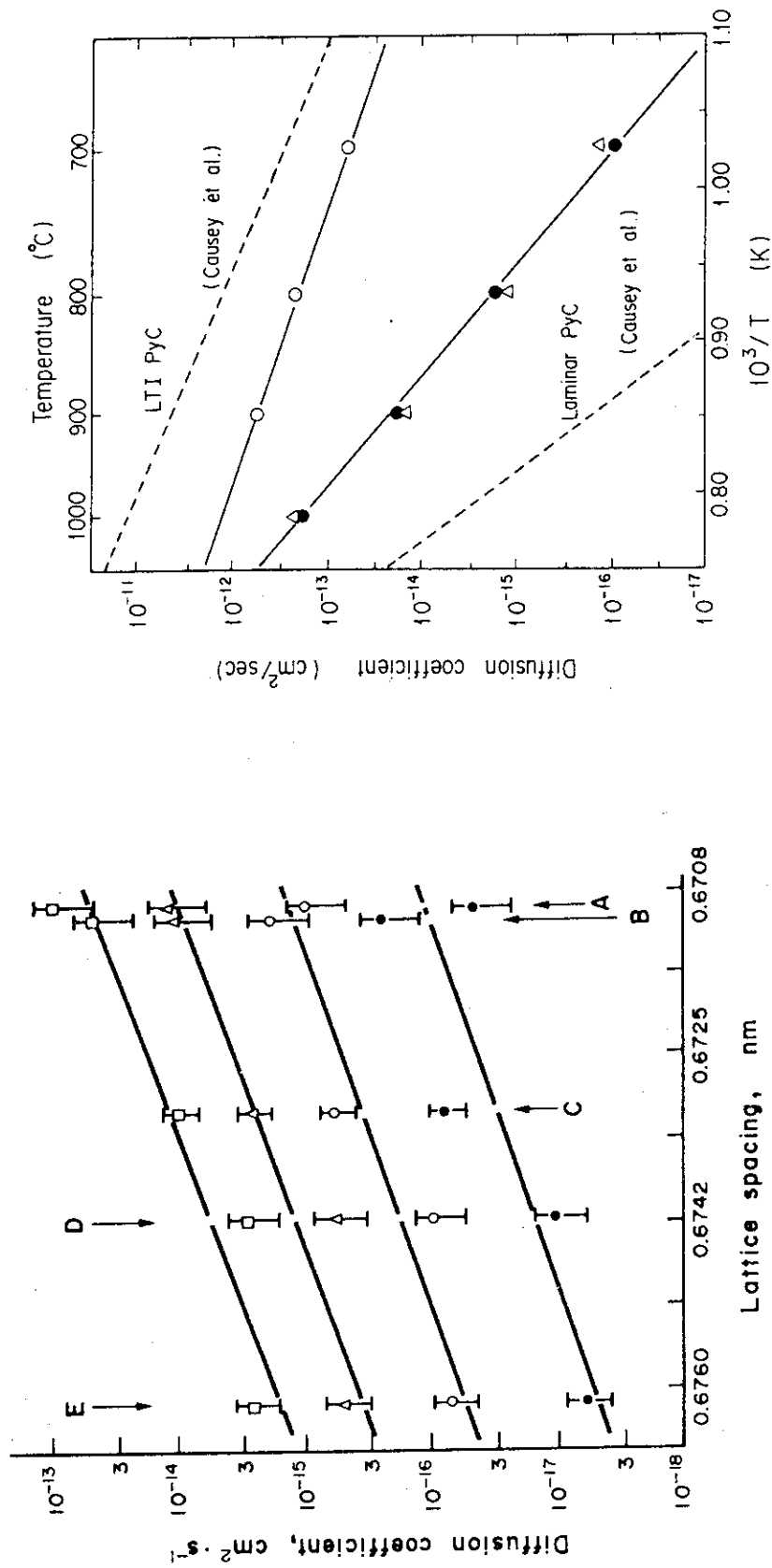


Fig. 1 Relationship between the lattice spacing of graphite and the diffusion coefficients. □: at 900°C; △: at 800°C; ○: at 700°C; ●: at 600°C. A: natural graphite; B: SiC decomposed graphite; C: Pechiney Q₁ (2.40 × 10¹⁶ n/cm²); D: Pechiney Q₁ (4.80 × 10²⁰ n/cm²); E: Pechiney Q₁ (1.66 × 10²¹ n/cm²).

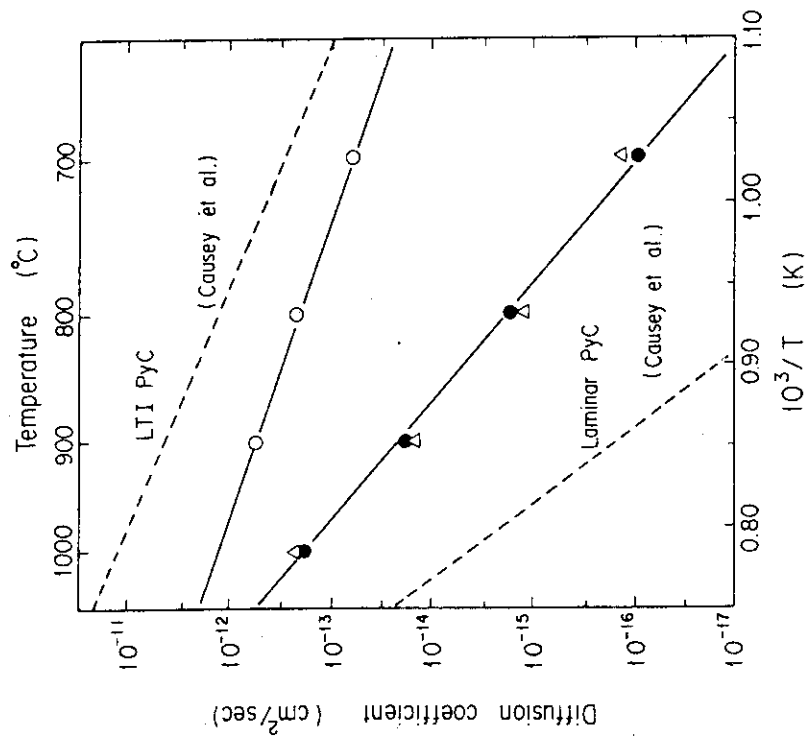


Fig. 2 Arrhenius plot for tritium diffusion in pyrolytic carbon. ○: G-32, △: H-2, ●: H-1.

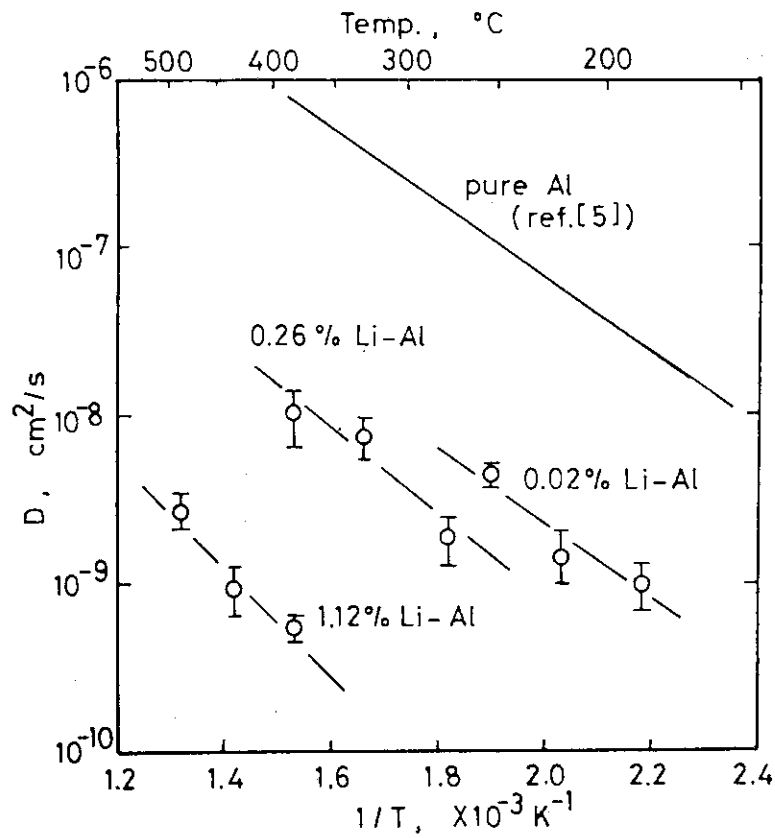


Fig. 5 Temperature dependence of diffusion coefficients of tritium.

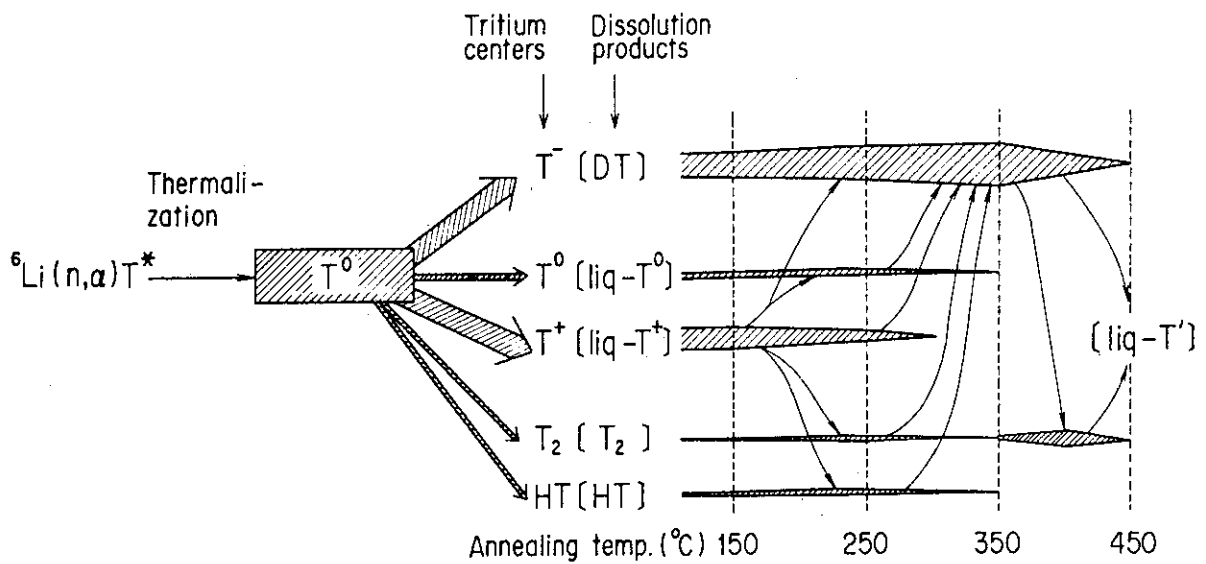


Fig. 6 Schematic presentation of the behaviors of the tritium centers against annealing temperature

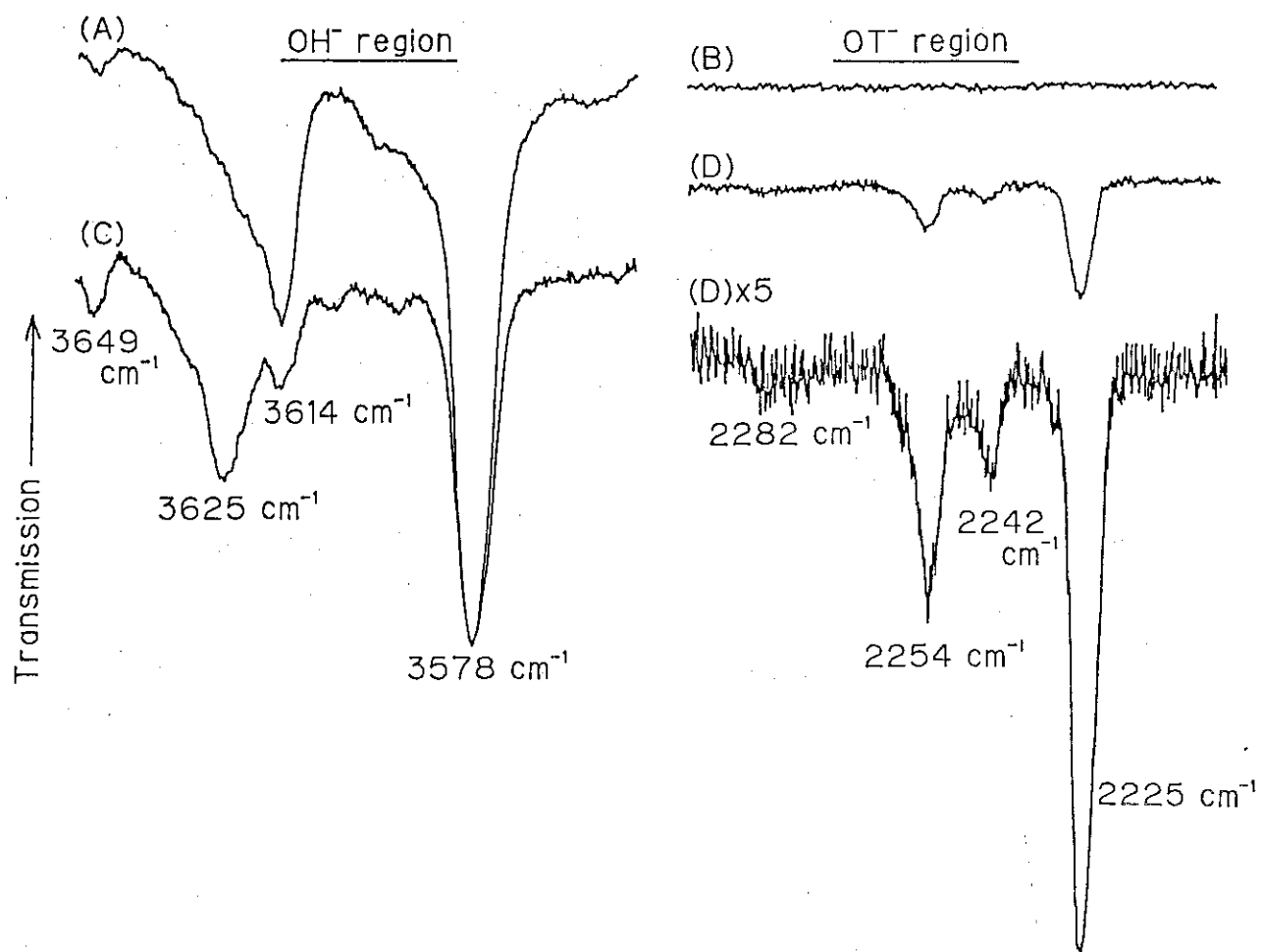


Fig. 7 Infrared absorption bands in OH^- and OT^- regions.
 (A), (B) : unirradiated.
 (C), (D) : annealed at 650 °C after neutron irradiation.

5.2 材料表面におけるトリチウムの収着と脱離

5.2.1 緒言

トリチウムは、水素の放射性同位体であるため、(i) 材料中を通過しやすく、(ii) 生体内に摂取され易い、という性質を有している。したがって、トリチウムの β 壊変による放出エネルギーが、最大でも 18.6 keV と弱いにもかかわらず、トリチウムの取扱いには、細心の注意を払う必要がある。

核融合炉の早期実現を目指して、トリチウムの製造、分離、精製、回収、貯蔵などに関する種々の研究が活発に進められている。今後、たとえば、核融合炉燃料循環系のように、比放射能の高いトリチウム・ガスを大量に取扱う場合には、測定器や装置の内壁へのトリチウムの収着（吸着および吸収）による汚染と、そのために起こるトリチウム損失が問題になるであろう。さらに、この収着トリチウムは、器壁深部にまで溶解・拡散して水素脆性、 β 壊変にともなう放射線脆性、生成する ^3He による脆性なども引き起こすことになるであろう。

このようなトリチウム安全取扱い技術上のあらゆる問題は、すべてトリチウムの「収着」を端緒とするものである。この観点から、材料表面上へのトリチウムの収着－脱離現象を正確に把握することを目的とし、一連の研究を行った。

5.2.2 ステンレス鋼表面におけるトリチウムの収着と脱離

(a) トリチウムの収着現象〔4〕

核融合実験炉の主要構造材として、316 ステンレス鋼または、これに微量の Ti などを加えた改良鋼が有力候補に上っている。そこで、316 ステンレス鋼表面におけるトリチウムの収着挙動を調べた。

ガス状のトリチウム (T_2 , HT, DT) がステンレス鋼表面に収着し、それが再放出される場合、大部分は水分子 (HTO) の状態に変わる。これは、トリチウムがステンレス鋼表面に形成されている酸化皮膜や吸着されている酸素と反応するためである。そこで、ガス状放出成分 (HT など) と水分子状放出成分 (HTO など) を区別しながら、トリチウムの収着現象を調べた。Fig. 1 は、トリチウム収着量の常温下におけるトリチウム・ガスとの接触時間依存性を成分別に示している。接触時間が長くなると、 HTO の化学形で放出される収着トリチウムは、一定値 (約 10^{15} 個分子/ cm^2) に達するが、HT の形で放出されるトリチウムの収着量は、トリチウム・ガスとの接触時間に比例して増加し続ける。このトリチウム収着量の増加は、

$$D = 4.6 \left(\begin{smallmatrix} +1.5 \\ -1.1 \end{smallmatrix} \right) \times 10^{-11} \times \exp \left[-32.8 \pm 0.7 \text{ (kJ} \cdot \text{mol}^{-1}) / RT \right] \text{ (m}^2 \cdot \text{sec}^{-1})$$

によって示される内部への拡散に従って進行していることを明らかにし、材料表面の汚染量あるいはトリチウムの貯蔵・移送時における物質収支等の予測を可能にした。たとえば、ステンレス鋼表面に 13.3 kPa のトリチウム・ガスを 298 K で 7 日間接触した際、トリチウムの全収着量は、約 $3.5 \text{ GBq} \cdot \text{m}^{-2}$ (約 1 Ci/m^2) に達する。

(b) トリチウムの収着状態〔4, 7, 8〕

ステンレス鋼表面におけるトリチウムの収着状態を昇温脱離法で調べた。トリチウムを収着したステンレス鋼を一定昇温速度 ($5 \text{ K} \cdot \text{min}^{-1}$) で加熱すると、Fig. 2 のような昇温脱離スペクトルが得られる。これは、ステンレス鋼との結合力の弱いトリチウムから順次脱離したことを示しており、収着トリチウムには少なくとも4種類の結合力の異なる状態があることがわかった。

一般に、一定昇温速度 (β) で脱離を行う場合、温度 T_m で脱離速度が極大になるならば、 T_m , β および収着種の脱離の活性化エネルギー E_d の間には、つぎの関係が成立つ。

$$\ln \left(\frac{T_m^2}{\beta} \right) = \left(\frac{E_d}{RT_m} \right) + \ln \left(\frac{E_d}{\chi R \nu N_m \chi^{-1}} \right)$$

ここで、 χ は脱離の反応次数、 ν は頻度因子、 N_m は温度 T_m における収着種の数である。この関係から、各収着状態のトリチウムが脱離するに要する活性化エネルギーを求めた。その他、DT ガスを用いた解離挙動の研究など、種々の実験結果を総合し、昇温脱離スペクトル中の各ピークに対応するトリチウムの収着状態について、つぎのような結論を得た。

(i) HTO ピーク

ステンレス鋼表面で解離し、原子状になったトリチウムは、表面や粒界の酸化皮膜中に存在する O^{2-} イオンとの結合または OH^- イオンの H との同位体交換によって、 OT^- イオンの状態になる。この OT^- イオンの形成には、表面に存在する鉄が関与する。全収着トリチウムの約 90 % は OT^- イオンの状態で収着されており、脱離のさい、周囲に存在する H と結合して HTO の形になる。この脱離に要する活性化エネルギーは、 $27 \text{ kJ} \cdot \text{mol}^{-1}$ である。

(ii) HT-I ピーク

全収着トリチウムの 5 % 程度は、解離されることなく、分子状 (HT または HT^+) のままステンレス鋼の最表面に弱く吸着している。この状態のトリチウムは、 $20 \text{ kJ} \cdot \text{mol}^{-1}$ 程度の小さい活性化エネルギーで再び脱離する。

(iii) HT-II ピーク

収着トリチウムの 2 % は、原子状に解離して、316 ステンレス鋼の粒界に偏析しているモリブデン炭化物によって捕捉されている。このトリチウムの脱離には、 $55 \text{ kJ} \cdot \text{mol}^{-1}$ 程度の活性化エネルギーを必要とする。

(iv) HT-III ピーク

収着トリチウムの 4 % は、原子状に解離して、ステンレス鋼表面層のニッケルが関与しているサイトに捕捉されており、970 K 程度まで加熱しなければ脱離しない程きわめて強く収着している。

(c) トリチウムの収着抑制〔7〕

ステンレス鋼のトリチウムによる表面汚染の防止を目的にして、ステンレス鋼を種々表面処理し、トリチウムの収着抑制効果を調べた。その結果、重クロム酸カリウムと硝酸の溶液を用いて不動態化処理することにより、ステンレス鋼表面を化学的に安定なクロム酸化物で覆うと、トリチウムの収着量を 1 桁以上も抑制しうることを見いだした。この表面不動態化処理法は、

トリチウムの材料内部への侵入を収着の段階で阻止するものであり、測定器内壁などの表面汚染防止法としてきわめて有効なものである。

なお、実験装置等の表面洗浄法として注目されているイオンスパッタ・エッチング法による表面処理を行うと、トリチウムの収着量は著しく増大した。したがって、トリチウムの収着抑制という観点からは、この表面処理を避けるべきである。

(d) 収着トリチウムの化学的除去〔8〕

収着トリチウムの存在状態に関する知見に基づき、トリチウムで表面汚染したステンレス鋼の除去法を検討した。前述の(a)～(c)で得られた結果と除去法との関係を Table 1 にまとめて示した。

希塩酸を用いる全面的な表面溶解法により、汚染表面をわずかに溶解すると、Fig. 3 の昇温脱離スペクトルの変化から明らかなように、表面に収着されているトリチウム (HT-I, HT-II および HTO の一部) はすべて容易に除去されるが、粒界に侵入しているトリチウムだけは除去できない。一方、硫酸銅-硫酸溶液を用いて、粒界部分を選択的に溶解した場合、Fig. 4 の昇温脱離スペクトルから明らかなように、表面層に強く収着されているトリチウムは除去できないが、粒界に収着されているトリチウム (HT-II および HTO の一部) はほぼ完全に除去しうることを見いだした。

そこで、希塩酸によるわずかな表面溶解 (深さ約 $2\ \mu\text{m}$) および硫酸銅-硫酸溶液による粒界選択溶解を組合せた化学的除去法について検討した。その結果、この組合せ除染法によれば、ステンレス鋼の腐食を抑制したまま $1/100$ 程度まで効率良く表面の除染ができることを見いだした。なお、アイソトープ部における $100\ \text{Ci}$ 規模のトリチウム製造試験に用いられた配管について、本法による汚染除去試験を行なった結果、内部深くまで拡散してしまったトリチウム以外は、効率良く除去できることが実証された。

5.2.3 ガラス表面におけるトリチウムの収着と脱離

(a) トリチウムの収着〔1,5〕

研究実験用の基本材料の一つであるホウケイ酸ガラス (パイレックスガラス) に対するトリチウムの収着速度 (v) は、多孔性物質の細孔内拡散を考慮した BANGHAM の定圧吸着速度式

$$v = kt^{1/m}, \quad k = 0.039, \quad m = 1.6, \quad t: \text{時間 (hr)}$$

によって近似できる。

ガラス表面におけるトリチウムの収着機構には、化学的および物理的な収着の2様式がある。化学的な収着は、主に最外表面上および深さ $2\ \mu\text{m}$ 程度の表面層に存在するマイクロクラックの内表面上で起こる。この収着は、トリチウムの OH 基の水素との同位体交換反応およびトリチウムと SiO_2 との反応によって、OT 基を形成することにより進行する。物理的な収着では、トリチウムがガラスの SiO_2 の網目構造の "free-volume" に侵入し、解離されることなく、分子状のまま捕捉されることを見いだした。このガス状で内部に侵入するトリチウムの量は、接触させるトリチウムのガス圧に正比例して増加した。

(b) 放射線照射効果 [5,9]

ガス状トリチウムのガラス表面上への化学的な収着は、トリチウム自身から放射される β 線あるいは外部から照射する γ 線によって促進されることを見いだした。ガラス表面（深さ0 - 3.0 μ m）へのトリチウム収着量は、接触させるトリチウム・ガスの比放射能に比例して増大する（Table 2）。また、Fig. 5に示したように、トリチウムの収着量は、 γ 線の照射線量とトリチウムのガス圧の積の平方根に比例して増大しており、 γ 線による収着促進効果のあることが明らかにされた。さらに、 SiO_2 の網目構造の中に侵入し、物理的に収着されている分子状のトリチウムが、放射線照射によって完全に化学的な収着状態に変化することも明らかにした。これらの事実から、軽水素や重水素を用いた実験では、トリチウムの挙動の推定が困難な現象のあることを再確認した。

(T. Hirabayashi)

Publication List

- [1] Hirabayashi, T., Tachikawa, E.: "Sorption and desorption of tritium on the surface of borosilicate glass", *Radiochim. Acta*, 33, 61(1983).
- [2] Saeki, M., Hirabayashi, T., Aratono, Y., Hasegawa, T., Tachikawa, E.: "Preparation of gas chromatographic column for separation of hydrogen isotopes and its application to analysis of commercially available tritium gas", *J. Nucl. Sci. Technol.*, 20, 762(1983).
- [3] Hirabayashi, T., Saeki, M.: "Sorption of gaseous tritium on the surface of type 316 stainless steel", *J. Nucl. Mater.*, 120, 309(1984).
- [4] Hirabayashi, T., Saeki, M., Tachikawa, E.: "A thermal desorption study of the surface interaction between tritium and type 316 stainless steel", *J. Nucl. Mater.*, 126, 38(1984).
- [5] Saeki, M., Hirabayashi, T.: "Sorption mechanisms of tritium on the surface of borosilicate glass", *Radiochim. Acta*, 35, 233(1984).

- [6] Saeki, M., Hirabayashi, T. : "Desorption behavior of carrier free tritium from the inner surface of glass ampoule", Radioisotopes, 33, 776(1984), (in Japanese).
- [7] Hirabayashi, T., Saeki, M., Tachikawa, E.: "Effect of surface treatments on the sorption of tritium on type 316 stainless steel", J. Nucl. Mater., 127, 187(1985).
- [8] Hirabayashi, T., Saeki, M., Tachikawa, E.: "Chemical decontamination of the tritium-sorbing surface of type 316 stainless steel", J. Nucl. Mater., 136, 179 (1985).
- [9] Saeki, M., Hirabayashi, T.: "Effects of ionizing radiations on the amount and the chemical forms of tritium sorbed on the surface of borosilicate glass", Radiochim. Acta, 38, 37(1985).

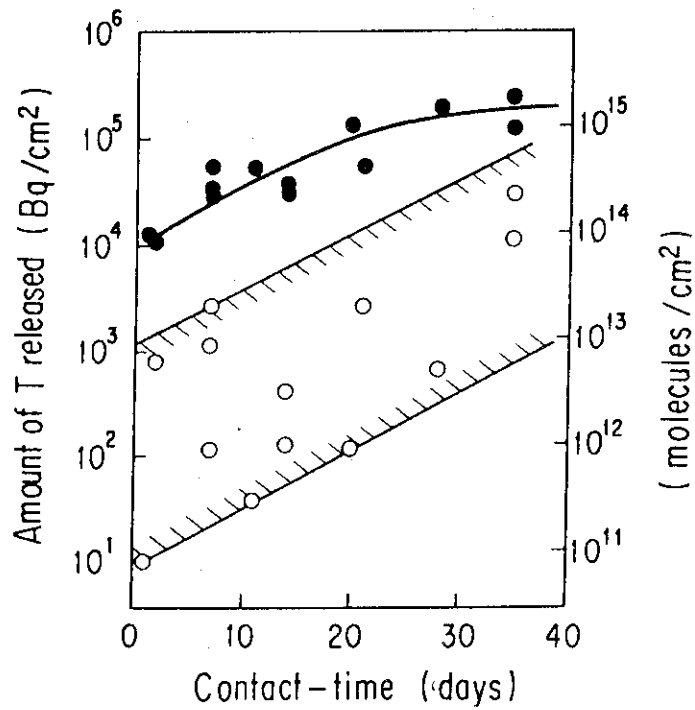


Fig. 1. Release of tritium as HT (○) and as HTO (●) from the stainless steel contacted with 13.3 kPa of HT-gas for various times at 293 K.

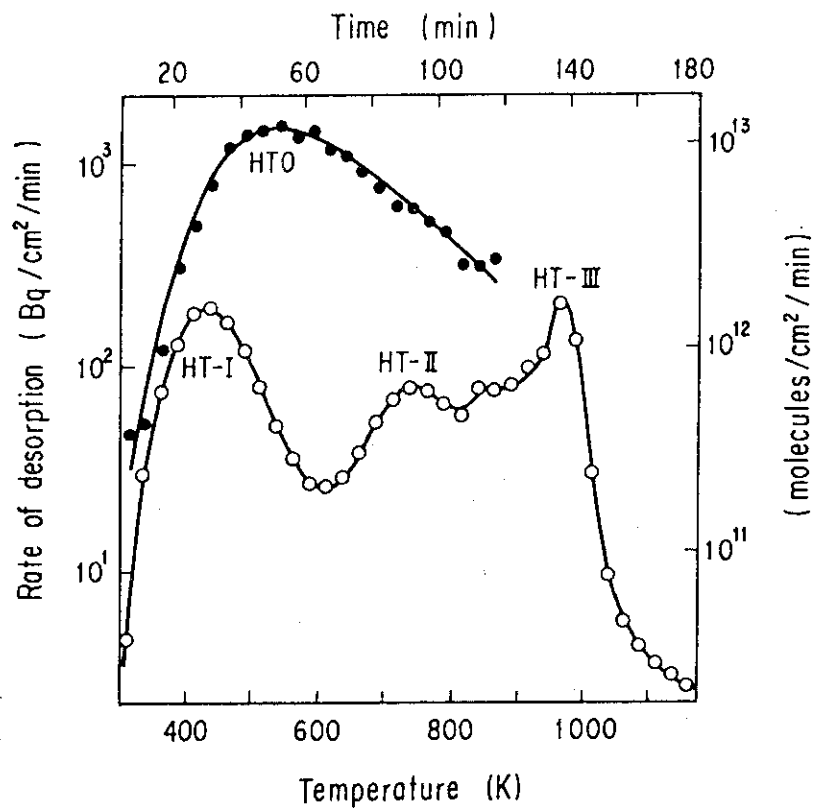


Fig. 2. The thermal desorption spectra of tritium (○: HT, ●: HTO) desorbing from the stainless steel sample.

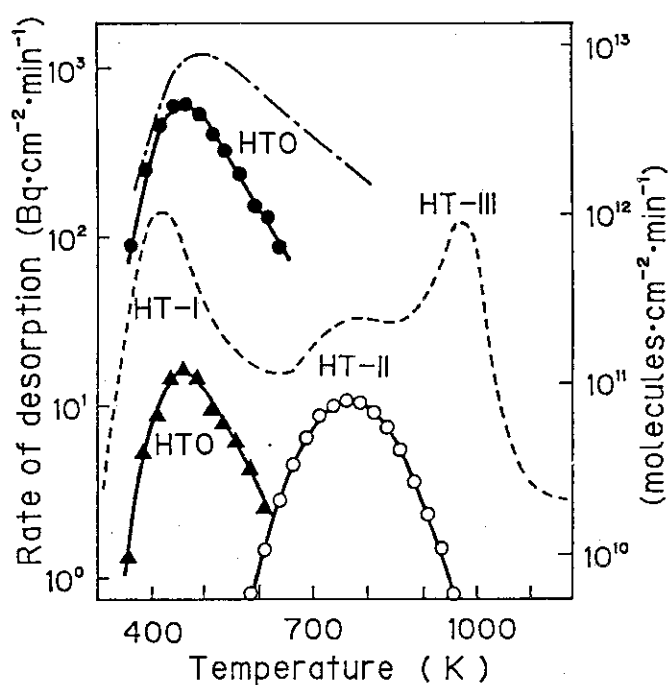


Fig. 3 Thermal desorption spectra of tritium desorbing from the specimens before [spectra (a); ----:HT, ---:HTO] and after dipping in dil. HCl for 2 h [spectra (b); ○:HT, ●:HTO] and 24 h [spectrum (c); ▲:HTO].

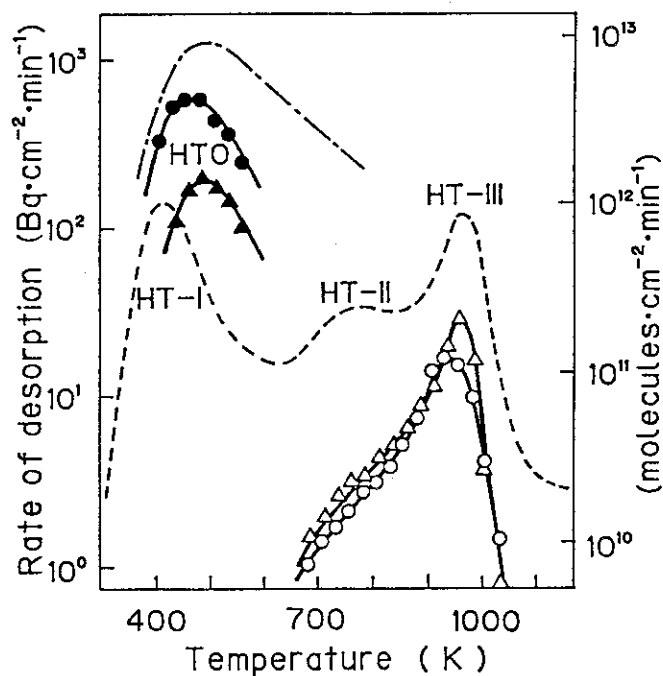


Fig. 4 Thermal desorption spectra of tritium desorbing from the specimens before [spectra (a); ----:HT, ---:HTO] and after dipping in $\text{CuSO}_4\text{-H}_2\text{SO}_4$ for 2 h [spectra (b); ○:HT, ●:HTO] and 24 h [spectra (c); △:HT, ▲:HTO].

Table 1 Summary of the results obtained

Name of thermal desorption peak	T_m^a (K)	E_d^b (kJ·mol ⁻¹)	Predictable form of sorbed tritium	Component related to the sorption site	Distribution of sorption site	Effective type of corrosion for decontamination
HT-I	430	20 ± 4	molecular species	(OT ⁻ , OH ⁻ , O ²⁻)	topmost surface	any
HTO	540	27 ± 7	OT ⁻ ion	Fe	surface + intergranule	whole surface intergranular
HT-II	750	55 ± 9	atomic species	Mo _x Cy	intergranule	intergranular
HT-III	970	> 55	atomic species	Ni	surface layer	whole surface

^a T_m is the temperature at maximal rate of thermal desorption peak.

^b E_d is the activation energy of desorption.

Table 2 Specific activity effect on the amount of tritium sorbed on Pyrex glass

Specific activity of tritiated gases (TBq/mol)	Sorbed tritium (10^{15} atoms/cm ²)		
	0 - 3.0 μm	3.0 - 11.4 μm	>11.4 μm
56.6	5.6 ± 0.3	0.22 ± 0.02	0.63 ± 0.04
19.6	3.2 ± 0.2	0.25 ± 0.02	0.78 ± 0.05
16.8	2.4 ± 0.3	0.22 ± 0.03	0.73 ± 0.08

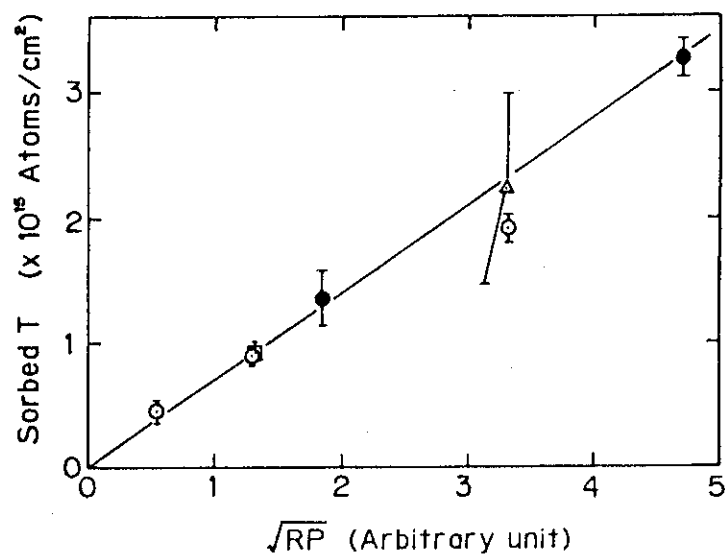


Fig. 5. Relationship between the amount of tritium sorbed on the surface and the square root of the product of the absorbed gamma ray dose (R) and pressure of the sorbing gas (P).

- : Pyrex glass was exposed to 6.65 kPa of the DT-gas for 21 h.
- : Pyrex glass was exposed to 13.3 kPa of the DT-gas for 21 h.
- : Fused silica was exposed to 6.65 kPa of the DT-gas for 21 h.
- △: Pyrex glass was gamma ray irradiated at the end of 135-day exposure to the DT-gas.

5.3 固体吸着剤によるトリチウムの捕集

5.3.1 緒言

トリチウムは従来最も毒性の低い放射性核種のひとつと考えられ、RI 実験室や原子炉施設などでは比較的安易に取扱われており、漏洩トリチウムのほとんどがそのまま、あるいは希釈して放出されている。本テーマは、核融合炉開発に伴なって取扱量の増加が予想されるトリチウムの環境放出低減化に関連した研究として開始された。トリチウムの捕集には、トリチウムガスを適当な酸化触媒によりトリチウム水として、乾燥剤に捕集する方法が一般的に用いられている。捕集剤としては、モレキュラーシーブ 4A または 5A、シリカゲル、活性アルミナなどが用いられる。本テーマでは、最初にシリカゲルによるトリチウムの捕集機構を調べ〔1〕、さらにこれら代表的な捕集剤の最大捕集容量、捕集速度の測定を行った〔2〕。また、トリチウムを捕集した捕集剤の保管、廃棄の際に問題となる、放射線分解による水素ガスの発生を調べる為に、シリカゲルに収着したトリチウム水の γ 線および β 線による放射線分解を調べた〔3〕。

5.3.2 シリカゲルによるトリチウム水の捕集〔1〕

600℃以下の種々温度で前処理されたシリカゲルにトリチウム水（48 $\mu\text{Ci}/\text{ml}$ ）蒸気を矩形パルスとして導入し吸着させ、これを Ar ガスを流しながら、5℃/min で 900℃まで昇温し、脱離スペクトルをとると、300℃以下の処理では二つのピークを示し、400℃以上の処理では三つのピークを示す（Fig. 1, 2）。これらの成分の割合は前処理温度に依存し、トリチウムの捕集サイトの違いを示している（Table 1）。シリカゲルは吸着水として、約 200℃以上で徐々に脱離する化学吸着水（表面水酸基）と、200℃までに脱離する物理吸着水（表面水酸基上に吸着）を有しており、これらの吸着水と HTO 蒸気との同位体交換反応が捕集機構において重要な役割を果たしている。すなわち一部物理吸着水を有するシリカゲルでは、HTO はすでに吸着している物理吸着水上に吸着し、同位体交換反応によりトリチウムが物理吸着水と表面水酸基とに分配されて平衡に達する。200℃以上で加熱処理されたシリカゲルでは、表面水酸基の脱離が始まっており、脱離の程度は処理温度とともに大きくなるが、300℃以下では水酸基の脱離サイトは水の吸着によって可逆的に水酸基を再生するものと考えられ、したがって 300℃以下で処理されたシリカゲルでは、残留水酸基上への HTO の吸着とそれに続く同位体交換反応による水酸基へのトリチウムの取込み、あるいは表面水酸基の再生（OT 基）という過程でトリチウムが捕集される。400℃～600℃の加熱処理では、水酸基の脱離した後の表面での水酸基の再生は必ずしも可逆的ではなく、その速度は前処理温度に依存し、高温で処理したものほど水酸基の再生の速度は遅くなる。このような表面へのトリチウム水の吸着は、水酸基の脱離した表面への吸着とそれに続く表面水酸基の再形成、残留水酸基上への吸着と同位体交換反応などがその表面状態に依存して起こると考えられる。このようにトリチウム水の捕集は、トリチウムそのものに注目した場合には単なる水の捕集とは異なり、吸着水や表面水酸基との同位体交換反応を考慮する必要があることが明らかとなった。これらの結果は、乾燥シリカゲルと水を含んだシリカゲルが同等の捕集能を示す事や、HTO の保持時間が H_2O に比べ大きいという他の研究報告に見られる実験事実も説明することができる。

5.3.3 各種固体吸着剤によるトリチウム水の捕集〔2〕

シリカゲル等の吸着剤を捕集カラムとして、実際に使用するさいに重要なパラメータは、最大捕集容量と捕集速度定数である。これらのパラメータは、捕集トリチウムのカラム内分布を測定することにより求めることができる。モレキュラーシーブ5A, 13X, シリカゲルおよび活性アルミナの小さなカラムを用いて得られた結果は一次の速度式(1)により解析することができた。

$$A = K \cdot A_m \cdot C_0 \cdot \exp \{ (-K A_m / v) \ell \} t \quad \dots\dots\dots (1)$$

- A : 捕集 HTO 量 (mmol/ml)
 K : 捕集速度定数 (ml/mmol・min)
 A_m : 最大捕集容量 (mmol/ml)
 C_0 : 気相中の HTO 初期濃度 (mmol/ml)
 C : 気相中の HTO 濃度 (mmol/ml)
 v : ガスの線流速 (cm/min)
 ℓ : カラムの入口からの距離 (cm)
 t : HTO の供給時間 (min)

シリカゲルおよび活性アルミナの最大捕集容量は、カラム温度 25℃においてモレキュラーシーブの約 1.5 倍と大きい、温度依存性が大きく 80℃ではモレキュラーシーブの約半分に減少する (Table 2)。またシリカゲル、活性アルミナではキャリアガス中の水蒸気分圧にも大きく影響され、0.67 kPa から 3.2 kPa の水蒸気圧の範囲で約 4 倍も最大捕集容量が変化する (Fig. 3)。一方、モレキュラーシーブの最大捕集容量は温度および水蒸気分圧の影響を受けにくい。また、みかけの吸着速度はいずれの捕集剤についても大きい、特にモレキュラーシーブ 5A で大きい。このようなモレキュラーシーブの優れた捕集特性は、結晶内の陽イオンが水のような極性分子を強く引きつけて吸着することに起因しており、シリカゲルや活性アルミナへの吸着が主に水素結合によるものであることと異なっている。

得られた最大捕集容量と捕集速度定数を用いて、トリチウムの破過時間をカラムの長さの関数として表わすことができる。

$$t = a \ell - b \ln (C_0 / C_B) \quad \dots\dots\dots (2)$$

$$a = A_m / v C_0, \quad b = 1 / 2 K C_0$$

(2)式は、長さ ℓ (cm) のカラムを用いたとき、出口濃度が C_B になるまでの時間が t (min) であることを表わしている。(2)式による計算値と実験値は良く一致した。

5.3.4 シリカゲルに捕集されたトリチウム水の γ 線分解

トリチウム水を捕集した捕集剤を保管、廃棄する場合の自己放射線分解による水素ガス (HT) の発生量評価の為に、まず ^{60}Co - γ 線照射による実験を行った。用いたシリカゲルは BET 表面積および表面水酸基濃度の異なる 3 種のガスクロマトグラフ用充填剤である (Table 3)。水素ガスの発生量はシリカゲル重量に対する吸着水量の割合 (P 値) に依存し、P 値一定においては、約 $4 \times 10^{20} \text{ eV/g}$ まで吸収エネルギーに一次に比例する (真空下)。試料全体のエネルギー

—吸収を考慮して求めた水素発生のG値 ($G(H_2)_{ES}$) はシリカゲルの種類によって異なる (Fig. 4)。SG-A 試料では純水における G_{H_2} 値 (0.45) の約2倍、他の2つの試料では G_{H_2} 値より小さい。また、いずれの試料でも、“Liquid line”^{*}より大きい $G(H_2)_{ES}$ 値を示した。これらの結果より、吸着水の分解においてはシリカゲルからのエネルギー移動が重要な役割を果たしており、その寄与の大きさはシリカゲル表面の水酸基濃度および吸着層の厚みと相関していると考えられる。そこで適当な吸着モデルを用いて、発生水素量を3種類のシリカゲルについて統一的に表わすことを試みた (Fig. 5)。その結果、発生水素量 (Y_{H_2}) を

$$Y_{H_2} = [\text{シリカゲルからのエネルギー移動による生成水素}] \\ + [\text{吸着水に直接吸収されたエネルギーによる生成水素}] \\ = R_{SGOH} \cdot P \cdot \frac{k_\gamma}{C_{OH}} \cdot \ell \cdot \mu_\gamma \theta + G_{H_2} \cdot \frac{R_{H_2O}}{100} \quad \dots\dots\dots (3)$$

と表わすことができた。ここで R_{SGOH} , R_{H_2O} はそれぞれシリカゲルと吸着水に吸収されたエネルギー (eV), C_{OH} はシリカゲルの表面水酸基濃度 ($1/\text{nm}^2$), θ は吸着層の数, k_γ と μ_γ は定数である。Fig. 5 は、シリカゲルからのエネルギー移動による水素生成量の補正值 (A) を吸着層の数 (θ) に対してプロットしたものである。

$$A = \frac{\left(Y_{H_2} - G_{H_2} \frac{R_{H_2O}}{100} \right) C_{OH}}{R_{SGOH} \cdot P} = k_\gamma \cdot \ell \cdot \mu_\gamma \theta \quad \dots\dots\dots (4)$$

この結果、シリカゲルからのエネルギー移動は表面水酸基を通して起こると考えられ、このエネルギー移動による水素生成量は C_{OH} に反比例することが解った。さらに水素生成量は吸着層の増加とともに減少することから、吸着水の増加によってエネルギーの分散が起こり、吸着水の分解確率が減少するものと考えられる。

5.3.5 シリカゲルに捕集されたトリチウム水の自己放射線分解

前節の $^{60}\text{Co}-\gamma$ 線の外部照射による吸着トリチウム水の放射線分解に続いて、トリチウムの β 線による自己放射線分解について調べた。吸着トリチウム水の濃度は 261 MBq/g (7.06 mCi/g) で、吸着水量は $P = 0.04 \sim 0.32$ である。試料の吸収したエネルギーは、トリチウムの壊変数と β 線の平均エネルギー 5.68 keV を用いて計算し、最高 $2 \times 10^{19} \text{ eV/g}$ であった。水素発生のみかけのG値を Fig. 6 に示す。水素発生量は、 γ 線照射の場合と同様シリカゲルからのエネルギー移動効果による生成促進を起こし、前節で得られた(3)式によって表わすことが出来た。

(Fig. 7) また、 γ 線による分解と自己放射線分解の差は顕著ではないが、 $\theta > 2$ でわずかに自己放射線分解による水素発生量が多い傾向が見られた。酸素の発生は、 γ 線照射の場合と同様、観測されなかった。

(M. Nakashima)

* 固体と吸着物質の間に相互作用は全くなく、固体は単に希釈剤としてのみ働き、固体に吸収されたエネルギーは吸着物質の分解に寄与しないと仮定し、さらに吸着物質は、それが液相の場合の G_{H_2} 値で分解生成物を与えるとした時の $G(H_2)$ 値。

Publication List

- [1] Nakashima, M., Tachikawa, E., Saeki, M. and Aratono, Y.:
"Removal mechanism of tritium by variously pretreated silica gel", J. Inorg. Nucl. Chem., 43, 369(1981).
- [2] Nakashima, M. and Tachikawa, E.: "Removal of tritiated water vapor by molecular sieve 5A and 13X, silica gel and activated alumina", J. Nucl. Sci. Technol., 19, 571(1982).
- [3] Nakashima, M. and Tachikawa, E.: "Hydrogen evolution from tritiated water on silica gel by gamma-irradiation.", Radiochim. Acta, 33, 217(1983).
- [4] Nakashima, M. and Tachikawa, E.: "Release of radioiodine from U_3O_8 . Possible chemical form of iodine", J. Inorg. Nucl. Chem., 43, 1686(1981).
- [5] Nakashima, M., Saeki, ., Aratono, Y. and Tachikawa, E.:
"Release of radioiodine from UO_2 during reactor operation", Int. J. Appl. Radiat. Isot., 32, 397(1981).
- [6] Nakashima, M., Aratono, Y. and Tachikawa, E.: "Diffusivity of recoil-injected or thermally-doped tritium in aluminum", J. Nucl. Mater., 98, 27(1981).
- [7] Yokoyama, A., Nakashima, M. and Tachikawa, E.: "Chemical form of tritium on the release from aluminum", J. Nucl. Mater., 101, 9(1981).
- [8] Nakashima, M., Saeki, M., Aratono, Y. and Tachikawa, E.:
"Diffusivity of tritium in Li-Al alloys", J. Nucl. Mater., 116, 141(1983).

Table 1 Distribution of tritium among each fraction in variously pretreated silica gels with 5-minutes pulse loading. (%)

Sample	Fraction A	Fraction B	Fraction C
SG-N	5	/	95
SG-100	1	/	99
SG-200	0.1	/	100
SG-300	2	/	98
SG-400	5	5	90
SG-500	18	18	64
SG-600	23	20	57

Table 2 Temperature dependence of the maximum adsorption capacity (mmol/ml).

Column Temp. (°C)	Silica Gel	Activated Alumina	Molecular Sieve 13X	Molecular Sieve 5A
25	16.0 ± 0.4	14.8 ± 1.7	10.0 ± 0.9	9.6 ± 0.6
40	6.2 ± 0.1	6.9 ± 0.4	7.5 ± 0.2	7.4 ± 0.5
55	4.1 ± 0.2	5.6 ± 0.1	6.7 ± 0.2	6.8 ± 0.1
70	3.0 ± 0.2	4.6 ± 0.2	6.2 ± 0.2	6.3 ± 0.1
80	2.6 ± 0.1	4.2 ± 0.2	5.4 ± 0.2	5.8 ± 0.4

Table 3 Specifications of the samples used in the present study

Sample	Surface area (A_{BET}), m ² /g	Concentration of surface hydroxyls (C_{OH}), OH/(nm) ²	Mesh
SG-A	546	4.6	60/80
SG-B	197	5.4	60/80
SG-C	99	12.2	80/100

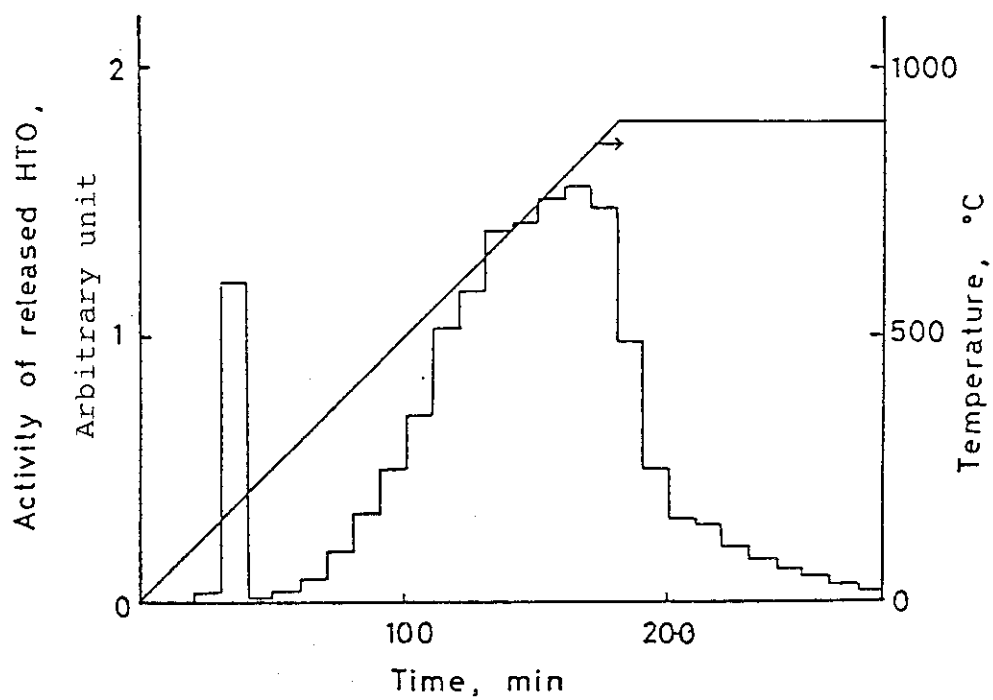


Fig. 1 Release of tritium from SG-N loaded with HTO for 5 min.

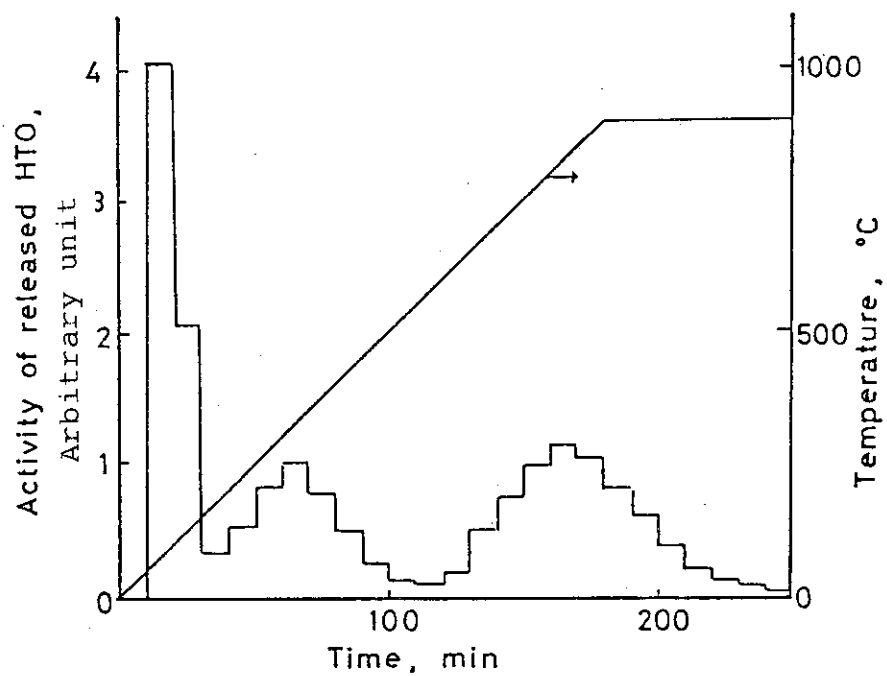


Fig. 2 Release of tritium from SG-600 loaded with HTO for 5 min.

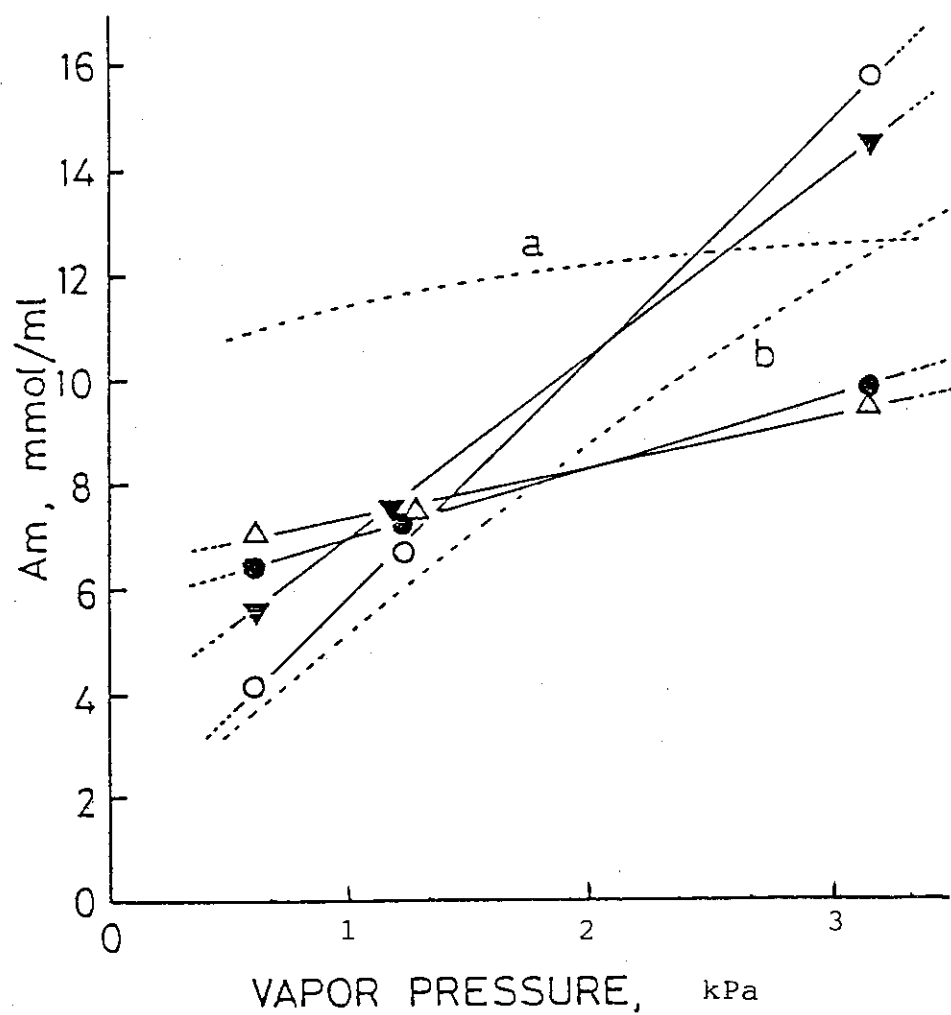


Fig. 3 Maximum adsorption capacity of silica gel(O), activated alumina(▼), molecular sieve 13X(●) and 5A(△) with varying HTO vapor pressure in feed gas. The dotted lines represent the results on type A zeolite(a) and silica gel(b) in Ref.113.

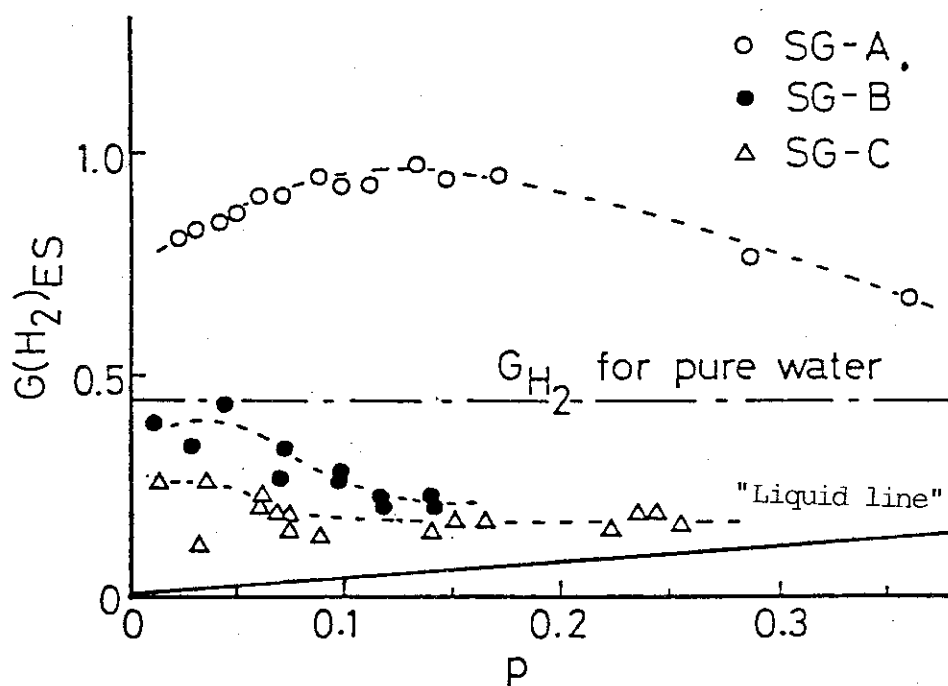


Fig. 4 $G(H_2)$ values calculated from energy absorbed by the entire system as a function of p value.

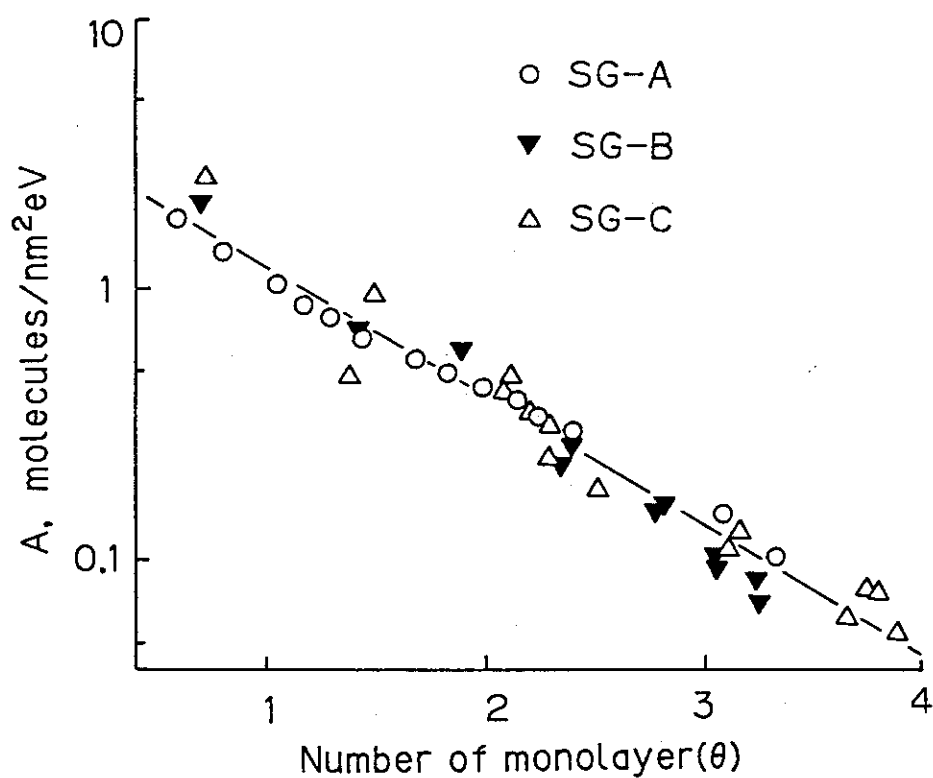


Fig. 5 Corrected value of hydrogen yields(A) arising from energy transfer effect vs. surface coverage(θ).

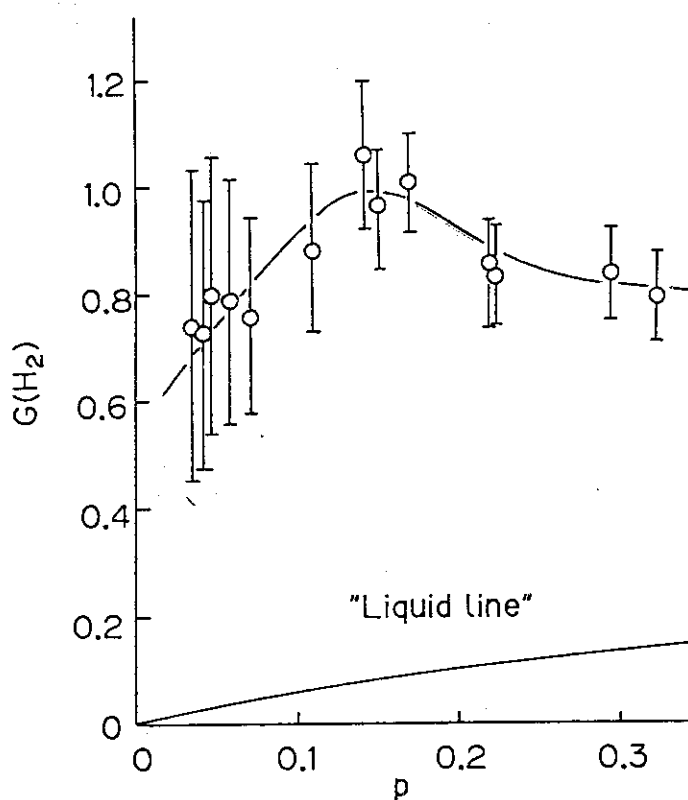


Fig. 6 Hydrogen yields per 100eV of the energy absorbed by entire system($G(H_2)$) as a function of p value.

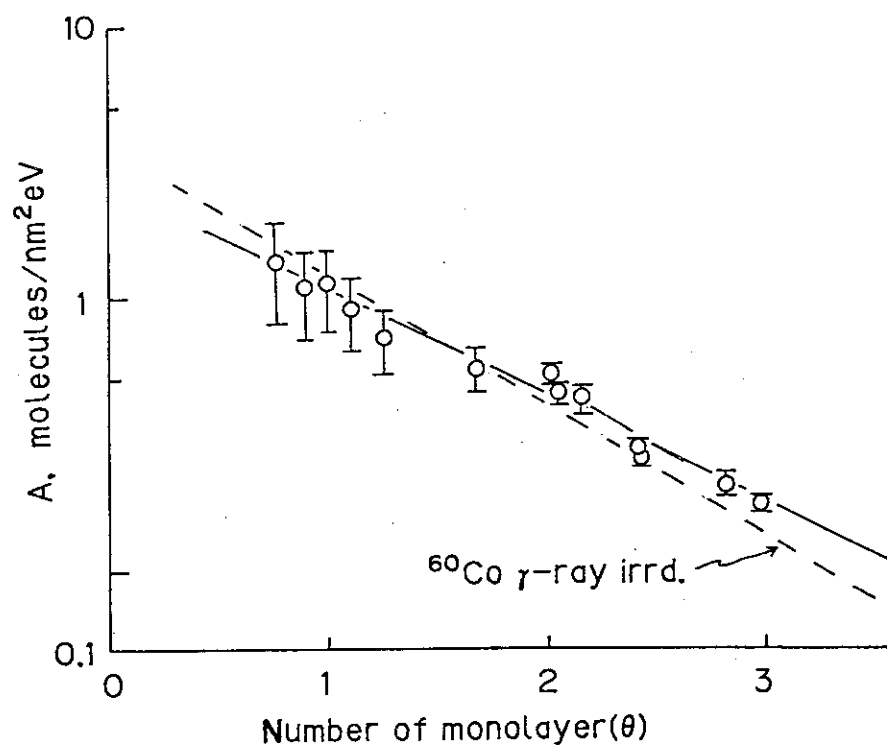


Fig. 7 Relation of corrected value (A) of hydrogen yields arising from energy transfer effect to surface coverage (θ).

6. CRUD BEHAVIOR AND CHEMICAL DECONTAMINATION FOR NUCLEAR REACTOR

E.Tachikawa, M.Hoshi, T.Suwa, C.Sagawa,
C.Yonezawa, S.Goto and N.Kuribayashi

6. クラッドおよび原子炉除染の化学

立川 圓造・星 三千男・諏訪 武・佐川 千明
米沢伸四郎・後藤 覚司・栗林 伸英

6.1 SUS-304の腐食と水中クラッドの挙動

6.1.1 はじめに

放射性腐食生成物（クラッド）は原子炉一次冷却系に蓄積し、原子炉関連技術者の被曝線量の増大をもたらすため問題にされている¹⁾。現在まで、蓄積低減化のため、種々の対策が講じられ、かなりの成果をおさめているが、クラッドの生成、移行、沈着、蓄積の過程に関して、不明の点も多い^{2,3)}、本研究ではクラッドの性状および挙動を把握することを目的とした。

6.1.2 SUS-304の腐食〔1〕

280℃、脱気静水中のSUS-304試験片から生成したクラッドは大部分がマグネタイトあるいはフェライトで構成される。全腐食金属量 (M_{total}) は水中に放出された金属量 (M_{rel})、試験片付着クラッドの外層 (M_{out}) および内層 (M_{inn}) 中の金属量の和になる。反応時間が100時間以上の定常状態では、Fig. 1に示すように、 M_{inn} は $(47 \pm 5) \mu\text{g}/\text{cm}^2$ と一定である。一方 ($M_{out} + M_{rel}$) は、式(1)のように表わされる。

$$M_{out} + M_{rel} = (11.2 \pm 6.7) + (3.34 \pm 0.23) \times \sqrt{t} \quad \mu\text{g}/\text{cm}^2 \quad (1)$$

t : 反応時間 (hour)

したがって、 M_{total} は式(2)のようになり

$$M_{total} = (58.2 \pm 4.4) + (3.34 \pm 0.23) \times \sqrt{t} \quad \mu\text{g}/\text{cm}^2 \quad (2)$$

SUS-304の腐食は放物線則に従うことを明かにした。式(2)から、1000時間での腐食速度として $0.39 \text{ mg} \cdot \text{dm}^{-2} \cdot \text{day}^{-1}$ (mdd) が得られるが、一般に受けいれられている値、0.1 mdd あるいは Lister がループ実験で得た 1.0 mdd と異なっている^{2,4)}。これは本実験が脱気静水中で行われたのに対し、他の場合は流動水でしかも数 ppb の溶存酸素量を含むなど実験条件が異なるためである。

一方、腐食に伴って発生する水素量、 $[H_2]$ は式(3)で

$$[H_2] = (8.74 \pm 0.66) + (0.50 \pm 0.04) \times \sqrt{t} \quad 10^{17} \text{ 分子}/\text{cm}^2 \quad (3)$$

表わされ、腐食が全体としては、式(4)で示すように



SUS-304 を構成する金属元素、Mと水との反応で進行するとして計算した値とよく一致し、水素ガスの測定により、腐食量が決定できることを示した。

SUS-304 を構成する金属元素の水中への溶出は $Fe > Mn > Co \simeq Ni > Cr$ の順になり、水中でのこれらの金属元素イオンの溶解度の順序に一致する⁵⁾。また、水中に溶出したクラッドと試験片クラッド外層の金属元素組成はほぼ同じであり、クラッド外層は水中クラッドが付着して生成すること、および内層にはCrが濃縮されることを明かにした⁶⁾。

原子炉で照射（中性子束が $5 \times 10^{13} S^{-1}$ で2時間照射）した試験片では腐食量が非照射のものより50%ほど大きくなる結果を得、照射により試験片に生じた欠陥が腐食を促進する効果を見出した。

6.1.3 ^{60}Co の存在状態〔2〕

Co(II)イオンはジエチルジチオカルバミン酸(DDC)と安定な錯体を生成し、pH 1～8でクロロホルム、四塩化炭素などの有機溶媒に定量的に抽出される(Fig. 2)。しかし、pH8以上では空气中に放置すると時間とともに抽出率が低下し、低下の度合はpHとともに大きくなることが観測された。報告されている安定度定数に基づいて計算するとCoがⅡ価で水溶液中に存在する限り、pHが1～14の範囲では定量的抽出が可能という結果になる^{8, 9)}。一方、pH8以上の領域で溶液中の溶存酸素濃度を変えた実験から、抽出されるCo量、 Co_{ext} の時間変化は

$$-d[Co_{ext}]/dt = k[Co_{ext}][O_2]^{1/4} \quad (5)$$

で表わされ、抽出率の低下は酸化還元電位が示すように低pH領域では起らない、Co(II)が酸素によりCo(III)に酸化されるためであることを明かにした。それとともに、室温付近の酸化で生成したCo(III)はpHを6以下にすると再び抽出可能な状態になること、および一次冷却水条件下(～280℃)で生成した不溶性クラッド(クラッド-P)中の ^{60}Co は濃塩酸などによりクラッドを完全に分解しない限り、抽出されないことがわかった。

この性質を材料試験炉(JMTR)・OWL-1のループ水に適用して、可溶性 ^{60}Co の75～95%が Co^{2+} 、5～22%がCo(III)、残りの数%が細粒状のクラッドで存在することを明かにした。この結果は従来のイオン交換法で得られた結果と一致するが、溶媒抽出法はあらかじめ可溶性クラッド(クラッド-F)とクラッド-Pを分離することなく適用できる、Co(II)とCo(III)の状態を識別できるなどの利点をもっている。

6.1.4 SUS-304 およびジルカロイ-2 試験片への水中クラッドの付着〔3〕〔4〕

JMTRの運転期間中に採取したOWL-1ループ水を0.45 μmのミリポアフィルターでろ過し、クラッド-Fとクラッド-Pに分類すると、金属元素濃度はクラッド-Fが20～30 μg/ℓ、クラッド-Pが～1 μg/ℓを示すが、両者とも主要元素はFe, Cr, Niでその構成比に差が認められないこと、 ^{60}Co のCo量に対する比放射能はクラッド-Fで0.005 μCi/μg、クラッド-Pで0.1 μCi/μgを示して、1オーダー以上異なること、さらにクラッド-Pには M_3O_4 型酸化物と M_2O_3 型酸化物が78:22の割合で存在することがわかった。

これに対して、ループ水中に浸漬した SUS-304 試験片上のクラッドは表面を剥離するにつれて M_3O_4 型酸化物が若干見られるものの大部分が M_2O_3 型酸化物であること、XMA によるスポット分析の結果は Fe 含量の多いクラッドと Cr 含量の多いクラッドが存在することを示した。ジルカロイ-2 試験片の場合には大部分が Cr 含量の多いクラッドであった。このように、試験片表面付着クラッドの元素組成と化合物組成は水中クラッドの分析結果と大きく異なることが明らかになった。また比放射能、 $^{60}\text{Co}/\text{Co}$ の値は SUS-304 およびジルカロイ-2 試験片とも表面からの剥離順に小さくなり、表面の値はループ水中のクラッド-P、母材に近い部分はクラッド-F の値にほぼ等しくなった。これらの結果は、はじめに試験片上に腐食によって形成された M_3O_4 あるいは ZrO_2 の表面にループ水中の M_2O_3 型酸化物が静電的相互作用により選択的に付着してクラッド外層が形成され、母材に近い酸化皮膜はクラッド-F が取り込まれて成長するためと考えた。

Table 1 に示すように、クラッド-F、-P には、 ^{60}Co 、 ^{58}Co 、 ^{54}Mn 、 ^{56}Mn 、 ^{51}Cr が検出されるが、同位体である ^{60}Co と ^{58}Co および ^{54}Mn と ^{56}Mn のクラッド-F / クラッド-P 中での存在割合を計算すると、 ^{60}Co と ^{58}Co ではともに約 1.0、 ^{54}Mn と ^{56}Mn ではともに約 6.0 の値が得られた。このように、これらの先行非放射性核種が ^{59}Co と ^{58}Ni あるいは ^{54}Fe と ^{55}Mn であり元素が異なるにもかかわらず同位体間で等しい値になったこと、さらには既に述べたように、クラッド-P と -F では ^{60}Co の比放射能が異なることは、i) Co と Ni および Fe と Mn の化学的性質が類似する、ii) 核反応が起っても ^{60}Co と ^{58}Co および ^{54}Mn と ^{56}Mn の化学形は最終的には先行核種の化学形を保持する。iii) クラッド-P と -F 間の同位体交換反応が非常に遅い結果として説明できる。

6.1.5 SUS-304 への ^{60}Co の拡散〔5〕

280℃水中から SUS-304 に付着した ^{60}Co はクラッド層ばかりでなく、一部は SUS-304 母材中に拡散する。拡散挙動は不活性ガス雰囲気で行った実験、さらには ^{63}Ni の場合と同じく、SUS-304 の表面に近い部分は見かけ上、拡散定数、 $D_v = (6.0 \pm 4.0) \times 10^{-19} \text{ cm}^2/\text{s}$ である体積拡散に支配され、内部は定数 $\delta D_{gb} = (1.4 \pm 1.0) \times 10^{-21} \text{ cm}^3/\text{s}$ (δ は粒界幅) である粒界拡散に支配される結果を得た。これらの D_v と δD_{gb} は Fig. 3 に示すように、JPDR 原子炉浄化系配管および OWL-1 試験片中の ^{60}Co の拡散挙動をよく説明した。しかし、600～1250℃で得た文献からの外挿値とは大きく異なる¹⁰⁾。これらは 280℃という低温では転位面などを経¹¹⁾由する拡散現象が現れるためと考えた。

(M. Hoshi)

Reference

- 1) Berry,W.E., Diegle,R.B.: EPRI-NP-522 (1979)
- 2) Izumiya,M., et al.: Karyoku Genshiryoku Hatsuden, 27, 419 (1976) (in Japanese)
- 3) Meguro,Y., et al.: Karyoku Genshiryoku Hatsuden, 30, 563 (1979) (in Japanese)
- 4) Lister,D.H.: Nucl. Sci. Enginner., 59, 406 (1976)
- 5) Cohen,P.: "Water Coolant Technology of Power Reactors", (1969), AEC Monograph, Gordon and Breach, Science Publishers, New York
- 6) Potter,E.C., Mann,G.M.W.: Proc. 1st Int. Cong. Metallic Corrosion, p.147 (1962), Butterworths, London
- 7) Stary,J., Kratzer,K.: Anal. Chim. Acta, 40, 93 (1968)
- 8) Usatenko,Yu.I., Barkalov,V.S., Tulyupa,F.M.: Zh. Anal. Khimii, 25, 1458 (1970)
- 9) Baes,C.F.,Jr., Mesmer,R.E.: "The Hydrolysis of Cations", p.238 (1976), John Wiley and Sons, Inc., New York
- 10) Perkins,R.A.: Metall. Trans., 4, 1665 (1973)
- 11) Mimkes,J., Wuttig,M.: Phys. Rev., B2, 1619 (1970)

Publication List

- [1] Tachikawa,E., Hoshi,M., Sagawa,C., Yonezawa,C., Nakashima,M.: "Investigation of oxide formed in the corrosion of SUS-304 in high-temperature water through the measurement of evolved hydrogen and radiochemical analyses", Nucl. Technol., 65, 138 (1984)
- [2] Hoshi,M., Tachikawa,E., Yonezawa,C., Goto,S., Yamamoto,K.: "Crud behaviors in high-temperature water III. Chemical form of ⁶⁰Co in JMTR OWL-1 loop water",

- J. Nucl. Sci. Technol., submitted for publication
- [3] Hoshi, M., Tachikawa, E., Suwa, T., Sagawa, C., Yonezawa, C., Aoyama, I., Yamamoto, K.: "Crud behaviors in high-temperature water I. Characterization of water in JMTR OWL-1 loop", J. Nucl. Sci. Technol., submitted for publication
- [4] Hoshi, M., Tachikawa, E., Suwa, T., Sagawa, C., Yonezawa, C., Tomita, M., Shimizu, M., Yamamoto, K.: "Crud behaviors in high-temperature water II. Characterization of corrosion layer on type 304 stainless steel and zircaloy-2", J. Nucl. Sci. Technol., submitted for publication
- [5] Hoshi, M., Tachikawa, E., Sagawa, C., Yonezawa, C., Goto, S.: "Tracer diffusion of ^{60}Co into SUS-304", J. Nucl. Mater., 120, 154 (1984)
- [6] Hoshi, M., Irumagawa, H., Sagawa, C., Tachikawa, E.: "Substoichiometric determination of cobalt in crud", Radioisotopes, 34, 201 (1985)

Table 1 Steady state concentration of constituents and their activities

Crud	Concentration							
	Sampling position	Fe ($\mu\text{g/l}$)	Cr ($\mu\text{g/l}$)	Ni ($\mu\text{g/l}$)	Co ($10^{-1}\mu\text{g/l}$)	Cr/Fe (10^{-1})	Ni/Fe (10^{-1})	Co/Fe (10^{-2})
Crud-F	T/S-1	17 \pm 9	7.6 \pm 2.4	2.4 \pm 1.7	1.7 \pm 1.2	4.5 \pm 2.8	1.4 \pm 1.2	1.0 \pm 0.9
	T/S-2	30 \pm 10	4.4 \pm 3.9	5.8 \pm 3.0	5.4 \pm 3.1	1.5 \pm 1.4	1.9 \pm 1.2	1.8 \pm 1.2
	Av.	23 \pm 7	6.0 \pm 2.3	4.1 \pm 1.7	3.6 \pm 1.7	2.6 \pm 1.3	1.8 \pm 0.9	1.6 \pm 0.9
Crud-P	T/S-1	----	-----	-----	0.2	0.2 [*]	1.1 [*]	1.4 [*]
	T/S-2	----	-----	-----	0.1	0.4 [*]	---	2.0 [*]
	Av.	----	-----	-----	0.2 \pm 0.1	0.3 \pm 0.1 [*]	1.1 [*]	1.7 \pm 0.3 [*]
Crud	Activity							
	Sampling position	^{60}Co 10^{-3} ($\mu\text{Ci/l}$)	^{58}Co 10^{-5} ($\mu\text{Ci/l}$)	^{54}Mn 10^{-5} ($\mu\text{Ci/l}$)	^{56}Mn 10^{-2} ($\mu\text{Ci/l}$)	^{51}Cr 10^{-2} ($\mu\text{Ci/l}$)	$^{60}\text{Co/Co}$ 10^{-2} ($\mu\text{Ci}/\mu\text{g}$)	
Crud-F	T/S-1	1.3 \pm 0.5	\leq 7.4 \pm 3.2	29 \pm 4	\leq 4.8 \pm 2.5	4.3 \pm 4.2	0.8 \pm 0.6	
	T/S-2	2.4 \pm 1.0	\leq 9.5 \pm 2.0	28 \pm 11	17 \pm 15	3.4 \pm 3.0	0.5 \pm 0.3	
	Av.	1.9 \pm 0.6	\leq 8.5 \pm 1.9	29 \pm 6	11 \pm 8	3.9 \pm 2.6	0.5 \pm 0.3	
Crud-P	T/S-1	1.7 \pm 1.5	4.2 \pm 2.5	\leq 5.0 \pm 4.1	0.8 \pm 0.4	0.2 \pm 0.1	9 \pm 8	
	T/S-2	2.0 \pm 1.2	5.1 \pm 2.1	\leq 3.4 \pm 3.4	2.5 \pm 0.6	0.3 \pm 0.1	20 \pm 10	
	Av.	1.9 \pm 1.0	4.7 \pm 1.6	\leq 4.2 \pm 2.7	1.7 \pm 0.4	0.3 \pm 0.1	10 \pm 7	

* The results were obtained with the crud-P released in the burst.

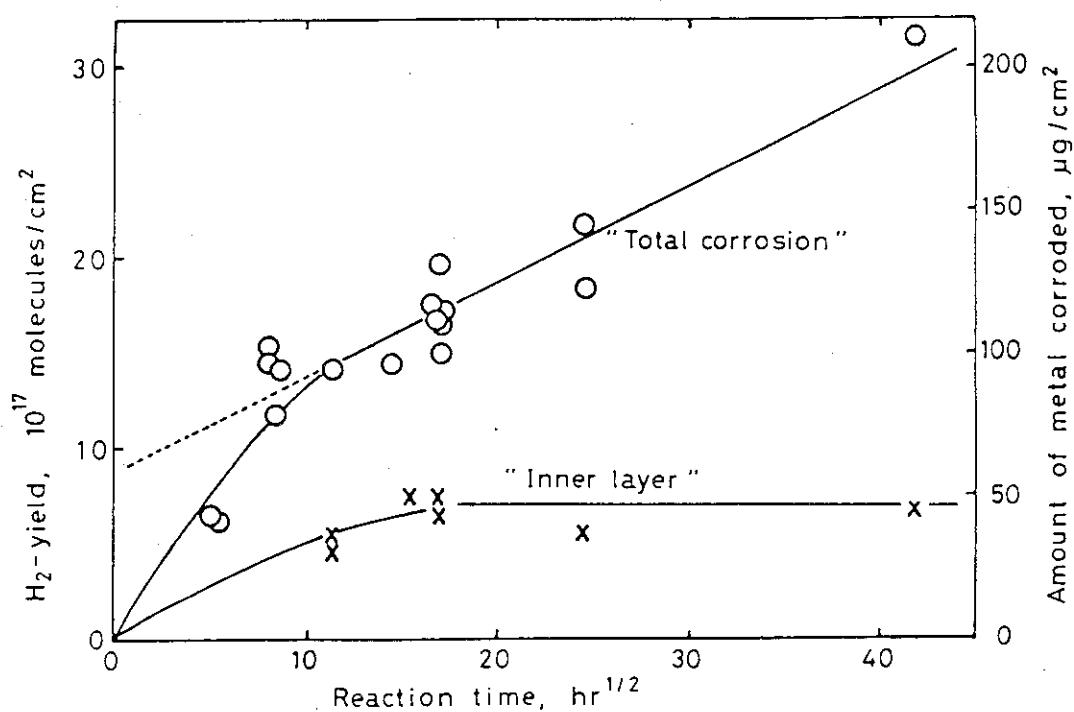


Fig. 1 Amount of metal corroded and hydrogen yield as a function of reaction time
The sample is SUS-304, 2.0x1.0x0.05 cm t.

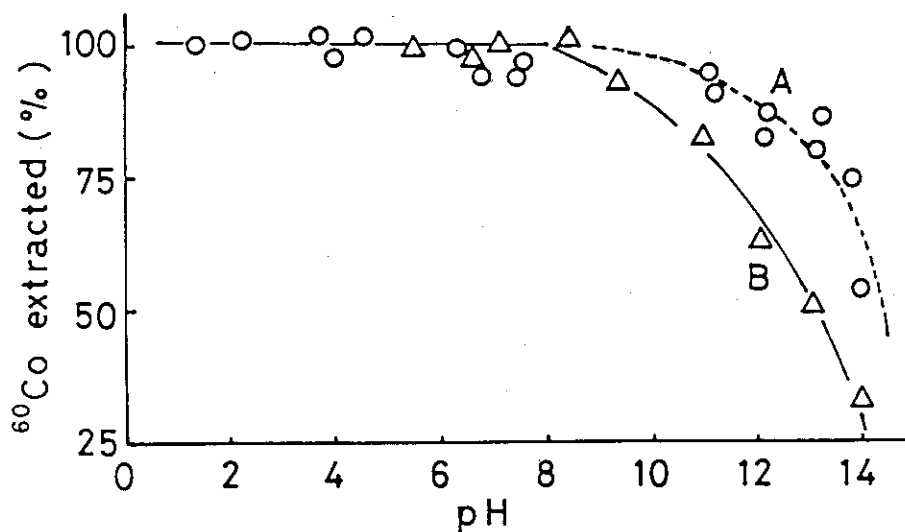


Fig. 2 Extraction of ⁶⁰Co at various pH

Aqueous phase: 50 ml, pH-adjustment: HCl or NaOH soln

A: NaDDC added immediately after pH-adjustment and extracted one hour later

B: NaDDC added one hour later pH-adjustment and extracted one hour later addition of NaDDC

Organic phase: CCl₄, 10 ml

(NaDDC: Sodium diethyldithiocarbamate)

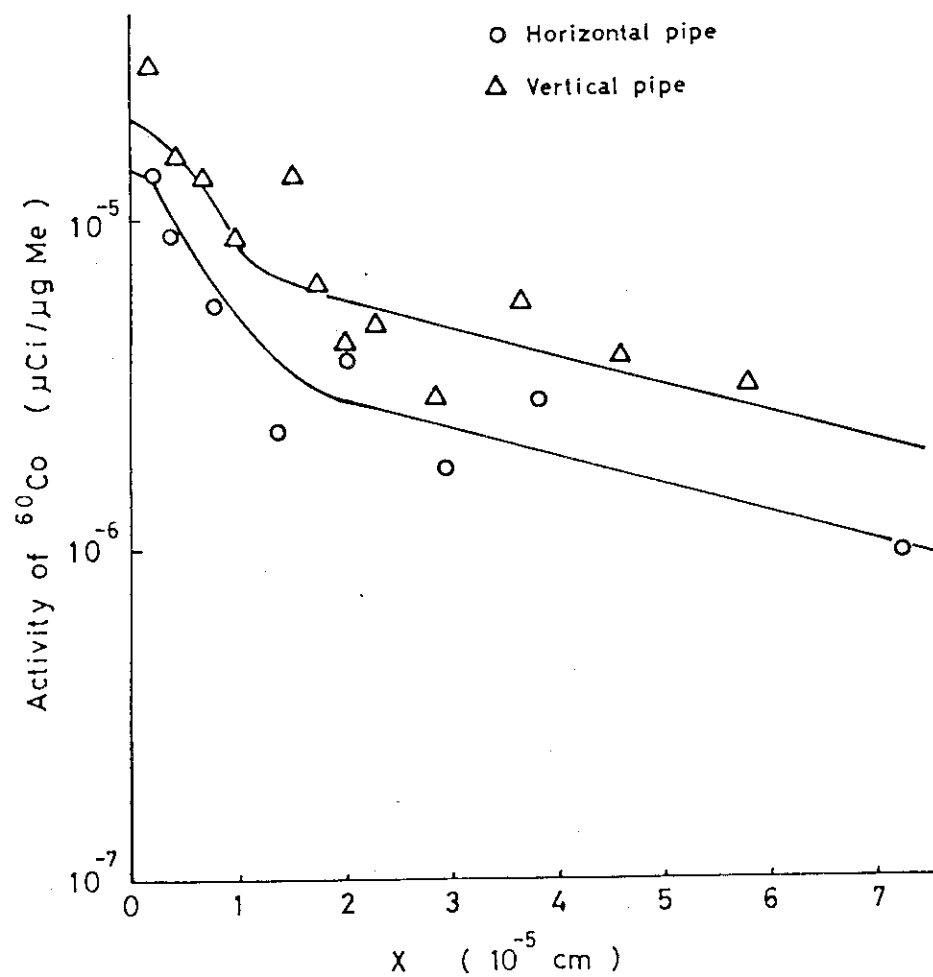


Fig. 3 The concentration profile of ^{60}Co in the specimens from the JPDR piping

Least square fitting: $D_v = 2.3 \times 10^{-19} \text{ cm}^2/\text{s}$

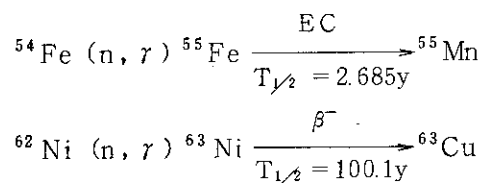
$\delta D_{gb} = 4.0 \times 10^{-22} \text{ cm}^3/\text{s}$

6.2 クラッド中の ^{55}Fe と ^{63}Ni の比放射能測定

6.2.1 はじめに

原子力発電所で作業員の被曝等の点から問題になっている放射性腐食生成物（クラッド）はヘマタイト、マグネタイトおよびフェライト等から構成され、一般的な化学組成は Table 1 のようなものである。表中の元素および放射能組成は Fe および ^{55}Fe を 1 とした各成分の割合を示す。クラッドの生成機構等を研究する上で原子炉一次冷却系各所に蓄積したこれらの元素の定量、および放射性核種の放射能測定が必要である。またクラッドを構成する放射性核種の比放射能に注目すると、中性子照射量および炉内滞留時間に関する情報が得られ、原子炉内でのクラッドの挙動を知る上で大きな手懸りとなる。特に元素量および放射能量ともその含有率の大きい ^{55}Fe および ^{63}Ni の場合には、その比放射能はかなり正確に求める事ができるので、より精度の高い情報提供源となり得る。これに対して、放射能的に多く含まれ、またその測定も容易な ^{60}Co 、 ^{54}Mn 等の γ 線放射体を用いる方法は、元素としての含有量が小さく、比放射能が求めにくいので、一般的ではあるが、信頼性に問題が残る。

^{55}Fe と ^{63}Ni は原子炉内で主に次の様な核反応で生成され、その放出する放射線は ^{55}Fe の場合 EC 壊変による Mn の特性 X 線およびそのオージェ電子で、 ^{63}Ni の場合は低エネルギー（ $E_{\text{max}} 65.87 \text{ keV}$ ）の β 線のみである。このためこれらの核種の放射能測定には計数効率およ



び試料調製の容易さの点から液体シンチレーション測定法が適している。 ^{55}Fe と ^{63}Ni の液体シンチレーションの測定は ^{55}Fe および ^{63}Ni 水溶液の乳化シンチレーターへの溶解、あるいは有機錯体としてトルエンおよびキシレン中への抽出により行われる。前者の乳化シンチレーターを用いる方法は一般的であり、広く使われているが、計数効率および計数率の安定性の点で問題がある。一方後者の方法は計数効率および、計数率の安定性の点で勝れているが、液液抽出操作を必要とする事から前者程一般的ではない。しかし後者の液液抽出による方法は、錯形成剤を適当に選ぶ事により、目的とする核種を共存する他の放射性核種から分離する事が出来る上に、その錯体が比色分析に用いられているものであれば、その吸光度測定により容易に元素量をも定量する事が出来る利点をもつ。この事から高感度比色試薬の中から ^{55}Fe に対してはバトフェナントロリン（BPT）、 ^{63}Ni に対してはジメチルグリオキシム（DMG）を選びその測定法を検討したところ、簡単な操作で、高感度、高計数効率の ^{55}Fe と ^{63}Ni の比放射能測定法を確立できた。さらに ^{55}Fe と ^{63}Ni の液体シンチレーションの同時測定法についても検討し、これらの方法をクラッドの分析に適用して、クラッドの原子炉内での挙動に関する情報を得た。

6.2.2 ^{55}Fe の比放射能測定法〔2〕

(a) 分析操作

^{55}Fe を含む溶液 ($\text{Fe } 2 \sim 20 \mu\text{g}$, $^{55}\text{Fe } 0.2 \sim 5000 \text{ Bq}$) をビーカーにとり、レーアスコルビン酸溶液 ($10 \text{ g}/100 \text{ ml}$) 4 ml , 酢酸ナトリウム溶液 ($10 \text{ g}/100 \text{ ml}$) 5 ml を加え、 7 M アンモニア水で pH を $4 \sim 5$ に調節する。溶液を分液ロートに移し、水で 50 ml に希釈する。過塩素酸アンモニウム溶液 ($10 \text{ g}/100 \text{ ml}$) 10 ml , バトフェナントロリン溶液 (BPT, $4,7\text{-diphenyl-1,10-phenanthroline}$, $0.1 \text{ g}/100 \text{ ml}$ エチルアルコール溶液) 10 ml を加え、約 10 分間放置する。PPO ($2,5\text{-diphenyloxazole}$) - キシレン溶液 ($5 \text{ g}/\ell$) 10 ml を加え、約 3 分間振り混ぜる。水相は捨て、 $\text{pH}=6.0$ 0.005 M EDTA - 0.05 M クエン酸溶液 10 ml , エチルアルコール 2 ml を加え、 10 分間振り混ぜ ^{60}Co を逆抽出する。有機相を液体シンチレーション測定用バイアルに移し、液体シンチレーションを測定し、 ^{55}Fe の放射エネルギーを求める。液体シンチレーションを測定後、 535 nm の吸光度を測定し、 Fe 量を求める。

(b) 結果および考察

通常 Fe-BPT 錯体の抽出に使用されるイソアミルアルコールおよびクロロホルムは、液体シンチレーション測定にはクエンチングが大きく不適当であり、抽出用の溶媒としてはクエンチングが無く、発光量の大きなキシレンを選び、液液抽出法を検討した。 Fe-BPT 錯体は $\text{Fe}(\text{BPT})_3^{2+}$ で示される様に電荷をもち、直接キシレンに抽出する事が出来ない。このためクロロホルム抽出の場合と同様に過塩素酸イオンを添加し、イオン会合体 $[\text{Fe}^{\text{II}}(\text{BPT})_3](\text{ClO}_4)_2$ として抽出する事にした。 ^{59}Fe をトレーサーとして用い、水相の pH とキシレンおよび PPO - キシレンへの ^{59}Fe の抽出率の関係を調べた結果、PPO の存在とは無関係に ^{59}Fe は $\text{pH } 3 \sim 8$ の範囲で Fe 量 $50 \mu\text{g}$ まで定量的に抽出されることが判明した。振り混ぜ時間は 1 分以上あれば十分である。

抽出液の吸収曲線の測定から、PPO の影響は無くその吸収極大は 535 nm で、 $\text{Fe } 2 \sim 30 \mu\text{g}/10 \text{ ml}$ の範囲でベールの法則が成立し、モル吸光係数は 22000 を示して、吸収極大位置とモル吸光係数ともイソアミルアルコールおよびクロロホルムの場合にほぼ等しい結果が得られた。 Fe の定量に対して、 Al , Cr , Mn , Zn は 10 倍量まで、 Co , Ni , Mo は等量まで、 Cu は $1/10$ 量まで共存しても Fe を $\pm 2\%$ 以内の誤差で定量出来た。抽出液の吸光度は少なくとも 6 日間は一一定であった。

Fe-BPT 錯体は赤色であり、液体シンチレーション測定の際色クエンチングの影響が考えられる。 Fe 濃度を変化させシンチレーターの溶質として PPO だけの場合と、PPO と DMPOPOP ($1,4\text{-bis}(4\text{-methyl-5-phenyl-2-oxazolyl})\text{benzene}$) を用いた場合の Fe 濃度と ^{55}Fe の計数効率の関係を調べた。PPO - DMPOPOP の場合には低 Fe 濃度域では計数効率が PPO だけの場合より高いが、 Fe 濃度が高くなるにつれ計数効率の低下が顕著である。PPO およびこれに DMPOPOP を加えた場合のシンチレーションの発光スペクトルと、 Fe-BPT 錯体の吸収曲線を Ni-DMG 錯体の吸収曲線とともに Fig. 1 に示す。図から、DMPOPOP を加えると、シンチレーションの発光スペクトルが Fe-BPT 錯体の吸収に近づき、PPO だけを用いる場合より色クエンチングの影響が大きいことがわかる。PPO 濃度は $50 \text{ mg}/10 \text{ ml}$ が最適であり、抽出液の計数値は少なくとも 6 日間 0.67% 以内で一一定であった。

クエンチングの補正は ^{226}Ra を用いる外部標準法により行った。 ^{55}Fe およびクラッドに含まれる $^{58,60}\text{Co}$, ^{63}Ni , ^{54}Mn , ^{59}Fe について得られたクエンチング補正曲線を Fig. 2 に示す。Fig. 2 はシンチレーションカウンターのウィンドウ幅を ^{55}Fe の測定に十分な 0 ~ 15 keV に設定して測定した。クエンチャーを添加しない試料の ^{55}Fe の計数効率率は 60% 以上である。 ^{55}Fe と同じ EC 壊変の ^{54}Mn と ^{58}Co は ^{55}Fe より計数効率は低いが、 ^{55}Fe と類似のクエンチング補正曲線を示す。 β^- 線放射体で低エネルギーの β^- 線を放出する ^{63}Ni は計数効率は高いが、高エネルギーの ^{59}Fe と ^{60}Co の計数効率は約 7% と低い。またこれらの β^- 線放出核種のクエンチングの影響は小さかった。 ^{51}Cr は抽出されなかった。 ^{55}Fe の補正曲線により、Fe 濃度の変化による色クエンチングの補正に適用した結果、Fe 30 $\mu\text{g}/10\text{m}\ell$ までの誤差は 0.85% 以内であった。バックグラウンド計数値をもとに、 ^{55}Fe の検出下限をバックグラウンドの計数値の標準偏差の 3 倍として求めると、0.2 Bq になる。

^{60}Co は液体シンチレーション測定での計数効率は低いが、クラッド中の含有率が高く ^{55}Fe の測定に対して最も影響が大きい。バトフェナントロリン抽出法で、Co も pH 2.5 ~ 8.0 の範囲で、50 μg 量まで抽出される。このため Fe^{2+} に比べて Co^{2+} とより安定な錯体を作る EDTA を用い、逆抽出による ^{60}Co の分離法を検討した。0.005 M EDTA 溶液の pH と ^{60}Co と ^{59}Fe の逆抽出率の関係を調べた結果、抽出液を pH = 6.0 0.005 M EDTA 溶液で振り混ぜると、 ^{60}Co は 99% 以上逆抽出されるが、 ^{59}Fe は 1% 以下であることがわかった。さらに、50 μg 量までの Co の逆抽出には EDTA 濃度が 0.005 M 以上、振り混ぜ時間が 10 分以上必要であり、エチルアルコール、2 m ℓ の添加により分離がより効果的になることが確認された。本法による ^{55}Fe の液体シンチレーション測定の際の共存する放射性核種の影響を調べた。クエンチングレベルにより各核種の計数効率が異なるため、一定のクエンチングレベルで比較した。結果を Table 2 に示す。 ^{54}Mn と ^{51}Cr は抽出および逆抽出により除かれる。 $^{58,60}\text{Co}$ は ^{55}Fe とともに抽出されるが、逆抽出により分離できる。 ^{63}Ni は抽出および逆抽出によっても除く事が出来ないが、2 チャンネル計数法により補正が可能であるとともに、これを利用して ^{55}Fe と ^{63}Ni の同時測定が可能となった。 ^{59}Fe もまた 2 チャンネル計数または γ 線計数により補正する事が出来るが、半減期が短く、クラッドの分析の際含まれる事が少く、 ^{55}Fe の測定に大きな障害とはならない。

(c) ^{55}Fe と ^{63}Ni の同時測定法の検討

バトフェナントロリン法に対して ^{63}Ni は ^{55}Fe と同じ抽出挙動をとるが、放出する放射線の種類とエネルギーが異なるため液体シンチレーション法による同時測定が可能となる。 ^{55}Fe の放射線は特性 X 線とそのオージェ電子のためそのシンチレーションは低エネルギー側に分布し、 ^{63}Ni のシンチレーションは ^{55}Fe より高エネルギー側まで分布する。ディスクリミネータレベルの検討をした結果 0 ~ 11 と 11 ~ 50 keV に設定した 2 チャンネルでの測定が最適である事がわかった。 ^{55}Fe と ^{63}Ni の標準溶液からクエンチング補正曲線を作り、Fe および Ni 濃度の変化による色クエンチングの補正に適用して、各々 30 $\mu\text{g}/10\text{m}\ell$ まで補正できる結果を得た。 ^{55}Fe と ^{63}Ni の混合比による 2 核種の測定誤差は、 ^{55}Fe は ^{63}Ni 中約 1/10 以上の濃度領域で、 ^{63}Ni は ^{55}Fe 中約 1/50 以上の濃度領域で各々 10% 以内であった。

6.2.3 ^{63}Ni の比放射能測定法〔1〕

(a) 分析操作

^{63}Ni を含む溶液 (Ni 5 ~ 40 μg , ^{63}Ni 0.3 ~ 5000 Bq) をビーカーにとり、クエン酸アンモニウム溶液 (30 g/100 ml) 10 ml を加えた後アンモニウム水で pH を約 9.5 に調節する。ジメチルグリオキシム溶液 (DMG, 1 g/100 ml エチルアルコール溶液) 1 ml を加え 3 分間振り混ぜる。有機相の吸光度 (333 nm) を石英製 1 cm セルを使用して測定した後、5 ml を液体シンチレーション用バイアルにとり、液体シンチレーター (PPO 10 g-DMPOPOP 0.6 g/l キシレン) 5 ml を加え、液体シンチレーションを測定する。

(b) 結果および考察

通常 Ni-DMG 錯体の抽出にはクロロホルムが用いられるが、 ^{55}Fe の場合と同様にクエンチングの観点から、キシレンによる抽出法の検討をした。 ^{63}Ni (半減期 2.52 h) をトレーサーとして、クエン酸アンモニウム存在下での水相の pH と ^{63}Ni の抽出率の関係を調べた結果 Ni はクロロホルム抽出の場合と同様 pH 8.5 ~ 11 の範囲で 95% 以上の抽出率を示した。定量的に抽出出来る最大の Ni 量を調べた結果クロロホルムでは 200 μg であるのに対してキシレンでは 40 μg であり、この差は Ni-DMG 錯体のそれぞれの溶媒における溶解度の差と考えられる。振り混ぜ時間は 30 sec 以上で十分であった。

抽出液の吸収曲線を測定した結果 333 nm と 379 nm に吸収極大があり、クロロホルムの場合より数 nm 長波長側へのシフトが見られた。Ni 濃度を変化させ、濃度と吸光度の関係を調べた結果、333 および 379 nm のピークとも 5 ~ 40 $\mu\text{g}/10\text{ml}$ の範囲で直線関係があり、モル吸光係数は 42000 (333 nm), 32000 (379 nm) であった。これはクロロホルムの場合の 47000 (327 nm), 35000 (377 nm) と比べやや小さな値であった。クロロホルム抽出の場合と比べ 333 nm 付近でのブランクの吸光度がほとんど 0 である事と、感度の点から 333 nm の吸収を定量に用いた。

Ni-DMG 錯体は黄色であるため ^{55}Fe で観測された色クエンチングの影響が考えられ、Ni 濃度を変化させその影響を調べた。 ^{55}Fe の場合と同様シンチレーターの溶質として PPO だけの場合と PPO-DMPOPOP の場合について調べた。PPO だけの場合 Ni 濃度の増加によるその計数効率の低下が著しいが、DMPOPOP を加える事により計数効率の低下をかなり抑える事が出来た。これは Fig. 1 からわかる様に、Ni-DMG 錯体の吸収スペクトルと PPO の発光スペクトルはかなり接近しているが、DMPOPOP を加えると発光スペクトルは長波側にシフトして、Ni-DMG 錯体の吸収からかなり分離できるためにこのような効果が得られると思われる。PPO 濃度を通常液体シンチレーション測定で用いられる 50 $\mu\text{g}/10\text{ml}$ にすると、DMPOPOP 濃度は 1 mg/10ml 以上が必要である。

ウィンドウ幅を ^{63}Ni の測定に充分な 0 ~ 100 keV に設定して、 ^{55}Fe の場合と同様に ^{226}Ra を用いる外部標準法によりクエンチング補正曲線を求めた。この補正曲線を、Ni 濃度変化による色クエンチングの補正に適用すると、Ni 濃度 30 $\mu\text{g}/10\text{ml}$ までの誤差は 0.67% 以内であった。クエンチャーを含まない試料の ^{63}Ni の計数効率は 80% 以上であった。バックグラウンド計数値より ^{55}Fe の場合と同様 ^{63}Ni の検出下限を求めると、0.3 Bq になる。 ^{63}Ni の比放射能 281 MBq/gNi の試料を用い、Ni 量として 0.6 ~ 120 μg の範囲で行った 10 個の試料の比

放射能測定誤差は5%以内であった。これにより抽出出来る最大量である40 μg 以上のNi量でもその比放射能は正確に測定出来る事がわかった。

6.2.4 クラッド中の ^{55}Fe および ^{63}Ni の分析例

PWR型原子炉の燃料被覆管より採取したクラッドの分析例をTable 3に示す。表には、試料に直接バトフェナントロリン錯体抽出分離と2チャンネル測定法を適用した場合の正確さを確認するため、イオン交換法によりFeとNiを分離後、比放射能測定から得られた ^{55}Fe と ^{63}Ni の値も一緒にまとめた。各分析法による測定値は非常によく一致し、試料を事前に分離することなく抽出操作だけで精度よく測定できることがわかった。

シュウ酸溶液へのマグネタイトとヘマタイトの溶解度差を利用した分別溶解法により、クラッドを構成するヘマタイトおよびマグネタイト中の ^{55}Fe および、存在量が微量である ^{63}Ni の比放射能測定を行った。85℃に加温した0.0079 Mシュウ酸50mlにクラッドを浸し、85℃に加温しながら30分間超音波照射をしてマグネタイトを溶解する。ミリポアフィルター(0.45 μm)で濾過し、残渣をもう一度シュウ酸による溶解操作を行った後、残渣のヘマタイトを濃塩酸で溶解をする。シュウ酸による溶解液のマグネタイト成分と、塩酸による溶解液のヘマタイト成分中の ^{55}Fe と ^{63}Ni の比放射能の測定結果をTable 4に示す。JMTR OWL-1ループより採取したクラッド、およびBWR型炉より採取したクラッドとも、ヘマタイト中の ^{55}Fe の比放射能がマグネタイト中のものより2~6倍高く、 ^{63}Ni の場合も ^{55}Fe と同様ヘマタイト中の方が2~6倍高くなっている。一般に、一次冷却系構成材料の腐食あるいは溶出により給水系から炉心に運搬される主としてFeのイオンあるいは化合物のクラッドは低酸化状態のFe(II)状態で存在する。炉心は水の放射線分解により生ずる H_2O_2 、OHなどの酸化種により高温の酸化雰囲気になっている。そのため、給水系からのクラッドは炉心での挙動で次のように分類される。

- i) 溶解度の低いFe(III)に酸化されるため、燃料被覆管などに付着して、比較的炉心での滞留時間が長くなるもの、これがヘマタイトである。
- ii) 滞留時間が短いため、酸化されずに比較的溶解度の大きい状態で炉心を通過するもの、これがマグネタイトである。
- iii) Niは存在量が少く、単独よりもむしろ、ヘマタイトあるいはマグネタイトに取り込まれた形で、これらと一緒に行動する。

今回のマグネタイトおよびヘマタイト成分中の ^{55}Fe と ^{63}Ni の比放射能測定結果はi) ii) iii)のようなこれらクラッドの炉心での挙動差の結果と考えられる。

(C. Yonezawa)

Publication List

- [1] Yonezawa, C., Sagawa, C., Hoshi, M., Tachikawa, E.: "Rapid determination of specific activity of nickel-63", J. Radioanal. Chem., 78, 7 (1983).

- [2] Yonezawa, C., Hoshi, M., Tachikawa, E.: "Determination of specific activity of iron-55 by spectrophotometry and liquid scintillation counting with bathophenanthroline complex", Anal. Chem., 57, 2961 (1985).
- [3] Hoshi, M., Tachikawa, E., Sagawa, C., Yonezawa, C., Goto, S.: "Tracer diffusion of ^{60}Co into SUS-304", J. Nucl. Mater., 120, 154 (1984).
- [4] Tachikawa, E., Hoshi, M., Sagawa, C., Yonezawa, C., Nakashima, M.: "Investigation of oxides formed in the corrosion of SUS-304 in high-temperature water through the measurement of evolved hydrogen and radiochemical analyses", Nucl. Technol., 65, 128 (1984).
- [5] Yonezawa, C., Komori, T.: "Determination of hafnium in zirconium and its alloys by stable isotope dilution-neutron activation analysis", Anal. Chem., 55, 2059 (1983).
- [6] Yonezawa, C.: "Determination of hafnium in reference materials of zirconium and Zircaloy by neutron activation analysis with hafnium-175 as a tracer", Bunseki Kagaku, 33, 336 (1984), (in Japanese).
- [7] Tamura, S., Toida, Y., Yonezawa, C., Tamura, K.: "Isotope-dilution analysis of boron in highly-irradiated U-Al-B alloy fuel-element specimens", JAERI-M 82-070 (1982), (in Japanese).
- [8] Yonezawa, C.: "Current topics on activation analysis", Department of research reactor operation Ed., "The upgraded JRR-3 and future scope of its utilization", p.114-121, JAERI-M 85-149 (1985), (in Japanese).

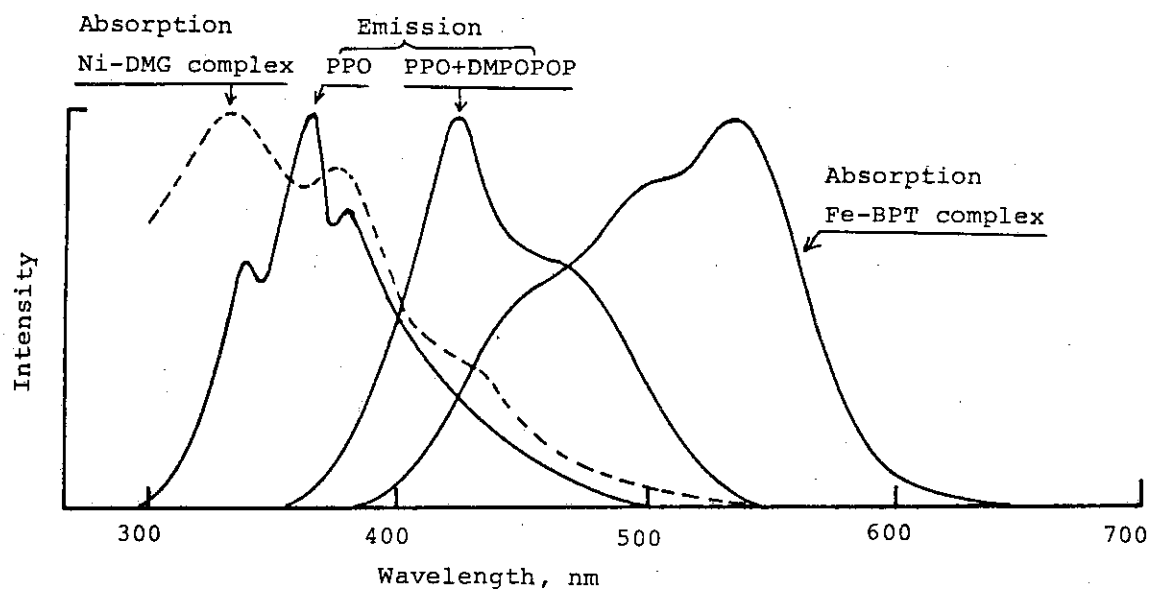


Fig.1 Emission and absorption spectra of scintillation and of the complexes

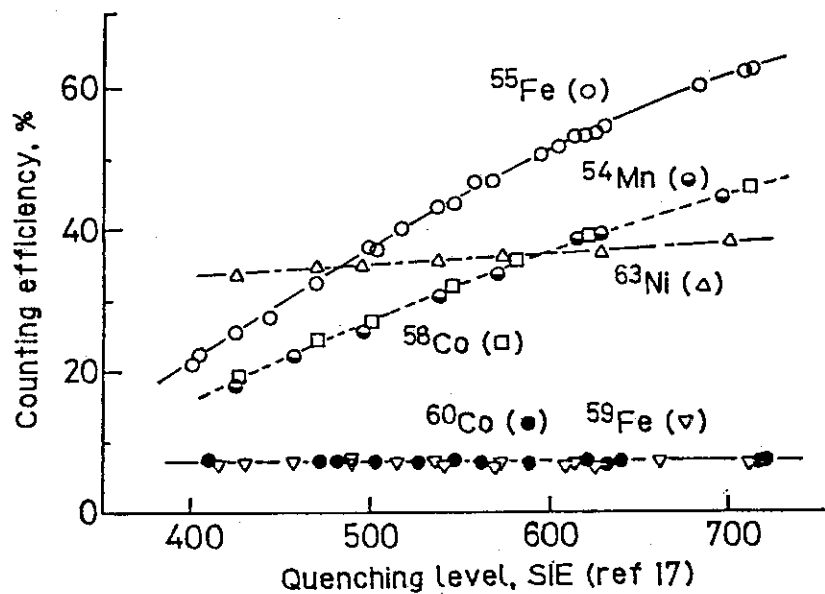


Fig. 2 Quenching correction curves

Window width of scintillation counter : 0-15 keV

Table 1 Chemical composition of fuel CRUD

Element and Radionuclide	BWR	PWR
Fe	1.0	1.0
Ni	0.070	0.50
Cr	0.021	0.023
Mn	0.075	0.0015
Co	—	0.00085
⁵⁵ Fe	1.0	1.0
⁶⁰ Co	3.6	0.14
⁵⁴ Mn	0.12	0.021
⁶³ Ni	0.01	0.098

Table 2 Effect of foreign radionuclides on extraction, back-extraction and liquid scintillation counting of ⁵⁵Fe

Nuclide	After first extn. Found, %	After back-extn.	
		Found, % Av.	Counted by L.S.C., %
			Av.
⁵⁵ Fe	99 ± 3 ^a (n=17)	99, 99, 96 98 ^a	100
⁵⁹ Fe	99 ± 3 ^a (n=17)	99, 99, 96 98 ^a	13, 14, 12, 12 13
⁶³ Ni	99.6 ± 0.5 ^b (n=7)	100, 100 100 ^b	69, 67 68
⁵⁸ Co	100 ± 2 ^c (n=7)	0.97, 1.4 1.2 ^c	0.16, 0.31 0.23
⁶⁰ Co	97 ± 2 ^c (n=13)	1.3, 0.80 1.0 ^c	0.05, 0.01 0.03
⁵⁴ Mn	61 ± 1 ^c (n=9)	0.07, 0.05 0.06 ^c	0.01, 0.00 0.005
⁵¹ Cr	0.12 ± 0.04 ^c (n=6)	<0.02, <0.02 <0.02 ^c	0.01, 0.007 0.008

The radionuclides taken were 584-10092 Bq in radioactivity, and 0.006-14 µg in weight. All the liquid scintillation counting was carried out at 53 ± 4 % in the counting efficiency of ⁵⁵Fe. a: Measured by gamma-ray counting of ⁵⁹Fe; b: Measured by liquid scintillation counting of ⁶³Ni; c: Measured by gamma-ray counting of the nuclides.

Table 3 Analytical results of CRUD collected from PWR type reactor

Radionuclide and element	Determined					
	Ion exchange sepn. Av.			BPT extn. Av.		
⁵⁵ Fe (MBq)	4.66, 4.62,	4.61, 4.57	4.61	4.76, 4.76,	4.72, 4.67	4.72
Fe (μg)	1192, 1232,	1240, 1224	1222	1168, 1200,	1200, 1187	1189
⁵⁵ Fe/Fe (GBq/g)	3.77			3.97		
⁶³ Ni (MBq)	0.610, 0.629,	0.607, 0.638	0.621	0.686, 0.692,	0.682, 0.682	0.686
Ni (μg)	648,	598	623	_____		
⁶³ Ni/Ni(GBq/g)	0.997			_____		
⁶⁰ Co (MBq)	0.932 ^a			_____		
⁵⁴ Mn (MBq)	0.114 ^a			_____		
⁶⁵ Zn (MBq)	0.0013 ^a			_____		
Cr (μg)	55 ^b			_____		
Mn (μg)	5.0 ^b			_____		
Co (μg)	1.6 ^b			_____		

a : Measured by gamma-ray spectrometry.

b : Determined by ICP emission spectrometry.

Analysis were carried out after 2.2 years cooling.

Table 4 Specific activity of ^{55}Fe and ^{63}Ni in the CRUD

Fraction	Specific activity, MBq/g			
	JMTR OWL-1 CRUD		BWR CRUD	
	^{55}Fe	^{63}Ni	^{55}Fe	^{63}Ni
Magnetite fraction	48.8	11.5	17.5	31.9
Hematite fraction	98.3	22.9	111	188

6.3 硫酸-セリウム(IV)系化学除染法の開発

6.3.1 はじめに

本研究は、原子炉解体プロジェクトの一環として、昭和57年度に発足したもので、原子炉解体関連除染技術の開発を目的に行っている。

原子炉一次冷却系配管表面等の放射性腐食生成物（以下クラッドと呼ぶ）は、一般に外層と呼ばれる付着性酸化物と、内層と呼ばれる成長性酸化物の二層から成っている。内層酸化物は母材表面における腐食により生成することから、母材の組成の影響を強く受ける。ステンレス鋼やインコネル上の内層は、腐食によりFeは炉水中へ溶出し難溶性のCrが濃縮されるため、Cr含有量が高い。高Cr含有クラッドに対する除染は、一般的には酸化前処理段階でCr(III)から水溶性のCr(VI)に酸化溶解し、ひきつづき未溶解のFe、Niを還元溶解するという二段階処理がとられている。この為に除染工程が複雑になり、除染廃液量も増えるという欠点がある。

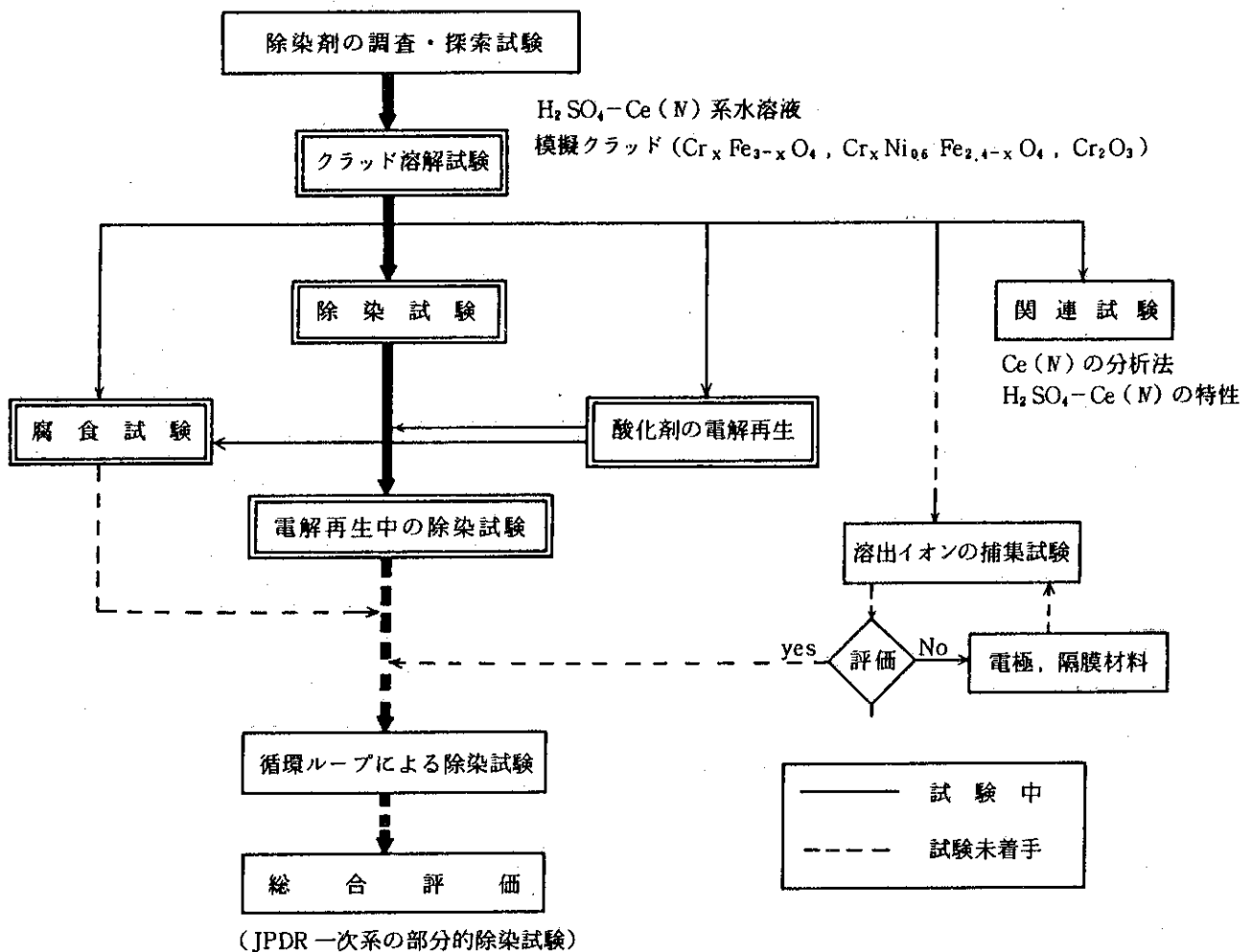
原子炉解体を目的とした化学除染法の開発では、高い除染係数(DF)を達成することが重要であり、この為にはCr含有量の高い内層をも効果的に溶解することが必要であるとの観点に立って、除染剤の探索を行い、硫酸-Ce(IV)溶液が優れていることを見出した。

本除染法の特徴は、高Cr含有クラッドに対し、CrだけでなくFeとNiをも同時に溶解することが可能であり、除染を一段処理で行うことができる。また、40～90℃という比較的低温度で使用できることから解体前一次系除染だけでなく、解体後の機器除染、さらには高温下での除染が不可能な系への適用も期待できる。

6.3.2 硫酸-セリウム(IV)系化学除染法の開発概要

本除染法をJPDR解体前除染のみならず、より一般的な除染技術として確立するために、下記に示す試験項目に分けて研究開発を進めている。

各種模擬クラッドの溶解挙動、JPDR汚染試験の除染効果および母材の腐食(SUS304)についての試験は昭和59年度ではほぼ終了しているので、これらの結果について述べる。60年度は溶出金属イオンの捕集(廃液処理法)の検討を中心に、61年度に本除染法をJPDR一次冷却系に適用するための工学的検討も合せて進めている。



6.3.3 模擬クラッドの溶解挙動

模擬クラッドの溶解挙動に関する検討目的は2つに大別される：i) 模擬クラッドの溶解機構の解明，ii) 除染剤の探索及び除染効果の向上．i) の反応動学的な研究を行う場合には，金属酸化物（模擬クラッド）の溶解速度は系の状態変化の小さい初期速度を用いる．一方，ii) の除染では，初期速度よりむしろ全体の溶解量の方が重要となる．

ここでは，ii) が主な目的であることから， $\text{Cr}_x\text{Fe}_{3-x}\text{O}_4$ ， $\text{Cr}_x\text{Ni}_{0.6}\text{Fe}_{2.4-x}\text{O}_4$ 等各種模擬クラッドについて先ず 60°C ，24 時間での溶解率を求め，これらの硫酸および Ce(IV) 濃度依存性を明らかにした．その後， $\text{Cr}_{0.6}\text{Ni}_{0.6}\text{Fe}_{1.8}\text{O}_4$ ， Cr_2O_3 および NiFe_2O_4 について，温度，濃度，pH 等の溶解条件を変えて，溶解率の経時変化（溶解曲線）を求め，初期速度と24 時間での溶解率に着目して検討を行った．以下に主な結果を列記する．

(a) 硫酸 - Ce(IV) と他の酸化性溶液との比較

Table 1 に $\text{Cr}_x\text{Ni}_{0.6}\text{Fe}_{2.4-x}\text{O}_4$ を用いた比較試験結果を示す．Cr の溶解率は：



である．他の3種類の溶液に比べ硫酸 - Ce(IV) 溶液は Cr だけでなく Fe と Ni に対しても溶解性の高いことが明らかになった．

上記模擬クラッドの溶解率 (f_{obs}) は、クラッド組成中のCr(Ⅲ)をCr(VI)に、Fe(Ⅱ)をFe(Ⅲ)に酸化するために必要なCe(Ⅳ)量の計算値 (C_{cal})と仕込濃度 (C_{exp})の比から求めた溶解率 $f_{cal} = C_{exp}/C_{cal}$ とほぼ一致する。即ち、クラッドの溶解に関して酸化還元当量が成立する。

(b) $Cr_{0.6}Ni_{0.6}Fe_{1.8}O_4$ の溶解挙動

Fig. 1 に 80 °C の 0.25 M 硫酸溶液中でCe(Ⅳ)無添加と5 mM 添加した場合の各組成別溶解曲線を示す。Ce(Ⅳ)無添加の場合、各組成別の溶解率は $f_{Fe} > f_{Ni} > f_{Cr} \approx 0$ である。Ce(Ⅳ)添加系では $f_{Cr} > f_{Ni} > f_{Fe}$ となり、CrとNiの溶解が促進される。

Fig. 2 は各組成別に溶解速度の温度依存性をアレニウスプロットで示している。Crの溶解速度はFeの約30倍、Niの20倍である。これらの直線の勾配から求めたみかけの活性化エネルギーはCr, Ni, Feでそれぞれ49.8, 55.3, 44.8 kJ/molである。

ここで溶解速度は、次式を用いて求めた。

$$1 - (1 - f)^{1/3} = Kt$$

Table 2 に 24 時間における溶解率と初期溶解速度 (h^{-1})について硫酸-Ce(Ⅳ)溶液と他の溶液との比較を示す。LND-101Aの場合、初期溶解速度は全体の平均で $1h^{-1}$ と最大であるが、24時間での溶解率は66.3%とあまり高くない。このように除染剤の溶解性能を評価する場合、初期速度だけから判断するのは危険である。

6.3.4 JPDR 汚染試料の除染効果

JPDR 浄化系配管から採取した汚染試験片を用いて、硫酸-Ce(Ⅳ)溶液の除染効果を検討した。比較のために、酸化性溶液として硝酸-Ce(Ⅳ)とPOD法(PWR Oxidative Decontamination)、還元性溶液としてLND-101A(Can-Decon法)、NS-1(Dow Chemical法)、ギ酸-ホルムアルデヒド溶液についても検討した。さらに硫酸-Ce(Ⅳ)溶液についてはCe(Ⅲ)からCe(Ⅳ)への電解再生下での除染も行った。

Table 3 に除染試験結果をまとめて示す。硫酸-Ce(Ⅳ)溶液では、40 °C でも24時間でDF=2、48時間でDF=13が得られた。90 °C では24時間でDF=33に達するが、48時間でもDF=36とほとんど大きくならない。このような場合にはCe(Ⅳ)析出物が試験片表面に付着していた。析出の起きていない80 °C の場合には、Fig. 3 に示すように、除染時間と共にDFは増大して、52時間で57を得た。問題点として、硫酸-Ce(Ⅳ)溶液で除染する場合には、Ce(Ⅳ)の析出を起こさない状態で除染を行うことが重要である。さらに、除染時のCe(Ⅲ)濃度が時間と共に減少し、酸化力が低下するために、高DFを得ることが困難である。

これらの問題を解決することを目的に、電解再生下で除染したところ、大きなDFを得ることができた。さらに、除染後の試験片を純水中で約5分間超音波洗浄すると、表面放射能は $1.5 \times 10^{-5} \mu Ci/cm^2$ 以下に達したことから、解体後の機器除染への適用も可能である。

6.3.5 母材の腐食

硫酸-Ce(Ⅳ)溶液は酸化性であるから、母材に対し腐食速度が大きくなることが予測される。原子炉解体を目的とした除染では、母材の腐食はある程度許容される。しかし、除染時の母材の

腐食は、i) Ce (IV) の消費による除染剤の劣化、ii) 除染廃液処理に大きな影響を及ぼすとの観点から検討を行った。

SUS 304 の腐食速度は温度と Ce (IV) 濃度に大きく依存する。腐食による溶出金属イオン量は母材の組成とほぼ一致し、選択溶解は認められなかった。Ce (IV) 消費量は $\text{Fe} \rightarrow \text{Fe(III)}$, $\text{Cr} \rightarrow \text{Cr(IV)}$, $\text{Ni} \rightarrow \text{Ni(II)}$ になるものと仮定して溶出金属イオン量から計算した値と一致した。

Fig. 4 に電解再生の有無による SUS 304 の腐食速度、試験片の重量減少量および溶液中の Ce (IV) の相対濃度 (Ce/Co) の経時変化を示す。電解再生を行わない場合、腐食速度と Ce (IV) 濃度は時間と共に急速に低下する。一方、電解再生下では腐食速度と Ce (IV) 濃度はほぼ一定である。

Fig. 5 は、電解再生下における腐食速度のアレニウスプロットを示したものである。モデル試験片と JPDR 汚染試験の腐食速度はほぼ同じ値を示した。これは初期の表面状態に差があっても、腐食速度が大きいために、短時間のうちに表面の粗さがほぼ同程度に近づくことによるものと考えられる。腐食速度 R_c (mdd) は次式で示される：

$$R_c = 9.31 \times 10^{11} C_{\text{exp}} (-43.2 \times 10^3 / RT)$$

ここで、 C は Ce (IV) 濃度 (mol/l), $R = 8.314 \text{ J/deg. mol}$ である。

(T. Suwa)

Publication List

- [1] Suwa, T., Kuribayashi, N., Tachikawa, E. : "Development of chemical decontamination process with sulfuric acid-cerium (IV) for decommissioning : A single step process to dissolve chromium-rich oxides", J. Nucl. Sci. and Tech., to be published.
- [2] Suwa, T., Yasunaka, H. : "Present state of decontamination technology for nuclear reactors", Corrosion Engineering (BOSHOKU GIJUTSU), 32, 721 (1983), in Japanese.
- [3] Suwa, T. : "Present status of chemical decontamination technology for nuclear reactor-coolant systems", Nuclear Engineering, 31, (3), 21 (1985), in Japanese.
- [4] Tachikawa, E., Yasunaka, H. : "Development of reactor decommissioning technology. (3) Decontamination for decommissioning", *ibid.*, 31, (4), 63 (1985), in Japanese.

Table 1 Dissolution test of $\text{Cr}_x\text{Ni}_{0.6}\text{Fe}_{2.4-x}\text{O}_4$ in $\text{H}_2\text{SO}_4\text{-Ce(IV)}$
and other oxidizing solutions for 24 hours at 60°C

X in oxide	Dissolution condition		Dissolution fraction(%)			
	Reagent	Conc.(mmol/l)	Cr	Fe	Ni	Overall
0.14	$\text{H}_2\text{SO}_4\text{-Ce}^{4+}$	100 - 5	100	33.7	95.0	51.6
0.3	"	100 - 5	100	49.9	74.4	59.7
0.6	"	100 - 5	84.5	34.9	21.0	41.3
"	"	200 - 10	98.8	67.1	86.4	77.1
1.0	"	100 - 5	64.7	21.8	10.2	32.8
"	"	200 - 10	100	62.5	47.0	71.9
0.6	$\text{HNO}_3\text{-Ce}^{4+}$	200 - 10	82.6	21.9	61.7	41.6
"	NaOH-KMnO_4	25 - 6.3	5.4	<0.1	<0.1	1.0
"	$\text{HNO}_3\text{-KMnO}_4$	3.5- 5.1	82.0	<0.1	2.6	15.9

Table 2 Dissolution test of $\text{Cr}_{0.6}\text{Ni}_{0.6}\text{Fe}_{1.8}\text{O}_4$ in $\text{H}_2\text{SO}_4\text{-Ce(IV)}$
and other typical decontamination reagents^{a)}

Dissolution condition			Dissolution fraction(%) at 24 hours				Initial dissolution rate(h ⁻¹)			
Reagent	Conc.(mmol/l)	Temp(°C)	Fe	Cr	Ni	Overall	Fe	Cr	Ni	Overall
$\text{H}_2\text{SO}_4\text{-Ce}^{4+}$	250 - 0	80	100	0	10.6	62.4	0.17	0	6.8×10^{-3}	0.08
"	250 - 5	"	96.2	100	100	97.7	0.11	2.0	0.18	0.17
$\text{HNO}_3\text{-Ce}^{4+}$	500 - 0	"	67.1	0	7.9	42.0	0.018	0	1.2×10^{-3}	0.011
"	500 - 5	"	54.5	86.2	100	70.0	0.028	4.0	0.82	0.16
LND 101 A	0.1 wt %	90	100	0.5	28.7	66.3	2.5	9.1×10^{-4}	0.046	1.0
NS-1	0.7 wt %	"	47.5	0	6.6	30.0	0.074	0	1×10^{-3}	0.044

a) Dissolution condition was 0.15g of the oxide in 0.7 dm³ solution.

Table 3 Comparison of decontamination factors(DF) obtained on JPDR specimens
in $\text{H}_2\text{SO}_4\text{-Ce(IV)}$ and typical decontamination reagents

No.	Reagents	Decontamination conditions		Specimen	Decontamination data			Notes
		Concentration ($\times 10^{-3}$ M)	Temp. ($^{\circ}\text{C}$)		DF at 24 hrs	Final DF	Time(hr)	
1	$\text{H}_2\text{SO}_4\text{-Ce}^{4+}$	250 - 10	40	F-18-2	2.3	13.3	48	
2	"	250 - 10	60	H- 2-3	9.0	9.3	48	LT
3	"	250 - 5	80	F-19-4	6.8	57.4	52	
4	"	250 - 5	90	F-19-3	32.8	36.4	48	P
5	"	500 - 10	90	F-73-4	—	41.5	27	
6	$\text{H}_2\text{SO}_4\text{-Ce}^{4+}$	250 - 1.3	80	F-40-1	460	1150	48	ER
7	"	250 - 5	80	F-40-2	87	420	48	ER
8	$\text{HNO}_3\text{-Ce}^{4+}$	500 - 5	90	F-14-3	4.3	5.3	96	
9	"	500 - 10	60	F-18-4	3.2	10.5	48	
10	$\text{HNO}_3\text{-KMnO}_4$	3.5 - 5.1	90	F-14-1	4.6	—	—	LT, POD
11	LND101A	0.1wt%	90	E-73-1	1.5	—	—	LT
12	NS-1	0.7wt%	90	E-73-2	—	1.2	48	LT
13	HCOOH-HCHO	2200 - 100	90	F-15-2	—	1.3	99	

P: Cerium hydroxide precipitated during decontamination.

LT: Decontamination with recirculation loop

ER: Electrolytic regeneration from Ce(III) to Ce(IV)

POD: Decontamination with POD process

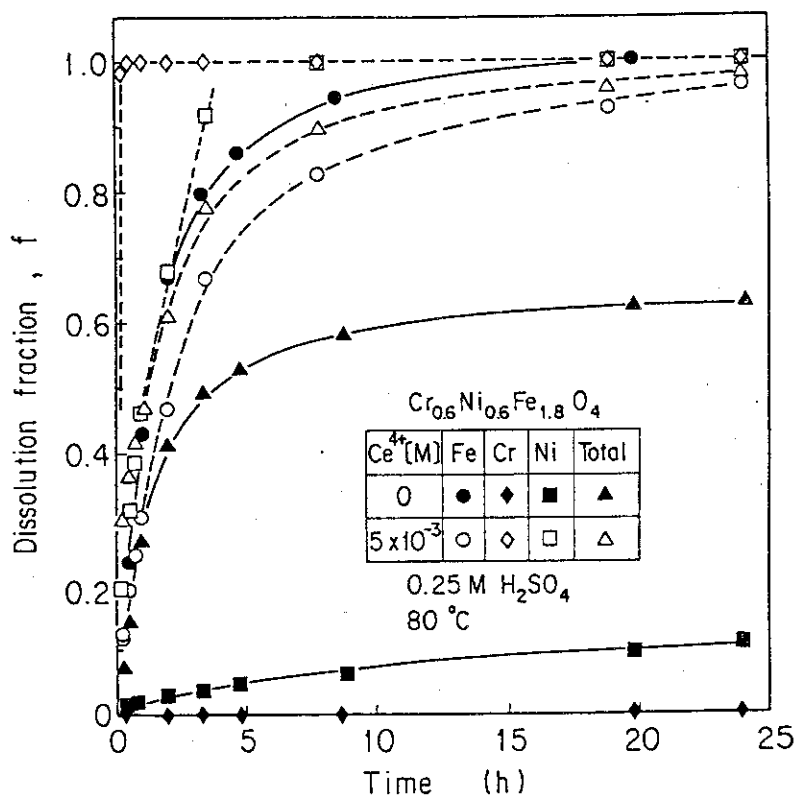


Fig. 1 Effect of the addition of Ce⁴⁺ on the dissolution behavior of Cr_{0.6}Ni_{0.6}Fe_{1.8}O₄

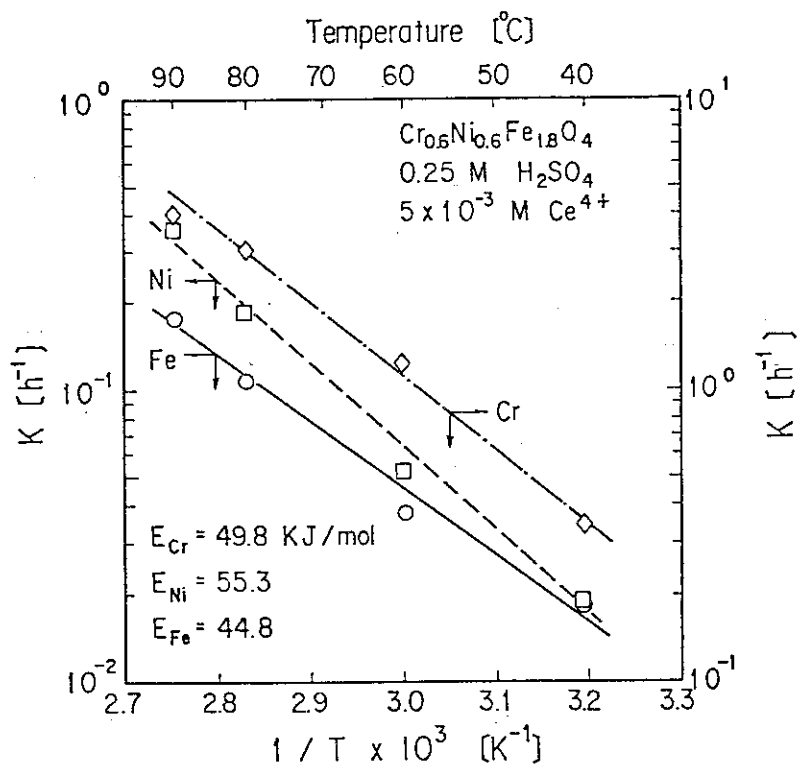
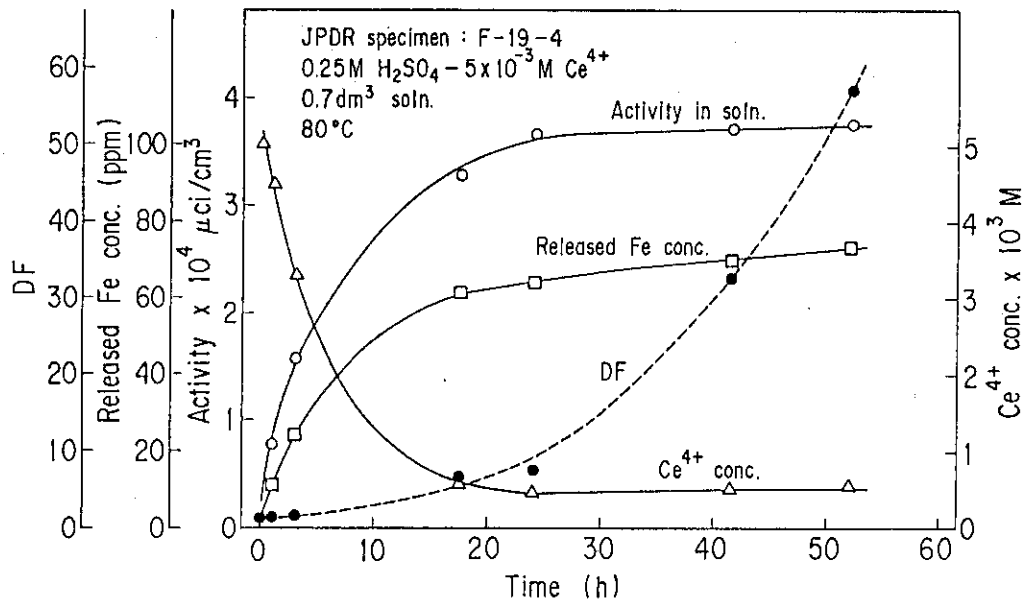
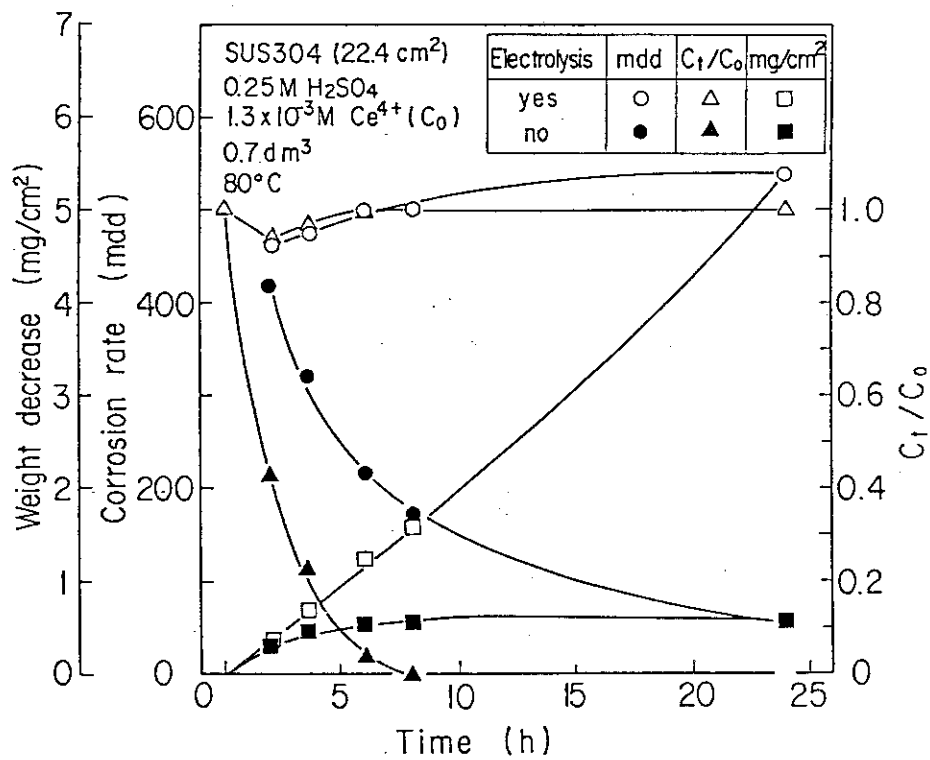


Fig. 2 Dissolution rate $K [h^{-1}]$ of Cr_{0.6}Ni_{0.6}Fe_{1.8}O₄ as a function of temperature

Fig. 3 Decontamination of JPDR specimen in H_2SO_4 - Ce^{4+} solutionFig. 4 Effect of electrolytic regeneration of Ce^{3+} on the corrosion rates of SUS304

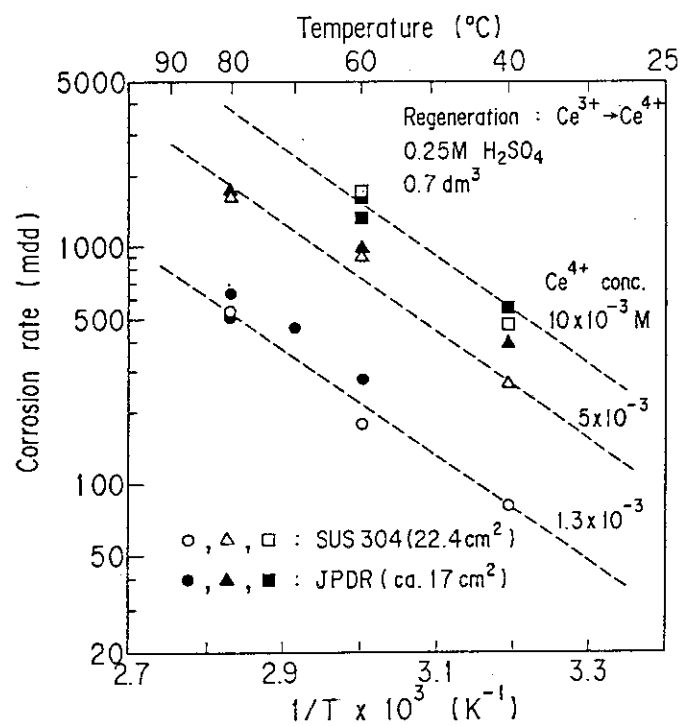


Fig. 5 Effect of temperature on the corrosion rates in H_2SO_4 - Ce^{4+} solutions under electrolytic regeneration of Ce^{4+} from Ce^{3+}

7. SOLID-STATE CHEMISTRY OF RADIATION DAMAGE

K.Izui, S.Ohno, T.A.Sasaki,
S.Furuno, H.Ohtsu, T.Soga,
K.Furukawa and K.Hojou

7. 放射線損傷の固体化学的研究

出井 数彦・大野 新一・佐々木貞吉・古野 茂美
大津 仁・曾我 猛・古川 勝敏・北条 喜一

7.1 低エネルギーイオン衝撃による化学反応

高速中性子の物質に対する化学的作用は、(i) 非弾性散乱によって発生する電離放射線(α , p, γ 線)ならびに(ii) 弾性散乱による反跳原子ないしイオン(~ 100 keV)の作用の重なったものと考えられる〔7, 10〕。これまでの研究により、電離放射線による反応過程をかなりの程度にまで予測することができる。そこで、従来ほとんど研究されなかった低エネルギー(100 keV)領域の化学反応の研究を開始した。

低エネルギーイオンが関係する化学反応には、そのイオン自身が化学反応にあずかる場合と、そうではなく、そのイオンの持つ運動エネルギーが媒体に移行し、媒体中の分子が化学反応を起こす場合とがある。本章は、このうち後者に関係するものである。まず媒体を走るイオンのエネルギー損失について考える。イオンが単位距離を走る間に失うエネルギー量(=阻止能)は、電子線に対しては $0.2 \text{ eV} \cdot \text{nm}^{-1}$ の程度であるが、重イオンに対しては $10^2 \sim 10^4 \text{ eV} \cdot \text{nm}^{-1}$ である。重イオンの場合の大きな阻止能の値は、第1には入射イオンと物質中の原子(分子)との衝突確率が高く、エネルギー移行(通常は外殻軌道の励起であり、エネルギー移行量は $10 \sim 20 \text{ eV}$ である)が頻ぱんに起こることによるが、第2には、1回の衝突にさいしてのエネルギー移行量が多い(たとえば数100 eV)によると考えられる。原子衝突物理の成果を参照すれば、このような大きなエネルギー移行が重イオンによる内殻励起ないし多電子励起に基づくことは容易に理解される。この内殻励起・多電子励起は、高速イオンつまり点電荷の通過によっては誘発されないで、構造をもつ粒子つまり低エネルギー重イオンの衝撃によって誘発される。入射イオンのエネルギーがもっと低くなると、電子励起以外に、媒体中の原子の運動を励起する、いわゆる弾性衝突が加わってくる。弾性衝突により、分子中の原子がはじき飛ばされると、それはすなわち化学反応の誘起である〔12〕。

以下では、まず低エネルギーイオン衝撃に特異な化学反応を起こす衝突過程として(a)内殻励起または多電子励起及び(b)弾性衝突の2つの観点から当研究室で得られた主要成果を報告し、つづいて(c)実験に必要な低エネルギーイオン照射装置と周辺機器の整備状況を報告する。

7.1.1 エネルギー移行量の大きい場合の鉄錯体の分解 [1, 2, 6]

エネルギー移行量の大きい衝突は、エネルギー移行量の小さい衝突に比してはるかにまれな現象である。したがってエネルギー移行量が大きい場合の化学効果が実際に観測されるためには、頻度の高いエネルギー移行量の小さい衝突の効果が観測を妨害しないような条件、たとえばその効果がアニールされて消失してしまうようなことが必要である。そこできわめて安定であることが知られている鉄(II)錯体 $K_4[Fe(CN)_6] \cdot 3H_2O$ を選び、種々の粒子線衝撃後の室温における ESR 測定を試みた。ESR 測定は微量の生成物の検出が可能なのであり、また室温における測定は頻度の高い外殻軌道励起をアニールするためである。

$K_4[Fe(CN)_6] \cdot 3H_2O$ 結晶は反磁性物質であるから ESR シグナルはでない。 10^7 rad までのガンマ線を照射してもやはり ESR シグナルは現われなかった (注: 液体窒素温度の照射及び測定を行うときはシグナルが現われる)。 10^8 rad 以上の照射では、 $g = 4.3$ の位置に配位子による縮退がとれた Fe^{3+} イオンによると考えられる ESR シグナルがあらわれる。配位子 CN の分解は CN 基の内殻励起ないしは多電子励起により誘発されたものと考えられる。ところが $10^9 - 10^{10}$ rad の照射を行い、かつ、たとえば $150^\circ C$ の熱処理を行うと、 $g = 2.0$ の位置に幅広い吸収があらわれる。この吸収は $Fe^{3+} - Fe^{3+}$ の交換相互作用によるものであり、クラスターになった $Fe^{3+} - Fe^{3+}$ 距離は $7 - 8 \text{ \AA}$ 以下と推定される。これが $K_4[Fe(CN)_6] \cdot 3H_2O$ に対するガンマ線照射の結果である。

これに対してイオン線照射の結果はつぎのようである。 1 MeV プロトンの照射によっても、また原子変位が効率的に起こると考えられる $20 - 40 \text{ keV Ar}^+$ 照射によっても、いずれも配位子が、こわれたと思われる孤立状態の Fe^{3+} スピンのシグナルだけである (Fig. 1)。ところが $0.45 - 1.8 \text{ MeV}$ の Ar^+ イオンの照射では、 $Fe^{3+} - Fe^{3+}$ クラスターの吸収 ($g = 2.0$) が観測される (Fig. 2)。ここで特に注目すべきことは、イオン飛跡が重なり合うことのない低線量照射でもこの吸収がみられること、さらに ESR 吸収の g 値にわずかながらあるがイオンビームの方向に関する異方性がみられたことである。つまり $\sim 1 \text{ MeV Ar}^+$ イオン照射によって移行エネルギーの大きい衝突 (Fe の内殻励起ないしは多重イオン化) が起こり、配位子がばらばらにこわれると同時にビーム方向に Fe の移動が起ったのである。

なお、鉄(III)錯体 ($K_3[Fe(CN)_6]$, $K_3[Fe(C_2O_4)_3]$) についても、同様の実験を行い、やはり Fe^{3+} クラスターの形成を確認している。

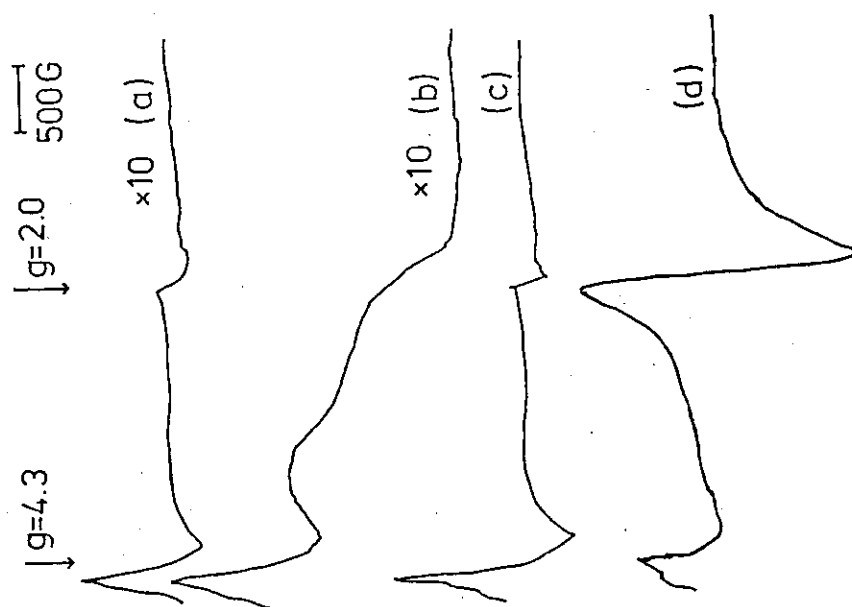


Fig. 1 EPR-spectra of irradiated pellets of $K_4[Fe(CN)_6] \cdot 3H_2O$.
 (a) 40 keV Ar^{+} -bombarded at $10 \mu A cm^{-2}$ for 10 min,
 (b) 40 keV Ar^{+} -bombarded at $10 \mu A cm^{-2}$ for 30 min,
 (c) 1.45 MeV H^{+} -bombarded at $1.5 \mu A cm^{-2}$ for 10 min,
 (d) $60Co-\gamma$ irradiated at 4×10^9 rad followed by heating at $150^\circ C$ for 30 min.

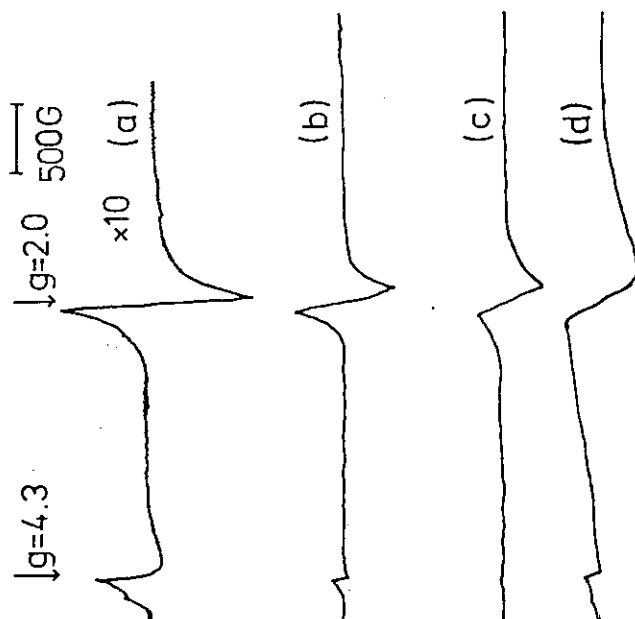


Fig. 2 EPR-spectra of 1.8 MeV Ar^{2+} -ion irradiated (010)-surface of $K_4[Fe(CN)_6] \cdot 3H_2O$. Current density: $0.75 \mu A cm^{-2}$; irradiation time: (a) 10 s, (b) 1 min, (c) 5 min, and (d) 15 min.

7.1.2 硝酸カリウムの分解に対する電子的衝突及び核的衝突の効果

硝酸カリウム (KNO_3) の結晶をガンマ線・電子線やプロトン線・アルファ線で照射すると、分解して亜硝酸イオン (NO_2^-) が生成する。 $G(\text{NO}_2^-)$ は $1.5 \sim 2$ である。これらの放射線では、エネルギーの大部分は電子的衝突 (電子励起) に費やされる。放射線を低エネルギーイオン線に置きかえることにより、電子的衝突から核的衝突 (弾性散乱による原子変位) の寄与を大きくしたときの反応の起こり易さを調べた。結果 (初期生成 G 値) を Table 1 に示す [3]。すなわち D_2^+ , He^+ の場合の値 1.8 はガンマ線の場合とはほぼ一致, N_2^+ , O_2^+ の場合の値 0.5 はかなり低い。これは KNO_3 の分解が、構成原子のはじき出しによるのではなく、 NO_3^- の電子励起によって分解が誘起されることを示唆する。

TABLE 1 COMPARISON OF $G(\text{NO}_2^-)$ FROM KNO_3 OBTAINED BY VARIOUS RADIATIONS.

i) This work (100 keV)

$\text{D}^+, \text{D}_2^+, \text{D}_3^+$	He^+	N_2^+	O^+, O_2^+
1.8 ± 0.2	1.8 ± 0.2	0.5 ± 0.1	0.5 ± 0.2

ii) Literature values

10 keV He^+	3.4 MeV α	1.5 MeV e^-	$^{60}\text{Co } \gamma$
1.54	2.2	1.48	1.46

このことを詳細に検討するために、逆反応等による複雑さの少ない希ガスイオン照射の場合の分解収率のデータの解析を試みた [5]。まず 20 - 100 keV の He^+ , Ar^+ , Xe^+ に対する KNO_3 の電子的阻止能 (S_e) と核的阻止能 (S_n) を求めておく。 He^+ に対しては $S_e > S_n$ であり, Xe^+ に対しては逆に $S_e < S_n$ である。他方、反応の起こり易さは反応断面積 Q で表わされる。これは収率 Y そのものとは違う。両者の関係は

$$Y(T_0) = N \int_0^{T_0} Q(T) y(T) dT$$

あるいは

$$dY/dT = NQ(T) y(T)$$

である。但し、入射イオンのエネルギー T が初期値 T_0 から 0 になるまでに標的物質 (原子密度 N) 中で生成物を生ずる断面積 $Q(T)$ が T に依存し、また入射イオンのエネルギーが T から $T - dT$ になるまでに走る距離を $y(T) dT$ とする。 $y(T)$ は阻止能から求められる。結果は 20 - 100 keV のエネルギー範囲で $\text{KNO}_3 \rightarrow \text{KNO}_2 + \text{O}$ の反応の Q にエネルギー依存性はあまりな

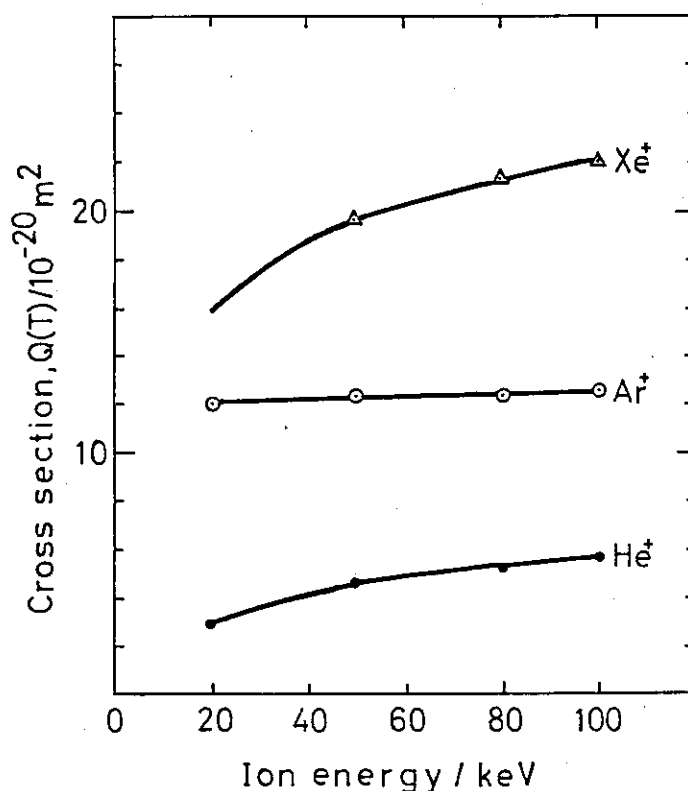


Fig. 3 Cross-sections for producing NO_2^- from KNO_3 as a function of incident ion energy.

く (Fig. 3), 入射イオン Xe^+ に対して $22.0 \times 10^{-16} \text{ cm}^2$, Ar^+ に対して $12.6 \times 10^{-16} \text{ cm}^2$, He^+ に対して $5.7 \times 10^{-16} \text{ cm}^2$ であり, これらの値は S_e と S_n が 5 対 1 の割合で分解反応に寄与しているとするとなつじつまの合うものである。

7.1.3 低エネルギーイオン照射装置の整備

53 年から 57 年にかけて設置されたイオン照射装置は, デュオプラズマ型と RF 型の 2 種類のイオン源, ビーム収束機構, イオン選別電磁石, ビームチョッパーなどを有している。加速可能なイオン種は, 希ガス, 水素, 酸素, 窒素などの気体放電によるものであり, 加速電圧は 0 - 100 kV である。また測定機器としては, 照射チェンバー, 電子放出率測定器, 電子エネルギー分析器, 二次イオン質量分析器などである。

58 年から 60 年にかけて以下の測定機器の整備を行い, 低エネルギーイオン照射装置の設置計画の予定を終了した〔1〕。なお現在の装置の配置図を Fig. 4 に示す。

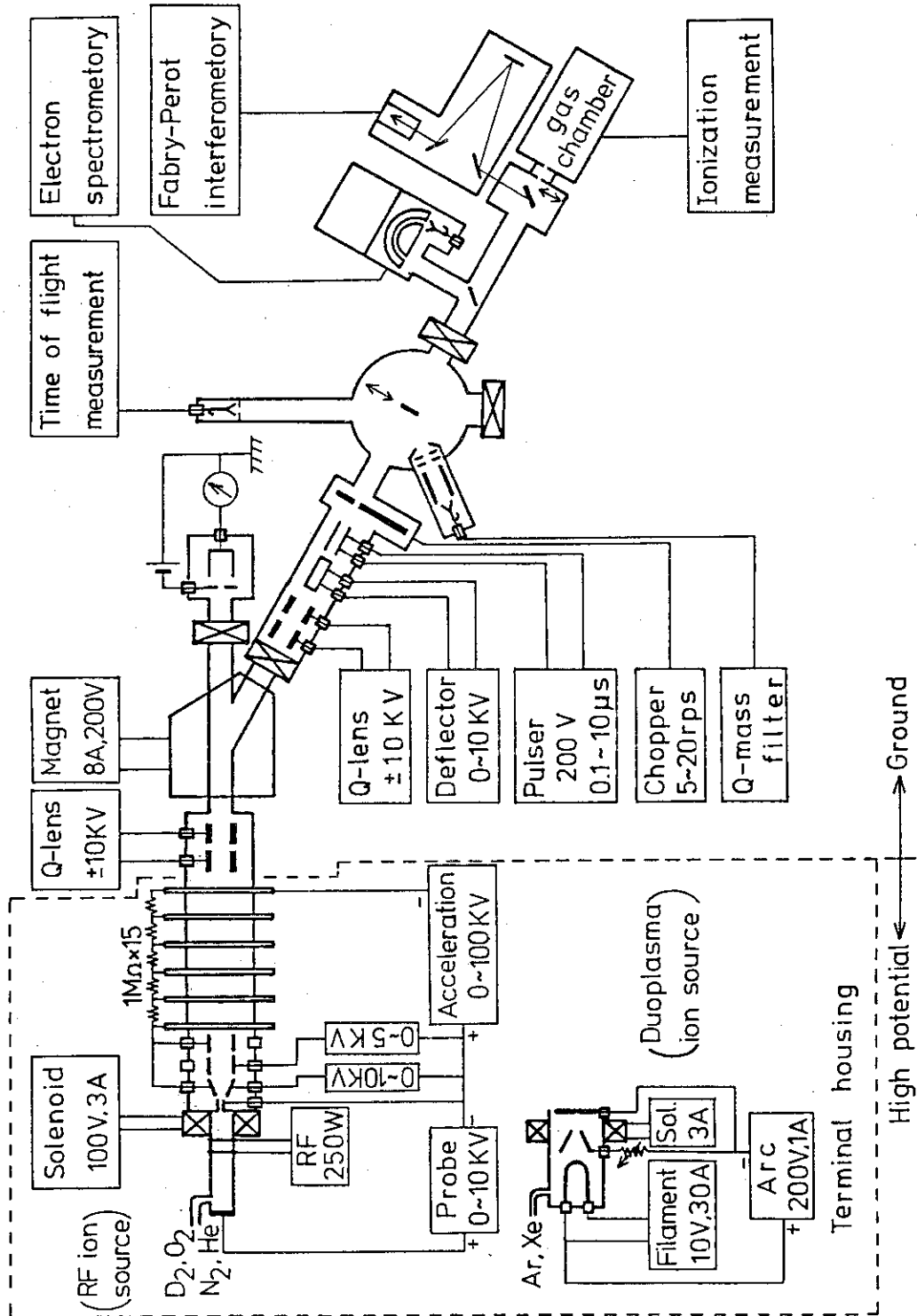


Fig. 4 A schematic illustration of the 100-kV ion accelerator and experimental equipments.

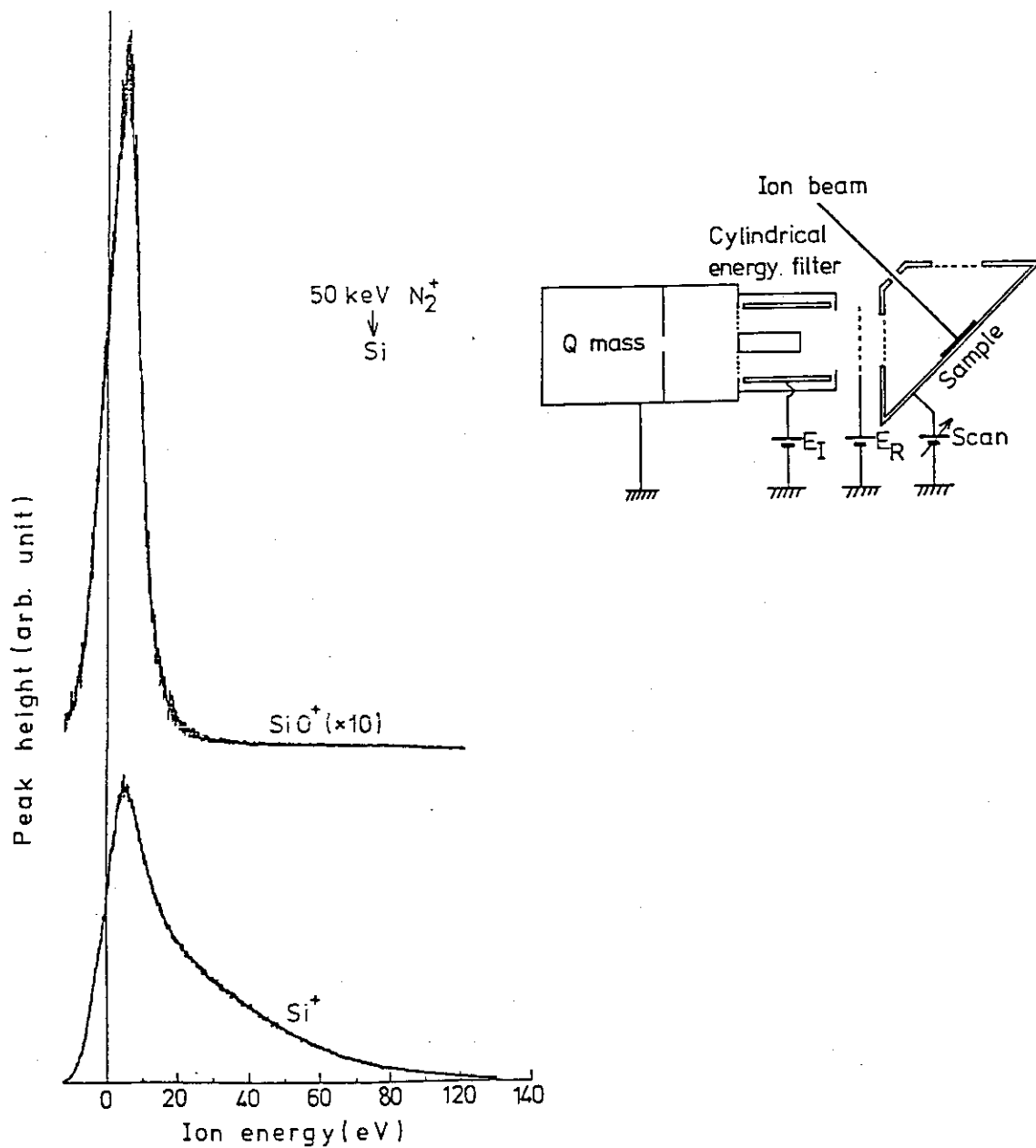


Fig. 5 (right) Measurement of the kinetic energy of emitted secondary ion from solid sample with use of an electrostatic energy filter and a retarding grid (left) Energy spectrum of Si^+ and SiO^+ emitted from Si bombarded with 50 keV N_2^+ ions.

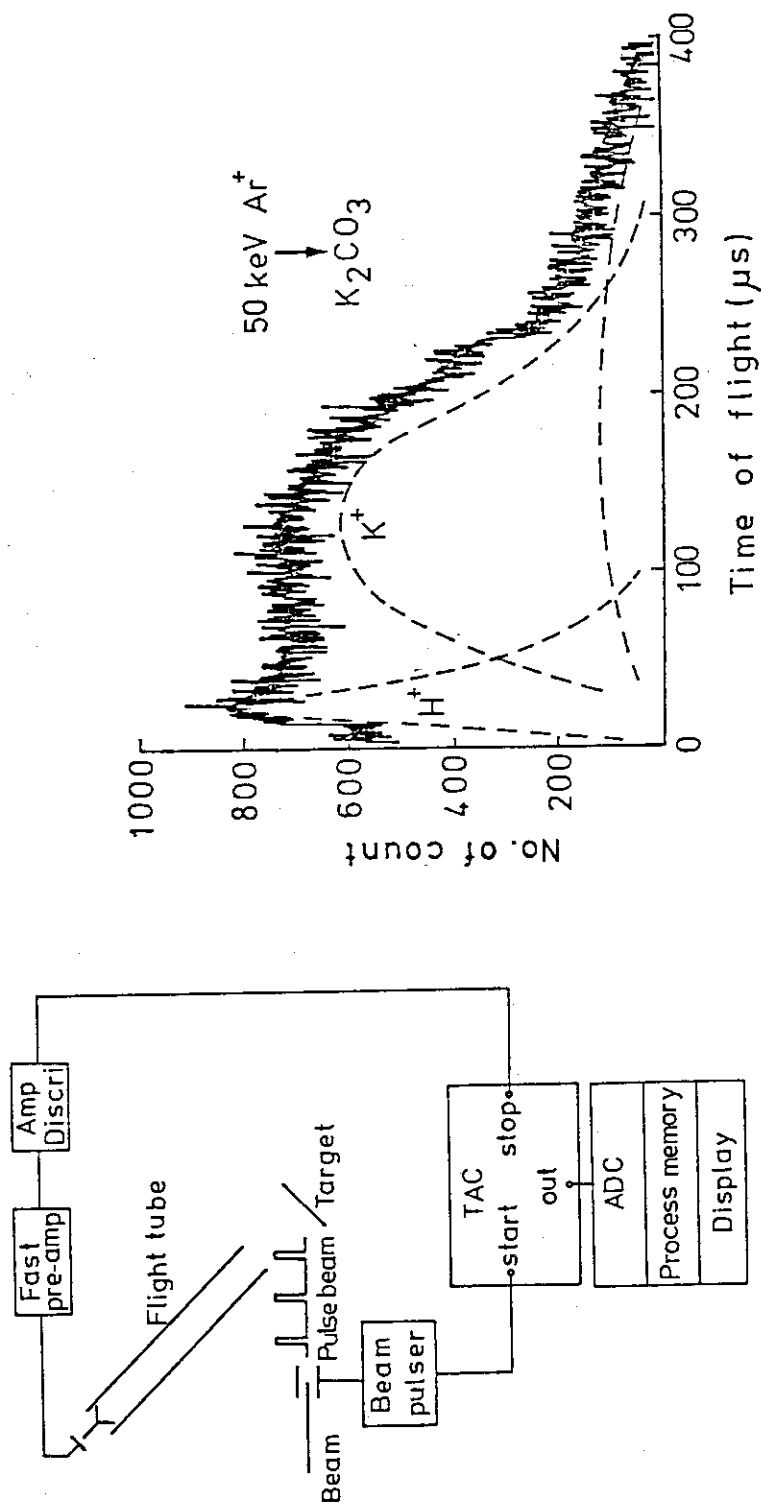


Fig. 6. Block diagram of the apparatus for ionization-yield measurements.

(a) 二次イオンエネルギーの測定

イオン衝撃による固体からの二次イオン放出に関する研究は、イオン衝撃による化学反応生成物の同定の観点から注目されている[8, 9]。二次イオン生成の機構を研究するために、二次イオンエネルギー測定の方法を検討した。

まず、日本真空(株)製の残留気体分析用四重極質量分析計(QMS-300)を用い、これに(i)円筒状エネルギーフィルターを取付ける、(ii)アナログ測定からパルス計測に切換えるの2点を改造する。さらに、エネルギーフィルターは二次イオンのうちの高エネルギー成分をカットするので、(iii)その直前に阻止グリッドをもうけて低エネルギー成分をカットする。Fig. 5に装置の模式図と50 keVの N_2^+ イオン衝撃のケイ素結晶から得られる二次イオンのエネルギー測定の例を示す。エネルギー分布の傾向はわかるが、エネルギーフィルターの分解能に改善の余地があることを示している。

また二次イオンのエネルギーは、静電方式によらなくても、飛行時間測定によって求めることもできる。装置のブロック図と測定結果をFig. 6に示す。

(b) 発光スペクトル測定

イオンビームを固体表面に照射するさいにみられる発光は、スパッター粒子からの発光、衝撃イオンからの発光、および固体励起(空孔-電子対再結合)による発光が知られている。このうちスパッター原子からの発光の線幅の解析からは、スパッター原子の飛行方向とエネルギーないし励起領域の温度の情報が得られる。

(c) 気体イオン化の測定

気体中に入射したイオンは、その飛跡に沿って気体分子をイオン化する。生成イオン対の数を測定するための電離箱を製作し、その電離電流の飽和特性を調べた。

(S. Ohno)

Publication List

- [1] Ohno, S., Furukawa, K.: "Chemical reactions induced by low-energy ions. Decomposition of ferrous cyanida complex due to Ar^+ -ion bombardment", "Proc. 7th Intern. Congr. Radiat. Res., ed by Broese, J.J. et al., Martinus Nijhoff Pub., Amsterdam, 1983, A2, p.23.
- [2] Ohno, S., Furukawa, K.: "Decomposition of crystalline postassium hexacyanoferrate (II) trihydrate by incident energetic argon ions", Bull. Chem. Soc. Jpn., 58, 1100 (1985).
- [3] Furukawa, K., Ohno, S.: "Decomposition of solid potassium nitrate by incident 100 keV ions", Bull. Chem. Soc. Jpn., 58, 1831 (1985).
- [4] Saeki, M., Ohno, S., Tachikawa, E., Azuma, N., Miyazaki, T., Fueki, T., Fueki, K.: "Comparison of 80-keV D^+ ion implantation with Thermal D_2 doping in silica by FTIR and ESR spectroscopy", J. Am. Chem. Soc., 68, 151 (1985).

- [5] Ohno, S., Furukawa, K., Soga, T.: "Chemical effectiveness of elastic and inelastic energy loss of He^+ , Ar^+ , and Xe^+ ions bombarding potassium nitrate", Bull. Chem. Soc. Jpn., to be published.
- [6] Ohno, S., Furukawa, K.: "Chemical reactions induced by low-energy ions. Decomposition of ferrous cyanide complex due to Ar^+ -ion bombardment", informal documents, (1983).
- [7] Ohno, S.: "Radiolytic decomposition of water for hydrogen production", (in Japanese), Radioisotopes, 29, 401 (1980).
- [8] Ohno, S.: "Secondary electron emission by ionic and electronic bombardment", (in Japanese), Report of Workshop on Particle Material Interactions for Fusion Research, JAERI-M 9775, p.75 (1981).
- [9] Ohno, S.: "Ion induced desorption process at solid surface", (in Japanese), 2nd Workshop on Particle Material Interactions for Fusion Research, JAERI-M 83-235, p.73 (1983).
- [10] Ohno, S.: "Hot atom chemistry in relation to fusion energy utilizations", ed by Matsuura, T., "Hot Atom Chemistry", Kodansha-Elsevier Pub., Tokyo, 1984, p.512.
- [11] Furukawa, K., Ohno, S.: "100 keV-Ion accelerator for study of chemical reaction", (in Japanese), JAERI-M85-110 (1985).
- [12] Ohno, S.: "Chemical reactions induced by low-energy ion bombardment", (in Japanese), Ioniz. Radiat., 11, 75 (1985).
- [13] Ohno, S., Izui, K., Sasaki, T.A., Furuno, S., Soga, T., Furukawa, K., Houjo, K., Komaki, Y., Baba, Y.: "A proposal for study of ion-beam induced chemical reactions using JAERI tandem accelerator", (in Japanese), JAERI-M85-164 (1985).

7.2 水素イオン衝撃による耐熱性材料の表面化学変化

核融合炉におけるプラズマ-壁相互作用の一つに、壁材料によるプラズマ粒子の捕捉がある。水素の場合、その捕捉状態は水素化物形成、水素透過などを通じて材料の脆化やトリチウムのリサイクリングに影響を及ぼす重要な因子となる。しかし、水素の検出法は限られているため、材料表面層における捕捉状態、とりわけ化学状態についての知見は極めて乏しい。そこで、捕捉水素の化学結合状態を光電子分光法により解析することを目標とし、金属-水素結合の電子状態をDV-X α クラスタ法に基づく分子軌道法で計算した〔4, 6〕。この手法を用いて、低エネルギー水素イオンを照射した高融点金属及びセラミックスのX線光電子分光(XPS)スペクトルを解析し、水素化物形成の有無、表面化学組成変化等に関する知見を得た。以下に、keV オーダ水素イオンで衝撃した3d 遷移金属（スカンジウム、チタン、バナジウム、クロム、ニッケル）、4d 遷移金属（イットリウム、ジルコニウム、ニオブ、モリブデン）及びケイ素含有セラミックス（炭化ケイ素、窒化ケイ素、酸化ケイ素）についての成果を記す。

7.2.1 水素イオン衝撃した単体金属の内殻XPS スペクトルと表面化学状態〔7, 9, 11, 13, 15〕

遷移金属の多くは核融合炉第一壁候補材料の主要な構成元素である。そこで、一連の単体金属にPIG型イオン銃からの8 keV H_2^+ イオンを室温照射し、表面化学状態の変化をXPSにより測定した。

H_2^+ イオンを 5×10^{14} ions/cm²・sec (100 μ A/cm²) のビーム束により 1×10^{18} ions/cm² まで照射した後の金属チタンのTi 2p XPS スペクトルをFig. 1に示す。比較のため、未照射金属チタン、TiO₂ 及び熱合成水素化物 (TiH_{1.97}) のスペクトルも示す。水素照射試料

(Ti:H_{imp}, H_{imp} はイオン注入水素を表わす) のTi 2p_{3/2} 線は、金属状態に比べ0.3 eV 高エネルギー側にシフトする。TiH_{1.97} のスペクトルには表面酸化物によるピークの重なりが認められるものの、454.6 eV の主ピークは水素化物からのTi 2p_{3/2} 線である。ピークエネルギーは、Ti:H_{imp} の主ピークに等しいことから、注入水素はターゲット表面層 (～1 nm) において、TiH_{1.97} に極めて近い化学組成の水素化物を形成したと考えられる。

Fig. 2 には、ジルコニウム化合物のZr 3d XPS スペクトルを示す。熱合成水素化物 (ZrH_{1.64}) の表面は酸化物に覆われているが、179.6 eV には水素化物に帰属しうる光電子ピークが認められる。一方、水素照射試料 (Zr:H_{imp}) のZr 3d 領域には、金属ジルコニウムの場合よりはるかに広いスペクトルが観測された。また、Zr 3d_{5/2} とZr 3d_{3/2} のピーク強度比は1.1で、理論値の3/2より小さい。これは、水素イオンビーム中に不純物として混在した酸素イオンが、ターゲット表面層に注入されたためと考えられる。すなわち、ジルコニウム中での8 keV H_2^+ イオンの飛程20 nm に対し、8 keV O_2^+ イオンの飛程は5 nm であるため、表面層が酸素リッチになりうる。実際、Zr:H_{imp} を5 keV Ar⁺ イオンで短時間エッチングしたところ、Zr 3d_{3/2} のピーク強度は急激に減少し、179.6 eV にシャープなピークが現われた。このことから、水素イオン照射したジルコニウム表面に生成する水素化物は、ZrH_{1.64} に近い化学組成をもつと推測される。

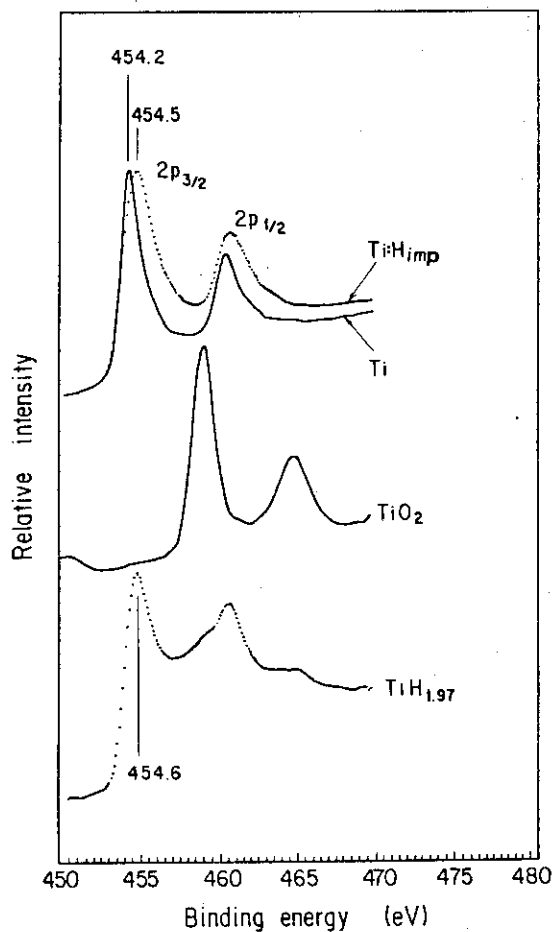


Fig. 1 Ti 2p XPS spectra of TiH_{imp} , Ti , TiO_2 and $\text{TiH}_{1.97}$.

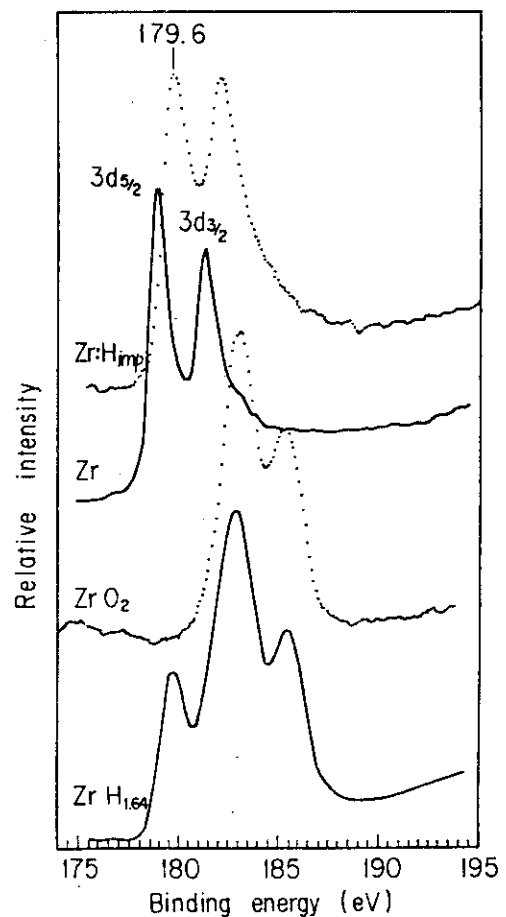


Fig. 2 Zr 3d XPS spectra of ZrH_{imp} , Zr , ZrO_2 , and $\text{ZrH}_{1.64}$. Note that the surface of the $\text{ZrH}_{1.64}$ sample is covered with a large amount of oxide(s).

スカンジウム、バナジウム、イットリウム、ニオブ等の単体金属ターゲットについても水素イオン衝撃を行って、水素化物特有の内殻軌道におけるケミカルシフトを見出した。

一方、クロム、ニッケル及びモリブデンの場合、 $2 \times 10^{18} \text{ ions/cm}^2$ までの水素照射でも、内殻軌道のケミカルシフトは観測されなかった。これは、これらの金属と水素の化学反応が吸熱的であり、熱力学的には常温で安定な水素化物層が存在しえないことによると理解できる。したがって上記金属中の注入水素は、金属の格子間あるいは欠陥等に原子状または分子状で捕捉されたと考えることができよう。

7.2.2 水素イオン衝撃した単体金属の価電子帯レベル構造 [9, 11, 13]

水素イオン注入法により、遷移金属の多くは金属水素化物を形成することを、内殻軌道のXPSスペクトル測定により確認した。注入層のレベル構造、捕捉水素の結合エネルギー等に関する知見を得るため、水素イオン衝撃した各種遷移金属について、価電子帯 (VB) のXPSスペクトル測定を行った。

Fig. 3 にチタン化合物のVB-XPS スペクトルを示す。水素イオン照射試料 (Ti:H_{imp}) のスペクトルには、 $E_b = 3.5 \text{ eV}$ に金属チタン及び TiO_2 には認められない新しいピークが出現する。ピークエネルギーは、白丸で図示した分子軌道法による $\text{Ti } 3d - \text{H } 1s$ 結合性軌道の計算値より 2.5 eV も低い。しかし、 3.5 eV ピークは酸素吸着、水素吸着などで出現しないことから、注入水素とチタンの反応により形成された Ti-H 結合性軌道の一部と考えられる。

Fig. 4 にジルコニウム化合物のVB-XPS スペクトルを示す。金属ジルコニウムを水素照射すると、 $E_b = 3.4 \text{ eV}$ に斜線部のような新しい光電子ピークが出現する。吸着酸素の影響を調べるため、金属ジルコニウムの清浄表面を $9 \times 10^{-5} \text{ Pa}$ の酸素雰囲気にし、 $\text{O } 1s / \text{Zr } 3d$ 比が水素照射試料 Zr:H_{imp} の場合と同じになるまで酸素を吸着させたが、 $\sim 3.4 \text{ eV}$ にピークは出現しなかった。また、金属ジルコニウムを $5 \sim 10 \text{ keV}$ の Ar^+ イオンで照射しても、VB-XPS スペクトルに変化は認められない。以上のことから、斜線部のピークは酸素吸着、照射損傷等によるものではなく、試料表面層の Zr-H 結合によると結論できる。

Fig. 4 の斜線部のピークエネルギーは、Fig. 3 の場合と同様、 $\text{DV-X}\alpha$ 法を用いた分子軌道法による計算値より $\sim 2.5 \text{ eV}$ 低い。この理由は、イオン照射により表面損傷が起こるためである。

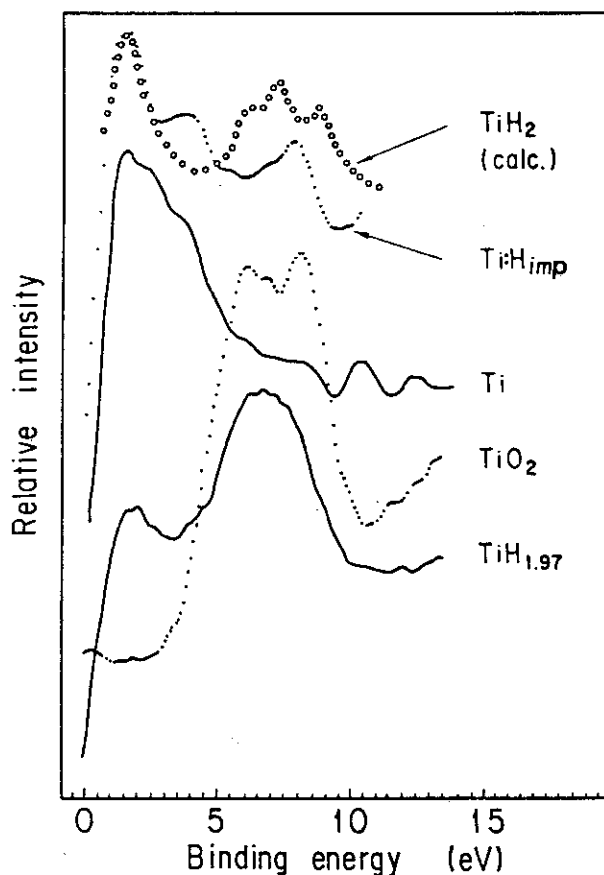


Fig. 3 VB XPS spectra of TiH_{imp} , Ti , TiO_2 and $\text{TiH}_{1.97}$. A curve with open circles is spectrum calculated for TiH_2 , taken from ref. [4]. Photopeaks at 5–9 eV which are observed for TiH_{imp} , TiO_2 and $\text{TiH}_{1.97}$ correspond to the surface oxides. The peak at 3.5 eV for TiH_{imp} is attributed to the $\text{Ti } 3d - \text{H } 1s$ bond.

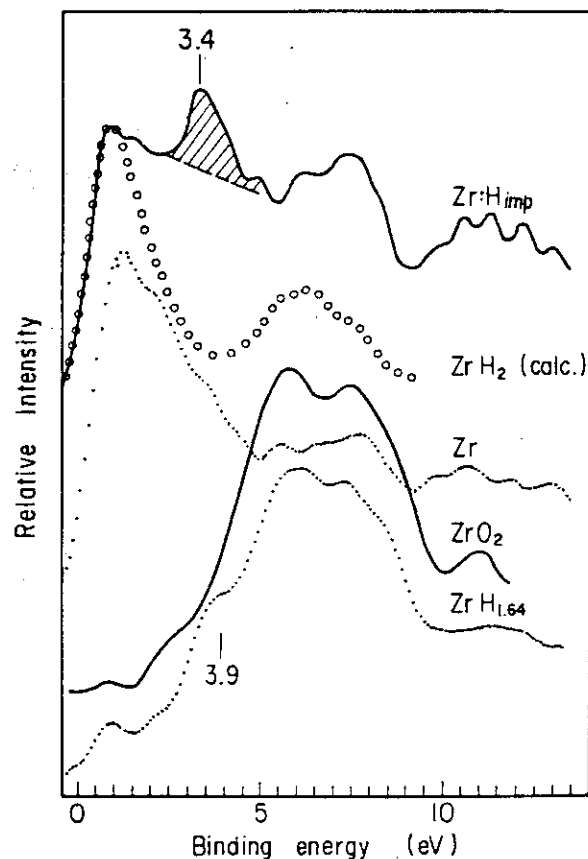


Fig. 4 Blowup of the XPS spectra near the Fermi level of Zr:H_{imp} , Zr , ZrO_2 , and $\text{ZrH}_{1.64}$. The curve using open circles is spectrum calculated for ZrH_2 , taken from ref. [4]. The photopeak at 5–9 eV which is observed for all samples is mainly due to oxide(s). The small bump at $\sim 3.9 \text{ eV}$ for the $\text{ZrH}_{1.64}$ sample is probably from the $\text{Zr } 4d - \text{H } 1s$ bond.

すなわち、DV-X α 法による計算は〔Zr₄H₈〕クラスターのレベル構造で、Zr-Hの原子間距離には熱合成水素化物ZrH_{1.64}結晶の値が用いられている。一方、水素イオンに衝撃により生成した水素化物では、結晶格子が乱れ、原子間距離が多少小さくなると予想される。Zr-Hの原子間距離を、熱合成水素化物の場合の60%として計算し直したところ、Fig. 4の4.5~8 eVピークが分裂し、~3.3 eVにレベル構造が出現した。これは、Zr4d-H1s相互作用が弱められた結果生じるH1sのコンポーネントを多く含む軌道である。Fig. 4の斜線部は、このレベル構造に対応するピークと考えられる。

水素イオン衝撃した金属表面のVB-XPSスペクトル測定は、スカンジウム、バナジウム、イットリウム及びニオブ等についても行った。いずれの場合も、水素化物特有のMetal d-H1s結合性軌道に起因する光電子ピークがE_b = 3.0~5.0 eVにあること、ピーク位置は熱合成水素化物のレベル構造に対する計算値より低エネルギー側になること等が明らかにされた。

7.2.3 注入水素の加熱放出挙動〔11, 13〕

イオン衝撃により注入された水素と母体金属の原子間距離が、熱合成水素化物における金属-水素の結合距離に比べ数10%も小さいならば、これら両者における水素の拡散速度は大きく異なると予想される。そこで、水素イオン衝撃実験において水素化物の生成が認められたTi:H_{imp}、V:H_{imp}、Y:H_{imp}、Zr:H_{imp}及びNb:H_{imp}について注入水素の加熱放出挙動を調べ、熱合成水素化物の場合と比較検討した。

水素イオン照射試料は7.2.2の方法により、また、熱合成試料は高温域における高純度単体金属の水素吸蔵・放出処理により得た。水素放出の確認は次のように行った。まず、照射試料の場合は、所定温度において30分間の等時アニーリングの後、室温においてXPS測定を行い、水素化物に帰属されるMetal d-H1s軌道のピーク強度を求めた。また、熱合成試料の場合は、真空電気炉中で試料を等速昇温（5℃/min）させ熱重量法（TG）から放出水素量を決定した。

Fig. 5には、XPSスペクトルのピーク強度変化及びTG曲線から求めたH/Me比を示す。照射試料のXPSピーク強度は、いずれの金属でも加熱に伴い上昇する。これは、金属中における8 keV H₂⁺イオンの飛程が10~20 nmで、XPSの検出深度（~1 nm）に比べはるかに大きく、深層部の注入水素が、加熱に伴い試料表面へ拡散したことによる。

注入水素の加熱放出温度が、熱合成水素化物の分解温度より高いというのも、照射試料の大きな特徴である。Fig. 5で明らかなように、熱合成試料VH_{0.55}では180℃で水素放出が完了するとともに、V 3d-H1s軌道のXPSスペクトルが消失する。一方、照射試料V:H_{imp}の場合では、300℃に加熱しても光電子ピークが認められる。熱合成水素化物の水素に比べ注入水素がより高温まで保持されるのは、照射損傷によりターゲット表面層が非晶質化し、これが水素の熱拡散を抑制するためと考えられる。

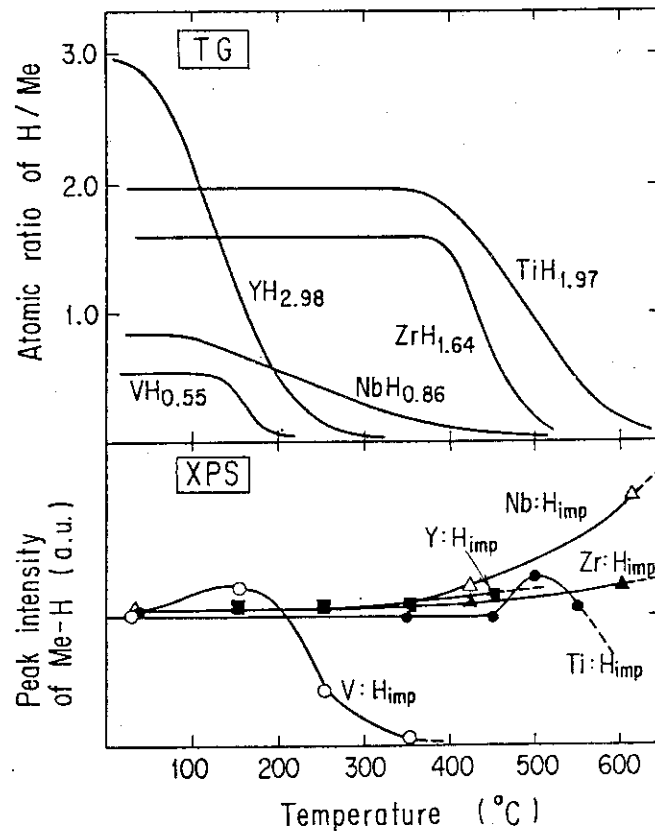


Fig.5 TG Curves of Hydrides and Changes in XPS intensities of Me : H_{imp}

7.2.4 X線励起オージェ電子分光法 (XAES) による注入水素化物の状態分析 [7, 9]

オージェ電子分光法 (AES) は、一次ビームに電子線を用いるので、S/N 比が低くエネルギー分解能も悪い。さらに、電子ビームによる表面損傷のため、これが化学状態分析に用いられることはほとんどない。しかし、一次ビームとして軟X線を用いることにより上記の困難を克服することができるので、XAESのケミカルシフトから化学状態に関する知見が得られる。しかも、オージェ電子は脱出深度が小さいので、XAESはXPSに比べより表面の化学状態に関する情報をもたらすという大きな特徴をもつ。そこで、水素イオン衝撃したイットリウム、ジルコニウム、ニオブについてXAESスペクトルの測定を試み、XPSによる結果と比較検討した。

Fig. 6にジルコニウム化合物の $M_{4,5}N_{2,3}V$ 遷移に伴うXAESスペクトルを示す。熱合成水素化物 ($ZrH_{1.64}$) の場合、XPSでは水素化物からの光電子ピークが観測された (Fig. 2)。しかし、XAESスペクトルには ZrO_2 が認められるのみである。XAESの結果がXPSのそれと全く異なるのは、検出深度がそれぞれ 0.5 nm, 1.5 nm で、前者が後者より表面に鋭敏であることによる。一方、水素照射試料 $Zr:H_{imp}$ の場合、XAESスペクトルは金属ジルコニウム及び ZrO_2 のそれとは異なり、表面層が水素化物であることを示唆する。オージェピークのケミカルシフトは 3.3 eV でXPSにおける $Zr 3d_{5/2}$ 線のケミカルシフト 0.6 eV よりはるかに大きい。このように大きいケミカルシフトは、 $Y:H_{imp}$, $Nb:H_{imp}$ についても見出された。Table 1には、XAES及びXPSのピークエネルギー及びケミカルシフトを示す。注入水素化物ではXAESのケ

ミカルシフトがXPSの場合の2.5～5.5倍に達することから、本法が金属水素化物の状態分析に極めて有用であることが分かった。

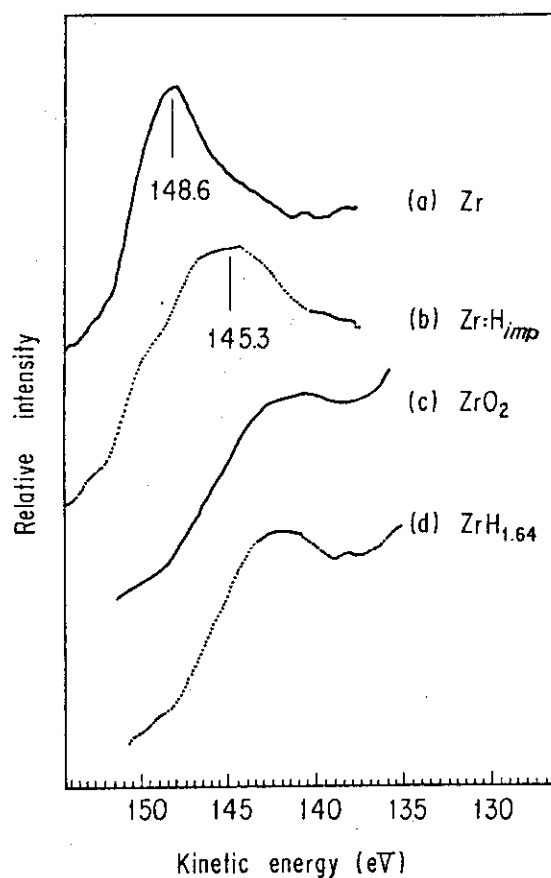


Fig. 6 X-ray-induced $M_{4,5}N_{2,3}V$ Auger spectra for (a) Zr, (b) ZrH_{imp} , (c) ZrO_2 and (d) $ZrH_{1.64}$.

Table 1 E_k of $M_{4,5}N_{2,3}V$ Auger electrons, E_b of $3d_{5/2}$ lines and their chemical shifts.

Sample	E_k (eV)	Auger Chemical Shift (eV)	E_b (eV)	$3d_{5/2}$ Chemical Shift (eV)
Y	124.3	-	155.9	-
Y:H _{imp}	123.3	1.0	156.2	0.3
Y ₂ O ₃	117.8	6.5	158.6	2.7
Zr	148.6	-	179.0	-
Zr:H _{imp}	145.3	3.3	179.6	0.6
ZrO ₂	141.9	6.7	183.3	4.3
Nb	167.8	-	202.4	-
Nb:H _{imp}	165.6	2.2	203.2	0.8
Nb ₂ O ₅	161.6	6.2	208.1	5.7

7.2.5 ケイ素含有セラミックスの表面化学組成に及ぼす水素イオン照射効果〔14, 16〕

炭化ケイ素の表面損傷は、プラズマ-壁相互作用と直接関連する問題であるため、注目すべき成果があいついで報告されてきた。化学的に興味ある結果として、低エネルギー水素イオン衝撃により化学スパッタの起こることが見出され、照射表面が炭素リッチになることも明らかにされている。しかし、注入水素の捕捉状態等に関する知見はほとんどない。そこで、炭化ケイ素のみならず、窒化ケイ素、酸化ケイ素についても水素イオン衝撃を行い、照射表面の化学変化、化学組成の照射量依存性等を調べるとともに、注入水素の捕捉状態について検討した。

ターゲットには高純度グラファイト、シリコン単結晶、CVD-SiC、CVD-Si₃N₄などの鏡面試料を用いた。これらを、電子分光装置の分析装置内ターゲットホルダー上で、6 keV H₂⁺イオンにより室温照射した。照射条件は7.2.1と同じであった。オージェ電子分光(AES)スペクトル測定は、5 keV電子線により行い、peak-to-peakの相対値から組成変化の大きさを見積った。

炭化ケイ素表面におけるC/Si比の照射量依存性をFig. 7に示す。H₂⁺イオンの照射に伴い表面の炭素量が増加し、 2.2×10^{18} atoms/cm²におけるC/Si比は、XPS, AESでそれぞれ照射前の1.1倍、2.5倍であった。AESによる値がXPSによる結果より大きくなるのは、組成変化が表面1~2原子層で起こることを示唆する。すなわち、Si 2s及びC 1s軌道からの光電子は約1.1 keVの運動エネルギーをもち、従ってXPSの検出深度は約1.5 nmとなる。一方、Si(LVV)及びC(KLL)のオージェ電子による検出深度は約0.5 nmである。これら両者における表面層検出感度の差異がFig. 7に示す結果をもたらしたと考えられる。AESで求めたC/Si

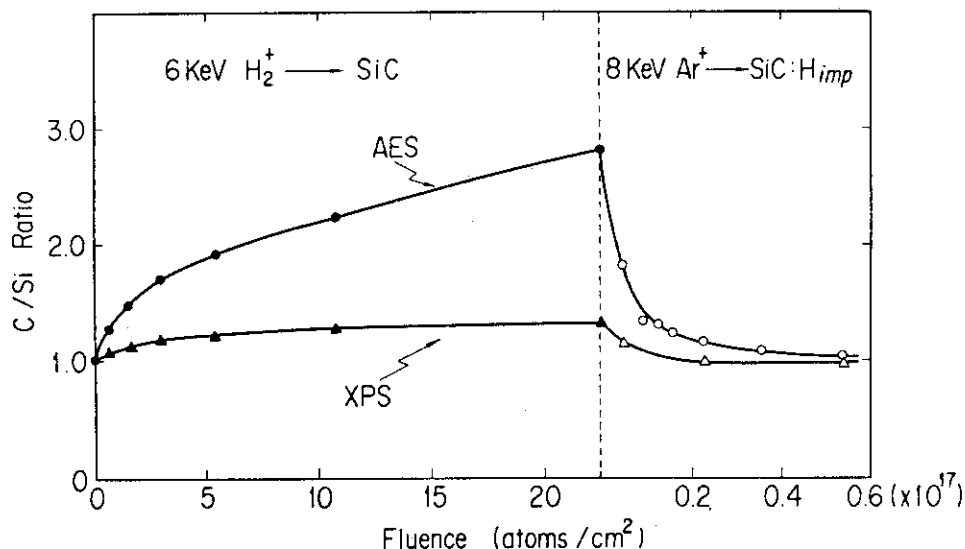


Fig. 7 Compositional changes in the C/Si ratios of the SiC sample as functions of hydrogen and Ar⁺-ion fluences. The AES data were determined from the signal ratio of C(KLL, 260 eV)/Si(LVV, 75 eV). The XPS data were estimated through the signal ratio of C1s(283.4 eV)/Si2s(151.8 eV).

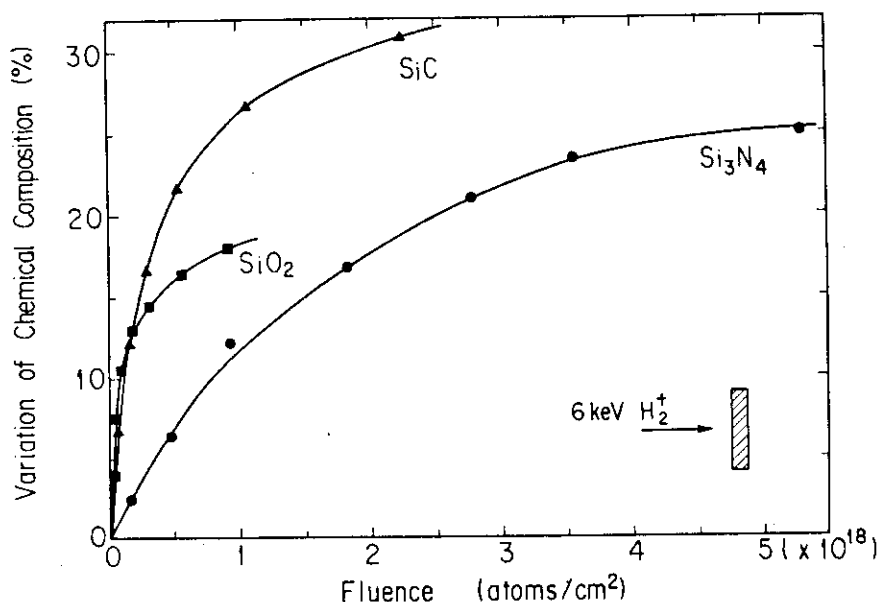


Fig. 8 Variations of the compositional changes for the SiC, Si₃N₄ and SiO₂ samples vs. hydrogen fluence. The values plotted are data by the XPS measurements.

比の最大値 2.5 は、グラファイト及びシリコンを 3 keV H⁺ イオン（衝撃の効果は 6 keV H₂⁺ イオン 0.5 個分と同じ）で衝撃したとき観測されるスパッタ収率の比 1.9 に近い値である。これまで、表面化学組成が変化する原因として、（１）照射イオンからの運動量移行による表面原子の深部注入、（２）表面原子のスパッタリング、という二通りのモデルが提案されている。本研究のデータはモデル（２）を強く支持する結果といえる。

次に、表面層で過剰に存在する炭素の化学結合状態を明らかにするため、グラファイトを水素イオン衝撃した場合と比較検討した。炭化ケイ素、グラファイトとも、照射後の C1s 線には 0.2 eV のケミカルシフトが認められた。ピーク位置が高分子材料の C1s 線のそれと類似することから、炭化ケイ素表面の過剰炭素は注入水素を捕捉し、C-H 結合を形成したと考えられる。VB-XPS スペクトルにも C-H 結合に帰属しうる光電子ピークが観測された。

窒化ケイ素及び酸化ケイ素を水素イオン衝撃すると、炭化ケイ素の場合とは逆にケイ素リッチになる。被照射試料の内殻軌道スペクトルは衝撃前と同一であるが、VB-XPS スペクトルには新しい光電子ピーク（E_b = 3.6 eV）が出現する。このピーク位置は Si-H の結合エネルギー 3.2 eV に近く、シリコン単結晶を水素イオン衝撃したときも認められた。イオン衝撃により多数の dangling bond が生成し、これが Si-H の結合形成をもたらしたと推測される。

Fig. 8 には表面化学組成変化率の照射量依存性を示す。変化率曲線において、初期勾配は表面構成原子と水素イオンとの反応速度の、また、重照射域での平衡値は反応量の目安となる。二酸化ケイ素についての初期勾配は比較的大きく、ケイ素含有セラミックスの中で水素イオンは二酸化ケイ素と最も反応しやすいことがわかる。

(T. A. Sasaki and Y. Baba)

Publication List

- [1] Sasaki, T.A., Soga, T.: "Electronic structure and x-ray photoelectron spectra of rutile-family dioxides calculated by DV-X α cluster method", *Physica*, 111B, 304 (1981).
- [2] Sasaki, T.A., Kiuchi, K.: "Electronic structures and x-ray photoelectron spectra of MoO₂ and Li₂MoO₄", *Chem. Phys. Lett.*, 83, 356 (1981).
- [3] Soga, T., Sasaki, T.A.: "Electronic structures and valence band XPS spectra of BeO and SiC calculated by X α cluster method", (in Japanese), JAERI-M 9769 (1981).
- [4] Sasaki, T.A., Soga, T.: "Calculations of electronic structures of TiH₂, VH₂, ZrH₂ and NbH₂ by the X α method", (in Japanese), *J. Surf. Sci. Soc. Japan*, 3, 17 (1982).
- [5] Sasaki, T.A., Soga, T., Adachi, H.: "Electronic structure of molybdenum dioxide calculated by the X α method", *Phys. St. Sol.*, 113(b), 647 (1982).
- [6] Sasaki, T.A.: "Calculation of electronic structures of ScH₂, NiH₂, YH₂ and PdH₂ by the X α method", (in Japanese), *J. Surf. Sci. Soc. Japan*, 3, 183 (1982).
- [7] Baba, Y., Sasaki, T.A.: "X-ray excited Auger electron spectra of hydrogen implanted 4d transition-metals and related compounds", informal communication, (1983).
- [8] Baba, Y., Sasaki, T.A.: "X-ray photoelectron and x-ray-induced Auger electron spectroscopic data, I 3d transition-metals (Sc, Ti, V, Ni) and related oxides", JAERI-M 84-005 (1984).
- [9] Baba, Y., Sasaki, T.A.: "Application of x-ray-induced Auger electron spectroscopy to state analyses of hydrogen implanted in Y, Zr and Nb metals", *Surf. Interface Anal.*, 6, 171 (1984).
- [10] Baba, Y., Sasaki, T.A.: "X-ray photoelectron and x-ray-induced Auger electron spectroscopic data, II 4d transition-metals (Y, Zr, Nb, Mo, Ru) and related oxides", JAERI-M 84-071 (1984).
- [11] Sasaki, T.A., Baba, Y.: "Chemical-state studies of Zr and Nb surfaces exposed to hydrogen ions", *Phys. Rev. B*, 31, 791 (1985).
- [12] Sasaki, T.A., Baba, Y., Hojou, K., Aruga, T.: "Transmission sputtering of titanium by 114 MeV fluorine ions", *J. Nucl. Mater.*, 132, 95 (1985).
- [13] Baba, Y., Sasaki, T.A.: "Chemical state and thermal stability of hydrogen-implanted Ti and V studied by x-ray photoelectron

- spectroscopy", J. Nucl. Mater., 132, 173 (1985).
- [14] Sasaki, T.A., Baba, Y.: "X-ray photoelectron and x-ray-induced Auger electron spectroscopic data, III graphite, Si, SiC, Si₃N₄ and SiO₂", JAERI-M 85-063 (1985).
- [15] Baba, Y., Sasaki, T.A.: "XPS observation of yttrium surface bombarded with hydrogen-ions", J. Nucl. Mater., 138 (1986).
- [16] Sasaki, T.A., Baba, Y.: "Surface compositional and chemical-state changes of SiC, Si₃N₄ and SiO₂ by energetic hydrogens", J. Nucl. Mater., 138 (1986).

7.3 金属及びセラミックスにおけるイオン照射欠陥

7.3.1 序

Al は低放射化材料, SiC は低原子番号の高温耐熱材料としてそれぞれ注目されているが, これらを核融合炉材料として使用した場合に受ける照射損傷は照射粒子の多様性に応じて複雑な様相を呈すると考えられる。例えば 14 MeV 中性子によるノックオン, (n, α) 反応による He, 燃料要素からの T, その他プラズマ中の種々の不純物イオンなどによる損傷である。これら個々のイオンによる損傷の形態を要素的に捕えておけば全体の複雑な現象を理解する上で有効な手がかりが得られるであろう。このような観点から固体材料の損傷に対するイオン種効果を電顕観察により研究しているが, 以下に Al および SiC について得られた成果の主なるものをまとめて述べる。

7.3.2 実験方法

用いたイオン種は H^+ , He^+ , O^+ , N^+ および Ar^+ の各イオンで, 照射量は $10^{14} \sim 10^{17}$, 照射温度は Al の場合は表 1 の照射条件に示すように 175 K \sim 723 K, SiC の場合は室温 \sim 1500 K であった。用いた試料は帯精製した高純度 Al (6 nine) と焼結して作った SiC 多結晶である。電顕観察用試料としては Al の薄板をエタノールと過塩素酸の 4 : 1 の混合液中で電解研磨して作った薄膜 (厚さ 100 \sim 1000 Å) を, また SiC の薄板を機械研磨して数 10 μ の厚さにした後, 更にイオンエッチング法により薄膜 (厚さ 100 \sim 数 1000 Å) にしたものをを用いた。照射後試料は JEM 100C 型電顕により観察した。特にバブル形成が顕著であった He^+ イオン照射した Al 試料については, バブル中の He 原子密度を測定するために, JEM 200 CX 型電顕に装着した ASE A3 型電子分光器を用いて透過電子エネルギー損失スペクトル分析 (Electron Energy Loss Spectroscopy : 以下 EELS と略) を行った。

7.3.3 Al の照射欠陥形成に対するイオン種効果 [5]

照射量が 10^{14} ions/cm² 程度以下の少い範囲で起こる照射欠陥形成の一般的傾向は, 始めに小さい転位ループが現れ, 次いで小さいキャビティが出来て次第にその数を増して行くという経過を辿り, イオン種による顕著な差異は見られなかった。しかし照射量が 10^{16} ions/cm² 以上になると, キャビティの成長挙動がイオン種により著しく異なることが見出された。すなわち O^+ および N^+ イオン照射では 173 K から 723 K 迄の照射温度範囲全体に亘って, キャビティの大きさは 30 Å 位の小さいまゝで, それ以上成長せず, 数丈が増加するが, それに対して H^+ , He^+ , Ar^+ イオン照射の場合には, Fig. 1 に示すように各イオン特有の温度領域でキャビティが著しく成長することが分った。代表的な観察例を Fig. 2, (a), (b), (c) に示す。要するに照射量が 10^{16} ions/cm² 以上では, H^+ イオンの場合は室温以下で, He^+ と Ar^+ イオンの場合はそれぞれ 473 K と 173 K 以上でキャビティが著しく成長するという結果が得られた。キャビティが大きく成長するためには, かなり大きな内部圧力が必要であると予想されるが, これを実験的に EELS により評価した。その結果を次に述べる。

7.3.4 Al 中 He バブルの透過電子エネルギー損失スペクトル分析 (EELS) [4]

Fig. 3 は 753 K で 20 keV He^+ イオンを 2×10^{16} ions/cm² 照射した Al 中に形成されたバブルの電顕写真である。この視野の中央部の直径 1500 Å の円形制限視野内を透過した 200 keV 電子のエネルギー損失スペクトルを Fig. 4 に示す。一方バブルを全く含まない未照射試料からのスペクトルを Fig. 5 に示す。これらの図で 15 eV と 30 eV に現われているピークはそれぞれ Al 中の第 1 および第 2 のプラズモン励起によるものであるが、Fig. 4 のみに現れている約 20 ~ 30 eV に互る幅広いスペクトルは He の 1s - 2p 遷移などの種々の K 殻励起によるものと同定された。He によるスペクトル強度を I_{He} とすると He 原子の数、 N_{He} は次式で与えられる。

$$N_{\text{He}} = I_{\text{He}} / (I_0 \cdot \sigma_{\text{He}}), \quad (\text{cm}^{-2}) \quad (1)$$

ここで I_0 は入射電子線強度、 σ_{He} は He の非弾性散乱断面積である。He によるスペクトルのバックグラウンドを試みに Fig. 4 の点線のように引くと I_{He}/I_0 の値は約 2×10^{-3} となる。 σ_{He} の値は Bethe 式に基いて井口が導出した式¹⁾を用いて計算すると約 3×10^{-19} cm² となる。これらの値を (1) 式に入れると、 $N_{\text{He}} \sim 6 \times 10^{15}$ cm⁻² となる。この値の正確度は主として I_{He} を求める時のバックグラウンドの引き方によるが、大きく見ても因子 2 の範囲で妥当であると考えられる。

次に Fig. 3 に示した電顕像から単位面積当り観察されるバブルの全体積、 V_R を測定し、 N_{He} 個の He 原子が総てこのバブル中に含まれているとするとバブル中の He 原子密度は 1×10^{22} cm⁻³ となる。この値を高密度ガスの状態方程式²⁾に入れて圧力を求め約 500 bar という値を得た。バブルがその表面張力による収縮力に打ち克って大きく成長するためには、内部圧力がかなり高くなければならないことを予想していたが、以上の実験でこれが定量的に実証されたことになる。以上の実験結果に基いて Al 中のバブルの成長挙動を点欠陥の移動と結合の立場から考察した結果を次に述べる。

7.3.5 Al における照射中のバブル成長機構 [5]

照射量が 10^{14} ions/cm² 程度の初期段階では、生成した点欠陥の中、動きの速い格子間原子 (移動エネルギー、 $E_m^I \sim 0.11$ eV³⁾) がかなりの部分表面シンクへ逃げると同時に互に集合して転位ループを作り、次いで動きの遅い空孔 (移動エネルギー、 $E_m^V \sim 0.67$ eV^{4), 5)}) が高密度に蓄積され互に集合して多数の小さいボイドを作る。重い Ar^+ イオンの場合にはカスケードクラスターの所にボイドの核形成が起こる可能性もある。何れにしてもその過程で注入されたガス原子がボイド中に入ってこれを安定化する役割を果しているであろう。以上がイオン種によらず照射の初期段階で起こる点欠陥の集合過程と考えられる。

照射量が 10^{16} ions/cm² 以上の場合には異なるイオン種間で観察されたバブルの成長挙動の著しい相違は、注入されたガス原子の挙動の差によるものとして次のように解釈した。7.3.4 節でバブルの内圧が極めて高いことを実証したが、このバブルが大きく成長するためには、内圧を高く保ったまま成長することが必要である。そのためには空孔とガス原子が殆んど同じ割合でバブル内に供給されなければならない。ガス原子は単独では高圧ガスバブル内には入り難いと考えられるので、空孔と一緒に複合体を作って、それが動いてバブルに供給されると考えた。すなわちバブルの成長のために必要な条件は、ガス原子と空孔の複合体、 $[\text{G}^S, \text{V}]$ が形成され、その

移動度が高いことであるというモデルを提案した。このモデルで主役を演ずる $[G^S, V]$ は次のような過程で形成されると考えられる。注入されたガス原子は先ず格子間を Al 自身の格子間原子と同程度の移動度で動き回っている間に空孔に掴まって置換型ガス原子となり、それが空孔と結合して $[G^S, V]$ となる。或は格子間ガス原子が複空孔と結合して $[G^S, V]$ となる場合もあるであろう。

Fig. 1 に纏めてあるキャビティについての観察結果は、 $[G^S, V]$ モデルを用いて次のように解釈できる。Ar⁺ イオン照射の場合、Ar 原子と空孔の複合体、 $[Ar^S, V]$ は全照射温度領域に亘って安定に形成され、十分速く動いてバブルに供給され、それを大きく成長させる。He の場合、 $[He^S, V]$ は安定に存在するが、移動エネルギーがやや高く、473 K 以下では動き難くなってバブルの成長は止まるが、この温度以上では動き易くなってバブル成長に寄与する。H の場合は、H 原子と空孔の結合エネルギーが前二者の場合よりも小さくて、 $[H^S, V]$ は 300 K 以下では安定に存在し、動いてバブル成長に寄与するが、この温度以上では分解して、複合体を作らず従ってバブル成長は困難となる。O および N の場合はそれぞれの原子と母体の Al 原子との結合性が強くそれに掴まって動き難くなるのでバブルを大きく成長させることは困難となる。

以上の如く、Al におけるバブルの成長挙動に対するイオン種効果についての実験結果は、 $[G^S, V]$ モデルで定性的に説明出来たが、より定量的な検証は今後の課題である。

7.3.6 SiC 結晶の He⁺ イオン照射による構造変化〔8〕

一般にセラミックス材料の照射損傷の研究は、機械的或は電氣的性質の変化に関するものが数多くあるが、照射による微細構造の変化については極めて少い。核融合炉材料として使用する場合 (n, α) 反応によって材料中に生成する He の効果は特に重要である。この問題をシミュレートするために He⁺ イオンで SiC を照射して、その構造変化を電顕および電子回折によって調べた結果を次に述べる。(照射条件は 7.3.2 節で記した通り)

(a) SiC 結晶の非晶質化

SiC の結晶を特定の結晶軸から外れた任意の方向から 30 keV He⁺ イオンで室温照射した場合、照射量が 6×10^{15} ions/cm² 以上で非晶質化が起きることを見出した。Fig. 6(a), (b), (c), (d) に照射と共に非晶質化が進行する様子を電顕像および電子回折像で示す。照射量、 6×10^{16} ions/cm² は損傷密度にすると約 1 dpa となることが、TRIM-code⁶⁾ による計算結果から判るが、これが非晶質化に必要な損傷密度の臨界値と考えられる。金属材料を室温で照射した場合、この程度の損傷密度では非晶化は起きない。SiC でこれが起きるのは、照射による点欠陥の移動が金属の場合と比べて遙かに困難であることを示唆するものである。

イオンビームの方向を SiC の特定の結晶軸、例えば $[001]$ 、または $[210]$ と一致させて照射した場合には、照射量が上に述べた値、 6×10^{15} ions/cm² 以上になっても非晶質化は起きない。これはイオンチャネリングの効果によるものと考えられる。即ちチャネリングによりイオンの飛程が 10 倍ないし 10 数倍になるので、任意方向入射の場合と比べ、同じ照射量に対する損傷密度は 1 桁以上小さくなり、非晶質化に必要な臨界値に達しないからであると考えられる。

上記の非晶質領域は、照射後 1000 K 以上の焼鈍で、再結晶することが判った。

(b) SiC 結晶の高温照射効果

SiC 結晶を 1000 K で 30 keV He⁺ イオンで、 1×10^{17} ions/cm² 照射すると、数 100 Å の微小結晶粒が多数、母体の結晶中に観察された。

更に照射温度を上げて行くと、微結晶粒は形成されなくなり、代わりにバブルが多数成長してくることが分った。Fig. 7 は 1300 K で 30 keV He⁺ ions を 1×10^{17} ions/cm² 照射した結果、生じたバブルを示す。これらのバブルは注入された He 原子が集合して出来た He バブルと考えられる。このバブルの内圧を推定した結果を次に述べる。

TRIM-code による計算結果に基づいて、SiC 試料の厚さ 1000 Å の場合の注入 He 原子の試料中での残存率を 10% と仮定し、この He が全て観察された He バブル内に入っているとすると、バブル内での He 原子密度は 2.4×10^{21} cm⁻³ となる。この値を高圧ガスの状態方程式²⁾に入れて、内圧を求めると約 100 bar となる。このように高温照射で生成した SiC 中の He バブルの内圧は、Al の場合と同様極めて高いと推定される。高温、重照射の場合は、バブルが更に成長して、結晶の体積が大きく膨脹すると共に表面ではブリストーが起ることが十分考えられる。

(K. Izui)

References

- 1) Inokuti, M., Kim, Y.K., Platzman, R.L.: Phys. Rev., 164, 55 (1967).
- 2) Brearley, I.R., MacInnes, D.A.: J. Nucl. Mater., 95, 239 (1980).
- 3) Shimomura, Y., Kuwabara, S.: J. Phys. Soc. Jpn., 42, 1221 (1977).
- 4) Hashimoto, E., Kabemoto, S., Kino, T.: J. Phys. Soc. Jpn., 43, 1247 (1977).
- 5) Ono, K., Kino, T.: J. Phys. Soc. Jpn., 44, 875 (1978).
- 6) Biersack, J.P., Haggmark, L.G.: Nucl. Inst. Meth., 174, 257 (1980).

Publication List

- [1] Furuno, S., Otsu, H., Izui, K.: "Electron microscopic observations of tracks of 130 MeV Cl⁹⁺ ions in solids", J. Electron Microsc., 30, 327 (1981).
- [2] Nishida, T., Izui, K.: "Identification of small point defect clusters by high resolution electron microscopy", Point Defects and Defect Interactions in Metals (Univ. Tokyo Press, 1982) p.705.
- [3] Hojou, K.: "Density measurements of boron films made by ion-beam sputtering", (in Japanese), J. Vac. Soc. Japan, 27, 21 (1984).
- [4] Izui, K., Hojou, K., Furuno, S., Ono, K., Kino, T.: "Electron energy loss spectroscopy of helium injected in aluminum at high temperature", J. Electron Microsc., 33, 381 (1984).

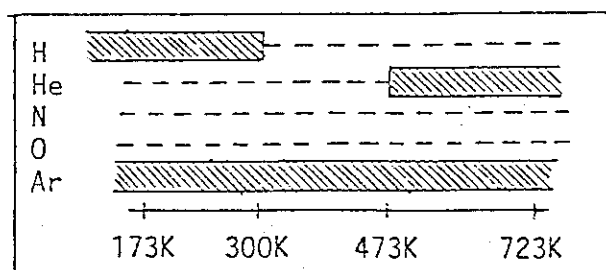
- [5] Furuno, S., Izui, K., Komaki, Y.: "High energy ion tracks in solids", JAERI-M 85-125, p.165-173 (1985).
- [6] Furuno, S., Izui, K., Ono, K., Kino, T.: "Effects of ion species on the evolution of structural damage in ion irradiated high-purity aluminium", J. Nucl. Mater., 133 & 134, 400 (1985).
- [7] Ono, K., Inoue, M., Kino, T., Furuno, S., Izui, K.: "Formation, coalescence and stability of helium bubbles in high purity aluminium and some dilute alloys", J. Nucl. Mater., 133 & 134, 477 (1985).
- [8] Hojou, K., Izui, K.: "Structural changes induced by helium ion irradiation in silicon carbide crystals", J. Nucl. Mater., 133 & 134, 709 (1985).

Table 1. Irradiation conditions for aluminium.

Irradiation condition

Ion	Energy (keV)	Fluence (cm ⁻²)	Temperature (K)
H	10-17	1.2×10^{14} - 6×10^{16}	173-723
He	20	1×10^{14} - 6×10^{16}	"
N	20	6.3×10^{14} - 6×10^{16}	"
O	20	6.3×10^{14} - 6×10^{16}	"
Ar	30-40	6×10^{14} - 6×10^{16}	"

SUMMARY OF RESULTS




 : Temperature regions in which cavities grow.
 ---- : Temperature regions in which no cavity grows.

Fig. 1 Summary of observed results.

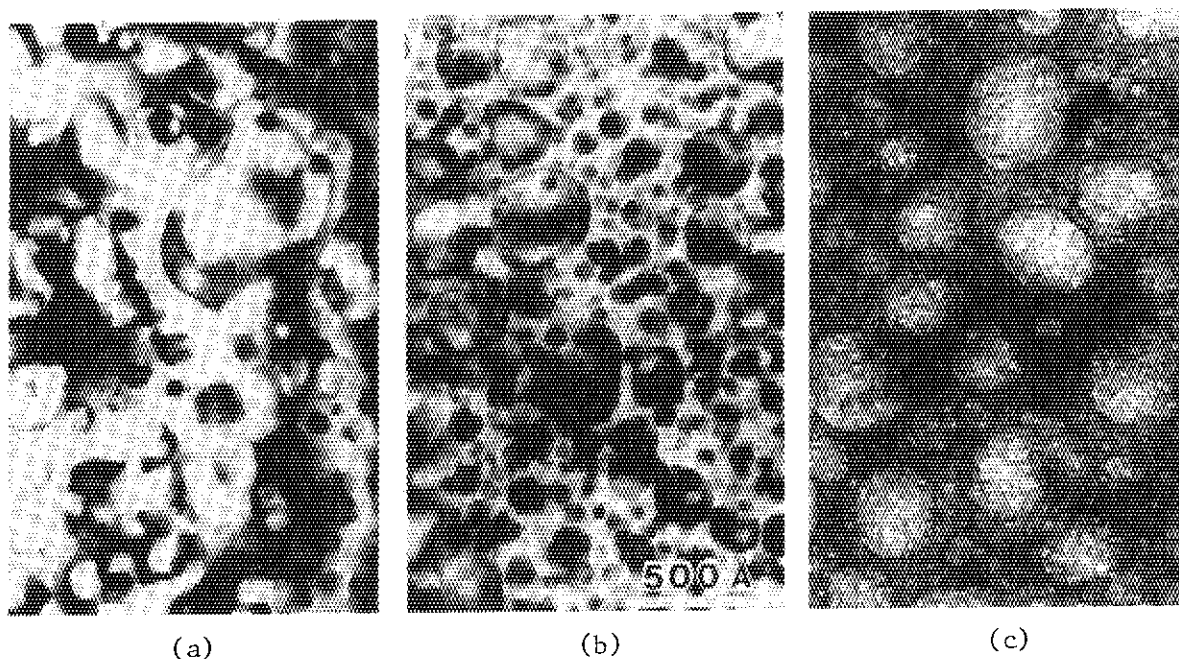


Fig. 2 Cavities produced in aluminium irradiated with various ions.
 (a) 20keV helium ion: 1.8×10^{16} ions/cm², at 574K
 (b) 30keV argon ion: 6×10^{16} ions/cm², at 574K
 (c) 15keV hydrogen ion: 6×10^{16} ions/cm² at 175K

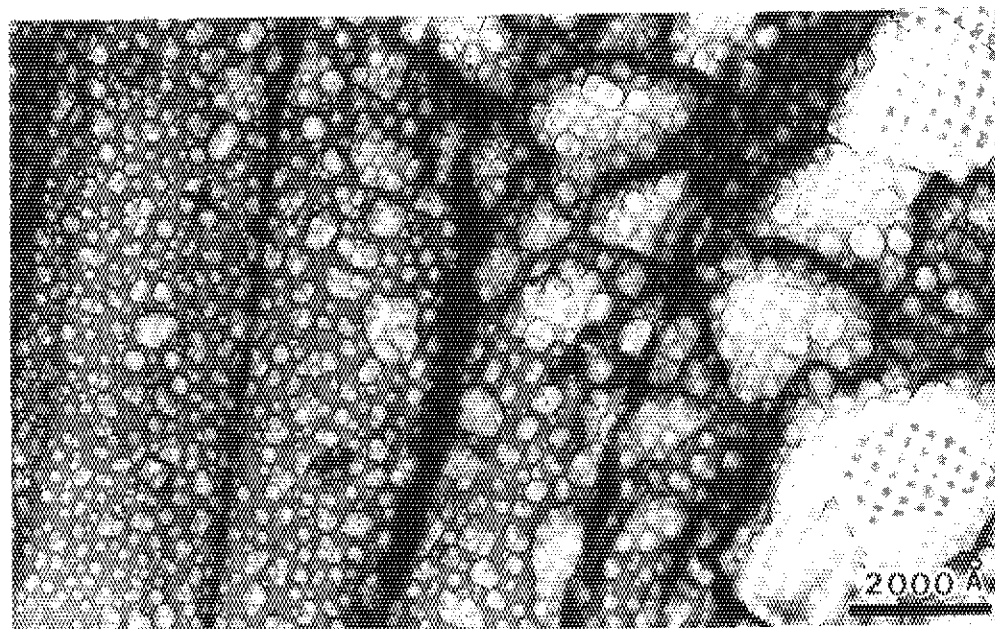


Fig. 3 Cavities produced in aluminium irradiated with 20keV He⁺ ions to the fluence of 2×10^{16} ions/cm² at 713K.

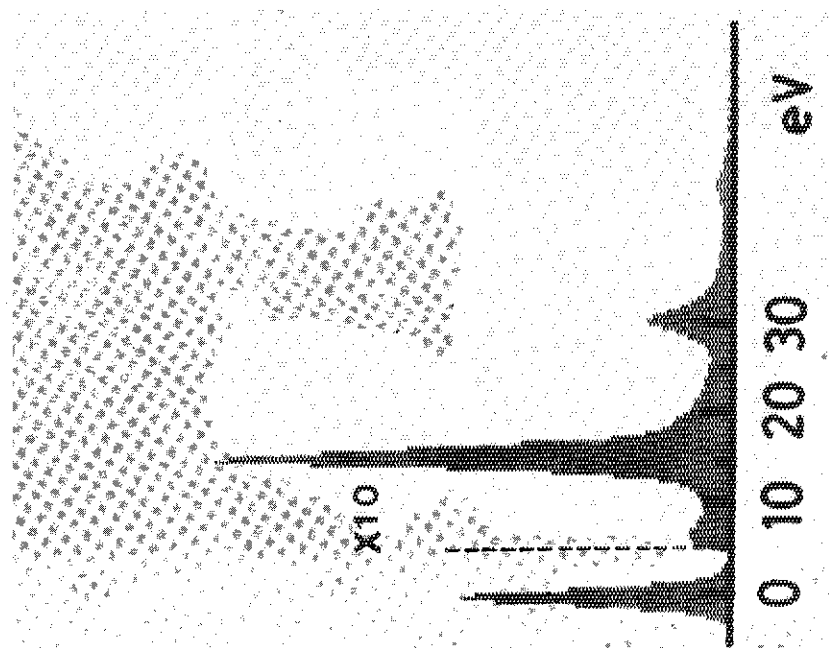


Fig. 5 EELS from area containing no cavities.

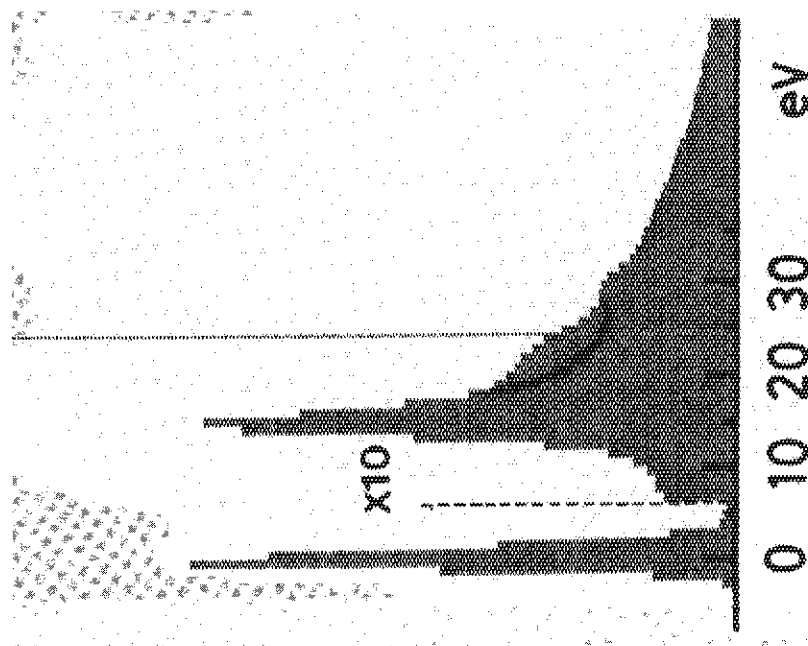


Fig. 4 EELS from the area containing some irradiation-induced cavities.

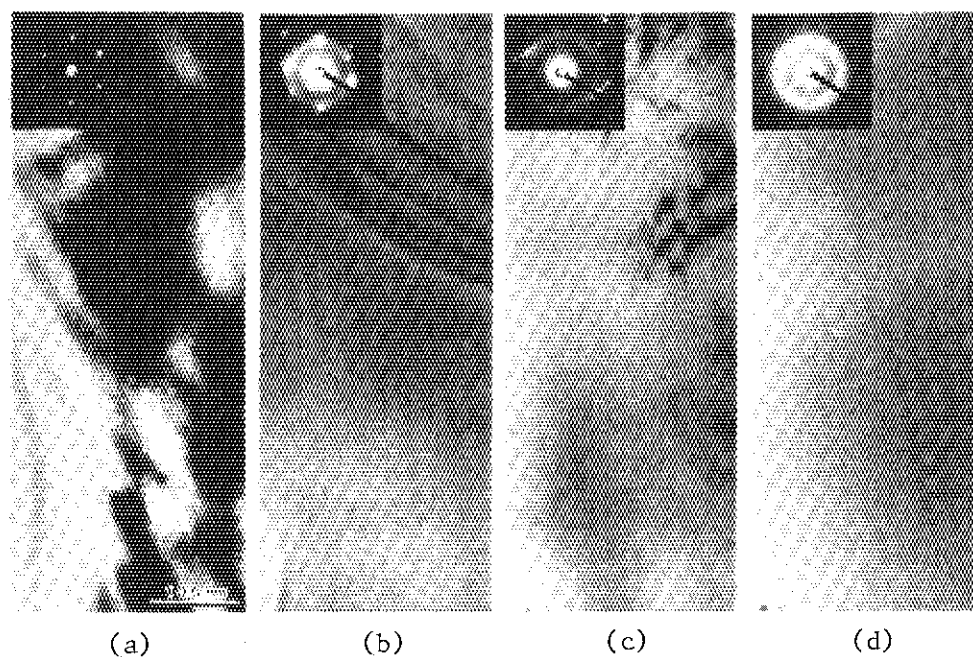


Fig. 6 Amorphization in SiC crystal due to irradiation with 30keV He^+ ions at room temperature.

(a) $3.8 \times 10^{15} \text{ ions/cm}^2$	(c) $1.3 \times 10^{16} \text{ ions/cm}^2$
(b) $6.4 \times 10^{15} \text{ ions/cm}^2$	(d) $2.9 \times 10^{16} \text{ ions/cm}^2$

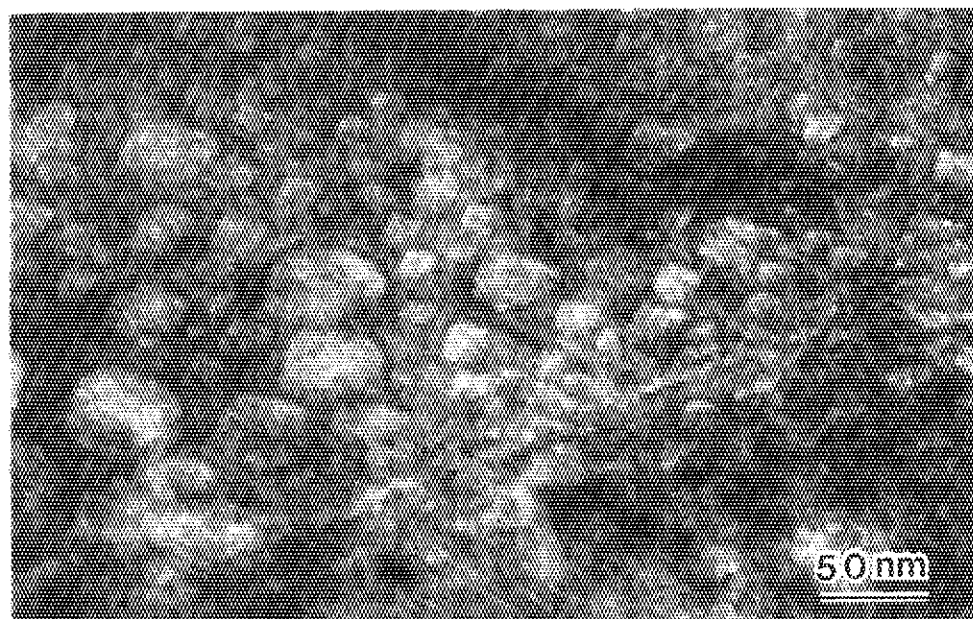


Fig. 7 He bubbles in SiC crystal produced by irradiation with 30keV He^+ ions: $1 \times 10^{17} \text{ ions/cm}^2$ at 1300K.

8. SERVICE WITH Co-60 IRRADIATION FACILITY AND ANALYTICAL EQUIPMENTS

K. Izui, H. Nagayama, T. Okubo,
H. Ohtsu, T. Soga and K. Furukawa

8. Co-60 照射室の運営並びに電顕等分析業務

出井 数彦・長山 尚・大久保 隆・大津 仁
曾我 猛・古川 勝敏

8.1 Co-60 照射室の運営

東海研 Co-60 照射室は、昭和 33 年 8 月完工以来、今日まで 27 年間に亘り、所内外の多様なガンマ線照射要求に応え、幅広い分野の照射サービスを実施して来た。当照射室の管理運営は最初、放射線応用部、放射線利用研究室、次いで所内組織改定に伴い化学部、炉化学研究室へ移り、現在、固体化学研究室が行っている。

この間、建家、設備の改造修理が数多く行われ、Co-60 線源も数回補充増強された。照射利用実績は現在までに件数にして、一般照射は 3 万 3 千件、実験照射は 1 千件を超えた。これら利用動向の推移および建屋、設備、線源等の変遷については、昨年 Co-60 25 周年記念事業の一つとして纏めた「東海研究所 Co-60 照射室 25 年史」に詳しく述べてあるのでそれを参照されたい〔1〕。今回は最近 2 年間（58、59 年度）に行った業務の概要を述べる。

8.1.1 施設の維持管理と更新

ケープは三つのセルからなり、中央の C セルを線源貯蔵用、左右の A および B セルを照射、実験用に使用しているが、A セル用放射線遮蔽窓（昭和 33 年設置）が放射線損傷により曇りが著しくなり透視が困難となった。それで 58 年度に予算措置がなされたので、更新の詳細仕様を検討して発注し、59 年 11 月に納入据付を完了した。

ケープ内ホイストは絶縁材料の交換等、大がかりなオーバーホールの時期になったので、60 年 2 月に絶縁材料やオイル類を耐放射線性用にし、小型ではあるが従来と同じ能力を持った電気チェーンブロックに交換した。

ケープ内面の塗装面が放射線劣化のため剥離を生じたので 59 年 9 月、技術部の協力を得て再塗装をした。

その他、ケープのバツステップドア、リフトドア、モニター、安全系統回路等の定期的点検を実施し、また毎年 4 月と 10 月に 14 kCi と 2.9 kCi（何れも公称値）の線源の線量測定を行い、定期的線量率改定をして利用関係者に通知した。

58年度はCo-60照射室25周年に当るので、記念行事として、10月7日に記念講演会を開催し、関係者多数の参会を得た。また25年間に亘る施設の変遷、利用動向の推移などについて、資料を整理して纏めた〔1〕。

8.1.2 照射利用実績

58年度と59年度の月別利用実績を表1および表2にそれぞれ示す。また利用者の分布を扇形グラフにしたものを図1および図2に示す。こゝで“照射”と“実験”の区別は次の通りである。前者は利用者から届けられた試料を利用者の指定する条件で照射して返却するものであり、後者は利用者が照射室に来室し、セル内に実験装置を設置し、照射しながら、各種の測定、試験を行うものである。“照射”の場合の“件数”は試料の数を意味し、“実験”の場合の“件数”は一連の実験を1件としており、1件の実験は1日で終るものから数ヶ月以上に及ぶものまでであるので、参考迄に実験の全日数を示してある。

最近の照射利用の動向を知る上での参考として、表3と表4にそれぞれ58年度と59年度の照射実験の利用者の所属と実験の目的を一覧表にして示す。

(K. Izui)

Publication List

- [1] Nagayama, H., Okubo, T., Izui, K., Tsujimura, S.: "Review of twenty-five years' activities of Co-60 irradiation facility in Tokai Research Establishment", (in Japanese), JAERI-M 84-175 (1984).

8.2 電顕等分析業務

最初にこの業務の由来を簡単に述べる。原研発足当時は、大型電子顕微鏡やX線回折装置、質量分析計、分光計などの高価な装置は所全体でも設置台数が極めて少く、その効率的利用のために1ヶ所で集中的に管理して共同利用を行い、当時の分析化学研究室（現在、分析センター）がその任に当たっていた。その活動状況については最近、纏められた“分析センターの活動”(JAERI-memo 60-006)に詳しく述べられているので、こゝではふれないが、その中で“電顕、X線グループ”の3名が、装置と共に47年度、固体化学研究室に移籍したのが、表記の業務の由来である。

電顕、X線装置を研究室自体の研究目的に使用するかたわら、希望者の利用に応じているが、最近の状況は、20年前頃とは隔世の感がある。日本の高度経済成長のおかげで、所内の研究関係の各部で必要とする台数はほぼ保有しているので、化学部への依頼は余りない。従って、主として化学部内の研究室の利用に供しているのが現状である。

表5に58年度および59年度の研究室別の共同利用実績を示す。

(K. Izui)

表1 58年度Co-60月別利用実績

()内は日数

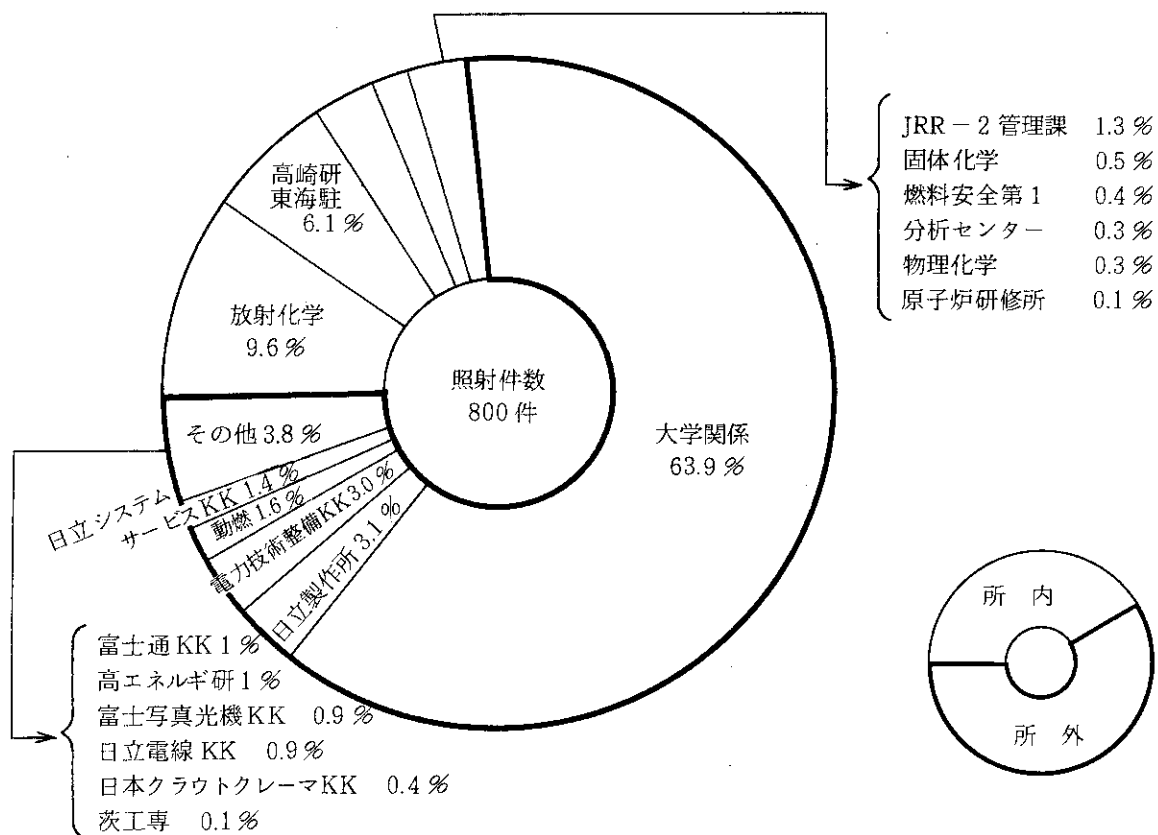
年月	照 射 個 数		実 験 件 数	
	所 内	所 外	所 内	所 外
58. 4	45	28	1 (1)	2 (8)
5	12	36	2 (6)	2 (9)
6	15	29	0	1 (2)
7	18	9	0	1 (1)
8	5	34	0	2 (7)
9	3	46	0	1 (3)
10	13	24	0	5 (27)
11	23	80	1 (5)	1 (3)
12	3	54	0	3 (13)
59. 1	23	58	1 (15)	1 (2)
2	7	135	0	2 (5)
3	19	81	0	5 (7)
計	186	614	5 (27)	26 (87)

表2 59年度Co-60月別利用実績

()内は日数

月日	照 射 個 数		実 験 件 数	
	所 内	所 外	所 内	所 外
59. 4	28	20	0	5 (17)
5	10	0	1 (11)	5 (14)
6	19	36	2 (11)	3 (22)
7	45	20	1 (5)	2 (9)
8	13	39	4 (22)	3 (7)
9	25	5	1 (11)	1 (2)
10	10	70	3 (25)	2 (2)
11	21	64	2 (9)	0
12	7	50	1 (8)	3 (11)
60. 1	7	110	0	2 (9)
2	17	26	0	5 (16)
3	22	125	0	3 (12)
計	224	565	15 (102)	34 (121)

(1) 照射件数



(2) 実験日数

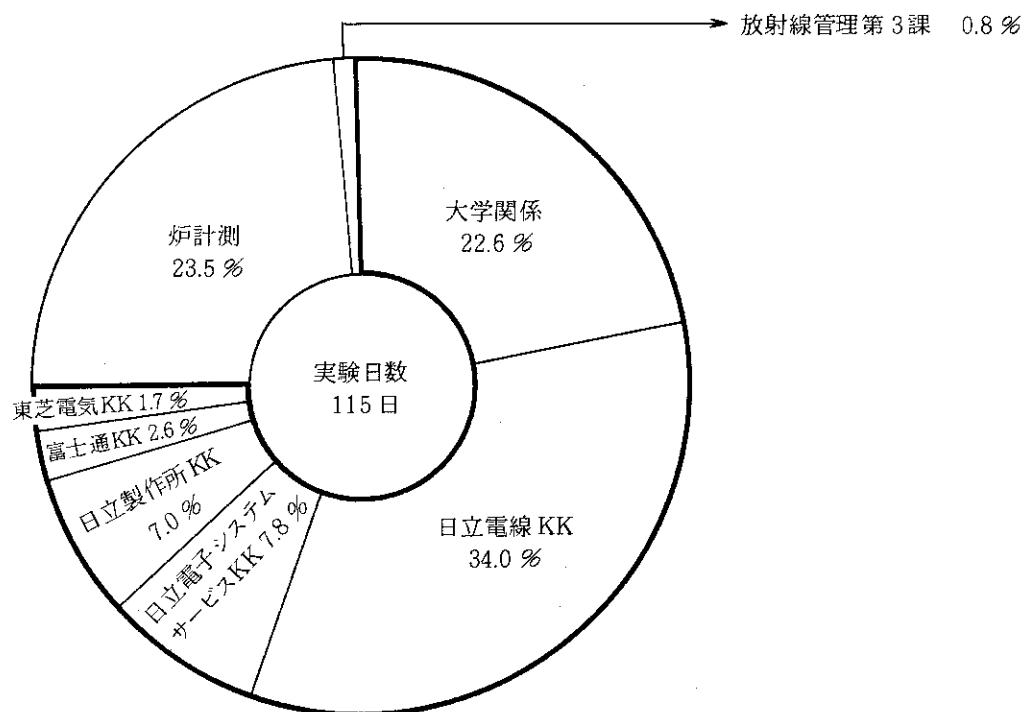
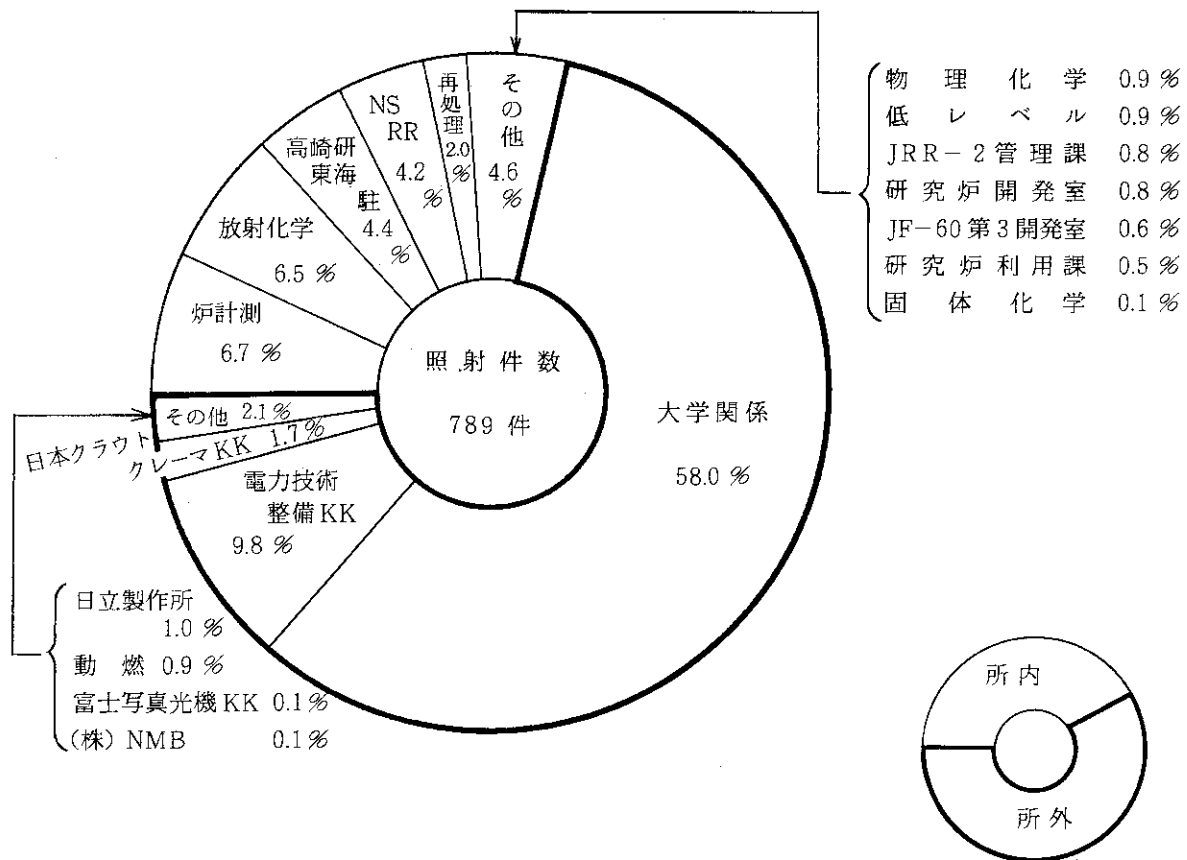


図 1 昭和 58 年度 Co-60 照射室利用状況

(1) 照射件数



(2) 実験日数

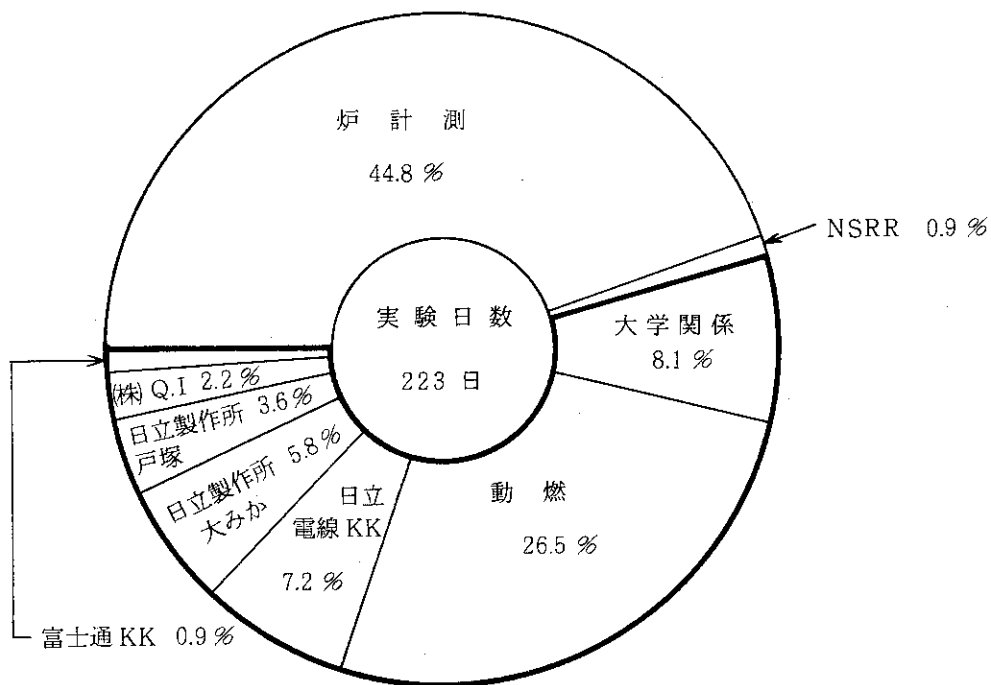


図2 昭和59年度 Co-60 照射室利用状況

表3 照射及び実験の利用目的(58年度)

照射実験	所内外	所 属	目 的 (内 容)
照 射	所 内	放射化学 高崎研(東海駐) 再処理 炉計測 JRR-2管理課 固体化学 燃料安全第1 分析センター 物理化学 原子炉研修所	水素吸着におよぼす照射効果 化学線量計の較正, 炭酸ガスの放射線分解 TBP-nDD-HNO ₃ -H ₂ O系におけるトリ チウム分配比の測定 ガラスの照射効果(SiO ₂ -B ₂ O ₃) 耐放射線性の確認(エポキシ樹脂) 固体の放射線損傷の研究 ジルカロイのCsIによるSCC実験 石英吸収セルに対する γ 線の影響 γ 線照射高分子のESR測定 磁気センサーの γ 線照射試験
	所 外	日立製作所 電力技術整備KK 動燃 日立システムサービスKK 富士通KK 高エネルギー物理研 富士写真光機KK 日立電線KK 日本クラウトクレマーKK 茨城工業高等専門学校	照射試験(ケーブル, モータ, バルブ) 年代測定 テフロン系パッキン類 γ 線照射 電気部品の耐放射線調査(トランジスターコン デンサー) 半導体集積回路の放射線に対する耐性の調査 放射線損傷による出力, ゲイン等の変化をし らべる TV用固定焦点レンズの耐放射線テスト 光ファイバー γ 線照射 電子部品の照射試験(リチウム電池) 卒業研究指導(砂: SiO ₂)
実 験	所 内	炉計測 放射線管理第3課	BF ₃ 比例計数管の γ 線感度測定 電離箱及びラドコン線量計の較正
	所 外	日立電線KK 日立電子システムサービスKK 日立製作所 富士通KK 東京芝浦電気KK	光ファイバー γ 線照射実験 CCTVカメラの γ 線に対する耐性調査 衛星搭載装置の耐放射線試験(LSI) 半導体集積回路の放射線に対する耐性調査 VLSIの耐放射線特性評価

表4 照射及び実験の利用目的 (59年度)

照射実験	所内外	所 属	目 的 (内 容)	
照 射	所 内	原子炉計測研	照射効果 (超音波センサー, 圧電ゴム, カメラレンズ, トランジスター)	
		放射化学研	水素吸着に及ぼす照射効果, Fe ₃ O ₄ 粒子の酸化反応	
		高崎研, 東海駐	放射線エネルギーの化学エネルギーへの変換, 線量測定	
		NSRR 管理室	歪ゲージ耐放射線試験	
		再処理研	溶媒抽出の測定, フィルム線量計の校正	
		物理化学研	高分子フィルムの照射損傷	
		低レベル廃棄物処理処分研	プラスチック固化体の耐放射線性	
		JRR-2 管理課	耐放射線性の確認 (ポリスチレン, コネクター)	
		研究炉開発室	ニッケル蒸着ガラス板の照射効果試験	
		JT-60 第3 開発室	JT-60 計測用 IC の耐 γ 線試験	
		研究炉利用課	TLD 素子の校正	
	固体化学研	容器の前処理		
	所 外	電力技術整備 KK	ESR 年代測定	
		日本クラウトクレマー KK	電子部品, Oリング等の照射効果	
		KK 日立製作所	耐放射線性の試験	
		動力炉核燃料事業団	TLD の校正	
		富士写真光機 KK	TV 用ズームレンズの耐放射線試験	
		(株) NMB	チューブの照射劣化試験	
		実 験	所 内	原子炉計測研
”				TVカメラ放射線照射効果, 光近接センサー照射効果
NSRR 管理室	γ チェンバーの検出感度校正			
所 外	動力炉核燃料事業団		光ファイバー γ 線照射試験	
	日立電線 KK		光ファイバー照射試験	
	KK 日立製作所		電子部品の耐放射線性を確認する	
	”	半導体の耐放射線試験		
	(株) Q.I	TV カメラの耐放射線試験		
富士通 KK	半導体集積回路の放射線に対する耐性の調査			

表 5 電顕共同利用実績

58 年度

研 究 室 名	件数	試料数	測定数	備考
材 料 物 性	2	5	68	電顕
高 崎 研(東海)	1	5	32	〃
合 計	3	10	100	

59 年度

研 究 室 名	件数	試料数	測定数	備考
放 射 化 学	2	21	74	電顕
高 崎 研(東海)	1	5	38	〃
合 計	3	26	112	

9. THERMODYNAMIC STUDY OF NUCLEAR FUEL

T.Fujino, J.Tateno, A.Nakamura,
K.Ohuchi, T.Yamashita, Y.Hinatsu

9.1 The Nature of Small Polarons and the Oxygen Potential in Nonstoichiometric Uranium Oxides

9.1.1 Introduction

Physical and thermodynamic characteristics of nonstoichiometric compounds are often determined by the defects and defect structure which are introduced by nonstoichiometry. Therefore it is important to elucidate the nature of defect and the interaction between them in nonstoichiometric compounds. In nonstoichiometric uranium oxides, UO_{2+x} , excess oxygen atoms corresponding to the composition x are distributed in the interstitial sites of the fluorite structure of UO_2 crystal lattice. The interstitial oxygen atoms are ionized to produce interstitial oxygen ions and holes as,



It has been reported that the hole in uranium oxides is localized and surrounded by lattice distortion to form "small polaron". In the following the nature of small polarons in uranium oxides is analysed based on the experimental results of dielectric properties of these compounds at microwave frequencies. In connection with this, the defect structures are also discussed thermodynamically.

9.1.2 Dielectric properties of UO_2 , UO_{2+x} and U_4O_9 at 9.1GHz

Dielectric constants of uranium oxides were measured at 9.1 GHz using the standing wave method in the temperature range 233-300K(4)(5). The results are shown in Fig.1, where ϵ' and ϵ'' at 300K are plotted against the excess oxygen concentration x . Both of them increase with increasing x . By considering different kinds of polarization, it may be concluded that the origin of these increments are attributed to the movement of charge carriers (holes in the present case) which increase with increasing x . The conductivity by the charge carriers is given by $\sigma = \epsilon' \epsilon_0 \omega$, where ω is the measurement frequency. The values of σ at 300K are shown in Fig.2. As the mobility μ is obtained by $\mu = \sigma / Ne$, we have $\mu = 1.2 \times 10^{-5} \text{cm}^2/\text{Vs}$ for $x=0.5$ at 300K. This value is smaller than the upper limit for the mobility in the small-polaron hopping region ($0.08 \text{cm}^2/\text{Vs}$ calculated by small polaron theory), so one can conclude that the conduction mechanism in uranium oxides can be described by hopping of small polarons.

At high frequency the dc conductivity of small polarons is given by $\sigma = (A/\sqrt{T}) \exp(-E_a/kT)$, where A is a constant, E_a is the activation energy of hopping.^{1,2)} This equation indicates that the graph of $\ln(\sigma\sqrt{T})$ against $1/T$ must be linear. From Fig.3 where Arrhenius plot of $\sigma\sqrt{T}$ are shown for several concentrations, one can conclude that the above equation holds good for the present case. The activation energy at large x is different from that at small x . The pre-exponent term A/\sqrt{T} is given by¹⁾,

$$A/\sqrt{T} = (Ne^2 a^2 \sqrt{\pi}/4h) \eta (\omega_0/\omega), \quad \eta = J^2 / \hbar \omega_0 \sqrt{E_a kT}, \quad (2)$$

where a is the distance of hopping, ω_0 is the characteristic frequency of optical phonon and J is the electron transfer integral. By the calculation using the characteristic values for uranium

oxides, one can obtain the parameters which describe the hopping conduction in uranium oxides. The results are listed in Table I for several concentrations.

Hopping of a small polaron can be classified into two types as adiabatic and nonadiabatic transition. In Fig.4 hopping process of a small polaron is shown. An electron or a hole in the potential well (small polaron) attains the same energy level as that of neighboring site by thermal activation process. This state is called coincidence event (fig.4(b)). If the electronic motion is quicker than the atomic motion (adiabatic process), then all electrons in the state the coincidence event are transferred to the neighboring site (c). However, if the electronic motion is so slow and cannot follow the atomic motion (nonadiabatic process), only a part of the electrons is transferred. This adiabaticity can be examined by parameter η ($1 < \eta$ for adiabatic case and $\eta < 1$ for nonadiabatic case). The result for adiabaticity are also shown in Table I.

Finally we shall refer the relaxation mechanism. When there exists a Debye-type relaxation mechanism, the relation between ϵ' and ϵ'' is described by

$$\epsilon'' = \omega\tau(\epsilon' - \epsilon_{\infty}), \quad (3)$$

where τ is the relaxation time and ϵ_{∞} is the dielectric constant at frequency for which $1 \ll \omega\tau$. Calculated values for $\omega\tau$ are shown in Fig.5.

From the experimental results described above, one can recognize that values for some parameters (such as A, E_a, J and τ) in high concentration region are clearly different from those in low concentration region. A boundary exists at about $x=0.15$. In high concentration region ($0.15 < x < 0.25$), the activation

energy for hopping is large and the Debye-type relaxation mechanism appears with $\tau \sim 2.7 \times 10^{-11}$ s. These facts suggest that different types of small polaron exist and that small polarons at high concentrations are bound to some centers. Bosman and van Daal³⁾ pointed out that there exist two types charge carriers in NiO and that they are free carriers (in large-polaron band) and carriers bound to centers (small polaron). In the present case both types of carriers fulfill the condition of small polarons as described above. So we infer that there are free carriers at low concentrations and carriers bound to centers (interstitial oxygen ions) at high concentrations and that both of them are in the state of a small polaron in UO_{2+x} .

This inference can be confirmed by the thermodynamic consideration. Small polarons bound to interstitial oxygen ions indicate that there must be considerable interactions between them. Here we suppose the Debye-Hückel type interactions. The oxygen potential of UO_{2+x} is given by,

$$\mu_{\text{O}} = \mu_{\text{O}}^{\circ} + vRT \ln \gamma x, \quad (4)$$

where v is the number of ions ($v=3$ in the present case), μ_{O}° is the oxygen potential in the standard state and γ is the activity coefficient. Then the excess potential (deviation from the reference potential $\mu_{\text{O}}^{\text{r}} = \mu_{\text{O}} + vRT \ln x$), $\mu_{\text{O}}^{\text{E}}$ is defined as,

$$\mu_{\text{O}}^{\text{E}} = vRT \ln \gamma. \quad (5)$$

According to the Debye-Hückel theory this excess potential can be described by the Debye-Hückel term as,

$$\begin{aligned} \mu_{\text{O}}^{\text{DH}} &= (Ne^2 / 2\epsilon'v) (\sum v_i Z_i) (\kappa / (1 + \kappa a)), \\ \kappa^2 &= (4\pi e^2 / \epsilon'kT) \sum N_i Z_i^2. \end{aligned} \quad (6)$$

From the numerical calculation for UO_{2+x} we have $\mu_{\text{O}}^{\text{DH}} = -3.57 \times 10^3 x$

$\sqrt{x/T}(1+\kappa a)^{-1}$ kcal/mol and $\kappa=1.18 \times 10^{10} \sqrt{x/T} \text{ cm}^{-1}$, where a is the distance of closest approaches of ions. In Fig.6 $\mu_{\text{O}}^{\text{E}}$ and $\mu_{\text{O}}^{\text{DH}}$ at 1100K are shown where we set $a=1.63\text{\AA}$. The curves agree well. However, concentration-dependent disagreements exist between them: disagreement at low concentrations (designated by A in Fig.6) and that at high concentrations (by B). The latter occurs in the usual application of the Debye-Hückel theory, because the approximation in the solution of the Poisson's equation is invalid in such concentrations. The disagreement at low concentrations means that excess potential is smaller than the evaluated value, that is, the interactions between ions and small polarons are weak in this region. This result agrees with the previous conclusion that charge carriers are rather free at low concentrations.

9.1.3 Interactions between defects in nonstoichiometric uranium oxides

Hitherto, complicated clusters of defects have been introduced in order to explain physical and thermodynamic properties of nonstoichiometric compounds⁴⁾. However, as we have stated above, these properties can be understood by taking into account interactions between defects which are used in usual liquid theory. In the case of multi-component nonstoichiometric systems (2)(3), the treatment of liquid solution such as Kirkwood-Buff theory are well applicable in order to elucidate their thermodynamic behaviors. As we have seen in the application of the Debye-Hückel theory, some modification must be done in the treatment. Further investigation is necessary as to this point.

(J. Tateno)

Reference

- 1) Böttger, H., and Bryksin, V.V.: Phys. Status Solidi B, **78**, 9 and 415(1976).
- 2) Emin, D.: Physics Today, June 1982, 34(1982).
- 3) Bosman, A.J., and van Daal, J.: Adv. Phys., **19**, 1(1981).
- 4) Sørensen, O.T. (ed): "Nonstoichiometric Oxides", (1981), Academic Press.

Publication List

- [1] Tateno, J.: "Quasi-chemical Treatment of Intermediate Phase Appearing in Nonstoichiometric Compounds", J. Solid State Chem., **36**, 305(1981).
- [2] Tateno, J.: "Application of Kirkwood-Buff Theory to the Study of Oxygen Potential of Nonstoichiometric Ternary Uranium Oxides", J. Nucl. Mater., **114**, 242(1983).
- [3] Tateno, J.: "Equi-chemical-potential Curves in Ternary Uranium Oxides $M_yU_{1-y}O_{2+x}$ ", J. Nucl. Mater., **119**, 37(1983).
- [4] Tateno, J.: "The Dielectric Properties at 9.1GHz and Nature of Small Polarons in Nonstoichiometric Uranium Oxides", J. Chem. Phys., **81**, 6130(1984).
- [5] Tateno, J.: "Dielectric Constants of Uranium Oxides Measured at Microwave Region", (in Japanese), J. Atomic Energy Soc. Japan, **27**, 15(1985).
- [6] Tateno, J.: "Temperature-dependence of Hopping Conduction", (in Japanese), Kagaku to Kogyo, **38**, 717(1985).

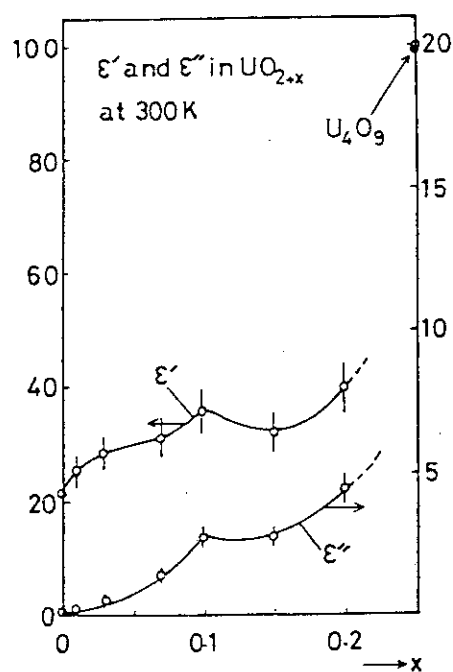


Fig. 1 Dielectric constants in UO_{2+x} as a function of x .

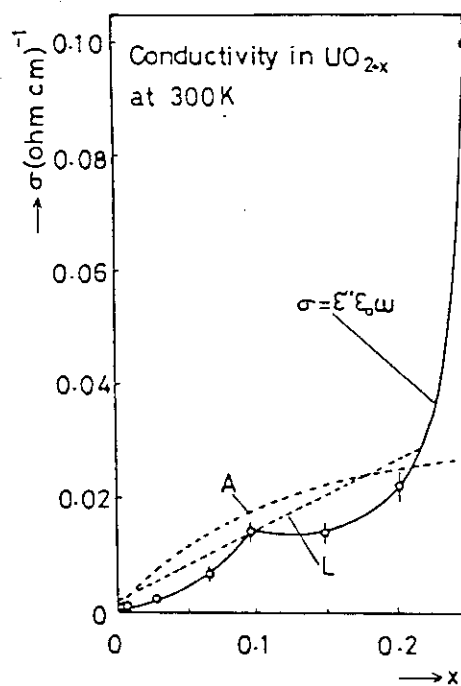


Fig. 2 Conductivity of UO_{2+x} at 9.1GHz (A: by Aronson, L: by Lee).

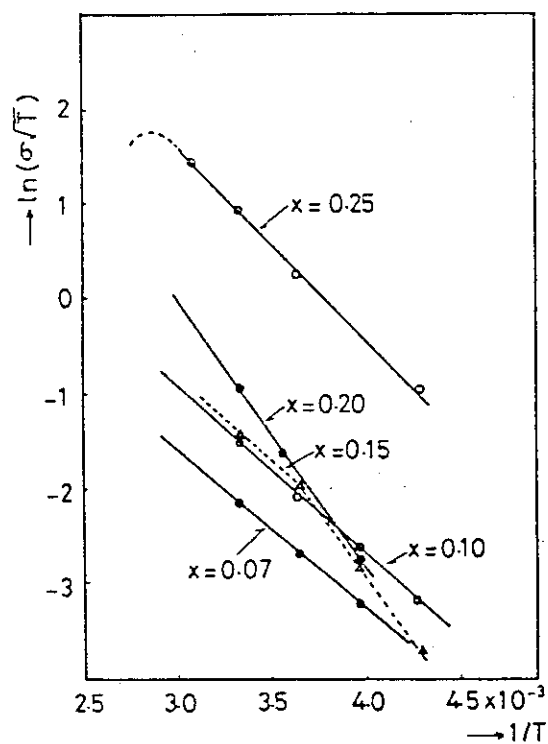


Fig. 3 Temperature dependence of conductivity in UO_{2+x} .

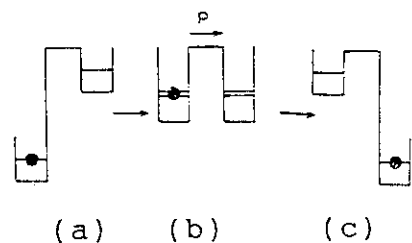
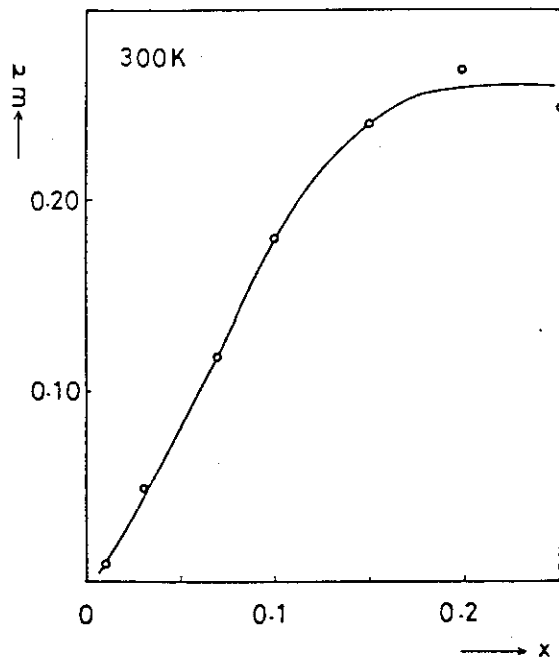
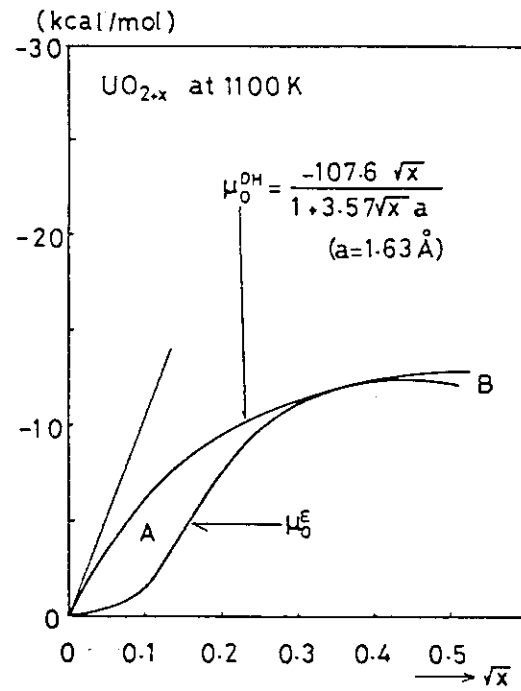


Fig. 4 Hopping process of a small polaron.

Fig. 5 Plot of $\omega\tau$ against x .Fig. 6 Excess potential of oxygen and the Debye-Hückel term in UO_{2+x} .Table I A , E_a , J and μ in UO_{2+x} .

	A	E_a (eV)	$J \times 10^3$ (eV)	$\mu \times 10^5$ (cm ² /V s) ^b	Adiabaticity
$x = 0.07$	33	0.15 ± 0.01	1.1 ± 0.1	1.3 ± 0.2	nonadiabatic
$x = 0.10$	90	0.15 ± 0.01	1.0 ± 0.1	1.8 ± 0.2	nonadiabatic
$x = 0.15^d$	90	0.15 ± 0.01	0.8 ± 0.1	1.2 ± 0.1	nonadiabatic
$x = 0.15^e$	6630	0.25 ± 0.01	8.2 ± 0.5	...	adiabatic
$x = 0.20$	6630	0.25 ± 0.01	7.4 ± 0.4	1.5 ± 0.2	adiabatic
U_4O_9 ^c	2440	0.16 ± 0.01	3.8 ± 0.2	5.4 ± 0.6	nonadiabatic

^a $\sigma = (A/\sqrt{T})\exp(-E_a/kT)$, $\sigma = Ne\mu$.^d $T > 275$ K.^b At 300 K.^e $T < 275$ K.^c $T < 350$ K.

9.2 On the Nonstoichiometry, Point Defects and Fe^{2+} - Mg^{2+} Interdiffusion in Olivine

9.2.1 Introduction

Olivine is an important earth mineral that determines to a large extent the mantle rheology.¹⁾ For deformation by dislocation climb, diffusional properties are involved. Zoning of natural olivine and ionic conductivity are essentially due to the mobilities of divalent cations. At high enough temperature, where transport via dislocations and grain boundaries can be neglected, the transport properties are determined by point defects. A careful theoretical analysis of the behaviour of point defect concentrations as a function of all the independent thermodynamic variables is therefore a prerequisite for the understanding of the transport properties of olivine together with appropriate experiments that determine the defect concentrations.

Accordingly, in this report, first, a point defect thermodynamic model of olivine is presented based on the thermogravimetric measurements of the nonstoichiometry as a function of the oxygen potential and temperature. Thereupon, results on Fe^{2+} - Mg^{2+} interdiffusion in olivines are presented and discussed, emphasizing the practical application of point defect thermodynamics to the geological processes.

9.2.2 Point Defect Thermodynamics of Olivine[1]

From the point of view of defect thermodynamics, the end member fayalite Fe_2SiO_4 is already representative and is analyzed in detail. The almost ideal admixture of Mg_2SiO_4 does not

alter the point defect disorder unless the $\text{Fe}_{\text{Me}}^{\bullet}$ defects become small in concentration relative to the inherent defect concentration of forsterite Mg_2SiO_4 .

In Fig.1a, the Gibbs phase triangle for the system Fe-Si-O is given, mainly indicating the three phase regions including fayalite. Fig.1b gives a (schematic) enlargement of the fayalite one phase field and the adjacent two- and three phase fields. According to Gibbs phase rule, at given P and T, the homogeneity range is extended in two dimensions and can be quantified by two variables η and ξ , which are conveniently defined as (n designates the mol number)

$$\begin{aligned}\bar{\xi} &= \xi - \frac{1}{3} ; & \xi &= \frac{n_{\text{Si}}}{n_{\text{Si}} + n_{\text{Fe}}} \\ \bar{\eta} &= \eta - \frac{4}{3} ; & \eta &= \frac{n_{\text{O}}}{n_{\text{Si}} + n_{\text{Fe}}}\end{aligned}\tag{1}$$

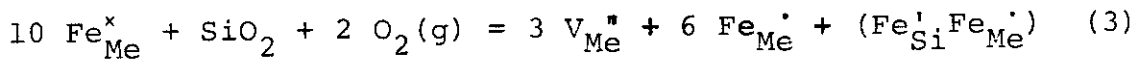
In the literature, one finds the stability region of fayalite given in terms of $\log(a_{\text{O}_2})$ and temperature. (Fig.2a). In conjunction with Fig.1b, one notes that this representation is not unambiguous as long as the composition of the fayalite is not specified with respect to $\bar{\eta}$ and $\bar{\xi}$. In other words, fayalite, at given T, in equilibrium with Fe_3O_4 and SiO_2 , has a composition different from fayalite in equilibrium with Fe and SiO_2 . Although small in absolute scale, nonstoichiometry ($\bar{\eta}/\bar{\xi}$) of fayalite is responsible for most of the point-defect-dependent properties, e.g. diffusion, electrical conductivity and optical absorption. It is thus necessary for an appropriate discussion of these phenomena to apply point defect thermodynamics in the calculation of the fayalite field ($\bar{\eta}/\bar{\xi}/P_{\text{O}_2}/a_{\text{SiO}_2}/T$), its oxygen- and SiO_2 - activity lines and the corresponding defect concen-

trations.

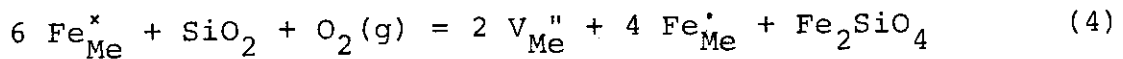
For this purpose, the most probable majority defect species: V_{Me}'' , $(Fe_{Si}'Fe_{Me}^{\bullet})$ and Fe_{Me}^{\bullet} are identified and introduced. Then the parameters η and ξ of Eq.(1) can be expressed as the unique functions of these point defect concentrations;

$$\begin{aligned}\xi &= \frac{1 - (Fe_{Si}'Fe_{Me}^{\bullet})}{3 - (V_{Me}'')} : & 3\bar{\xi} &= \frac{1}{3}(V_{Me}'') - (Fe_{Si}'Fe_{Me}^{\bullet}) \\ \eta &= \frac{4}{3 - (V_{Me}'')} : & 3\bar{\eta} &= \frac{4}{3} (V_{Me}'')\end{aligned}\quad (2)$$

The corresponding defect equilibrium equation which describes the interaction of fayalite crystal with these defect species and gaseous oxygen is ;



whereas the additional interaction with the second independent component SiO_2 can be formulated as ;



Applying the mass action law to Eqs. (3) and (4) and combining the resultant eqs. with Eq. (2), together with the electroneutrality condition; $2(V_{Me}'') = (Fe_{Me}^{\bullet})$; yield,

$$\bar{\eta} = \frac{8}{9} \left(\frac{K_4}{16}\right)^{1/6} \cdot P_{O_2}^{1/6} \cdot a_{SiO_2}^{1/6} \quad (5)$$

$$\bar{\xi} = \frac{2}{9} \left(\frac{K_4}{16}\right)^{1/6} \cdot P_{O_2}^{1/6} \cdot a_{SiO_2}^{1/6}$$

$$\left[1 - \frac{3}{2} K_3 \left(\frac{16}{K_4}\right)^{1/6} \cdot P_{O_2}^{1/6} \cdot a_{SiO_2}^{-5/3} \right] \quad (6)$$

From Eqs. (5) and (6), one can immediately derive the boundaries of the phase field of fayalite by letting a_{SiO_2} , $a_{Fe_3O_4}$, a_{FeO} , a_{Fe} be one, respectively. (See Fig.1b)

For the numerical evaluation, equilibrium constants K_3 and K_4 , therefore the absolute values of the point defect concentrations must be known. To this end, thermogravimetric determination of the nonstoichiometry of olivine was performed in the range; $0.2 \leq x \leq 1.0$ and $1000 \text{ C} \leq T \leq 1280 \text{ C}$. Fig.3 shows its result at 1130°C for olivines of various composition x . (Here $\delta =$

$$\frac{1}{3} (V_{\text{Me}}^{\bullet}) = \frac{3}{4} \bar{n})$$

In thermogravimetric experiment, fayalite (and olivine) are prepared by usual ceramics methods to be a single phase material, and \bar{n} of these samples is changed by changing the oxygen potential at given composition $\bar{\xi}$ (i.e. at fixed $(\text{Fe} + \text{Si})/\text{Si}$ ratio). In this case, let us, for example, set $\bar{\xi} = 0$. From Eqs. (5) and (6), it follows then that

$$\bar{n} = \frac{8}{9} \cdot \left(\frac{3}{2}\right)^{1/10} : \left(\frac{K_4}{16}\right)^{3/20} \cdot K_3^{1/10} \cdot P_{\text{O}_2}^{1/5} \quad (7)$$

As is apparent from Fig.3, the experimentally observed P_{O_2} dependence of \bar{n} ($\propto P_{\text{O}_2}^{1/5}$ for $1.0 \geq x \geq 0.4$) is in fair agreement with this prediction of Eq.(7). Finally, by numerically determining K_3 and K_4 , point defect concentrations along various phase boundaries of fayalite (Fig.4), and also the stability field of fayalite at 1130°C can be determined explicitly. (Fig. 5a-b). Also in Table 1, various defect reactions involved are listed, only two of which (such as Eqs.(3) and (4)) are independent. It is seen from Fig.5a that fayalite is always cation deficient ($\bar{n} \geq 0$), and has a larger Fe- ($\bar{\xi} \leq 0$) than Si- ($\xi \geq 0$) excess. These excess Fe are mainly accommodated in olivine crystals as defect complexes $(\text{Fe}_{\text{Si}}' \text{Fe}_{\text{Me}}^{\bullet})$.

9.2.3 Fe^{2+} - Mg^{2+} Interdiffusion in olivine[2]

Interdiffusion experiments were performed in the quasibinary system Fe_2SiO_4 and Mg_2SiO_4 . Typical concentration profiles of Fe and Mg, which are determined by electron microprobe analysis, are shown in Fig.6. From these profiles, the Fe/Mg-interdiffusion coefficient \tilde{D} was determined for the quasibinary silicate solid solution in intervals of 10 mol% by the Boltzmann-Matano analysis. Fig.7 summarizes all the results on interdiffusion coefficients; both the composition and the oxygen potential dependence is given for various temperatures. In addition, the numerical values of \tilde{D} shown in Fig.7 are summarized in Table .2 in parametric form.

Interdiffusion is a coupled process. In silicate, where the selfdiffusion coefficients: D_{Si} and D_{O} are very small in comparison to D_{Me} ($\text{Me}=\text{Fe}, \text{Mg}, \text{Co}, \text{Ni}, \dots$), one can safely assume that the interdiffusion of Fe and Mg in olivine occurs in the fixed frame of silicon-oxygen tetrahedra.

The formal treatment of the diffusional process under this condition leads to the following expression of the interdiffusion coefficient \tilde{D} in terms of selfdiffusion coefficients of divalent cations: D_{Fe} and D_{Mg} ;

$$\tilde{D} = \frac{D_{\text{Fe}} D_{\text{Mg}}}{x D_{\text{Fe}} + (1-x) D_{\text{Mg}}} \quad (8)$$

If the vacancy mechanism is operating in the diffusional process of Fe and Mg, and therefore in \tilde{D} , it follows from Eq. (8) that \tilde{D} at given x is proportional to (V_{Me}'') (or δ), should exhibit the same isothermal oxygen potential dependence as (V_{Me}'') . Results are given in Fig.8a/b. The slope $(\partial \log \tilde{D} / \partial \log p_{\text{O}_2})$

is approximately 1/5 both at 1130 C and 1200 C, which are in good agreement with the slope $(\partial \log \delta / \partial \log P_{O_2})$, see Fig.3.

Dividing \tilde{D} by $(V_{Me}^{''})$, the effective vacancy diffusion coefficient $\tilde{D}_{V_{Me}^{''}}$ results. In Fig.9a, it is seen that this quantity is almost independent of the composition variable x . Since the ratio (D_A/D_B) has been found to be only weakly dependent on x in other oxide solid solutions $(A,B)O^{(2)}$, it is concluded that effects due to the correlation and due to the explicit dependence of \tilde{D} on x essentially cancel each other. For the sake of comparison, the same evaluation has been performed with experimental data found in literature for Co-olivine $(\tilde{D}^{(3)}, V_{Me}^{''(4)})$. Results of this evaluation are shown in Fig.9b. It is seen that this system behaves in the same manner as does $(Fe,Mg)_2SiO_4$. Fig.10 gives the temperature dependence of $\tilde{D}_{V_{Me}^{''}}$ for olivine with several compositions x . At given temperature, the mobility of vacancies in the divalent cation sublattice and its activation energy (~ 2.0 eV) are almost independent of composition x . This is an important feature from a practical point of view. It allows to estimate diffusion coefficients in various olivine systems with incomplete experimental data.

The present study is summarized as follows:

In the first part of this report, the point defect thermodynamics for fayalite and olivine solid solutions $(Fe_xMg_{1-x})_2SiO_4$ was presented based on the thermogravimetric determination of the metal to oxygen ratio of these silicates as a function of P_{O_2} and T . Experiments were performed in the range of $0.2 \leq x \leq 1.0$ and $1000^\circ C \leq T \leq 1280^\circ C$. It was found that $V_{Me}^{''}$, Fe_{Me}^{\bullet} and the associate $(Fe_{Si}^{\bullet}Fe_{Me}^{\bullet})$ are majority defects. With this knowledge it was possible to calculate the nonstoichiometry at given

temperature as a function of P_{O_2} and a_{SiO_2} . The cation vacancy concentration shows a $P_{O_2}^{1/5}$ -dependence ($x \approx 0.4$) and increases almost exponentially with composition x . In the composition range studied here, the silicate shows an oxygen excess, and FeO is more soluble in olivine than SiO_2 .

In the second part of this report, results on Fe^{2+} - Mg^{2+} interdiffusion in olivine were presented and discussed in connection with above mentioned point defect model of olivine. It was found that the interdiffusion coefficient \tilde{D} exhibits the same P_{O_2} dependence as $(V_{Me}^{''})$, demonstrating that the vacancy mechanism is indeed operating in the diffusion of Fe^{2+} and Mg^{2+} and therefore in \tilde{D} . \tilde{D} also shows almost the same compositional variation with x as $(V_{Me}^{''})$ at given T and P_{O_2} , giving almost composition independent apparent vacancy diffusion coefficient for interdiffusion. This conclusion was reinforced by the same evaluation on Co-olivine reported in literature and might be important in dealing with diffusion data of various olivine systems with incomplete experimental background.

(A. Nakamura)

References

- 1) Donath, F.A., et.al. (eds.): "High Temp. Creep of Rock and Mantle Viscosity", In; Annual review of earth and planetary sciences, Vol.3, pp293-315(1975)
- 2) Schnehage, M., Dieckmann, R., Schmalzried, H.: Ber. Bunsenges. Phys. Chem., 86, 1061(1982)
- 3) Morioka, M.: Geochim. Cosmochim. Acta., 44, 759(1980), 45, 1573(1981)
- 4) Schwier, G., Dieckmann, R., Schmalzried, H.: Ber. Bunsenges. Phys. Chem., 77, 402(1973)

Publication List

- [1] Nakamura, A., Schmalzried, H.: "On the nonstoichiometry and point defect of olivine", Phys. Chem. Mineral, 10, 27(1983).
- [2] Nakamura, A., Schmalzried, H.: "On the Fe^{2+} - Mg^{2+} interdiffusion in olivine (II)", Ber. Bunsenges. Phys. Chem., 88, 140(1984).

Table 1. Incorporation and exsolution reactions of the coexisting phases along various phase boundaries

Type of phase boundary	Phase boundary reaction	$\frac{\partial \log [\text{defect}]}{\partial \log p_{\text{O}_2}} = \frac{1}{n}$ upper value for $[V_{\text{Me}}^{\bullet}] = \frac{1}{2} [Fe'_{\text{Me}}]$ lower value for $[Fe'_{\text{Fe}}]$
$\text{SiO}_2/\text{Fe}_2\text{SiO}_4$	$6Fe_{\text{Me}}^{\bullet} + \text{SiO}_2 + (\text{O}_2(\text{g}) = 2V_{\text{Me}}^{\bullet} + 4Fe'_{\text{Me}} + Fe_2\text{SiO}_4) \quad (3)$ $Fe_{\text{Me}}^{\bullet} + Si_{\text{Si}}^{\bullet} + \frac{1}{2} Fe_2\text{SiO}_4 + \frac{1}{2} \text{O}_2(\text{g}) = (Fe'_{\text{Fe}}) + \frac{1}{2} SiO_2$	1/6 1/2
$Fe_3O_4/\text{Fe}_2\text{SiO}_4$	$9Fe_{\text{Me}}^{\bullet} + 2\text{O}_2(\text{g}) = 6Fe_{\text{Me}}^{\bullet} + 3V_{\text{Me}}^{\bullet} + Fe_3O_4$ $Fe_3O_4 + Fe_{\text{Me}}^{\bullet} + Si_{\text{Si}}^{\bullet} = (Fe'_{\text{Fe}}) + Fe_2\text{SiO}_4$	1/4.5 0
$FeO/\text{Fe}_2\text{SiO}_4$	$6Fe_{\text{Me}}^{\bullet} + \text{O}_2(\text{g}) = 2V_{\text{Me}}^{\bullet} + 4Fe'_{\text{Me}} + 2FeO$ $3FeO + Fe_{\text{Me}}^{\bullet} + Si_{\text{Si}}^{\bullet} + \frac{1}{2} \text{O}_2(\text{g}) = (Fe'_{\text{Fe}}) + Fe_2\text{SiO}_4$	1/6 1/2
$Fe/\text{Fe}_2\text{SiO}_4$	$6Fe_{\text{Me}}^{\bullet} = 2V_{\text{Me}}^{\bullet} + 4Fe'_{\text{Me}} + 2Fe$ $4Fe + Si_{\text{Si}}^{\bullet} + 2\text{O}_2(\text{g}) = (Fe'_{\text{Fe}}) + Fe_2\text{SiO}_4$	0 2
$Fe_2\text{SiO}_4$ one-phase field	$10Fe_{\text{Me}}^{\bullet} + Si_{\text{Si}}^{\bullet} + 2\text{O}_2(\text{g}) = 3V_{\text{Me}}^{\bullet} + 6Fe'_{\text{Me}} + (Fe'_{\text{Fe}}) + Fe_2\text{SiO}_4 \quad (19)$	1/5 (only for $\xi=0$ these 1/5-slopes are the same)

Table 2
Parameters D^0 and ε for the interdiffusion coefficient
 $\bar{D} = D^0 \cdot \left(\frac{p_{\text{O}_2}}{p_{\text{O}_2}^0} \right)^{1/5} \cdot \exp(\varepsilon x)$ of olivine $(\text{Fe}_x\text{Mg}_{1-x})_2\text{SiO}_4$ at
various temperatures ($p_{\text{O}_2}^0 = 1$ bar)

T [°C]	composition range x	D^0 [cm ² /s]	ε
1050	$0 \leq x \leq 1.0$	$4.30 \cdot 10^{-11}$	4.14
1130	$0 \leq x \leq 1.0$	$1.15 \cdot 10^{-10}$	4.10
1200	$0 \leq x \leq 0.8$	$2.70 \cdot 10^{-10}$	4.69
1280	$0 \leq x \leq 0.6$	$3.83 \cdot 10^{-10}$	6.38

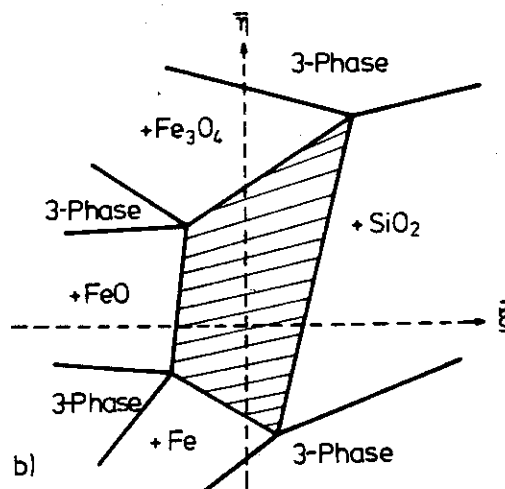
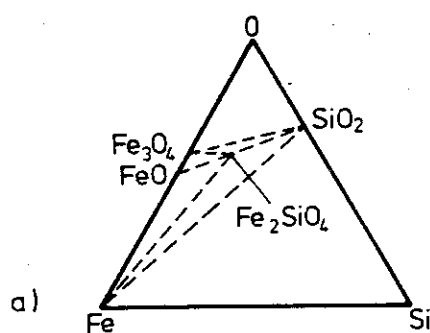


Fig. 1a. Schematic Gibbs phase triangle for the system Fe-Si-O showing three-phase fields around fayalite Fe_2SiO_4 at $T \approx 1,130^\circ\text{C}$

Fig. 1b. Enlargement of a schematic fayalite one-phase field and the adjacent two- and three-phase fields in terms of the coordinates ξ and η (see text)

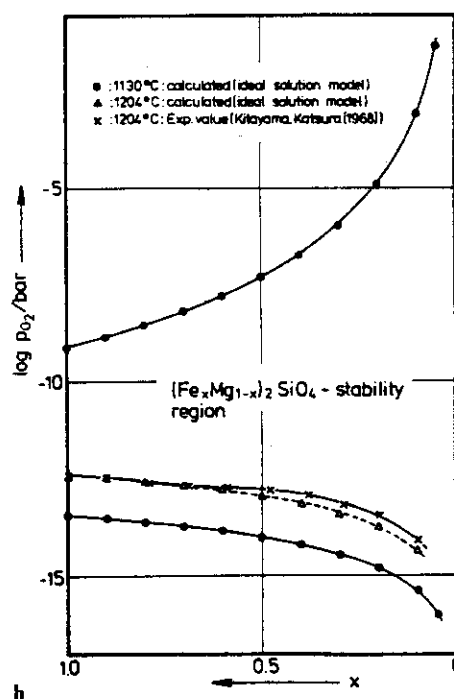
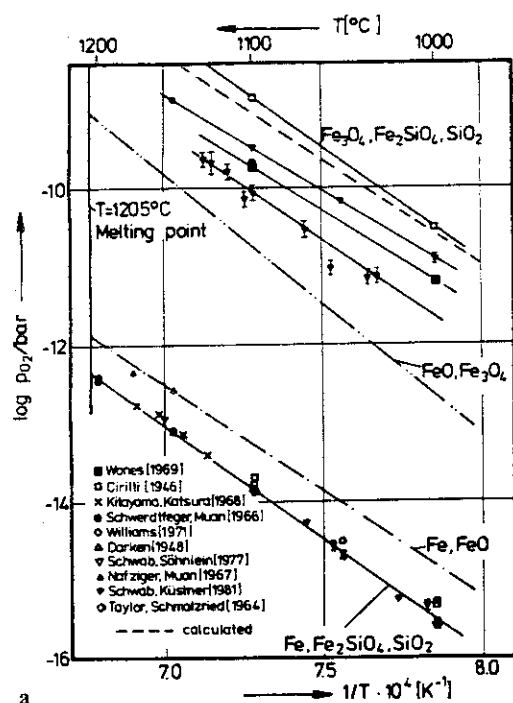


Fig. 2a. Stability region $\log p_{\text{O}_2}$ vs. $1/T$ of fayalite at $1,000^\circ < T < 1,200^\circ\text{C}$ reported by various authors. Stability limit at high oxygen potential:
 $3\text{Fe}_2\text{SiO}_4 + \text{O}_2 = 2\text{Fe}_3\text{O}_4 + 3\text{SiO}_2$
 Stability limit at low oxygen potential:
 $2\text{Fe} + \text{SiO}_4 + \text{O}_2 = \text{Fe}_2\text{SiO}_4$
 ---: calculated in the present work.
 The oxygen potentials of the nonvariant equilibria between Fe/FeO and FeO/Fe₃O₄ are also given in this figure

Fig. 2b. Stability region of olivine solid solution $(\text{Fe}_x\text{Mg}_{1-x})_2\text{SiO}_4$ at $T = 1,130^\circ\text{C}$ and $1,204^\circ\text{C}$; ●: $T = 1,130^\circ\text{C}$, calculated in analogy to Figure 2a assuming an ideal solution model between Fe_2SiO_4 and Mg_2SiO_4 ; △: $T = 1,204^\circ\text{C}$; ×: $T = 1,204^\circ\text{C}$; exp. value from Kitayama and Katsura

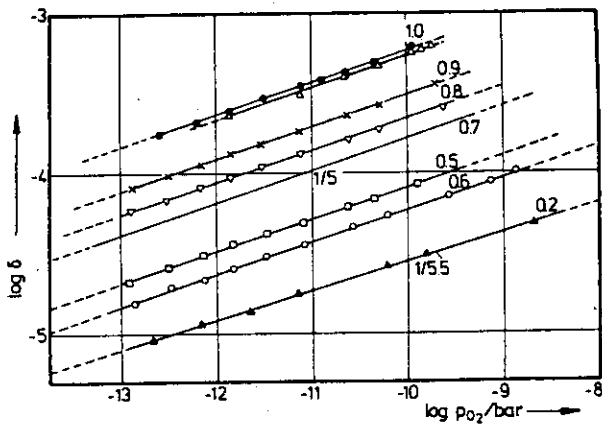


Fig. 3. Log δ vs. $\log p_{O_2}$ -plots at $T=1,130^\circ\text{C}$ for the data in Figure 3. In addition Δ : single crystal for $x=1.0$

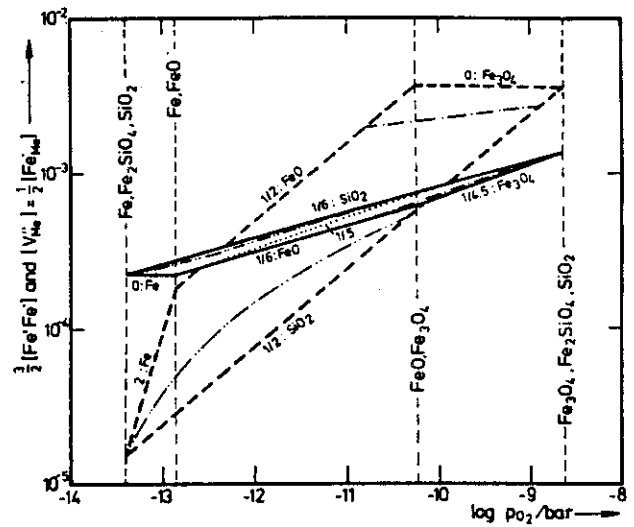


Fig. 4. 1) Concentrations of defects along the various phase boundaries of fayalite: $\log [V_{Me}'']$, $\log \frac{1}{2} [Fe'Fe']$ and $\log \frac{1}{2} [Fe'Fe']$ vs. $\log p_{O_2}$ plots at $T=1,130^\circ\text{C}$, along the phase boundaries Fe, FeO, Fe_3O_4 and SiO_2/Fe_2SiO_4 —: $[V_{Me}'']$ ($=\frac{1}{2} [Fe'Fe']$) ----: $\frac{1}{2} [Fe'Fe']$. 2) Lines inside the fayalite phase field show the variations of $[V_{Me}'']$ ($=\frac{1}{2} [Fe'Fe']$) and $\frac{1}{2} [Fe'Fe']$ with $\log p_{O_2}$ for different compositions: (a) ----: $\xi = 0.46 \cdot 10^{-4}$ (Si-excess), (b): $\xi = 0$ (stoichiometric), (c) -----: $\xi = -3.33 \cdot 10^{-4}$ (Fe excess)

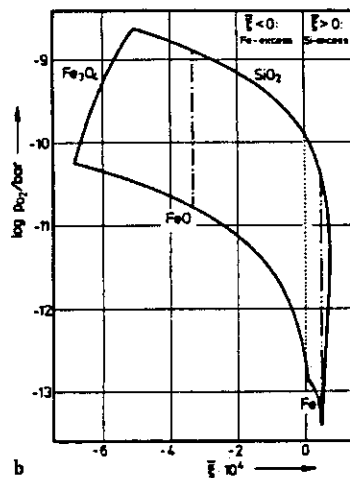
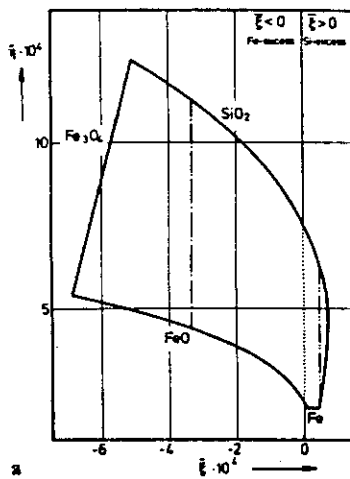


Fig. 5. a and b. Stability region of fayalite at $T=1,130^\circ\text{C}$. a $\log p_{O_2}$ vs. ξ plot along phase boundaries. b η vs. ξ -plot of the phase boundaries

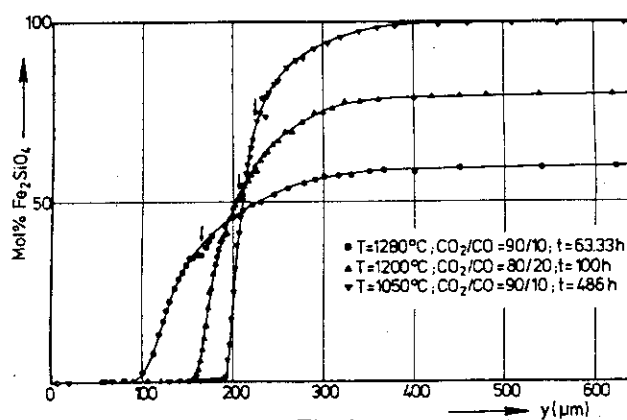


Fig. 6.

Typical concentration profiles of Fe-Mg interdiffusion in olivine

diffusion couple	T [°C]	CO ₂ /CO ratio	log p _{O₂} /bar	diffusion anneal time [hrs]
▼ Fe ₂ SiO ₄ /Mg ₂ SiO ₄	1050	90/10	-11.223	486
▲ (Fe _{0.8} Mg _{0.2}) ₂ SiO ₄ /Mg ₂ SiO ₄	1200	80/20	-9.655	100
● (Fe _{0.6} Mg _{0.4}) ₂ SiO ₄ /Mg ₂ SiO ₄	1280	90/10	-7.918	63.33

Boltzmann-Matano-interface

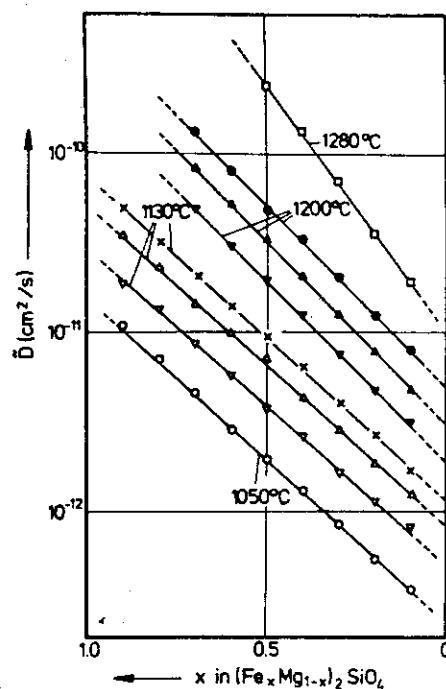


Fig. 7.

Summary of the interdiffusion data: \bar{D} vs. composition x -plots at various temperatures.

	T [°C]	CO ₂ /CO ratio	log p _{O₂} /bar
○	1050	90/10	-11.223
▽	1130	50/50	-11.855
△	1130	80/20	-10.655
×	1130	90/10	-9.940
▼	1200	50/50	-10.859
▲	1200	80/20	-9.655
●	1200	92/8	-8.737
□	1280	90/10	-7.918

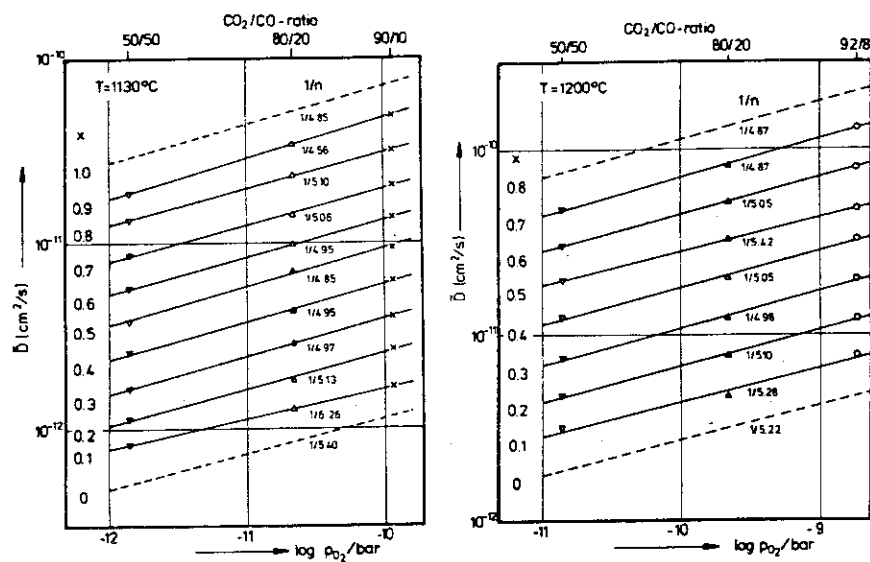


Fig. 8a and b.

log \bar{D} vs. log p_{O_2} -plots at various compositions x . a) $T = 1130^\circ\text{C}$; b) $T = 1200^\circ\text{C}$. Numbers beneath each line indicate the slope $\partial \log \bar{D} / \partial \log p_{O_2} = 1/n$. Numbers before each line indicate the composition variable x .

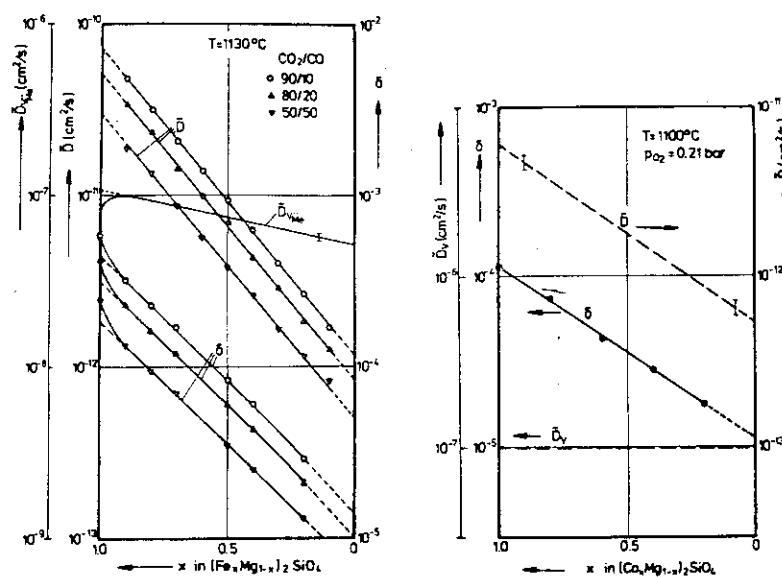


Fig. 9

a) $\log \bar{D}$, $\log \delta$, $\log \bar{D}_{V_{Me}}$ vs. composition x -plots at $T = 1130^\circ\text{C}$ for Fe-olivines. \bar{D} : obtained in the present investigation; δ : cited from 6; $\bar{D}_{V_{Me}}$: calculated as $\bar{D}_{V_{Me}} = \bar{D}/[V_{Me}'] = \bar{D}/(\frac{1}{2}\delta)$;

b) $\log \bar{D}$, $\log \delta$, $\log \bar{D}_{V_{Me}}$ vs. composition x -plots at $T = 1100^\circ\text{C}$ for Co-olivines $(\text{Co}_x\text{Mg}_{1-x})_2\text{SiO}_4$. \bar{D} : estimated values from an extrapolation of Morioka's data at $1150^\circ\text{C} \leq T \leq 1400^\circ\text{C}$ in air [10]; δ : measured values at $T = 1100^\circ\text{C}$ [11]; $\bar{D}_{V_{Me}}$: calculated as $\bar{D}_{V_{Me}} = \bar{D}/[V_{Me}']$

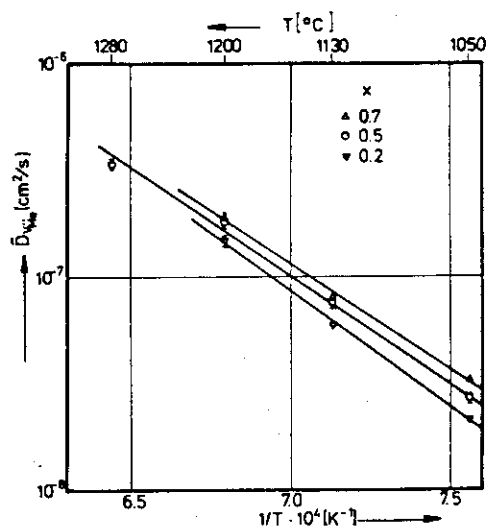


Fig. 10

Arrhenius-plots of $\bar{D}_{V_{Me}}$ in $(\text{Fe}_x\text{Mg}_{1-x})_2\text{SiO}_4$ at several compositions $x = 0.7; 0.5; 0.2$. Data are taken from Fig. 4a and the corresponding plots at other temperatures

9.3 Phase Relations and Thermodynamics of Ternary Uranium Oxides

9.3.1 Introduction

Some metal oxides have been known to dissolve in UO_2 at high temperatures forming substitutional solid solutions, $\text{M}_y\text{U}_{1-y}\text{O}_{2+x}$, where M denotes a foreign metal ion. This type of solid solution should be the most probable form in low oxygen pressures, but it is possible in some cases that the other phases could coexist with the solid solution phase. The knowledge of phase relations and thermodynamic properties of these systems is very important to clarify the irradiation behavior of UO_2 fuels. Here, we state the phase relation studies on Ca-U-O and Pr-U-O systems.

Interests are attached to the Ca-U-O system in relation to Sr-U-O and Ba-U-O systems in which the foreign metals have high fission yields. There have been a few reports on Ca-U-O system. However, these data for the single phase region do not agree to each other, nor the lattice parameter change of $\text{Ca}_y\text{U}_{1-y}\text{O}_{2+x}$ with y. This may be because the previous reports did not take into account the oxygen nonstoichiometry.

In the present work, the phase behavior of $\text{Ca}_y\text{U}_{1-y}\text{O}_{2+x}$ solid solution was studied as a function of y and x in the temperature range between 1200 and 1400 °C. The oxidation state of uranium in the compound was discussed using an ionic model of spheres of ions. With these results, the partial molar enthalpy of oxygen for the solid solution was obtained.

Lighter rare earth elements(RE's) are produced in nuclear fuel with high yields. Although there have been a relatively

large number of works concerned with the RE-U-O systems¹⁾, studies on Pr-U-O ternary system are meager and the phase relations are not well resolved. In the present work, efforts were made to determine the phase regions to find the defect characteristics of the Pr-U-O system at temperatures from 1200 to 1500 °C under the atmospheres of air, helium stream and high vacuum. The relations between lattice parameters and compositions of the fluorite solid solution were determined. Discussion was made for the oxidation state of uranium and praseodymium in the solid solution by evoking some thermodynamic data [1,2].

9.3.2 Experimental

Reagent grade CaCO_3 and 99.99 % metallic purity $\text{PrO}_{1.833}$ were purchased from Wako Pure Chemical Co. Ltd. and Shin-Etsu Chemical Co. Ltd., respectively. CaCO_3 was mixed with U_3O_8 ($\text{Ca}/\text{U}=1$), and heated in air at 1000 °C to form CaUO_4 with the final heating at 700 °C to have stoichiometric CaUO_4 ²⁾. U_3O_8 was obtained either by heating high purity uranium metal³⁾ or by heating uranium peroxide, precipitated from uranyl nitrate solution, in air at 900 °C. UO_2 was prepared by reducing the U_3O_8 in a stream of purified hydrogen at 1000 °C for 10 h.

Mixed oxides in the Ca-U-O system were made by heating CaUO_4 , UO_2 and U_3O_8 mixture pellets with Ca/U ratio ranging from 0 to 0.4 in purified He at temperatures between 1200 and 1400 °C.

To prepare the mixed oxides in the Pr-U-O system, the mixtures of Pr_2O_3 and UO_2 (Pr/U atom ratio: 0.1-0.9) were first oxidized in air at 800 °C. Then, the oxidized pellets were heated in air, helium or vacuum at temperatures between 1200 and

1500 °C.

Chemical analysis was performed for the products by determining the amount of total uranium and U(IV) with cerimetric titration after dissolving the specimen into 1.5 M sulfuric acid containing excess Ce(IV) [3].

X-ray diffraction patterns were taken for powdered specimens in glass capillaries with a Norelco 114.6 mm Debye-Scherrer camera using Ni-filtered $\text{CuK}\alpha$ radiation. Lattice parameters of cubic solid solutions were obtained by least square calculations for eight diffraction peaks higher than 90 degrees (2θ). For the specimens showing broad peaks, patterns were also taken with a Philips PW-1390 diffractometer using $\text{CuK}\alpha$ radiation monochromatized with curved pyrolytic graphite.

9.3.3 Results and Discussion

1. Ca-U-O system

Figure 1 shows the plots of the mean valency of uranium against the contents of calcium ($=y$) at 1200 and 1400 °C. In the range $0 \leq y \leq 0.1$, the valency remains almost constant, while the curve becomes steeper over $y=0.1$ and intersects the horizontal line of mean valency 5.0 at $y=0.33$. This calcium concentration coincides with that of a phase boundary between fcc solid solution and rhombohedral phase determined from the break in the lattice parameter of the fcc solid solution (Fig.3). The mean valency of uranium is, therefore, between 4 and 5, which is different from RE-U-O systems where the solid solution range extends to U(VI) region^{7,8}.

The O/M ($M=\text{Ca}+\text{U}$) ratios as a function of y are shown in Fig. 2. The O/M ratio decreases linearly with increasing y up

to ca. $y=0.1$ and thereafter the curves are flattened around the O/M ratio of 2.

The following can be drawn from Figs. 1 and 2. In the range $0 \leq y \leq 0.1$, concentration of oxygen interstitialcy decreases without the oxidation of uranium atom in the solid solution with increasing calcium concentration. In the range $\sim 0.2 \leq y \leq 0.33$, however, the concentration of oxygen vacancy does not materially change while U(IV) atoms are oxidized to the higher valence states.

X-ray diffraction analyses were made to identify the phases in the products and to determine the lattice parameters. All specimens containing calcium showed diffraction lines of the fcc structure either in a single phase or in two phase mixture. Figure 3 shows the variation of lattice parameter of the products heated in helium at 1200 and 1400 °C together with the literature values^{4,5,6}). It is seen that the lattice parameter becomes larger as the heating temperature is higher, which is caused by the liberation of oxygen from the specimens when heated at higher temperatures.

Results of X-ray diffraction analysis show that the phase behavior of this system could be discussed in three regions. 1) The first region is $0 \leq y \leq 0.03$, where two fcc phases exist and the lattice parameter of both the phases seems to decrease with increasing y . 2) In the range $0.03 \leq y \leq 0.33$, the solid solution exists in a single phase of which lattice parameter decreases linearly with increasing y . 3) Above $y=0.33$, there exists a mixture of the phase and a rhombohedral phase.

The lattice parameters of the rhombohedral phase were found to be $a=6.273(6)$ Å and $\alpha=35.99(3)$ deg. According to the

literatures, six compounds having Ca/U atom ratio less than unity have been known. Inspection of the lattice parameters of these compounds revealed that those of CaUO_4 , $a=6.267(1)$ Å and $\alpha=36.03(1)$ deg.⁹⁾ are in good accordance with the present values. Therefore, the rhombohedral phase is considered to be $\text{CaUO}_{4(-x)}$.

The phase boundary of the fcc single phase is at $y=0.33$, which well accords with the literature⁶⁾. As indicated in Fig. 3, however, the samples heated at high temperatures and/or in strong reducing atmospheres have been reported to show extended solubility ranges up to 0.4 ⁵⁾ or 0.47 ⁴⁾. Under these heating conditions, the oxygen deficient solid solution would be formed keeping the mean valency of uranium below +5 until $y=0.4$ or 0.47 although no description has been made about the oxygen nonstoichiometry in these reports^{4,5)}.

To examine the effect of x on the lattice parameter of the fcc solid solution, the parameter was plotted against the O/M ratio ($=2+x$) in Fig. 4. The lattice parameters of the specimens containing the same calcium content are represented by a straight line. Then, by using these parameters and O/M ratios, least square calculations were performed to express the change of the lattice parameter as

$$a = 5.4704 - 0.102x - 0.310y \quad (x \geq 0) \quad (1)$$

This equation shows that the lattice parameter decreases with increasing x and y , while the effect of y is about three times larger than that of x . The observed change rates of the lattice parameter with y , -0.255 and -0.262 , are smaller than the coefficient of y . This means that x decreases monotonously with increasing y . The coefficient of x in Eq. (1), -0.102 , is

well comparable with -0.094 , -0.117 and -0.119 for UO_{2+x} ¹⁰⁾, $\text{Mg}_y\text{U}_{1-y}\text{O}_{2+x}$ ¹¹⁾ and $\text{Sr}_y\text{U}_{1-y}\text{O}_{2+x}$ ¹²⁾; respectively. Since the defect structure in these solid solutions are found to be oxygen interstitials from density measurements, these coefficients of x are considered to express the effect of oxygen interstitials on the lattice parameter. Therefore, the defect type of oxygen in the present solid solution can be considered to be the same as that in UO_{2+x} , i.e. oxygen interstitials.

Ohmichi et al.¹²⁾ explained the rate of change of lattice parameter with y in $\text{RE}_y\text{U}_{1-y}\text{O}_{2+x}$ solid solutions by means of an ionic model with rigid spheres. By applying this model to the present system, the value da/dy should be -0.277 and -0.046 for U(V) and U(VI) , respectively. The experimental value, -0.310 , is in accordance with the one for U(V) , which indicates that U(V) exists in preference to U(VI) in the present solid solutions.

For $x < 0$, the lattice parameter can be expressed as

$$a = 5.470 - 0.19x - 0.31y \quad (x < 0) \quad (2)$$

The coefficient of x in the region $x < 0$, -0.19 , is about twice as large as that in the region $x \geq 0$. For the solid solutions containing trivalent rare earth elements, it has been reported that the lattice parameter dependence on x changes at $x=0$ and that the rate of the change of the lattice parameter by x in the region $x < 0$ is twice or three times larger than that in the region $x \geq 0$ ^{8,13)}. The present result is in accordance with the changes in these systems.

The partial molar enthalpy of oxygen $\Delta\bar{H}_{\text{O}_2}$ for the single phase $\text{Ca}_y\text{U}_{1-y}\text{O}_{2+x}$ solid solution was estimated using an equation for the partial molar entropy of oxygen $\Delta\bar{S}_{\text{O}_2}$ derived by Fujino

and Naito¹¹⁾:

$$\Delta \bar{S}_{O_2} = -2R \cdot \ln\left(\frac{x}{1-x}\right) - 4R \cdot \ln\left(\frac{2x+2y}{1-2x-3y}\right) + Q, \quad (3)$$

where the first and second terms of Eq. (3) are due to the configurational entropy change and the factor Q includes the vibrational term which does not vary greatly with the composition. Using the estimated Q value, -167 J/K mol, the partial molar enthalpy was obtained by $\Delta \bar{H}_{O_2} = \Delta \bar{G}_{O_2} + T\Delta \bar{S}_{O_2}$. These values are shown in Fig. 5 as a function of x in $Ca_yU_{1-y}O_{2+x}$. Sharp increase of $\Delta \bar{H}_{O_2}$ near $x=0$, maximum in the vicinity of $x=0.01$ and slow decrease of $\Delta \bar{H}_{O_2}$ over $x=0.1$ were observed.

The phenomenon giving maximum of $\Delta \bar{H}_{O_2}$ has been observed also in the other systems: $x=0.01$ ¹⁴⁾ and $x=0.002$ ¹⁵⁾ for UO_{2+x} and near $x=0$ for $Gd_yU_{1-y}O_{2+x}$ ¹⁶⁾. In the figure, the $\Delta \bar{H}_{O_2}$ values for $Mg_{0.05}U_{0.95}O_{2+x}$ ¹⁷⁾ are also shown. These values are about -25 kJ/mol smaller than the present values in the range $x \geq 0.1$. The difference is due to the smaller Q values, -188 to -196 J/K·mol, in the solid solutions of magnesium.

2. Pr-U-O system

The variation of cubic lattice parameter with y for the specimens heated in air is shown in Fig. 6 together with literature values^{18,19,20)}. The data can be connected by three straight lines with different slopes. The present values are in good accordance with those of Hund and Peetz¹⁸⁾, whereas somewhat different from those of Jocher²³⁾. At $y=0$, the X-ray diffraction pattern revealed an existence of $\beta-U_3O_8$ with orthorhombic lattice parameters $a=7.070$, $b=11.45$ and $c=8.302$ Å, and of a small amount of $\alpha-U_3O_8$ with $a=6.73$, $b=11.95$ and $c=4.15$ Å. Coexistence of $\alpha-U_3O_8$ in $\beta-U_3O_8$ may be caused by rather rapid cooling rate, 100 C/min. or higher at the first stage since

$\beta\text{-U}_3\text{O}_8$ was obtained only by slow cooling (100 °C per day)²¹⁾. It is seen from the figure that breaks occur on the line (curve 1) at $y=0.32$ and 0.60 . Below $y=0.32$, the lattice parameter of the fcc phase remained unchanged at 5.443 Å, and $\alpha\text{-}$ and $\beta\text{-U}_3\text{O}_8$ lines were also detected: Two phase mixture exists in this range. From $y=0.32$ to 0.60 , the lattice parameter increases linearly with y . The value reaches 5.4727 Å at $y=0.60$. Above $y=0.60$, the lattice parameter increases with a steeper slope, which is consistent with literatures^{18,19)}. The extrapolated value of the lattice parameters to $y=1.0$, 5.540 Å, is close to the half-cell value of 5.530 Å for nonstoichiometric C-type rare earth sesquioxide quenched from 1250 °C¹⁹⁾.

At $y=0.8$, the diffraction lines corresponding to another fcc phase with smaller lattice parameter became distinct, and they grew clearer and stronger with the increase of y value. The lattice parameter change of this phase is shown in Fig. 6 as curve 3. The parameter diminishes with increasing y and reaches that of $\text{PrO}_{1.833}$ at $y=1.0$.

A rhombohedral phase known as $\text{Pr}_6\text{UO}_{12}$ ¹⁹⁾ coexisted with $\text{PrO}_{1.833}$ at $y=0.9$ when heated at 1350 °C. The lattice parameters obtained were $a=10.24$ and $c=9.570$ Å in hexagonal indexing. By heating at 1200 °C, however, this rhombohedral phase was not formed: The product was a mixture of the fcc solid solution and the $\text{PrO}_{1.833}$ phase.

The variation of the fcc lattice parameter with composition for the samples heated in helium is shown in Fig. 7, where the broken line is that for samples heated in air at 1350 °C for comparison. It is seen from Fig. 7 that the lattice parameter of the samples heated in helium can be followed by two straight

lines with different slopes. The difference between the lattice parameters heated in helium and those in air is that the parameter increases with y almost linearly from $y = 0$ to 0.52 .

The rhombohedral phase appeared both at $y=0.8$ and 0.9 when heated in helium at 1200 or 1350°C . At $y=0.8$, it coexisted with the cubic solid solution, and at $y=0.9$, with A-type (hexagonal) rare earth sesquioxide phase.

The lattice parameter change for the fcc solid solutions of the specimens heated in vacuum are also shown in Fig. 7. In this case, the lattice parameter decreases with increasing y in the range $0 \leq y \leq 0.38$ when heated at 1200 or 1350°C . On the other hand, when heated at 1500°C , the lattice parameter does not change at $y \leq 0.38$ but increases steeply with y at $y > 0.38$. The rhombohedral phase was observed at $y=0.8$ and 0.9 provided that the heating temperature was either 1200 or 1350°C . This phase, however, did not appear at 1500°C .

The lattice parameter of the fluorite single phase is plotted as a function of $O/M (=2+x)$ in Fig. 8. It is seen that the fluorite lattice contracts with increasing x . The data can be followed by two straight lines of which the slope changes at $O/M=2.00$. Similar sharp breaks at the stoichiometric $\text{MO}_{2.00}$ have been noted in the systems $\text{La-U-O}^{22)}$, $\text{Gd-U-O}^{8)}$ and $\text{Nd-U-O}^{13)}$.

By using the observed lattice parameters in the cubic single phase region, least squares calculations were performed to express the change of lattice parameter as linear equations of x and y under the condition that the parameter is $5.4704 \text{ \AA}^{10)}$ for both x and y being zero. The results are:

$$a = 5.4704 - 0.127x - 0.007y \quad (x \geq 0) \quad (4)$$

and

$$a = 5.4704 - 0.397x - 0.007y \quad (x < 0) \quad (5)$$

These equations show that the lattice parameter diminishes with increasing x and y . The coefficient of x in Eq.(4), which expresses the effect of oxygen on the lattice parameter in the $O/M \geq 2$ region, 0.127, is well comparable with -0.10, -0.117 and -0.094 for $Nd_yU_{1-y}O_{2+x}$ ¹³⁾, $Mg_yU_{1-y}O_{2+x}$ ¹¹⁾ and UO_{2+x} ¹⁰⁾, respectively. Since these coefficients have been verified to correspond to the defect structure with oxygen interstitial type, the present result can be considered to give a strong support that the " x " oxygen atoms are in interstitial sites in the range $O/M \geq 2$ in this system.

The coefficient of y , which is equivalent to $\partial a / \partial y$, indicates the rate of change of lattice parameter with content of rare earth elements. The present value is shown as a star mark in Fig. 9 together with literature data^{7,8,12,13,22,23,24)}. The figure shows that $\partial a / \partial y$ changes linearly with ionic radius. These results suggest that the lattice parameter change with y in the solid solutions of $RE_yU_{1-y}O_{2+x}$ depends only on the trivalent ion size of rare earth elements which substitute for uranium.

Figure 10 shows the mean valency of uranium for the samples heated in air at 1350 °C. The value decreases with increasing y until $y=0.32$, and then it increases steeply up to $y \sim 0.70$. The points of $y=0.32$ and ~ 0.70 can be considered to express the phase boundaries. For samples heated in helium, the mean valency increases from $y=0$ to ~ 0.6 with increasing slope. The curve crosses the horizontal line of mean valency of 5.0 at $y=0.52$. Above $y \sim 0.70$, the points scatter.

When heated in vacuum, the curve crosses the line of mean valency of 5.0 at $y=0.62$. At $y \geq 0.70$, the valency fluctuates along the curve with smaller increasing rate. There may be a phase boundary around this concentration of y .

Phase relations and lattice parameter change in the present system could be classified by the uranium valency and the type of oxygen nonstoichiometry. These are shown in Table 1. The table shows that when heated in air at 1350 °C, the fcc solid solution having fluorite type structure is formed as a mixture with U_3O_8 in the range $0 < y \leq 0.32$. In the range $0.32 < y \leq 0.38$, the uranium valencies of the fcc phase are U(IV)-U(V) with excess oxygen atoms on interstitial sites, while those in the range $0.38 < y \leq 0.60$ are U(V)-U(VI). In the range $0.60 < y \leq 0.71$, oxygen vacancies are formed instead of interstitials. The change of slope in lattice parameter was seen at $y=0.6$ in Fig. 6. Above 0.71, the solid solution phase does not exist in single phase.

When heated in helium, the fcc solid solution was in a single phase even below $y=0.1$, which is in contrast with the case of heating in air. The uranium valencies of the fcc phase in the range of $0 < y \leq 0.38$ are U(IV)-U(V) with interstitial oxygen, and it has oxygen vacancies in the range $0.38 < y \leq 0.52$. As seen from Fig. 7, the lattice parameter increases with a slope of 0.027 per y in these ranges. The uranium valencies change from U(IV)-U(V) to U(V)-U(VI) at $y=0.52$. In the range $0.52 < y \leq 0.77$, the fcc phase is in the region U(V)-U(VI) and oxygen vacancies. The lattice parameter increases more rapidly in this range. Above $y=0.77$, the fcc phase exists as a mixture with Pr_6UO_{12} phase or $A-PrO_{1.5}$ phase.

Let us calculate the slope in the range $0 < y \leq 0.38$

theoretically. Since partial molar entropy of oxygen, $\Delta\bar{S}_{O_2}$, can be obtained by the equation discussed previously¹¹⁾, and since partial molar free energy, $\Delta\bar{G}_{O_2}$, is given by $RT \cdot \ln p_{O_2}$,

$$\Delta\bar{G}_{O_2} = \Delta\bar{H}_{O_2} - T(-2R \cdot \ln \frac{x}{1-x} - 4R \cdot \ln \frac{2x+y}{1-2x-2y} + Q). \quad (6)$$

Since the values of $\Delta\bar{H}_{O_2}$ and Q do not change greatly with composition and temperature except near $x=0$ ¹⁶⁾, let these values are taken to be constant. The total derivative of $\Delta\bar{G}_{O_2}$ with y is expressed by

$$d(\Delta\bar{G}_{O_2}) = \frac{\partial(\Delta\bar{G}_{O_2})}{\partial x} dx + \frac{\partial(\Delta\bar{G}_{O_2})}{\partial y} dy. \quad (7)$$

Under the condition of constant oxygen partial pressure,

$$d(\Delta\bar{G}_{O_2}) = 0.$$

Then,

$$\frac{dx}{dy} = - \frac{2x(1-x)(1+2x)}{4x^2y-8x^2-10xy-2y^2+6x+y} \quad (8)$$

and from Eq.(4)

$$\frac{da}{dy} = - 0.127 \frac{dx}{dy} - 0.007. \quad (9)$$

The dx/dy values were calculated to be -0.441 , -0.426 and -0.275 for $y=0.1$, 0.2 and 0.3 , respectively, with Eq.(8). Therefore, by substituting these values in Eq.(9), da/dy values of 0.049 , 0.0471 and 0.0279 were obtained for $y=0.1$, 0.2 and 0.3 , respectively. These are in reasonable agreement with the observed slope.

(T. Fujino, T. Yamashita and K. Ohuchi)

References

- 1) See, for example, the review by Keller, C. in: "Ternäre und

- Polynäre Oxide des Urans", Gmelins Handbuch der anorganischen Chemie, 8. Ergänzungswerk, Band 55, Teil C3, p.197, (1975), Verlag Chemie, GmbH, Weinheim/Bergstrasse.
- 2) Tagawa, H., Fujino T., Yamashita, T.: J. Inorg. Nucl. Chem., **41**, 1729 (1979).
 - 3) Hashitani, H., Hoshino, A., Adachi, T.: Japan Atomic Energy Research Institute Report, JAERI-M-5343, (1973).
 - 4) Alberman, K.B., Blakey, R.C., Anderson, J.S.: J. Chem. Soc., 1352 (1951).
 - 5) Voronov, N.M., Sofronova, R.M. in Ivanov, O.S.(ed.): "Physical Chemistry of Alloys and Refractory Compounds of Thorium and Uranium", p.204, (1972), Jerusalem.
 - 6) Brisi, C., Montorsi, M., Burlando-Acquarone, G.: Atti Acad. Sci. Torino Classe Sci. Fis. Mat. Nat., **106**, 257 (1972).
 - 7) Keller, C., Boroujerdi, A.: J. Inorg. Nucl. Chem., **34**, 1187 (1972).
 - 8) Beals, R.J., Handwerk, J.H.: J. Amer. Ceram. Soc., **48**, 271 (1965).
 - 9) Zachariasen, W.H.: Acta Crystallogr., **1**, 265 (1948).
 - 10) Nickel, H.: Nukleonik, **8**, 366 (1966).
 - 11) Fujino, T., Naito, K.: J. Inorg. Nucl. Chem., **32**, 627 (1970).
 - 12) Ohmichi, T., Fukushima, S., Maeda, A., Watanabe, H.: J. Nucl. Mater., **102**, 40 (1981).
 - 13) Wadier, J.F.: CEA-R-4507, (1973).
 - 14) Markin, T.L., Bones, R.J.: AERE-R-4042, (1962).
 - 15) Gerdanian, P.: J. Phys. Chem. Solids, **35**, 163 (1974).
 - 16) Une, K., Oguma, M.: J. Nucl. Mater., **110**, 215 (1982).
 - 17) Fujino, T., Tateno, J., Tagawa, H.: J. Solid State Chem.,

24, 11 (1978).

- 18) Hund, F., Peetz, U.: Z. Elektrochem., **56**, 223 (1952).
- 19) Jocher, W.G.: KFK-2518, (1978).
- 20) Lowe, A.T.: Diss. Arizona State Univ., (1974).
- 21) Loopstra, B.O.: Acta Crystallogr., B**26**, 656 (1970).
- 22) Hill, D.C.: J. Amer. Ceram. Soc., **45**, 258 (1962).
- 23) Shannon, R.D.: Acta Crystallogr., A**32**, 751 (1976).
- 24) Kollar, D., Handwerk, J.H., Beals, R.J.: ANL-6631, (1962).

Publication List

- [1] Yamashita, T., Fujino, T., Tagawa, H.: J. Nucl. Mater., **132**, 192 (1985).
- [2] Yamashita, T., Fujino, T.: J. Nucl. Mater., in press.
- [3] Fujino, T., Yamashita, T.: Fresenius Z. Anal. Chem., **314**, 423 (1983).
- [4] Fujino, T., Yamashita, T., Tagawa, H.: to be submitted to J. Solid State Chem.

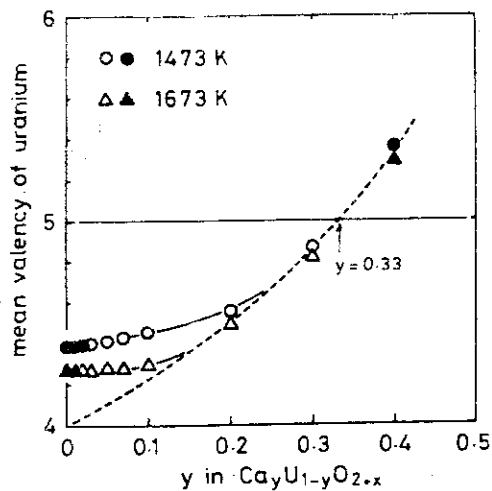


Fig. 1. Mean valency of uranium as a function of y in $\text{Ca}_y\text{U}_{1-y}\text{O}_{2+x}$ solid solution. The open marks indicate a single phase and filled marks the two phase mixture. The broken line shows the mean valency of uranium calculated theoretically for the case where no change occurs in the O/M ratio of the solid solution by the incorporation of calcium.

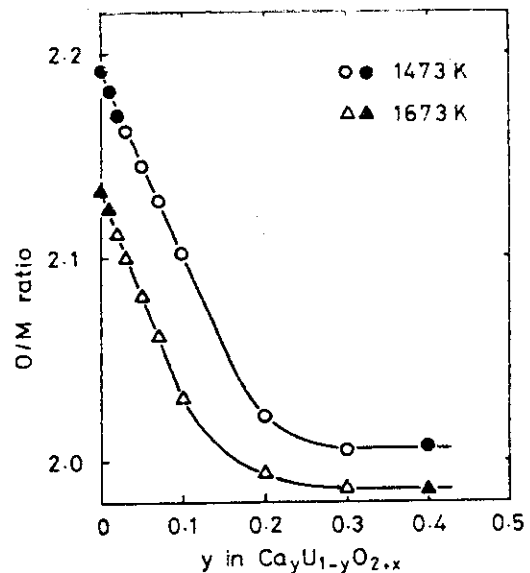


Fig. 2. Oxygen to metal atom ratios as a function of y in $\text{Ca}_y\text{U}_{1-y}\text{O}_{2+x}$ solid solution. Open marks indicate a single phase and filled marks the two phase mixture.

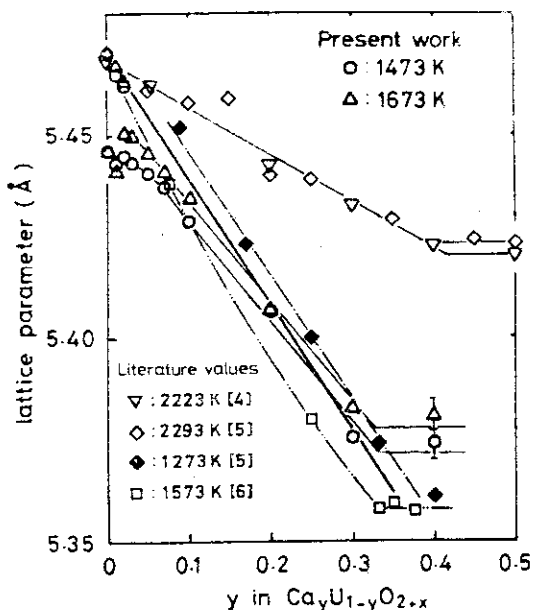


Fig. 3. Lattice parameter change of cubic solid solutions. The bold line shows the change of the lattice parameter for stoichiometric $\text{Ca}_y\text{U}_{1-y}\text{O}_{2.00}$.

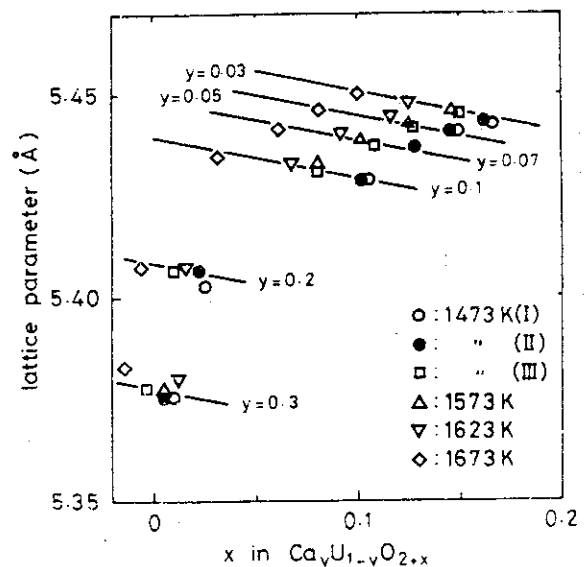


Fig. 4. Effect of excess oxygen content ($=x$) on the lattice parameter of the $\text{Ca}_y\text{U}_{1-y}\text{O}_{2+x}$ solid solution.

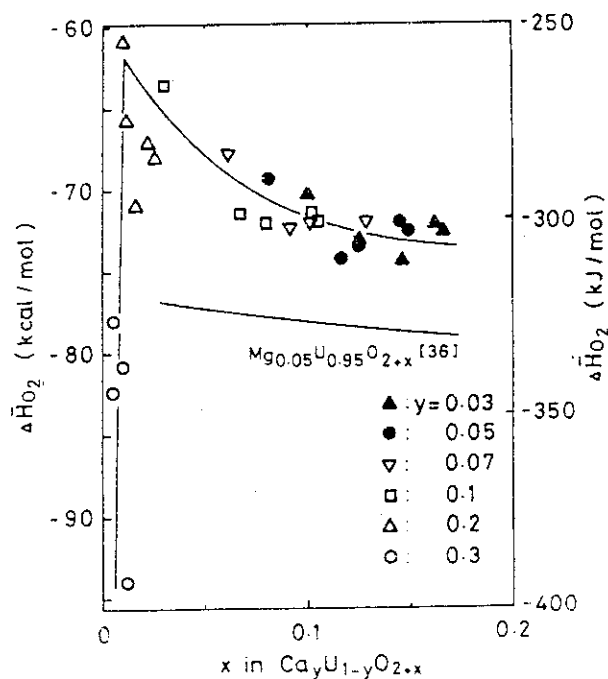


Fig. 5. The partial molar enthalpy of oxygen as a function of excess oxygen content ($=x$).

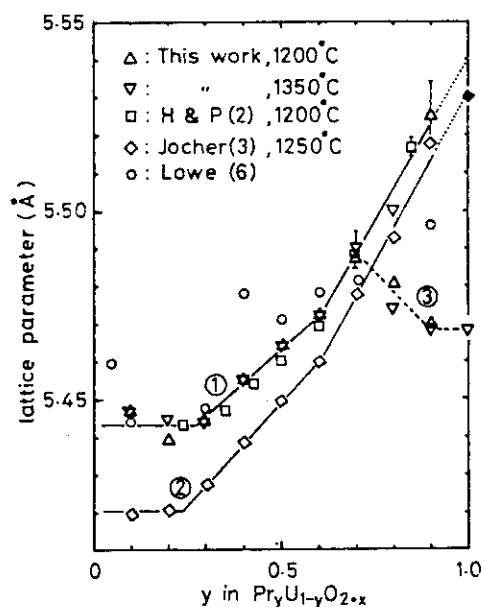


Fig. 6. Lattice parameter change of cubic solid solutions obtained by heating in air; ◆ = half of the lattice parameter of body centered cubic cell of C-type praseodymium sesquioxide heated at 1250°C [19].

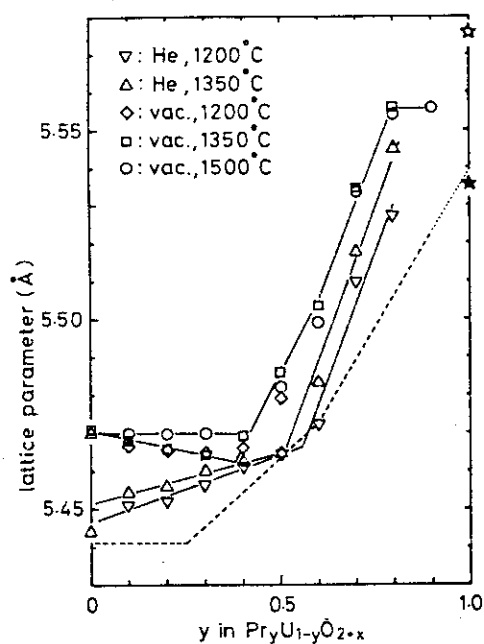


Fig. 7. Lattice parameter change of cubic solid solutions obtained by heating in helium or in vacuo; ★, ★ = half the lattice parameter of body centered cubic cell of C-type $\text{PrO}_{1.5}$ and $\text{PrO}_{1.65}$. Broken line indicates the lattice parameters for those heated in air at 1350°C.

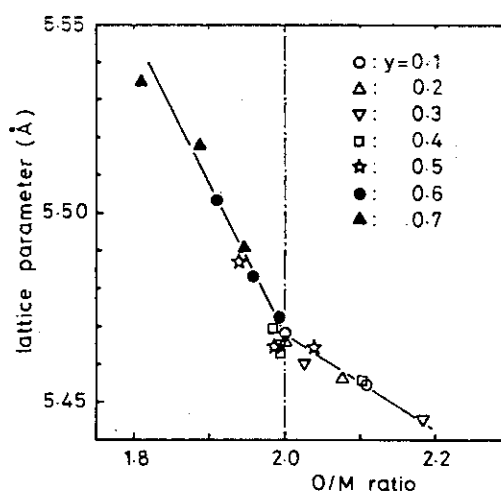


Fig. 8. Effect of oxygen-to-metal-atom ratios on the lattice parameter for cubic solid solutions with praseodymium oxide and uranium oxide.

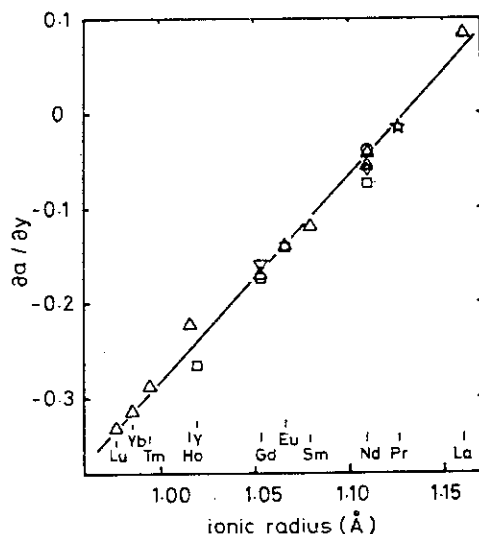


Fig. 9. Partial derivative of lattice parameter with γ as a function of ionic radius of RE^{3+} [23]; \square [12], \diamond [13], ∇ [10], \circ [24], Δ = calculated from the lattice parameters of $\text{RE}_{0.5}\text{U}_{0.5}\text{O}_{2.00}$ [22, 7, 20] assuming that linear relationships hold between the lattice parameters of UO_2 and these phases.

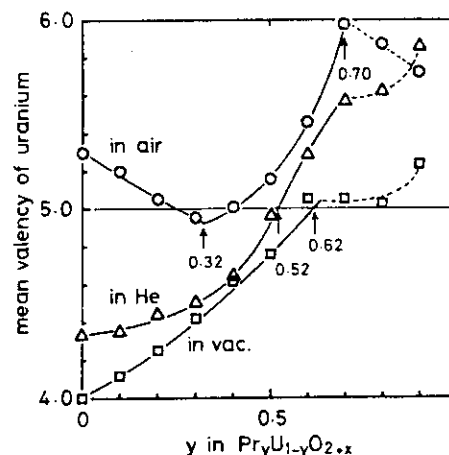


Fig. 10 Mean valency of uranium of the products obtained by heating at 1350°C in air, helium or vacuo.

Table 1
Phases in relation to uranium valency and oxygen non-stoichiometry

Region	Phase	Uranium valency and type of defect
(1) in air at 1350°C		
$0 < y \leq 0.32$	fcc s.s. + α - β - U_3O_8	
$0.32 < y \leq 0.38$	fcc s.s.	$\text{U}^{4+} \sim \text{U}^{5+}$ oxygen interstitial
$0.38 < y \leq 0.60$	fcc s.s.	$\text{U}^{5+} \sim \text{U}^{6+}$ oxygen interstitial
$0.60 < y \leq 0.71$	fcc s.s.	$\text{U}^{5+} \sim \text{U}^{6+}$ oxygen vacancy
$0.71 < y < 1.0$	fcc s.s. + $\text{Pr}_6\text{UO}_{12}$ or $\text{PrO}_{1.833}$ phase	
(2) in helium at 1350°C		
$0 < y \leq 0.38$	fcc s.s.	$\text{U}^{4+} \sim \text{U}^{5+}$ oxygen interstitial
$0.38 < y \leq 0.52$	fcc s.s.	$\text{U}^{4+} \sim \text{U}^{5+}$ oxygen vacancy
$0.52 < y \leq 0.77$	fcc s.s.	$\text{U}^{5+} \sim \text{U}^{6+}$ oxygen vacancy
$0.77 < y < 1.0$	fcc s.s. + $\text{Pr}_6\text{UO}_{12}$ or A- $\text{PrO}_{1.5}$ phase	
(3) in vacuo at 1350°C		
$0 < y \leq 0.38$	fcc s.s.	$\text{U}^{4+} \sim \text{U}^{5+}$ no oxygen defect
$0.38 < y \leq 0.62$	fcc s.s.	$\text{U}^{4+} \sim \text{U}^{5+}$ oxygen vacancy
$0.62 < y \leq 0.70$	fcc s.s.	$\text{U}^{5+} \sim \text{U}^{6+}$ oxygen vacancy
$0.70 < y < 1.0$	fcc s.s. + $\text{Pr}_6\text{UO}_{12}$ or A- $\text{PrO}_{1.5}$ phase	

9.4 Magnetic Susceptibilities of $\text{UO}_2\text{-ThO}_2$ Solid Solutions

9.4.1 Introduction

The magnetic susceptibilities of $\text{UO}_2\text{-ThO}_2$ solid solutions have been measured by several researchers. Slowinski and Elliott ¹⁾ measured the magnetic susceptibilities in the temperature range of 66~296 K, and showed that the solid solutions obey the Curie-Weiss law. They also showed that the magnetic moment of the U^{4+} ion decreases with dilution with ThO_2 and approaches the "spin only value". The configuration of the valence electrons of the U^{4+} ion was considered to be $6d^2$, because the quenching of the orbital angular momentum, which is characteristic of the d electrons, was thought to be responsible for the observed magnetic moment. Contrary to that, Hutchison and Candela ²⁾ indicated that this "spin only value" could be interpreted in terms of a ground state configuration of $5f^2$ perturbed by the crystalline field with cubic symmetry. After a decade, Comly ³⁾ made the magnetic susceptibility measurements down to 1.7 K. His results on the diluted samples of 5~10 mole% UO_2 in ThO_2 were explained on the basis of the paramagnetic ground state of the U^{4+} ion in UO_2 to be not singlet, but triplet, which was in accord with the results of the spin-wave dispersion branch experiments ⁴⁾. Comly also observed a linear dependence of Néel temperature, T_N , on the concentration in the range of 60~100 mole% UO_2 . By extrapolation, the critical concentration at which antiferromagnetism disappears was found to be 58 mole% UO_2 .

However, there are some problems left to be clarified:

(1) The problem of whether the reaction to form the solid solutions was complete or not. Regarding the relation between lattice parameter and composition, it has been known that the solid solutions of $\text{UO}_2\text{-ThO}_2$ obey the Vegard's law, whereas at very high concentrations of UO_2 , Cohen and Berman ⁵⁾ reported deviation from the linearity. The lattice parameters of the samples used for magnetic susceptibility measurements by Trzebiatowski and Selwood ⁶⁾ show scattering, and the samples of Slowinski and Elliott ¹⁾ were prepared by heating at $1000 \sim 1200^\circ\text{C}$ for $2 \sim 4$ hr. These reaction temperatures seem not to be sufficiently high for forming $\text{UO}_2\text{-ThO}_2$ solid solutions.

(2) Change of magnetic moment and Weiss constant with composition. There have been few reports concerning this point. The magnetic moment obtained by Slowinski and Elliott ¹⁾ does not change up to 25 mole% ThO_2 , whereas the Weiss constant decreases monotonously with increasing ThO_2 concentration ^{1, 6, 7)}.

(3) Néel temperature change with composition. According to the recent data of neutron diffraction ⁸⁾ and thermal expansion ⁹⁾ measurements, the linear dependence of T_N on the concentration of ThO_2 does not hold at high concentrations, which is inconsistent with magnetic susceptibility data ³⁾.

We report here the results of the magnetic susceptibility measurements for $\text{UO}_2\text{-ThO}_2$ solid solutions prepared at 1650°C . The temperature range of the measurements was

from 2.0 K to room temperature. We will discuss the variation of three magnetic parameters, i.e., magnetic moment (μ_{eff}), Weiss constant (θ), and Néel temperature (T_N) with the concentration of uranium ion. The molecular field theory which includes interaction between next-nearest neighbor spins is used for discussing the results.

9.4.2 Experimental

(a) Sample preparation

Samples were prepared by the coprecipitation method. Chemically pure grade reagents of $\text{UO}_2(\text{NO}_3)_2 \cdot 6\text{H}_2\text{O}$ and $\text{Th}(\text{NO}_3)_4 \cdot 4\text{H}_2\text{O}$ were weighed out to the intended U/Th ratios, dissolved in water, and stirred well. By adding ammonia water, an intimate mixture of ammonium diuranate and thorium hydroxide was obtained. The precipitate was washed with dilute ammonium nitrate solution, dried, and preliminary calcined in air. The mixtures thus obtained were pressed into pellets and reduced at 1650°C in flowing hydrogen for about 7 hr. After cooling, the samples were crushed into powder, repressed, and reduced under the same conditions.

(b) X-ray diffraction measurements

An X-ray diffraction study on the solid solutions was performed using $\text{Cu-K}\alpha$ radiation with a Philips PW 1390 diffractometer with curved graphite monochromator. The lattice parameter of the samples was determined by the Nelson-Riley extrapolation method to the diffraction lines.

(c) Magnetic susceptibility measurement

Magnetic susceptibility was measured by a Faraday-type torsion balance in the temperature range from 2.0 K to room temperature. The apparatus was calibrated with Mn-Tutton's salt as a standard. The temperature of the sample was measured by normal Ag vs. Au-0.07 at% Fe thermocouple¹⁰⁾ and Au-Co vs. Cu thermocouple.

9.4.3 Results and discussion

(a) Lattice parameter

Figure 1 shows the variation of the lattice parameters of the samples used in this study. These solid solutions have a fluorite-type structure, and obey Vegard's law; the lattice parameters change linearly in whole range of ThO_2 concentration between 5.4704 Å for UO_2 and 5.5975 Å for ThO_2 .

(b) Magnetic susceptibility

The magnetic susceptibilities per mole of uranium as a function of temperature for UO_2 and for the solid solutions in concentrated UO_2 range, i.e., $\text{Th}_{0.1}\text{U}_{0.9}\text{O}_2$, $\text{Th}_{0.2}\text{U}_{0.8}\text{O}_2$, $\text{Th}_{0.3}\text{U}_{0.7}\text{O}_2$ and $\text{Th}_{0.4}\text{U}_{0.6}\text{O}_2$ are shown in Fig. 2. For the solid solutions in the dilute range, the inverse magnetic susceptibilities per mole of uranium vs. temperature are shown in Fig. 3. For all the solid solutions examined here, the Curie-Weiss law holds over the temperature range from liquid nitrogen temperature to room temperature.

(c) Magnetic moment

In the previous reports, the Weiss constant decreased with increasing ThO_2 concentration, but the magnetic moment

obtained by Slowinski et al.¹⁾ did not vary up to 25 mole% ThO₂. However, the Néel temperature, as will be described later, decreased monotonously with increasing ThO₂ concentration^{3, 8, 9)}. Therefore, the magnetic moment is also expected to vary at low ThO₂ concentrations. In Fig. 4, the magnetic moment determined in this work is plotted as a function of ThO₂ concentration. The value decreases monotonously with increasing ThO₂ concentration. The magnetic moment of the U⁴⁺ ion infinitely diluted in ThO₂ is 2.78 B.M. from Fig. 4, which is a little lower than that obtained by Slowinski et al.¹⁾ and slightly larger than that of an infinitely diluted solid solutions in UP-ThP system¹¹⁾. Theoretical calculation gives 2.83 B.M. for the moment of the ground state configuration 5f² in the crystalline field produced by eight oxygens with cubic symmetry. Our experimental moment agrees well with the theoretical value which is for the uranium ion without any magnetic interaction with the adjacent uranium ions. The larger magnetic moment in the concentrated range of UO₂ in Fig. 4 is possibly due to the increased effect of adjacent uranium ions in this range as with the case of Fe₂O₃-Al₂O₃^{12, 13)}.

(d) Weiss constant

The effect of dilution on the Weiss constant, θ , is also shown in Fig. 4. There exists a nearly linear relation between θ and uranium concentration. In general, the Weiss constant is indicative of the magnitude of the magnetic exchange interaction. Thus it can be said that as the ThO₂ concentration increases, the interaction is weakened. The linear dependence can be obtained by assuming that the

exchange interaction for any one U^{4+} ion is proportional to to the number of nearest and next-nearest neighbor U^{4+} ions.

First, we consider only nearest neighbor spins¹⁴⁾. The U^{4+} ions are divided into groups having 0, 1, ---, 12 nearest neighbors. The average value of θ will then be given by

$$\bar{\theta} = \sum_{k=0}^{12} f_k \cdot k \cdot \delta, \quad (1)$$

where f_k is the fraction of the U^{4+} ions having k U^{4+} nearest neighbors and δ represents the contribution to the total θ of one of the equivalent nearest neighbors. The fraction f_k is expressed as

$$f_k = \frac{12!}{k! \cdot (12-k)!} x^k \cdot (1-x)^{12-k}, \quad (2)$$

where x is the mole fraction of UO_2 . By direct summation, $\bar{\theta}$ is obtained as

$$\bar{\theta} = x \cdot 12\delta = x \cdot \theta_{\text{pure } UO_2}. \quad (3)$$

In the case where next-nearest neighbor interaction also significantly contributes to the Weiss constant, the average value of θ will be given by

$$\bar{\theta} = \sum_{k=0}^{12} f_k \cdot k \cdot \delta + \sum_{k=0}^6 f'_k \cdot k \cdot \delta', \quad (4)$$

where f'_k is the fraction of the U^{4+} ion having k U^{4+} next nearest neighbors and δ' represents the contribution of one of the equivalent next nearest neighbors to the total θ .

The fraction f'_k is given by

$$f'_k = \frac{6!}{k! \cdot (6-k)!} x^k \cdot (1-x)^{6-k}. \quad (5)$$

Then a following equation is obtained,

$$\begin{aligned}\bar{\theta} &= x (12\delta + 6\delta') \\ &= x \cdot \theta_{\text{pure UO}_2}.\end{aligned}\quad (6)$$

Equation (6) shows that θ is a linear function of UO_2 concentration in the solid solutions even if next nearest interaction is taken into account. It also shows that the Weiss constant is zero if UO_2 is infinitely diluted with ThO_2 . The experimental curves, however, do not approach 0 K at 100 % ThO_2 . This discrepancy has been observed fairly often in the other systems, and in some cases it is discussed on the basis of clustering of magnetic ions in the dilute limit ^{11, 15)}, but there is no reason that clustering of uranium ions occurs in this case, i.e., Vegard's law holds in the lattice parameter change. It is likely that Van Vleck's temperature-independent susceptibility contributes to the experimental susceptibility to some extent.

(e) Néel temperature

The variation of T_N with uranium concentration is shown in Fig. 5. The data seem to be followed by a straight line which falls to $T_N = 0$ at ~54 mole% UO_2 , although the point at 60 mole% UO_2 deviates slightly from the line. According to the experimental results for the samples with 50 mole% UO_2 shown in Fig. 3, antiferromagnetism does not appear at this concentration of the solid solution. From these facts, it can be safely estimated that the critical concentration is between 50~55 mole% UO_2 , which is close to the results of Comly. The linear dependence of

T_N on concentration supports the idea that the ground state of the U^{4+} ion in UO_2 is triplet^{3,16)}. The T_N change in the UO_2 - ThO_2 system has been also determined by the measurements of the linear thermal expansion coefficient⁹⁾ and by the measurements of intensity of the (100) magnetic reflection in neutron diffraction⁸⁾. The results indicated that a linear dependence of T_N on concentration does not hold at low UO_2 concentrations and that the critical concentration of U^{4+} ion is lower than that determined by magnetic susceptibility measurements. A plausible reason for this difference is the oxidation of the solid solution during heating. The deviation from linearity might be also observed if the U^{5+} ion is contained in the solid solution of U^{4+} ion¹⁷⁾.

(f) Change in J_1 and J_2

The magnetic structure of UO_2 determined by neutron diffraction experiments^{18~21)} is of type I. Smart²²⁾ gave the molecular field relation for θ and T_N in terms of two exchange interactions J_1 and J_2 for various lattices and for various types of order. J_1 and J_2 represent magnetic interactions between nearest neighbor spins and next-nearest neighbor spins, respectively. For face-centered cubic lattices with the first kind of magnetic ordering, the molecular field relations between T_N , θ , J_1 and J_2 are given by

$$T_N = 2/3S(S+1)(-4J_1+6J_2), \quad (7)$$

$$\theta = 2/3S(S+1)(12J_1+6J_2), \quad (8)$$

where J_1 and J_2 are given in Kelvin. It can be said that

T_N is a lattice-dependent quantity which is a measure of the lowest energy of the magnetic ions in the lattice, whereas θ gives the strength of total interactions. The values of J_1 and J_2 determined are plotted against composition in Fig. 6. Both J_1 and J_2 decrease monotonously with ThO_2 content. This is considered to reflect the dilution effect with ThO_2 . A slow decrease of J_2 may be due to a fact that the magnetic interaction between next-nearest uranium ions is through oxygen ions intervening between them. The effect of dilution with ThO_2 should be alleviated in the indirect interaction of J_2 . Consequently, the effect would be much smaller on the interaction between next-nearest neighbor spins than on that between nearest neighbor spins.

(Y.Hinatsu and T.Fujino)

References

- 1) Slowinski, E., Elliott, N.: Acta Cryst., **5**, 768 (1952).
- 2) Hutchison, Jr. C.A., Candela, G.A.: J.Chem.Phys., **27**, 707 (1957).
- 3) Comly, J.B.: J.Appl.Phys., **39**, 716 (1968).
- 4) Cowley R.A., Dolling, G.: Phys.Rev., **167**, 464 (1968).
- 5) Cohen, I., Berman, R.M.: J.Nucl.Mater., **18**, 77 (1966).
- 6) Trzebiatowski, W., Selwood, P.W.: J.Amer.Chem.Soc., **72**, 4504 (1950).
- 7) Dawson, J.K., Lister, M.W.: J.Chem.Soc. 5041 (1952).
- 8) Sabine, T.M., Smith, G.B., Reeve, K.D.: J.Phys. C, **7**, 4513 (1974).
- 9) White, G.K., Sheard, F.W.: J.Low Temp.Phys., **14**, 445

- (1974).
- 10) Sparks, L.L., Powell, R.L.: J.Res.,Nat.Bur.Stand.(U.S.)
76A, 263 (1972).
 - 11) Chechernikov, V.I., Shavishvili, T.M., Pletyushkin, V.A.,
Slovyanskikh, V.K.: Sov.Phys.JETP **28**, 81 (1969).
 - 12) Selwood, P.W., Lyon, L., Ellis, M.: J.Amer.Chem.Soc.,
73, 2310 (1951).
 - 13) Selwood, P.W.: "Magnetochemistry", (1956), Interscience.
 - 14) Corliss, L., Delabarre, Y., Elliott, N.: J.Chem.Phys.,
18, 1256 (1950).
 - 15) Wang, F.F., Kestigian, M.: Phys.Stat.Sol., **23**, 289 (1967).
 - 16) Erdos, P., Robinson, J.M.: "The Physics of Actinide
Compounds", (1983), Plenum Press.
 - 17) Hinatsu, Y., Fujino, T.: to be submitted.
 - 18) Frazer, B.C., Shirane, G., Cox, D.E., Olsen, C.E.:
Phys.Rev., **140**, A1448 (1965).
 - 19) Willis, B.T.M., Taylor, R.I.: Phys.Lett., **17**, 188 (1965).
 - 20) Faber, Jr. J., Lander, G.H., Cooper, B.R.: Phys.Rev.
Lett., **35**, 1770 (1975).
 - 21) Faber, Jr. J., Lander, G.H.: Phys.Rev., **B14**, 1151 (1976).
 - 22) Rado, G.T., Suhl, H.(ed): "Magnetism III", (1963),
Academic Press.

Publication List

- (1) Hinatsu, Y., Fujino, T.: "Magnetic susceptibilities of
UO₂-ThO₂ Solid Solutions", J.Solid State Chem., **60**, No.2
(1985) in press.

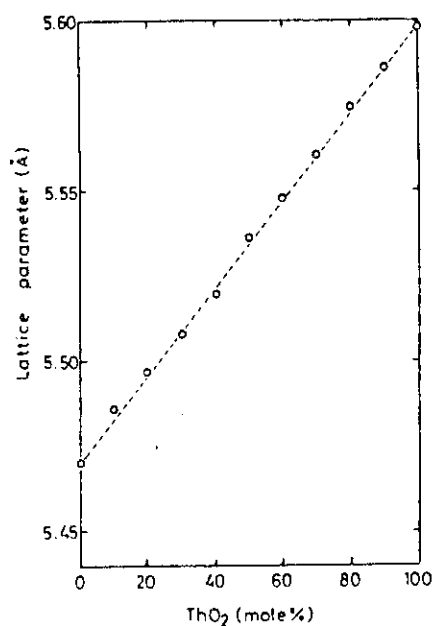
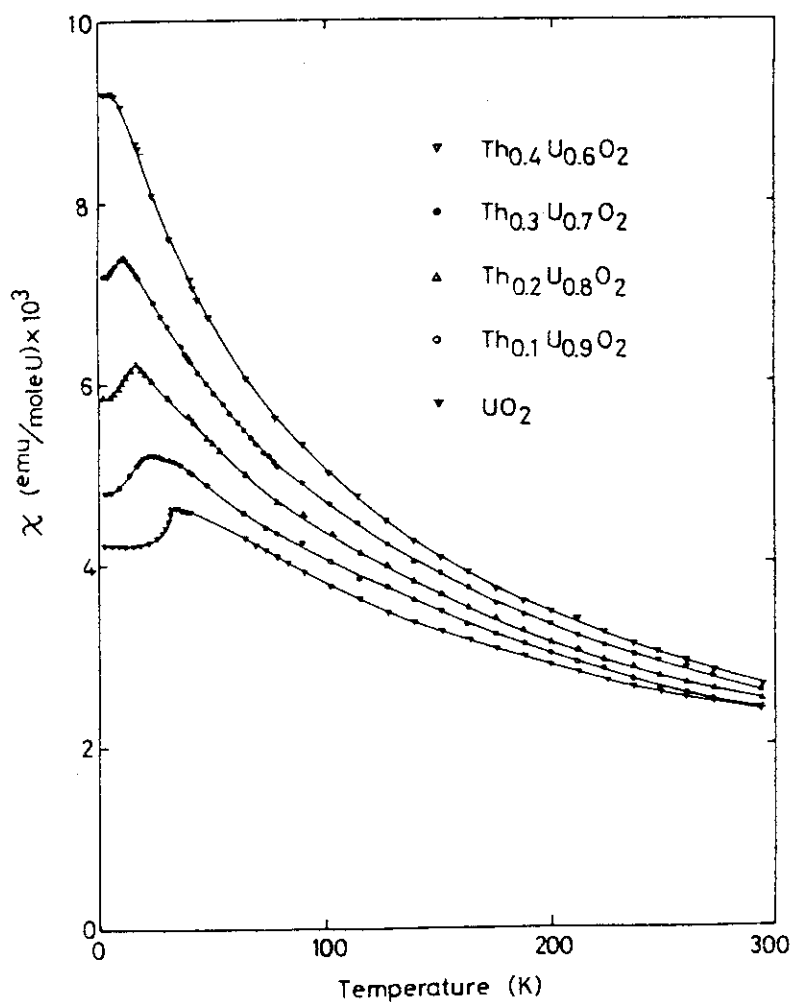


FIG. 1. Variation of lattice parameter with composition.

FIG. 2. Magnetic susceptibilities per mole uranium ion versus temperature for the solid solutions of the concentrated UO₂ range.

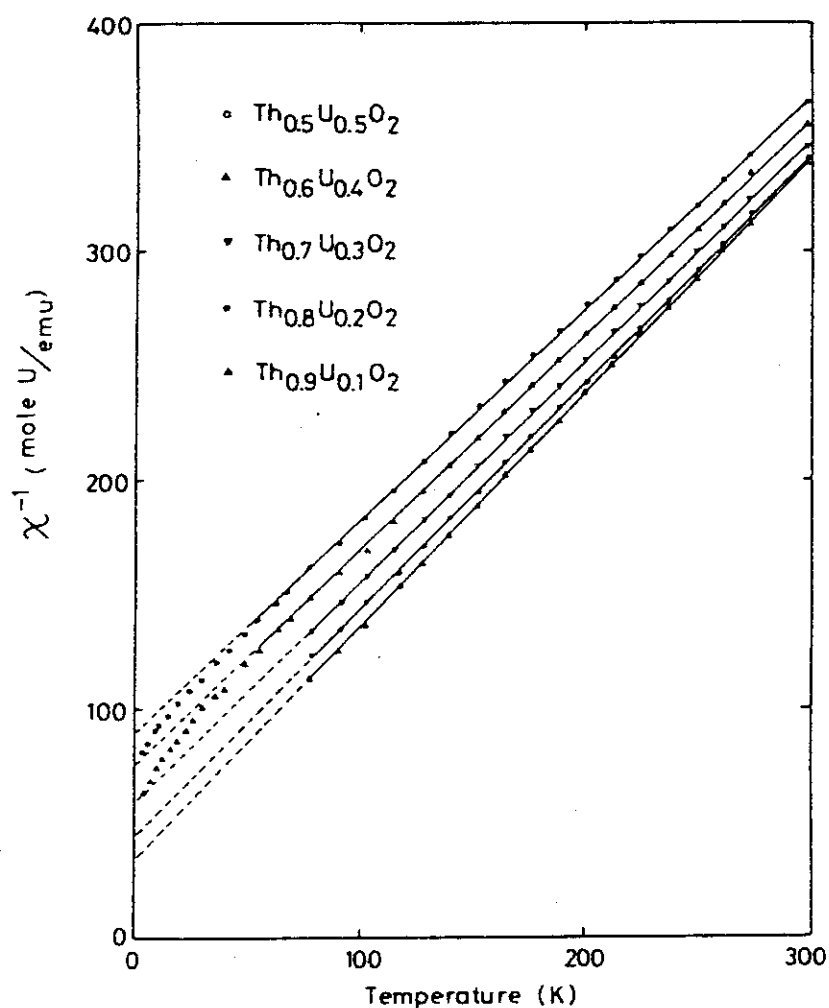


FIG. 3. Inverse magnetic susceptibilities per mole uranium ion versus temperature for the solid solutions of the dilute UO_2 range.

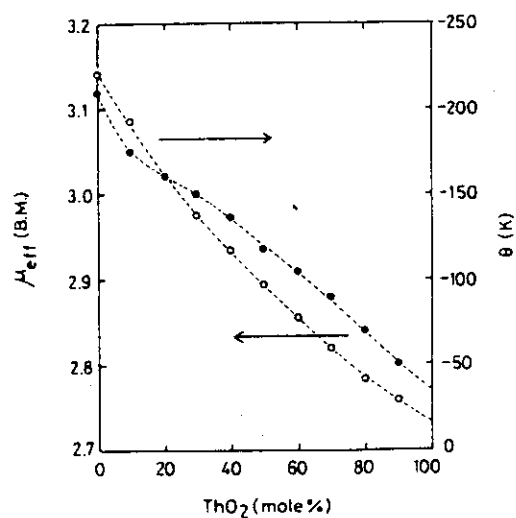


FIG. 4. Variation of magnetic moment and Weiss constant with composition.

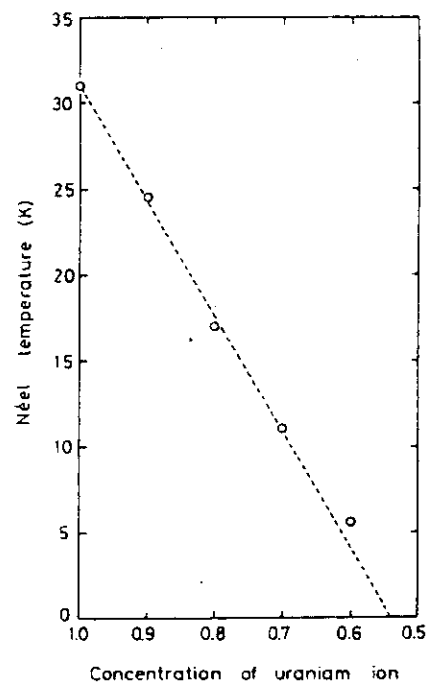


FIG. 5. Variation of Néel temperature with concentration of uranium ion.

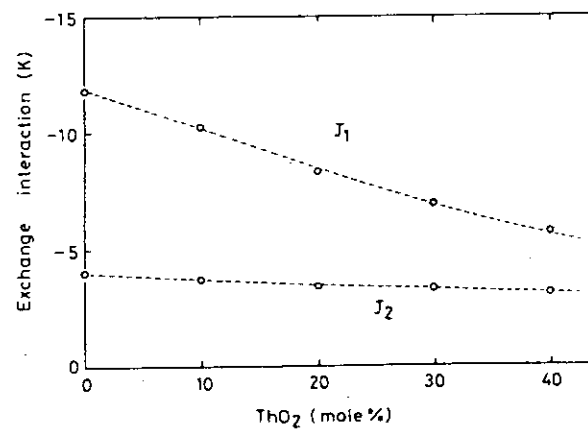


FIG. 6. Variation of J_1 and J_2 with composition.

10. SOLIDIFICATION OF HIGH-LEVEL RADIOACTIVE WASTE INTO SYNTHETIC MINERAL-LIKE COMPOUNDS

T. Muromura, Y. Hinatsu and

T. Fujino

10.1 Phase Study

10.1.1 Introduction (1,2)

The waste forms of high-level radioactive waste (HLW) resulting from reprocessing of spent nuclear fuels can be classified into two groups. The one is the glass waste form, in which radioactive elements in HLW are homogeneously dissolved with frit by melting. The other is the crystalline form such as alumina-based ceramics, titania-based ceramics, SYNROC, and phosphate-tailored ceramics. They are made by modifying the composition of HLW with selected additives, so that an assemblage of mutual compatible crystalline phases is produced. Generally, the phases thus produced are designed to be synthetic mineral-like compounds that would be stable under weathering, change of circumstances, and irradiation for long time of 10^3 - 10^6 years¹⁾.

This study represents one approach on the immobilization of HLW using stabilized zirconia with fluorite structure as a host phase of the actinide elements, and is devoted primarily to the examination of phase behaviors of the crystalline waste form produced. The major techniques used in this study are mixing of HLW and additive solutions by usual way in glass beakers, and heat-treatments under high and low oxygen pressures. The products are identified by X-ray diffraction

diffraction analysis. The reaction behavior has been observed by thermogravimetric and chemical analyses.

10.1.2 Consideration

(1) Additives

The roll of additives is to modify the composition of HLW, so that the crystalline waste form consisting of two or more phases would be produced. These phases are required to be thermodynamically compatible and chemically stable under various conditions. Furthermore, the additives are desirable to be chemically stable especially in the presence of water, fully abundant and easily available. These requisites seem to be satisfied by such ceramic materials as alumina Al_2O_3 , magnesia MgO and zirconia ZrO_2 . There is another advantage in the chemical properties of these ceramic materials: the nitrates of Al, Mg and Zr are soluble into water and/or in dilute nitric acid solutions. Accordingly, it becomes possible to obtain an intimate mixture of additives and HLW solutions. This seems to be favorable for fast completion of solid state reactions during heat-treatment at high temperatures.

(2) Host phases

Host phase of actinides²⁾: Many kinds of radioactive elements are dissolved in HLW. Among them, the actinide elements such as Pu, Am and Cm appear to have great biological hazards because of their long half-lives and alpha activities. For their immobilization, there are many candidates as their host phase: monazite, perovskite, zirconolite, stabilized zirconia with fluorite structure and others, as shown in Table 1. In the present study, the stabilized zirconia has been chosen as

Table 1 Comparison of some properties of host phases of the actinide elements

	Monazite	Perovskite	Zirconolite	Stabilized zirconia
(1) Leaching resistivity	++	++	++	++
(2) Radiation stability	++	+	++	++
(3) Phase stability	++	+	++	++
(4) Solid solubility	++	+	+	++
(5) Technol. background	+	++	+	++

+: good, ++: better

the host phase of the actinide elements because of its high irradiation stability, chemical stability and considerably wide ranges of solid solubilities. The selection of this phase would also satisfy the choice of additives in the present study.

It is well known that the stabilized zirconia can be made by addition of bivalent ions(Ca, Mg), trivalent ions(Y, Nd) and quadrivalent ions(Ce, U, Pu) into ZrO_2 ³⁾. In the present study, CaO- and Y_2O_3 -stabilized zirconias would be examined from the stand points of phase equilibria and chemical stabilities.

Host phase of alkali and alkaline earth elements⁴⁾: For the immobilization of Sr and Ba in HLW, which would be apt to be excluded from the fluorite phase, alumina Al_2O_3 seems to be an effective additive because of its high chemical reactivity with the alkaline earth metals. Many compounds have been formed in the binary systems, Al_2O_3 -CaO, Al_2O_3 -SrO, and Al_2O_3 -BaO. Among them the magnetoplumbite type phases, $CaO \cdot 6Al_2O_3$, $SrO \cdot 6Al_2O_3$, $BaO \cdot 6Al_2O_3$ and their mutual solid

solutions, seem to be promising as the host phase of the Sr and Ba.

The beta-alumina phases such as $\text{Na}_2\text{O} \cdot 11\text{Al}_2\text{O}_3$ and $\text{Na}_2\text{O} \cdot \text{MgO} \cdot 15\text{Al}_2\text{O}_3$ are also some of the magnetoplumbite type phases. They would be able to be the host phase of alkali metals in HLW such as Cs and Rb.

Accordingly, provided that alumina is thermodynamically in equilibrium with the stabilized zirconia phase, the Sr and Ba excluded from the stabilized zirconia would react with the alumina and make the magnetoplumbite. Thus, the beta-alumina phase would be also produced by the reaction between the alkali metals and excess alumina.

Host phase of Fe, Cr and Ni⁵⁾: Most of Fe, Cr and Ni come from scales of equipments in the reprocessing plants. If ZrO_2 , MgO and Al_2O_3 are used as the additives for the solidification of HLW, it is likely that the spinel phase $\text{MgO} \cdot \text{Al}_2\text{O}_3$ would be produced with the fluorite and magnetoplumbite phases. The site of Mg in this phase can be substituted by Fe(II), Co(II) and Ni(II), and that of Al by Cr(III). Hence it seems that the spinel phase would become a host phase of most of nonradioactive elements in HLW.

Host phase of noble metals⁶⁾: Ruthenium in HLW is one of the most radioactive elements. The vapor pressures of its oxides are considerably high, so that it is desirable to reduce them into low valency states, e.g. into its metallic state. It is well known that the platinum group elements, Ru, Rh and Pd, make alloys with Mo and Tc in the irradiated nuclear fuels under low oxygen pressures. The alloys become non-soluble

residues in the reprocessing of the spent fuels.

Thus, the noble metals will become alloys in the waste form with Mo and Tc in the atmosphere of low oxygen pressures. If the oxygen pressure is higher than 10^{-14} atm at 1,200-1,300°C, some amounts of Mo and Tc are oxidized and incorporated into the other phases, and Pd-Rh base alloys will be produced in the waste form. The scheelite type phase (Sr,Ba)MoO₄ will be also produced in the products as in the case of irradiated (Th,U)O₂ fuel under high oxygen pressures.

(3) Reaction atmosphere

The oxides of Mo, Tc, Ru and the alkali metals in HLW would tend to vaporize during solidification reaction at high temperatures especially in the atmosphere of high oxygen pressures. The reaction conditions of the calcination and heat-treatment processes are considered in the following.

Ruthenium oxides vaporize in the atmosphere of high oxygen pressures at high temperatures. This may be attributed to the formation of RuO₄ depending on temperature and oxygen pressure. When the temperature is raised above 1,100°C, the vapor pressure of RuO₄ becomes above 10^{-3} atm under 1 atm O₂. Molybdenum oxides would also vaporize during calcination and heat-treatment due to formation of MoO₃ under the atmosphere of high oxygen pressures. The oxides would be reduced to metal with low vapor pressures in the atmosphere of low oxygen pressures. Cesium oxide Cs₂O has a melting point of 490°C and vaporizes in the atmosphere of high oxygen pressures through formation of higher oxides such as Cs₂O₂ and CsO₂. Under the atmosphere of low oxygen pressures, it will vaporize predominantly by decomposition

to the elements.

In the present study, therefore, an atmosphere of low oxygen pressures, 4% H_2 + 96%He, will be employed for the calcination and heat treatment of the residues obtained after evaporation of the solutions containing simulated HLW. In this atmosphere, the oxides of Mo, Tc and Ru will be reduced to their metallic states with low vapor pressures, which will make the alloys as described above.

10.1.3 Experimental (3)

The reaction between simulated HLW and CaO-stabilized zirconia with fluorite structure has been studied at temperatures from 1,000 to 1,500°C in air and in a mixture of 4% H_2 + 96%He.

Table 2 Simplified formulation for high-level radioactive waste(HLW) corresponding to 33,000MWD/TMU burn-up

	Element		Oxide form		Stand-in role
	at%		Oxide	wt%	
(1) Cs	11.1		Cs_2O	10.5	15% of Cs acts as a stand-in for Rb.
(2) Sr	9.9		SrO	7.0	50% for Ba.
(3) Ce	15.5		CeO_2	16.4	33% for Pr, Pu, Am and Cm.
(4) Nd	24.2		Nd_2O_3	27.6	46% for La, Sm, Y, Eu, Gd and Pm.
(5) U	4.3		UO_2	7.8	44% for Np.
(6) Mo	24.5		MoO_2	21.3	18% for Tc.
(7) Ru	10.5		RuO_2	9.4	24% for Rh.

Corresponding to 33,000 MWD/TMU

Simplified formulation of HLW: The HLW contains more than 30 radioactive elements. In the approach presented here, the composition of HLW has been simplified, as shown in Table 2. Several types of substitutions or chemical stand-ins are presented in the last column of the table.

Experimental procedure: The composition of CaO-stabilized zirconia was 8 wt% CaO + 92 wt% ZrO₂. Mixtures of the stabilized

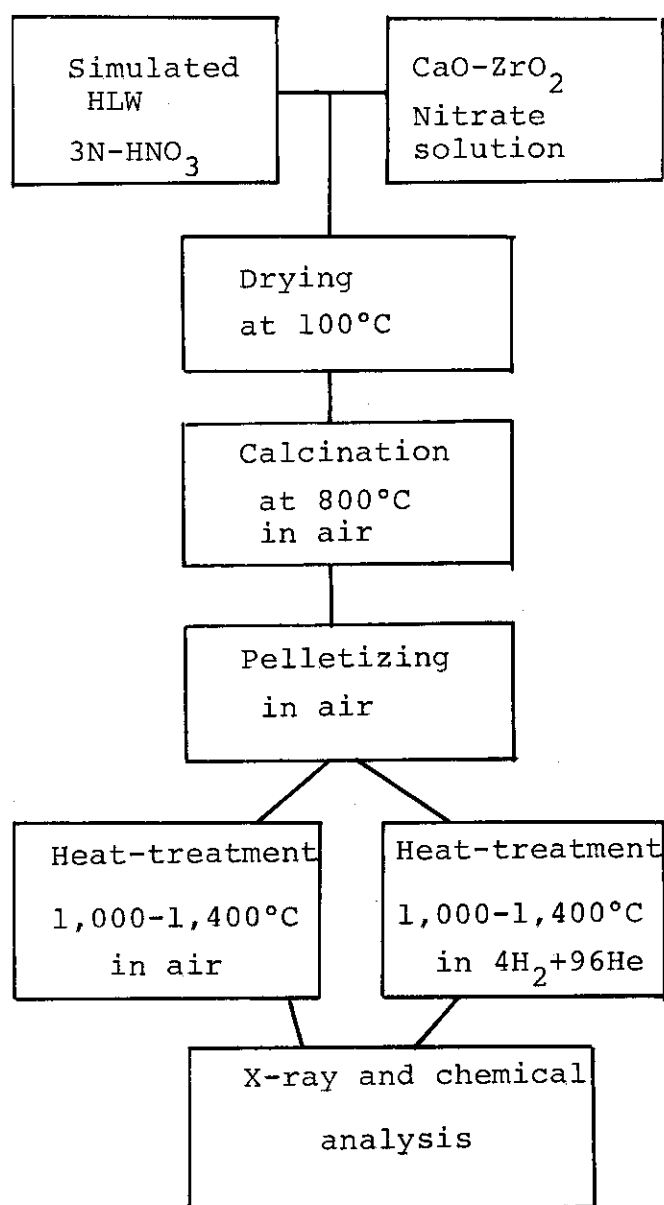


Figure 1. Experimental procedure

zirconia and simulated HLW solutions were prepared in various mixing ratios. They were evaporated to dryness in air. The resulting materials obtained were calcined in air at 800°C. The products were then compacted into pellets and heat-treated in air or in a mixture of 4% H_2 + 96%He. After the heat-treatment, the pellets were crushed and then submitted to X-ray and chemical analyses. The procedure is shown in Figure 1.

10.1.4 Conclusion

- (1) In the evaporation of mixtures of the stabilized zirconia and simulated HLW solutions, it has been shown that considerable amount of Ru was lost by vaporization due to formation of RuO_4 .
- (2) In the calcination process, dehydration and denitration proceed below 500°C.
- (3) About 4 wt% of simulated HLW was homogeneously incorporated into the fluorite phase, of which lattice parameter increased with HLW content according to the equation:

$$a = 0.5134 + 0.00028x \quad (\text{nm}),$$

where x is HLW content in wt%, as shown in Figure 2.

When the HLW content was in the range of 4-20 wt%, two phases were in equilibrium: the fluorite and scheelite phases. The lattice parameter of the fluorite phase varies with HLW content in the form:

$$a = 0.5141 + 0.00014x \quad (\text{nm})$$

The actinide and rare earth elements were incorporated in the fluorite phase.

Molibdenum and strontium excluded from the fluorite phase combined and made a scheelite phase.

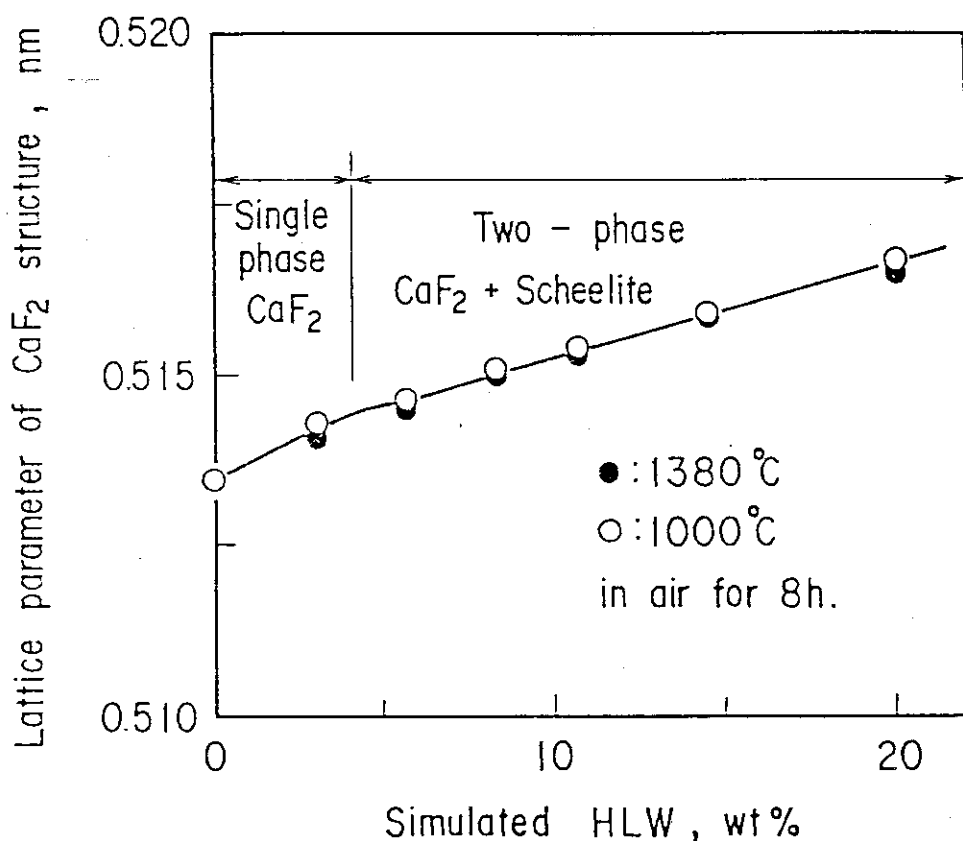


Figure 2. Phases produced and the lattice parameter variation of the fluorite phase with HLW content
Heat-treatment: in air for 8 h

- (4) Under the heat treatment in a mixture of H_2+He , three phases were formed: the fluorite phase, perovskite phase and Mo alloy. The actinide and rare earth elements were soluble in the fluorite phase, of which lattice parameter increased with HLW content by the expression:

$$a = 0.5134 + 0.00022x \quad (\text{nm})$$

The phases and lattice parameter variation of the fluorite phase is shown in Figure 3.

From these results described above, it has been shown that the stabilized zirconia with fluorite structure would be an excellent host phase for the immobilization of the actinide

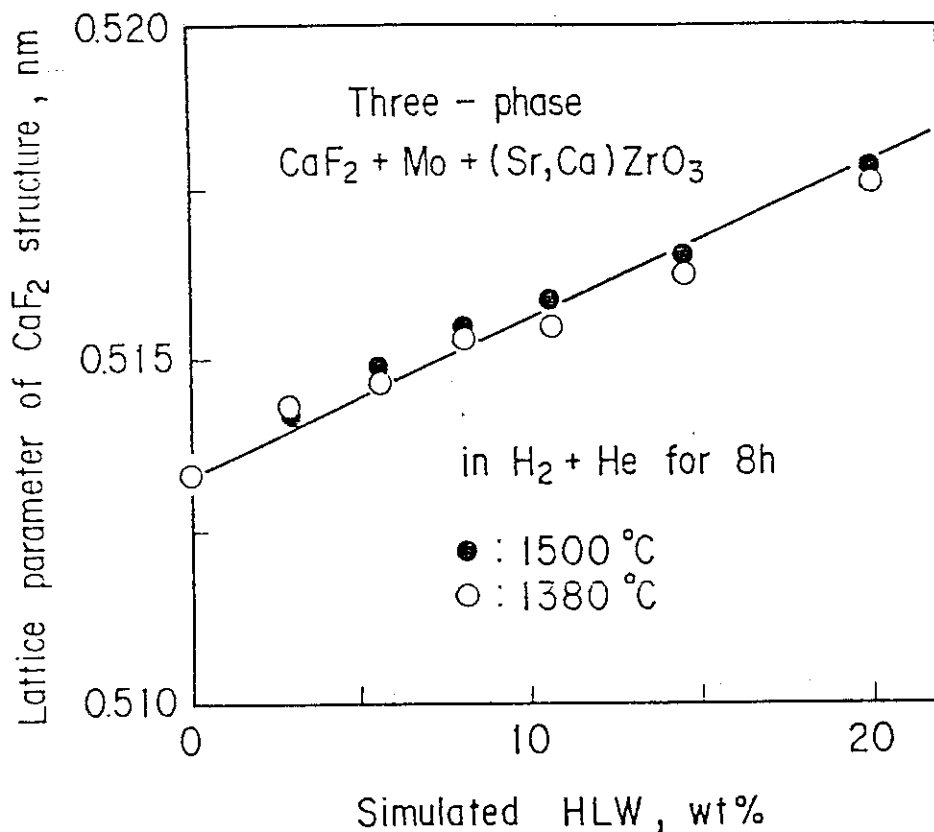


Figure 3. Phases produced and lattice parameter variation of the fluorite phase with HLW content

Heat-treatment: in 4%H₂+96%He for 8 h

elements.

(T. Muromura)

Reference

- 1) Bernadzikowski, T. A. et al., J. Am. Ceram. Soc. Bull., 62, 1364 (1983)
- 2) Vance, E. R. and Pillary, K. K. S., DOE/ET 41900-5(1981)
- 3) Garvie, R. G., J. Am. Ceram. Soc., 51, 553 (1968)
- 4) Morgan, P. E. D. and Cirlic, E. H., J. Am. Ceram. Soc., 65, C-114 (1982)
- 5) Wyckoff, R. W. G., "Crystal Structure, vol. 3", p 75 (1965)

Interscience Pub., New York

- 6) Jenkins, I. L. and Brown. P. E., *Radiochimica Acta.*,
36, 25 (1984)

Publication list

- (1) Tachikawa, A. et al., "Chemical Aspects on the Treatments
of Radioactive Wastes(in Japanese)", *J. At. Energy Soc. Jpn.*,
21, 159 (1981)
- (2) Muromura, T., "Phosphate waste forms on High-level Radio-
active Waste(in Japanese)", *Kagaku-to-kogyo(Japan)*,
38(10), 183 (1985)
- (3) Muromura, T. and Hinatsu, Y., "Solubility of Simulated
High-level Radioactive Waste in CaO-stabilized Zirconia",
J. Nucl. Sci. Technol., 21, 764 (1984)

11. NUCLEAR CHEMISTRY RESEARCH

H.Okashita, T.Suzuki, S.Okazaki^{*},
T.Sonobe, M.Ohnuki, Y.Nakahara^{*},
N.Kono, S.Usuda, S.Ichikawa,
N.Shinohara and M.Magara

11.1 Measurements on Burnup Characteristics of the Japan Power Demonstration Reactor-I Full-Core Fuel Assemblies

11.1.1 Introduction

Most of the nuclear reactors have their burnup calculation codes for the fuel management. The accuracy of the calculation, however, is scarcely verified through comparison with the actual burnup measurements. On the occasion of the full-core discharge of the Japan Power Demonstration Reactor-I (JPDR), burnup measurements of all the fuel assemblies were performed in collaboration with the Tank-type Critical Assembly (TCA) group of the JAERI and the Tokai Reprocessing Plant group of the PNC.

Non-destructive gamma-ray spectrometry is the most effective method to examine the burnup characteristics of numerous fuel assemblies in detail, although the data obtained by this method, which gives only relative values, should be calibrated by destructive (chemical) data for evaluation in absolute base. It is well recognized that the amount of ^{137}Cs in a spent fuel is a good measure for burnup and the ratio $^{134}\text{Cs}/^{137}\text{Cs}$ for plutonium formation¹⁾. Both the nuclides are the most easily detectable

* Present address: Nuclear Material Control Center (NMCC).

ones in the spent fuel by gamma-ray spectrometry.

The JPDR-I was operated from October 1963 to August 1969 with frequent shutdowns for several experimental purposes. The assembly burnups were estimated to be in the range from 110 to 5,640 MWd/t by means of FLARE code utilizing the operation data²⁾. Detailed description of the JPDR-I core and operation history is given elsewhere¹⁾.

Seventy two spent fuel assemblies discharged from the JPDR-I were subjected to the non-destructive gamma-ray spectrometry and dissolved at the Tokai Reprocessing Plant. The respective 19 batch-samples were taken out of the dissolver vessels and analyzed chemically in detail.

11.1.2 Non-destructive Gamma-ray Spectrometry

The non-destructive measurements were carried out in two steps. The first was a series of rod-wise measurements for a typical assembly A20 and the second a series of assembly-wise measurements for the full-core assemblies except 3 assemblies which had been destroyed for post irradiation examination.

In the rod-wise measurements, correlation between the non-destructive gamma-ray spectrometry data (96 points for selected 7 rods) and the burnup or the Pu/U atom ratio were established with the corresponding destructive measurement data (Figs. 1 and 2)¹⁾. The average burnup and the Pu/U ratio in the assembly A20 were derived from the correlations for the 8 rods measured and interpolation for the other rods assuming their quadratic distribution and diagonal symmetries in the assembly.

Assembly-wise measurements were performed for the 72 assemblies prior to shipment to the Tokai Reprocessing Plant. Twelve

assemblies were measured at 10 points on every four sides, while the other 60 were at 4 points on selected one side only. Among the 12 assemblies, A8, which had the same irradiation history of A20 in the symmetrical position of the core, was chosen as a reference and the others were representatives of the 11 positions in one-octant region of the core. The measured gamma-ray intensities and the intensity ratios at the 40 points on assembly surfaces were summed up with weights to obtain their averages in each assembly. For the assembly measured at only the four points, the averages were calculated by assuming that their relative distributions were the same as those in the assemblies submitted to the detailed measurements. Details of the assembly-wise gamma-ray spectrometry are provided elsewhere³⁾. The average burnup and the Pu/U ratio of each assembly were derived from the averaged ^{137}Cs intensity and the averaged $^{134}\text{Cs}/^{137}\text{Cs}$ ratio using the correlation obtained by the assembly A20 with correction for decay time and detector efficiency and assuming the A8 had the same values of burnup and Pu/U ratio as the A20.

11.1.3 Destructive Measurements

At the Tokai Reprocessing Plant, the JPDR-I assemblies were arranged into 19 batches in consideration of similar irradiation history (burnup) and dissolved in 3M HNO_3 solutions. An appropriate aliquot of the dissolver solution in each batch was taken and evaporated gently to near dryness. Then, the 19 batch-samples were set back to the JAERI.

Each dried sample received was dissolved in HNO_3 including Cs carrier. Appropriate aliquots were weighed and subjected to analysis. Precise gamma-ray spectrometry was applied to one of the

aliquots for determination of gamma-ray emitting fission product nuclides. By using the other aliquot, Am, Cm, Nd, Pu and U were subsequently separated by ion exchange⁴⁾. Amounts of Nd, Pu and U were determined by means of mass-spectrometric isotope-dilution method, and ^{237}Np , ^{238}Pu , ^{241}Am , ^{242}Cm (as $^{242\text{m}}\text{Am}$) and ^{244}Cm by alpha-ray spectrometry.

Burnups were evaluated for the individual batch-samples using the following equation:

$$\text{BU (\%)} = \frac{100 \text{ K } R_{\text{FP}/\text{U}}/Y_{\text{FP}}}{1 + R_{\text{Pu}/\text{U}} + \text{K } R_{\text{FP}/\text{U}}/Y_{\text{FP}}},$$

where $R_{\text{FP}/\text{U}}$, $R_{\text{Pu}/\text{U}}$: Atom ratio of ^{137}Cs or ^{148}Nd to U, and Pu to U,

Y_{FP} : Cumulative fission yield of ^{137}Cs or ^{148}Nd ,

and K : Inpile-outpile decay factor of the fission product nuclides, which was precisely evaluated according to the detailed irradiation history.

Comparison of the burnups obtained showed that the values from ^{137}Cs were systematically lower than those from ^{148}Nd , 2.3% in average. This discrepancy would be ascribed to ambiguities in the nuclear data used, since the experimental errors were confirmed to be within 1%.

11.1.4 Discussion

The evaluated values on burnup characteristics of the JPDR-I fuels based on the destructive (DA) and the non-destructive assembly-wise (NDA) measurements are summarized in Table 1 for the 19 batches, where the NDA values were obtained by averaging or summing those among the assemblies relevant to the same repro-

cessing batch. The NDA overestimated systematically both of burnups and Pu/U ratios by 2 to 4%. Causes of the differences are considered: some overestimation in the averaging method on the reference assembly A20, failure of the assumption that the assemblies A20 and A8 had the same power histories and so forth. Apart from the remaining problems, these results show that applicability of the non-destructive gamma-ray spectrometry to the spent fuel examination is well demonstrated in a practical sense.

The ratios of ^{237}Np , ^{241}Am , $^{242\text{m}}\text{Am}$ and ^{244}Cm to U are plotted against the $^{134}\text{Cs}/^{137}\text{Cs}$ ratio in both logarithmic scales, as shown Figs. 3 to 6. The former ratios, y , are expressed fairly well as the function of the latter, x , as

$$y = c x^p,$$

where c and p are constants in the individual combinations. Since all of the transuranium nuclides are produced mainly by successive neutron captures of ^{238}U , the exponent p should correspond approximately to the number of captured neutrons, and hardly affected by power histories and cooling time in this case. Therefore it is suggested that the amounts of the transuranium nuclides accumulated in spent fuels may be estimated from non-destructively measured activity ratios of $^{134}\text{Cs}/^{137}\text{Cs}$, when the constant C is determined by some reference measurements. However, further examination should be required to assure the applicability of this method to higher burnup fuels.

Comprehensive data and discussions are given elsewhere [1].

(H.Okashita)

References

- 1) Natsume, H., Okashita, H., Umezawa, H., Okazaki, S., Suzuki, T., Ohnuki, M., Sonobe, T., Nakahara, Y., Ichikawa, S., Usuda, S., Matsuura, S., Tsuruta, H., Suzaki, T., Komori, T., Tamura, S., Gunji, K., Tamura, T.: J.Nucl.Sci.Technol., 14, 745(1977).
- 2) Ezure, H., Tanaka, T., Naito, T., Sekiguchi, K., Kawasaki, M., Shimooke, T.: JAERI-memo(open) 4083(1970)(in Japanese).
- 3) Suzaki, T., Tsuruta, H. Matsuura, S.: JAERI-1296(1985).
- 4) Natsume, H., Umezawa, H., Okazaki, S., Suzuki, T., Sonobe, T., Usuda, S.: J.Nucl.Sci.Technol., 9, 737(1972).

Publication List

- [1] Suzaki, T., Okazaki, S., Okashita, H., Kobayashi, I., Suzuki, T., Kohno, N., Ohnuki, M., Shinohara, N., Sonobe, T., Ohno, A., Murakami, K., Umezawa, H., Tsuruta, H., Matsuura, S., Asakura, Y., Araya, S., Yamanouchi, T.: "Non-Destructive and Destructive Measurements on Burnup Characteristics of the Japan Power Demonstration Reactor-I Full-Core Fuel Assemblies", J.Nucl.Sci.Technol., 23(No.1) 53(1986).

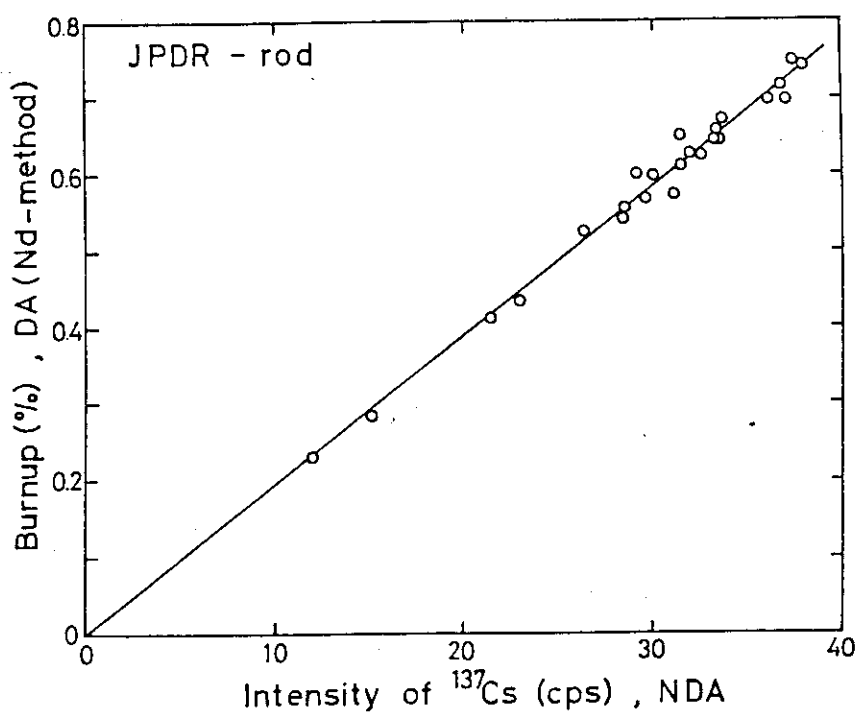


Fig. 1 Correlation between ^{137}Cs intensities by non-destructive gamma-ray spectrometry and burnups by the ^{148}Nd method on the fuel rods in Assembly A20.

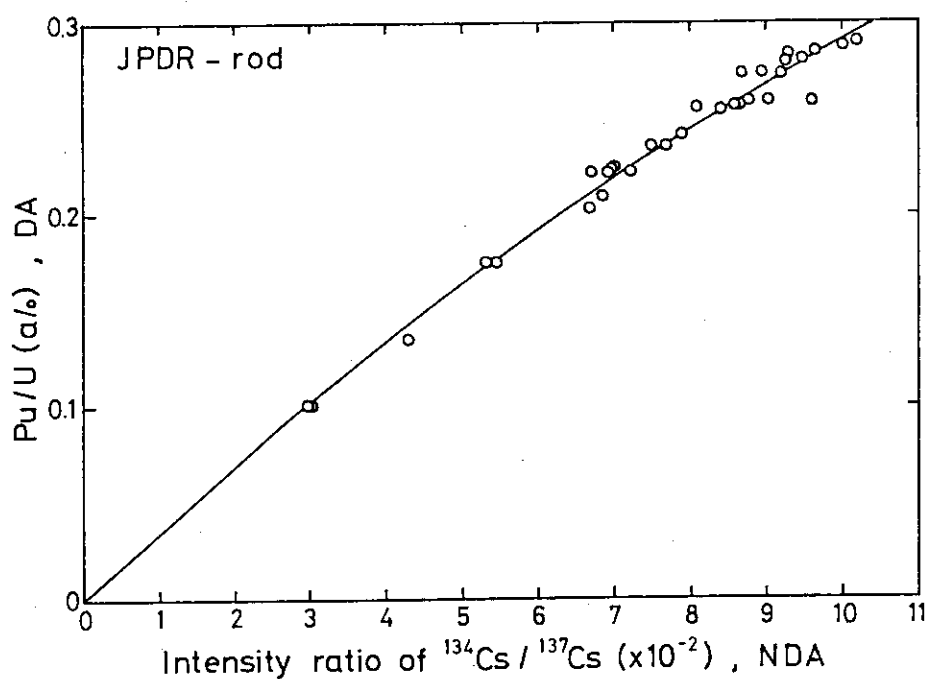


Fig. 2 Correlation between $^{134}\text{Cs}/^{137}\text{Cs}$ ratios measured non-destructively and Pu/U ratios determined destructively on the fuel rods in Assembly A20.

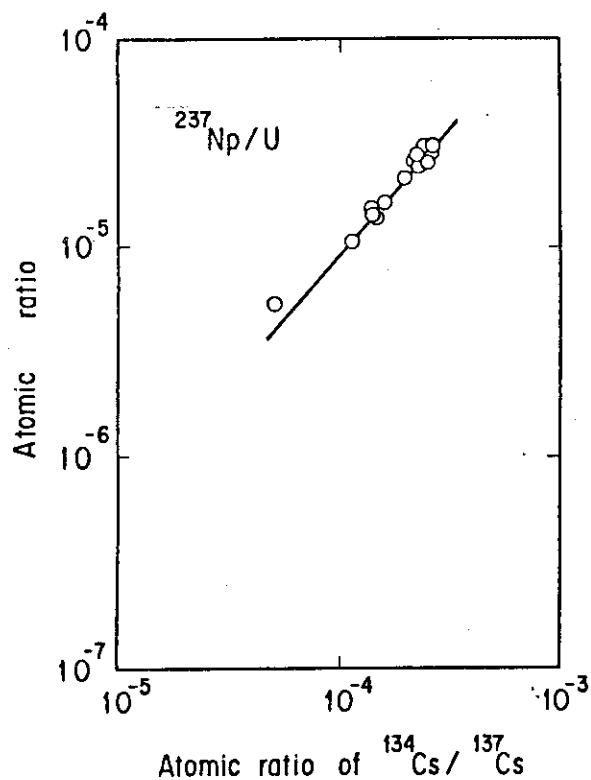


Fig. 3 Correlation between atom ratios of $^{237}\text{Np}/\text{U}$ and $^{134}\text{Cs}/^{137}\text{Cs}$.

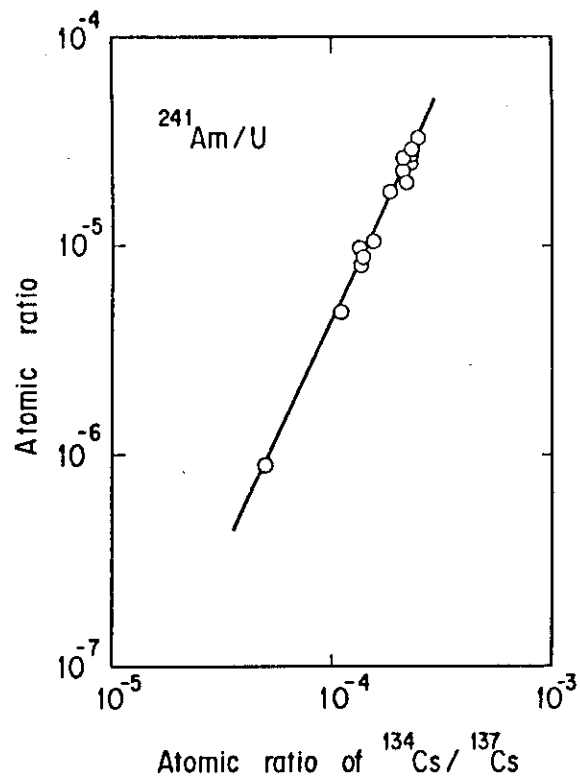


Fig. 4 Correlation between atom ratios of $^{241}\text{Am}/\text{U}$ and $^{134}\text{Cs}/^{137}\text{Cs}$.

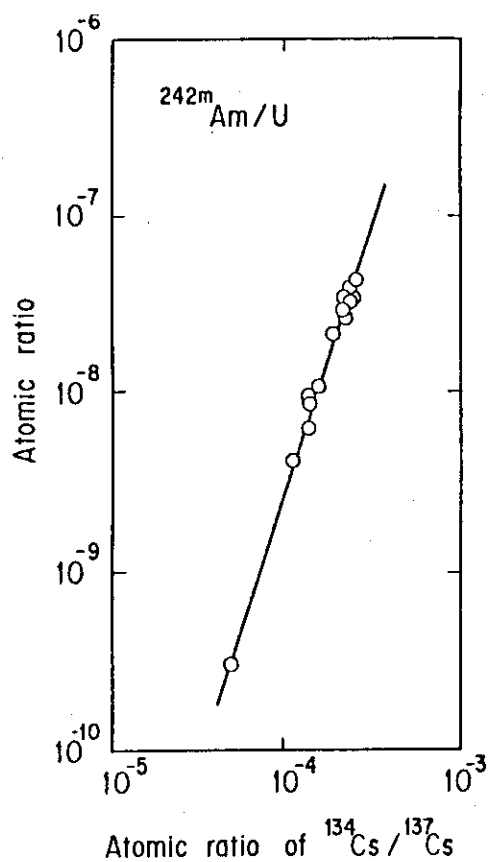


Fig. 5 Correlation between atom ratios of $^{242\text{m}}\text{Am}/\text{U}$ and $^{134}\text{Cs}/^{137}\text{Cs}$.

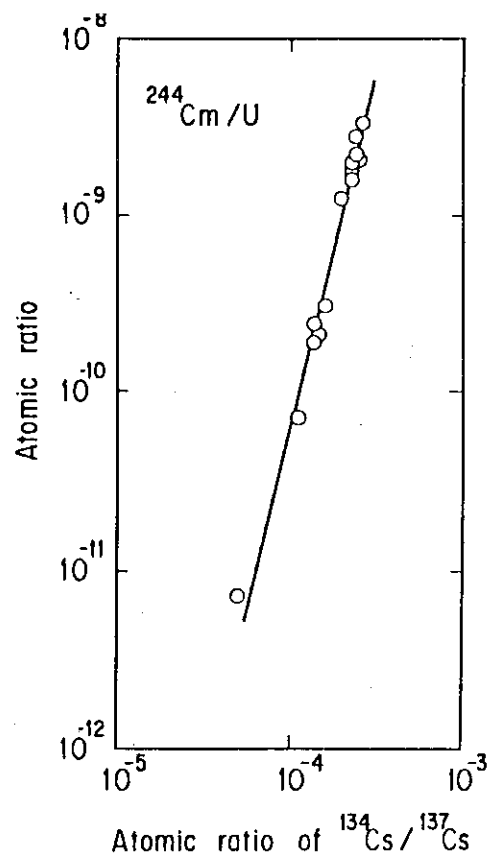


Fig. 6 Correlation between atom ratios of $^{244}\text{Cm}/\text{U}$ and $^{134}\text{Cs}/^{137}\text{Cs}$.

Table 1 Summary of destructive and non-destructive analyses
on the 19 reprocessing batches.

Reproc.	Init. U (kg)	D A				N D A						
		^{#1} 134Cs/137Cs (x10 ⁻⁴)	B U (%)	^{#2} Pu/U (x10 ⁻³)	^{#2} Pu (g)	U (kg)	^{#3} 137Cs (cps)	^{#3} 134Cs/137Cs (x10 ⁻³)	B U (%)	^{#4} Pu/U (x10 ⁻³)	^{#4} Pu (g)	U (kg)
JP-001	116.05	0.019	0.011	0.057	6.7	116.03	19.2	—	0.011	—	—	116.04
JP-002	230.69	0.516	0.140	0.638	147.6	230.22	247.1	3.73	0.131	0.52	120	230.26
JP-003	232.15	1.13	0.295	1.052	244.4	231.23	632.1	8.75	0.335	1.17	270	231.10
JP-004	232.05	1.41	0.362	1.289	299.1	230.93	690.6	9.89	0.366	1.30	303	230.90
JP-005	232.26	1.39	0.331	1.280	297.4	231.20	658.0	9.90	0.348	1.30	301	231.15
JP-006	174.08	1.39	0.378	1.355	235.8	173.19	774.3	10.32	0.410	1.36	236	173.13
JP-007	232.39	1.59	0.397	1.486	345.2	231.13	814.5	12.18	0.431	1.57	365	231.02
JP-008	232.14	2.50	0.468	2.031	470.7	230.60	868.5	17.24	0.460	2.12	490	230.58
JP-009	232.07	1.93	0.461	1.710	396.3	230.62	940.5	14.55	0.498	1.83	424	230.49
JP-010	232.08	2.54	0.482	2.090	484.1	230.49	923.1	18.21	0.489	2.21	513	230.43
JP-011	231.86	2.25	0.440	1.704	394.7	230.46	1011.4	16.45	0.535	2.04	470	230.15
JP-012	232.54	2.22	0.473	1.935	449.2	231.01	964.5	16.56	0.511	2.05	475	230.88
JP-013	231.71	2.24	0.531	2.045	472.8	230.02	1048.7	17.18	0.555	2.11	487	229.93
JP-014	232.21	2.45	0.525	2.159	500.2	230.50	1059.9	18.02	0.561	2.20	508	230.40
JP-015	232.05	2.59	0.559	2.217	513.1	230.26	1107.1	19.33	0.586	2.32	537	230.16
JP-016	232.12	—	0.495	2.174	503.6	230.49	930.4	17.35	0.492	2.13	493	230.49
JP-017	231.72	—	0.500	1.854	428.8	230.14	978.4	15.20	0.518	1.90	440	230.08
JP-018	173.83	—	0.481	1.975	342.7	172.66	949.9	15.78	0.503	1.96	340	172.61
JP-019	173.98	—	0.455	1.828	317.6	172.88	890.6	15.68	0.471	1.94	337	172.82

*1) Atom ratio as of April 1, 1982. *2) As of March 10, 1982. *3) Activity or activity ratio as of June 1, 1977.

*4) As of March 1, 1973.

11.2 Experiments of Nuclides far from β -Stability by JAERI ISOL

11.2.1 Introduction

On-line isotope separators (ISOL) connected to various types of accelerators are widely used in the study of nuclei far from β -stability^{1,2)}. The ISOL supplied by Danfysik was installed at the tandem accelerator in the JAERI. A series of investigation of short-lived neutron deficient isotopes was performed on cesium, barium and rare earths. A surface-ionization ion source, which can ionized effectively these elements, was developed to facilitate the aimed experiments.

The ISOL first tested in off-line and now frequently used in on-line operation. Using fusion-evaporation reaction, neutron-deficient isotopes for the following elements were mass-separated and investigated by decay-spectroscopy: Cs-Xe, Ba-Cs and Nd-Pr.

The present paper describes the performed of the surface ionization ion-source and the results of on-line experiments.

11.2.2 Description of the ISOL

The JAERI ISOL facility is shown schematically in Fig.1. It is constituted of four major equipments; an isotope separator (included an ion-source), connection system of the separator to the accelerator beam line, a tape-transport system and a data acquisition system.

The isotope separator has a 55° deflection and 1.5 m radius-of-curvature. Resolving power of the separator is more than 1200 and mass dispersion at the focal plane is 1500 mm/M (M =mass).

Oil-diffusion vacuum pumps are used to keep high vacuum in the ion-source and other parts. The ion-source is connected to

the beam line of tandem accelerator through a differential-pumping system and a thin window (2 μm HAVAR foil), which keep a hydrocarbon "free" vacuum (10^{-5} pa) in the accelerator side.

The data-acquisition system is based on a PDP 11/04 computer system interfaced to A/D converters. The tape-transport system is also connected to the PDP 11/04 computer performing the tape control and the data accumulation automatically.

11.2.3 Design and Performance of the Ion-source

The surface-ionization ion source constructed is shown in Fig.2. The ion-source consists of a vaporizer, an ionizer, a couple of tungsten filaments and a heat shield. The tungsten ionizer is a form of hollow cylinder and its inner surface is covered with rhenium foil. A recoil catcher, carbon or tantalum foil, is mounted inside the vaporizer. A target is usually placed at the vaporizer entrance. If the target is likely to melt due to the high temperature, it is moved 5 mm outward and the vaporizer entrance is sealed by a thin foil (20 $\mu\text{g}/\text{cm}^2$ carbon or 1.5 μm tantalum foil). The reaction products emerge from target at a small angle with respect to the projectile direction. The energy of recoil nuclei is enough to enable them to pass the thin foil to the vaporizer cavity. For instance, in bombarding Nb target by 160 MeV ^{32}S ions and Au target by 120 MeV ^{16}O ions the kinetic energies are equal to about 40 MeV and 6 MeV respectively.

The ionizer and vaporizer are heated by electron bombardment from the tungsten filaments. The maximum voltage between the filament and ionizer is equal to 600 V and maximum electron current is 5 A. The temperature around ionizer was measured by an optical pyrometer; it reached about 2700 K.

The efficiency of the ion source was determined in off-line operation for cesium and barium isotopes by comparing the activity collected in the focal plane with that inserted into the vaporizer. The cesium and barium isotopes were obtained by the $^{nat}\text{Ag}(^{16}\text{O},\text{xn})^{125,127}\text{Cs}$ and $^{93}\text{Nb}(^{37}\text{Cl},\alpha\text{n})^{126}\text{Ba}$ reactions, respectively. The ion-source efficiency was estimated to be 30 % for cesium and 18 % for barium atoms. The transport efficiency from the focal plane to the detection point was also found to be 50 %. In on-line operation the over-all efficiency was measured for the cesium isotopes produced by the $^{93}\text{Nb}(^{32}\text{S},\alpha)^{121}\text{Cs}$ reaction; it proved to be 15 %.

11.2.4 On-line Experiment

The elements Cs, Ba, La, Pr, Nd and Pm have been separated in the on-line operation. The neutron deficient nuclides for these elements were supplied by the heavy-ion fusion-evaporation reaction, such as $^{93}\text{Nb}(^{35}\text{Cl},\alpha\text{xn})^{131-134}\text{Nd}$, separated by the ISOL and collected on an aluminum coated Mylar tape in the tape-transport system. The nuclides thus collected were moved to the measuring port in 1 sec. The X- and γ -ray spectra were taken with Ge detectors to identify the different elements in the mass chain selected by the separator. The results are shown in Figs. 3 and 4 for masses $A=121$ and $A=132$, respectively. With respect of the mass $A=121$ nuclei, γ - γ coincidence spectra were obtained by using an event-by-event recording system and Ge detectors. Also, the decay of γ -rays emitted from the isobars were traced. It is newly found that the γ -rays 99.2, 111.6, 210.8 and 341.9 keV are assigned to be ^{121}Ba [1,2].

(S.Ichikawa)

References

- 1) Ravn, H.L.: Physics Report, 54, 201(1979).
- 2) Bruske, C., Burkand, K.H., Hüller, W., Kirchner, R., Klepper, O.,
Roeckl, E.: Nucl.Instr.Meth., 186, 61(1981).

Publication List

- [1] Ichikawa, S., Sekine, T., Hata, K., Tamura, T., Minehara, E.,
Takahashi, N., Fujiwara, I., Imanishi, N.: JAERI-M 84-129,
60(1981).
- [2] Ichikawa, S., Sekine, T., Hata, K., Shinohara, N.,
Takahashi, N.: JAERI-M 85-104, 139(1984).

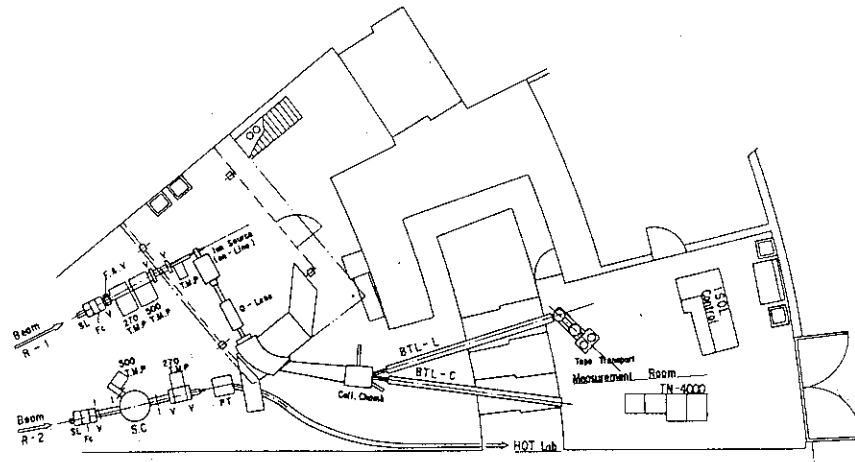


Fig.1 Isotope separator and associated instruments in the JAERI tandem accelerator facility.

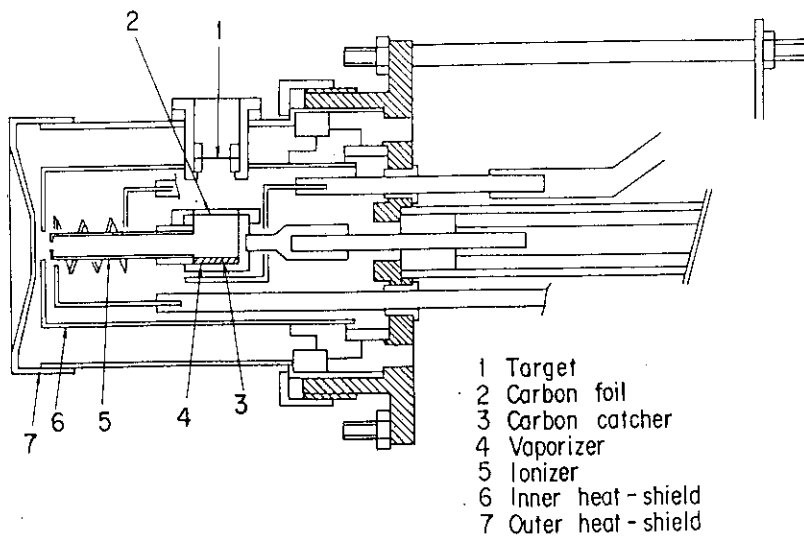


Fig.2 The integrated ion source system.

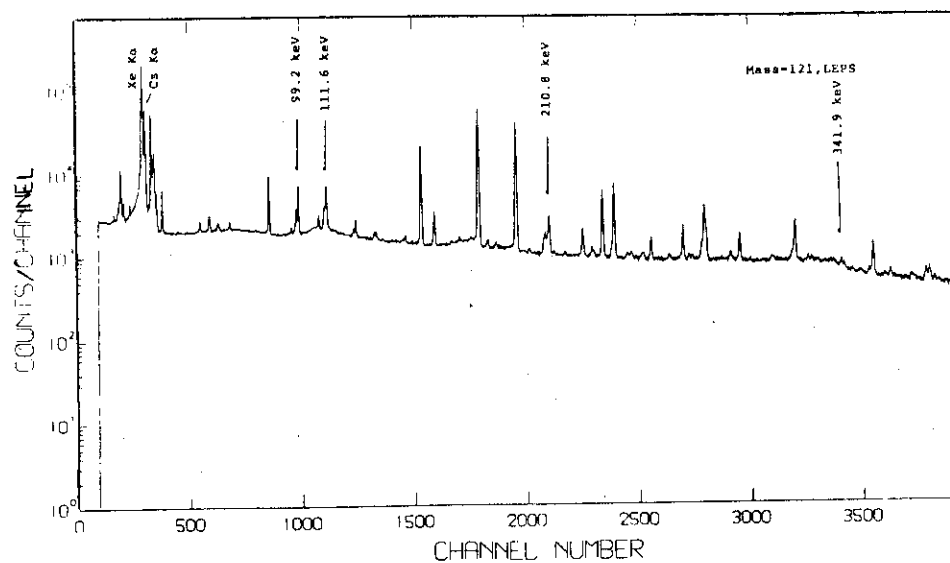


Fig.3 The X-and γ -ray spectrum measured for Mass A=121 in the bombardment of ^{93}Nb with 180 MeV ^{35}Cl ions.

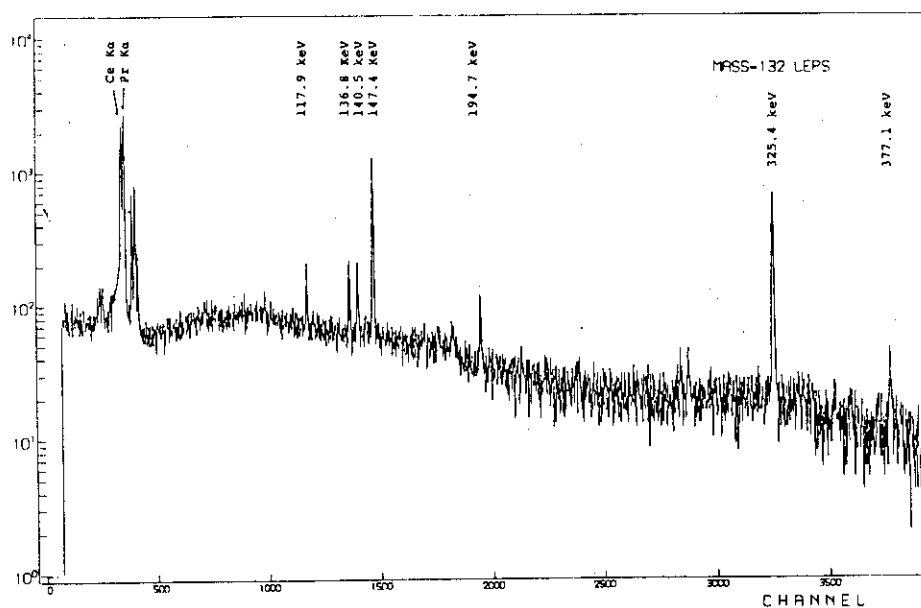


Fig.4 The X-and γ -ray spectrum measured for mass A=132 in the bombardment of ^{103}Rh with 180 MeV ^{35}Cl ions.

11.3 Actinides Synthesized by Heavy-Ion Nuclear Reaction

11.3.1 Introduction

In concert with the development of nuclear reactors and accelerators, most of actinide isotopes have been synthesized artificially by nuclear reactions, where various targets have been irradiated by light particles such as neutrons, protons, deuterons and He-ions. In order to produce heavier actinides by such light-particle irradiation, it is necessary to prepare heavy-element targets, but usually such targets, especially transcurium elements, are difficult to obtain easily. Consequently, the heavy-ion (which are generally defined as heavier nuclei than helium) irradiations have appeared on the stage. So far studies of the production of new actinide isotopes have performed mainly by the heavy-ion nuclear reactions, and synthesized up to the 109th element¹⁾.

For the purpose of clarifying the nuclear and chemical properties of the heavy actinides which have relatively short lives, a systematic study of the heavy-ion nuclear reactions by using radiochemical methods have been initiated: The formation of the actinides in the bombardments of ^{242}Pu with ^{12}C ions and ^{238}U with ^{12}C or ^{16}O ions at energies not far in excess of the Coulomb barriers has been investigated.

11.3.2 Experimental

The ^{242}Pu and ^{238}U targets were prepared by electrodeposition from isopropyl alcohol solution onto aluminum foils²⁾. A target assembly consists of a stack of aluminum foils for degrading the beam energy at the upstream side of the target and an aluminum

foil for catching the recoil nuclei at the down stream side. Irradiations by ^{12}C or ^{16}O ions were performed by the Tandem accelerator of the JAERI. After irradiation, a rapid ion-exchange separation was carried out for the aluminum catcher foil. Radioactivity of each actinide fraction after the chemical separation was measured with Si-surface-barrier and Ge(Li) detectors.

11.3.3 Results and Conclusion

(1) Fermium

After bombardment for 30 minutes, the fermium fraction was separated from the irradiated sample by the ion-exchange method and subjected to alpha-spectrometry. The chemical behavior, the alpha-energy and the half-life observed indicated formation of the ^{250}Fm isotope. The alpha-spectrum of transplutonium fraction for the $^{16}\text{O} + ^{238}\text{U}$ reaction is shown in Fig. 1.

(2) Californium and Curium

By measuring the alpha-spectra of the aluminum catcher foils for long periods after irradiation and examining the chemical behaviors and half-lives, it was confirmed that the ^{244}Cf , ^{245}Cf and ^{246}Cf were formed by any reactions of $^{12}\text{C} + ^{242}\text{Pu}$, $^{16}\text{O} + ^{238}\text{U}$, and $^{12}\text{C} + ^{238}\text{U}$ reactions. The curium isotopes, ^{242}Cm and $^{243,244}\text{Cm}$, were formed by $^{12}\text{C} + ^{242}\text{Pu}$, and ^{242}Cm by $^{16}\text{O} + ^{238}\text{U}$ reaction.

(3) Neptunium and Uranium

The formation of the target-like isotopes emitting gamma-rays was investigated. After irradiation, the gamma-spectrum of the aluminum catcher foil was measured with a Ge(Li) detector and the chemical behavior of the gamma-emitter was studied.

The formation of the isotopes ^{238}Np , ^{239}Np , ^{237}U and ^{239}U was confirmed in the $^{16}\text{O} + ^{238}\text{U}$ reaction. The gamma-spectrum of the target assembly after bombardment of ^{238}U with 92 MeV ^{16}O beam is shown in Fig. 2.

(4) Formation Mechanism of the Actinides by Heavy-Ion Reaction

The isotope of ^{250}Fm is produced via compound nucleus reactions: $^{242}\text{Pu}(^{12}\text{C}, 4n)^{250}\text{Fm}$ or $^{238}\text{U}(^{16}\text{O}, 4n)^{250}\text{Fm}$. In the $^{12}\text{C} + ^{238}\text{U}$ reaction, the californium isotopes of $^{244-246}\text{Cf}$ are also produced by the compound nucleus reactions $^{238}\text{U}(^{12}\text{C}, 6n-4n)^{244-246}\text{Cf}$. The curium, americium, neptunium and uranium isotopes are formed by transfer reactions, in which several nucleons are transferred from the projectile to the target nucleus without the formation of compound nucleus. Details are given elsewhere[1-4].

(N.Shinohara)

References

- 1) Münzenberg, G., et al.: Z.Phys.A, 309, 89(1982).
- 2) Kono, N.: informal communication, (1982).

Publication List

- [1] Shinohara, N., Ichikawa, S., Usuda, S., Suzuki, T., Kono, N., Umezawa, H., Okashita, H., Sekine, T., Hata, K., Yoshizawa, Y., Horiguchi, T., Fujiwara, I.: "Nuclear Chemistry of Actinoids, Synthesis of Transuranium Nuclides from Interaction of ^{16}O with ^{238}U ", JAERI-M 83-095, 53(1983).
- [2] Shinohara, N., Ichikawa, S., Usuda, S., Suzuki, T., Okashita, H., Sekine, T., Hata, K., Horiguchi, T., Yoshizawa, Y., Shibata, S., Fujiwara, I.: "Nuclear Chemistry of Actinoids

II. Formation Cross sections of Transuranium Nuclides from Interaction of ^{16}O with ^{238}U ", JAERI-M 84-129, 57(1984).

- [3] Shinohara, N., Usuda, S., Ichikawa, S., Suzuki, T., Okashita, H., Yoshikawa, H., Iwata, Y., Horiguchi, T., Yoshizawa, Y., Shibata, S., Fujiwara, I.: "Nuclear Chemistry of Actinoids III. $^{16}\text{O} + ^{238}\text{U}$ and $^{12}\text{C} + ^{242}\text{Pu}$ Reactions", JAERI-M 85-104, 129(1985).
- [4] Shinohara, N., Ichikawa, S., Usuda, S., Suzuki, T., Okashita, H., Sekine, T., Hata, K., Horiguchi, T., Yoshizawa, Y., Shibata, S., Fujiwara, I.: "Synthesis of Transuranium Nuclides from Interaction of ^{16}O with ^{238}U ", Americium and Curium Chemistry and Technology, Edelstein, N.M., et al.(eds), D. Reidel Publishing Co., Dordrecht, 251(1985).

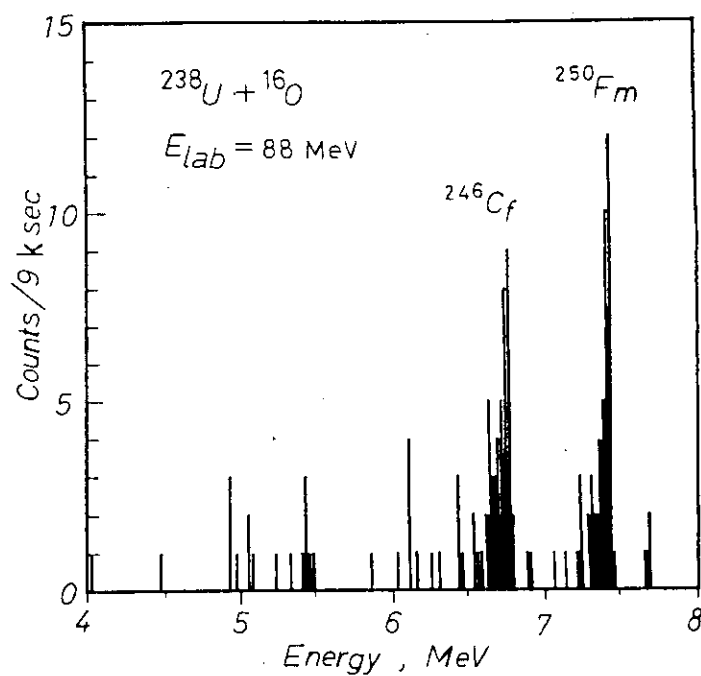


Fig. 1 Alpha-spectrum of the transplutonium fraction after the ion-exchange separation.

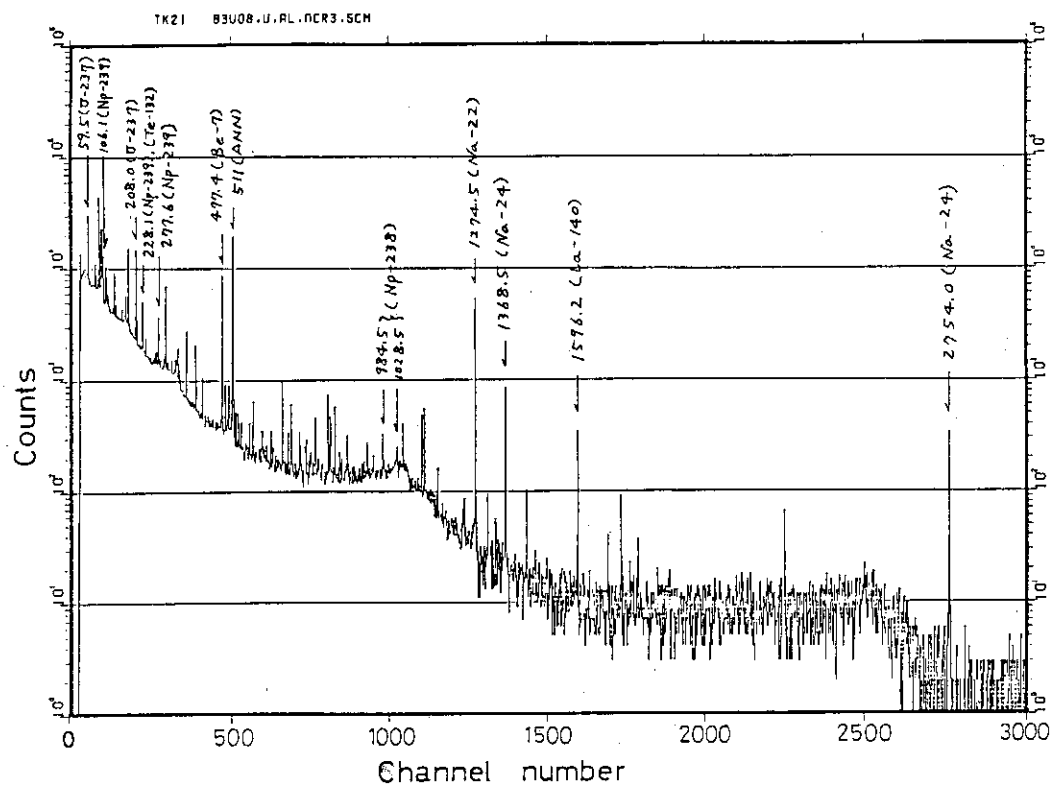


fig. 2 Gamma-spectrum of the ^{238}U target assembly after 6.7 days of 3-hours bombardment with 92-MeV ^{16}O beam.

11.4 Isotope Correlation Techniques for Verifying Input Accountability Measurements at a Reprocessing Plant

11.4.1 Introduction

Measurements of nuclear material input to a reprocessing plant, in particular of plutonium, are of great importance, since it is the starting point of plutonium accountancy based on direct measurements. Isotope correlation techniques (ICTs) provide very promising means for verification of the input measurement data.

The present study deals with the method of analyzing data from the input accountability measurements by means of the isotope correlation of heavy nuclides and a system which can be operated in a very small computer and used by safeguards inspectors to collect data generated at the key measurement point (KMP) and evaluate promptly the data in the field.

11.4.2 Fundamentals

Estimation of uranium and plutonium input amounts to a reprocessing plant by the ICTs is based on a technique so-called "Pu/U ratio method", in which values of initial uranium amount, burnup and Pu/U ratio of the spent fuel to be dissolved must be known. Initial uranium amount, which is only an absolute datum used, is brought by fabricator as well as its isotopic ratio data. Both the burnup and Pu/U ratio are, therefore, estimated by the ICTs developed. The burnup is calculated from isotopic ratio data of uranium in pre- and post-irradiation, and of plutonium in post-irradiation. A value of Pu/U ratio is also used in the burnup calculation. Initial value of Pu/U ratio is created from uranium and plutonium concentration data in accountability measurements,

and substituted by the ICTs-estimated value later, in which new value of Pu/U ratio is estimated by using the correlation between Pu/U and heavy isotopic variables, relating with the burnup.

1) Determination of uranium and plutonium amounts in a given spent fuel

Material balance of heavy metals in pre- and post-irradiation of the fuel is expressed as

$$U^0 = U + Pu + F + TU,$$

where F stands for the number of fission occurred, and U^0 , U, Pu and TU denote the number of atoms of pre-irradiation uranium, post-irradiation uranium and plutonium accumulated, and the other transuranium elements formed, respectively. Term TU is usually small enough to be neglected. Introducing burnup B in unit of FIMA (Fission per Initial Metal Atoms), defined as F/U^0 , the above equation is reduced to

$$U + Pu = U^0 (1 - B).$$

Since $Pu = (Pu/U) U$, the equation is rewritten as

$$U (1 + Pu/U) = U^0 (1 - B),$$

hence, $U = U^0 (1 - B) / (1 + Pu/U)$,

and $Pu = (Pu/U) U^0 (1 - B) / (1 + Pu/U)$.

If the relationship between the plutonium-to-uranium ratio and some isotopic data or reduced parameters can be drawn, the plutonium-to-uranium ratio will be predicted from isotopic data of either heavy elements or fission products for a given reprocessing batch of spent fuel, and the amount of plutonium in the batch will be independently determined on the basis of the fabrication data U^0 and its burnup B.

2) Burnup determination

The established method to determine burnup of spent fuel

needs to measure neodymium-148 formed as fission product by the mass-spectrometric dilution analysis as well as uranium and plutonium. Under the present circumstances of the data availability in safeguards implementation, burnup has to be evaluated from only uranium and plutonium data including isotopic compositions besides the burnup calculated by reactor operator.

Burnup in FIMA is given by

$$B = F_{25}/U^{\circ} + F_{28}/U^{\circ} + F_{49}/U^{\circ} + F_{41}/U^{\circ},$$

and each term in the right side is obtained by the following equations;

$$F_{25}/U^{\circ} = A_{28}^{\circ} | R(25/28)^{\circ} + R(26/28)^{\circ} - f | R(25/28) + R(26/28) | |.$$

$$F_{28}/U^{\circ} = p(f/a_{28}) | 1 + (A_{40} + A_{41} + A_{42}(1 + a_{49} + a_{41})/a_{41}/a_{49}) |.$$

$$F_{49}/U^{\circ} = p(f/a_{49}) | A_{40} + A_{41} + A_{42}(1 + 1/a_{41}) |,$$

$$F_{41}/U^{\circ} = p(f/a_{41}) A_{42},$$

$$1/f = | (1 + Pu/U) | 1 + A_{40}/a_{49} + A_{41}/a_{49} + A_{42}(1 + a_{49} + a_{41})/(a_{49}a_{41}) | \\ (1 + 1/a_{28})/A_{28} |^{-1},$$

$$\text{and, } p = (A_{28}^{\circ}/A_{28})(Pu/U),$$

where symbol A stands for isotope fraction in atom unit, F number of fissions, R atom ratio, Pu/U atom ratio of total uranium and plutonium, a the ratio of capture to fission cross section, and the first digit of suffix represents the atomic number and the second the mass number of heavy metal atoms concerned. $^{\circ}$ refers to its initial (pre-irradiation) value.

Since the a values depend upon burnup and type of reactor, those obtained from burnup calculation of typical LWR fuels are fitted as a function of burnup to use. Details are given elsewhere [1].

3) Isotopic variables and correction with plutonium-to-uranium ratio

In order to estimate the most probable Pu/U ratio, correlations between the respective isotopic variables and the Pu/U ratio are fitted to the following linear function within a limited range of burnup, considering the dependency of correlation upon burnup.

$$\text{Pu/U} = (a_i + b_i \times B) \times V_i ; i = 1, 2, 3, \dots, 9,$$

where V_i stands for isotopic variable computed from isotopic data of uranium and plutonium as follows:

$$V1 = (A25^\circ - A25) \times 100,$$

$$V2 = (A26 - A26^\circ) \times 100,$$

$$V3 = \ln \left| (A28 / A24) \times (A24^\circ / A28^\circ) \right|,$$

$$V4 = \ln \left| (A28 / A25) \times (A25^\circ / A28^\circ) \right|,$$

$$V5 = 100 - A49 \times 100,$$

$$V6 = A40 / A49,$$

$$V7 = A41 / A40,$$

$$V8 = (A41 + A42) / A40, \text{ and}$$

$$V9 = A49 \times A42 / A40^2.$$

All the variables correspond to quantities approximately proportional to the time-integrated neutron flux. The coefficients determined from the fitting, a_i and b_i , vary in different initial enrichment and type of reactor. Therefore the values would be better established as more data are accumulated.

11.4.3 Analysis of the Input Measurement Data by ICTs

The data obtained by the operator (reprocessor) are analyzed batch by batch. Accordingly results of the analysis for the previous batch have always to be kept and referred to correct for mixing with the heel of the previous batch solution. The input accountability tank is usually different from the dissolver and some intermediate vessels are in between. Therefore the dis-

solved fuels is, in general, not completely transferred into the accountability tank. Correction for the mixing thus occurred should be taken into account.

From the data thus corrected, burnup is estimated taking at first the measured plutonium-to-uranium ratio and a set of initial a values which correspond with those of fresh fuel. After the first estimate of burnup, the a values are computed by the following equation,

$$a = k B^m \exp (n B),$$

where B is the burnup, and k , m and n are the fitted parameters provided separately for typical LWR reactors and given in [1]. The computation is continued iteratively to converge on reasonably constant values.

The next step is to calculate the isotopic variables as defined in the preceding section. By choosing an appropriate set of coefficients for the equation given in 11.4.2.3) based on reactor type and initial enrichment, the plutonium-to-uranium ratio can be calculated from each isotopic variable. Consequently the nine data obtained for the ratio are averaged and subjected to the 3-sigma rejection examination until the rest of the data remains within the limiting range.

The final averaged value of the plutonium-to-uranium ratio is substituted for the measured value that was taken at first to obtain burnup, and then a values, burnup and plutonium-to-uranium ratio are again calculated iteratively until the plutonium-to-uranium ratios converge within 1% difference.

From the most probable plutonium-to-uranium ratio eventually estimated by the procedures described above, the masses of uranium and plutonium input to the reprocessing batch can be determined

in connection with the initial mass of uranium. At the same time, the most probable isotope abundance of uranium and plutonium may also be computed from the finally determined plutonium-to-uranium ratio and the correlation with the isotopic variables.

11.4.4 Development of a Small-Computer-Based System

The analysis described above can be performed in a small pocketable computer that may be very convenient for safeguards inspectors to bring in the field for examining and collecting the input accountability data generated every day.

To demonstrate the feasibility of such techniques, a soft-system was developed with a Sharp PC-1500 pocket computer which can be supported by battery power and be operated in a completely independent fashion from the operator's system. Details of the software and the operation are given elsewhere[1].

(Y.Nakahara and H.Okashita)

Publication List

- [1] Umezawa, H., Nakahara, Y.: "Isotope correlation techniques for verifying input accountability measurements at a reprocessing plant", "Nuclear Safeguards Technology 1982", IAEA, Vienna, 1, 473(1983).

11.5 Measurements and Evaluation of Gamma-Ray Intensities of ^{239}Pu

11.5.1 Introduction

Gamma-ray spectrometry with Ge detector has attracted major interest in the non-destructive analysis of nuclear fuels. The accurate analysis requires a very knowledge of gamma-ray energies and intensities for the relevant nuclides in the fuel. Gamma-ray intensities in the decay of ^{239}Pu were measured recently by several authors¹⁻³⁾ but the values are still open to be evaluated. Some of the present authors have established precision measurement techniques of gamma-ray intensities which achieved accuracies better than 1% in the region above 120 keV^{4,5)}. By using this method, gamma-ray intensities of ^{239}Pu were measured with intent of below 1% uncertainties.

In order to reduce ambiguity of source-absorption for low energy gamma-ray, absorption of plutonium source was measured and careful correction was made for the self-absorption. Weight and isotopic abundance of plutonium in the source were measured with a mass-spectrometer to determine intensities per decay.

11.5.2 Experimental

The plutonium samples which were recovered from spent fuels of the Japan Research Reactor 3 (JRR-3), were carefully purified on uranium and americium, prepared in 4N HCl solution, and sealed in geometrically identical vials, 16 mm diameter and 48 mm high, and 34 mm diameter and 5 mm high, of acrylic

acid resin. Plutonium content in the vials was about 220 mg for the cylindrical type and about 100 mg for the disk type. The former sources were used to determine the intensities per decay of ^{239}Pu gamma-rays with ^{133}Ba , ^{152}Eu and ^{154}Eu standard solutions which contained the same concentration of plutonium or uranium and are sealed in the cylindrical vials. The latter were provided for self-absorption measurements to compare with an empty source of the same disk. Sources of a mixture of ^{152}Eu and ^{182}Tm were also made for calibration with disks of the same dimensions.

Gamma-ray spectrum measurements were performed with a vertical type ORTEC 6.6% Ge(Li) detector with a resolution of 2.1 keV for the 1332-keV gamma-ray shielded with lead blocks, placing at 18 cm above surface of the detector. All the sources including the standard sources were measured normally more than twenty times.

11.5.3 Analysis

Gamma-ray spectra were analyzed by subtracting Compton background and peeling off of complex peaks with correction for the coincidence sum effects of cascade and cross-over gamma-rays. Details of the spectrum analysis method are given elsewhere⁴⁾.

The self-absorption correction was made by the following manner. Three different measurements were performed using the disk sources with and without plutonium solution as follows:

- i) The disk containing plutonium solution was placed in the upper position and an empty one in the lower position,
- ii) Two disks containing plutonium solution were put on top of each other,

iii) An empty disk was placed in the upper position and the one filled with plutonium solution in the lower position.

Relation between counting rates for the three kinds of source configuration is given by

$$I_1 \exp(-m d) + I_3 = I_2,$$

where I_1 , I_2 and I_3 are counting rates for the source configurations i), ii) and iii), respectively, and m stands for the absorption coefficient and d the thickness of the source solution. Therefore md is obtained as

$$m d = \log \left| I_1 / (I_2 - I_3) \right|.$$

Self-absorption in the measurements with the source configuration iii) is corrected as follows:

$$I'_3 = m d I_3 / \left| 1 - \exp(-m d) \right|,$$

which were used for the detector calibration and the intensity determination. The correction ranged between 3 to 7% for the ^{239}Pu gamma-rays.

The relative efficiencies of the detector were obtained from the measurements of the standard ^{152}Eu , ^{154}Eu and ^{182}Ta gamma-rays and the absolute efficiency was from the ^{133}Ba measurements. The entire efficiency curve was eventually derived by fitting the efficiencies obtained above to the following equations:

$$e_f = a_1 \exp(-b_1 E) + a_2 \exp(-b_2 E) \quad 180 \text{ keV}$$

$$\text{and} \quad e_f = a_1 \exp(-b_1 E) + a_2 \exp(-b_2 E) \\ + c_1 E^3 + c_2 E^2 + c_1 E + c_0 \quad 180 \text{ keV,}$$

where e_f and E denote the efficiency and the gamma-ray energy,

respectively, and a_i , b_i and c_i are fitting parameters. Details of efficiency curve determination was given elsewhere[1]. The absolute efficiencies were obtained from the relative efficiency curve and the absolute efficiency at 356.0 keV of ^{133}Ba . The experimental errors associated with the absolute efficiencies were varied from 0.7 to 1.8% (0.78% at 356.0 keV).

11.5.4 Results and Evaluation

The 70 gamma-ray emission probabilities obtained were compared with the reported values¹⁻³⁾. Detailed discussion is made elsewhere[1]. For the selected major gamma-rays a critical evaluation was performed for the IAEA Coordinated Research Programme on the Measurement and evaluation of trans-Actinium Isotope Nuclear Decay Data (1978-1985). Comparison with other measurements and the final recommended values are listed in Table 1. The accuracies requested for the gamma-ray emission probabilities of ^{239}Pu were quite high, greater than 1%. It is, however, recognized from the table that several values meet satisfactorily the requirement.

(H.Okashita)

References

- 1) Gunnink, R., Evans, J. E., Prindle, A. L.: UCRL 52193 (1976).
- 2) Depres, M.: CEA-R-5065(1980).
- 3) Helmer, R. G., Reich, C. W., Gehrke, R. J., Baker, J. D.:
Int.J.Appl.Radiat.Isot., 33, 23(1982).
- 4) Yoshizawa, Y., Iwata, Y., Kaku, T., Katoh, T., Ruan, J.,
Kojima, T., Kawada, Y.: Nucl.Instrum.Methods, 174, 109(1980).
- 5) Yoshizawa, Y., Iwata, Y., Katoh, T., Ruan, J., Kawada, Y.:

Nucl.Instrum.Methods, 212, 249(1983).

Publication List

- [1] Iwata, Y., Yoshizawa, Y., Suzuki, T., Ichikawa, S.,
Okazaki, S.: Int.J.Appl.Radiat.Isot., 35,1(1984).

Table 1 Comparison with Other Measurements and Evaluation
of Gamma-Ray Emission Probabilities of ^{239}Pu (photons/ 10^7 decays).

E (keV) ¹⁾	Gunnink ¹⁾	Depres ²⁾	Helmer ³⁾	Iwata ¹⁾	Evaluated
129.296(1)	626(13)	623(4)	641(5)	648(10)	631(6)
144.201(3)	28.3(6)	32.4(15)	30.7(6)	30.8(8)	29.9(7)
161.482(12)	12.0(3)	12.5(7)	12.5(3)	12.4(6)	12.3(2)
171.396(6)	11.05(24)	10.5(6)	11.1(3)	11.0(6)	11.0(2)
179.220(12)	6.58(15)	6.5(5)	6.65(20)	6.5(3)	6.6(1)
189.360(10)	8.30(23)	8.30	8.31(15)	8.27(19)	8.3(1)
195.679(8)	10.64(22)	10.2(7)	10.7(2)	10.88(25)	10.7(1)
203.550(5)	56.0(11)	55.7(26)	56.8(4)	58.0(9)	56.9(3)
255.384(15)	8.05(23)	7.9(6)	8.12(20)	7.94(18)	8.0(1)
297.46(3)	5.02(14)	4.8(5)	4.98(13)	4.96(13)	4.98(8)
332.80(4)	50.6(10)	47.6(20)	49.2(4)	49.5(7)	49.4(3)
345.013(4)	55.9(11)	54.5(19)	55.4(10)	55.8(7)	55.6(5)
375.054(3)	157.0(31)	155(5)	154.7(12)	156.5(18)	155.4(9)
413.713(5)	148.9(30)	148(5)	145.5(9)	149.6(40)	146.6(11)
422.598(19)	11.93(24)	11.9(9)	12.00(25)	11.93(24)	12.2(2)
445.81(10)	0.870(25)	0.908	1.15(13)	0.85(7)	0.88(6)
451.481(10)	18.9(4)	19.2(12)	18.92(22)	18.99(28)	18.94(16)
481.78(12)	0.460(10)	0.477	0.71(6)	0.448(29)	0.46(2)
639.99(10)	0.820(17)	0.867	1.03(13)	0.92(3)	0.87(2)
645.98(3)	1.489(30)	1.55	1.34(13)	1.53(4)	1.52(3)
651.79(10)	0.655(14)	0.657	0.79(10)	0.66(3)	0.66(2)
658.63(15)	0.969(21)	0.991	0.79(9)	0.97(3)	0.97(2)
718.0(5)	0.274(6)	0.296	----	0.274(23)	0.28(2)
769.19(4)	1.120(23)	1.25	----	1.21(3)	1.19(2)

12. DEVELOPMENT OF RADIOCHEMICAL ANALYSIS METHODS

H.Okashita, T.Suzuki, S.Okazaki*,
T.Sato, N.Kono, S.Usuda,
S.Ichikawa, N.Shinohara, M.Magara
and H.Yoshikawa**

12.1 Rapid Ion Exchange Separation of Transplutonium Elements

12.1.1 Introduction

Most of transplutonium nuclides, especially produced by heavy-ion bombardments, have short half-lives and small formation cross sections, and emit alpha particles. In various rapid chemical separation methods, ion exchange has advantages of isolating and concentrating trace amounts of such elements with quantitative yield.

In order to study the nuclear chemistry of the transplutonium nuclides, a pressurized ion exchange system was developed. The present paper deals with the system and its application.

12.1.2 Experimental

A strongly acidic cation exchange resin (MCI GEL CK08Y) and strongly basic anion exchange resins (MCI GEL CA08Y and CA08S), which supplied by Mitsubishi Chemical Industries, were

* Present address : Nuclear Material Control Center (NMCC)

** JAERI Scholarship in the fiscal years of 1984-1985 from Tokyo Metropolitan University

used for the system. After washing, the resins were packed into fluoroplastic tube columns (i.d.: ca. 1.5 mm) and fixed with quartz wool plugs at both ends.

Nitric acid-alcohol mixed eluent was prepared by adding calculated amount of the concentrated acid to the required volume of alcohol, and by bringing the solution up to a definite volume with distilled water.

As tracers, ^{241}Am , ^{244}Cm , ^{252}Cf and long-lived fission products were employed. Alpha- and beta-activities were measured with a silicon surface barrier detector.

The pressurized ion exchange separation system developed consists of a pressurized ion exchange column under controlled temperature and flow rate, a continuous eluent supplier and a direct drop evaporator of effluents for immediate alpha source preparation(Fig.1).

12.1.3 Cation Exchange with Hydrochloric Acid Solution

Cation exchange of transplutonium elements was examined for separation from mg order of U and Al in hydrochloric acid solution. The overall recovery of the transplutonium elements was 90 ± 10 % and the separation time within 15 minutes.

The procedure was applied to separation of ^{250}Fm ($T_{1/2}$: 30 min) and ^{246}Cf ($T_{1/2}$: 35.7 hr) synthesized by the $^{16}\text{O} + ^{238}\text{U}$ reaction from the target and the aluminium catcher foil[1].

12.1.4 Anion Exchange with Nitric Acid-Methyl Alcohol Solvents

It is reported that light rare earth^{1,2)} and transplutonium elements³⁻⁵⁾ can be mutually separated by anion exchange with nitric acid-methyl alcohol mixed solvent. The procedure, however,

is not so effective to rapid separation because of slow exchange rate.

To improve this point, the temperature effect was examined at the range of room temperature to elevated one, over the boiling point of methyl alcohol (64.65°C) at 1 atmosphere. Dependence of adsorbability on both concentrations of nitric acid and methyl alcohol was also investigated in detail at the elevated temperature. Based on these results, optimum conditions were determined for effective and rapid separation of the trans-plutonium and rare earth elements. Figure 2 shows the typical elution curves of actinoid and rare earth mixture[2].

(S. Usuda)

References

- 1) Faris, J.P., Warton, J.W.: Anal.Chem., 34, 1077(1962).
- 2) Korkisch, J., Hazan, I., Arrhenius, G.: Talanta, 10, 865(1963).
- 3) Hines, J., Wahlgren, M.A., Lawless, F.: TID-7655, 247(1962).
- 4) Guseva, L.I., Myasoedov, B.F., Tikhomirova, G.S., Pavlenko, L.I., Babicheva, G.G.: J.Radioanal.Chem., 13, 293(1973).
- 5) Lebedev, J.A., Myasoedov, B.F., Guseva, L.I.: J.Radioanal. Chem., 21, 259(1974).

Publication List

- [1] Shinohara, N., Ichikawa, S., Usuda, S., Suzuki, T., Okashita, H., Sekine, T., Hata, K., Horiguchi, T., Yoshizawa, Y., Shibata, S., Fujiwara, I.: "Nuclear Chemistry of Actinoids II. Formation Cross Sections of Transuranium Nuclides from Interaction of ^{16}O with ^{238}U ", JAERI-M 84-129, 57 (1984).

- [2] Shinohara, N., Ichikawa, S., Usuda, S., Suzuki, T., Okashita, H., Sekine, T., Hata, K., Horiguchi, T., Yoshizawa, Y., Shibata, S., Fujiwara, I.: "Synthesis of Transuranium Nuclides from Interaction of ^{16}O with ^{238}U ", Americium and Curium Chemistry and Technology, N.M. Edelstein et al. (eds.), D. Reidel Publishing Company, Dordrecht, 251(1985).

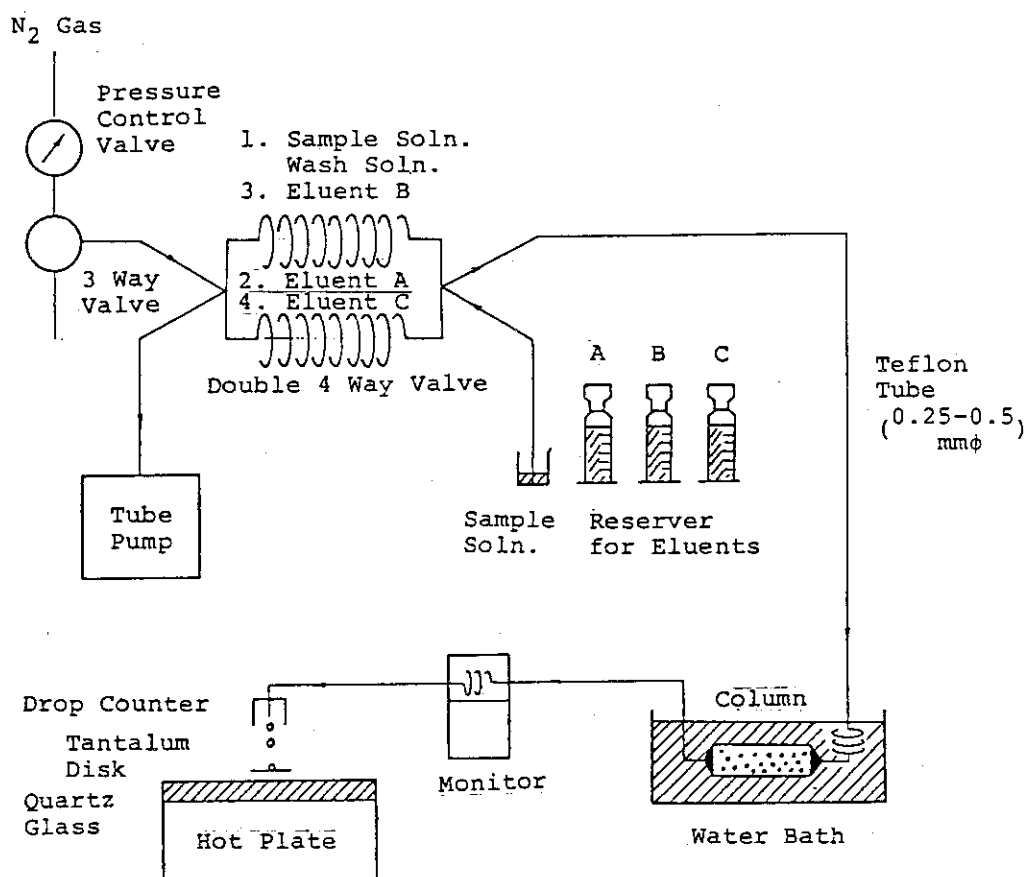


Fig.1 Pressurized ion exchange separation system.

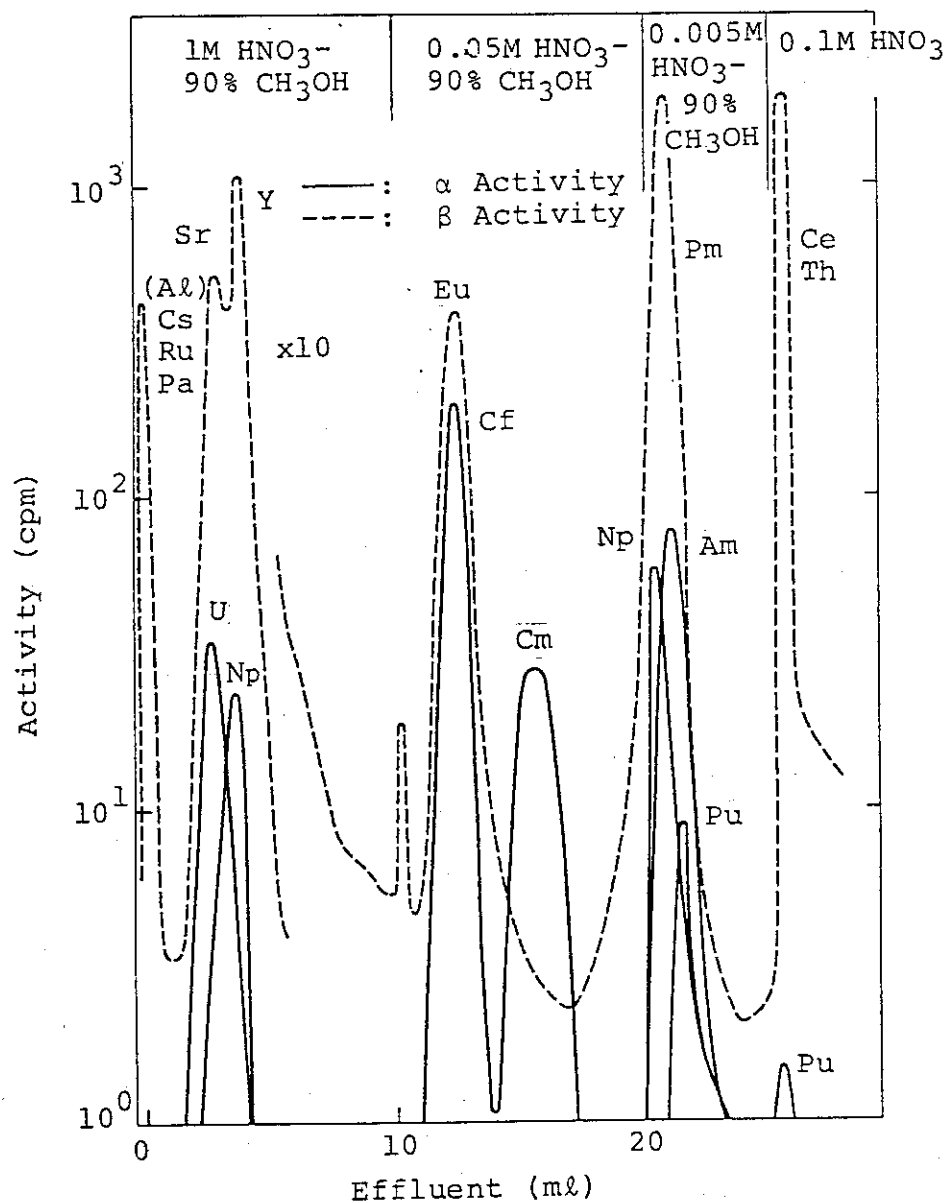


Fig.2 Elution curves for separation of actinoid and rare earth mixture from about 2 mg of Al and U.

Column bed : 1.5 mm ϕ x 14 cm

Resin : CA08Y (23.5 \pm 4 μ m)

Flow rate : 10-15 cm/min

Temperature: 80-90 °C

12.2 Electrodeposition of Actinides

12.2.1 Introduction

Alpha spectrometry is a quite useful technique for the measurements of the amount and the isotopic composition of the heavy elements such as Np, Pu, Am and Cm. To analyze the alpha spectrum accurately, it is important to prepare the measuring sources with high resolution. Although many electrodeposition techniques have been reported¹⁻⁴⁾, actual application of these methods often encounter some difficulties. Hence we have developed a novel and rapid electrodeposition method for preparation of the high resolution sources.

12.2.2 Experimental

The electrodeposition cell assembly is illustrated in Fig. 1. Its effective deposition area is 0.78 cm^2 (1 cm diameter). The electrolytic solution is agitated by a rotated Pt wire anode (1 mm diameter) and cooled by flowing water in jacket. Platinum plate (24 mm diameter and 0.05 mm thick) is used as backing. Uranium, Np, Pu, Am and Cm are purified by an anion-exchange method⁵⁾. Each solution of the purified actinides is dried gently, dissolved with 50 μl of 12M HCl and diluted with 2 ml of water, and then kept as stock solution, which contains about 100 μCi as alpha activity of the major nuclides. The electrolytic solution is composed of 5 to 100 μl of the stock solution, 4 ml of isopropyl alcohol and 20 μl of 0.1M HCl.

12.2.3 Results

Deposition yield higher than 99% can be achieved within 15 to 20 minutes under the condition of 3 to 5 mA/cm² current density and 400 to 800 V of electrolytic voltage. Duration of the electrolysis over 25 minutes makes decrease of deposition yields for Am and Cm. The resolution of alpha spectra of the sources obtained falls in the range of 14 to 18 keV (FWHM) by a silicon surface barrier detector (ORTEC A-14-100-100) with 4096 pulse height analyzer system. The results are summarized in Table 1.

The present method has been applied successfully to the preparations of sources for precise measurements of transuranium in spent fuels⁶⁾, of targets for heavy-ion bombardment for the study of nuclear chemistry of transplutonium nuclides⁷⁾ and of fission chambers for the use in the Fast Critical Assembly in the JAERI⁸⁾.

(S.Okazaki and N.Kono)

References

- 1) Getoff, N., Bildstein, H.: Nucl.Instr. and Methods, 36, 173(1965).
- 2) Evans, J.E., et al.: ibid., 102, 389(1972).
- 3) Mullen, G., Aumann, D.C.: ibid., 128, 425(1975).
- 4) Kressin, I.K.: Anal.Chem., 49, 842(1977).
- 5) Natsume, H., et al.: J.Nucl.Sci.Technol., 12, 9(1972).
- 6) Suzaki, T., et al.: ibid., 23(No.1)(1986), in press.
- 7) Shinohara, N., et al.: JAERI-M 84-129, 57(1984).
- 8) Ohbu, M.: JAERI-M 9795 (in Japanese)(1981).

Table 1 Electrodeposition yields and energy resolutions of alpha-ray spectra.

Element	Deposition yield (%)	Thickness ($\mu\text{g}/\text{cm}^2$)	Resolution (KeV) [FWHM]
U-235	99.7	13.	17.0
	99.9	25.	17.9
Np-237	99.1	10.	16.2
	99.6	23.	16.9
Pu-238	99.2	.004	14.2
	99.1	.007	14.0
Pu-242	99.4	1.8	15.0
	99.7	2.9	15.8
Am-243	99.2	1.7	15.3
Cm-244	99.3	.007	14.9

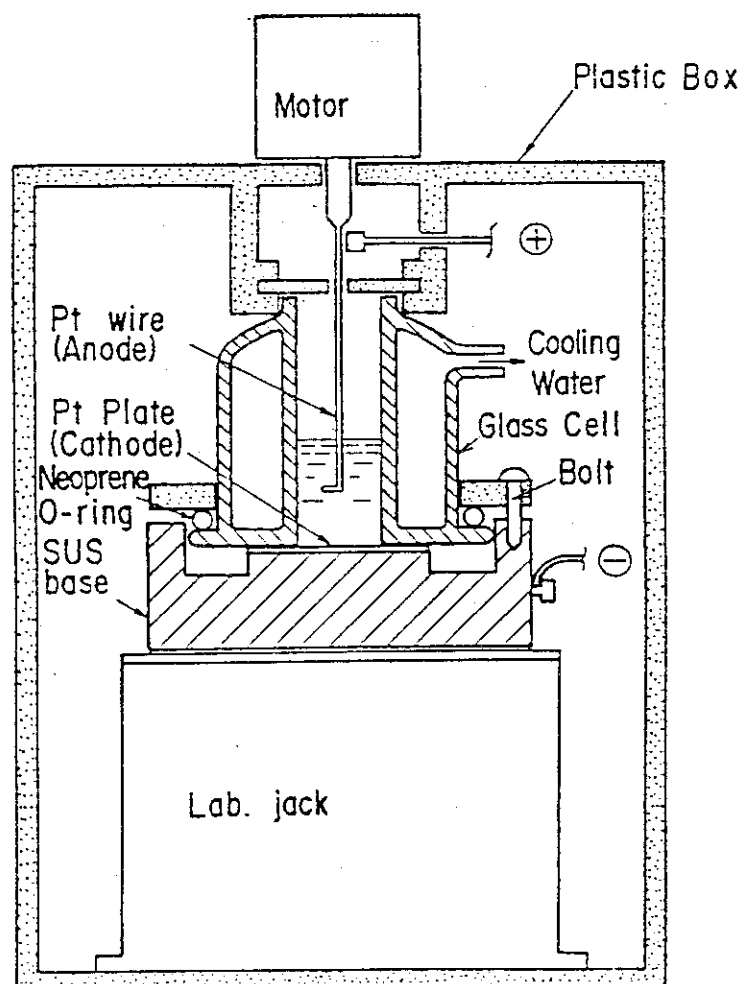


Fig. 1 Electrodeposition cell assembly.

12.3 Analysis of Biological Shielding Concrete of JPDR

12.3.1 Introduction

Evaluation of radioactivity inventory in a nuclear power plant is essential to the planning of decommission of the plant. Although the biological shielding concrete is less activated in comparison with reactor core material, it accounts for main parts in volume and weight of radioactive waste. The inventory evaluation is performed by radioactivity measurement of the samples taken out from the entire shield, which might be laborious work to depict in three dimensional radioactivity distribution for the whole shield.

It is required to develop a computer code to facilitate evaluation of activity inventory in the biological shielding of power plant. In order to compute the activity inventory with the evaluation code, it is necessary to know bulk composition of concrete together with activable micro constituents and water content. Since the concrete is composed of various elements, instrumentals analysis which can perform simultaneous multielemental measurements such as ICP is preferred to treat a number of samples. Analysis of micro constituents with the analytical instruments might be affected by the matrix elements, and the effects should be calibrated independently by other methods.

The evaluation code can be justified by comparing of the measured value of radioactivity at a certain position with composition of the concrete.

The present paper describes elemental analysis and radioactivity measurement of the samples taken out from the

biological shielding concrete of the Japan Power Demonstration Reactor(JPDR).

12.3.2 Experimental and Results

Samples: Concrete disks cutting out from the D core, which was bored from biological sheilding concrete of JPDR, were ground by a ball mill into fine powder.

Radioactivity measurements: The samples were sealed doubly in polyethelene bag. The weight of the samples was adjusted to 50~100mg depending on the intensity of the activities. The radioactivities were measured by Ge(Li) detector with 4000 ch pulse height analyzer. The results were shown in Table 1.

Chemical analysis of matrix elements: Main components of the concrete were analyzed by gravimetry used for the usual refractory material analysis as shown in Fig. 1. The results were tabulated in Table 2 together with the nickel content measured by spectro photomeroty and the water content determined by heating weight loss at 1000 °C.

Activation analysis: The very samples measured radioactivities were irradiated in JRR-2 reactor for 20 min. Nuclides induced by the neutron irradiation were measured with the same detector system for the radioactivity measurements. The results were listed in Table 3. It is obvious that nineteen elements can be analyzed without chemical procedure.

Determination of ^{63}Ni : After determination of nickel content by photometry, the extract, nickeldimethyglyoxime, was decomposed by aqua regia, and then was precipitated as nickel

hydroxide with sodium hydroxide. After rinsing with water twice and ethyl alcohol twice, the precipitate was redissolved by n-caproic acid. The solution thus prepared was mixed with toluene-based scintillation cocktail. The activity of ^{63}Ni was counted by liquid scintillation counter at carbon channel. The counting efficiency of ^{63}Ni exceeded more than 65 % with 1 mg of nickel carrier.

(T.Sato)

Table 1 Radioactivity in the biological shielding concrete.

	Sample			
	D-73		D-76	
Nuclide	Activity* (Bq/g)	Error (%)	Activity* (Bq/g)	Error (%)
^{152}Eu	2.03×10^3	1.2	1.73×10^3	3.8
^{154}Eu	1.73×10^2	3.3	1.77×10^2	6.0
^{60}Co	7.30×10^2	1.5	6.24×10^2	3.7
^{134}Cs	6.64×10^1	4.6	9.39×10^1	6.0

*) As of Dec. 31, 1980

Table 2 Macro components of the concrete sample(D-73 ,D-76) determined by gravimetry.

	Sample			
	D-73		D-76	
Component	Contents	Error	Contents	Error
SiO ₂ (%)	60.0	1.2	62.6	1.0
CaO (%)	13.3	0.5	12.4	1.0
Al ₂ O ₃ (%)	8.2	0.4	9.2	0.4
Fe ₂ O ₃ (%)	5.5	0.01	4.7	0.01
K ₂ O (%)	1.8	0.1	2.2	0.1
H ₂ O (%)	9.04	0.08	6.3	0.1
Ni (ppm)	17.6	1.0	83.6	5.0

Table 3 Micro constituents in the concrete sample(D-76) determined by activation analysis.

Element	Content (ppm)	Error (%)	Element	Content (ppm)	Error (%)
Na	1.12×10^4	4	Ba	6.38×10^2	13
K	1.48×10^4	5	La	1.75×10^1	8
Ca	7.55×10^4	6	Ce	3.11×10^1	5
Cr	3.07×10^1	4	Eu	6.10×10^{-1}	8
Mn	3.18×10^2	4	Tb	4.84×10^{-1}	5
Fe	1.98×10^4	4	Lu	4.30×10^{-1}	9
Co	6.53×10^0	4	Hf	2.78×10^0	5
Rb	8.34×10^1	10	Ta	6.00×10^{-1}	10
Sb	1.29×10^0	10	Th	5.73×10^0	4
Cs	2.00×10^0	8			

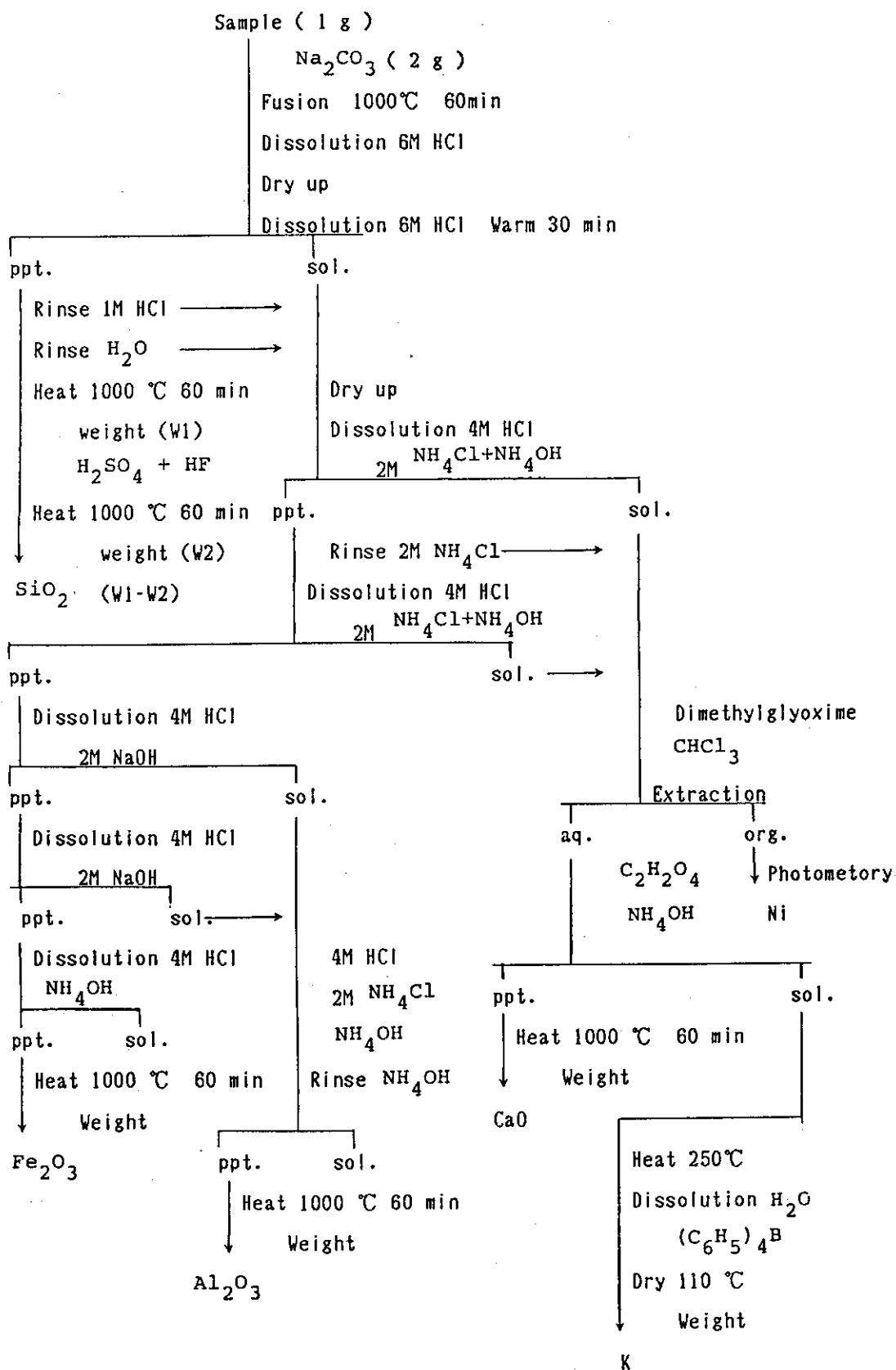


Fig. 1 Analytical procedure

13. SOLUTION CHEMISTRY OF RADIOACTIVE ELEMENTS

F. Ichikawa and T. Sato

13.1 On the Particle Size Distribution of Hydrolyzed
Plutonium(IV) Polymer

13.1.1 Introduction

Tetravalent plutonium is hydrolyzed to form colloidal polymers in aqueous solution¹⁾. This polymerization has a great influence on the behavior of this element in an aqueous chemical process such as the reprocessing of spent nuclear fuel.²⁾ The particle size or molecular weight of colloidal plutonium has been reported by some authors.³⁻¹²⁾ However, the reported values differ from each other even in orders of magnitude. The present paper [1] deals with the particle size distribution of plutonium polymer colloid and its aging effect examined by means of high speed centrifugation.

13.1.2 Experimental

1 ml of 4N nitric acid solution of tetravalent plutonium, which contained 36 mg plutonium, was evaporated under an infrared lamp. The residue was dissolved with heating in 9 ml of distilled water to obtain a yellowish green solution of plutonium colloid. The absorption spectrum of this solution is consistent with the reported spectrum.^{8,13)} One part of this stock solution is diluted with 1000 parts of 0.1N nitric acid, and used for further experiments. The final concentration of plutonium was 1.7×10^{-5} M.

5 ml of the colloidal plutonium solution was transferred into three polyethylene centrifuging tubes, sealed within a rotor basket of a swing rotor. Centrifuging was carried out by using an ultracentrifuge (Hitachi, Model 65P). The rotor chamber was evacuated to 10^{-4} torr. The temperature of the rotor was controlled to 25°C by a refrigerator. The maximum rotation rate was 65000 ± 500 rpm, which corresponds to 4×10^5 times the gravity acceleration. The conditions of the experiments were changed between 5000 and 65000 rpm in rotation rate and between 1 and 73 hr in rotation time. After the sample was centrifuged under given conditions, $50 \mu\text{l}$ of the supernatant solution was pipetted out and dried up in a counting dish under an infrared lamp. The alpha radioactivity of the sample was measured with a gas flow proportional counter. In order to estimate the loss of colloidal plutonium by adsorption on the wall of the centrifuging tube, the same procedure was repeated without centrifugation. The experiments were carried out the first time between 7 and 11 days after preparation of the colloidal solution, and the next time, after one year of aging of the solution.

13.1.3 Results and Discussion

The adsorption ratio of colloidal plutonium from 0.1N nitric acid solution on the wall of polyethylene centrifuging tube was plotted against the adsorption time (Fig.1). The rates of fresh and aged colloids are drawn by solid and dashed lines, respectively. The fresh colloid of plutonium reaches an adsorption equilibrium within a few hours and the adsorption ratio is about 25% at equilibrium. The adsorption ratio of the aged colloid is higher than that of the fresh colloid and reaches

about 50% after 50 hrs.

The fraction decreased by centrifuge (C) for fresh and aged colloid of plutonium is shown in Tables 1 and 2 with the conditions of centrifuging.

In both cases, most part of the colloidal plutonium is precipitated under maximum centrifugal force and rotation time. However, the fraction of aged colloidal plutonium precipitated at lower centrifugal forces is higher than those for the fresh one.

When a particle is centrifuged for rotation time t at an angular velocity ω , the particle size r is described by Eq. (1)

$$r = \frac{3.22}{\omega} \sqrt{\frac{\log(a_t / a_0) \times \eta}{t(\rho - \rho_m)}} \quad (1),$$

where, a_0 and a_t — distances of the particle from the rotation center at time 0 and t , ρ and ρ_m — density of the particle and the medium, η — the viscosity of the medium.

It is very difficult to calculate the absolute value of r from Eq. (1) because of two reasons. The first is the uncertainty of a_0 and a_t . Experimentally, C is obtained from the decreased radioactivity of the surface layer of the centrifuged sample solution. Therefore, the path of removed particles cannot be determined uniquely from these data. The second reason is the lack of confirmed data on the composition of colloidal particles of plutonium and, consequently, on its value of density ρ . Therefore, some assumption must be made in the present work.

The following values were applied:

$$\eta = 0.01 \text{ poise (0.1N HNO}_3\text{)},$$

$$\rho_m = 1.0 \text{ g/cm}^3 \text{ (0.1N HNO}_3\text{)},$$

$a_t = 6.4$ cm (The middle point between surface and the bottom of solution)

$a_0 = 3.8$ cm.

The value of ρ is assumed to be 11 g/cm^3 which is a rough estimated value for PuO_2 .

Substituting these values into Eq. (1), r is described as a reciprocal function of ω and t :

$$r = \frac{4.85 \times 10^{-2}}{\omega \sqrt{t}} \quad (2)$$

The limiting particle size which does not precipitate by centrifuging because of its brownian motion is calculated to be about $1 \text{ }\mu\text{m}$ in the case of maximum rotation rate of this centrifuge.

On the basis of the above considerations, the distribution of particle size should be discussed. Fig. 2 shows a histogram of the relative particle size of both fresh and aged plutonium colloids. About one half of the fresh colloid belongs to the smallest particle group. If Eq. (2) is applicable, the r values of this group are below $1 \text{ }\mu\text{m}$. Also 94% of the fresh colloid has a value of $1/\omega \sqrt{t} \times 10^6$ lower than 5.3. On the contrary, 35% of the aged colloid belongs to the largest group. According to Eq. (2), the r values of this group are above $15 \text{ }\mu\text{m}$. The fraction of the finest group decreases to 10% in the aged colloid.

These facts suggest that very fine polymer particles (probably a few \AA in diameter) of plutonium are formed at the early stage of colloid formation, and that the diameter of these particles will grow up to the $\text{ }\mu\text{m}$ order.

Most of the centrifugal studies given in references were carried out in a low speed centrifuge such as 3000 rpm, with hydroxide precipitation or adsorption colloid (pseudo-colloid) of plutonium.

One exception is the case of ref. 8 reported by Ockenden and Welch. They used a centrifuge with a centrifugal force of 7000 times gravity acceleration. At a maximum centrifuging time of 300 min, the fresh and aged plutonium colloids precipitated in 5 and 85%, respectively. According to our calculations, the diameter of the precipitated particles is about 4 μ if the parameters are taken as the same as in the present work. Lloyd studied the size of fresh colloidal particles of plutonium polymer by electron microscopy and found them less than 2 μ .¹²⁾ These results are consistent with the present work.

(F. Ichikawa)

References

- 1) Kraus, K. A.: CN-3399(1945).
- 2) Cleveland, J. M.: "The Chemistry of Plutonium", Gordon & Breach Sci. Publ., 83(1970).
- 3) Werner, L. B.: CN-2034(1944).
- 4) Werner, L. B. : CN-P-327(1944).
- 5) Werner, L. B. : CN-2214(1944).
- 6) Hindman, J. C. : " The Actinide Elements", NNES IV, 14A, 301(1954).
- 7) Schubert, J., et al : CN-2197 (1944).
- 8) Ockenden, D. W. and Welch, G. A. : J. Chem. Soc., 3358(1956).
- 9) Grebenschikova, V. I. and Davydov, Yu. P. : Radiokhimiya, 3, 155(1961).
- 10) Grebenschikova, V. I. and Davydov, Yu. P. : Radiokhimiya, 7, 191(1965).
- 11) Andelman, J. B. and Rozzell, T. C. : RH 322-04, ESEA (1968).
- 12) Lloyd, M. H. and Haire, R. G. : Conf. 730927-2 (1973).
- 13) Constanzo, D. A. and Biggers, R. E. : ORNL-TM-585 (1963).

Publication List

- [1] Ichikawa, F. and Sato, T. : " On the Particle Size Distribution of Hydrolyzed Plutonium (IV) Polymer ", J. Radioanal. and Nucl. Chem., Articles, 84, 269(1984).

Table 1 Fraction of fresh plutonium colloid precipitated by centrifuging.

Rotation rate, rpm	Rotation time, hr.	C, %
5000	1	6.2
30000	1	6.1
50000	1	1.4
55000	1	10.3
60000	1	20.1
65000	1	36.5
65000	4	31.5
65000	8	63.3
65000	12	57.1
65000	18	59.6
65000	25	84.9
65000	70	98.2

Table 2 Fraction of aged plutonium colloid precipitated by centrifuging.

Rotation rate, rpm	Rotation time, hr.	C, %
5000	1	35.9
15000	1	37.8
30000	1	47.3
50000	1	53.7
55000	1	58.9
60000	1	68.4
65000	1	57.3
65000	4	68.0
65000	8	79.2
65000	13.5	86.7
65000	18	89.6
65000	25	92.5

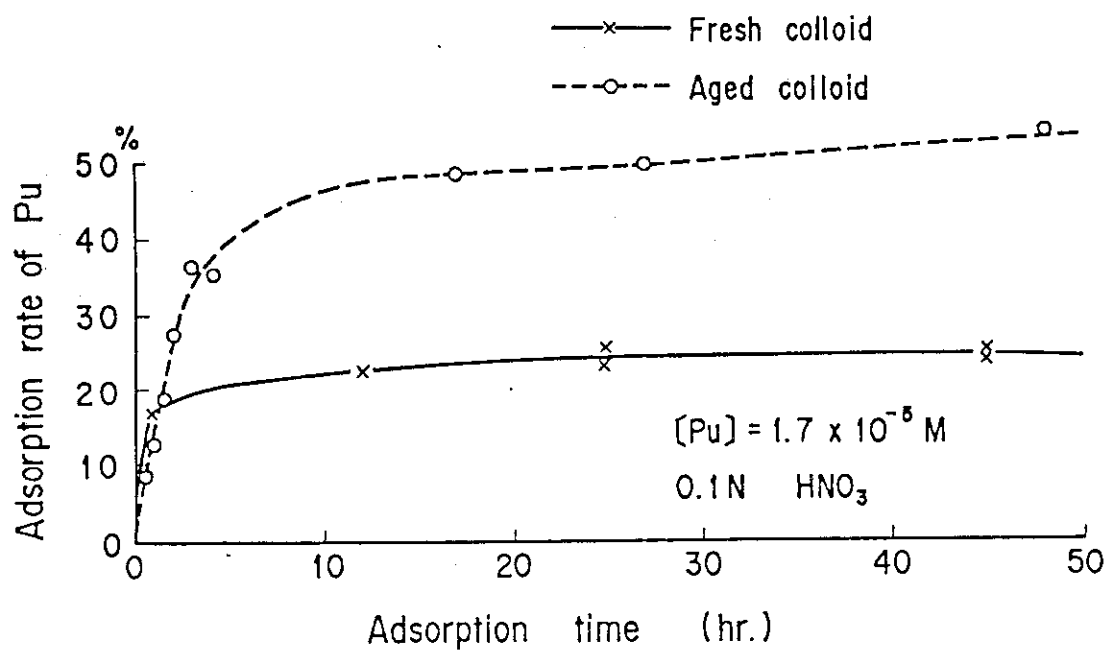


Fig. 1 Adsorption rate of colloidal plutonium on the wall of the centrifuging tube.

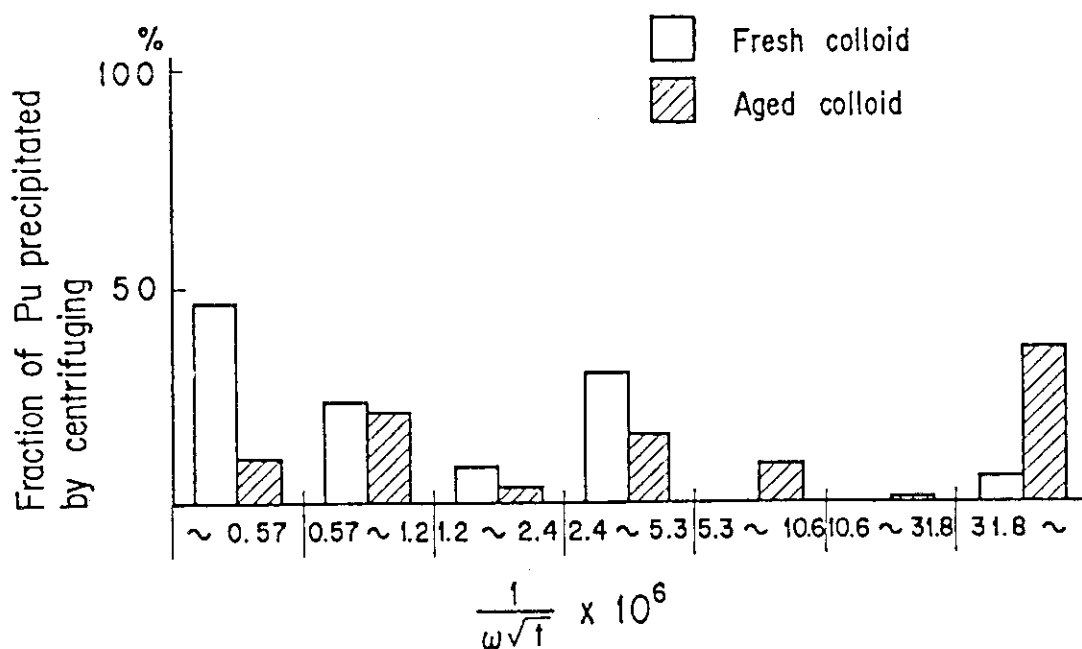


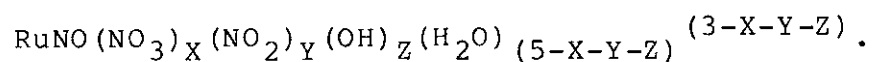
Fig. 2 A histogram of relative particle size of colloidal plutonium

13.2 Solution Chemistry of Ruthenium

13.2.1 Introduction

In nuclear fissions of uranium and plutonium, ruthenium is produced in relatively high fission yield. The element behaves in a quite different way from other fission products in nitric acid solution which is widely used in reprocessing of nuclear spent fuel by Purex process. It is difficult to describe completely the behavior of the element in solvent extraction separation in Purex process. For instance, a part of ruthenium remains in the uranium and plutonium products and increases the radiation level: some appear in the medium level aqueous waste stream and account for main activity in the waste.

Studies¹⁾ have been devoted to clarifying the behavior of the element in nitric acid solution. Fletcher et al.²⁾ first pointed out that in nitric acid solution, ruthenium formed ruthenium nitrosyl ion RuNO^{3+} , stable in various concentrated mineral acids and that nitrosyl made many complexes with various ligands including NO_3^- , NO_2^- , OH^- , and H_2O in general formula:



The complexities of the element in nitric acid solution are ascribed to the existence of such nitrosyl ruthenium complexes and to the transformation of one species to others.

The present work was aimed to separate these ruthenium species and to clarify the chemical behaviors.

13.2.2 Experimental

Fission products stock solution: The solution was prepared by dissolving irradiated uranium dioxide in concentrated nitric acid followed by gentle drying and redissolving in 1N nitric acid.

Separation method: High performance liquid chromatograph equipped with radiation detector was applied to the experiments. Two kinds of column, different in length, (60 cm and 1360 cm), with the same strongly acidic cation exchanger of sulfonic acid type were used to separation of cationic, anionic and neutral ruthenium species. The 60-cm column was used for the separation of cationic species and the 1360-cm one for neutral and anionic species.

13.2.3 Results and Discussion

Immediately after the dissolution of irradiated uranium dioxide in nitric acid, most of the fission product ruthenium were observed as anionic species. Cationic and neutral species increased in the solution with aging. At 100- days aging, the separated ruthenium species were four anionic, six neutral and fourteen cationic ones. While the charge of the cationic ruthenium species in 1N nitric acid can be estimated by comparing the K_d values of ruthenium species with those ions having definite charge such as Cs^+ , Sr^{2+} and Eu^{3+} , charge of the cationic ruthenium species separated were determined from the slope of $\log -\log$ plot of K_d value of the species versus activity of nitric acid used for elution. It was found that there were seven monopositives, three dipositives and four tripositive ruthenium species.

According to the theory of dissociation of nitrosyl ruthenium complex³⁾, the tripositive species should be uncomplexed nitrosyl ruthenium ion, RuNO^{3+} . If there exist non nitrosyl species in the solution, the species with tripositive charges is but one species, Ru^{3+} . The present results, existence of four tripositive ruthenium species can not be explained from current understanding of ruthenium chemistry.

All the ruthenium species separated by high performance liquid chromatograph were offered to determine distribution coefficient for 100 % TBP- 1N nitric acid extraction. One mononegative and one monopositive charged species were only extracted appreciably by the 100 % TBP. Fletcher et al.²⁾ described that extractable ruthenium species by TBP extraction were tetranitrate nitrosyl and trinitrate nitrosyl. As tetranitrato nitrosyl ruthenium was not stable in dilute nitric acid, only trinitrato nitrosyl ruthenium was responsible for high ruthenium extraction in Purex process. Trinitrato nitrosyl ruthenium has no electric charge. In the present work, no neutral species was extracted by 100 % TBP. This results also contradict the Fleacher's report²⁾.

(T.Sato)

Reference

- 1) Diana, J., : CEA-R-4813(1977).
Guegueniat, P., : CEA-R-4644(1975).
- 2) Fletcher, J., et al. : J.Inorg.Nucl.Chem.,1, 378(1955).
- 3) Siczek, A.,Steindler, M.: Atomic Energy Rev.,16, 575(1978).

14. ANALYTICAL SERVICES FOR IRRADIATED FUELS

H.Okashita, S.Okazaki*, T.Suzuki,
T.Sonobe, M.Ohnuki, Y.Nakahara*,
N.Kono, S.Usuda, S.Ichikawa,
N.Shinohara, S.Tsubakizaki and
M.Magara

14.1 Burnup Measurements of Spent Fuels from Power Reactors

14.1.1 Introduction

Burnup is an inevitable value in evaluation of spent fuels, since the burnup characteristics, the integrity and the nuclear transmutation of the fuel should be referred to the burnup. Based on the system we developed, burnup measurements have been performed for the spent fuel samples from several power reactors such as JPDR, Mihama, Genkai, Tsuruga and Oi, as well as from experimental and research reactors such as JRR-2, -3 and -4, JMTR and Fugen. Various irradiation test fuels have been also measured, especially of coated particle fuels for HTGR.

The present paper deals with the procedure used for the measurements of these irradiated fuels.

14.1.2 Procedures for Burnup Measurements

The most accurate method for burnup measurement is based on evaluating the fission numbers from ^{148}Nd content in the fuel sample. To determine the atom number of ^{148}Nd , the sample should be treated chemically to isolate the neodymium from the other elements. Major fission product and transuranium nuclides have

to be also measured for an evaluation of the burnup characteristics. The procedures for routine measurements are as follows:

- 1) The sample specimens received are subjected to direct gamma-ray spectrometry for determining the sample size to be treated. The specimens are dissolved in nitric acid with appropriate carriers such as Cs for avoiding loss by adsorption of important nuclides on glassware wall.
- 2) Appropriate aliquots of the solution are weighed and the two aliquots are subjected to chemical separation. An aliquot is measured immediately with Ge detector for gamma-emitting fission products.
- 3) A definite amount of spike mixture which contain ^{233}U , ^{242}Pu and ^{150}Nd is added to one of the two aliquots for isotope dilution analysis with mass-spectrometer. Chemical separation by ion exchange is carried out for the spiked and non-spiked aliquots. Details of the separation and purification procedure are given schematically in Fig. 1.
- 4) The purified elements are measured by mass-spectrometer for uranium, plutonium and neodymium and by alpha spectrometer for transuranium elements such as Np, Am and Cm.

14.1.3 Burnup Evaluation

Using the data measured, burnup is calculated as the following equation:

$$\text{BU (\%)} = \frac{100 \text{ K } R_{\text{FP/U}}/Y_{\text{FP}}}{1 + R_{\text{Pu/U}} + \text{K } R_{\text{FP/U}}/Y_{\text{FP}}}$$

where $R_{\text{FP/U}}$, $R_{\text{Pu/U}}$: Atom ratio of ^{137}Cs or ^{148}Nd to U, and Pu to U,

Y_{FP} : Cumulative fission yield of ^{137}Cs or ^{148}Nd ,
and K : Inpile-outpile decay factor of the ^{137}Cs .
Details of the procedure are given elsewhere¹⁾.

(H.Okashita)

Reference

- 1) Natsume, H., et al.: J.Nucl.Sci.Technol., 14, 745(1977).

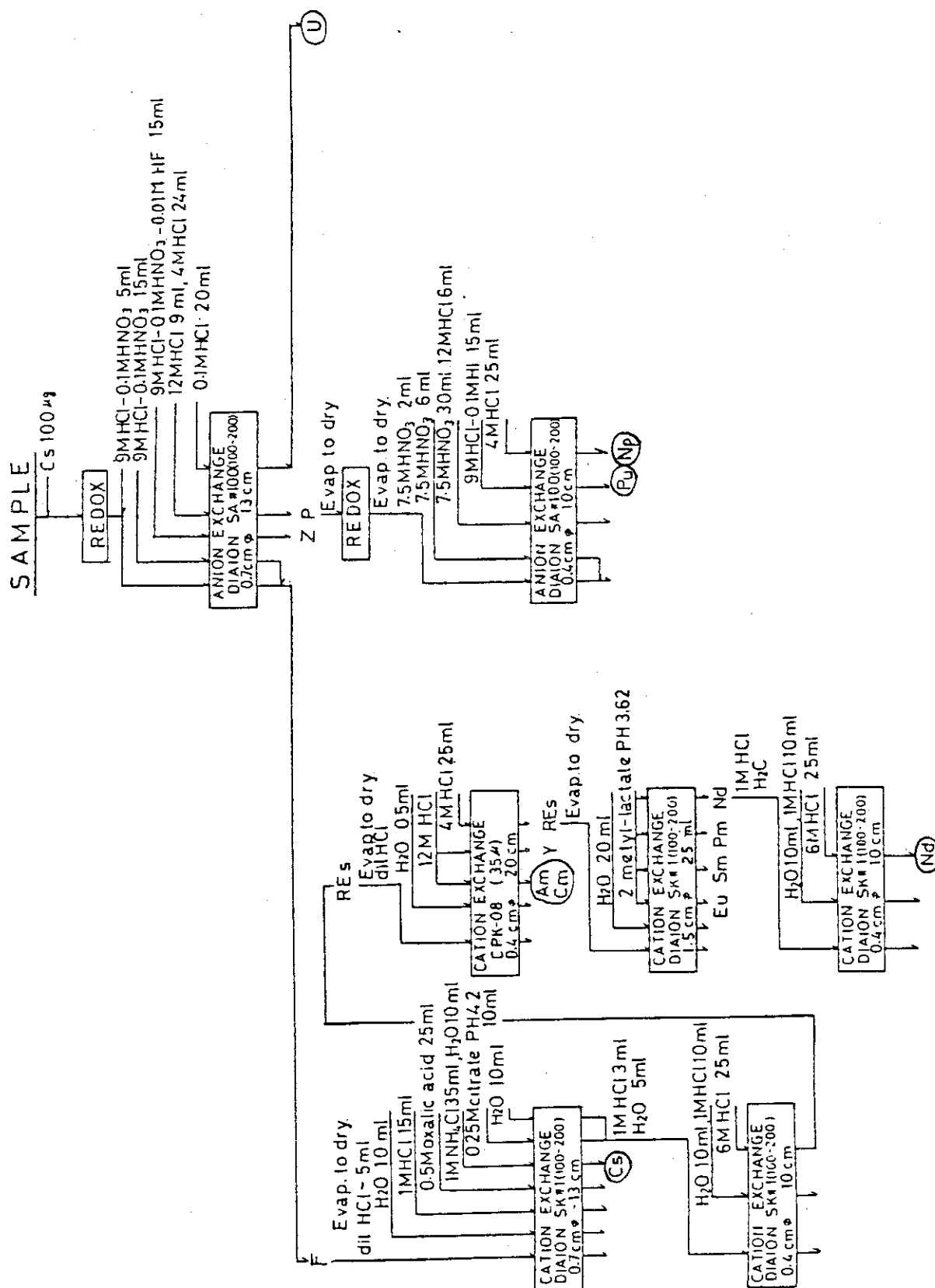


Fig. 1 Flow chart of the chemical procedures by ion exchange.

14.2 Measurements of Absolute Fission Number of NSRR Test Fuels

14.2.1 Introduction

In the case of abnormal operation of nuclear reactor, for instance, out of control of the reactor power accidentally, there is a possibility of the excess energy deposition in the fuel elements leading to the fuel failure. To evaluate such phenomena, the Nuclear Safety Research Reactor (NSRR) group in the JAERI has been continued the fuel tests irradiating pulsely with high neutron flux. The energy deposited to the fuel is the main parameter for analysing behavior of the fuel in such extraordinary situation. The absolute values of energy deposition are obtained from evaluating the number of fissions occurred in the test fuels (UO_2 , $\text{UO}_2\text{-Gd}_2\text{O}_3$ and $\text{UO}_2\text{-PuO}_2$).

As the one-pluse irradiation only causes very small number of fissions compared with spent fuels from power reactors, weak radioactivities from the fission products are the unique clue to trace the fissioning. Gamma-ray spectrometry is the most effective method for determination of such micro amount of fission products. The following section outlines the measurements of the absolute fission numbers by gamma-ray spectrometry.

14.2.2 Procedures for Measurements of Very Small Numbers of Fissions

General flow of the measurement procedures is described as follows:

- 1) The test fuel assembly which was irradiated in the NSRR is discharged from the experimental hole passing through the reactor core.

- 2) For radioactivity measurement, certain pellets are taken out from the fuel rod and weighed. The pellet is dissolved in 6 M HNO_3 solution (about 50 ml) with Cs carrier (about 1 mg) and then diluted to 100 ml with distilled water. A definite weight (about 4 ml in volume) of the solution is taken as the measuring sample.
- 3) Radioactivity of the sample is measured with Ge detector referring to some gamma-ray standard sources such as Eu-152 or Cs-137. The gamma-ray spectrum analysis is made by using code "BOB"¹⁾.
- 4) Absolute fission number per UO_2 or $\text{UO}_2\text{-PuO}_2$ can be evaluated from the activities of the selected fission products considering the half-lives and the fission yields of the nuclides, and the cooling time.

Table 1 shows typical radioactivities of the relevant fission product nuclides in different cooling times.

Besides, an alternative procedure is usually applied to the measurement of $\text{UO}_2\text{-PuO}_2$ fuels for avoiding tedious chemical handling: The sample pellets are directly subjected to gamma-ray spectrometry. Attenuation of the gamma ray by the sample itself is calibrated by an internal correction method which use the 413 KeV peak of ^{239}Pu gamma-ray for normalization of the fuel attenuation equation. The fission product nuclides to be measured are the same as the one listed in Table 1.

Details of the procedures are given elsewhere [1].

(N.Shinohara and T.Suzuki)

Reference

- 1) Baba, H.: JAERI-M 7017, (1977).

Publication List

- [1] Yanagihara, S., Suzuki, T.: "Evaluation of Energy Deposition in Various Test Fuel Rods in the NSRR Experiments", (in Japanese), JAERI-M 85-208 (1986).

Table 1 The radioactivities of the selected fission products for the evaluation of energy deposition in the NSRR Test Fuels.

Nuclide	$T_{1/2}$	FY (%)	Activity (Bq/g·UO ₂)*			
			Cooling Time (day)			
			0	30	60	90
Y-91	58.5 d	5.93	285,000	200,000	140,000	98,100
Zr-95	64.0 d	6.52	286,000	207,000	149,000	108,000
Ru-103	39.35 d	3.04	217,000	128,000	75,400	44,500
Ru-106	371.6 d	0.40	3,020	2,860	2,700	2,550
I-131	8.02 d	2.89	101,000	7,560	565	42
Cs-137	30.17 y	6.19	1,580	1,580	1,580	1,570
Ba-140	12.75 d	6.19	1,360,000	266,000	52,100	10,200
Ce-141	32.5 d	5.82	503,000	265,000	140,000	73,800
Ce-144	284.6 d	5.50	54,200	50,400	46,800	43,500
Nd-147	10.98 d	2.26	578,000	87,000	13,100	1,970

FY : fission yield (U-235, thermal)

*Number of the fission : 3.5×10^{13} fissions/g UO₂ (236 cal/g UO₂).

15. STUDIES ON FIXATION OF VOLATILE RADIONUCLIDES

T. Sakurai, Y. Komaki,
A. Takahashi, G. Fujisawa,
Y. Hinatsu and M. Izumo

15.1 Application of Silver-free Zeolites to Remove Iodine from
the Dissolver Off-gas

15.1.1 Introduction

The caustic scrubbing is the most widely used in the world for iodine removal process of the dissolver off-gas (DOG). This process has however disadvantages that it produces large amounts of waste and also that its efficiency is relatively low, especially for removal of organic iodides. An alternative process with high iodine-removal efficiency has to be established for treatment of DOG from highly burnt LWR fuels. A dry process using silver-impregnated adsorbents has been attracting concern of the people in this field. They can remove both elemental iodine and organic iodides with high decontamination factors ($DF > 10^4$) and their efficiencies are relatively not affected by the presence of such impurities as NO_x and H_2O . However, since their recovery process has not been sufficiently established yet,¹⁾ the adsorbents loaded with iodine have to be fed to the long-term storage or disposal without being reproduced. This situation makes the process expensive.

On the other hand, silver-free zeolites were not taken up for the off-gas treatment. The reason seems to be that they lose their abilities of adsorbing iodine when co-adsorption of

water occurs.²⁾ Recently, addition of dehumidification unit to DOG line is under consideration in our country from the viewpoint of controlling tritium release to environment: water content of DOG is expected to be decreased to considerably low levels. This situation has urged us to reconsider the use of less expensive silver-free zeolites for iodine removal process of DOG.

On this assumption, silver-free zeolites have been studied in our laboratory, in order to probe their abilities of adsorbing iodine in the presence of NO_x which is one of the main impurities present in DOG [1]. At present, 13X zeolite is in use because of its high adsorption capacity. The results so far obtained were summarized below.

15.1.2 Adsorption of elemental iodine

The adsorption capacity of 13X zeolite for elemental iodine (I_2) was already reported by earlier workers; it amounted to a value of 364 mg- I_2 /g-zeolite at 150 °C.³⁾ In the present work, we checked the thermal stability of the iodine adsorbed on 13X zeolite and a silver-impregnated zeolite "AgX" [2].

An air flow including about 150 ppm- I_2 (labeled with ^{131}I) and 2 %- NO_x was passed through a vertical adsorption column (Pyrex, 16 mm i.d. x 200 mm length) packed with either 13X zeolite or AgX at room temperature for 2 h. About 6 mg of I_2 was trapped at the bottom of the zeolite bed in the column; iodine was not released from the column during this period of time in both cases. The adsorption column was then heated in an air flow of 50 cc/min up to 550 °C; in the course of heating, the column was kept for each 1 h at 100, 200, 300, 400 and 550 °C.

After each step, the distribution of I_2 in the column was checked with γ -spectrometry. Fig. 1 shows the temperature dependence of migration of the adsorbed iodine in the 13X zeolite bed. Adsorbed iodine was retained at the place up to 100 °C; beyond 100 °C, it began to travel in the direction of flow. On the other hand, AgX fixed iodine so tightly that the migration of iodine did not occur even at 550 °C (Fig. 2).

Zeolite 13X is inferior to AgX with respect to the thermal stability of adsorbed iodine; if stated reversely, this means that the reproduction is easier for the former than for the latter. In the process using 13X zeolite, adsorbed iodine should be desorbed again in order to be changed into its stable form suitable for long-term storage. The role of 13X zeolite is in enrichment of dilute iodine contained in DOG.

15.1.3 Adsorption of organic iodides

It is said that organic iodides constitute 1~10 % of the total iodine quantity in DOG. The main species of the organic iodides has been postulated to be methyl iodide (CH_3I). Since no experimental data were available for its interaction with silver-free zeolites in the presence of NO_x , we checked behavior of CH_3I in this system. Nitrogen dioxide (NO_2) represented NO_x in the present work. Radioactive methyl iodide was prepared through the reaction between dimethyl sulfate and sodium iodide labeled with ^{131}I . Behavior of the methyl iodide was traced by γ -spectrometry.

An air flow including ~ 100 ppm- CH_3I and ~ 1 %- NO_2 was fed to the adsorption column (mentioned already) packed with 13X zeolite at 241 cc/min. The column was kept at room temperature

($\sim 20^\circ\text{C}$). The air flow from the column was then passed through a back-up filter of triethylenediamine (TEDA)-impregnated charcoal which was effective for capturing organic iodides.

Methyl iodide was accumulated at the bottom of the zeolite bed increasingly with elapse of time [3]. Fig. 3 shows the distribution of ^{131}I in the column. No radioactivity was detected at the TEDA filter downstream of the column. It is evident therefore that 13X zeolite can remove dilute CH_3I effectively from DOG.

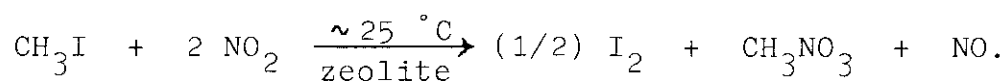
When supply of the gas was started, a yellow adsorption band of NO_2 was first noticed at the bottom of the zeolite bed. Behind this band, the zeolite bed turned pink due to the adsorption of iodine. Appearance of the pink adsorption band means that the decomposition of CH_3I into I_2 has taken place in the presence of NO_2 . The adsorption front of NO_2 traveled much faster than that of I_2 in the direction of flow. After 20 h of the gas supply, the former reached a position of 14 cm distant from the inlet of the column, whereas the latter was at a distance of only 3.5 cm from the inlet (Fig. 3). Heating the column in air flow resulted in the release of NO_2 at $100\sim 200^\circ\text{C}$ and then the desorption of I_2 beyond 300°C .

Since the decomposition of CH_3I was found to occur in the presence of NO_2 , we studied it further in order to establish its stoichiometry [4]. A static method was adopted. About 500 mg of dried 13X zeolite (1/16" pellets) were put in a Monel reactor (24 mm i.d. x 150 mm length). The reactor was evacuated and cooled with liq- N_2 . Then prescribed amounts of CH_3I and NO_2 were introduced in it (119.4 and 17.4 mg, respectively). After kept at room temperature for 1 h, the system was fed to IR ana-

lysis.

Fig. 4 shows the results of IR analysis. In the figure, (1) and (2) are the spectra of pure CH_3I and NO_2 , respectively; (3) shows the spectrum of the free gas which remained in the reactor after the adsorption. The spectrum reveals presence of NO , N_2O and other unknown substances. Mass spectrometry of the gas indicated that its main component was NO and further that no free oxygen was present in it.

After evacuation, the reactor was warmed slowly in order to desorb the unknown substances. Beyond 50°C , the desorption became observable. In Fig. 4, (4) shows the spectrum of the gas desorbed. Analyses of IR and mass spectra revealed that the substance desorbed was methyl nitrate (CH_3NO_3). When a gaseous mixture of CH_3I and NO_2 was kept in the absence of the zeolite for 1 h, its IR spectrum was merely superposition of those of the two substances. The reaction needs the presence of the zeolite.



The same reaction was noticed on AgX and also on a natural mordenite hydrogenated. A similar reaction was also confirmed for $\text{C}_2\text{H}_5\text{I}$ [4]. Thus, it was found that such organic iodides as CH_3I and $\text{C}_2\text{H}_5\text{I}$ were decomposed by NO_2 on the zeolites to change into I_2 .

15.1.4 Experiments by simulated DOG

In order to see the behavior of the I_2 which was produced through the foregoing reaction, simulated DOG — an air flow

including ~ 10 ppm- CH_3I , ~ 100 ppm- I_2 and ~ 1 %- NO_2 — was supplied to the adsorption column (described already) packed with 13X zeolite (1/16" pellets) at 25 °C and at a linear gas velocity of ~ 2.3 cm/s for 25 h. Prior to the experiments, either I_2 or CH_3I was labeled with ^{131}I in order to distinguish their behavior, and the experiments were repeated under the same conditions.

Fig. 5 shows the distribution of iodine in the column. Both of the iodines — one was originally in the DOG and the other came from CH_3I through the reaction — were trapped at almost the same place near the inlet of the column [5]. It is evident therefore that the presence of such an organic iodide as CH_3I in DOG brings about no additional problems into the iodine removal process using 13X zeolite.

15.1.5 Conclusion

Dehumidification of DOG makes it possible to use less expensive silver-free zeolites for removal of iodine. Both elemental iodine and organic iodides are adsorbed effectively on the zeolites. Organic iodides are decomposed into I_2 by NO_2 in the presence of the zeolites. For its long-term storage, the adsorbed iodine should be desorbed again by heating and changed into its stable solid form, e.g. CuI . Reproduction of 13X zeolite is much easier than that of AgX.

(T. Sakurai)

References

- 1) Burger, L.L., Scheele, R.D.: PNL - 4689, (1983).
- 2) Wilhelm, J.G. : KFK - 1065, (1969).

- 3) Staples, B.A., Murphy, L.P., Thomas, T.R. : CONF - 760822, (1976).

Publication List

- [1] Sakurai, T., Izumo, M., Takahashi, A., Komaki, Y.: "Application of zeolites to remove iodine from dissolver off-gas, (I) Follow-up of Wahlgren and Meinke's experiments", J. Nucle. Sci. Technol, 20, 264 (1983).
- [2] Sakurai, T., Izumo, M., Takahashi, A., Komaki, Y.: "Application of zeolites to remove iodine from dissolver off-gas, (II) Thermal stability of iodine adsorbed on 13X, 5A and silver-exchanged zeolites", ibid., 20, 784 (1983).
- [3] Sakurai, T., Komaki, Y., Takahashi, A., Izumo, M.: "Application of zeolites to remove iodine from dissolver off-gas, (III) Adsorption of methyl iodide on zeolite 13X", ibid., 20, 1046 (1983).
- [4] Sakurai, T., Komaki, Y., Takahashi, A., Izumo, M.: "Reaction of CH_3I and $\text{C}_2\text{H}_5\text{I}$ with NO_2 on zeolite 13X", ibid., 21, 877 (1984).
- [5] Sakurai, T., Komaki, Y., Takahashi, A., Izumo, M.: "Application of silver-free zeolite to remove iodine from dissolver off-gas in spent fuel reprocessing plants", IAEA-TECDOC -337, (1985), P.53-62.

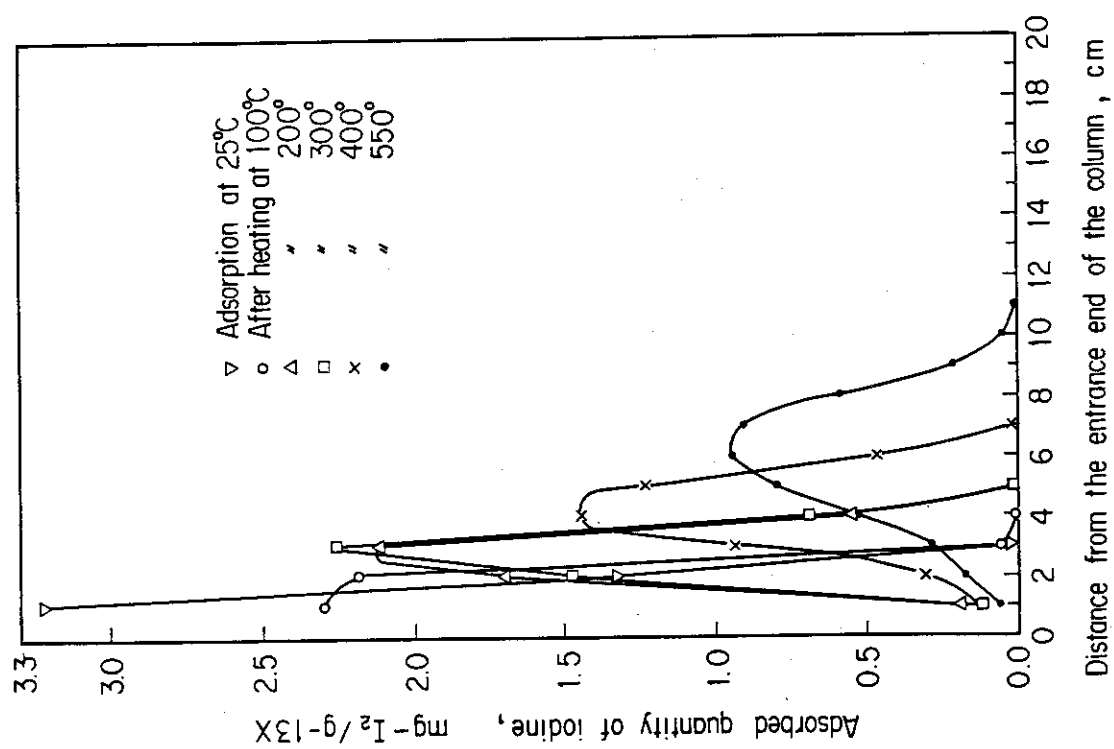


Fig. 1 Thermal behavior of iodine adsorbed on zeolite 13X (iodine content in the bed, ~ 6 mg) [2].

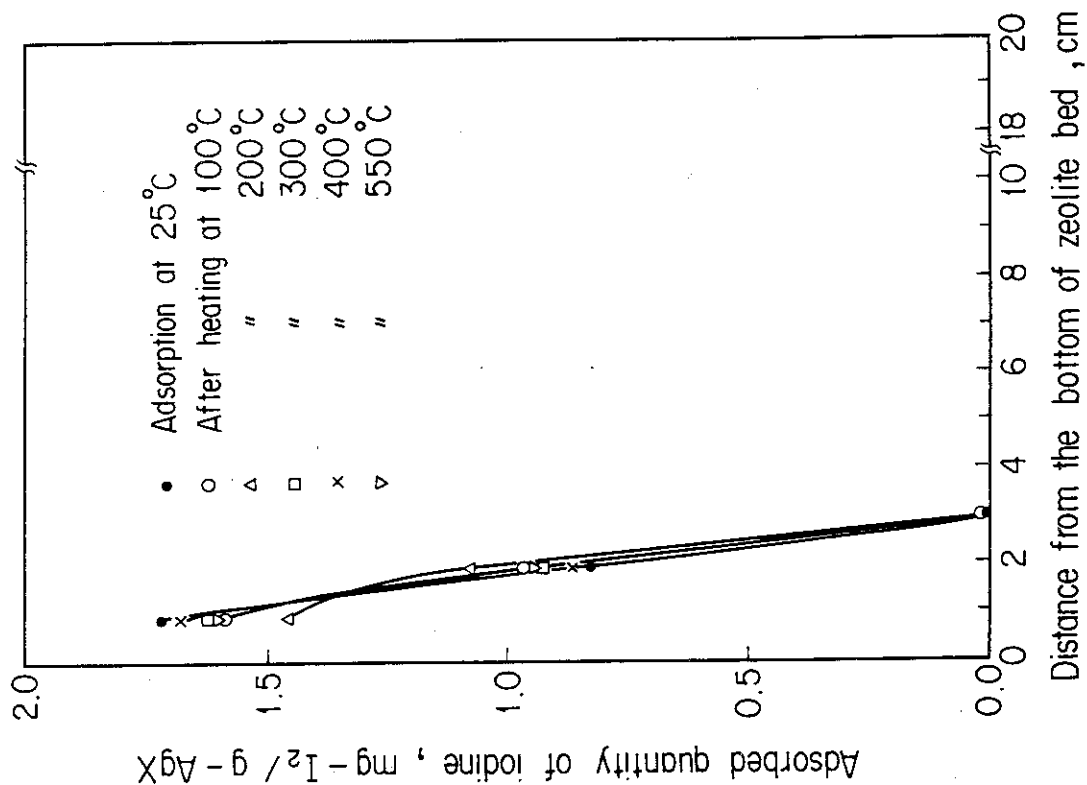


Fig. 2 Thermal behavior of iodine adsorbed on silver-exchanged zeolite 'AgX' (iodine content in the bed, ~ 6 mg) [2].

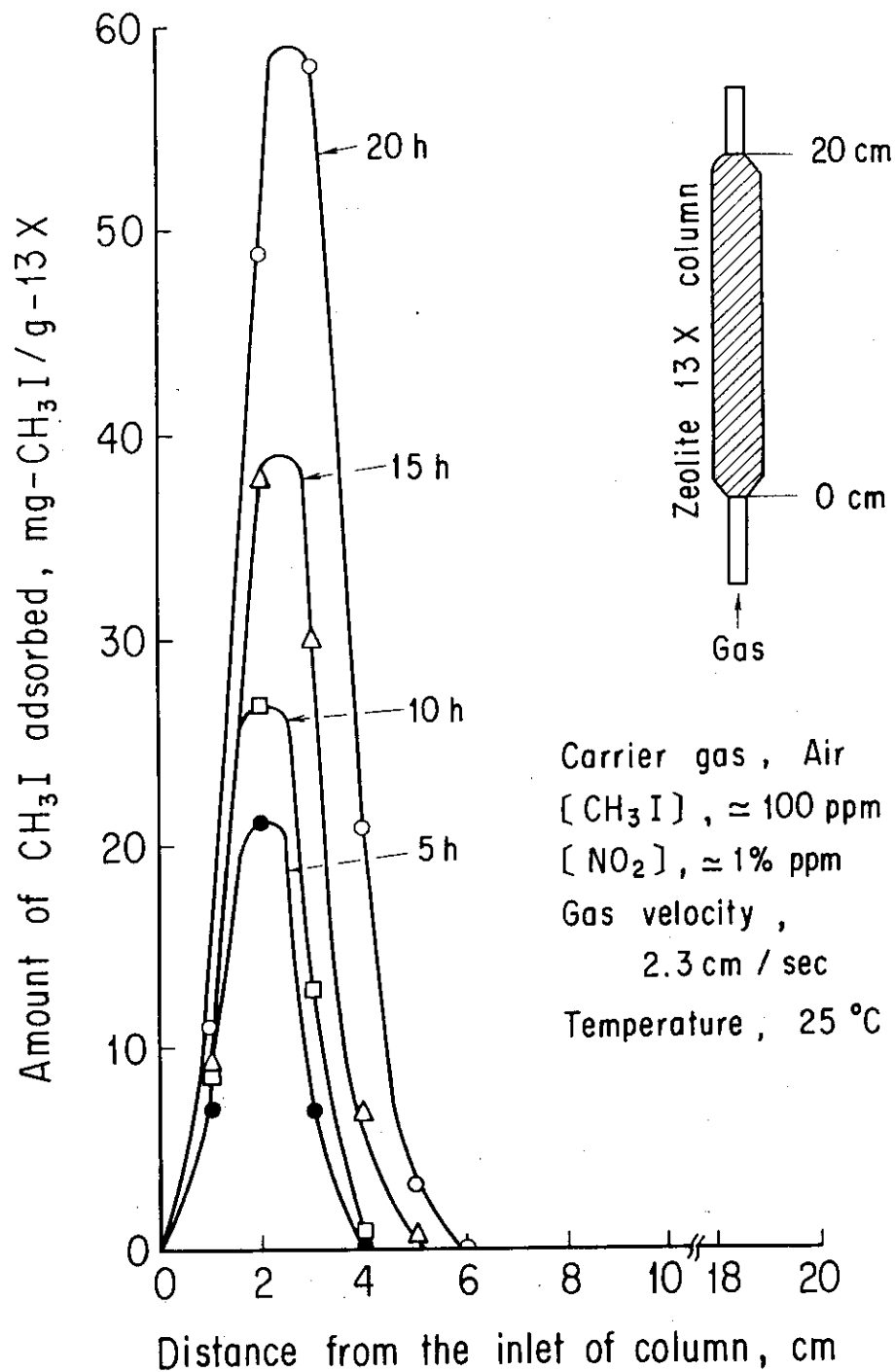


Fig. 3 Distribution of CH_3I in the zeolite 13X column after supply of the process gas of 5, 10, 15 and 20 h at 25°C [3].

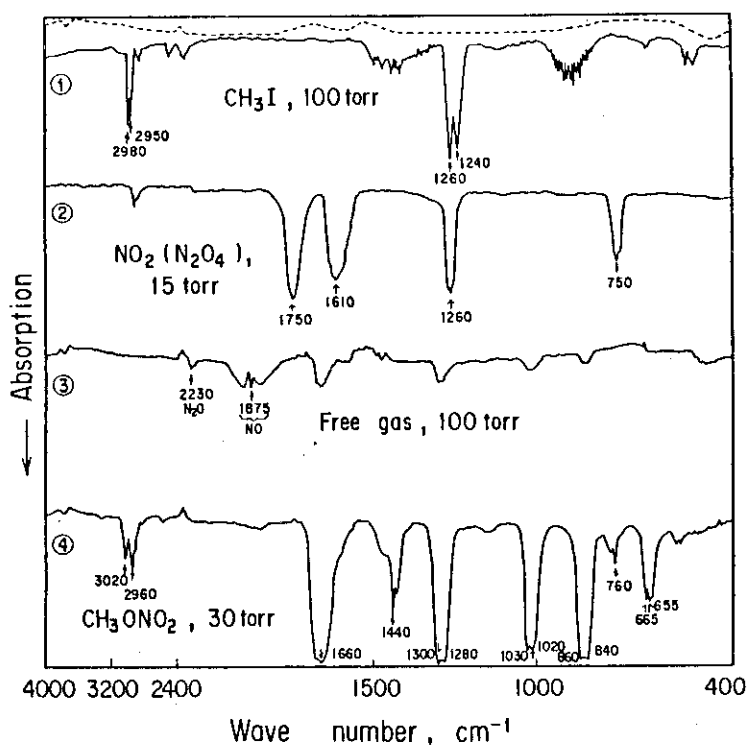


Fig. 4 Infrared spectra of ① CH_3I , ② NO_2 ($2\text{NO}_2 \rightleftharpoons \text{N}_2\text{O}_4$), ③ the free gas remaining after the adsorption process, ④ a reaction product CH_3ONO_2 [4].

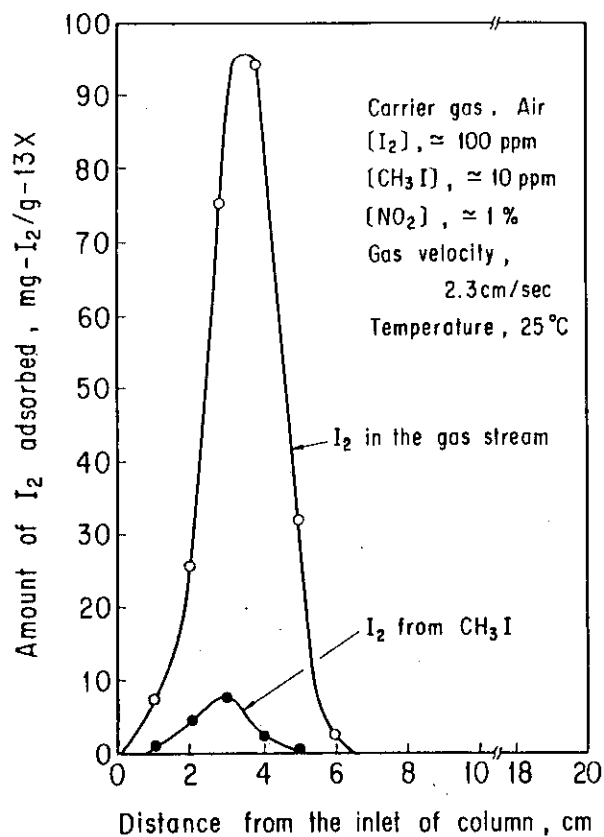


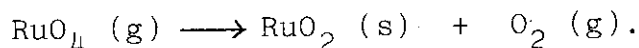
Fig. 5 Distribution of the adsorbed iodine (I_2) along the length of the zeolite 13X column (the gas supply, 25 h) [5].

15.2 Interaction of RuO_4 with Metal surfaces

15.2.1 Introduction

Volatile ruthenium species include RuO_4 , RuOF_4 , RuF_5 and RuF_6 ; they show complex behavior associated with their instabilities [1]. Ruthenium tetroxide (RuO_4) is a troublesome substance in the waste treatment of spent nuclear fuels. When contacted with gaseous RuO_4 , a number of materials are covered with a nonvolatile black deposit of ruthenium even at room temperature. Because of the substantial quantity of ruthenium in high level liquid waste of commercial nuclear reprocessing plants, any appreciable volatilization of RuO_4 during the waste treatment has potential for plugging off-gas piping of the equipment due to the deposition.¹⁾ Clarification of the volatilization/deposition mechanisms and establishment of an effective counterplan are necessary for successful operation of the process.

The deposition of ruthenium has been postulated to be due to decomposition of reactive and unstable RuO_4 into nonvolatile RuO_2 :²⁾



However, it seems likely that there are no fundamental works which proved this decomposition. Instead, there are evidences that the tetroxide is stable enough to exist at temperature higher than 500 °C.^{3),4)} The decomposition may be a hypothesis arising probably from the similarity in color between RuO_2 and the deposit.

From both chemical interest and practical necessity, we were motivated to study the interaction between gaseous RuO_4

and metal surfaces. Stainless steel (SUS-304), nickel, copper and gold were exposed to gaseous RuO_4 , and the generation of free oxygen and the character of the deposit on the metals were examined with mass spectrometry, XPS (X-ray photoelectron spectroscopy), X-ray diffraction analysis, IR analysis and chemical analysis. The conclusion derived is that the deposit is not RuO_2 but a modification of RuO_4 , i.e., $(\text{RuO}_4)_n$. Details leading to this conclusion will be described below.

15.2.2 Oxygen produced during the process

Mass spectrometry and chemical analysis were used to see whether oxygen was liberated by the interaction of RuO_4 with the metals [2]. First, a preliminary experiment was carried out to check its interaction with the wall of the Monel container which the pieces of the sample metals were to be put in. The tetroxide alone was transferred into the container and was kept for 24 or 50 h at 25 °C. It was then cooled to -196 °C to solidify the excess RuO_4 , and the pressure and composition of the residual gas were examined by mass spectrometry. After the measurements, excess RuO_4 was removed by pumping at room temperature and then the container was filled with a $\text{NaOH-K}_2\text{S}_2\text{O}_8$ solution for determination of the ruthenium deposited on the wall.

When the amount of ruthenium in the deposit was 7.5 mg, the pressure of the residual gas in the container was far less than 1 mm Hg ($< 1.33 \times 10^2$ Pa) at -196 °C and its composition was the same as that of background gas. If decomposition of RuO_4 had taken place, an oxygen pressure of 4.6 mm Hg (612 Pa) would have been reached in the container under the present experimental conditions. Hence, we first confirmed that no free

oxygen was released by the process depositing the ruthenium on Monel.

This preliminary experiment was followed by those using sample metals. The Monel container was packed with pieces of one of the metals, and they were treated in the same manner as in the preliminary experiment. In a day, they were covered with the black deposit of ruthenium. Table 1 summarizes the results [2]. Only in the case of copper was a measurable release of oxygen detected; the amount was only 0.8 % of the theoretical value predicted for the decomposition. The deposition occurred even on the nonoxidizable metal, i.e., gold, without releasing oxygen. The results indicate that the interaction of RuO_4 with metals does not bring about its decomposition accompanied by liberation of O_2 .

15.2.3 Binding energy of electrons in the deposit

A piece of each metal covered with the deposit was subjected to XPS. The binding energy of electrons was referenced to the $\text{Au } 4f_{7/2}$ level of Au at 84.0 eV. The XPS spectra of the deposits on Ni, SUS and Cu were the same; they were similar to that of RuO_2 [2],[3]. Fig.1 shows the spectrum of the deposit on Ni [2]. In the binding energy range up to 1000 eV, the peaks of the Ru 3d, Ru 3p, Ru 4s and O 1s levels are observable. However, no peaks due to the electrons of the substrate metal were observed. These findings attest to the absence of substrate metal atoms on the surface of the deposit and also within a depth of about 20 Å below the surface.⁵⁾

The XPS spectrum of RuO_2 is different from those of the deposits in both binding energies of inner-shell electrons and

abundance of oxygen. Table 2 lists the observed binding energies of the Ru $3d_{5/2}$ and O $1s$ levels for the deposits and RuO_2 , together with those for Ru metal and its oxides obtained by Kim and Winograd⁶⁾ [2]. The difference in binding energy of the Ru $3d_{5/2}$ level between RuO_2 and the deposits, ~ 0.7 eV, is beyond the experimental error of ± 0.1 eV, inherent in XPS.

On the other hand, the binding energy of the Ru $3d_{5/2}$ level of the deposits is considerably lower than those of both RuO_3 and RuO_4 . Since the binding energies of inner-shell electrons are qualitatively proportional to the valence of the atom, this finding indicates that the adsorption reduces the net charge density of the Ru atoms.

The valency of ruthenium in the deposits is lower than the VI state. Assuming the V state for the ruthenium requires the presence of terminal oxygen, i.e., $Ru=O$ bonds; however, the results of IR analysis (to be described later) show that the deposits do not contain $Ru(V)$. Ruthenium is in the IV state in the deposits. The small difference in binding energy of the Ru $3d_{5/2}$ level between RuO_2 and the deposits are ascribable to the difference in the immediate environment of each Ru atom.⁵⁾

The XPS has also revealed that the abundance of oxygen is much greater in the deposits than in RuO_2 . Fig. 2 shows the binding energies of Ru $3p_{3/2}$ and O $1s$ levels for (a) the deposit on the Ni plate and for (b) RuO_2 [2]. The area ratio of the O $1s$ peak to the Ru $3p$ peak was 2.0 for the deposit and 1.6 for RuO_2 .

15.2.4 X-ray analysis of the deposit

Before the present study, no data were available for the

structure of the deposit. So, we tried to find a clue to its structure. For the X-ray diffraction study, a plate of each metal (Ni, Cu and SUS) was exposed to gaseous RuO_4 for 4 months at 25 °C. The amounts of ruthenium in the deposits on the Ni, Cu and SUS plates were 0.450, 0.483 and 0.450 mg of Ru/cm^2 , respectively. In addition to strong reflection from the substrate metals, those from the deposit were observed [2]. However, the oxides of the metals, e.g., NiO , Fe_2O_3 , CuO , etc., did not show any peaks in the diffraction patterns. The tetroxide did not oxidize the metal surfaces significantly during the process.

Although differences were seen among the patterns of the deposits, the strongest reflected beam for all of the three cases always gave an interplanar spacing of $d = 4.7 \sim 4.8 \text{ \AA}$. In the case of RuO_2 , the most intense diffraction occurred at an interplanar spacing of $d = 3.1865 \text{ \AA}$, which is the widest in the pattern of the dioxide. The deposits have structures different from that of RuO_2 . Successive planes of atoms with high electron density (i.e., Ru) exist in the deposits, holding their spacings of $4.7 \sim 4.8 \text{ \AA}$. The possibility that the deposits may be mixed oxides of Ru and the substrate metals is ruled out by the results of XPS, as described already.

Each of the three patterns of the deposits consisted of multiple phases. As the amount of the deposit increased, additional spacings wider than 4.8 \AA became observable on the patterns. The presence of the multiple phases makes it difficult to define a crystal structure for the deposits. We found only that the deposits had such a structure that successive planes of Ru atoms were piled up at intervals of $4.7 \sim 4.8 \text{ \AA}$. These

intervals are ascribable to the presence of "Ru-O-O-Ru" bonds as will be discussed later.

15.2.5 Other evidences

In order to check the thermal stability of the deposit, the metal pieces covered with the deposit were placed in a quartz tube and heated to 700 °C in vacuum. Mass spectrometry was used to check the release of oxygen from the sample pieces; no evidence of the release was obtained during heating. No changes were observable on the deposit up to 500 °C; beyond 500 °C a brown substance was deposited on the quartz wall around the sample metal. The XPS of the residual deposit on the metal showed that the area ratio of the O 1s peak to the Ru 3p peak increased to 6.5. The binding energy of Ru 3d_{5/2} electrons decreased to a value of 280.1 eV, which was equivalent to that of Ru metal (280.0 eV) cited in Table 2. Part of the deposit volatilized during heating and the remainder was reduced via RuO₂ to Ru along with oxidation of the substrate metals. In this XPS, spectra of the substrates were obtained besides those of ruthenium and oxygen, e.g., Ni 2p and Fe 2p.

Infrared spectra of the deposit were scanned in a wavenumber range of 4000 to 400 cm⁻¹ by means of the ATR method. No absorption bands appeared between 900 and 4000 cm⁻¹: the spectra showed neither the ν_3 band of RuO₄ molecules (919.7 cm⁻¹, the Ru=O bond stretching frequency)⁷⁾ nor the bands of adsorbed water. Below 900 cm⁻¹, transmittance decreased gradually with decreasing wavenumber. Combination of the results of IR analysis and XPS indicates that the valency of Ru is four in the deposits.

15.2.6 Conclusion — character of the deposit

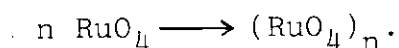
The experimental results obtained are summarized as follows.

- (1) Since the deposit is nonvolatile and increases in amount with the elapse of time, the phenomenon is neither the mere physical adsorption nor the chemisorption of RuO_4 .
- (2) Mass spectrometry of the residual gas ruled out the possibility that RuO_4 decomposed into RuO_2 and O_2 (Table 1).
- (3) The deposit is different from RuO_2 in crystal structure.
- (4) It is not a mixed oxide of ruthenium and the metals.
- (5) The abundance of oxygen is much greater for the deposit than for RuO_2 (Fig. 2).
- (6) The results of XPS and IR analysis indicate that ruthenium is in the IV state in the deposits.

It is, therefore, concluded that the deposit still retains the composition of RuO_4 . This requires oxygen atoms to form -O- bonds in the deposit, by which RuO_4 units are linked one another through Ru-O-O-Ru bonds.

The spacings of ~ 4.8 Å with the strongest relative intensity would be the Ru-Ru distance in the peroxide bonds. The Ru-O distance in a gaseous RuO_4 molecule is 1.7083 Å,⁷⁾ and subtracting twice this length from 4.8 Å gives ~ 1.4 Å, which is almost the same magnitude as the O-O distance in peroxide molecules, e.g., 1.49 Å of the O-O distance in a H_2O_2 molecule.⁸⁾ The distance of 4.7 ~ 4.8 Å would be reasonable as the Ru-O-O-Ru bond length. Ruthenium atoms form four σ bonds with oxygen atoms in the deposit.

Thus, for the RuO_4 -metal system, we have concluded that RuO_4 is polymerized on the metals without being decomposed:



The weak π bonds of RuO_4 molecules and their chemisorption make them link one another through the peroxide bond formation [2]. As the thickness of the deposit increases, thermal vibration of the Ru-O-O-Ru bond would become more active near the outer surface of the deposit and consequently the bond length is increased. We have attributed the appearance of spacings wider than 4.8 Å to the effect of thermal vibration.

(T. Sakurai)

References

- 1) Christian, J.D.: "Proceeding of the American Nuclear Society and American Institute of Chemical Engineers Meeting, August 5-6, 1976", Vol. 1, (1977), P. 2-1 2-34.
- 2) Rimshaw, S.J., Case, F.N.: CONF-801038-4, (1980).
- 3) Bell, W.E., Tagami, M.: J. Phys. Chem., 67, 2432 (1963).
- 4) Ortner, M.H., Anderson, C.J., Campbell, P.E.: IDO-14504, USAEC, (1961).
- 5) Roberts, M.W., McKee, C.S.: "Chemistry of the Metal-Gas Interface", Clarendon Press, Oxford, (1978).
- 6) Kim, K.S., Winograd, N.: J. Catal., 35, 66 (1974).
- 7) "Gmelins Handbuch der Anorganischen Chemie", Vol. 63, Verlag Chemie, GmbH, Berlin, (1970), p. 232.
- 8) Cartmell, E., Fowles, W.A.: "Valency and Molecular Structure", Butterworths, London, (1977), p.167.

Publication List

- [1] Sakurai, T., Takahashi, A.: "Behavior of ruthenium in fluoride-volatility processes. 3. Thermal decomposition of

- RuOF_4 ", J. Phys. Chem., 82, 780 (1978).
- [2] Sakurai, T., Hinatsu, Y., Takahashi, A., Fujisawa, G.: "Adsorption of ruthenium tetroxide on metal surfaces", *ibid.*, 89, 1892 (1985).
- [3] Sakurai, T., Takahashi, A.: "Interaction of ruthenium tetroxide with Stainless steel", J. Nucl. Sci. Technol., 20, 81 (1983).

Table 1 Theoretical and observed amounts of oxygen liberated by the deposition of RuO_4 at 25 °C [2].

Metal	Duration of contact, h	Ru quantity in the deposit, mg	Theoretical amount of O_2 released, ^{a)}		Amount of O_2 observed,	
			μmol	mm Hg, ^{b)}	μmol	mm Hg
Monel	24	7.5	74.2	4.6	<0.1	<0.01
"	50	14.0	138.4	8.7	"	"
Ni	24	4.9	48.5	3.0	"	"
"	"	4.4	43.5	2.7	"	"
SUS	"	8.4	83.1	5.2	"	"
"	"	7.6	75.2	4.7	"	"
Cu	"	16.0	158.3	9.9	1.3	0.08
Au	50	1.6	15.8	1.0	<0.1	<0.01

a) The oxygen quantity which would be produced if the amount of RuO_4 corresponding to the Ru quantity decomposes to RuO_2 and O_2 .

b) Oxygen pressure which would be attained in the present apparatus.

Table 2 Binding energies (eV) of Ru $3d_{5/2}$ and O 1s electrons of Ru - oxygen systems ^{a)} [2].

System	Ru $3d_{5/2}$	O 1s	
Deposit on a Ni plate	281.5	530.4	Present work
" a SUS plate	281.4	530.9	"
" a Cu plate	281.5	530.9	"
RuO_2	280.8	529.3	"
<hr/>			
Ru	280.0	—	Kim and Winograd ⁶⁾
RuO_2	280.7	529.4	"
RuO_3	282.5	530.7	"
RuO_4 (frozen)	283.3	b)	"

a) Referenced to Au $4f_{7/2}$ level of Au at 84.0 eV.

b) Not observed because of the interference of water at -80 °C.

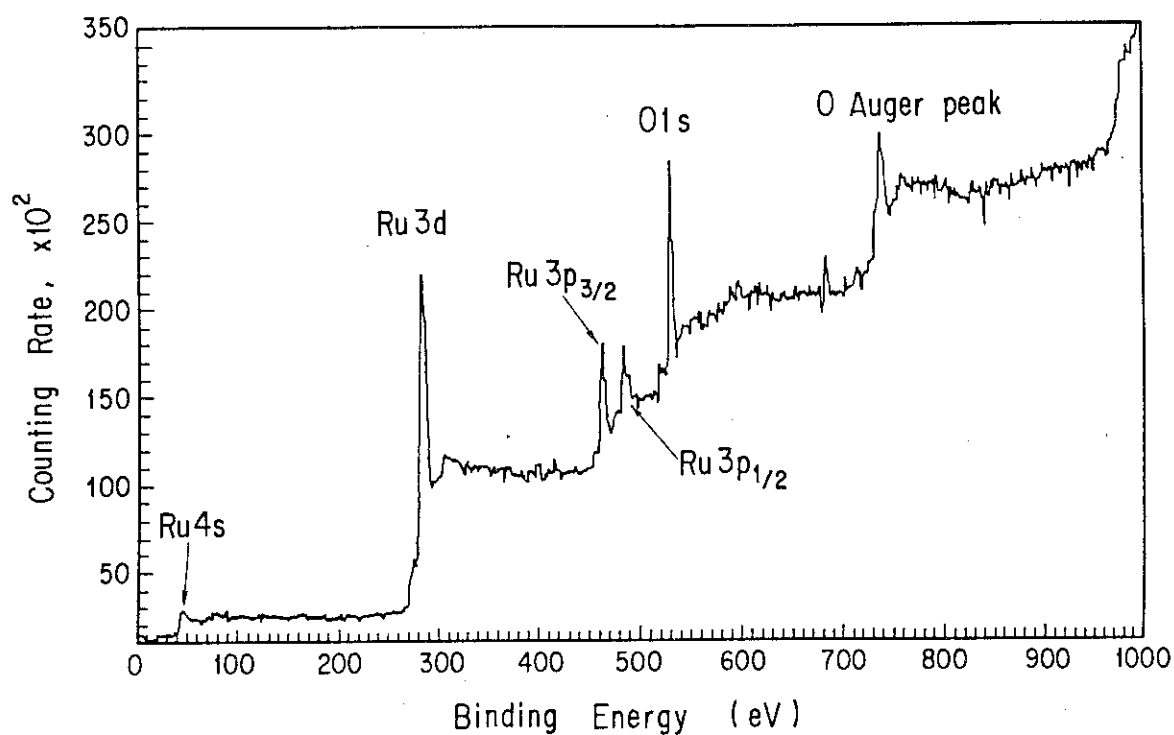


Fig. 1 X-ray photoelectron spectrum of the Ru deposit on a Ni plate [2].

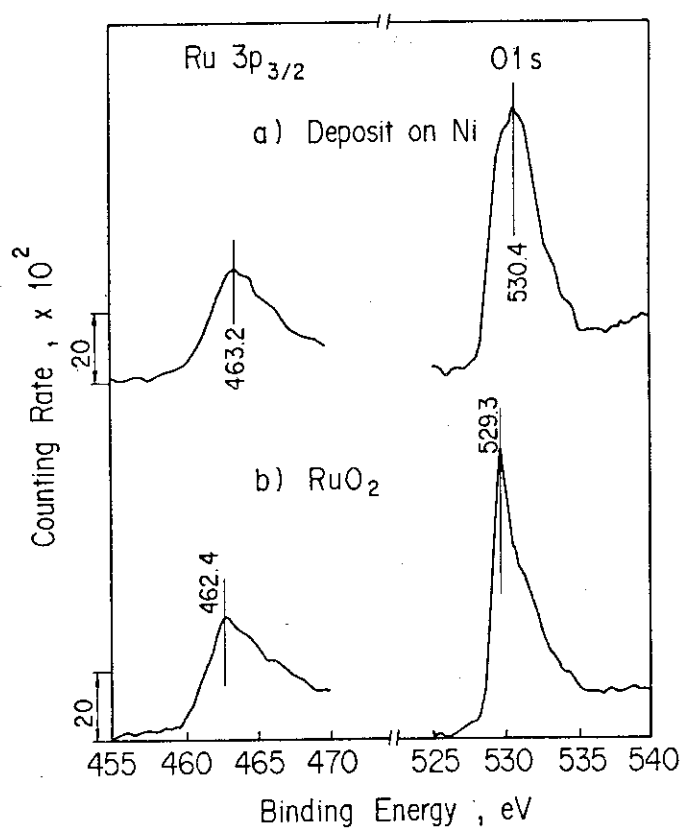


Fig. 2 X-ray photoelectron spectra of Ru 3p and O 1s levels of (a) the Ru deposit on a Ni plate and of (b) RuO_2 [2].

16. STUDIES OF TRITIUM SEPARATION BY ISOTOPICALLY SELECTIVE LASER EXCITATION OF MOLECULES

K.Suzuki, A.Yokoyama, G.Fujisawa,
J.Ishikawa and M.Iwasaki^{*}

16. 励起法によるトリチウム分離の化学的研究

鈴木 和弥・横山 淳・藤沢 銀治・石川 二郎
岩崎 又衛^{*}

16.1 同位体分離用レーザーの開発

レーザーの応用は、非常に広いが、光ファイバー通信用半導体レーザーと、核融合等のための大出力レーザーが二本の大きな柱となっている。大出力レーザーとしては炭酸ガスレーザー（9 - 11 μm ）フッ化水素レーザー（HF, 3 - 4 μm DF 3 - 4 μm ）ヨウ素レーザー（1.3 μm ）ネオジウムガラスレーザー（1.1 μm ）フッ化クリプトンエキシマレーザー（0.25 μm ）などがあり、 10^{12}W （パルス）に達するものも出現した。しかしながら、レーザー照射による同位体分離を行う場合の照射物質は、吸収波長が、赤外部（4 - 18 μm ）と真空紫外部（0.2 - 0.1 μm ）にあり、上の大出力レーザーは、ほとんど使用できない。炭酸ガスレーザーのみが使用できるが、それでも、照射物質が非常にかぎられてしまうので、赤外または、ラマン変換による波長変換を行うか、新しいレーザーの開発を行わなければならないという状況下にある。本稿では、炭酸ガスレーザーとその波長変換であるアンモニアレーザーの開発およびエキシマレーザーのラマン変換について述べる。

16.1.1 炭酸ガスレーザーの開発

レーザー発振の原理は、Fig. 1 に示すように、二酸化炭素分子の振動エネルギーをとり出すものである。放電、光等によって、 $v_3=1$ に励起されたものが、 $(v_1=1, v_2=2)$ （フェルミ共鳴によって二準位に分裂）のふたつの準位に落ちるとき、それぞれ、10 μ と 9 μ の光を放出する。レーザーが大出力となるための条件のひとつは、上下のエネルギー準位にある分子数の逆転比が大きいことであり、下のエネルギー準位の分子は速く除去されることが必要である。そのためには、さらに下にエネルギー準位があることが望ましい。炭酸ガスレーザーは、この条件を備えたレーザーである。

* Institute of Atomic Energy, Kyoto University

* 京都大学原子エネルギー研究所

当研究室では、はじめにネオントランス（15KV）を電源にした連続レーザー（2台、ガラス工作で製作）で20 - 30 Wの発振を確認したのち、主に、負極に抵抗付ピンを用いた横放電型パルスレーザー（7台）を試作し、出力8J/パルスを得た。しかしながらこれらのレーザーは、抵抗をつけた分だけ放電パルスが長くなり、レーザー出力パルスも長くなるため、赤外多光子吸収を用いた同位体分離には、不利であると判明したので、新しく、パルス巾の小さいレーザーの開発の必要にせまられた。種々の試行錯誤の後、予備放電により均一グロー放電をおこすことのできるTEA（Transversely Excited Atomspheric）型レーザーの試作を開始した。予備放電の必要な理由は、次のようである。二酸化炭素分子の振動励起を効率よく行うためには、電子の加速電圧が高いと電子励起が主になるので、加電圧は低い方がよい。炭酸ガスは絶縁体であり、低い電圧で放電を開始することはできない。そこであらかじめ予備放電（電子線、X線、紫外線でもよい）によって低濃度のイオン種をつくっておき、主放電を行うという二重放電方式が採られる。

予備放電の方法および電源等は種々考えられるがこれらの得失については省略し、当研究室で選択した型について述べる。Fig. 2は、もっとも性能のよいレーザー（Mark 11）の電源およびレーザー回路である。これで作動ガス1気圧でのグロー放電が可能になった。直流電源（H.V.）からコンデンサー（Cs）に充電された電荷は、レーザーのA \oplus 、K \ominus 極に移動する。ここで、予備放電用コンデンサーCtを通った電荷の一部は、グリット電極GとK \ominus 極間に放電を起す。この放電による紫外光が、A \oplus とG間の作動ガスを電離し、A \oplus とG間にグロー放電を起すことができる。予備放電と主放電の時間差は、コンデンサーCtの容量とKG間の距離およびGA間の距離によって決まる。また予備放電の均一性は、主にKG間の距離によって左右されるので最適になるよう設計する必要がある。

レーザーハウスの構造は、Fig. 3のようであり光軸方向と直角に放電が起るようになっている。正極Aは、ロブスキー型アルミ板、負極Kはニッケルメッキネジ（2mm ϕ ）である。グリット電極Gは、黄銅板に4mm ϕ の穴を一面に開けたものである。GとA間には、予備放電用セラミックコンデンサー（500 pF）10個が入っている。光の共振系については、全反射ミラー（金メッキ）と半透ミラー（セレン亜鉛ZnSe製）の間で、光の増幅がおこり、セレン亜鉛ミラーより出力がとり出せる。ミラーの角度は、マイクロメーターにより調節される。レーザー作動ガスは、二酸化炭素CO₂ガスに窒素およびヘリウムHeを混合したものが使われる。混合比は、CO₂ : N₂ : He = 10 : 10 : 80 または 10 : 5 : 85 のものが主に使われている。ここで窒素は、エネルギー準位図に示すように、励起されたN₂がCO₂分子に衝突して、振動エネルギーを移行させレーザー出力の増加に役立っている。しかしながら、この移行速度は、上記ガス組成（1気圧）中で約0.5 μ sec程度であるので、パルスレーザーの場合は、パルス巾が大きくなるという不利な点が出てくる。ヘリウムHeは、CO₂分子の下準位のものの除去に役立つとともに、放電の均一性に役立っている（イオン化電圧 He 24.6 eV CO₂ 13.8 eV）。Fig. 4（上）は、レーザー発振の様子を示したものである。放電条件は、コンデンサーCs = 0.05 μ F, 60 kV, 作動ガス CO₂ : N₂ : He = 10 : 5 : 85 1気圧である。この場合の出力は、5 J/パルスであり、パルス出力の波形は、同図（下）のようになった。半値巾60 nsecの尖頭パルスに続いて約1 μ secの尾があることがわかる。この尾は、励起された窒素からのエネルギー移動によるものである。同位体分離用レーザ

ーとしては、レーザーのパルス巾が小さいことが分離係数を上げるため必要であるので、窒素の混合割合を減らすか、出力ミラーの反射率を下げるかして、パルスの尾をなくすようにしなければならない。

このレーザーを使って、三塩化ホウ素 (BCl_3) を照射し、 $^{10}\text{B}/^{11}\text{B}$ 比が 1.3 倍に濃縮することを確めた。現在まで報告されているかぎりでは、炭酸ガスレーザーによる ^{10}B の濃縮は、実用化される程の結果はどこでも得られていない。今後とも研究を続ける必要がある。

炭酸ガスレーザーの今後の課題としては、高気圧 (8 - 10 atm) 炭酸ガスレーザーの開発がある。1 気圧作動の炭酸ガスレーザーは、回転エネルギー準位に沿ったとびとびの発振波長が示すが、5 気圧以上になると圧力による回転線巾のひろがりによって連続化してくるので、波長可変となる。また、パルス巾は、作動ガスの圧力に反比例するので、10 分の 1 になり、同位体分離用レーザーとして有用なものとなる。これは、次のアンモニアレーザーの励起源としても、出力波長範囲の拡大のためにも必要なものである。

16. 1. 2 アンモニアレーザーの開発

炭酸ガスレーザーは、波長範囲が 9 - 11 μm と狭いので、11 - 13 μm に吸収をもつ分子を照射したいときは、波長変換の必要がある。アンモニアレーザーは、はじめ UF_6 分子の照射のため開発されてきたようであるが、当研究室では、トリチウム化クロロホルム (CTCl_3) 照射のために開発された。アンモニアレーザー発振の原理は、Fig. 5 のように、炭酸ガスレーザー光で励起されたアンモニア分子 ($v_2=1$, 変角振動) が基底状態 $v_2=0$ へ落ちるとき発光するものであるが、次のような特長と問題点を有する。

- ① 励起光源の炭酸ガスレーザーの波長がとびとびであるので、またアンモニア分子の吸収波長もとびとびであるので、両者の一致は偶然のもので、9.22 μ (R (30)) と 9.29 μ (R (16)) でしか一致しない。したがって出力波長の数も少い。
- ② 室温で、下のエネルギー準位 ($v_2=0$) にアンモニア分子がすでに存在するので、レーザー発振光の自己吸収があり出力が小さい原因となっている。これを打開するには、作動ガスを冷却することであり、当研究室でも液体窒素または冷凍機による冷却を試みて、出力の増加を確認したが、冷凍機的能力不足等で、実際の照射には使われなかった。また、冷却法としては、管径を小さくした Wave Guide 型レーザー管 (2.5 mm ϕ) とすることも有力であり、変換効率が 40 % 以上になるという報告もある。

アンモニアレーザーの配置は、Fig. 6 のようであり炭酸ガスレーザー R (30) 光により、共振管 (5 $\phi \times 3.6$ m) 中のアンモニア分子が励起され発光するものである。使用された作動ガスは、アンモニアと窒素の混合ガスであり、窒素は、圧力効果によりアンモニアの回転線巾を増加させ、炭酸ガスレーザーの吸収をよくするのに役立っている。なお図中のフロン 12 の入ったフィルターは炭酸ガス光を吸収してとり除くものである。Fig. 7 は種々の混合比のアンモニア/窒素ガスを使用した場合のレーザー出力を示す。炭酸ガスレーザー入力 8 J/パルスに対して最大 800 mJ の出力を得た。出力光の波長成分は、アンモニア窒素混合比によって異なる。6 % アンモニアを作動ガスとして使用した場合、大部分波長 12.08 μm である。0.5 % アンモニアを使用した場合は、12.26 μm が大部分となる。さらに、0.25 % 以下の濃度のアンモニアガスを使った場合は、

主な波長成分は $11.71 \mu\text{m}$ となる。このように、アンモニア/窒素の混合割合によって、発振波長が変わってくるのは、Fig. 5 のように、励起されたアンモニアが $v_2=1$, $a(J=6, K=0)$ の準位で、すぐに、発光する場合 ($12.08 \mu\text{m}$) と衝突または遠赤外線発光により下の回転準位に移ってから発光する場合 ($12.26 \mu\text{m}$) があるためと説明されている。

入力炭酸ガスレーザーパルスと出力アンモニアレーザーの時間変化を、Fig. 8 に示す。作動ガスのアンモニア濃度 0.5%, 全圧力 160 torr で、波長 $12.26 \mu\text{m}$ が主である。炭酸ガスレーザーのパルスが最大になり、 $v_2=1$ でのアンモニア分子の数が最大になったところで発振がはじまる様子がよくわかる。

アンモニアレーザーで照射可能な物質は、トリチウム化物以外は、 SeF_6 (780 cm^{-1}), UF_6 (816 cm^{-1}) などであるが、高気圧炭酸ガスレーザーを励起源にすればより多くの発振線が得られると考えられ、今後とも研究を続ける必要がある。

16. 1. 3 エキシマーレーザーのラマン変換 (ラマンレーザー)

ラマン散乱光は、通常は入射光に対して百分の一以下であるが、入射光強度が 10 MW/cm^2 以上になると急に大きくなる。この効果は、波長が短いほど大きくまた照射物質の密度の大きい高圧ガスまたは液体では、特に大きくなる (ラマンレーザー)。

本レーザーは、ホルムアルデヒド ($\text{HDCO}/\text{H}_2\text{CO}$) 照射による重水素分離のためつくられたもので、エキシマーレーザー ($\text{Xecl } 308 \text{ nm}$) を液体窒素 ($\nu = 2327 \text{ cm}^{-1}$) により波長変換 (332 nm) するものである。

Fig. 9 に示すように、エキシマーレーザーは、レンズ (CaF_2 製, 30ϕ , $f = 20 \text{ cm}$) でしぼられ、石英窓付デュワー (60ϕ 内径, 石英製) 中の液体窒素に入り波長変換される。エキシマー光入力 75.6 mJ (30ϕ , パルス巾 20 nsec) のとき、液体窒素通過後の波長 $\lambda = 332 \text{ nm}$ 成分は、 10.8 mJ であり、もとの波長 $\lambda = 308 \text{ nm}$ 成分は、 37.8 mJ であった。この出力光を厚さ 10 cm のパイレックスガラスを通過させ、 $\lambda = 308 \text{ nm}$ 成分を吸収 (96% 吸収) させ、天然組成のホルムアルデヒドを照射 (照射パルス数 3600) した結果、重水素の濃縮率 3.5 を得た。

上記のラマン変換は、出力光中のもとの光が半分以上残っていて最適配置ではなくレンズの焦点距離を大きく液体窒素デュワーを大きくする必要がある。また、光の通過する液体窒素窓が研磨された平行平面になっていないのでこれを改良する必要がある。重水素の濃縮率を上げるためには、ホルムアルデヒドの回転線まで分解可能な高分解性能分光器 (分解能 0.001 nm) により、吸光比 ($\text{HDCO}/\text{H}_2\text{CO}$) 最大の波長を求めるとともに、レーザー光を干渉計等を通してその波長にしぼることが必要である。

(K. Suzuki)

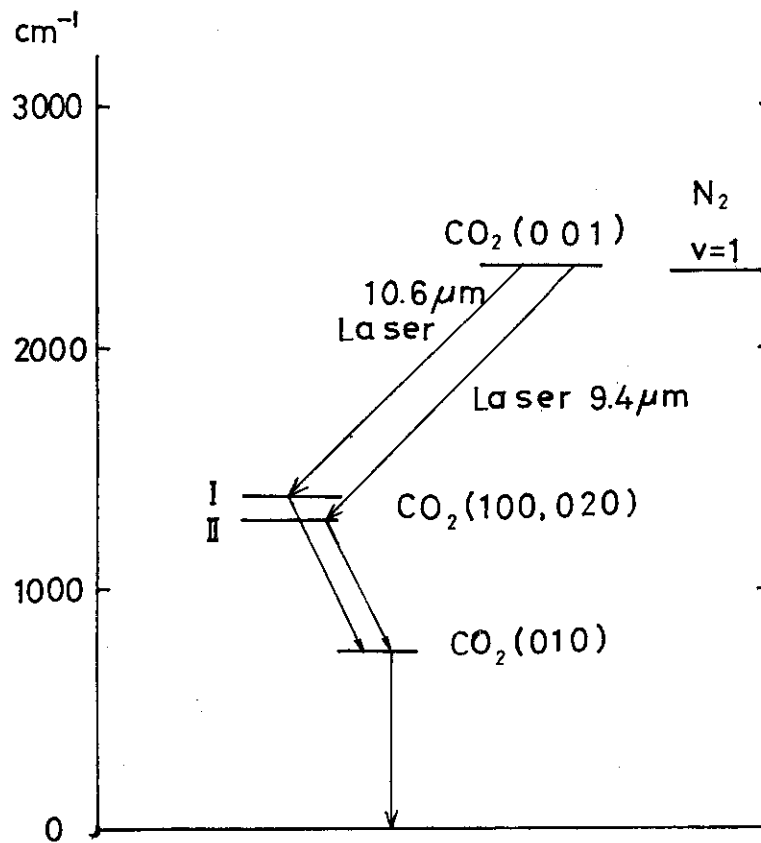


Fig. 1 Vibrational energy level of carbon dioxide.
(v_1 , symmetric stretching, v_2 , bending, v_3 , antisymmetric stretching) and nitrogen.

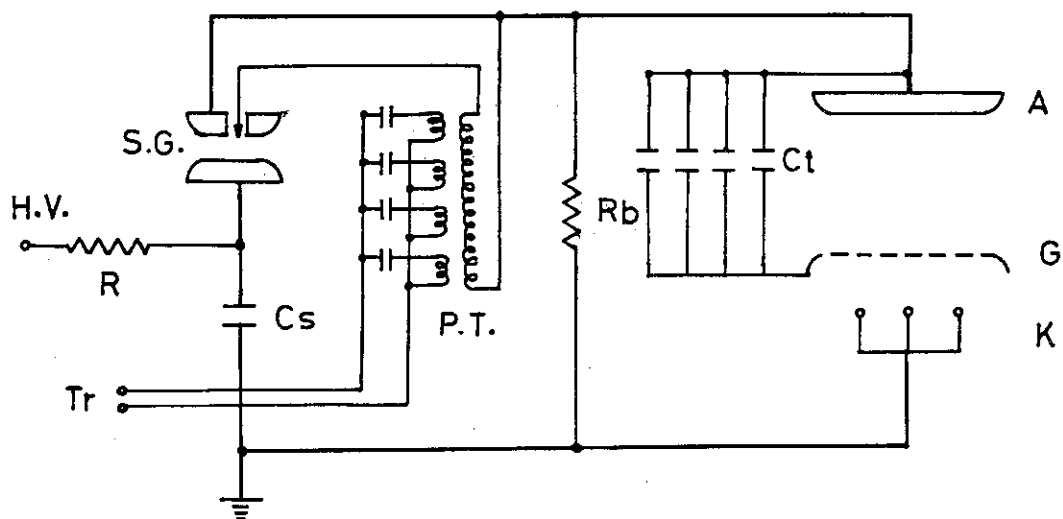


Fig. 2 Electric circuit of TEA carbon dioxide laser.
A) anode, G) grid, K) cathode, C_t) condenser for preionization,
H.V.) dc high voltage, R_b) resistor, P.T.) pulse transformer,
 C_s) main condenser, Tr) trigger for driving pulse transformer.

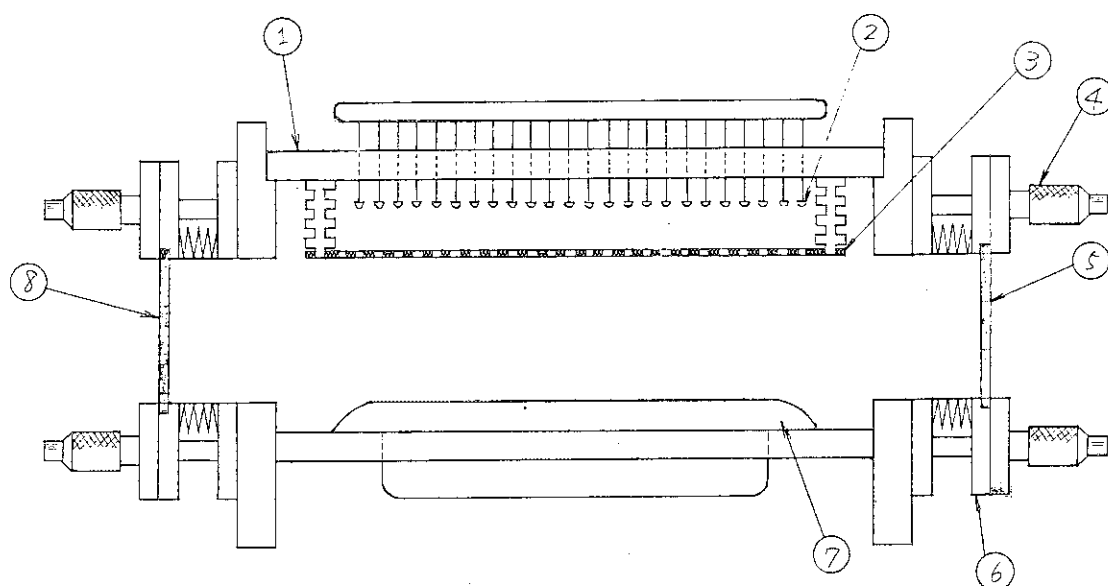
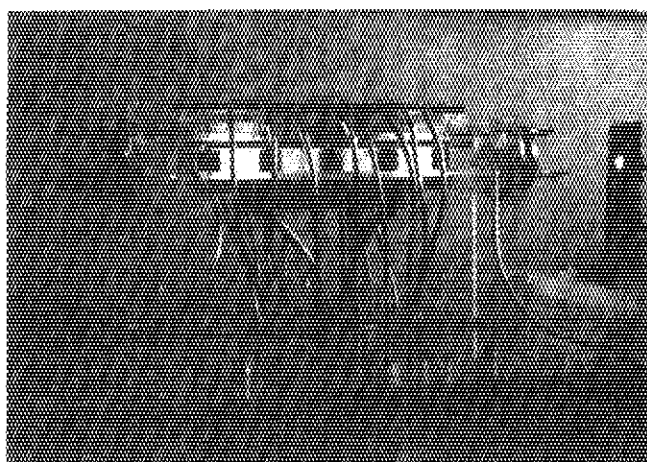
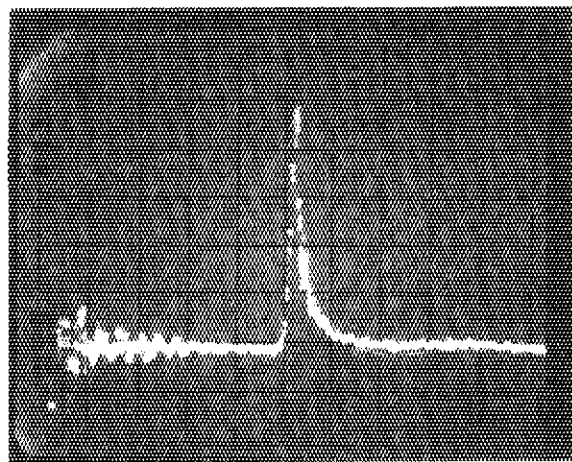


Fig. 3 Structure of TEA carbon dioxide laser.
 1) laser house, 85×85×800 mm, acrylite, 2) cathode, screw coated with nickel, 3) grid, perforated brass plate, 4) micrometer, 5) out put mirror (ZnSe 70φ, 5t) 6) mirror holder, 7) anode 60×15×500 mm, aluminum, 8) mirror coated with gold (70φ, 5t).



A



B

Fig. 4 Photograph of carbon dioxide laser oscillation. (A) discharge voltage 60 kv, working gas, $\text{CO}_2:\text{N}_2:\text{He} = 10:5:85$, 1 atm. Pulse form of the laser beam. (B)

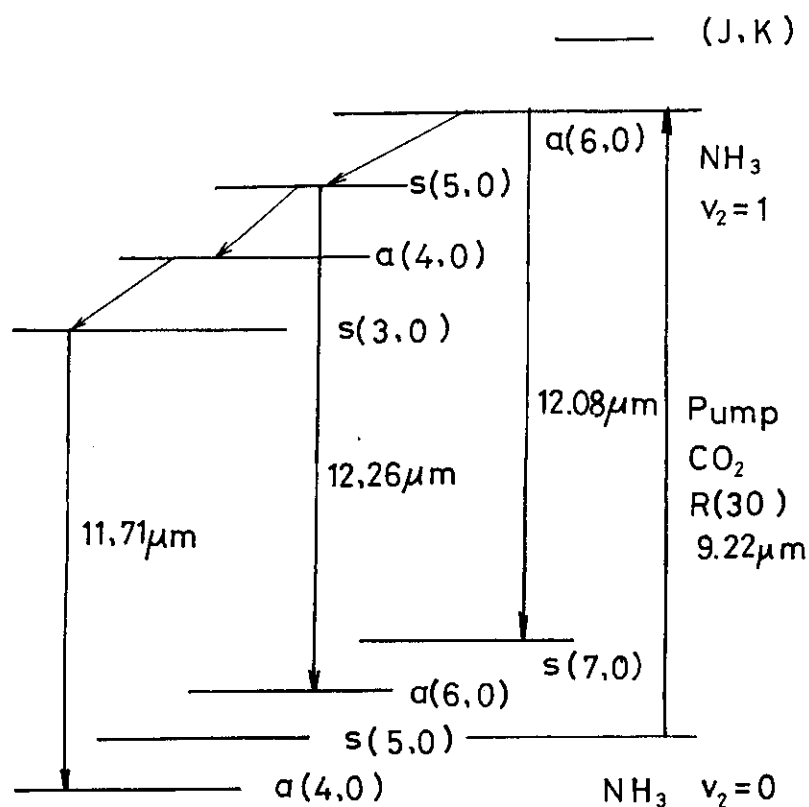


Fig. 5 Vibration-rotational energy level of ammonia (v_2 , bending).

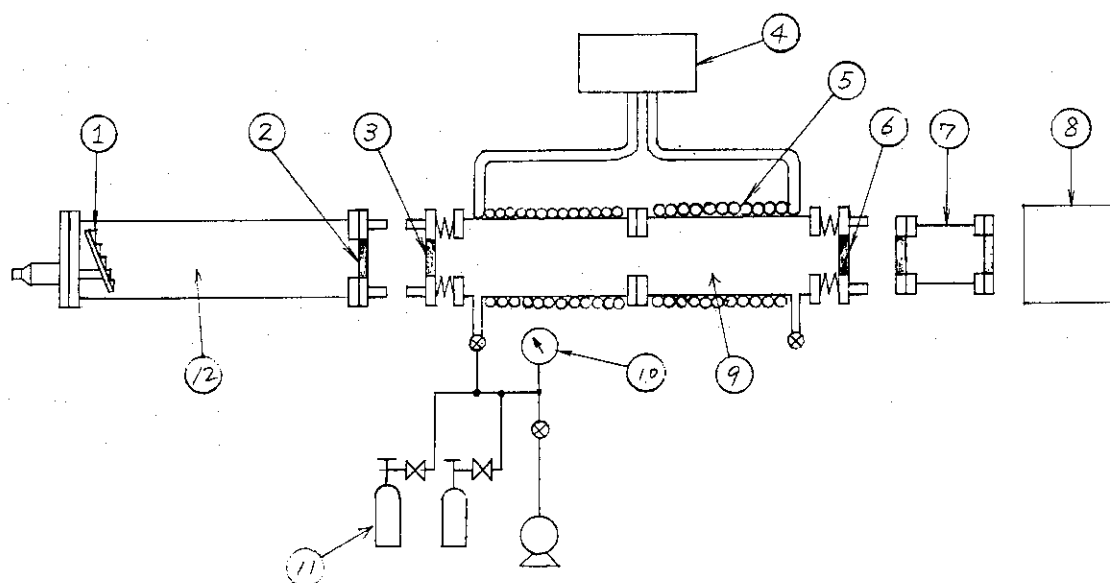


Fig. 6 Arrangement of ammonia laser system.
 1) grating, 2) output mirror of carbon dioxide laser (ZnSe 50%R 50 ϕ), 3) sodium chloride plate (50 ϕ , 50t), 4) refrigerator, 5) pipe for cooling, 6) Zinc selenide plate (17%R 50 ϕ), 7) filter (freon 12 60 torr and oxygen gas 180 torr, sodium chloride windows), 8) spectrometer and photodetector, 9) ammonia laser tube (5 $\phi \times 3.6$ m) 10) manometer, 11) carbon dioxide laser for pumping.

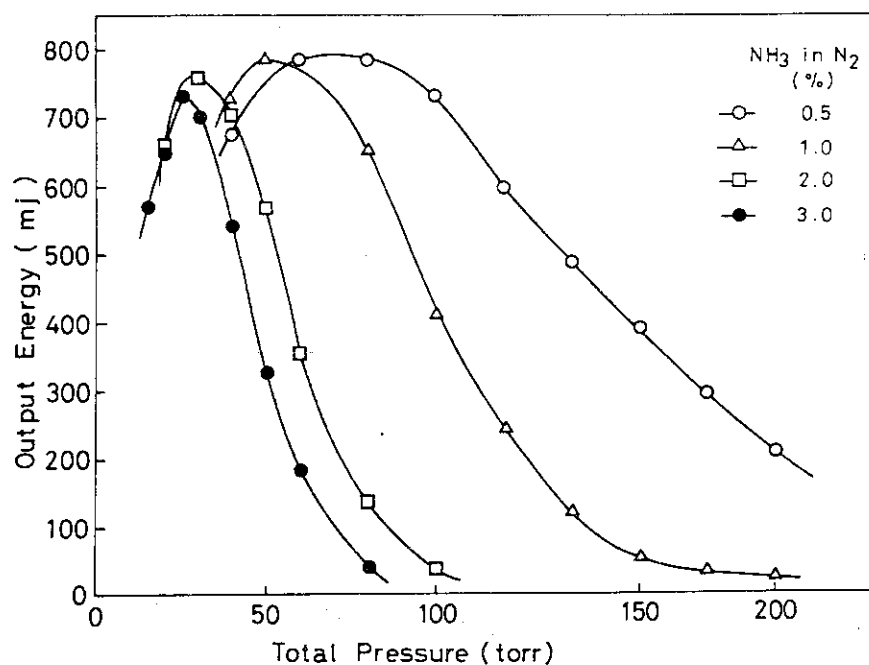


Fig. 7 Output of ammonia laer.
Input carbon dioxide laser is 8J/ pulse, R(30) 9.22 μ m.

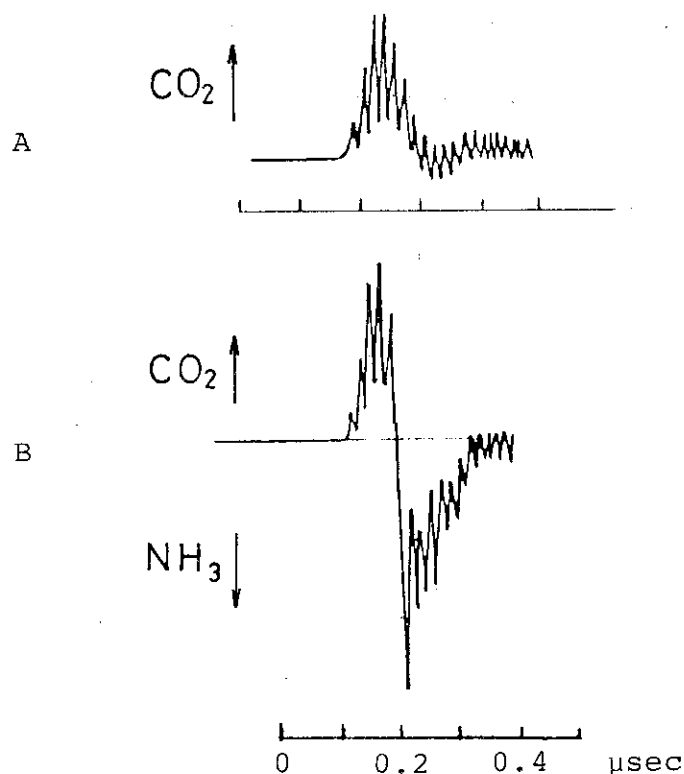


Fig. 8 Temporal behavior of ammonia laser oscillation pumped by carbon dioxide laser.
A), Pumping carbon dioxide laser pulse.
B), Pumping carbon dioxide laser pulse (upper trace) and ammonia laser pulse (lower trace). Working gas, 0.5% ammonia in nitrogen, total pressure 160 torr.

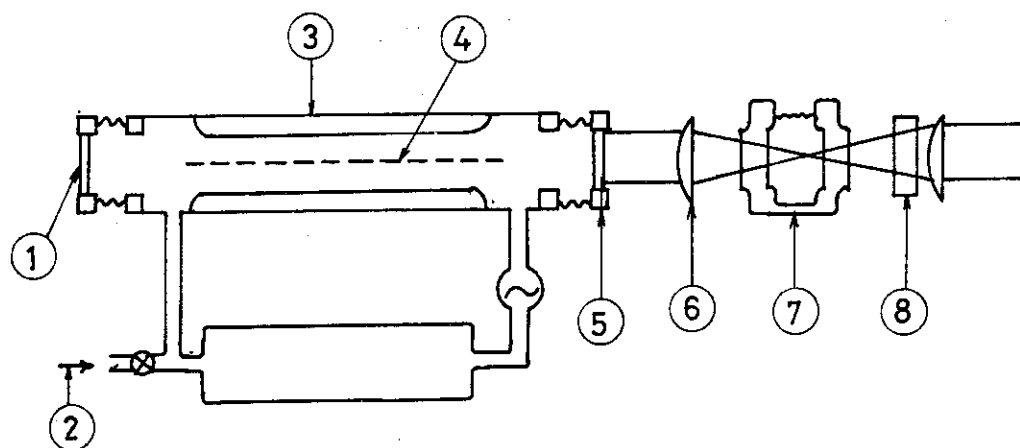


Fig. 9 Raman laser by stimulated Raman scattering of excimer laser (XeCl 308 nm) in liquid nitrogen.
 1) total reflection mirror (Al, 30 ϕ), 2) working gas, HCl 0.2% in Ar 1500mbar + Xe 50mbar, 3) excimer laser 4) pre-ionization electrode, 5) output mirror (CaF₂ 30 ϕ), 6) lens CaF₂ f=20cm, 7) Dewar of liquid nitrogen 60 ϕ , 8) filter (pyrex 10 cmt).

16.2 赤外多光子解離を用いた水素同位体（トリチウム）分離

16.2.1 序 論

レーザー同位体分離法は、他の分離法に比べて非常に大きい分離係数が得られることから、極低濃度同位体の分離に有効である。我々は、原子力施設に水の化学形で蓄積するトリチウムを分離・除去する為に、レーザー同位体分離に適切な作業物質へ水からトリチウムを同位体交換反応により移し、そのトリチウム化した作業物質をレーザー光照射により選択的に解離する方法を研究して来た。

本報告では、赤外パルスレーザー光照射による赤外多光子解離を利用したジクロロメタン ($\text{CDTCl}_2/\text{CD}_2\text{Cl}_2$) 系での T/D 分離, およびクロロホルム ($\text{CTCl}_3/\text{CHCl}_3$) 系での T/H 分離について述べる。

16.2.2 実験方法

16.2.2.1 試 料

CDTCl_2 は、 CD_2Cl_2 と $\text{tert-C}_4\text{H}_9\text{OT}$ との間の $\text{tert-C}_4\text{H}_9\text{O}^-$ を触媒とした同位体交換反応により合成した。また $\text{tert-C}_4\text{H}_9\text{OT}$ は、トリチウムを含んだ重水 ($\text{DTO}/\text{D}_2\text{O}$; 比放射能 $\sim 1\text{ mCi/g}$) と $\text{tert-C}_4\text{H}_9\text{OK}$ との反応により得た。 CD_2Cl_2 (重水素化率 $> 99\%$) および $\text{tert-C}_4\text{H}_9\text{OK}$ (純度 $> 97\%$) は Merck 社から購入したものをを用いた。

CTCl_3 は、トリチウム水 ($\text{HTO}/\text{H}_2\text{O}$; 比放射能 $\sim 1\text{ mCi/g}$) と CHCl_3 との間の OH^- を触媒とした同位体交換反応により合成した。 CHCl_3 (純度 99%) は関東化学より購入したものを蒸留水で洗浄してアルコールを取り除いた後に用いた。トリチウム水は、New England 社より購入した。 Xe (純度 $> 99\%$) は巴商会より購入し、脱ガスをした後に用いた。

16.2.2.2 照射および分析

照射用レーザーは、ジクロロメタンの T/D 分離では TEA CO_2 レーザー (Lumonics 203-2; パルス幅 $\sim 200\text{ nsec}$; パルスエネルギー 0.32 J) を、クロロホルムの T/H 分離では、16.1.2 に記した CO_2 レーザー励起の NH_3 レーザーを用いた。 NH_3 レーザーの発振線は、 NH_3/N_2 混合ガスを入れた共振管中の NH_3/N_2 比、全圧および照射用セルの前に置いたフィルター用セル中の気体の種類によって異なり、実験に用いた発振線を NH_3 レーザーの操作条件とともに Table 1 にまとめている。

照射用試料は、 BaF_2 または NaCl 窓付パイレックス製円筒形セルに入れ、レーザー光を ZnSe レンズ (焦点距離 25 または 50.8 cm) でセルの中央に集光して 500 から 15000 パルス照射した。照射後、試料は、ジクロロメタンの場合ラジオガスクロマトグラフを用いて、クロロホルムの場合赤外分光光度計と液体シンチレーションカウンターを用いて測定した。

16.2.3 結果および考察

16.2.3.1 ジクロロメタンの T/D 考察

CO_2 レーザー発振領域付近における CD_2Cl_2 の赤外吸収スペクトルおよび Dennen¹⁾ によって報告されたジクロロメタンの力の定数¹⁾を用いて計算した CDTCl_2 の基本振動数を Fig.1 に示す。

1100 から 900 cm^{-1} の間で CDTCI_2 の基準振動は、 ν_3 (基本振動数 1002 cm^{-1}) と ν_7 (基本振動数 929 cm^{-1}) の二つ存在するが、 ν_3 バンドは CD_2CI_2 の結合バンド ($\nu_4 + \nu_9$) と重なるので、 ν_7 バンド付近の振動数のレーザー光を用いて実験を行った。

CDTCI_2 および CD_2CI_2 の分解速度 (それぞれ W_T および W_D) のレーザー光振動数依存性と、一パルス照射当たりに生成する分解生成物におけるトリチウム濃縮係数 (β_{prod}) の振動数依存性を Fig. 2 (a) および (b) に示す。分解速度は、照射前後の分子の量 (それぞれ M_0 および M_n)、照射レーザー光パルス数 (n) を用いて、

$$W = \ln (M_0 / M_n) / n \quad (1)$$

と表わされ、トリチウム濃縮係数は、

$$\beta_{\text{prod}} \simeq W_T / W_D \quad (2)$$

と近似的に表わされる。 W_T は、927 cm^{-1} の所で最大値を示し、これは計算による CDTCI_2 ν_7 バンドの基本振動数 (929 cm^{-1}) と計算の精度内で一致する。また、917 cm^{-1} 付近に小さなピークがありそうだが、測定誤差を考えるとはっきりしない。一方、 W_D は 960 cm^{-1} を中心にした ν_8 バンドの励起により、照射レーザー光振動数が増加するに従って単調に増大している。また β_{prod} は W_D の振動数依存性が大きく影響して、振動数が小さくなるに従って増大している。 W_T 、 W_D および β_{prod} の試料圧依存性を Fig. 3 に示す。ここでレーザー光振動数は、Fig. 2 に示した β_{prod} の振動数依存性で最大の値が得られた 907.8 cm^{-1} である。 W_T は圧力とともに増大するが、 W_T は全圧 5 torr で最小値を持つ傾向が見られるものの、実験誤差範囲内で全圧にほとんど依存しない。その結果、 β_{prod} は全圧が低下するに従って増大し、本実験の最低圧である 3 torr で 29^{+156}_{-15} を得た。

16. 2. 3. 2 クロロホルムの T/H 分離

CTCI_3 の分解速度のレーザー光振動数依存性を Fig. 4 に示す。照射に用いた NH_3 レーザーは、Table 1 に示すように、同時に二つないし三つの振動数の光が出るので、そのうちの主出力光の振動数に対してプロットした。また、レーザー光のパルスエネルギーは、圧力 2 torr, 816 cm^{-1} 光でのデータ (123 mJ) を除いて 138 mJ である。 $\text{CTCI}_3/\text{CDCI}_3$ 混合系での単一振動数の光による赤外多光子解離では、分解速度が約 825 cm^{-1} で最大になるが²⁾、本実験の場合、主出力光の振動数が 816 cm^{-1} の場合の方が、828 cm^{-1} 光の場合に比べて大きい。同程度の分解速度を与える。これは、本実験では 816 cm^{-1} 光と同時に 828 および 833 cm^{-1} 光も照射されており、以下に述べる三振動数光同時照射下での赤外多光子解離過程が分解速度の増加に寄与しているためであると考えられる。すなわち、 CTCI_3 ν_4 バンドの基本振動数 (835 cm^{-1}) に近い 828 ないし 833 cm^{-1} 光による基底状態にある CTCI_3 の励起と、それに続く 816 cm^{-1} 光での振動励起 CTCI_3 の解離という励起・解離過程が、高励起状態になるに従って振動準位間隔がせまくなる非調和性 (非調和定数 $X_{44} = -8.9 \text{ cm}^{-1}$ ²⁾) を補償して、有効に CTCI_3 を解離させるものと考えられる。

CTCI_3 の分解速度のクロロホルム圧依存性を Fig. 5 に、Xe 圧依存性を Fig. 6 に示す。振動励起した CTCI_3 の CHCl_3 との衝突による振動緩和で、クロロホルム圧が増加するに従って

CTCl_3 の分解速度は減少する。また、クロロホルム圧が 2 torr 以下では、Xe 圧が増加するに従って分解速度は増加していき、最大値を経た後に減少していく。Xe 圧の低い所での分解速度の増加は、Xe と CTCl_3 との衝突によるボルトネック効果の解消に起因し、Xe 圧の高い所での分解速度の減少は、振動励起した CTCl_3 と Xe との衝突による振動緩和に起因すると考えられる。また、クロロホルム圧 5 torr では、ボルトネック効果は CHCl_3 と CTCl_3 との衝突によりほとんど解消しているので、Xe を加えても分解速度の増加は見られない。

CHCl_3 の分解速度は、クロロホルム圧 2 torr 以上で、照射前後における CHCl_3 ν_4 バンドの吸光度変化より求めた。照射後、分解しないで残っている CHCl_3 の割合は、レーザーフルエンス、パルス数、レーザー光振動数等に対して系統的な依存性を示さず、吸光度の測定誤差範囲内で分布した（平均値 0.995；標準偏差 0.012）。このことから、 CTCl_3 の分解速度の最大値 $[(1.48 \pm 0.12) \times 10^{-3} \text{ pulse}^{-1}]$ が得られた条件下でも測定誤差範囲内で CHCl_3 の分解は認められず、 CHCl_3 の分解速度は $2.4 \times 10^{-6} \text{ pulse}^{-1}$ 以下である。そこで一パルス照射当たりに生成する分解生成物におけるトリチウム濃縮係数は、クロロホルム圧 2 torr で 570 以上であると推定される。

16.2.4 おわりに

ジクロロメタンの T/D 分離では、Fig. 2 に示したように、 CO_2 レーザー発振領域にある CDTCl_2 の基本振動数が CD_2Cl_2 の ν_8 および $\nu_4 + \nu_9$ バンドと近接しており、 CD_2Cl_2 の分解もかなり起こる。そのために CO_2 レーザー光を用いたジクロロメタンの T/D 分離では、トリチウム濃縮係数の向上はあまり望めない。一方、クロロホルムの T/H 分離では、 CHCl_3 の分解は測定誤差範囲内で認められず、トリチウム濃縮係数はクロロホルム圧 2 torr で 570 以上であると推定される。またアルカリ触媒によるクロロホルムと水の水素同位体交換反応速度定数は、T/H 分離が行われているフルオロホルム (CHF_3)³⁾ の場合と比べて非常に大きい^{4,5)}。以上のことから、クロロホルムは T/D 分離²⁾ と同様に T/H 分離でも有力な作業物質に成り得るだろう。

(A. Yokoyama)

References

- 1) Dennen, R.S.: J. Mol. Spectry. 29, 163 (1969).
- 2) Magnotta, F., Herman, I.P.: J. Chem. Phys. 81, 2363 (1984).
- 3) Takeuchi, K., Inoue, I., Nakane, R., Makide, Y., Kato, S., Tominaga, T.: J. Chem. Phys. 76, 398 (1982).
- 4) Hine, J., Peek, Jr., Oakes, B.D.: J. Am. Chem. Soc. 76, 827 (1954).
- 5) Symons, E.A., Clermont, M.J.: J. Am. Chem. Soc. 103, 3127 (1981).

Publication List

- [1] Yokoyama, A., Suzuki, K., Fujisawa, G., Ishikawa, N., Iwasaki, M.:
"Selective Multiple-Photon Dissociation of Chloroform-d", J. Nucl.
Sci. Technol. 18, 737 (1981).
- [2] Yokoyama, A., Suzuki, K., Fujisawa, G., Ishikawa, N., Iwasaki, M.:
"Tritium Separation by Laser Multiple-Photon Dissociation of CDTCI_2
/ CD_2Cl_2 Mixture", Chem. Phys. Lett. 99, 221 (1983).
- [3] Yokoyama, A., Suzuki, K., Fujisawa, G., Ishikawa, N., Iwasaki, M.:
"Selective T/H Separation by NH_3 Laser Multiple-Photon Dissociation
of CTCl_3 ", Appl. Phys. B 38(2), 99 (1985).

Table 1 Output distributions of the NH_3 laser

NH_3/N_2 Ratio in NH_3 cell	Total Pressure in NH_3 cell	Filter ^a	Output Radiation Frequency ^b
0.5 %	140 torr	$\text{CCl}_2\text{F}_2/\text{O}_2$	816 cm^{-1} (77.6 %)
		(50/190)	828 cm^{-1} (12.8 %)
			833 cm^{-1} (9.6 %)
6 %	18 torr	$\text{CCl}_2\text{F}_2/\text{CCl}_4/\text{O}_2$	828 cm^{-1} (73.4 %)
		(50/140/190)	816 cm^{-1} (17.0 %)
		+	833 cm^{-1} (9.6 %)
		$\text{CH}_3\text{F}/\text{He}$ (200/560)	
0.28%	220 torr	$\text{CCl}_2\text{F}_2/\text{O}_2$	854 cm^{-1} (88.0 %)
		(60/180)	869 cm^{-1} (12.0 %)
		+	
		liq. CCl_4 ^c	

^a Numbers in parentheses are partial pressures of the respective gases in units of torr.

^b Numbers in parentheses are the ratios of the energy at the frequency to the total output energy.

^c The optical path length is about 0.1 mm.

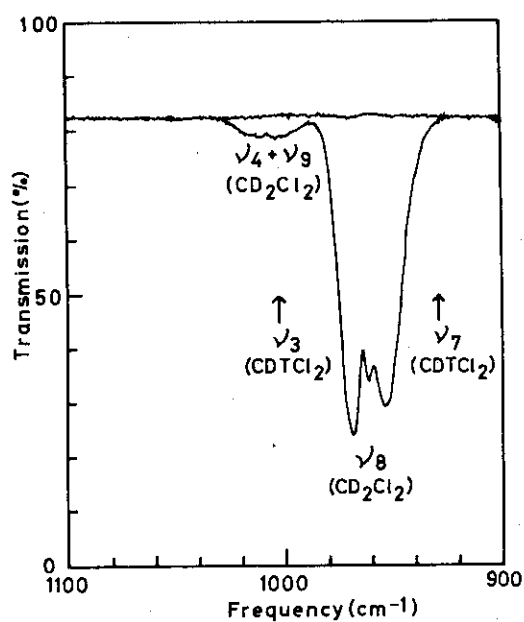


Fig. 1 IR spectrum of CD_2Cl_2 . Arrows indicate the calculated normal mode frequencies of CDTCl_2 .

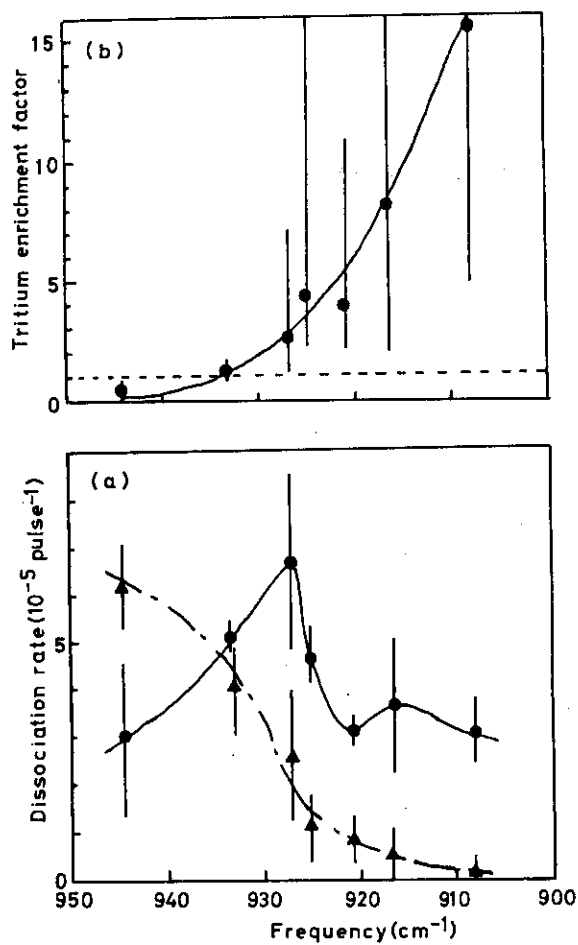


Fig. 2 Irradiating laser frequency dependence of (a) dissociation rates of CDTCl_2 (\bullet) and CD_2Cl_2 (\blacktriangle) and of (b) tritium enrichment factors. The total pressure is constant at 5.0 torr.

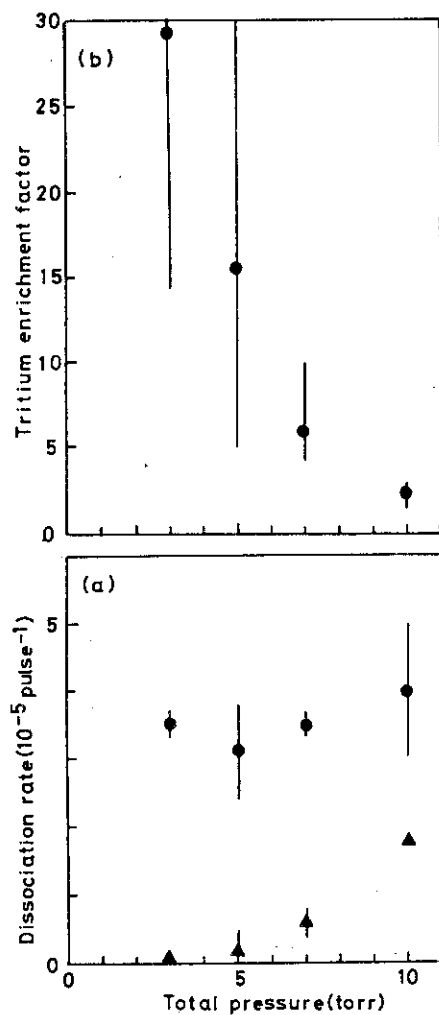


Fig. 3 Total pressure dependence of (a) dissociation rates of CDTCI_2 (●) and CD_2Cl_2 (▲) and of (b) tritium enrichment factors. The irradiating laser frequency is constant at 907.8 cm^{-1} .

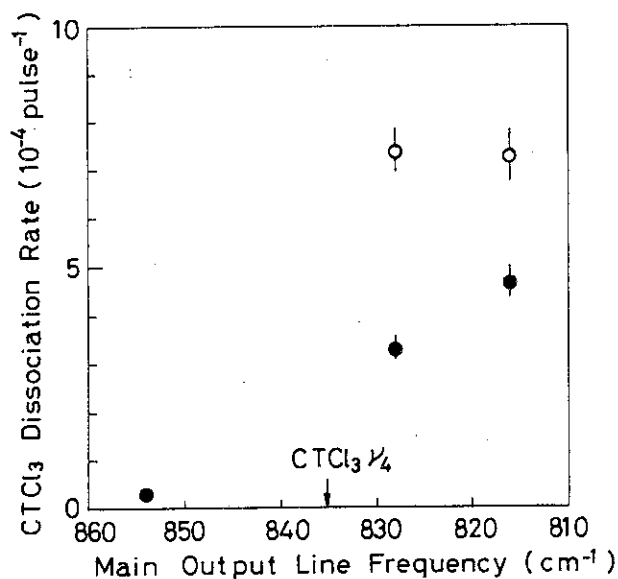


Fig. 4 Main output line frequency dependence of the CTCl_3 dissociation rate at chloroform pressures of 0.2 (○) and 2.0 torr (●). The arrow indicates the (0,0) band peak of the $\text{CTCl}_3 \nu_4$ mode observed in ref. 3. The focal length of the lens is 50.8 cm.

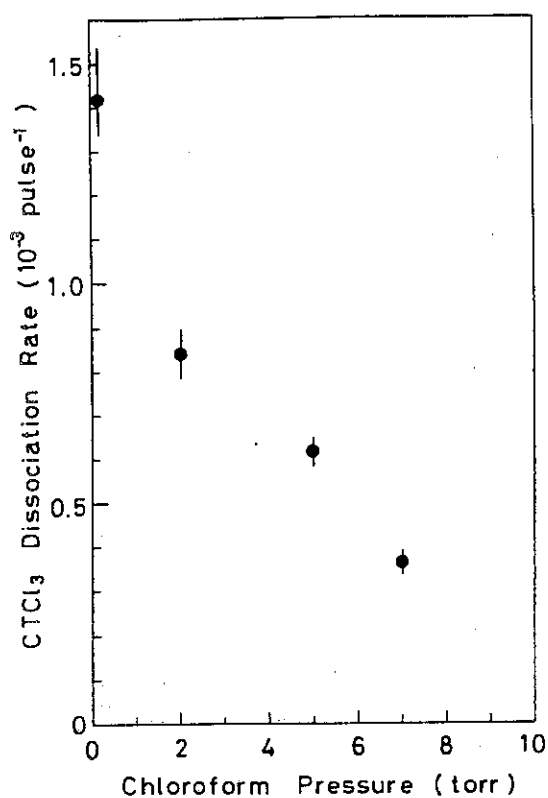


Fig. 5 Chloroform pressure dependence of CTCl₃ dissociation rate (50.8 cm focal length lens, 195 mJ at 816 cm⁻¹).

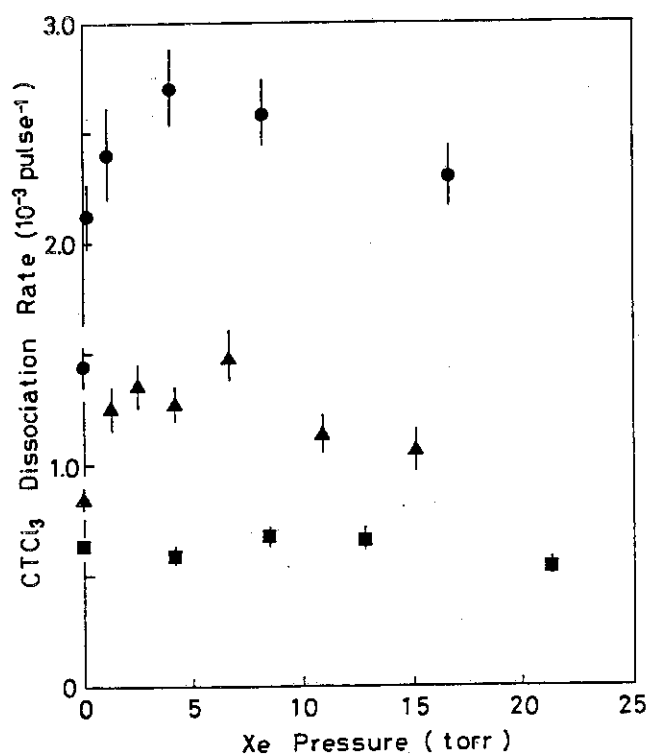


Fig. 6 Xe partial pressure dependence of the CTCl₃ dissociation rate (50.8 cm focal length lens, 195 mJ at 816 cm⁻¹) at chloroform pressure of 0.2 (●), 2.0 (▲), and 5.0 torr (■).

17. STUDIES OF FLUORINE COMPOUNDS

K.Ohwada, Y.Komaki and H.Shinohara

17. フッ素化合物の物理化学的研究

大和田 謙・古牧 睦英・篠原 遥

17.1 FF 照射ポリフッ化ビニリデン多孔膜の化学エッチング時の UV 照射効果

17.1.1 序 論

高エネルギー重イオンが絶縁性固体（マイカ類や高分子など）を通過すると、その通路に沿った固体内に強い局所的放射線損傷を与える。これらの重イオンの飛跡、即ちトラックは、 MoO_3 、 MoS_2 、マイカ等では、直接、電顕下で観察されるが、高分子では報告がない。しかし損傷の結果生じる固体内の溶解性の相異を利用して、エッチングした後では、トラック像が原型に忠実に拡大されることが知られた。従って、こうして現像された形像は、物質に固有の重イオン種と入射エネルギーを示す鍵を与え、物理学上多大な影響を及ぼしたが、他方、損傷生成物とエッチング剤との反応などの化学的考察は充分ではない。¹⁾

重イオンを垂直に高分子フィルムに入射しエッチングすると、多孔膜を作ることが出来る。その時の化学的反応は、まず固体表面が液と接触してトラック部分に、すばやく小さなくぼみが形成される。次にトラック中心部分から同心円状に溶解が進み、旦つ深さ方向へ液がすみやかに浸透し、損傷物質が溶出されてくる。最初は、バルクの固体が、損傷と無関係の一定速度で溶解し飛跡または孔を拡大する過程となる。このような溶解機構が可能なのは、バルクの侵蝕速度に比べて、トラック部分の溶出速度が大きい必要がある。このことから、フィルムの貫通した孔は、円筒状ないしは円錐状を示す。多孔膜の形成にあたっては、貫通孔の様々な形状を支配する因子の究明は欠かせない。重イオン種やエネルギーは勿論、濃度、温度などのエッチング条件や照射前後の雰囲気の影響することが分かった。

FF 照射ポリカーボネート（Lexan, Makrofol）ではエッチングに先立って酸素存在下で紫外線（UV）を照射してからエッチングすると、FF トラックの現出時間を短縮するのに効果が顕著であり、同時に孔のテイパー角が鋭角になることが報告された。^{2) 3)} 一方、硝酸セルローズに形成されたアルファ粒子は、一定量以上の UV 光で消去した。⁴⁾ これらは、それぞれの高分子に特有の重イオン照射損傷生成物が、酸素と UV 光のもとで結合して変化することを裏付けている。筆者は、フッ素樹脂のポリフッ化ビニリデン膜（PVDF）を対象に、FF を貫通させ、貫通孔のエッチングによる拡大挙動を、UV の影響下で調べた。その結果、UV 光照射は、PVDF 上の FF トラックの現象を特に早める効果はなく、かえって UV 照射量を増すと、孔径の拡大は一定値を示したまゝで、エッチング時間を増しても、それ以上に増大しなくなることが分かった。この現

象を理解するため、ガンマ線(γ)照射PVDFのアルカリによる溶解速度が、UV光照射でどのように影響されるのかを調べた。

γ 線吸収線量が大きくなると、UV光量と共にPVDFは溶け易く、 γ 線量が小さい時には、UV光下で溶け難くなることが分かった。後者に対しては、光による分子間橋かけの効果が大きく、前者に対しては、酸化物形成の効果が寄与するのだと説明された[1-3]。

17.1.2 実験

JRR-4にて、天然ウランを熱中性子照射し、ウラン膜と一定の距離をへだてた9 μ m PVDFフィルムに、 $3 \times 10^8/\text{cm}^2$ のFFトラックを得た。膜は、10 N水酸化ナトリウム水溶液中、85℃と65℃でエッチングした。拡大した孔の孔径は、孔を通るガスの流れを測定し、Knudsenの式を適用⁵⁾して算出した(有効孔径)。必要に応じて透過(JEM-1000)および走査電顕(JSM-35C)でも観察した。水銀ランプ(東芝製, SHL-100, UV-2)からのUV光を150時間まで、85℃の温度下で照射むらを防ぐため、回転させて照射した。利用した主な波長は、254, 313, 366, 435 nmである。

γ 線照射、50 μ mフィルムは、 1×10^4 から 2×10^6 Gyの範囲で、Co-60の γ 線で得た。

UV照射直後の膜のIR, UVスペクトルを測定し、溶解速度は、10 N水酸化ナトリウム水溶液中、85℃で一定時間攪拌したのち、水洗、乾燥し、重量測定により求めた。常法に従い、ゲル分率も測定し、また短冊型フィルム($1 \times 5 \text{ cm}^2$)の引張り強度を測定した(Instron model 1130)。

17.1.3 結果

FF照射後、エッチングに先立ってあらかじめUV光を照射すると、エッチングによって拡大するPVDF上のFFトラックの孔径は、どのように影響されるかを示したのがFig. 1である。

UV光照射3分から4時間までは、エッチング時間の増大と共に、孔径は、未照射の場合と同様に、直線的に拡大することを示す。UV光量が増えると、拡大速度は同じでも、一定時間経過後の孔径が小さくなることも分かる。照射から50時間を越えると、エッチングを延長しても、孔は比例的に拡大しなく、一定の値、 $\approx 100 \sim 200 \text{ \AA}$ の孔径のまゝにとどまることが示された。透過電顕写真観察から次のことが分かった。UV光を照射しないPVDFのFFトラックは、充分エッチングされると、円筒状を示し、FFがPVDFフィルムを一つの表面から他の表面まで貫通している様子がよく分かるのに対し、UVフィルムでは、両表面近傍でのみ孔径が拡大され、膜厚の中心部分では、太い円筒に生長しないまゝのくびれたクサビ型像が観察された。

この現象を理解するため、FF照射とは別に、 γ 線を照射したPVDF膜のアルカリ溶解性について、UV照射量を変化させて調べた。一定時間ごとにフィルムの重量変化からフィルム片面の溶解量を算出し溶解速度とし、UVを22, 50, 100および150時間照射した時の溶解速度とUVを全く照射しない時の値の比をとると、Fig. 2の如くに示された。比が1の時は、UVの効果を全く示さず、1より大であれば、UVによって溶解速度が大きくなること、1より小さければ、その逆であることを示している。従って図は、 γ 線吸収線量 10^5 Gyまでは、UV光照射すると、次第に溶解し難くなり、 10^6 Gyまででは、UV光照射で逆に大きく溶解性が増大し、UV光を照射しない場合の3倍にまで達することが分かる。 10^6 Gyを越えた試料に対しては、複雑に再び

低下する。そこで、これらフィルムの物性変化をスペクトル的に調べた。 5×10^5 Gyまでの吸収線量のPVDFのUVスペクトルは、Fig. 3(a)の如く、227, 274, 315 nmに明らかな吸収を持ち、すでにジェン、トリエンおよびテトラエン等の共役2重結合であることが知られた。このスペクトルは、空气中、室温下では長期間に亘り安定であるが、UV光を照射してゆくとFig. 3(b)の如くに吸収が次第に縮小することが見い出された。同時に、 γ 線吸収による着色が、30%近く退色することが確かめられた。これらの効果は、酸素中でUV光照射する時のみ現出し、窒素中では生じない。 γ 線照射済みフィルムIR測定から、1850, 1830, 1760, 1720 および 1600 cm^{-1} 近傍に吸収帯が現われ、これらの内 1850, 1760 および 1720 cm^{-1} では、UV光照射によりFig. 4のように、その強度が変化した。図から、 1850 cm^{-1} と 1760 cm^{-1} では、UV光量の増大に伴い、吸収強度が増大するが、 1720 cm^{-1} では、逆に減少する。

PVDFは γ 線照射の結果、酸素が共存すれば、これと結合して酸素化物を形成するのみならず橋かけ構造や主鎖の切断も生じると考えられている⁶⁾。一般に、PVDFでは、橋かけは酸素中では真空中 γ 線照射に比べて形成され難く、 $9 \mu\text{m}$ フィルムでは 10^6 Gyくらいの吸収線量までは、酸素中においた場合、橋かけが生じ難いとされている。 4×10^5 Gyと 1×10^6 GyのフィルムについてUV光照射を行うと、しばらくの間ゲル分率が低下するが、やがてその値は、UV光量と無関係にはば一定値をとる。この結果をFig. 5に示す。最後に、 γ 線吸収線量 10^4 GyのPVDFフィルムにおいて、UV光照射した場合と照射しない場合の引張りのびテストを行った。これによれば、 10^4 GyではUV光量と無関係に引張り強度は変化が見られないが、 5×10^5 Gyフィルムにおいては長時間UV光にさらされると、引張り強度は突然小さくなることが分かった。

17.1.4 検 討

高分子に蝕刻されたFFトラックを、エッチングで現出する際、ポリカーボネートであれば、UV光照射は、現出時間を短縮することに顕著な効果があるが、PVDFでは全く示されなかった。

Fig. 2に示すように、UV照射時間が長くなるにつれ、貫通孔の孔径が成長する誘導時間（フィルム両面から貫通したトラック通路に沿ってエッチングが進行し、孔が拡大し、中央で結合して貫通孔となるに要する時間）が長くなり、50時間を越えると孔の成長は一定値以上に拡大されない。これには、UVによる2つの効果を考えることが出来る。一つは、トラック内にUV光照射により安定化学種が形成されること、誘導時間は、この安定化学種がエッチングされるに要する時間のことと理解し、従って誘導時間後のエッチング速度は、UV光と無関係となる。もう一つは、UV光照射で $(\text{Na}^+, \text{OH}^-)$ イオンがFFトラック深部に浸透し難くなること、UVによって、トラック周辺に光架橋的構造変化が生じたためと推定される。長くエッチングした後のFFトラックのクサビ型の入口を示す電顕写真は、NaOHが深部に浸透して溶解し難いことを裏付けている。これらの諸事実を γ 線吸収したPVDFのUV照射効果から考察してみる。

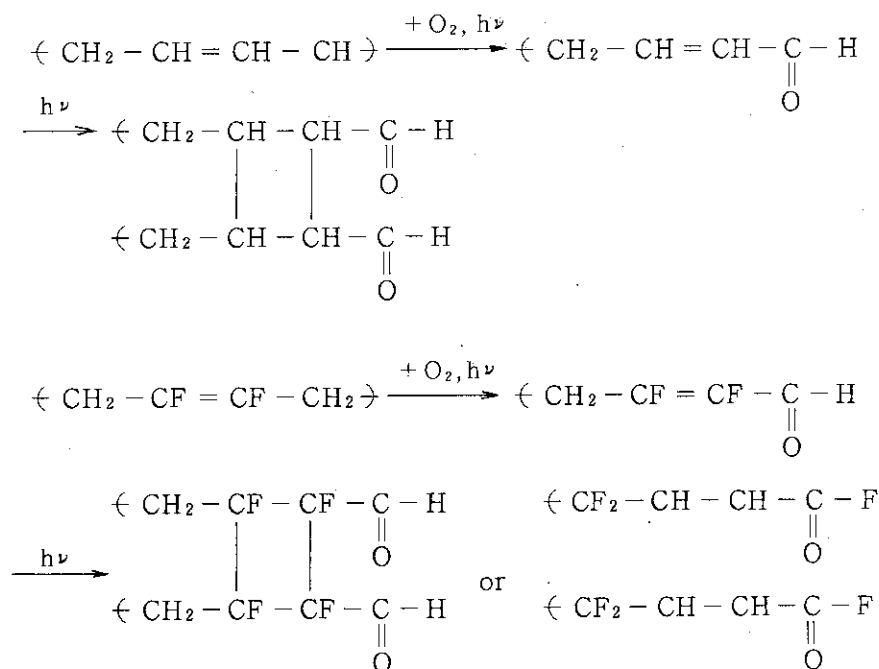
γ 線吸収済みPVDFのアルカリ溶解は、UV光照射でかなり影響を受けることを第2図に示しているが、この前後でフィルムは物性的にも明らかな変化を示す。Fig. 3のUVスペクトルは、UV光照射によって、 γ 線吸収済みPVDF中に生成したジェンやトリエン類の2重結合が消去することを示している。しかし完全に元の γ 線未照射PVDFのスペクトルに復帰する訳ではない。着色現象が2重結合形成に基因すると考えられていることから、UV光照射により色が希薄化す

る事実も、上記の考えを裏付けている。Fig. 4 の IR スペクトルの特色は、酸素化生成物形成と考えられている 1850 cm^{-1} と 1760 cm^{-1} の 2 者では、UV 照射と共に吸収がやや大になるのに対し 1720 cm^{-1} では減少することである。 1720 cm^{-1} の帰属は今のところ明確ではないが、2 重結合に関与した振動と考えられる。一般に高分子の架橋度の推定にゲル分率の測定がある。Fig. 5 は γ 線吸収した 2 種類の PVDF に、次第に UV 光照射量を増加した時のゲル分率の変化を示すが、これによって、一旦形成された架橋が UV 光量とほとんど無関係に持続することが分かる。従って、 γ 線吸収試料は、IR とゲル分率の結果とから、UV 光照射により 2 重結合が破れ、一方では酸素との結合基を増加させ、一方では架橋が保持され、これらのために 2 重結合部分が消化されると推定される。高分子フィルムの引張り強度変化は、厳密には複雑な要因がからんで定まるが、一般に分子間の橋かけが増大すると共に、引張り強度は小さくなる。表は特に $5 \times 10^5\text{ Gy}$ 以上で光による架橋の進行の傾向が大きいことを示唆し、 γ 線吸収量が小さい時は効果も小さいことが分かる。

上記の事実をふまえ、また瀬口、幕内ら⁶⁾⁷⁾が、PVDF の γ 線照射効果の解釈で示した見解を参考にして Fig. 2 を解釈し、Fig. 1 の結果を説明してみる。

まず、 10^5 Gy までの γ 線吸収量段階では、分子の切断と架橋化は共に生成するが、程度は大きくはない。UV 光照射が加わると、2 重結合に吸収されて光架橋化が進む。この時点で高分子は溶解し難くなる。一方酸素化も進行する。 10^5 Gy を越えると、切断と架橋化は同じ率 ($G \div 0.6$)_(s,c) で生成し、大きな割合を占めてくる。高分子内ではクラックなどの物理的損傷も生じ溶解し易い状態が出来る。UV が照射されても、もはや光架橋のみで構造が強化される状態ではなく、一方において進行する酸素との結合を基に溶解性が増大する。 $2 \times 10^6\text{ Gy}$ ともなると、 γ 線損傷生成物に UV 照射が影響を与えることはほとんどなくなる。

γ 線照射 PVDF 中に存在する共役 2 重結合が UV 光照射化で架橋化と酸素と結合して酸化が進行する過程は、cis-trans 1,4 polybutadiene が UV 下で酸素を仲介に架橋化して行く過程と類似して考えることが出来ると思われる。



FFトラックの微小体積内の線量分布を正確に知ることは不可能であるが、トラック通路に沿って同心円状に様々な線量吸収帯がとりかこみ、UV下で酸素などとの反応が進行し、アルカリエッチングされることが γ 線照射で得られた知見から、かなりよく理解出来ると考えられる。

(Y. Komaki)

References

- 1) Fleischer, R.L., Price, P.B., and Walker, R.M.: "Nuclear Tracks in Solids, Principles and Applications", (1975), University of California Press.
- 2) Crawford, M.T., DeSorbo, W., and Hunphrey, J.S., Jun.: Nature., 200, 1313(1968).
- 3) Henke, R.R and Benton, E.V., and Heckman, H.H.: Radiat. Effects., 3, 43(1970).
- 4) Hasegawa, H., Matsuo, M., Yamakoshi, K., and Yamawaki, K.: Radioisotope., 17, 419(1968).
- 5) Komaki, Y.: Nucle.Tracks., 3, 33(1979).
- 6) Makuuchi, K., Seguchi, T., Suwa, T., Abe, T., Tamura, N., and Takehisa, M.: Nippon Kagaku Kaishi., 1973, 1574(1973).
- 7) Seguchi, T., Makuuchi, K., Suwa, T., Abe, T., Tamura, N., and Takehisa, M.: Nippon Kagaku Kaishi., 1974, 1309(1974).
- 8) Beavan, S.W and Phillips, D.: Europ.Polym.J., 10, 593(1973).

Publication List.

- [1] Komaki, Y.: "UV effect on the alkaline dissolution of γ -irradiated Polyvinylidene fluoride film", J.Radiat. Phys & Chem., in press, (1986).
- [2] Komaki, Y.: "UV effect on etching of fission tracks in

Polyvinylidene fluoride film", J.Radiat.Phys & Chem.,
in press, (1986).

- [3] Komaki, Y.: "Nuclear track filter-preparation, property
and applications", informal communication, (1985).

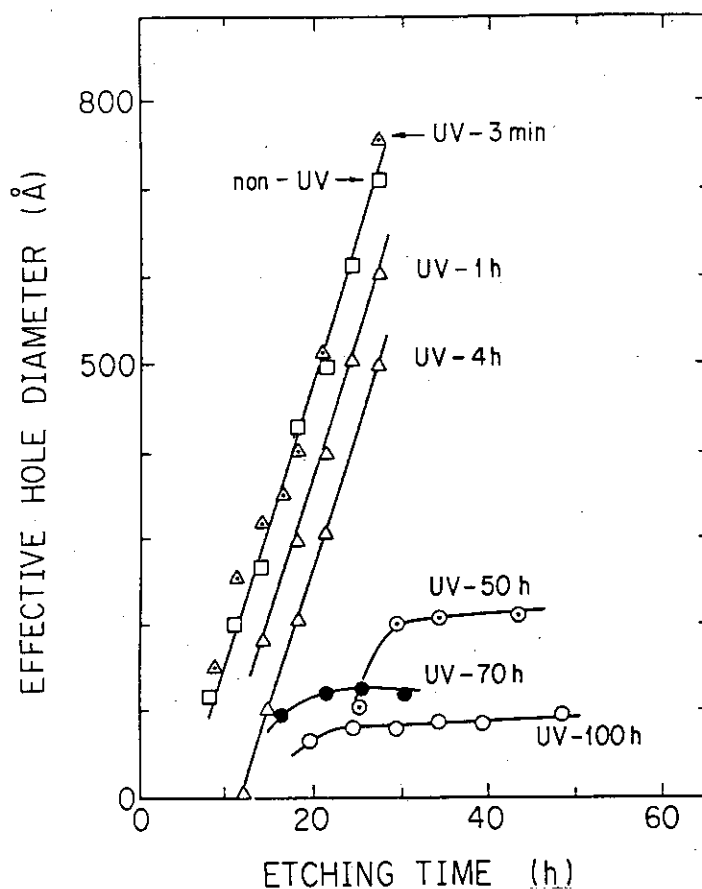


Fig. 1 Effective hole diameter vs etching time for PVDF film (9 μm) bombarded by fission fragments of ^{235}U . Etching condition : 10 N NaOH solution at 85 $^{\circ}\text{C}$ after UV exposure prior to etching.

Table 1 The elongation at break of the γ -irradiated PVDF film (50 μm) exposed to UV for some periods.
The rate of elongation : 20 cm/min at 20 $^{\circ}\text{C}$.

Sample No	γ radiation (Gy)	UV exposure (hr)	Elongation (%)
A	0	0	420
		20	400
		160	570
B	1×10^4	0	410
		20	360
		160	310
C	5×10^5	0	60
		20	90
		160	3

rate of elongation : 20 cm/min

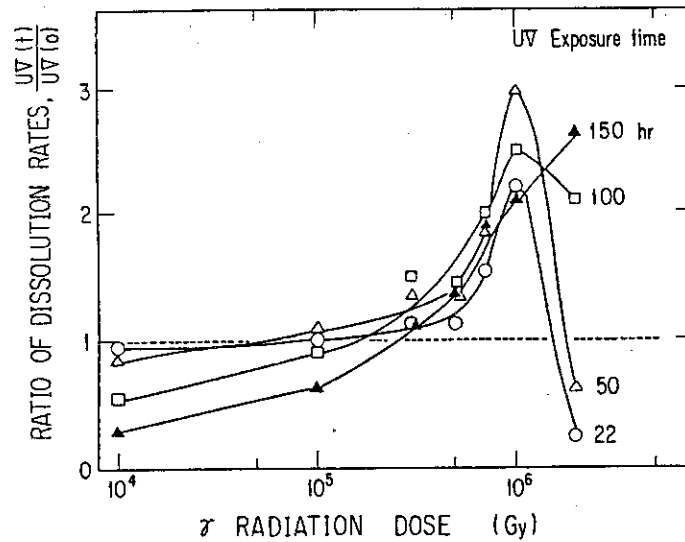


Fig. 2 The ratio of dissolution rates vs γ radiation dose.
The dissolution rate means the weight dissolved from a single face of the film per hour. The dissolution rates, $UV(t,0)$, indicate the one after UV exposure for some periods and the one without UV exposure, respectively.

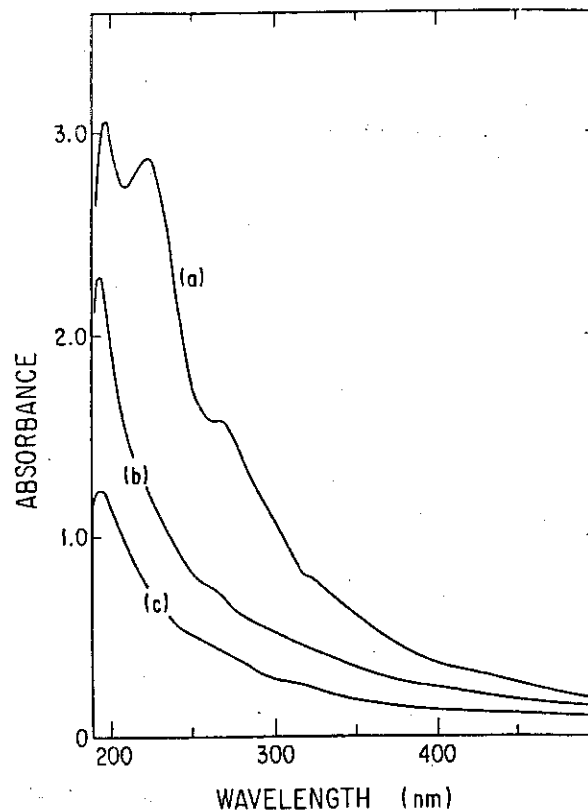


Fig. 3 The UV absorption spectrum of γ -irradiated PVDF film(a), the one of γ -irradiated PVDF film after UV exposure, and the one of a virgin PVDF film, vs wavelength.
(a) γ radiation (5×10^5 Gy) induced absorbance.
(b) The absorbance after UV exposure for 100 h.
(c) The absorbance in the virgin PVDF film.

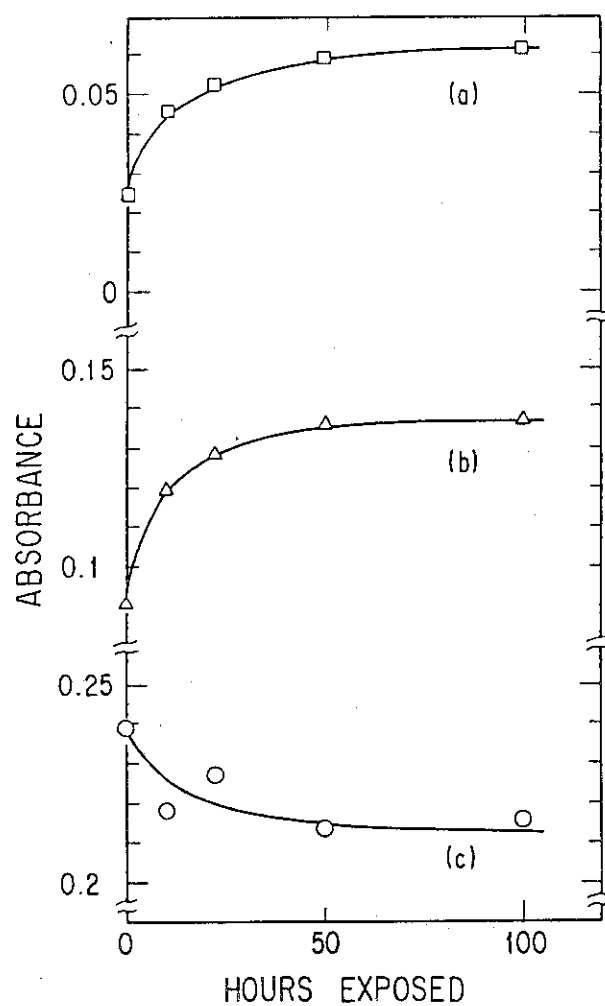


Fig. 4 The UV exposure induced relative intensities of the IR transmittances for frequencies at 1850(a), 1760(b), and 1720(c) cm^{-1} vs UV exposure time.

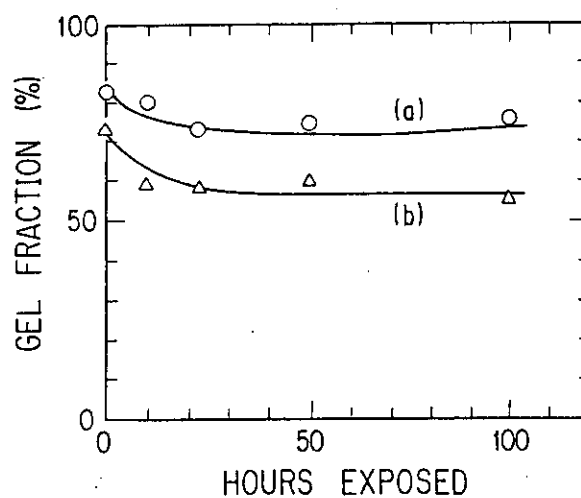


Fig. 5 The gel fractions of γ -irradiated PVDF film (50 μm) in vacuum after UV exposure, vs UV exposure time.

- (a) The PVDF film was irradiated to the dose of 1×10^6 Gy.
- (b) The PVDF film was irradiated to the dose of 4×10^5 Gy.

17.2 ポリマーの直接フッ素化に関する研究

ポリマーの直接フッ素化による親水性表面の形成（ポリフッ化ビニリデン）

17.2.1 緒言

ポリマー表面層を直接フッ素化するとき、フッ素 (F_2) 中に不純物として少量の酸素 (O_2) が含まれていると、フッ素化反応と共にポリマー主鎖の切断に伴い酸フッ化物が副生し、これが加水分解してカルボキシル基 ($-CO_2H$) となるために、表面が以前より親水性となることがある。そこで反応挙動が比較的良好に調べられたポリフッ化ビニリデン (PVdF) 膜を対象にして、その表面層をほとんどフッ素化することなくオキシフッ素化 (OF 化) することにより $-CO_2H$ を形成し親水性を増すことを試みた。

17.2.2 実験

ポリフッ化ビニリデン膜はPennwalt Chemicals製 Kynar-200 より製したインフレーションフィルム、厚約 $50\mu m$ を用いた。オキシフッ素化、水蒸気処理 (H_2O 処理) 及び水の接触角の測定の方法などは既報の通りである。アンモニア処理 (NH_3 処理) は試料を室温でアンモニア水に浸漬するか、湯浴上でアンモニア水から揮発する NH_3 と接触させて行った。

17.2.3 結果及び考察

図1にPVdF膜(a)のOF化(b)、 H_2O 処理(c)、及び NH_3 処理(d)を引き続き行ったときの赤外吸収 (IR) スペクトルの変化を、 $2000-1500\text{ cm}^{-1}$ の $C=O$ 伸縮振動領域について示す。

O_2/F_2 比を1:9、全圧を $1.0 \times 10^5\text{ Pa}$ (1 atm) として 40°C で 72 h OF 化したとき、 $4000-400\text{ cm}^{-1}$ 領域のスペクトルに認められる変化は図示した領域に限られており (図1b)、反応前後の試料の重量変化は、200-250 mg の膜につき約 1 mg の増加に過ぎなかった。これらはフッ素化はほとんど行われていないことを示している。

オキシフッ素化に続く H_2O 処理により膜中に形成された $-CO_2H$ (図1c) は、 NH_3 と速やかに反応して $-CO_2NH_4$ を形成した (図1d)。約 1550 cm^{-1} に現われる吸収帯は、PVdF膜をOF化及び後フッ素化した後に熱濃アルカリ処理を行って製したペルフルオロカルボン酸型陽イオン交換体を NH_3 処理しても出現せず、その帰属を検討中である。

図2に O_2/F_2 比を9:1として全圧 $1.0 \times 10^5\text{ Pa}$ 、 40°C でPVdF膜をOF化した後 H_2O 処理したときのIRスペクトルの 1762 cm^{-1} ($-CO_2H$) の吸光度の増加をOF化時間の関数として示す。反応は直線的に進行し、 F_2 分圧を変えずに O_2/F_2 比を1:1に減ざると反応速度は約0.6倍に減じた。オキシフッ素化反応の機構については検討中である。

図3に未処理PVdF膜(a, b)及び図1と同様にOF化- H_2O 処理を行った膜(c, d)上の水滴像を示す。未処理膜では前進及び後退接触角がそれぞれ約 75° 及び約 60° であったが (図3a, b)、処理後には約 70° と約 35° となり (図3c, d)、さらに NH_3 処理により約 70° と約 25° となった。図2に示した反応時間の範囲ではOF化の進行と共に接触角が減少する傾向が認められた。官能基の密度と濡れとの関係は今後の課題である。

このようにして親水性としたPVdF膜表面は、傾斜したときに水滴を保持する力に優れるほかに、未処理膜では不可能であった水性インキによる鮮明な筆記が可能であり、結露水の落下防止や印刷・染色などへの応用が考えられる。

(H. Shinohara)

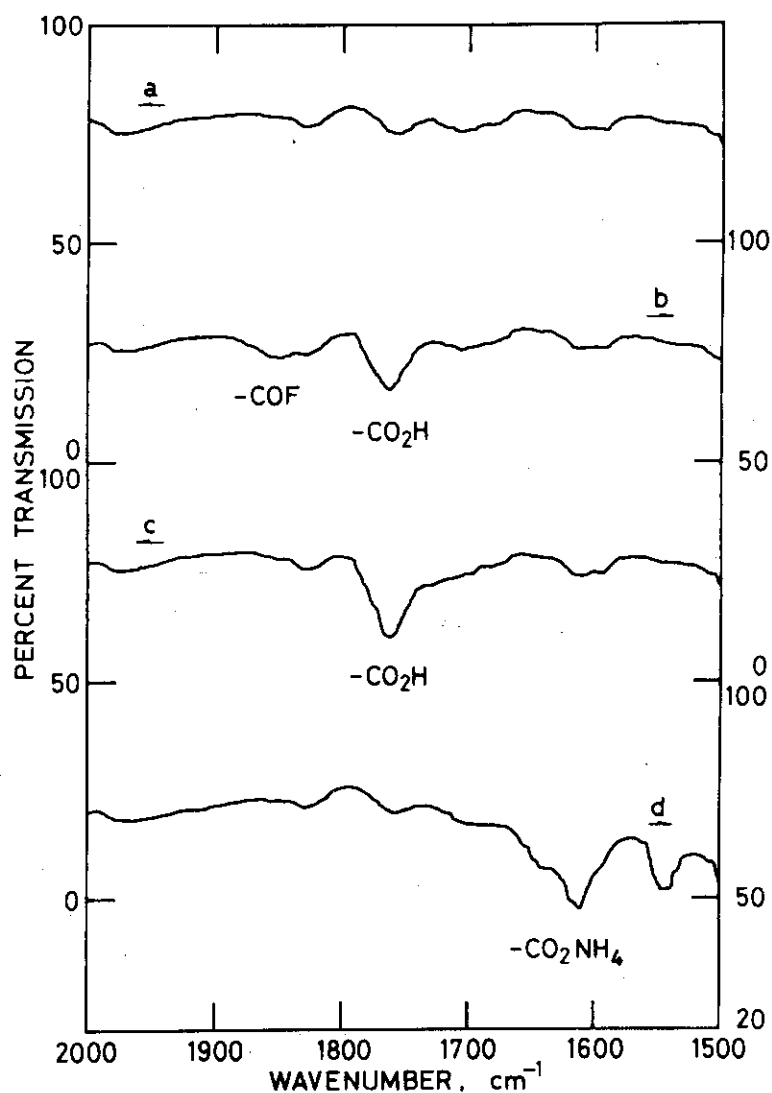


Fig.1 IR spectral changes of PVdF films after successive oxyfluorination, water vapor treatment, and ammonia treatment: (a) unfluorinated; (b) oxyfluorinated, $O_2/F_2 = 9$, total pressure 1.0×10^5 Pa, $40^\circ C$, 72h; (c) water vapor-treated, about $90^\circ C$, 24h; (d) ammonia-treated, room temperature, 1h.

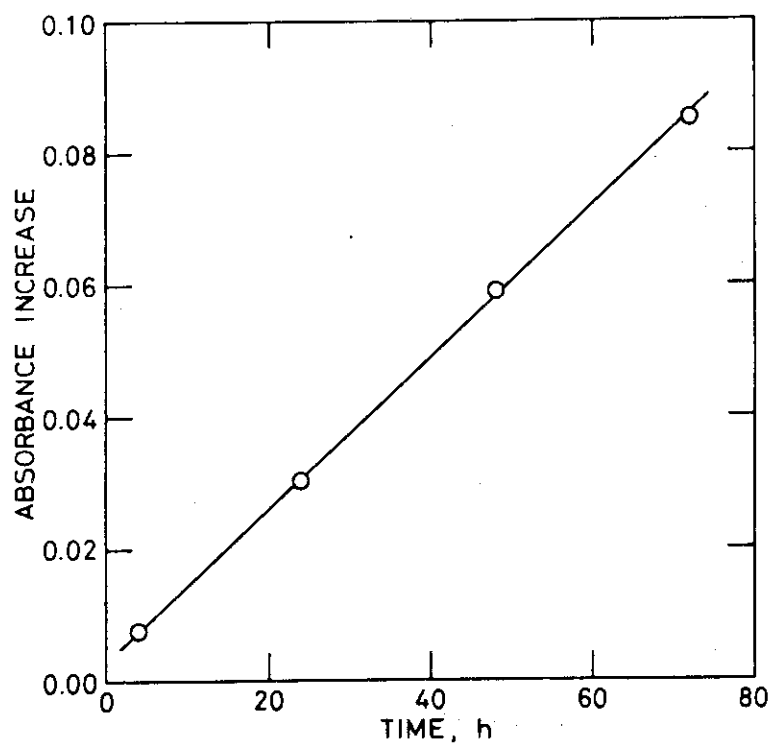


Fig.2 Increase in IR spectral absorbance of PVdF films at around 1762 cm^{-1} ($-\text{CO}_2\text{H}$) after oxyfluorination and water vapor treatment as a function of oxyfluorination time: Film thickness about $50\text{ }\mu\text{m}$, $\text{O}_2/\text{F}_2 = 9$, total pressure $1.0 \times 10^5\text{ Pa}$, 40°C .

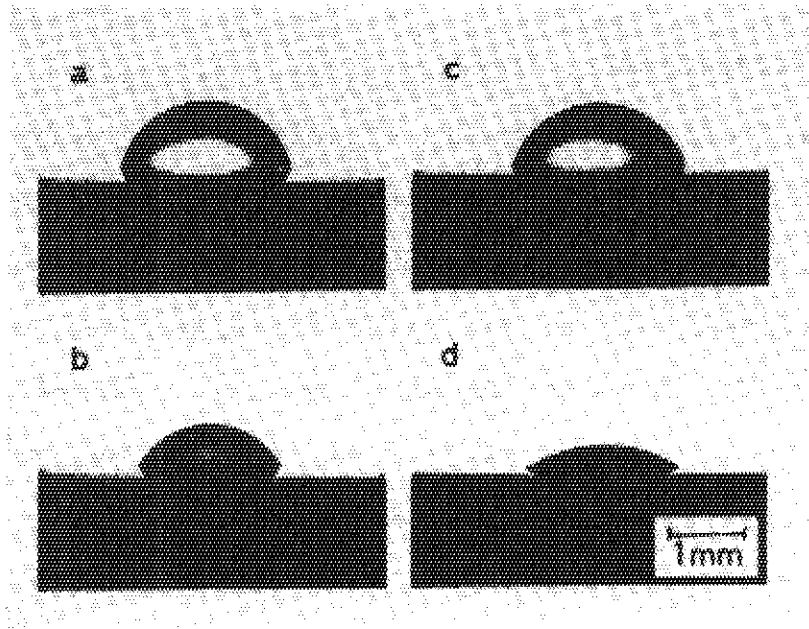


Fig.3: Photographic image of water drops on PVdF films unfluorinated and oxyfluorinated, 22 - 24°C: (a,b) unfluorinated, advancing (a) and receding (b); (c,d) oxyfluorinated and treated with water vapor, advancing (c) and receding (d). Treating conditions are equivalent to those in Fig. 1b and 1c. Films were washed with 1M-HCl solution and with water before applying water drops. Photographs were taken vertically so that real image is seen above each pair of reflection points and reflected image below.

17.3 The Application of an Effective Nuclear Charge Model to the Prediction of Valence Force Constants in Uranyl Tetrachloride and Pentafluoride Complexes

17.3.1 Introduction

In the field of molecular vibrational spectroscopy, one of the most significant problems which has been challenged for a long time by many investigators, both experimentally and theoretically, is to determine the exact molecular force field. For this purpose, we have recently proposed an effective nuclear charge (ENC) model¹⁾ in which effective nuclear charges are defined from the force constant expressions derived by the application of second order perturbation theory to homonuclear diatomic molecules. The ENC model, which allows us to predict approximately the various types of valence force constants such as bond stretching, angle deformation, bond-bond interaction, angle-angle interaction and bond-angle interaction, has recently been applied to the calculation of force constants in simple polyatomic molecules^{2,3)}. The results suggest that such a model is favorable to the prediction of valence force constants in more complicated polyatomic molecules.

In the present study, we focus attention on some complex ion molecules in uranyl tetrachloride and pentafluoride complexes [1] and their valence force constants are calculated on the basis of the ENC model. The calculated force constants are compared with those obtained by the normal coordinate analyses using observed vibrational frequencies. Based upon such results, we briefly discuss the reliability of the model

force constants as well as the utility of the ENC model.

17.3.2 Theory

Let us begin by describing the outline of the ENC model proposed in our previous paper¹⁾. In that model, the effective nuclear charge Z_i^* on the nucleus i in a homonuclear diatomic molecule is defined by the formula

$$Z_i^* = (K_{ii} \bar{R}_{ii}^3 / 2)^{1/2} = Z_i e(1 - f_{ii})^{1/2} \quad (1)$$

where K_{ii} and \bar{R}_{ii} are the quadratic force constant and the equilibrium internuclear distance, Z_i and e are the atomic number and the electronic charge, and f_{ii} is termed the molecular shielding factor⁴⁾ as given by

$$f_{ii} = \bar{R}_{ii}^3 \left\langle \rho_{00}(ii) \left| \frac{\cos^2 \theta_i}{r_i^4} \right| \right\rangle / [\bar{E}(ii) - E_0(ii)], \quad (2)$$

$\rho_{00}(ii)$ being the electron density in the molecular ground-state, $\bar{E}(ii)$ the average energy of excited electronic states, $E_0(ii)$ the ground-state energy, and the brackets indicating integration over the electronic coordinate $\cos \theta_i$ and r_i . Equation (1) can be derived by the application of second order perturbation theory to a homonuclear diatomic molecule.

By using Eqn. (1), the effective intramolecular potential function V for a polyatomic molecule is constructed on the basis of the Hellmann-Feynman theorem and the electron density separation as follows:

$$V = \sum_{i \neq j} \frac{Z_i^* Z_j^*}{R_{ij}} + \sum_{j \neq k} \frac{Z_j^* Z_k^*}{q_{jk}} - N(r; R), \quad (3)$$

where Z^* s are of course the effective nuclear charges defined in Eqn. (1), R_{ij} and q_{jk} are the bonded and non-bonded

internuclear distances, and $N(\vec{r}; \vec{R})$ is the correction term arising from the non-perfectly following density $\rho_{\text{NPF}}(\vec{r}; \vec{R})$. Recently, it has been confirmed that the potential form of Eqn. (3) can also be derived from Wilson's molecular energy formula⁵⁾ which has been given quantum-mechanically as a four-dimensional electron density function [2].

In order to derive the relationships between valence force constants and effective nuclear charges, the effective intramolecular potential function of Eqn. (3) is expanded to second order in the displacements of ΔR_{ij} and Δq_{jk} as follows:

$$\begin{aligned}
 V = \text{const.} - \sum_{i \neq j} \left[\frac{Z_i^* Z_j^*}{\bar{R}_{ij}^3} + \frac{1}{\bar{R}_{ij}} \left(\frac{\partial N}{\partial R_{ij}} \right)_0 \right] (\bar{R}_{ij} \Delta R_{ij}) \\
 + \frac{1}{2} \sum_{i \neq j} \left[\frac{2Z_i^* Z_j^*}{\bar{R}_{ij}^3} - \left(\frac{\partial^2 N}{\partial R_{ij}^2} \right)_0 \right] (\Delta R_{ij})^2 \\
 - \sum_{i \neq j \neq k} \left(\frac{\partial^2 N}{\partial R_{ij} \partial R_{ik}} \right)_0 (\Delta R_{ij}) (\Delta R_{ik}) \\
 - \sum_{j \neq k} \left(\frac{Z_j^* Z_k^*}{\bar{q}_{jk}^3} \right) (\bar{q}_{jk} \Delta q_{jk}) \\
 + \frac{1}{2} \sum_{j \neq k} \left(\frac{2Z_j^* Z_k^*}{\bar{q}_{jk}^3} \right) (\Delta q_{jk})^2 + \dots
 \end{aligned} \tag{4}$$

where \bar{R} and \bar{q} are the bonded and non-bonded equilibrium internuclear distances, and the subscripts 0 indicate that the partial differentials of the correction term $N(\vec{r}; \vec{R})$ in parentheses are evaluated at the equilibrium position. Here it should be noted that the force constant associated with the repulsive energy is dominant over that associated with the attractive energy. By the way, the correction term $N(\vec{r}; \vec{R})$ arising from the delocalized electron density in Eqn. (3) mainly expresses the attractive energy. Therefore, we may neglect to a first approximation the second order differentials of the correction term $N(\vec{r}; \vec{R})$ in Eqn. (4).

With this assumption, Eqn. (4) becomes

$$\begin{aligned}
V = \text{const.} - \sum_{i \neq k} \left[\frac{Z_i^* Z_k^*}{\bar{R}_{ij}^3} + \frac{1}{\bar{R}_{ij}} \left(\frac{\partial N}{\partial R_{ij}} \right)_0 \right] (\bar{R}_{ij} \Delta R_{ij}) \\
+ \frac{1}{2} \sum_{i \neq j} \left(\frac{2Z_i^* Z_j^*}{\bar{R}_{ij}^3} \right) (\Delta R_{ij})^2 - \sum_{j \neq k} \left(\frac{Z_j^* Z_k^*}{\bar{q}_{jk}^3} \right) (\bar{q}_{jk} \Delta q_{jk}) \\
+ \frac{1}{2} \sum_{j \neq k} \left(\frac{2Z_j^* Z_k^*}{\bar{q}_{jk}^3} \right) (\Delta q_{jk})^2 + \dots
\end{aligned} \quad (5)$$

which is similar to a central force potential, but is not identical with a quadratic central force potential since the first order terms are not equal to zero. It is here possible to make most of the first order terms vanish by introducing the condition of gem redundancy:

$$\begin{aligned}
\Delta q_{jk} = s_{jik} \Delta R_{ij} + s_{kij} \Delta R_{ik} + (t_{jik} t_{kij} \bar{R}_{ij} \bar{R}_{ik})^{1/2} \\
\times \Delta \phi_{jik} [t_{jik}^2 (\Delta R_{ij})^2 + t_{kij}^2 (\Delta R_{ik})^2 \\
- s_{jik} s_{kij} \bar{R}_{ij} \bar{R}_{ik} (\Delta \phi_{jik})^2 - 2t_{jik} t_{kij} (\Delta R_{ij}) (\Delta R_{ik}) \\
+ 2t_{jik} s_{kij} (\Delta R_{ij}) (\bar{R}_{ik} \Delta \phi_{jik}) \\
+ 2t_{kij} s_{jik} (\Delta R_{ik}) (\bar{R}_{ij} \Delta \phi_{jik})] / 2\bar{q}_{jk},
\end{aligned} \quad (6)$$

where

$$\begin{aligned}
s_{jik} &= (\bar{R}_{ij} - \bar{R}_{ik} \cos \phi_{jik}) / \bar{q}_{jk}, \\
t_{jik} &= \bar{R}_{ik} \sin \phi_{jik} / \bar{q}_{jk}, \\
s_{kij} &= (\bar{R}_{ik} - \bar{R}_{ij} \cos \phi_{jik}) / \bar{q}_{jk}, \\
t_{kij} &= \bar{R}_{ij} \sin \phi_{jik} / \bar{q}_{jk}.
\end{aligned} \quad (7)$$

By using this condition, Eqn. (5) can be transformed to the valence force potential as follows:

$$\begin{aligned}
V &= f(\dots, \Delta R_{ij}, \Delta R_{ik}, \dots, \Delta q_{jk}, \dots) \\
&\quad + \lambda g(\dots, \Delta R_{ij}, \Delta R_{ik}, \dots, \Delta \phi_{jik}, \dots, \Delta q_{jk}, \dots) \\
&= V_{\text{VFF}}(\dots, \Delta R_{ij}, \Delta R_{ik}, \dots, \Delta \phi_{jik}, \dots)
\end{aligned} \quad (8)$$

where λ is Lagrange's multiplier which is termed the intramolecular tension constant.

Applying the above procedure to both the distorted octahedral $(\text{UO}_2\text{Cl}_4)^{2-}$ ion (D_{4h} ; Fig. 1) and pentagonal bipyramidal $(\text{UO}_2\text{F}_5)^{3-}$ ion (D_{5h} ; Fig. 2) molecules [1], and collecting only the second order terms, we have ultimately the following potential function of the form:

$$\begin{aligned}
2V = & \sum K_{ij} (\Delta R_{ij})^2 + \sum H_{ijk} \bar{R}_{ij} \bar{R}_{ik} (\Delta \phi_{jik})^2 \\
& + 2 \sum k_{ij, ik} (\Delta R_{ij}) \times (\Delta R_{ik}) \\
& + 2 \sum g_{ij, jik} (\Delta R_{ij}) (\bar{R}_{ik} \Delta \phi_{jik})
\end{aligned} \tag{9}$$

where K_s are the bond stretching, H_s the angle deformation, k_s the bond-bond interaction and g_s the bond-angle interaction force constants. It is here to be noted that Eqn. (9) does not include interaction terms such as the angle-angle $(\Delta \phi_{jik})(\Delta \phi_{kil})$ interactions. The lack of such terms is due to the simplification of the effective intramolecular potential function, Eqn. (3). In this point of view, we cannot regard Eqn. (9) as the "general" valence force potential.

17.3.3 Force constant calculations and discussion

According to the method described in Section 2, we are now able to evaluate the force constants for $M_2UO_2Cl_4$ and $M_3UO_2F_5$ (M : K, Rb, Cs, NH_4) from both the effective nuclear charges on the nuclei and the known geometric parameters without need of any intrinsic frequency data. The effective nuclear charges used in the calculation are shown in Table 1, in which those of oxygen, fluorine and chlorine are determined from the homonuclear diatomic force constants using Eqn. (1). In particular, the charges of uranium are obtained from consideration of the UO_2 and UO_3 molecules. Of these effective nuclear charges, those of chlorine ($M_2UO_2Cl_4$) and fluorine ($M_3UO_2F_5$) are slightly modified so as to give the best agreement between the experimental and calculated diagonal force constants (K_s and H_s) when keeping the other charges (uranium and oxygen) constant. Such modifications are necessarily required from the result of neglecting the second

order differentials of the correction term $N(\vec{r}; \vec{R})$ in Eqn. (4) and further from the poor transferability of the effective nuclear charges defined for homonuclear diatomic molecules to polyatomic molecules. We here should note that the effective nuclear charges in Table 1 are reasonable but may not be unique ones as seen from the above arguments. The other requirements for the calculation are the structural parameters; these are also listed in Table 1.

The calculated force constants for $M_2UO_2Cl_4$ and $M_3UO_2F_5$ are shown in Tables 2 and 3, respectively. When the results obtained are compared with the experimental force constants which have been determined by normal coordinate analyses, we see that the agreement between the calculated and experimental values is moderately good for most force constants though there are small deviations from the experimental ones. Specifically, it is worth noting that the results for the force constants of bond stretching are fairly good. These results show that our method of approach, in other words, the effective nuclear charge model, is useful for the prediction of approximate valence force constants in $M_2UO_2Cl_4$ and $M_3UO_2F_5$ complexes and in even more complicated polyatomic molecules.

However, it is necessary to bear in mind the reasons why the calculated force constants of the complexes under investigation deviate from the experimental values. There are at least three main reasons: (1) neglect of the second order differentials of $N(\vec{r}; \vec{R})$ in Eqn. (4), (2) poor transferability of the effective nuclear charges defined for homonuclear diatomic molecules to polyatomic molecules and

(3) uncertainty of the experimental force constants determined by normal coordinate analyses. Since these problems have already been discussed in detail elsewhere, we intend to avoid the repetition of such a discussion in the present study.

(K.Ohwada)

References

- 1) Ohwada, K., J. Chem. Phys. 72, 1 (1980).
- 2) Ohwada, K., J. Chem. Phys. 72, 3663 (1980).
- 3) Ohwada, K., J. Chem. Phys. 73, 5459 (1980).
- 4) Murrell, J. N., J. Mol. Spectrosc. 4, 446 (1960).
- 5) Wilson, E. B., J. Chem. Phys. 36, 2232 (1962).

Publication List

- [1] Ohwada, K., Spectrochim. Acta, 41A, 1009 (1985).
- [2] Ohwada, K., J. Chem. Phys. 77, 5040 (1982).

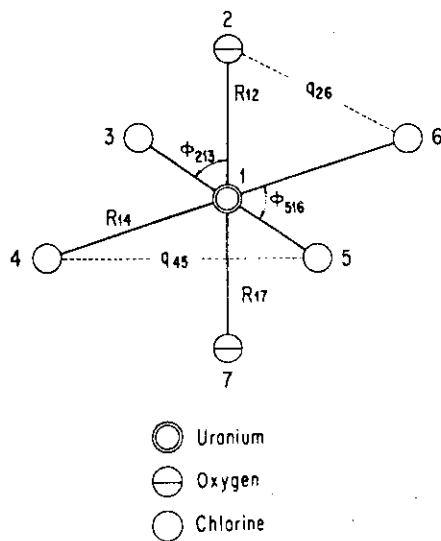


Fig. 1. Internal coordinates for the uranyl tetrachloride ion (point group: D_{4h}).

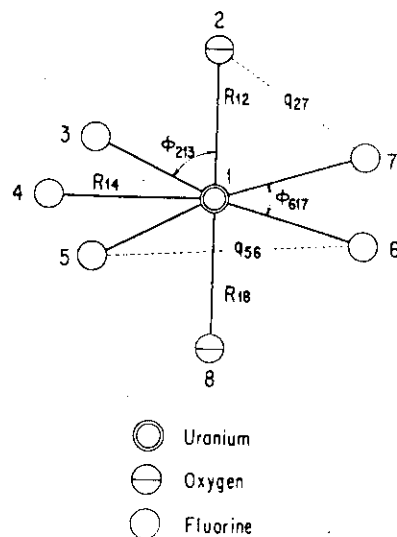


Fig. 2. Internal coordinates for the uranyl pentafluoride ion (point group: D_{3h}).

Table I. Effective nuclear charges (ENC) and bond lengths used in the calculation of force constants for uranyl tetrachloride and pentafluoride complexes

Complex	Z_U^*	ENC		Bond length (Å)	
		Z_O^*	$Z_X^{*†}$	R_{UO}	$R_{UX}^†$
$(NH_4)_2UO_2Cl_4$	3.349	2.118	1.073	1.744	2.82
$K_2UO_2Cl_4$	3.349	2.118	1.073	1.744	2.82
$Rb_2UO_2Cl_4$	3.337	2.118	1.073	1.745	2.82
$Cs_2UO_2Cl_4$	3.362	2.118	1.073	1.743	2.82
$(NH_4)_3UO_2F_5$	3.264	2.118	0.665	1.751	2.24
$K_3UO_2F_5$	3.182	2.118	0.665	1.758	2.24
$Rb_3UO_2F_5$	3.136	2.118	0.665	1.762	2.24
$Cs_3UO_2F_5$	3.068	2.118	0.665	1.768	2.24

† X = Cl or X = F.

Table 2. Experimental and calculated force constants (in mdyne/Å) for uranyl tetrachloride complexes

Force constant	$(\text{NH}_4)_2\text{UO}_2\text{Cl}_4$		$\text{K}_2\text{UO}_2\text{Cl}_4$	
	Calc.	Exp.	Calc.	Exp.
K_{12}	6.560	6.665	6.560	6.659
K_{13}	1.147	1.085	1.147	1.133
H_{213}	0.193	0.193	0.193	0.193
H_{314}	0.0628	0.067	0.0628	0.086
$k_{12,13}$	0.193	—	0.193	—
$k_{13,14}$	0.0628	0.151	0.0628	0.149
$k_{12,17}$	0.488	-0.102	0.488	-0.033
$k_{13,15}$	0.0296	—	0.0296	—
$g_{12,213}$	-0.0245	—	-0.0245	—
$g_{13,213}$	0.168	—	0.168	—
$g_{13,314}$	0.0209	—	0.0209	—

	$\text{Rb}_2\text{UO}_2\text{Cl}_4$		$\text{Cs}_2\text{UO}_2\text{Cl}_4$	
	Calc.	Exp.	Calc.	Exp.
K_{12}	6.527	6.612	6.595	6.702
K_{13}	1.144	1.108	1.151	1.088
H_{213}	0.193	0.163	0.193	0.115
H_{314}	0.0628	0.087	0.0628	0.090
$k_{12,13}$	0.193	—	0.193	—
$k_{13,14}$	0.0628	0.145	0.0628	0.144
$k_{12,17}$	0.487	-0.097	0.489	-0.234
$g_{13,15}$	0.0296	—	0.0296	—
$g_{12,213}$	-0.0243	—	-0.0246	—
$g_{13,213}$	0.168	—	0.168	—
$g_{13,314}$	0.0209	—	0.0209	—

Table 3. Experimental and calculated force constants (in mdyne/Å) for uranyl pentafluoride complexes

Force constant	$(\text{NH}_4)_3\text{UO}_2\text{F}_5$		$\text{K}_3\text{UO}_2\text{F}_5$	
	Calc.	Exp.	Calc.	Exp.
K_{12}	6.521	6.408	6.300	6.183
K_{13}	1.184	1.157	1.159	1.198
H_{213}	0.206	0.243	0.205	0.263
H_{314}	0.0924	0.180	0.0924	0.205
$k_{12,13}$	0.205	—	0.205	—
$k_{13,14}$	0.0752	0.377	0.0752	0.415
$k_{13,15}$	0.0251	—	0.0251	—
$k_{12,18}$	0.482	-0.087	0.476	-0.092
$g_{12,213}$	0.0195	—	0.0202	—
$g_{13,213}$	0.122	—	0.121	—
$g_{13,314}$	0.0266	—	0.0266	—

	$\text{Rb}_3\text{UO}_2\text{F}_5$		$\text{Cs}_3\text{UO}_2\text{F}_5$	
	Calc.	Exp.	Calc.	Exp.
K_{12}	6.178	6.059	5.999	5.891
K_{13}	1.158	1.162	1.124	1.138
H_{213}	0.205	0.265	0.204	0.257
H_{314}	0.0924	0.197	0.0924	0.185
$k_{12,13}$	0.205	—	0.204	—
$k_{13,14}$	0.0752	0.399	0.0752	0.363
$k_{13,15}$	0.0251	—	0.0251	—
$k_{12,18}$	0.473	-0.073	0.468	-0.099
$g_{12,213}$	0.0206	—	0.0212	—
$g_{13,213}$	0.120	—	0.119	—
$g_{13,314}$	0.0266	—	0.0266	—